



Randle, Rebecca (2022) Aggregation dependent naphthalimide diimides for electrochromic windows. PhD thesis.

<https://theses.gla.ac.uk/83096/>

Copyright and moral rights for this work are retained by the author

A copy can be downloaded for personal non-commercial research or study, without prior permission or charge

This work cannot be reproduced or quoted extensively from without first obtaining permission in writing from the author

The content must not be changed in any way or sold commercially in any format or medium without the formal permission of the author

When referring to this work, full bibliographic details including the author, title, awarding institution and date of the thesis must be given

Enlighten: Theses

<https://theses.gla.ac.uk/>
research-enlighten@glasgow.ac.uk



University
of Glasgow

**Aggregation Dependent
Naphthalimide Diimides for
Electrochromic Windows**

PhD Thesis submitted by:

Rebecca Iona Randle

June 2022

College of Science and Engineering
School of Chemistry

University of Glasgow

College of Science and Engineering

School of Chemistry

Statement of Originality to Accompany Thesis: Aggregation Dependent Naphthalimide Diimides for Electrochromic Windows

Registration Number:

I certify that the thesis presented here for examination for PhD degree of the University of Glasgow is solely my own work other than where I have clearly indicated that it is the work of others (in which case the extent of any work carried out jointly by me and any other person is clearly identified in it) and that the thesis has not been edited by a third party beyond what is permitted by the University's PGR Code of Practice. The copyright of this thesis rests with the author. No quotation from it is permitted without full acknowledgement. I declare that the thesis does not include work forming part of a thesis presented successfully for another degree. I declare that this thesis has been produced in accordance with the University of Glasgow's Code of Good Practice in Research. I acknowledge that if any issues are raised regarding good research practice based on review of the thesis, the examination may be postponed pending the outcome of any investigation of the issues.

Signature:

Date:24/06/2022.....

ABSTRACT

We describe the synthesis of naphthalene diimides (NDI) appended with simple amino acids and dipeptides. These systems can form a highly coloured reduced species by photo- and electrochemical reduction, which is reversible upon oxidation. In their neutral state these systems are transmissive and pale in colour. This transition from transmissive to coloured occurs quickly, using small potentials, and is reversible, making NDI systems a promising candidate for electrochromic devices. Their chromic properties, as well as their water solubility and tuneable aggregation, give such self-assembling small organic molecules many advantages over conductive polymers and transition metal oxides, which dominate the literature in this field.

The behaviour of five NDIs in different pH solutions is explored, and we identify ideal aggregated states for each chemical structure (found by altering pH) and identify parameters of their ideal structures that stabilise the formation or stability of the reduced species. These parameters facilitating highest contrast between neutral and reduced states changes with chemical structure, highlighting the sensitivity and importance of aggregation. We also identify aggregate types consistent with poor chromic behaviour and use this information to explain poor colouration of one NDI system.

Using neutron scattering we evaluate the long-term stability and cyclability of our best performing systems. Using *in situ* electrochemical techniques, we critically analyse our prior methodology and facilitate a truly representative measurement of the electrochemically reduced state of some NDI systems and analyse the susceptibility of NDIs to changes in aggregation with cycling between states.

We report multicomponent systems using two NDIs mixed with a transparent low molecular weight gelator (LMWG) in different ratios and observe that the chemical structure of the NDI, the pH and the component ratio affects their aggregation and chromic properties. We observe the decrease and enhancement of radical anion formation upon reduction in different multicomponent systems and select certain systems to evaluate long-term use. A combination of diffusion and aggregation dependent factors contribute to the cyclability of these systems.

Lastly, the effect of heat-cooling upon multicomponent systems is investigated. We find that different ratios of components respond differently. Radical anion formation and cyclability are affected. We identify different methods of improving cyclability (buffering, electrochemical scripting, multicomponent tuning) and open possibilities for future work using hydrogels with these multicomponent systems. At every point we try to understand and link aggregation types or parameters to desirable chromic properties such as colour intensity and efficiency of electrochemical processes.

ACKNOWLEDGMENTS

It's the end... but the moment has been prepared for.

I would firstly like to thank the University of Glasgow, the College of Science and Engineering and the chemistry department for the opportunity to study and complete a PhD. My thanks go to all the technicians, the careers development advisors and all staff at the university. I would like to thank everyone from around the department who made the transition to Glasgow welcoming and fun (Jake, Mike, Hallam, Tom...if you knew the pub Embargo as Gumbo, that's probably you).

I thank everyone in the Draper group past and present for their support and encouragement throughout the PhD. It has been a privilege to see this group grow and I'll miss my desk neighbours Jakki (my COVID support Canadian), Rebecca and Nick. I want to thank Dr Bart Dietrich for his help with synthesis and for 3D printing so many useful (and sometimes less useful) things for my work. Thanks to the Adams group past and present (all the "post-apocalypse PhDs" and the wonderful international students) for their friendship and help in the Raphael Lab. Special thanks to Ana Maria for all her support with job applications, to Libby and Chloe for their vintage fashion advice, and to (soon to be Dr) Dan McDowall and Lisa Thomson, I couldn't ask for better people to start and end my PhD with. You've both achieved so much, and you'll be so successful in the future. I would also like to thank Prof. Dave Adams for his supervision and help during periods of maternity leave during my PhD. Thanks also to Dr Leide Cavalcanti for her in person support and company for lunch during my visit to ISIS neutron source.

A big thank you to my supervisor Dr Emily Draper for giving me the opportunity to do this PhD, her help and support, her insight and her encouragement throughout my PhD (as well as her dedication to keeping up with the Ru Paul's Drag Race chat). It was exciting to be there at the infancy of your group as well as of your actual children! From conferences to writing to new techniques, I feel I have developed into a better scientist and collected some lovely data with you.

Huge thanks to all my family and close friends for their endless support, not just in this PhD but every day. Thanks to my hiking family, Anna, Matt, Alex, Liad, Rob, Katie, Elli, Jon, Cleo, Mary and Kate. Thanks to David, Ashleigh, Triss, Jonas and Hannah for all the games of Quiplash. Thanks to Matt for all the music recommendations. Thank you to my Mom, Nan and Mike for ferrying my stuff, letting me practice presentations and cheering my every achievement. It is sad to be completing this thesis without my biggest cheerleader, my Grandad. A special thank you to Harriet Smith for being the most wonderful friend, supporting me and making me laugh through every hardship in my PhD and since we were 12 years old. I would lastly like to thank Niall Brown for the last 3 years together, for all the times you've been there, for all the times you have pretended to be interested in chemistry and for every gig and show we've been to together.

Love you all.

PUBLICATIONS DURING PHD PERIOD

"Aggregate dependent electrochromic properties of amino acid appended naphthalene diimides in water" R. Randle, L. Cavalcanti, S. Sproules and E. Draper, *Mater. Adv.*, 2022, **3**, 3326-3331.

"Investigating Aggregation using *in situ* Electrochemistry and Small Angle Neutron Scattering" R. Randle, A. M Fuentes-Caparrós, L. Cavalcanti, R. Schweins, D. J. Adams and E. Draper, *J. Phys. Chem. C*, 2022, Accepted.

"Process dependent complexity in multicomponent gels" R. Randle, R. Ginesi, O. Matsarskaia, R. Schweins and E. Draper, 2022, Submitted.

"Assessing Stability and Cyclability of Single and Multicomponent Electrochromic Naphthalene Diimides Systems" R. Randle, C. Edwards-Gayle, L. Cavalcanti, and Emily Draper, 2022, In preparation.

"Tuning reduction potential whilst maintaining mechanical properties in perylene bisimide hydrogels at physiological pH" J. A. Mena Jimenez, J. Egan, R. Randle, R. Schweins and E. R. Draper, 2022, In preparation.

LIST OF ABBREVIATIONS

2D	Two dimensional
Br	Broad
CAD	Computer aided design
Car	Aromatic carbons
CD	Circular dichroism
CE	Colouration efficiency
CIE	Commission on illumination
CP	Conductive polymer
CV	Cyclic voltammetry
DLS	Dynamic light scattering
DMF	Dimethylformamide
DMSO	Dimethyl sulfoxide
DOSY	Diffusion ordered spectroscopy
EPR	Electron paramagnetic resonance
eSANS	Electrochemical small angle neutron scattering
ESI	Electrospray ionisation
FTO	Fluorine-doped tin oxide
Har	Aromatic hydrogens
HOMO	Highest occupied molecular orbital
HRMS	High resolution mass spectrometry
IR	Infrared
ITO	Indium tin oxide
LED	Light emitting diode
LMWG	Low molecular weight gelator
LUMO	Lowest unoccupied molecular orbital
MOF	Metal organic framework
Nap	Naphthalene
NDI	Naphthalene diimide
NIST	National institute of standards and technology
NMR	Nuclear magnetic resonance
NTCDA	1,4,5,8-Naphthalenetetracarboxylic dianhydride

PAH	Polycyclic aromatic hydrocarbons
PBI	Perylene bisimide
SANS	Small angle neutron scattering
SAS	Small angle scattering
SAXS	Small angle X-ray scattering
SEM	Scanning electron microscopy
SLD	Scattering light density
STFC	Science and technology facilities council
TEM	Transmission electron microscopy
TFA	Trifluoroacetic acid
TMO	Transition metal oxide
UV	Ultraviolet

TABLE OF CONTENTS

CHAPTER ONE: Introduction	1
1.1 Smart materials.....	2
1.1.1 Chromic materials.....	2
1.1.2 Electrochromic materials.....	2
1.2 Smart Windows.....	3
1.2.1 Requirements for Smart Windows.....	4
1.3 Existing Smart Window systems.....	5
1.3.1 Metal oxides.....	6
1.3.2 Conducting polymers.....	8
1.3.3 Small organic molecules.....	11
1.3.3.1 Self-assembling systems.....	12
1.3.3.1.1 Characterisation.....	13
1.3.3.2 Viologens.....	15
1.3.3.3 Naphthalene diimides.....	17
1.4 Aqueous systems.....	20
1.5 Transmissive to dark materials.....	23
1.6 Colour mixing and multicomponent systems.....	25
1.6.1 Mixing for other reasons.....	27
1.7 Measuring the structures formed from small organic molecules.....	28
1.7.1 SANS vs SAXS.....	29
1.8 Introduction to the work in this thesis.....	31
1.9 References.....	32

CHAPTER TWO: Investigation into the effect of pH on solubility, colour, redox values, and reversibility of colour change	47
2.1 Introduction.....	45
2.2 Results and discussion.....	48
2.2.1 Solubility.....	49
2.2.2 Apparent pK_a determination.....	50
2.2.3 Neutral state colour.....	51
2.2.4 Electrochromic response.....	56
2.2.4.1 pH and redox potential values.....	56
2.2.4.2 Electrochemically reduced colour.....	61
2.2.4.3 Ideal pH.....	66
2.2.4.4 Switchability.....	67
2.3 Conclusions.....	70
2.4 Experimental.....	70
2.4.1 Synthetic procedures.....	70

2.4.1.1	Purification of Isochromeno[6,5,4-def]isochromene-1,3,6,8-tetraone (NTCDA)	71
2.4.1.2	Synthesis of (2S,3S)-2-{13-[(1S,2S)-1-carboxy-2-methylbutyl]-5,7,12,14-tetraoxo-6,13-diazatetracyclo[6.6.2.0 ^{4,16} .0 ^{11,15}]hexadeca-1,3,8,10,15-pentaen-6-yl}-3-methylpentanoic acid (NDI-I)	72
2.4.1.3	Synthesis of (2S)-2-{13-[(1S)-1-carboxy-2-methylpropyl]-5,7,12,14-tetraoxo-6,13-diazatetracyclo[6.6.2.0 ^{4,16} .0 ^{11,15}]hexadeca-1,3,8,10,15-pentaen-6-yl}-3-methylbutanoic acid (NDI-V)	73
2.4.1.4	Synthesis of (2S)-2-{13-[(1S)-1-carboxy-2-phenylethyl]-5,7,12,14-tetraoxo-6,13-diazatetracyclo[6.6.2.0 ^{4,16} .0 ^{11,15}]hexadeca-1,3,8,10,15-pentaen-6-yl}-3-phenylpropanoic acid (NDI-F)	74
2.4.1.5	Synthesis of (2S)-2-{2-[13-{{{(1S)-1-carboxy-2-phenylethyl}carbamoyl)methyl}-5,7,12,14-tetraoxo-6,13-diazatetracyclo[6.6.2.0 ^{4,16} .0 ^{11,15}]hexadeca-1,3,8,10,15-pentaen-6-yl}acetamido}-3-phenylpropanoic acid (NDI-GF)	75
2.4.1.5.1	Synthesis of tert-butyl (2S)-2-(2-{{{tert-butoxy}carbonyl}amino}acetamido)-3-phenylpropanoate (GF-Protected).....	75
2.4.1.5.2	Synthesis of (2S)-2-(2-Aminoacetamido)-3-phenylpropanoic acid trifluoroacetate (GF-Deprotected)	76
2.4.1.5.3	Synthesis of (2S)-2-{2-[13-{{{(1S)-1-carboxy-2-phenylethyl}carbamoyl)methyl}-5,7,12,14-tetraoxo-6,13-diazatetracyclo[6.6.2.0 ^{4,16} .0 ^{11,15}]hexadeca-1,3,8,10,15-pentaen-6-yl}acetamido}-3-phenylpropanoic acid (NDI-GF)	76
2.4.1.6	Synthesis of (2S)-2-[(2S)-2-{13-[(1S)-1-{{{(1S)-1-carboxy-2-phenylethyl}carbamoyl)-2-phenylethyl]-5,7,12,14-tetraoxo-6,13-diazatetracyclo[6.6.2.0 ^{4,16} .0 ^{11,15}]hexadeca-1,3,8,10,15-pentaen-6-yl}-3-henylpropanamido]-3-phenylpropanoic acid (NDI-FF)	77
2.4.1.6.1	Synthesis of tert-butyl (2S)-2-[(2S)-2-{{{tert-butoxycarbonyl}amino}-3-phenylpropanamido]-3-phenylpropanoate (FF- Protected).....	77
2.4.1.6.2	Synthesis of (2S)-2-[(2S)-2-ammonio-3-phenylpropanamido]-3-phenylpropanoic acid trifluoroacetate (FF- Deprotected).....	78
2.4.1.6.3	Synthesis of Synthesis of (2S)-2-[(2S)-2-{13-[(1S)-1-{{{(1S)-1-carboxy-2-phenylethyl}carbamoyl)-2-phenylethyl]-5,7,12,14-tetraoxo-6,13-diazatetracyclo[6.6.2.0 ^{4,16} .0 ^{11,15}]hexadeca-1,3,8,10,15-pentaen-6-yl}-3-henylpropanamido]-3-phenylpropanoic acid (NDI-FF)	79
2.4.2	Experimental protocols and equipment	79
2.4.2.1	Freeze-dryer.....	79
2.4.2.2	Nuclear magnetic resonance (NMR) spectroscopy.....	80
2.4.2.3	High resolution mass spectroscopy (HRMS)	80
2.4.2.4	Preparation of solutions.....	80
2.4.2.5	pH measurements.....	80
2.4.2.6	Absorption spectroscopy	80
2.4.2.6.1	Dilution series	80
2.4.2.7	Apparent pK _a titrations	81
2.4.2.8	FTO windows.....	81
2.4.2.9	Cyclic voltammetry (CV).....	82
2.4.2.10	Spectroelectrochemistry.....	83

2.4.2.11	Electrochromic behaviour	83
2.4.2.11.1	Tracking electrochemical oxidation	83
2.5	References	84

CHAPTER THREE: Exploring stability and cyclability of NDI systems.....86

3.1	Introduction	88
3.2	Results and discussion	91
3.2.1	Buffering.....	92
3.2.2	Comparing ideal states.....	96
3.2.3	High pH.....	97
3.2.4	Aggregation at pD 9 and 6	99
3.2.4.1	Comparison of NDIs	103
3.2.5	The reduced state at ideal pH.....	104
3.2.6	Cyclability	108
3.2.6.1	Initial set-up	108
3.2.7	Initial assessment of cyclability.....	111
3.2.8	Assessing aggregation after electrochemical use	113
3.2.8.1	Investigation with CV	114
3.2.8.2	Investigation with spectroscopy	116
3.2.8.3	Investigation with SANS	117
3.2.9	Using <i>in situ</i> SANS to assess aggregation.....	122
3.2.9.1	Using <i>in situ</i> SANS to assess the differences between NDI-I and NDI-V	128
3.3	Conclusions	131
3.4	Experimental.....	133
3.4.1	Synthetic procedures.....	133
3.4.2	Experimental protocols and equipment	133
3.4.2.1	Preparation of solutions.....	133
3.4.2.2	pH measurements.....	133
3.4.2.3	Absorption spectroscopy	133
3.4.2.3.1	Dilution series	134
3.4.2.4	pH logs.....	134
3.4.2.5	Cyclic voltammetry (CV).....	134
3.4.2.6	Viscosity measurements	134
3.4.2.7	Small angle neutron scattering (SANS)	134
3.4.2.8	FTO windows.....	135
3.4.2.9	Spectro-electrochemistry.....	135
3.4.2.9.1	Transmittance	135

3.4.2.10	Electron paramagnetic resonance (EPR) spectroscopy	136
3.4.2.11	Cycling tests	136
3.4.2.11.1	Tracking redox potential	137
3.4.2.11.2	Temperature controlled cycling.....	137
3.4.2.12	High temperature NMR Spectroscopy.....	138
3.4.2.13	Diffusion-ordered spectroscopy (DOSY)	138
3.4.2.14	SANS after cycling and electrochemistry in the beamline.....	138
3.4.2.14.1	Electrochemistry in the beamline.....	139
3.5	References	141

CHAPTER FOUR: Improving Cyclability with Multicomponent Electrochromic

Systems	143	
4.1	Introduction	146
4.2	Results and discussion	149
4.2.1	Proof of concept showing diffusion influence	149
4.2.2	Screening trends in multicomponent systems	149
4.2.3	pK_a	151
4.2.4	Trends in viscosity	152
4.2.5	Trends in neutral state	154
4.2.6	The reduced state	157
4.2.6.1	Trends in CV	157
4.2.6.2	Trends in reduced state colouration.....	160
4.2.6.3	Trends in oxidation rate.....	163
4.2.7	Trends in SAXS data	164
4.2.7.1	Individual components.....	165
4.2.7.2	Multicomponent systems	167
4.2.7.3	NDI-GF:1-NapFF	169
4.2.7.4	NDI-F:1-NapFF	172
4.2.7.5	Comparisons	176
4.2.8	Effect of second component upon cyclability.....	177
4.2.8.1.1	<i>Buffering</i>	178
4.2.8.1.1.1	NDI-F containing systems	179
4.2.9	Effect of use upon aggregation	185
4.2.10	Heat-cooling NDI-F containing systems.....	187
4.2.10.1.1	<i>Aggregation and heat-cooling</i>	189
4.2.10.1.2	<i>The reduced state</i>	191
4.2.10.1.3	<i>Oxidation rates</i>	194
4.2.11	SAXS analysis.....	195

4.2.11.1.1	<i>Heat-cooling multicomponent systems</i>	196
4.2.11.1.2	<i>Trends in heat-cooled multicomponent systems</i>	199
4.2.12	Cyclability	202
4.2.13	Comparing our best performing systems	212
4.3	Conclusions	217
4.4	Experimental	219
4.4.1	Synthetic procedures	219
4.4.1.1	Synthesis of 2-{2-[2-(naphthalen-1-yloxy)acetamido]-3-phenylpropanamido}-3-phenylpropanoic acid (1-NapFF).....	220
4.4.1.1.1	Synthesis of ethyl 2-(2-[[tert-butoxy]carbonyl]amino)-3- phenylpropanamido)-3-phenylpropanoate (FF-OEt – Protected)	220
4.4.1.1.2	Synthesis of ethyl 2-(2-azaniumyl-3-phenylpropanamido)-3-Phenylpropanoate (FF-OEt – Deprotected)	221
4.4.1.1.3	Synthesis of ethyl 2-{2-[2-(naphthalen-1-yloxy)acetamido]-3-phenylpropanamido}-3-phenylpropanoate (1-NapFF – Protected)	221
4.4.1.1.4	Synthesis of 2-{2-[2-(naphthalen-1-yloxy)acetamido]-3-phenylpropanamido}-3-phenylpropanoic acid (1-NapFF).....	222
4.4.2	Experimental protocols and equipment	223
4.4.2.1	Nuclear magnetic resonance (NMR) spectroscopy.....	223
4.4.2.2	Preparation of solutions.....	223
4.4.2.3	Cycling tests	223
4.4.2.4	Apparent pK _a titrations	224
4.4.2.5	Absorption spectroscopy	224
4.4.2.6	Viscosity measurements	224
4.4.2.7	FTO windows.....	224
4.4.2.8	Spectro-electrochemistry.....	224
4.4.2.9	Cyclic voltammetry (CV).....	225
4.4.2.10	Small angle X-ray scattering (SAXS)	225
4.4.2.10.1	Dawn analysis of scattering data	225
4.5	References	225

CHAPTER FIVE: Summary, Conclusions and Future Work.....232

TABLE OF FIGURES

All images reproduced within the permission guidelines of the respective sources. Figures are reprinted or adapted from the referenced articles in figure captions with permission from the respective publishers (Royal Society of Chemistry, Elsevier or American Chemical Society).

Figures

Figure 1.1. Transition of colour of a Smart Window from Gesimat as reported by Baetens <i>et al.</i> ¹²	3
Figure 1.2. CIE 1931 XYZ colour space at 50% luminosity (mid-tones). ⁴³	6
Figure 1.3. Photographs of the AuPR/WO ₃ film on fluorine-doped Sn oxide (FTO) at the bleached state and the coloured state. Reproduced from Xu <i>et al.</i> ⁵⁸	8
Figure 1.4. Experimental observation of mechanical breathing of a film and after every 60 cycles reproduced from Wang <i>et al.</i> ⁷⁴	9
Figure 1.5. (a) Representative electrochromic polymers. Colours are representations of thin films based on measured CIE 1931 Y _{xy} colour coordinates. 0 = neutral, I = intermediate, + = oxidised - and -- = reduced states. Reproduced from Argun <i>et al.</i> ⁷⁰ from a compilation of reported systems ⁷⁵⁻⁹² (b) Chemical scheme of electropolymerisation formation of a copolymer. ⁹³ Photographs of neutral copolymer films on conductive glass with varying ratio of component parts. ⁷⁰	10
Figure 1.6. Cartoon of self-assembly into a variety of structures.....	13
Figure 1.7. Example of viologen in the dicationic, radical cationic and neutral state.	15
Figure 1.8. Colour change from transparent achieved using a TiO ₂ moderated film alongside corresponding chemical structures (colour coded) Adapted from Cinnsealach <i>et al.</i> (chemical structures and scale bar added to figure). ¹⁷⁶	16
Figure 1.9. Images of the device reported by Alesanco <i>et al.</i> demonstrating multicoloured responses. ¹⁸³	16
Figure 1.10. Redox states and triggers of NDIs.....	18
Figure 1.11. Patterned solutions (a–d) and gels (e–h) of an NDI based electrochromic device as reported by Gonzalez <i>et al.</i> ²⁹ a and e show the initial solution and gel, respectively. The photographs were taken at 0 minutes (a and e), after 1 minute (b and f), 5 minutes (c and g) and 10 minutes (d and h) after applying a reducing potential. The scale bar represents 1 cm.	19
Figure 1.12. Photographs of the colour change in one cycle including bleaching and colouring processes with the applied voltages of +0.5 V and -0.5 V. Systems contain acid-base indicator, (a) Phenolphthalein, (b) Thymolphthalein and (c) 3-Nitrophenol. Reproduced from Huang <i>et al.</i> ²²²	22
Figure 1.13. (a) Schematic of a 25 cm ² 2-electrode window containing a Cu-Ag gel. (b) Photographs of the window during switching outside (top) and inside with a white background (bottom) after 0, 15, and 30 seconds of metal electrodeposition by applying - 0.6 V and subsequently 30 seconds of metal stripping at 0.8 V (from left to right). Reproduced from Barile <i>et al.</i> ²²¹	23
Figure 1.14. (a) Chemical structure of the reported p-aminotriphenylamine system (b) photographs of the off (-0.47 V vs Fc/Fc+) and on states off state and coloured on state (1.13 V vs Fc/Fc+). Reproduced from Nguyen <i>et al.</i> ⁵⁵	24
Figure 1.15. Colouration from MnO ₂ (a) and Mo-doped WO ₃ (b) separately and then combined (c) into a device on FTO glass with a Pt foil counter electrode. 2 V and -2 V vs Ag/AgCl reference applied to achieve the coloured and bleached state. Reproduced from Xie <i>et al.</i> (scale bar added). ³⁹	26
Figure 1.16. Colouration achieved in a device reported by Stec <i>et al.</i> (scale bar added) ¹⁰⁵	26
Figure 1.17. Cartoon representation of SAS. θ is the scattering angle of the beam from the sample.	29
Figure 1.18. Transparent-to-dark colour change achieved hydrogel NDI based electrochromic device, reproduced from Gonzalez <i>et al.</i> ²⁹	31
Figure 2.1. Reversible formation of the different reduced species of NDI-R.	46
Figure 2.2. Cartoon showing NDI molecules forming different aggregation as pH changes and NDI-R is in various forms of deprotonation. A single amino acid R groups are assumed for simplicity.	47
Figure 2.3. Chemical structures of NDI-I , NDI-V , NDI-F , NDI-GF and NDI-FF	48
Figure 2.4. Images of solutions of (a) NDI-I , (b) NDI-V , (c) NDI-F , (d) NDI-GF and (e) NDI-FF in a thin gap of 0.1 mm (left) and in a vial (right) at 10 mg/mL, pH 9.	49
Figure 2.5. Absorption spectra of (a) NDI-I , (b) NDI-V , (c) NDI-F , (d) NDI-GF and (e) NDI-FF in neutral state at 5 (black), 2.5 (red), 1.25 (blue) and 0.625 (green) mg/mL at pH 9.....	50

Figure 2.6. Photographs of neutral solutions of (a) NDI-I , (b) NDI-V , (c) NDI-F , (d) NDI-GF and (e) NDI-FF at 5 mg/mL at pH 6 (red), 7 (pink), 8 (orange), 9 (black), 10 (turquoise), 11 (purple) and 12 (blue dashed) and after (blue solid) sitting for 30 minutes.	52
Figure 2.7. Absorbance spectra of NDI-I in neutral state at 5 mg/mL at pH 12. Measurements taken before (solid line) and after (dashed line) noted colour change of bulk solution.	53
Figure 2.8. Absorbance of neutral solutions of (a-b) NDI-I and (c-d) NDI-V and (e-f) NDI-F at 5 mg/mL at pH 6 (red), 7 (pink), 8 (orange), 9 (black), 10 (turquoise), 11 (purple) and 12 (blue). (b), (d) and (f) show absorbance spectra of pH 6-11 between 250-600 nm normalised between 0 and 1.....	54
Figure 2.9. Absorbance of neutral solutions of (a-b) NDI-GF and (c) NDI-FF at 5 mg/mL at pH 6 (red), 7 (pink), 8 (orange), 9 (black), 10 (turquoise), 11 (purple) and 12 (blue). (b) show absorbance spectra of NDI-GF between pH 6-10 normalised between 0 and 1 for clarity.	55
Figure 2.10. Cyclic voltammogram collected from 10 mg/mL solution of NDI-I (green) and NDI-V (blue) adjusted to pH 9. Voltammograms measured using a referenced glassy carbon set up (vs Ag/AgCl). The scan rate of the cyclic voltammograms was 0.2 V/s.....	57
Figure 2.11. Cyclic voltammogram collected from 10 mg/mL solutions of NDI-I adjusted to pH 6 in a 1 x 1 FTO window cell. The scan rate of the cyclic voltammograms was 0.1 V/s.....	58
Figure 2.12. (a) Absorbance spectra of 10 mg/mL solutions of NDI-I after a 10 second application of -2.5 V. Solutions adjusted to pH 6 (red), 7 (pink), 8 (orange), 9 (black), 10 (turquoise), 11 (purple) and 12 (blue) (b) Images of the resulting colouration in FTO windows are shown. Any bubbles caused by loading.....	62
Figure 2.13. (a) Absorbance spectra of 10 mg/mL solutions of NDI-V after a 10 second application of -2.5 V. Solutions adjusted to pH 6 (red), 7 (pink), 8 (orange), 9 (black), 10 (turquoise), 11 (purple) and 12 (blue) (b) Images of the resulting colouration are shown. Any bubbles caused by loading.....	63
Figure 2.14. (a) Absorbance spectra of 10 mg/mL solutions of NDI-F after a 10 second application of -2.5 V. Solutions adjusted to pH 6 (red), 7 (pink), 8 (orange), 9 (black), 10 (turquoise), 11 (purple) and 12 (blue) (b) Images of the resulting colouration are shown. Any bubbles caused by loading.....	64
Figure 2.15. (a) Absorbance spectra of 10 mg/mL solutions of NDI-FF after a 10 second application of -2.5 V. Solutions adjusted to pH 6 (red), 7 (pink), 8 (orange), 9 (black), 10 (turquoise), 11 (purple) and 12 (blue) (b) Images of the resulting colouration are shown. Any bubbles caused by loading.....	65
Figure 2.16. (a) Absorbance spectra of 10 mg/mL solutions of NDI-GF after a 10 second application of -2.5 V. Solutions adjusted to pH 6 (red), 7 (pink), 8 (orange), 9 (black), 10 (turquoise), 11 (purple) and 12 (blue) (b) Images of the resulting colouration are shown. Any bubbles caused by loading.....	66
Figure 2.17. Absorbance normalised between 0 and 1 showing trend in absorbance (at 490 nm for NDI-I , NDI-V , NDI-F , and NDI-FF and 450 nm for NDI-GF) characteristic of the radical anionic species electrochemically generated between pH 6 and 12. Measurements taken from spectra of (a) NDI-I (green), NDI-V (blue) and NDI-F (purple) and (b) NDI-GF (brown) and NDI-FF (black) at 10 mg/mL.	67
Figure 2.18. Absorbance spectra (lines) collected from electrochemically reduced solutions of (a) NDI-I and (c) NDI-V at 10 mg/mL after 20 second application of -2.5 V and a measure of absorbance at 540 nm (squares) taken every 30 seconds as oxidising potential of oxidation potential of 0.5 V was applied for 300 seconds to electrochemically reduced solutions of (b) NDI-I at and (d) NDI-V 10 mg/mL after 20 second application of -2.5 V. Solutions adjusted to pH 6 (red), 9 (black) and 12 (blue).	68
Figure 2.19. Absorbance spectra (lines) collected from electrochemically reduced solutions of (a) NDI-F and (c) NDI-GF at 10 mg/mL after 20 second application of -2.5 V and a measure of absorbance at 540 nm (squares) taken every 30 seconds as oxidising potential of oxidation potential of 0.5 V was applied for 300 seconds to electrochemically reduced solutions of (b) NDI-F at and (d) NDI-GF 10 mg/mL after 20 second application of -2.5 V. Solutions adjusted to pH 6 (red), 9 (black) and 12 (blue).	69
Figure 2.20. Reaction scheme of the purification of NTCDA.	71
Figure 2.21. Synthesis of NDI-I	72
Figure 2.22. Synthesis of NDI-V	73
Figure 2.23. Synthesis of NDI-F	74

Figure 2.24. 1st step, synthesis of GF-Protected.	75
Figure 2.25. 2nd step, deprotection of GF-Protected.....	76
Figure 2.26. 3 rd Step, synthesis of NDI-GF	76
Figure 2.27. 1st step, synthesis of FF-Protected.	77
Figure 2.28. 2nd step, deprotection of FF-Protected.	78
Figure 2.29. 3 rd step, synthesis of NDI-FF	79
Figure 2.30. Schematic diagram of the FTO window set-up described above.	82
Figure 2.31. The redox reaction of hydroquinone/benzoquinone measured by CV as a control.	82
Figure 2.32. CAD image of 3D printed holder designed to secure a 10 x 10 mm window into the absorption spectrometer.	83
Figure 3.1. Cartoon representation of the overestimation of radius which may occur using DLS.....	88
Figure 3.2. Set-up used for <i>in situ</i> SANS by Prabhu <i>et al.</i> ⁴⁸	90
Figure 3.3. Absorbance spectra of the neutral state of 5 mg/mL buffered (dashed line) and unbuffered (solid line) of NDI-I , (b) NDI-V , (c) NDI-F and (d) NDI-GF adjusted to their respective ideal pH (pH 9 for NDI-I and NDI-V and pH 6 for NDI-F and NDI-GF).	92
Figure 3.4. pH of 10 mg/mL buffered, and unbuffered solutions of NDI-I (green), NDI-V (blue), NDI-F (purple) and NDI-GF (brown) logged between 50-70 hours. Solutions were adjusted to their respective ideal pH (pH 9 for NDI-I and NDI-V and pH 6 for NDI-F and NDI-GF) at the start of the log. Buffered solutions are represented by NDI-I (light green), NDI-V (light blue), NDI-F (light purple) and NDI-GF (light brown)	94
Figure 3.5. Photographs of neutral and electrochemically reduced buffered (dashed line) and unbuffered (solid line) solutions of NDI-I (green), NDI-V (blue), NDI-F (purple) and NDI-GF (brown) at 10 mg/mL and at their respective ideal pH (pH 9 for NDI-I and NDI-V and pH 6 for NDI-F and NDI-GF). Reduction was achieved by application of -2.5 V for 10 seconds. Any bubbles caused by loading.	95
Figure 3.6. Absorbance at 540 nm taken every 30 seconds as oxidising potential of oxidation potential of 0.5 V was applied for 300 seconds to electrochemically reduced unbuffered (filled square) and buffered (open square) solutions of (a) NDI-I , (b) NDI-V , (c) NDI-F and (d) NDI-GF at 10 mg/mL after 20 second application of -2.5 V. Solutions adjusted to respective ideal pH (pH 9 for NDI-I and NDI-V and pH 6 for NDI-F and NDI-GF).	96
Figure 3.7. (a) Absorbance spectra of the neutral state of 5 mg/mL buffered NDI-I (green), NDI-V (blue) adjusted to pH 9, NDI-F (purple) and NDI-GF (brown) adjusted to pH 6 (b) Viscosity measurements under increasing shear rate for buffered solutions of NDI-I (green) and NDI-V (blue) at pH 9 and NDI-F (purple) and NDI-GF (brown) at pH 6 at 10 mg/mL. Measurements are taken as an average of triplicate measurements and error bars calculated from standard deviation.	97
Figure 3.8. Small angle neutron scattering data (open circles) for 10 mg/mL solutions, in their neutral state, of NDI-I (green), NDI-V (blue), NDI-F (purple), NDI-GF (brown) and NDI-FF (black) at pD 12. ...	98
Figure 3.9. Small angle neutron scattering data for a neutral solution of NDI-FF at pD 7 (black) and pD 12 (pink).	99
Figure 3.10. Small angle neutron scattering data for a 10 mg/mL neutral buffered solution of (a) NDI-I and (b) NDI-V at pD 6 (red), pD 12 (blue) and buffered at pD 9 (black).	100
Figure 3.11. Small angle neutron scattering data for a 10 mg/mL neutral buffered solution of (a) NDI-F and (b) NDI-GF at pD 9 (black), pD 12 (blue) and buffered at pD 6 (red).	101
Figure 3.12. Absorbance spectra of NDI-GF containing NaCl in a neutral state at 5 mg/mL. Solutions recorded at pH 6 (red), 9 (black) and 12 (blue).	103
Figure 3.13. SANS (open circles) and fits (lines) for solutions of 10 mg/mL NDI-I (green), NDI-V (blue), NDI-F (purple), NDI-GF (brown) at their respective ideal pD (pD 9 for NDI-I and NDI-V and pD 6 for NDI-F and NDI-GF). Fits are to flexible cylinder, flexible cylinder, hollow cylinder and flexible elliptical cylinder (all combined with a power law) for NDI-I (green), NDI-V (blue), NDI-F (purple), NDI-GF (brown).	104
Figure 3.14. (a) Absorbance spectra of the reduced state of 10 mg/mL buffered NDI-I (green), NDI-V (blue) NDI-F (purple) and NDI-GF (brown) adjusted to their respective ideal pH (pH 9 for NDI-I and	

NDI-V and pH 6 for NDI-F and NDI-GF) after 20 seconds of application of -2.5 V, (b) Photographs of solutions of NDI-I , NDI-V , NDI-F and NDI-GF at their respective ideal pH in coloured (top) and neutral states (bottom). Coloured states achieved by application of -2.5 V for 20 seconds in 1 x 1 cm windows.	106
Figure 3.15. Absorbance spectra of the reduced state of 10 mg/mL buffered NDI-GF adjusted to pH 6 at 10 mg/mL (black) and 14.5 mg/mL (red). Spectra taken after 20 seconds of application of -2.5 V.	107
Figure 3.16. EPR signal measured for electrochemically reduced buffered solutions of 10 mg/mL (a) NDI-I (green), (b) NDI-V (blue), (c) NDI-F (purple) and (d) NDI-GF (brown) adjusted to their respective ideal pH (pH 9 for NDI-I and NDI-V and pH 6 for NDI-F and NDI-GF). Data collected by Dr Stephen Sproules.	108
Figure 3.17. Images of the neutral and electrochemically reduced (10 seconds of -2.5 V) and oxidised (2 minutes of 0.5 V) states of buffered (a) NDI-I , (b) NDI-V , (c) NDI-F and (d) NDI-GF at their respective ideal pH (pH 9 for NDI-I and NDI-V and pH 6 for NDI-F and NDI-GF).....	110
Figure 3.18. Images of the reduced state at the start (left) and end (right) of cycling experiments. Buffered solution of 10 mg/mL NDI-I adjusted to pH 9 is shown. The start time of (a) is offset as the stopwatch was not restarted at the beginning of this experiment in error. Images of other NDIs are available in Figure A.3.30, Appendix. Bubble in window caused by loading.	111
Figure 3.19. (a-d) Photographs of colouration of solutions before cycling experiment (left) and after being collected from window cells after excessive cycling (right). Solutions are at 10 mg/mL and buffered to their respective ideal pH (pH 9 for NDI-I and NDI-V and pH 6 for NDI-F and NDI-GF). Shown are (a) NDI-I , (b) NDI-V , (c) NDI-F and (d) NDI-GF . (e) Images of oxidised state after periods of cycling. Solution of buffered 10 mg/mL NDI-I at pH 9 used. Corresponding images for other NDIs are available in Figures A.3.32-A.3.34, Appendix. Bubble in window is caused by loading.....	112
Figure 3.20. Plot showing how time to reach a state without colouration fluctuates with electrochemical cycling between a reduced and oxidised state. Measurements carried out using solutions of NDI-I (green), NDI-V (blue), NDI-F (purple) and NDI-GF (brown) at their respective ideal pH (pH 9 for NDI-I and NDI-V and pH 6 for NDI-F and NDI-GF). Measurements are taken as an average of triplicate measurements and error bars calculated from standard deviation.	113
Figure 3.21. Cartoon showing show a build-up of radical anionic species could occur through a cycle of (a) reduction, (b) diffusion, (c) incomplete oxidation and (d) reduction.....	114
Figure 3.22. Cyclic voltammograms collected from neutral buffered 10 mg/mL solution of (a) NDI-I , (b) NDI-V , (c) NDI-F and (d) NDI-GF adjusted to their respective ideal pH (pH 9 for NDI-I and NDI-V and pH 6 for NDI-F and NDI-GF). Voltammograms measured using a 5 x 5 cm FTO window cell with a scan rate of 0.5 V/s. Measurements shown from scan number 1 (red) and 100 (purple). Full data sets are available in Figure A.3.35-A.3.38, Appendix.	115
Figure 3.23. Absorbance spectra of the neutral state of 10 mg/mL buffered (a) NDI-I , (b) NDI-V , (c) NDI-F and (d) NDI-GF , adjusted to their respective ideal pH (pH 9 for NDI-I and NDI-V and pH 6 for NDI-F and NDI-GF), before (dashed lines) and after (solid lines) 50 electrochemical cycles. Spectra taken after a period of 24 hours of relaxation following cycling.....	116
Figure 3.24. (a) Chemical structure of NDI-R showing two environments of the core protons (b) ¹ H NMR spectra of the neutral state of 10 mg/mL buffered NDI-GF adjusted to pH 6 before (black) and after (red) excessive electrochemical cycling. Latter spectra taken after a period of 24 hours of relaxation following cycling. The peaks corresponding to a fully equivalent (black) and inequivalent (green/blue) core are marked in (b) as spanning lines.	117
Figure 3.25. Small angle neutron scattering data for a neutral buffered 10 mg/mL solution of (a) NDI-I and (b) NDI-V at pD 9 (black), after relaxation following one electrochemical cycle (green) and after 50 electrochemical cycles (blue).....	118
Figure 3.26. Small angle neutron scattering data for a neutral, 10 mg/mL buffered solution of (a) NDI-F and (b) NDI-GF at pD 6 (black), after relaxation following one electrochemical cycle (green) and after 50 electrochemical cycles (blue).....	119

Figure 3.27. Cartoon representation of the hypothesised (a) elongation or (b) joining of fibres, leading to an increase in axis ratio of NDI-GF with cycling.	121
Figure 3.28. Diagram of the process of transferring solution from a FTO window cell to a cuvette for measurement with SANS.	123
Figure 3.29. Diagram of the experimental set-up of spectro-electrochemical cell in the neutron beam.	124
Figure 3.30. (a) Diagram of the experimental set-up control, (b) an expanded diagram of the electrochemical reduction and oxidation of NDI solution at the working electrode of the cell where the beam is positioned.	125
Figure 3.31. Small angle neutron scattering data for a 10 mg/mL buffered solution of NDI-GF at pD 6 in a neutral state before electrochemical reduction (open circles) and after one electrochemical reduction and oxidation (red filled circles). Measurements taken in (a) spectro-electrochemical cell and (b) in a standard quartz cuvette.....	126
Figure 3.33. Small angle neutron scattering data for a 10 mg/mL buffered solution of NDI-GF at pD 6 (black), during reduction (red) and after electrochemical oxidation (blue) Data taken in spectro-electrochemical cell.	127
Figure 3.34. Small angle neutron scattering data for a buffered solution of (a) NDI-I and (b) NDI-V at pD 9 (black), during reduction (red) and after electrochemical oxidation (blue) Data taken in spectro-electrochemical cell.	129
Figure 3.35. Cyclic voltammograms collected from 10 mg/mL solutions of buffered (a) NDI-I , (b) NDI-V , (c) NDI-F and (d) NDI-GF adjusted to their respective ideal pH (pH 9 for NDI-I and NDI-V and pH 6 for NDI-F and NDI-GF), using a scan rate of 0.1 (black), 0.2 (red) and 0.5 (blue) V/s. Voltammograms performed in 5 x 5 cm window cell (unreferenced).	131
Figure 3.36. Schematic diagram of the FTO window set-up described above	135
Figure 3.37. Photograph showing the set-up in which cycling test are run.	137
Figure 3.38. Schematic of how <i>ex situ</i> electrochemically used samples were transferred into cuvettes.	139
Figure 3.39. Image of manually setting the position of the beam on the rack at ISIS beamline.....	139
Figure 3.40. Connection to PalmSense Potentiostat to cell in the beamline (covered by protective foil). Potentiostat is highlighted by red arrow.	140
Figure 3.41. Schematic of spectro-electrochemical cell used in SANS experiments. Reference electrode is Pt wire.....	141
Figure 4.1. Cartoon representation of (a/c) reduction and diffusion (b/d) away from the electrode surface within the cell. (a-b) shows the current set-up and (c-d) shows what may occur with the addition of a viscous component.....	146
Figure 4.2. Image reported by Alesanco <i>et al.</i> showing a “slime” based electrolyte. ¹⁵	147
Figure 4.3. Cartoon representation of hetero- (left) and homo- (right) type aggregates forming as pH is lowered in theoretical multicomponent systems.	148
Figure 4.4. Plot showing how time to reach a state without colouration fluctuates with electrochemical cycling between a reduced and oxidised state. Measurements carried out using solutions of buffered NDI-F at 10 mg/mL and adjusted to pH 6 (purple). The same experiment was repeated whilst heavy bass music played (black) at pH 6. Measurements are taken as an average of triplicate measurements and error bars calculated from standard deviation.....	149
Figure 4.5. (a) Chemical structure of 1-NapFF (b) colour by eye of 5 mg/mL solutions at pH 6, 9 and 12.	150
Figure 4.6. Viscosity measurements of 5 mg/mL 1-NapFF (black) and 5:5 mg/mL, NDI-F:1-NapFF (purple), and NDI-GF:1-NapFF (brown) at (a) pH 6, (b) 9 and (c) 12 containing 50% 0.1 M NaCl. Measurements are taken as an average of triplicate measurements and error bars calculated from standard deviation.	153

Figure 4.7. Images of (a) NDI-F:1-NapFF and (b) NDI-GF:1-NapFF neutral solutions containing 50% 0.1 M NaCl at pH 6, 9 and 12 at 5:5 (black), 5:2.5 (red), 5:1.25 (blue), 5:0.625 (green) and 5:0 (dashed line) mg/mL.....	155
Figure 4.8. Absorbance spectra of neutral single components at 5 mg/mL of (a) 1-NapFF and (b) NDI-F , (c) NDI-GF at pH 6 (red), 9 (black) and 12 (blue) containing 50% 0.1 M NaCl.....	156
Figure 4.9. Absorbance spectra of neutral 5:5 mg/mL (a) NDI-F:1-NapFF , (b) NDI-GF:1-NapFF at pH 6 (red), 9 (black) and 12 (blue) containing 50% 0.1 M NaCl.....	157
Figure 4.10. Images of NDI-F:1-NapFF 5:5 (black), 5:2.5 (red), 5:1.25 (blue), 5:0.625 (green) and 5:0 (dashed line) mg/mL at pH 6 (a), 9 (b) and 12 (c) following application of -2.5 V for 10 seconds. Any bubbles are a result of loading. Solutions contain 50% 0.1 M NaCl.....	161
Figure 4.11. Images of NDI-GF:1-NapFF 5:5 (black), 5:2.5 (red), 5:1.25 (blue), 5:0.625 (green) and 5:0 (dashed line) mg/mL at pH 6 (a), 9 (b) and 12 (c) following application of -2.5 V for 10 seconds. Any bubbles are a result of loading. Solutions contain 50% 0.1 M NaCl.....	162
Figure 4.12. Measurement of absorbance at 540 nm as an oxidising potential of 0.5 V was applied for 5 minutes after 20 seconds of reduction with -2.5 V. Solutions of NDI-F:1-NapFF at 5:5 (black), 5:2.5 (red), 5:1.25 (blue), 5:0.625 (green) and 5:0 (open square) mg/mL at pH 6 (a), 9 (b) and 12 (c) were used.....	163
Figure 4.13. Measurement of absorbance at 540 nm as an oxidising potential of 0.5 V was applied for 5 minutes after 20 seconds of reduction with -2.5 V. Solutions of NDI-GF:1-NapFF at 5:5 (black), 5:2.5 (red), 5:1.25 (blue), 5:0.625 (green) and 5:0 (open square) mg/mL at pH 6 (a), 9 (b) and 12 (c) were used.....	164
Figure 4.14. SAXS measurements of (a) 1-NapFF , (b) NDI-F and (c) NDI-GF at 5 mg/mL. Solutions adjusted to pH 6 (red), 9 (black) and 12 (blue). Solutions contain 50% 0.1 M NaCl.....	165
Figure 4.15. Cartoon representation of a flexible cylinder and Kuhn length.....	167
Figure 4.16. Raw detector data of 2D scattering plots of measurement taken from for a solution of NDI-F:1-NapFF 5:5 mg/mL adjusted to pH 9 (a) and 6 (b). Histogram plots are shown at a range of 0 to 100. Small angle X-ray scattering data for a solution of the same system at pH 9 (c) and 6 (d). (a) and (c) shows alignment causing a kink (red) highlighted in (c).....	168
Figure 4.17. SAXS measurements of neutral NDI-F (purple) and NDI-GF (brown) at 5 mg/mL, 1-NapFF (5mg/mL, black), and NDI-R:1-NapFF (5:5 mg/mL, blue) at pH 6 (a,d), 9 (b,e) and 12 (c,f). Multicomponent systems contain NDI-F (a-c), and NDI-F (d-f). Solutions contain 50% 0.1 M NaCl..	169
Figure 4.18. SAXS measurement of NDI-GF:1-NapFF at 5:5 (black), 5:2.5 (red), 5:1.25 (blue) and 5:0.625 (green) mg/mL at pH 6 (a), 9 (b) and 12 (c).....	171
Figure 4.19. SAXS measurement of NDI-F:1-NapFF at 5:5 (black), 5:2.5 (red), 5:1.25 (blue) and 5:0.625 (green) mg/mL at pH 6 (a), 9 (b) and 12 (c). (d) plot showing how Kuhn length of model fits varies with concentration of 1-NapFF in NDI-F:1-NapFF systems at pH 6 (red), 9 (black) and 12 (blue).....	174
Figure 4.20. Plot showing how radii of 1-NapFF (filled squares) and NDI-F (open squares) components fluctuates in models with concentration of 1-NapFF in NDI-F:1-NapFF systems at pH 9 (a) and 12 (b).	175
Figure 4.21. Absorbance spectra of solutions of reduced NDI-F:1-NapFF at pH 12 at ratios of 5:5 (black), 5:2.5 (red), 5:1.25 (blue), 5:0.625 (green) and 5:0 (dashed line) mg/mL. Spectra taken after 10 seconds of -2.5 V application.....	176
Figure 4.22. Plot showing how time to reach a state without colouration fluctuates with electrochemical cycling between a reduced and oxidised state. Measurements carried out using solutions of 5 mg/mL of NDI-F (purple) and mixes of 5:5 mg/mL NDI-F:1-NapFF at pH 6 (black), 5:1.25 mg/mL NDI-F:1-NapFF at pH 9 (blue). Measurements are taken as an average of triplicate measurements and error bars calculated from standard deviation.....	178
Figure 4.23. (a) Absorbance spectra (b) SAXS measurement of 1-NapFF 5 mg/mL at pH 6. Solutions are buffered (grey) and unbuffered (black).	179
Figure 4.24. Absorbance spectra of neutral state of buffered (dashed line) and unbuffered (solid line) (a) NDI-F 5 mg/mL and (b) NDI-F:1-NapFF 5:5 mg/mL adjusted to pH 6.	180

Figure 4.25. (a-b) Absorbance spectra of reduced state after application of -2.5 V for 10 seconds (c-d) Measurement of absorbance at 540 nm as an oxidising potential of 0.5 V was applied for 5 minutes after 20 seconds of reduction with -2.5 V. Solutions of buffered (dashed line/open square) and unbuffered (solid line/filled square) (a/c) NDI-F 5 mg/mL and (b/d) NDI-F:1-NapFF 5:5 mg/mL all adjusted to pH 6 were used. Images showing colouration by eye after reduction are included as insets of (a-b).....	182
Figure 4.26. Plots showing how time to reach a state without colouration fluctuates with electrochemical cycling between a reduced and oxidised state. Measurements of buffered (open shape) and unbuffered (filled shape) NDI-F 5 mg/mL (purple) and NDI-F:1-NapFF 5:5 mg/mL (black) adjusted to pH 6. Measurements are taken as an average of triplicate measurements and error bars calculated from standard deviation.....	183
Figure 4.27. SAXS measurement of neutral (a) NDI-F 5 mg/mL and (b) NDI-F:1-NapFF 5:5 mg/mL at pH 6. Solutions are buffered (light lilac and grey) and unbuffered (purple and black colour).	184
Figure 4.28. SAXS measurement of relaxed buffered (a) NDI-F:1-NapFF 5:1.5 mg/mL and (b) NDI-F 5 mg/mL at pH 6. Solutions are measured after 0 (black/purple), 1 (grey/lilac) and 50 (light grey/light lilac) electrochemical cycles.....	186
Figure 4.29. Absorbance spectra of neutral NDI-F:1-NapFF at pH 12 before (solid line) and after (dashed line) a heat-cool transition (heating to 40 °C and allowing to cool for 30 minutes) at (a) 5:0, (b) 5:5, (c) 5:2.5, (d) 5:0.625 mg/mL.....	190
Figure 4.30. Absorbance spectra of neutral NDI-F:1-NapFF at pH 6 before (solid line) and after (dashed line) a heat-cool transition (heating to 40 °C and allowing to cool for 30 minutes) at (a) 5:1.25 and (b) 5:0.625 mg/mL.....	191
Figure 4.31. Images of NDI-F:1-NapFF 5:5 (black), 5:2.5 (red), 5:1.25 (blue), 5:0.625 (green) and 5:0 (dashed line) mg/mL after heat-cooling (heating to 40 °C and allowing to cool for 30 minutes) at pH 6 (a), 9 (b) and 12 (c) following application of -2.5 V for 10 seconds. Any bubbles are a result of loading.	194
Figure 4.32. Measurement of absorbance at 540 nm as an oxidising potential of 0.5 V was applied for 5 minutes after 20 seconds of reduction with -2.5 V. Solutions of NDI-F:1-NapFF after heat-cooling (heating to 40 °C and allowing to cool for 30 minutes) at 5:5 (black), 5:2.5 (red), 5:1.25 (blue), 5:0.625 (green) and 5:0 (open square) mg/mL at pH 6 (a), 9 (b) and 12 (c) were used.....	195
Figure 4.33. SAXS data of 5 mg/mL (a) 1-NapFF and (b) NDI-F before (grey) and after (open circles) a heat-cool transition (heating to 40 °C and allowing to cool for 30 minutes) at pH 6 (red), 9 (black) and 12 (blue).	196
Figure 4.34. SAXS data of NDI-F:1-NapFF before (filled circles) and after (open circles) a heat-cool transition (heating to 40 °C and allowing to cool for 30 minutes) at 5:2.5 mg/mL (a) pH 6 and (b) 9.	197
Figure 4.35. Plot showing how axis ratio of cylindrical model fits varies with concentration of 1-NapFF in NDI-F:1-NapFF systems at pH 6 (red), 9 (black) and 12 (blue) after heat-cooling (heating to 40 °C and allowing to cool for 30 minutes). NDI-F kept at a constant concentration of 5 mg/mL.....	200
Figure 4.36. Plot showing how Kuhn length of 1-NapFF component fluctuates in cylindrical models with concentration of 1-NapFF in heat-cooled NDI-F:1-NapFF systems at pH 6 (red), 9 (black) and 12 (blue). Data after heat-cooling (heating to 40 °C and allowing to cool for 30 minutes). NDI-F kept at a constant concentration of 5 mg/mL.	201
Figure 4.37. Plot showing how radii of 1-NapFF (filled squares) and NDI-F (empty squares) components fluctuates in cylindrical models with concentration of 1-NapFF in heat-cooled (heating to 40 °C and allowing to cool for 30 minutes). NDI-F:1-NapFF systems at (a) pH 6 and (b) 9. Where data is missing, no NDI component was used in the model. NDI-F kept at a constant concentration of 5 mg/mL.	202
Figure 4.38. Plot showing how time to reach a state without colouration fluctuates with electrochemical cycling between a reduced and oxidised state. Measurements carried out using solutions of heat-cooled (heating to 40 °C and allowing to cool for 30 minutes) 5:0.625 mg/mL NDI-	

F:1-NapFF at pH 6 (red) and 9 (black). Measurements are taken as an average of triplicate measurements and error bars calculated from standard deviation.....	203
Figure 4.39. (a and c) Absorbance spectra of neutral state, (b and d) SAXS measurements at pH 6. Solutions of heat-cooled (heating to 40 °C and allowing to cool for 30 minutes) (a-b) NDI-F:1-NapFF 5:0.625 mg/mL and (c-d) NDI-F 5 mg/mL are buffered (dashed line or a lighter colour of orange and lilac) and unbuffered (solid line or a darker colour of red and purple).	204
Figure 4.40. (a/c) Absorbance spectra of reduced state after application of -2.5 V for 10 seconds, (b/d) measurement of absorbance at 540 nm as an oxidising potential of 0.5 V was applied for 5 minutes after 20 seconds of reduction with -2.5 V. Solutions of heat-cooled (heating to 40 °C and allowing to cool for 30 minutes) (a-b) NDI-F:1-NapFF 5:0.625 mg/mL and (c-d) NDI-F 5 mg/mL are buffered (dashed line or open squares) and unbuffered (solid line or filled squares).....	207
Figure 4.41. Plot showing how much time is needed to reach a transmissive state fluctuates with electrochemical cycling between a reduced and oxidised state. Measurements carried out using solutions of heat-cooled (heating to 40 °C and allowing to cool for 30 minutes) (a) NDI-F 5 mg/mL and (b) NDI-F:1-NapFF 5:0.625 mg/mL at pH 6 buffered (open shapes, lilac and red) and unbuffered (filled shapes, purple and orange). Measurements are taken as an average of triplicate measurements and error bars calculated from standard deviation.	208
Figure 4.42. SAXS measurement of relaxed buffered (a) NDI-F:1-NapFF 5:0.625 mg/mL heat-cooled (heating to 40 °C and allowing to cool for 30 minutes) and buffered at pH 6. Solutions are measured after 0 (red), 1 (orange) and 50 (yellow) electrochemical cycles.	209
Figure 4.43. (a) Absorbance spectra after 10 second application of -2.5 V and (b) plot showing how time to reach a state without colouration fluctuates with electrochemical cycling between a reduced and oxidised state. Measurements carried out using solutions of 5 mg/mL NDI-F buffered to pH 6 before (light purple) and after heat-cooling (heating to 40 °C and allowing to cool for 30 minutes) (purple). Measurements are taken as an average of triplicate measurements and error bars calculated from standard deviation.	210
Figure 4.44. (a) SAXS measurement and (b) absorbance spectra of neutral buffered NDI-F 5 mg/mL pre- (open circles and dashed lines) and post- (filled circles and solid lines) heat-cooling (heating to 40 °C and allowing to cool for 30 minutes).....	211
Figure 4.45. SAXS measurement of buffered relaxed NDI-F 5 mg/mL heat-cooled (heating to 40 °C and allowing to cool for 30 minutes) and buffered at pH 6. Solutions are measured after 0 (purple), 1 (lilac) and 50 (light lilac) electrochemical cycles.....	212
Figure 4.46. (a) Absorbance and (b) normalised absorbance spectra of the neutral state of NDI-F 5 mg/mL (purple), NDI-F:1-NapFF 5:0.625 mg/mL (red) and NDI-F:1-NapFF 5:5 mg/mL (black). All solutions buffered to pH 6. Dashed lines indicate heat-cooling (heating to 40 °C and allowing to cool for 30 minutes).....	213
Figure 4.47. (a) Absorbance spectra of reduced state after application of -2.5 V for 10 seconds and (b) measurement of absorbance at 540 nm as an oxidising potential of 0.5 V was applied for 5 minutes after 20 seconds of reduction with -2.5 V. Spectra taken with NDI-F 5 mg/mL (purple), NDI-F:1-NapFF 5:0.625 mg/mL (red) and NDI-F:1-NapFF 5:5 mg/mL (black). All solutions buffered to pH 6. Dashed lines and open squares indicate heat-cooling (heating to 40 °C and allowing to cool for 30 minutes).	214
Figure 4.48. (a) Viscosity measurements and (b) plot showing how time to reach a state without colouration fluctuates with electrochemical cycling between a reduced and oxidised state. Measurements taken with NDI-F 5 mg/mL (purple), NDI-F:1-NapFF 5:5 mg/mL (black), heat-cooled NDI-F 5 mg/mL (lilac) and heat-cooled NDI-F:1-NapFF 5:0.625 mg/mL (red). All solutions buffered to pH 6. Heat-cooled systems (heating to 40 °C and allowing to cool for 30 minutes) are shown as open shapes. Measurements are taken as an average of triplicate measurements and error bars calculated from standard deviation.	215
Figure 4.49. Plot showing how time to reach a state without colouration fluctuates with electrochemical cycling between a reduced and oxidised state. Measurements taken with heat-cooled	

(heating to 40 °C and allowing to cool for 30 minutes) NDI-F 5 mg/mL (lilac) and NDI-F:1-NapFF 5:0.625 mg/mL (red). All solutions buffered to pH 6. Measurements are taken as an average of triplicate measurements and error bars calculated from standard deviation.....	216
Figure 4.50. 1st step, synthesis of FF-OEt – Protected.	220
Figure 4.51. 2 nd step, deprotection of FF-OEt – Protected.	221
Figure 4.52. 3 rd step, synthesis of 1-NapFF – Protected.	221
Figure 4.53. 4 th step, deprotection of 1-NapFF – Protected.....	222
Figure 4.4.54 Cartoon representation of cycling test set-up with the vibration of music.....	224
Figure 5.1. Chemical structure of NDIs that could be investigated in future work.....	234

Tables

Table 2.1. Tabulated pK _a values calculated from pH titrations of different NDIs.....	51
Table 2.2. Reduction and oxidation potentials taken from cyclic voltammograms of 10 mg/mL hydroquinone with 10 % 0.1 M NaCl. Cyclic voltammograms performed in referenced set-up or in a 1 x 1 FTO window set-up. The scan rate of the cyclic voltammograms was 0.5 V/s.	57
Table 2.3. Reduction and oxidation potentials taken from cyclic voltammograms of 10 mg/mL solutions of NDI-I , NDI-V , NDI-F and NDI-GF adjusted to pH 9. Cyclic voltammograms performed in referenced set-up. The scan rate of the cyclic voltammograms was 0.2 V/s. The values for NDI-GF are shown at 0.2 and 0.5 V/s to see the oxidation potential.	58
Table 2.4. Reduction and oxidation potentials taken from cyclic voltammograms of 10 mg/mL solutions of NDI-I adjusted to different pH values. Cyclic voltammograms performed in FTO windows. The scan rate of the cyclic voltammograms was 0.1 V/s.	59
Table 2.5. Reduction and oxidation potentials taken from cyclic voltammograms of 10 mg/mL solutions of NDI-V adjusted to different pH values. Cyclic voltammograms performed in FTO windows. The scan rate of the cyclic voltammograms was 0.1 V/s.	59
Table 2.6. Reduction and oxidation potentials taken from cyclic voltammograms of 10 mg/mL solutions of NDI-F adjusted to different pH values. Cyclic voltammograms performed in FTO windows. The scan rate of the cyclic voltammograms was 0.1 V/s.	60
Table 2.7. Reduction and oxidation potentials taken from cyclic voltammograms of 10 mg/mL solutions of NDI-GF adjusted to different pH values. Cyclic voltammograms performed in 1x1 cm FTO windows. The scan rate of the cyclic voltammograms was 0.1 V/s.	61
Table 2.8. Reduction and oxidation potentials taken from cyclic voltammograms of 10 mg/mL solutions of NDI-FF adjusted to different pH values. Cyclic voltammograms performed in FTO windows. The scan rate of the cyclic voltammograms was 0.1 V/s.	61
Table 3.1. Molar absorbance coefficient calculated from the gradient of a plot of concentration vs. absorbance at λ_{max} . Calculated from data shown in Figure 2.5 in main text of Chapter 2.....	91
Table 3.2. Reduction and oxidation potentials taken from cyclic voltammograms of 10 mg/mL buffered and unbuffered solutions of NDI-I , NDI-V , NDI-F and NDI-GF adjusted to their respective ideal pH (pH 9 for NDI-I and NDI-V and pH 6 for NDI-F and NDI-GF). Cyclic voltammograms performed in referenced set at 0.2 V/s.	93
Table 3.3. Reduction and oxidation potentials taken from cyclic voltammograms of 10 mg/mL buffered and unbuffered solutions of NDI-I , NDI-V , NDI-F and NDI-GF adjusted to their respective ideal pH (pH 9 for NDI-I and NDI-V and pH 6 for NDI-F and NDI-GF). Cyclic voltammograms performed in 1x1 FTO windows at 0.2 V/s.....	93
Table 3.4. Tabulated absorbance at 540 nm for buffered and unbuffered solutions of NDI-R after a 10 second application of -2.5 V. Full data set available in Figure A.3.6, Appendix.	94
Table 3.5. Tabulated parameters from SANS model fits of systems at pD 12. The parameters for NDI-FF at pD 7 are also shown. Full data sets available in Figures A.3.7-A.3.12 and Tables A.3.1-A.3.6, Appendix.	98

Table 3.6. Tabulated parameters from SANS model fits of NDI-I . Full data sets available in Figures A.3.13-A.3.14 and Tables A.3.7-A.3.8, Appendix.	100
Table 3.7. Tabulated parameters from SANS model fits of NDI-V . Full data sets available in Figures A.3.15-A.3.16 and Tables A.3.9-A.3.10, Appendix.	101
Table 3.8. Tabulated parameters from SANS model fits of NDI-F . Full data sets available in Figures A.3.17-A.3.18 and Tables A.3.11-A.3.12, Appendix.	101
Table 3.9. Tabulated parameters from SANS model fits of NDI-GF . Full data sets available in Figures A.3.19-A.3.20 and Tables A.3.13-A.3.14, Appendix.	102
Table 3.10. Tabulated colouration efficiency calculated using transmittance taken at the λ_{\max} of the reduced state for buffered NDI-I , NDI-V , NDI-F , and NDI-GF after application of -2.5 V. Colouration efficiency calculated using charge density in a 1 x 1 cm FTO window set-up.	105
Table 3.11. Reduction and oxidation potentials taken from cyclic voltammograms of 10 mg/mL hydroquinone with 10 % 0.1 M NaCl. Cyclic voltammograms performed in a 1 x 1 and 5 x 5 FTO window set-up at 0.5 V/s. Data available in Figure A.3.21, Appendix.	109
Table 3.12. Redox potentials collected from cyclic voltammograms of buffered NDI-I , NDI-V , NDI-F and NDI-GF collected at their ideal pH at 10 mg/mL within a 5 x 5 cm FTO window set-up. The scan rate of the cyclic voltammograms was 0.1 V/s. Full data available in Figure A.3.22, Appendix.	109
Table 3.13. Tabulated parameters from SANS model fits of NDI-I after periods of cycling. Full data sets available in Figures A.3.62-A.3.63 and Table A.3.16, Appendix.	118
Table 3.14. Tabulated parameters from SANS model fits of NDI-V after periods of cycling. Full data sets available in Figures A.3.64-A.3.65 and Table A.3.17, Appendix.	119
Table 3.15. Tabulated parameters from SANS model fits of NDI-F after periods of cycling. Full data sets available in Figures A.3.66-A.3.67 and Table A.3.18, Appendix.	120
Table 3.16. Tabulated parameters from SANS model fits of NDI-GF after periods of cycling. Full data sets available in Figures A.3.68-A.3.69 and Table A.3.19, Appendix.	121
Table 3.17. Redox potentials collected from cyclic voltammograms of buffered NDI-GF collected at pH 6 at 10 mg/mL within spectro-electrochemical cell set-up. The scan rate of the cyclic voltammograms was 0.2 V/s. Full data available in Figure A.3.70, Appendix.	125
Table 3.18. Tabulated parameters from SANS model fits of NDI-GF taken from the electrochemical cell. Full data sets available in Figures A.3.72-A.3.74 and Table A.3.20, Appendix.	127
Table 3.19. Redox potentials collected from cyclic voltammograms of buffered NDI-I and NDI-V collected at pH 9 at 10 mg/mL within spectro-electrochemical cell set-up. The scan rate of the cyclic voltammograms was 0.2 V/s. Full data available in Figure A.3.77, Appendix.	128
Table 3.20. Tabulated parameters from SANS model fits of NDI-I and NDI-V taken from the electrochemical cell. Full data sets available in Figures A.3.80-A.3.85 and Table A.3.21-A.3.22, Appendix.	129
Table 4.1. Tabulated data from apparent pK_a titrations showing pH at which buffering occurs from raw data in Figure A.4.1-A.4.5, Appendix.	151
Table 4.2. Tabulated average apparent viscosity at a shear rate of 1 s^{-1} for 1-NapFF and NDI-R as single components at different pH. Full data sets available in Figure A.4.6-A.4.8, Appendix.	152
Table 4.3. Tabulated average apparent viscosity at a shear rate of 1 s^{-1} for NDI-R:1-NapFF at different ratios and pH. Full data sets available in Figure A.4.7-A.4.9, Appendix.	154
Table 4.4. Tabulated reduction and oxidation potentials found by CV of solutions of NDI-F:1-NapFF at various ratios at pH 6. Scan rate 0.2 V/s. Full data set found in Figure A.4.12, Appendix.	158
Table 4.5. Tabulated reduction and oxidation potentials found by CV of solutions of NDI-F:1-NapFF at various ratios at pH 9. Scan rate 0.2 V/s. Full data set found in Figure A.4.12, Appendix.	158
Table 4.6. Tabulated reduction and oxidation potentials found by CV of solutions of NDI-F:1-NapFF at various ratios at pH 12. Scan rate 0.2 V/s. Full data set found in Figure A.4.12, Appendix.	158
Table 4.7. Tabulated reduction and oxidation potentials found by CV of solutions of NDI-GF:1-NapFF at various ratios at pH 6. Scan rate 0.2 V/s. Full data set found in Figure A.4.13, Appendix.	159

Table 4.8. Tabulated reduction and oxidation potentials found by CV of solutions of NDI-GF:1-NapFF at various ratios at pH 9. Scan rate 0.2 V/s. Full data set found in Figure A.4.13, Appendix.	159
Table 4.9. Tabulated reduction and oxidation potentials found by CV of solutions of NDI-GF:1-NapFF at various ratios at pH 12. Scan rate 0.2 V/s. Full data set found in Figure A.4.13, Appendix.	160
Table 4.10. Tabulated absorbance intensity at λ_{\max} (after 10 seconds of application of -2.5 V) for NDI-F:1-NapFF at different ratios and pH. Full data sets available in Figure A.4.14, Appendix.	160
Table 4.11. Tabulated absorbance intensity at λ_{\max} (after 10 seconds of application of -2.5 V) for NDI-GF:1-NapFF at different ratios and pH. Full data sets available in Figure A.4.15, Appendix.	162
Table 4.12. Tabulated parameters from fits to SAXS data from single component systems. Full data set available in Figures A.4.16-A.4.25 and Tables A.4.1-A.4.9, Appendix.	166
Table 4.13. Tabulated parameters from fits to SAXS data from NDI-GF:1-NapFF systems. Full data set available in Figures A.4.28-A.4.40 and Tables A.4.10-A.4.21, Appendix.	170
Table 4.14. Tabulated parameters from fits to SAXS data from NDI-F:1-NapFF systems. Full data set available in Figures A.4.41-A.4.55 and Tables A.4.22-A.4.33, Appendix.	173
Table 4.15. Tabulated data from cyclic voltammograms performed in 5 x 5 FTO window cell at 0.2 V/s scan rate. Full data available in Figure A.5.59, Appendix.	177
Table 4.16. Tabulated average apparent viscosity at a shear rate of 1 s^{-1} for single and multicomponent systems buffered and unbuffered. All solutions adjusted to pH 6. Full data set in Figure A.4.60, Appendix.	178
Table 4.17. Tabulated parameters from fits to SAXS data from single component systems. Full data set available in Figures A.4.22 and A.4.61 and Tables A.4.7 and A.4.34, Appendix.	179
Table 4.18. Tabulated data of redox potentials taken from cyclic voltammograms taken at 0.2 V/s of NDI-F 5 mg/mL and NDI-F:1-NapFF 5:5 mg/mL, buffered and unbuffered at pH 6 in different sizes of FTO window cell. Full data sets available in Figure A.4.62, Appendix.	181
Table 4.19. Tabulated parameters from fits to SAXS data from NDI-F and NDI-F:1-NapFF systems. Full data set available in Figures A.4.16, A.4.41 and A.4.63-A.4.64 and Tables A.4.1, A.4.22 and A.4.35-A.4.36, Appendix.	185
Table 4.20. Tabulated parameters from fits to SAXS data from NDI-F and NDI-F:1-NapFF systems. Full data set available in Figures A.4.16, A.4.41 and A.4.65-A.4.68 and Tables A.4.1, A.4.22 and A.4.37-A.4.40, Appendix.	186
Table 4.21. Tabulated average apparent viscosity at a shear rate of 1 s^{-1} for NDI-F 5 mg/mL and 1-NapFF and NDI-F:1-NapFF at different ratios and pH after heating to 40 °C and allowing to cool for 30 minutes. Full data sets of available in Figures A.4.6 and A.4.69-A.4.70, Appendix. Heat-cooled data is shown as red text.	188
Table 4.22. Tabulated reduction and oxidation potentials found by CV of solutions of NDI-F:1-NapFF at various ratios at pH 6 after heat-cooling. Scan rate 0.2 V/s. Full dataset available in Figure A.4.72, Appendix.	191
Table 4.23. Tabulated reduction and oxidation potentials found by CV of solutions of NDI-F:1-NapFF at various ratios at pH 9 after heat-cooling. Scan rate 0.2 V/s. Full dataset available in Figure A.4.72, Appendix.	192
Table 4.24. Tabulated reduction and oxidation potentials found by CV of solutions of NDI-F:1-NapFF at various ratios at pH 12 after heat-cooling. Scan rate 0.2 V/s. Full dataset available in Figure A.4.72, Appendix.	192
Table 4.25. Tabulated absorbance intensity at λ_{\max} (after 10 seconds of application of -2.5 V) for NDI-F:1-NapFF at different ratios and pH before and after heat-cooling Full data sets available in Figure A.4.73, Appendix. Heat-cooled data is shown as red text.	193
Table 4.26. Tabulated parameters from fits to SAXS data from single component systems after heat-cooling. Full data set available in Figures A.4.74-A.4.79 and Tables A.4.41-A.4.46, Appendix.	196
Table 4.27. Tabulated fit parameters data from NDI-F:1-NapFF systems after heat-cooling. Full data of heat cooled measurements available in Figures A.4.81-A.4.92 and Tables A.4.47-A.4.58, Appendix. Heat-cooled data is shown as red text.	198

Table 4.28. Tabulated average apparent viscosity at a shear rate of 1 s^{-1} for heat-cooled single and multicomponent systems buffered and unbuffered. All solutions adjusted to pH 6. Full data set available in Figure A.4.94, Appendix.....	204
Table 4.29. Tabulated fit parameters of SAXS data from for heat-cooled single and multicomponent systems buffered and unbuffered. All solutions adjusted to pH 6. Full data set of buffered data found in Figures A.4.95-A.4.96 and Tables A.4.59-A.5.60, Appendix.....	205
Table 4.30. Tabulated data of redox potentials taken from cyclic voltammograms taken at 0.2 V/s of heat-cooled NDI-F:1-NapFF 5:0.625 mg/mL and NDI-F 5 mg/mL, buffered and unbuffered at pH 6 in different sizes of FTO window cell. Full data sets available in Figure A.4.97, Appendix.	206
Table 4.31. Tabulated parameters from fits to SAXS data from NDI-F:1-NapFF systems. Full data set available in Figures A.4.49 and A.4.98-A.4.99 and Tables A.4.59 and A.4.61-A.4.62, Appendix.....	209
Table 4.32. Tabulated parameters from fits to SAXS data from for heat-cooled systems buffered and unbuffered. All solutions adjusted to pH 6. Full data set available in Figures A.4.63 and A.4.96 and Tables A.4.35 and A.4.60, Appendix.	211
Table 4.33. Tabulated parameters from fits to SAXS data from NDI-F systems. Full data set available in Figures A.4.50 and A.4.100-A.4.101 and Tables A.4.60 and A.4.63-A.4.64, Appendix.	212
Table 4.34. Tabulated parameters from fits to SAXS data from single and multicomponent systems.	217

CHAPTER ONE

Introduction

1.1 Smart materials

Smart materials are responsive to external stimuli such as temperature, pH, electrical or magnetic fields, light or secondary chemical compounds.¹ This response could be a change in shape, electrical charge or colour for example. Shape-memory materials are used in products such as glasses that return to their original shape after deformation.² Piezoelectric materials are used in products such as lighters and pickups in acoustic-electric guitars.³

1.1.1 Chromic materials

Chromic materials that change their colouration upon exposure to stimulus are perhaps the broadest ranging in their application.⁴ A change in colour is recognisable and obvious to the eye. Chromic changes are marketable as they can be universally identified and require little or no training to be understood (*i.e.*, no need for scientific understanding or of different languages.). Chromic materials can be used for many categories of product. They have aesthetic (colour changing mugs⁵ and clothing^{6,7}), safety (thermochromic baby clothing⁸ and thermometers⁹), medical (pregnancy tests¹⁰, lateral flow COVID-19 tests) and environmental (Smart Windows^{4,11-13}) applications. They are already apparent in everyday use (reusable price labels, protective eyewear, glare-reduction systems, camouflage materials and displays).¹⁴ Commercial chromic materials often change colour reversibly when exposed to external stimulus such as temperature, light, pressure, electricity, and pH.¹⁵

1.1.2 Electrochromic materials

Electrochromism is defined as the reversible and visible change in transmittance and/or reflectance associated with an electrochemically induced redox reaction.^{4,16} Electrochromic materials change colour as the result of an electrochromic species within the system changing from a bleached or coloured state to a (differently) coloured state.^{14,16} Each state has distinct electronic and optical properties. Electrochromic devices include at least two electrodes and an electrolyte.¹⁷

Electrochromic materials have advantages over chromic materials that are triggered by other stimuli. Electricity is perhaps one of the simplest stimuli to control with ease compared to pH, temperature or light, as it can be done on demand. Electrochromic devices were initially outperformed by liquid crystal displays.¹⁸ However, it was then reported that liquid crystal displays have disadvantages such as poor contrast (except when back lighting is provided), decreased legibility from some viewing angles and narrow temperature operation range.¹⁸ Electrochromic materials can be used in a wide range of display applications. This wide usage is due to properties such as multicolour appearance, high contrast, optical memory, and no visual dependence upon viewing angle.⁴

1.2 Smart Windows

Among the many applications of electrochromic materials, so called Smart Windows are one of the most relevant to a growingly environmentally conscious society. Smart Windows have a focus towards reducing the effects of climate change and are in line with a growing public interest in more efficient energy systems.^{16,19–21} Smart Windows can change transmittance on demand, changing the tinting, optical depth, or colour of a window, Figure 1.1. They are of great interest because energy consumption in a building's heating, ventilation, and air conditioning systems accounts for 25% of the world's total energy use.²²

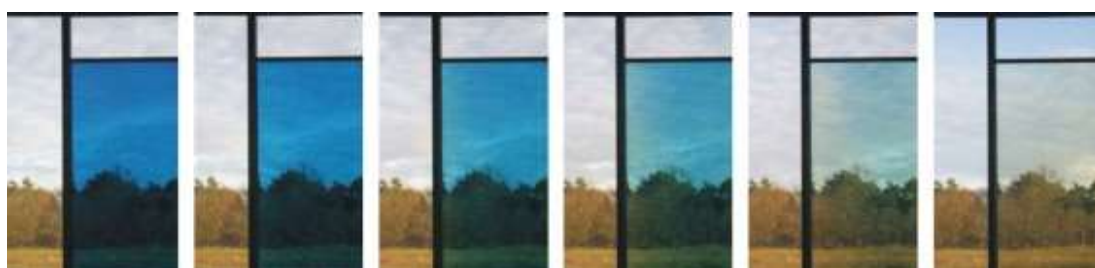


Figure 1.1. Transition of colour of a Smart Window from Gesimat as reported by Baetens *et al.*¹²

In the winter, windows are the cause of a lack in energy efficiency in buildings as they let out heat but are needed to let in light for workers.²³ In the summer, windows heat up buildings by letting in ultraviolet and infrared light and so money is spent on air conditioning. This problem is something that tintable (or smart) windows are seeking to solve.¹² Sustainable Technologies Australia Ltd stated in 2001 that electrochromic windows that were able to achieve absorbance of 95% of solar infrared (IR) could cut 30% of working environment costs.²⁴ The “potential for savings” is thought to be higher for certain building types, for example “highly glazed facades in modern urban office design”.²⁵

Smart Windows have been reported to provide a 54% energy reduction when compared to standard single-glazed windows for a 25-year life cycle.²⁶ This figure suggests that initial set-up costs are outweighed over a long term use. A $\text{WO}_3 + \text{Ag}$ nanocomposite layer based Smart Window with a change in transmittance of 39.65% between bleached and coloured states was reported.¹⁹ It facilitated a reduction in thermal energy consumption in different climates in Iran between 25–45% relative to a typical window.¹⁹ Recent studies have used electrochromic windows within a new classroom design in school buildings in Nanjing.²⁷ These studies found that annual energy consumption decreased by around 250 kWh, and that parameters such as the number of hours of “thermal discomfort” were significantly decreased.²⁷

Not all Smart Windows are electrochromic. The term Smart Window has been applied to windows that do not alter transmittance or colour at all. These windows instead are composed of systems of thin-film coatings designed to modulate near-infrared absorption.²⁸ The disadvantage of these systems is that static tinted windows are inconvenient. They may unnecessarily darken rooms during winter months (driving up lighting costs) and therefore offset any heating savings. The ability to alter transmission of radiation on-demand is preferable as it can allow a window to be tailored to seasonal and daily weather changes. This ability has the potential to drastically reduce energy consumption.¹² Altering the transmission of windows is also beneficial for privacy within buildings.²³ Smart Windows also have the potential to significantly improve running costs of vehicles, aircraft *etc.*²⁹

Flexibility is advantageous for application to Smart Windows as the specific requirements of each environment may be different. Factors such as frequency of use, desired colour, ambient temperature *etc.* will alter and therefore tunability is important.³⁰

1.2.1 Requirements for Smart Windows

There are several requirements that an electrochromic material must possess to be commercially viable for use in Smart Windows. These criteria have been defined within the literature:^{23,24,26,30-33}

- Reversibility of colour change
- uniformity and intensity of colour change that can be maintained
- fast switching (a few minutes) between coloured states using potentials no more than 5 V^{31,34}
- operating glass surface temperatures of -20 – 80 °C.^{31,34} Although currently available electrochromic windows have been tested in hot climate regions within the USA (giving an 80 – 4% transmission change over a few minutes, on a 28 cm x 35 cm scale²⁴), performance in cold climates is not as fully validated²³
- low maintenance, processing, and set-up costs
- an acceptable colour for the non-coloured state. This state must be transmissive enough not to compromise the visibility of the window
- the ability to achieve a device with large area
- acceptable material cost (around \$100 m⁻²).^{31,34} The quoted maximum permissible additional cost per m² of electrochromic glass over a period of 10 years is 33.44 €²⁶
- durability for lifetime use over 20 years (around 100,000 cycles)³⁵
- transparent, high conductivity electrolyte durable to solar irradiation and resistant to moisture³³
- low toxicity and/or non-hazardous to the public.²⁶

There are also some factors that, while not essential, would be beneficial commercially for such as:

- photosensitivity (which can be easily controlled)
- easily tailoring of the colour response
- the ability to create patterns (for potential branding applications)

1.3 Existing Smart Window systems

Common examples of electrochromic material classes are metal oxides or metal coordination complexes, conducting polymers (CPs) and small organic molecules.¹⁴ Electrochromic devices are commonly characterised in terms of their transmittance, speed of change (of approximately 90-95% of the transmittance change³⁶) and cyclability.

Cyclic voltammetry (CV) is used to show the required redox potentials for devices. Occasionally chronoamperometry plots are also shown.³⁷ Depending upon the type of device, imaging can also be included in articles to indicate either structure or changes, to a film surface for example.^{38,39}

Absorbance spectra (specifically spectro-electrochemical spectra) are commonly shown to indicate the changes in colour with an applied voltage, showing absorbance in the visible region of light in a particular state. This technique can also assess transmittance in “on and off” states. Taking these values, colouration efficiency is often quoted. This property depends upon the total transmittance change, the size of the device and the electrochemical measurement of current through the cell. The dependence upon these factors makes it easier to compare across reported systems which may be of different sizes, require different potentials etc.

The international commission on illumination (CIE) colour space is often used to report specific colours in coloured-to-coloured devices, Figure 1.2.⁴⁰⁻⁴² The parameters that determine the exact position in the space depend upon thickness of material and light source.³⁶ Coordinates a^* and b^* are used to indicate the colour itself while L^* describes brightness.

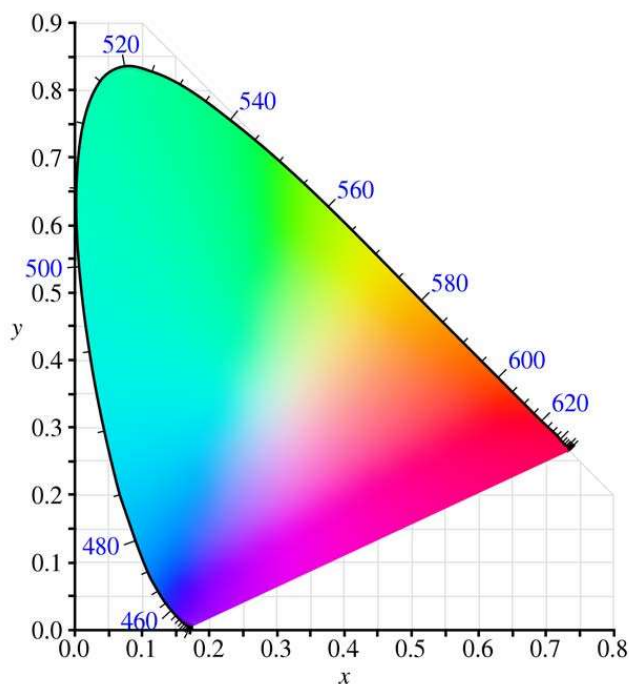


Figure 1.2. CIE 1931 XYZ colour space at 50% luminosity (mid-tones).⁴³

Cyclability is typically measured by switching between the states of a device and measuring how the transmittance or colouration efficiency is altered through cycling. Typically, the number of cycles achieved without detriment to these properties is quoted as a measure of stability, or a plot of transmittance with cycling is shown.^{38,39,42} Less commonly is the specific aggregation or structure reported and how this may change with electrochemical use.

1.3.1 Metal oxides

Transition metal oxides (TMOs) such as Ir^{44,45}, W^{17,46–48}, Co, Mn and Ru⁴ oxide make up a large section of the electrochromic field. TMO films are the most common usage.⁴ There have also been reports of Smart Windows constructed using metal oxides and polyester-based foils (such as W and Ni oxide films laminated together).^{17,34} TMO films are electrochemically switched to a non-stoichiometric redox state. An absorption band due to optical intervalence charge transfer causes an intense coloured state.⁴ While effective, the use of such materials are generally energy intensive.²⁹

An advantage of TMO based materials such as doped metal oxides is that they can sometimes act both as electrochromic devices and pseudo capacitors in a sandwich-like configuration. This factor is an advantage because a single system can act as both a Smart Window and an energy storage system.³⁹ A reported example can power a light emitting diode (LED) for 90 seconds in a coloured state.³⁹

A common example used in electrochromics is WO₃ systems, achieving a transparent to blue colour change.^{12,17,34,46,49–51} WO₃ has an almost cubic crystal structure with empty space inside.⁴ These spaces

allow the process of insertion of guest ions such as Li^+ , altering the oxidation state. For example, WO_3 is a transparent film when all W sites have the oxidation state W^{6+} whereas W^{5+} has a blue colour.⁴ Intervalence charge transfer between adjacent W^{5+} and W^{6+} sites allow an intense blue colour in M_xWO_3 systems when x (of M_x) has a low value.⁴ At higher x values, there is an irreversible formation of a bronze colour.⁴ Irreversible colour changes are a large disadvantage, causing a significant loss in suitability of use.⁵²

Coatings based on TMOs are not always practical. For example, VO_2 coatings can have poor transmittance of $\sim 40\%$ ³³ (although this can be improved by adding a band gap widening agent such as magnesium).³³ TMO films often require complex techniques such as vacuum evaporation, spray deposition, electrodeposition, electrochemical oxidation, chemical vapor deposition and sol-gel methodology^{33,46,53,54} to be deposited onto electrode surfaces. The complicated nature of these techniques is a disadvantage as they require specific equipment and training, high temperatures and vacuum.^{55, 56} Such techniques may encounter problems or high costs when scaled up. This factor can only be calculated in a commercial setting as literature examples of devices are typically under 5-10 cm in size.⁵⁰

A general issue with scaling up metal-based devices is that quality and cost are restrictions.^{56,57} Maintaining good optical transparency with electrical conductivity is also challenging for heat sensitive polymer substrates in electrochromic films.³³ Even transmissive bleached states may not be optically clear enough for use in windows, creating a yellowish or cloudy view through the metal film. For example, a gold nanoparticle-gold nanorod system deposited on a porous WO_3 substrate (AuPR/WO_3) show in Figure 1.3.⁵⁸ The coloured state in this case is very intense and shows a good contrast to the bleached state. Nevertheless, the yellowish colour of the transmissive state makes this system less appealing for application in Smart Windows. The requirement of high temperatures to achieve a coloured state is a disadvantage, as it would be energy intensive and offset Smart Window savings.



Figure 1.3. Photographs of the AuPR/WO₃ film on fluorine-doped Sn oxide (FTO) at the bleached state and the coloured state. Reproduced from Xu *et al.*⁵⁸

Ion insertion and extraction can be used to change the lattice structure of an inorganic electrochromic material.²² Changing the potential applied and the thickness of a film can impact colouration to form tuneable devices. However, these systems are reported to suffer from issues with irreversible side reactions, instability and slow switching times in large area devices.²²

One of the advantages of TMOs is the variety of colour achieved. Phthalocyanines are compounds with a metal ion at either the centre of a phthalocyanine ring or between two rings.^{59,60} [Lu(Pc)₂] has a range of colours from orange to violet, although mostly a blue-green transition is used in electrochromic devices.⁴ While performing reversible and uniform chromic changes in a range of tuneable colours, TMOs are not without fault. They are costly,⁵⁴ with examples such as IrO₂ described as “excessively expensive”.¹² TMOs are also inherently brittle and often require long switching times to achieve colouration.^{52,61} Finally, TMOs tend to have high stability to ultraviolet (UV) radiation. Although not a direct disadvantage for Smart Windows, it takes away the possibility of windows that respond to sunlight.³⁵ The ability to respond to natural light automatically is a property that other classes of material can achieve.

Overall, TMOs offer many beneficial properties that fulfil the criteria of a Smart Window. Nevertheless, the disadvantages in terms of stability and cost can outweigh these benefits. Some systems also have poor colour intensity in a coloured state.⁶² Other classes of material could fulfil these criteria without the challenges associated with mining, processing and recycling TMOs, creating a ‘greener’ alternative.

1.3.2 Conducting polymers

CPs are more processable than inorganic electrochromic materials and have a higher propensity to tune colour *via* functionalisation, copolymerisation, blending and lamination.^{4,63} Redox processes (accompanied by ion insertion or expulsion) result in changes to the polymer’s electronic properties

and thus changing the colour of the material.⁴ CPs have advantages such as the ability to finetune band gap, high colouring efficiency and contrast and fast switching speeds.⁶⁴⁻⁶⁷

Unfortunately, transmissive states of electrochromic polymers are rarely reported. Electrochromic responses are either between two differently coloured states, or between a dark and yellowish or white transmissive state.⁶⁸⁻⁷² Although transparent CPs exist, they may not be electrochromic themselves. They are instead used as electrodes for the construction of flexible devices.⁷³ The lack of a visually colourless state is a large disadvantage of CPs in the application for Smart Windows.

For organic polymers to achieve a contrast ratio of over 60%, thick films of over 1 μm are often required which comes at a detriment to switching times between coloured and non-coloured states.⁵⁵ Polymer films are also susceptible to degradation if there is a large amount of charge insertion and deinsertion.⁶⁴ Size changes and cracking of electrode with cycling (mechanical breathing) are a large issue, which effect the lifetime of organic film electrochromic devices. This issue arises from electron transport and ion intercalation in a redox active material, Figure 1.4.⁷⁴

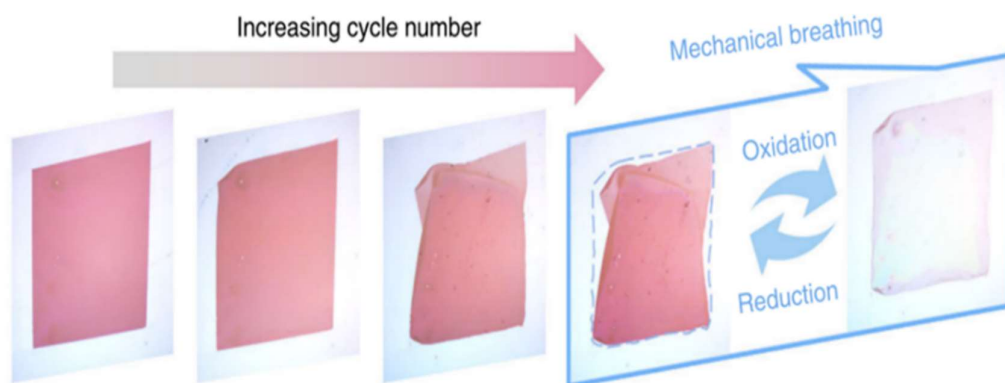


Figure 1.4. Experimental observation of mechanical breathing of a film and after every 60 cycles reproduced from Wang *et al.*⁷⁴

The multicoloured aspect of polymer systems is an advantage in electrochromic applications such as displays (although this ability is not essential for Smart Windows). Multicoloured responses can be achieved by systems with different reduction processes produced by; metal centred and ligand centred reduction,⁴ different states of oxidation or reduction or different ratios of mixes, Figure 1.5.⁷⁰

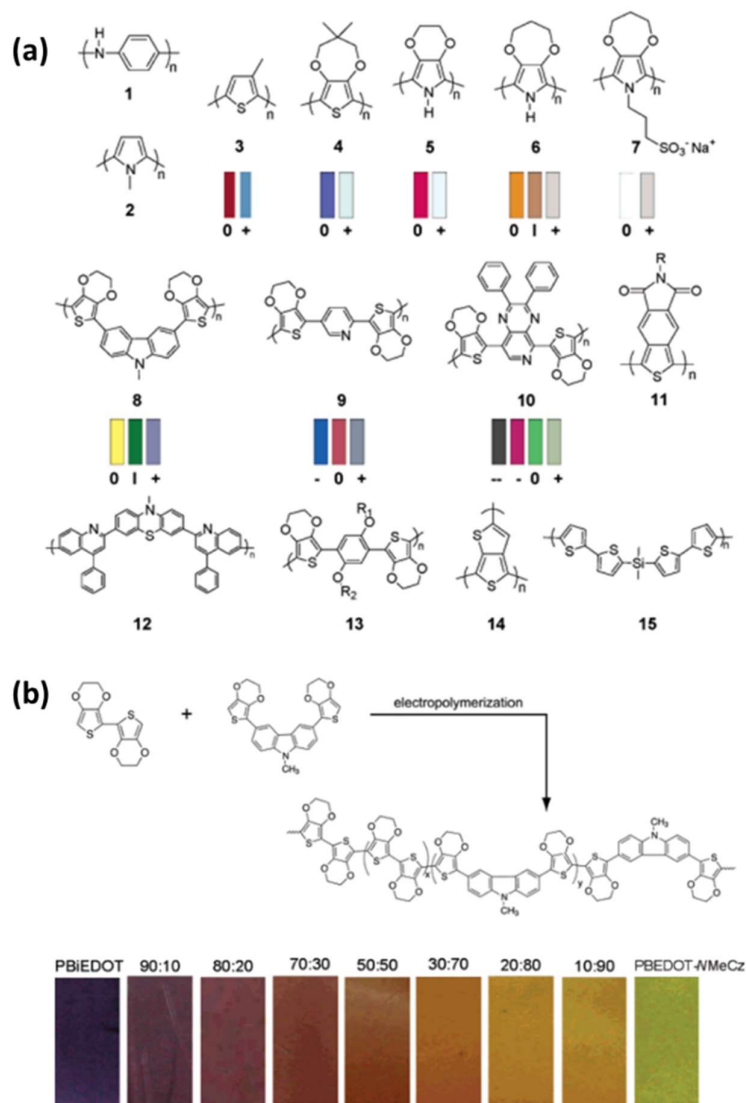


Figure 1.5. (a) Representative electrochromic polymers. Colours are representations of thin films based on measured CIE 1931 Y_{xy} colour coordinates. 0 = neutral, I = intermediate, + = oxidised - and -- = reduced states. Reproduced from Argun *et al.*⁷⁰ from a compilation of reported systems^{75–92} (b) Chemical scheme of electropolymerisation formation of a copolymer.⁹³ Photographs of neutral copolymer films on conductive glass with varying ratio of component parts.⁷⁰

Another category of polymer-based devices is a polymer gel. Polymer gel electrolytes are a combination of copolymer, electrolyte and high boiling point solvent (such as butane-1,4-diol). One of the key advantages of a polymer gel electrolyte is that these systems can be “self-sticking”,⁹⁴ eliminating the need for binders to stick onto an electrode surface. This property also facilitates a system that stands up to some amount of mechanical strain. These systems demonstrate good ionic

conductivity and tuneable mechanical properties.⁹⁴ However the solvents used may be harmful. Gelation can also require additional processing such as heating to high temperatures, which may not be practical on a large scale. Scalability must be considered, for example, while methods such as electropolymerisation are suitable for low surface area films, they may be unsuitable for larger areas.⁹⁵

The flexibility of polymer devices is advantageous. Wang *et al.* reported a co-assembled nanowire network used to produce flexible transparent electrochromic devices.⁵⁶ Films could be bent more than 1000 times without significant reduction in performance. The level of colouration could be tailored by stacking layers of film and a dark blue reversible electrochemically induced colouration was achieved.⁵⁶ Flexibility, although not essential for Smart Windows, could have potential application in displays or wearable technologies^{17,56,96,97} giving organic systems another advantage over TMOs. The use of films could also mean that technology could be added to existing windows as a coating rather than replacing the whole windowpane, another advantage to reduce set-up costs.

Polymers have many advantageous properties, but their sensitivity to common weather conditions can make them unsuitable for Smart Windows. Issues have been reported where device stability is compromised by oxygen or moisture.⁹⁸ Moisture is likely to be a particular issue due to rain and condensation formed by the difference in outdoor and indoor temperature. Some devices must be made inside glove boxes, which is unsuitable for a scale up.⁹⁸ Electrochromic polymers can also degrade under UV irradiation.³⁸ This property poses an issue of durability as well as suitability for use in Smart Windows, which are exposed to UV radiation regularly in the form of daylight.

1.3.3 Small organic molecules

Many organic species have redox states with distinct electronic absorption spectra that absorb along the UV-visible region.⁹⁵ Organic compounds have many advantages over inorganic oxides. Domination of the field by TMOs is most likely due to initial reports of organic electrochromic materials suffering from secondary reactions during switching between states.⁹⁵ More stable systems have since been reported.⁹⁵ With precious metals being mined from the Earth (posing many social and environmental issues⁹⁹) a move towards organic materials which can be sourced from more sustainable feedstocks³⁶ could be a better, 'greener' approach to this field. One report found that 84% of Pt resources and 70% of Co resources are located in "high-risk contexts".⁹⁹

Advantages of organic systems include processability, fast switching times, multiple coloured states, colour tunability, switching stability, high colouration efficiency and a great variety of colours.^{100,101} Surface-bound organic electrochromes have been reported to demonstrate better colouration efficiency and switching responses than TMOs.⁶⁹

Small organic molecules can demonstrate chromic effects *via* multiple processes such as redox, isomerisation, bond breaking or forming. These processes are not all triggered by application of a potential.¹⁰² Small organic molecules have an advantage over larger systems such as polymers in terms of facile production and low cost.^{70,103} Polymers have faced challenges related to efficient electrochemical bleaching and can require extra processing such as doping.

Organic systems can suffer from degradation (from mechanical stress, UV exposure or moisture) and slow kinetics.¹⁰² These drawbacks could affect reversibility and processing costs. Thermal instability can also be an issue.¹⁰⁴ However, these disadvantages are not the case for all organic systems.

Polycyclic aromatic hydrocarbons (PAHs) have been reported to exist as stable species (stabilised by resonance structures) with the addition or removal of an electron. Neutral PAHs are mostly colourless as they have large HOMO-LUMO energy gaps.¹⁰⁵ In charged states however, they are highly coloured. As both reduced and oxidised species are stable, these systems can be dual coloured. A reported system using perylene can exist in a blue, olive and pale yellow colour in anionic, cationic and neutral states respectively.¹⁰⁵ A large variety of PAHs exist and some have been reported to show electrochromic behaviour in organic solvents.^{106,107} A disadvantage is that some of these reported systems are dissolved in tetrahydrofuran¹⁰⁷ which is flammable and a health hazard.

1.3.3.1 Self-assembling systems

Small organic molecules often have the ability to self-assemble into stable, complex structures or networks^{108,109} through non-covalent molecular (intra- and inter- depending on the size of the molecule) interactions such as electrostatic attraction, Van der Waals forces, π - π stacking and hydrogen bonding and/or through solvent interaction with phobic/philic parts of the system.^{108,110-112} This process occurs either spontaneously (thermodynamic and kinetically driven¹¹³) or in response to a trigger (for example, a change in solvent or pH).^{108,114} A variety of shapes can be formed depending upon the systems used and some can be seen in Figure 1.6.

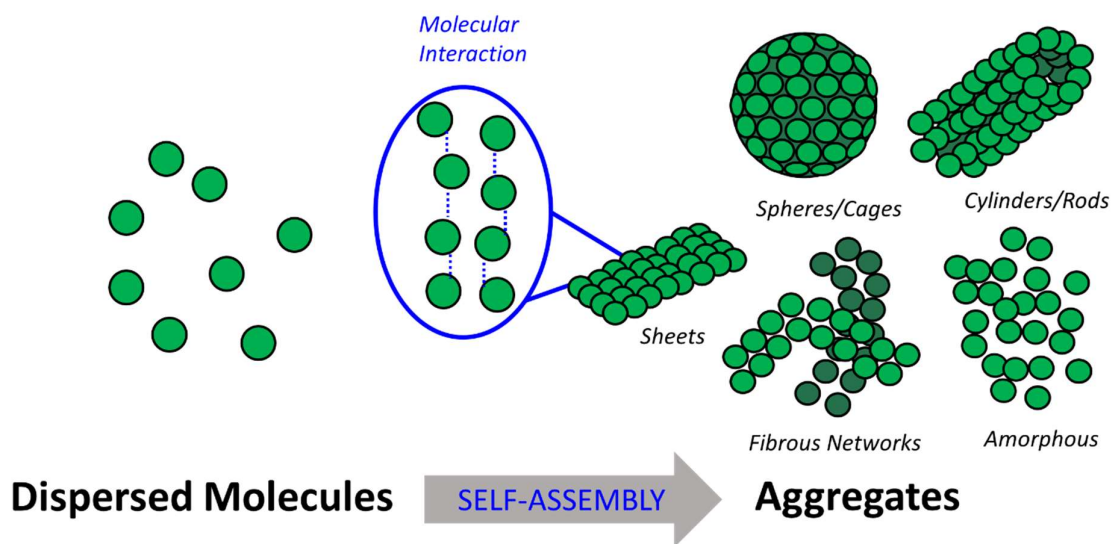


Figure 1.6. Cartoon of self-assembly into a variety of structures.

The interactions holding together these assemblies are weaker than covalent bonds and more labile.¹⁰⁸ The assemblies can therefore be easily changed, broken apart or reformed by changing the chemical structure of the molecules, changing solvent, adding components, or adding energy to the system.¹¹³ This tunability has made organic self-assemblies attractive to different fields of research such as pigments, sensors, bioprobes, and photovoltaics.¹¹⁵

Host-guest chemistry is also utilised in multicomponent systems where one molecule can fit inside of a larger structure or self-assemble with another.¹⁰⁸ Such co-assembly can be useful in donor acceptor systems, where assembly can affect photophysical and charge transfer properties.^{116,117} Larger assemblies and networks can be made up of smaller parts and linked together by entanglement or salt bridging.^{108,111,118,119}

The self-assembling nature of small organic molecules has some advantages for electrochromics. Assembly can be tuned simply by alteration of functional groups or chemical structure or lengthening of a repeating unit.⁶¹ Formation of fibrous networks has also been shown to be able to aid electron transfer and result in more efficient redox reactions.¹²⁰

1.3.3.1.1 Characterisation

The self-assemblies of small organic molecules are commonly measured with a variety of techniques. Depending upon the specific systems, each technique has different advantages and disadvantages. Some common examples are absorbance spectroscopy,^{121–127} nuclear magnetic resonance (NMR) spectroscopy,^{128–132} rheology,^{133–138} dynamic light scattering (DLS),^{114,139–143} small angle scattering (SAS),^{136,144–150} circular dichroism (CD),^{151–156} and microscopy.^{142,143,157–160}

Absorbance spectroscopy is an effective technique to probe molecular packing¹⁶¹ but cannot tell information about the specific structures formed (i.e. a sphere, a cylinder, a sheet etc). Similarly, NMR spectroscopy is a useful *in situ* technique to assess the kinetics of assembly but cannot tell information about the types of aggregates forming. Instead, this technique can provide information about the percentage of molecules that are assembled (for example over the course of gelation).¹²⁹ Absorbance spectroscopy is of particular use in chromic materials as it can be used to assess how much of the visual spectrum of light is absorbed or transmitted by a sample as well as noting any significant aggregation changes. However, the absorbance wavelengths of some systems are out of the range of a spectrometer, and highly coloured dyes can be challenging to measure even at relatively low concentrations.

CD can give information about packing and chiral assemblies¹⁶¹ and is most commonly used in biochemical fields, for example to assess the secondary structures of proteins.¹⁶² CD can also be used to monitor gelation of chiral monomers.¹⁶³ However, properties such as turbidity, birefringence and anisotropies of the sample may “seriously affect the data”.^{163,164}

The rheological properties of gels can be indicative of network type and rheology can be used to understand the kinetics of assembly.¹⁶¹ Trends in viscosity with shear or the magnitude of viscosity can indicate the presence of micelle assemblies or of networks.^{165,166} Similarly to absorbance and NMR spectroscopy, we cannot infer specific information about the structures. This technique provides information about bulk properties only.

Optical microscopy is not commonly used to assess self-assembly due to the need for very large structures. Fibrous structures can be imaged using scanning electron microscopy (SEM) or transmission electron microscopy (TEM) to give information about fibre thickness or porosity. The drawback of this technique is that drying is required which means one may not gather a true representation about the sample in solution or gel state.^{160,167–169} The use of a stain in TEM can also change structures during imaging.¹⁶¹ For electrochromics, where a background electrolyte is often required, the presence of salt would not be conducive for drying samples. Another issue with microscopy as a technique is that it could be challenging to see the structures of smaller aggregates (in other words, if a well-defined fibrous network is not formed as in gels). Alternatively, if a multicomponent system is used, it can be challenging to determine components from each other, although some examples are reported.^{170–172}

DLS and SAS are both scattering techniques. SAS is the most commonly reported technique for assessing the self-assembly of small organic molecules. This technique will be discussed in more detail later in this chapter. As a non-destructive technique which measures aggregation in the sample

without pre-processing, over a variety of length scales, it is an attractive tool with some drawbacks such as the time scale of measurement and availability of neutron and X-ray sources. DLS is effective in assessing the size of aggregates but cannot discern molecular organisation and structure.¹⁴¹ It is a more readily available instrument but is more suited for spherical particles than more complex aggregate types. DLS can also be sensitive to impurities in the sample such as dust.

The best understanding of structures comes from a combination of bulk measurements with molecular level measurements. By combining techniques, a variety of length scales of assembly can be investigated, giving as much understanding as possible for each system.

1.3.3.2 Viologens

Viologens are salts of quaternised 4,4'-bipyridine. The starting material for viologens (4,4'-bipyridine) is readily available and synthetic routes are relatively simple.¹⁴ Viologens dominate the organic electrochromic field^{4,14,32,38,173–180} due to the intense colour (attributed to optical charge transfer between nitrogen atoms with different valences)^{95,14,176,177,181,182} of their radical species. The radical cations of viologens are stable due to delocalisation of the radical electron throughout a π -framework, Figure 1.7.^{16,95}

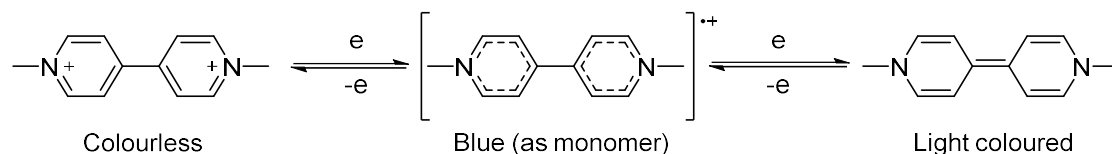


Figure 1.7. Example of viologen in the dicationic, radical cationic and neutral state.

The functionalisation of viologens influences colouration, which makes them easy to tune. For example, alkyl groups promote blue or violet colours and aryl groups promote green colouration,⁹⁵ Figure 1.8. Dimerised viologens also have different spectral properties to monomers, exhibiting very different coloration in some cases.⁹⁵

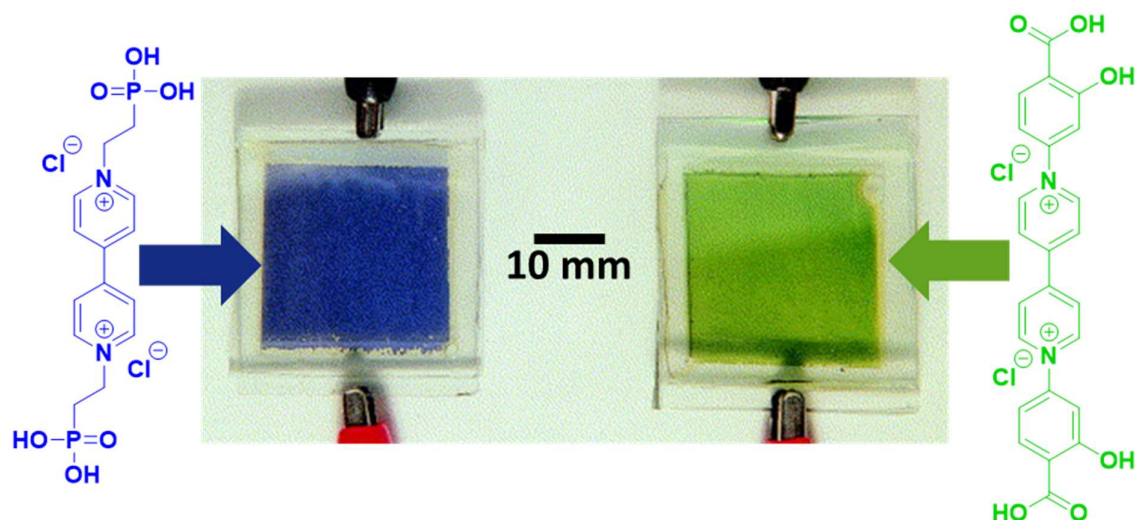


Figure 1.8. Colour change from transparent achieved using a TiO_2 moderated film alongside corresponding chemical structures (colour coded) Adapted from Cinnsealach *et al.* (chemical structures and scale bar added to figure).¹⁷⁶

Viologens are also capable of multicoloured responses when different potentials are applied corresponding to different states of reduction and oxidation, and mixing multiple species together can increase the number of colours achieved, Figure 1.9.¹⁸³ There are many examples of viologens as modified films^{173,184–186} or gels^{32,94,187–189} used in electrochromic devices but solution based devices are less commonly reported due to issues such as leakages and side reactions.¹⁷³

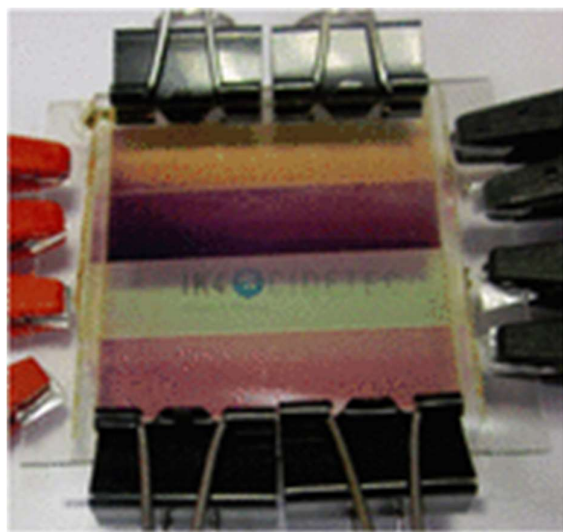


Figure 1.9. Images of the device reported by Alesanco *et al.* demonstrating multicoloured responses.¹⁸³

Switching times may rely on diffusion rates which can slow the chromic changes.¹⁹⁰ Fading in intensity of colour and poor cyclability long term efficiency are also issues.^{179,180,185} Prolonged cycling has been reported to cause irreversible colouration.¹⁹¹ Viologen systems can often form a residue due to crystallisation (which is referred to as ageing).^{102,185} Sometimes ageing causes colouration to appear patchy within films, which causes a “ghost image”.¹⁸⁵ Redox mediators such as hexacyanoferrate can resolve these issues; adding cost to the system.⁹⁵ Unfortunately, mediators themselves can cause coloured residues or precipitates.¹⁸⁵

Incomplete conversion to a transmissive state can also be compromised by the presence of side reactions.^{189,192} These side reactions (such as dimerisation) occur during the electrochemical operation. Such side reactions can cause “incomplete bleaching” of the highly coloured viologen radical cation.¹⁸⁹ This occurrence can be removed by a number of approaches, for example, using bridging ions¹⁹³ or bulky substituents,¹⁹⁴ anchoring to a substrate¹⁷⁷ or incorporating a polymer network.¹⁹⁵ Aggregation of coloured viologen species can also cause issues with “bleaching”.¹⁸⁹ In cases like this, thermal curing is required to avoid this phenomenon which adds cost and additional processing to the system, which is a disadvantage to the application of Smart Windows.

In addition to cyclability issues, although highly coloured, viologens still may not be best suited for the application of Smart Windows due to a lack of neutral transparent state.⁹⁷ A colourless to coloured state is not always viable, rather coloured to coloured is seen. Some reported examples are yellow⁷² or white¹⁹² in colour. Some can appear transparent in a neutral state in a thin gap.¹⁸⁸ The intensity of colour is also not very powerful in non-radical states of viologens. This phenomenon is due to a lack of optical charge transfer or internal transition (which correspond to wavelengths in the visible region).⁹⁵ The toxicity of viologens is also a disadvantage¹⁹⁶ as concerns to public safety will likely outweigh most other advantages.

1.3.3.3 *Naphthalene diimides*

1,4,5,8-Naphthalenediimides (NDIs) are neutral, planar, chemically robust, electron-deficient and easily functionalised.^{197,198} They have many of the same advantages of viologens such as easy synthesis, high colouration intensity and stability of radical species through a π network, Figure 1.10. NDIs are easily photo- and electrochemically reduced to form their stable radical anion and dianion in high yield. These reduced species can be identified easily through absorbance spectroscopy or electron paramagnetic resonance (EPR) spectroscopy as well as by eye due to high colouration.^{197,199} NDI radical anions can be oxidised electrochemically or slowly relax over time.²⁰⁰ One advantage of some NDI systems (for example, those appended with simple amino acids) is that they are soluble in

water. Water is a cheap and benign solvent which is advantageous for Smart Windows. Aqueous systems are a greener approach to electrochromics and preferable to be used in public places.

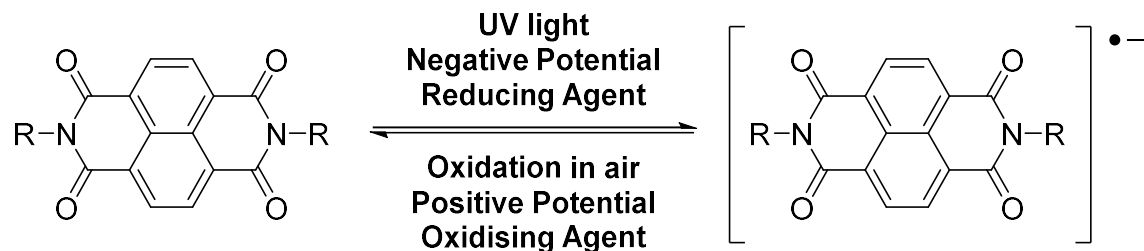


Figure 1.10. Redox states and triggers of NDIs.

The radical anions of NDIs are effective chromophores, absorbing strongly in the visible and near infrared regions.^{29,42,174,199} This property makes them well suited for application in Smart Windows. Zheng *et al.* reported an NDI-based gel which undergoes colour changes from brown to purple upon electrochemical reduction.²⁰¹ These colours can be characteristic of the radical anion and dianionic species of NDIs respectively.^{199,201} Pink and yellow colours have also been associated with the radical anion.¹⁹⁷

NDIs have been reported to give uniform, dark colour changes at low potentials that can be maintained without the need for constant application of potential.²⁹ Low potentials not only save energy consumption, but also prevent degradation and are safer to use.¹⁹⁷ Reducing the magnitude of potential required for colour change (as well as the frequency of applying potential) gives NDIs advantages over viologens. Viologens require bursts of potential in order to replenish dark colouration in aqueous systems.^{95,179} A replenishing potential is required as the coloured species diffuse into bulk solution easily and are quenched by water.^{95,179}

NDIs can self-assemble into a variety of structures in solution depending on solvent and chemical structure. NDIs have been reported to form assemblies such as π -stacks,^{174,197,202} nano-tubes, honeycomb like structures and nano-sheets¹¹⁶ as well as vesicles,²⁰³ nano-belts and microcup structures in chloroform.²⁰⁴ This variety of structure is an advantage of self-assembling organic molecules generally. Self-assembly can be achieved spontaneously as well as through methods such as metal-ion coordination and solvophobic control.¹⁹⁸ Influencing assembly by external stimuli as well as changes within the molecules chemical structure or functionalisation is facile for small organic molecules such as NDIs and tuning ability can be used to fit to a set of criteria for a commercial product.^{116,200,204,205}

Certain NDIs can form organogels²⁰⁶ and hydrogels,²⁹ a property which allows them the additional advantage of application in patterning, Figure 1.11. Due to slower diffusion rates, gel-based devices hold the shape of a pattern for longer than solutions. The photo- and electro-chromic sensitivity of NDIs allow multi-stimuli systems which can respond to light as well as on-demand electricity. This is an advantage for Smart Windows as it facilitates a dual trigger, meaning the windows could be automatically tinting as well as responsive on demand.

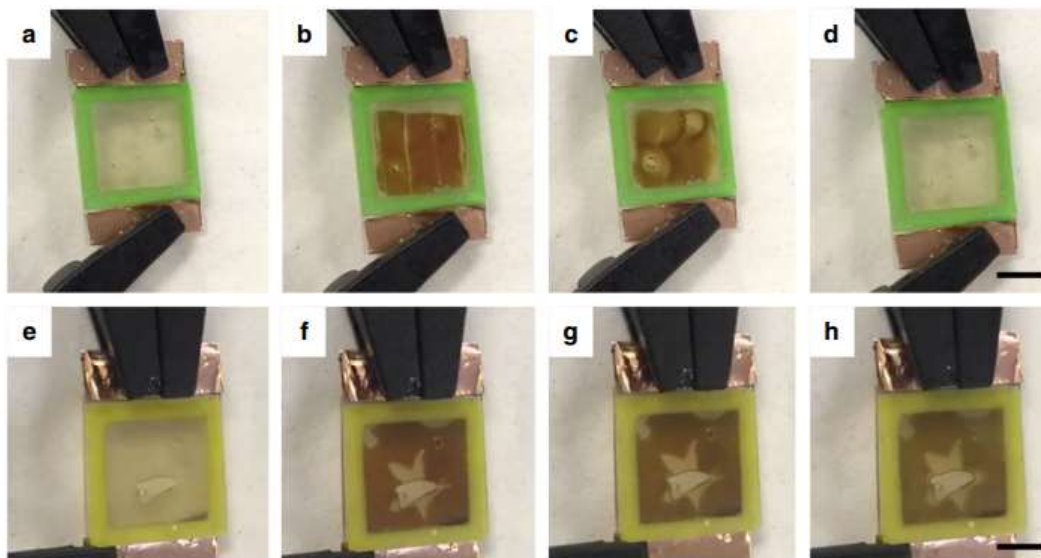


Figure 1.11. Patterned solutions (a–d) and gels (e–h) of an NDI based electrochromic device as reported by Gonzalez *et al.*²⁹ a and e show the initial solution and gel, respectively. The photographs were taken at 0 minutes (a and e), after 1 minute (b and f), 5 minutes (c and g) and 10 minutes (d and h) after applying a reducing potential. The scale bar represents 1 cm.

NDIs have not been as commonly reported as viologens, although some examples with good cyclability have been reported.^{207,208} Viologens may be preferred because the range of colouration is not as wide or because some examples of NDIs show weak colouration.^{208,209} However, in an ideal Smart Window, only a transition to a dark colour is required. Another reason may be this class of molecule is more commonly reported as part of semiconducting applications.^{210,211}

The chromic properties of NDIs have been used in combination with metal organic frameworks (MOFs)^{207,212–214} to form chromic systems but MOFs can be challenging and costly to synthesise and sometimes the colour change by eye is weak in such systems.²¹⁴

The highly pale colour of neutral NDIs makes these devices appear almost transparent to the eye in a thin gap,^{29,207,208} Figure 1.11(a and e). The coloured state of devices can be highly contrasting.^{29,199,207,212,215} Both of these factors are very great advantage for the application of Smart Windows. NDIs have great potential but are not commonly reported as Smart Window systems.

1.4 Aqueous systems

Many electrochromic systems operate within organic media (polar organic solvents are conventionally used as electrolytes due to high dielectric constants needed to facilitate ion migration^{35,174}). The use of volatile or harmful solvents (organic solvents are very commonly skin irritators or harmful if inhaled or swallowed)²¹⁶ offsets some of the advantages of organic materials such as their derivability from renewable resources.³⁶ Such hazards will increase the safety procedures required during scale up and will be more harmful if products were to leak or break. Some systems can alternatively be dissolved into an aqueous solution.²¹⁷ In general, these systems are more likely to be organic.

Using any solution as an electrolyte can cause issues and challenges with device set-up. Common problems include leaking, containing the solution whilst sealing²¹⁸ and bubbles or gaps in the filling process. Hydrogels are an example of aqueous systems which can solve issues such as leakage.^{29,49,219} For example, a reversible thermally triggered system using hydroxypropyl methyl cellulose switches between optically clear and opaque states.²¹⁹ The reported system uses an application of 8 V through a tin mesh to generate the heat required for this process. This potential is very high and energy intensive which is non ideal for Smart Windows.

Aqueous solutions have restrictions in operating potentials of approximately ± 1 V due to water limits.²²⁰ Another limit is that the temperature range of water as a solvent is acceptable for buildings but unsuitable for automotive glass.²²¹ The drop in temperature in winter could prove a complication for aqueous systems due to freezing. One solution is that adding ethanol or glycerol to aqueous electrolytes can aid functionality in cold temperatures by lowering the freezing point.²²²

Water soluble systems are, nevertheless, preferable to organic systems. Volatile or toxic solvents are hazardous and unsuitable for Smart Windows. Conventional liquid electrolytes using organic solvents can also have issues with contamination.⁹⁴ Furthermore, as aqueous systems offer advantages such as minimised cost, ease of handling and disposal, environmental friendliness and safety to the public, and so would be good candidates for Smart Windows.^{64,65}

Solution-type electrochromic devices are not always possible. CPs can become redox-inactive when interfaced with aqueous salt solutions⁶⁵ and are commonly non-aqueous due to the hydrophobic nature of some polymers. Side chain modification with amide functional groups has been reported as a way to facilitate aqueous systems for CPs.⁶⁵ Water soluble polymer-based electrolytes have some

disadvantages. Their thin films often need post-modification in order to prevent delamination or dissolution in aqueous electrolytes.²²³

Dimerisation of viologens is particularly prevalent in aqueous solutions.⁹⁵ The electro-oxidation of the radical cation dimer of a viologen is slow and therefore this phenomenon effects switching times of aqueous devices.⁹⁵ It has also been reported that the efficiency of displays based on short-alkyl chain viologens in aqueous electrolytes is lowered by the coloured species diffusing away from the electrode surface due to high solubility.^{95,224} Aqueous environments also facilitate quenching of the viologen radical by H₂O and O₂.¹⁷⁹ This quenching gives rise to a requirement of a continuous small current in order to replenish the coloured state.⁹⁵ This drawback should be considered a flaw of viologen systems rather than a disadvantage of solution-type devices.

Metal based aqueous devices have been reported but are not common. Using water as a solvent is an issue in such systems as electrochemical redox of metal compounds is usually performed at high potentials which would cause H₂ production from water and cause bubbles.²²¹ More oxophilic metals have a greater likelihood of irreversibly forming metal oxides on the surface of electrodeposited metals as well as insoluble hydroxides in basic solution.²²¹

Huang *et al.* reported a pH-tunable aqueous electrolyte which exhibits electrochemical switching in pseudocapacitive devices *via* reactions of Co₃O₄.²²² This system relies on two redox reactions converting between Co²⁺ and Co³⁺ or Co³⁺ and Co⁴⁺. "Large amounts" of OH⁻ ions are generated and used up as a potential of ±0.5 V is applied.²²² Colour changes (pink, blue and yellow) in this system are brought about as the pH of solution changes.²²² The yellow colour change is not particularly intense, Figure 1.12(c). This chromic effect is facilitated by pH indicators (phenolphthalein, thymolphthalein and 3-nitrophenol) which allow different three colour changes, and mixing of the indicators could allow a further range of colours. An issue with this system is the chemical stability of the pH indicators is poor due to the application of high voltages and CO₂ dissolving into the electrolyte.²²² Another issue is that the bleaching process takes 10 times as long as the colouring process (100 and 10 seconds respectively) which is not ideal.²²² This difference is due to ion diffusion processes.

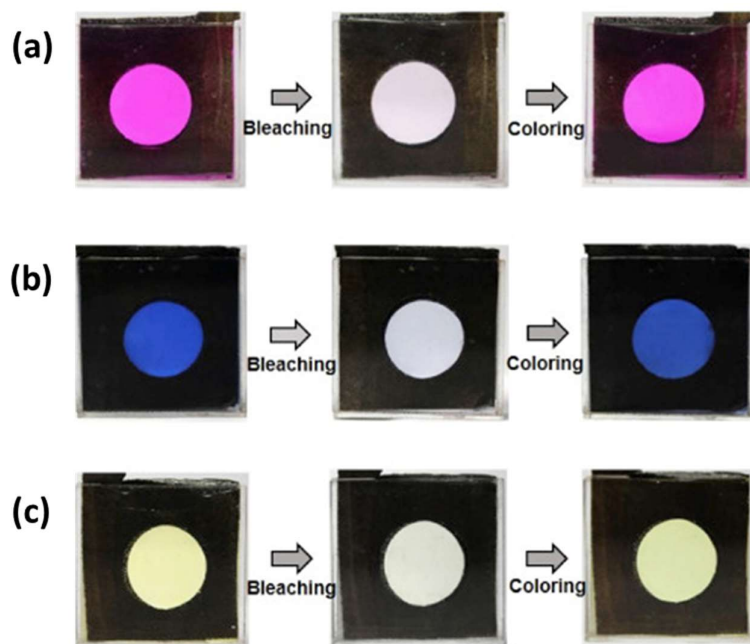


Figure 1.12. Photographs of the colour change in one cycle including bleaching and colouring processes with the applied voltages of +0.5 V and -0.5 V. Systems contain acid-base indicator, (a) Phenolphthalein, (b) Thymolphthalein and (c) 3-Nitrophenol. Reproduced from Huang *et al.*²²²

Metal based electrochromic windows have been reported using an aqueous media (agitated to form a gel electrolyte) using metal deposition and dissolution to form coloured and transparent states.²²¹ This system provides a high contrast transmissive to dark colour change and so is a very good candidate for Smart Windows, Figure 1.13. Such examples shows that aqueous based systems can yield promising results and that such choices can be made to maximise the safety and minimise the cost of such systems if they were to be scaled up. Lower cost is of particular benefit to metal containing systems, which can be very costly.

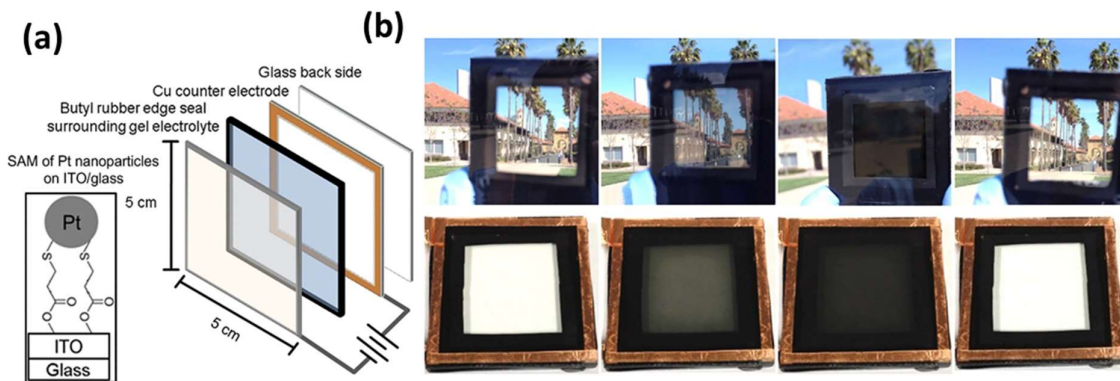


Figure 1.13. (a) Schematic of a 25 cm² 2-electrode window containing a Cu-Ag gel. (b) Photographs of the window during switching outside (top) and inside with a white background (bottom) after 0, 15, and 30 seconds of metal electrodeposition by applying -0.6 V and subsequently 30 seconds of metal stripping at 0.8 V (from left to right). Reproduced from Barile *et al.*²²¹

1.5 Transmissive to dark materials

It is not common for one system to be able to transmit and/or absorb all the visible region of light on demand. It is challenging to synthesise or fabricate materials with the significantly large band gap required to be both transmissive and broadly absorbing in bleached and coloured states.^{55,63} A transparent native state is also hard to achieve, with a light yellow being commonly seen and accepted.²⁴ The transition from transparent to black has been referred to as the “holy grail” of organic optoelectronics.²²⁵

The transition from a transmissive state to a coloured state is essential to Smart Windows and a visually transparent to black transition is the most aesthetically pleasing. Transition between two coloured states compromises the visibility through a window. Black is a neutral colour and is associated with privacy windows already and so this transition would be most desired for a chromic window device.

The transmittance of the window must be sufficiently altered in order to achieve significant energy savings and so a high contrast between states is important.²⁴ Grey or black coloured devices can filter light in an effective way. However, colourless to black or grey electrochromic materials are challenging due to slow switching responses and issues tuning absorption properties.³²

Transmissive to black electrochromic films have been prepared from aromatic polyamides¹⁰¹ which are soluble in organic solvents. Although this material shows broad absorbance in the visible and near

infrared region, the colouration is not dark enough for an application in Smart Windows and the use of organic solvents is a disadvantage.

One strategy to achieve a transmissive to dark colour change was reported by Hernandez *et al.*³⁸ Reversible metal electrodeposition was used to achieve a uniform black colour. This colouration was facilitated *via* electrochemical reduction of metal cations in the electrolyte of the window to a film. Windows based on this method of electrodeposition tend to suffer from poor durability if scaled up to areas beyond 1-4 cm².³⁸

Single electro-chromophores are not common in transmissive to black devices. Sometimes two colouring materials are instead used.⁵⁵ An example of a single electro-chromophore is reported by Nguyen *et al.*⁵⁵ based upon *p*-aminotriphenylamine anchored to a mesoporous Sn-doped In oxide (ITO) electrode surface. This system achieved fast switching times of 4 and 2 seconds and contrast ratios of 64% but still required additional steps such as annealing and drop casting.⁵⁵ The colour change itself is also not of very high contrast as an image can still be seen through the glass, Figure 1.14. Depending upon requirements, this factor could be a disadvantage to Smart Windows.

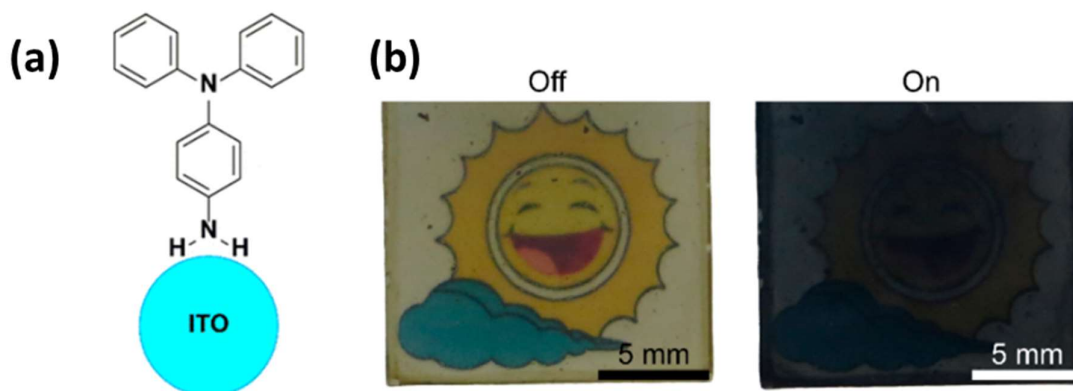


Figure 1.14. (a) Chemical structure of the reported *p*-aminotriphenylamine system (b) photographs of the off (-0.47 V vs Fc/Fc+) and on states off state and coloured on state (1.13 V vs Fc/Fc+). Reproduced from Nguyen *et al.*⁵⁵

This system has poor cyclability, with solution becoming “progressively bluer during electrochemical cycling”.⁵⁵ There is also partial loss after 50 cycles and complete loss after 270 cycles⁵⁵ of switching performance due to deterioration of the scaffold of mesoporous ITO. A long life time is required for a Smart Window to warrant the initial set-up costs. A radical cation is responsible for a black state in this system. It is generated upon oxidation which itself means that oxidation in the air could discolour

the device. This occurrence is a disadvantage in Smart Windows as colouration should be on demand. As the transmissive state is seen upon application of a potential, a constant potential would be required to maintain a transmissive colour. This aspect is another disadvantage of this system.

Polymerised materials have been reported in black to transmissive devices. Copolymerisation, blending and layering is used in order to create a material which can absorb the largest amount of the visible spectrum.^{63,69} However, reported systems experience issues with cycling.⁶³

Switching from dark to light colouration is less suitable than light to dark states.^{70,94,226} As a transmissive state is likely the default state for a window, the energy expended maintaining that state in a dark to light system would offset the energy savings facilitated by a Smart Window. Safety hazards must also be considered with constant potential flow through windows.

1.6 Colour mixing and multicomponent systems

Some methods of achieving a transmissive to dark colour change are through colour mixing, multi-layered devices and multielectrode systems.^{32,227} By combining the absorbance in the visible region of multiple components, the device can appear closer to black by eye. Colour matching is an example of mixing components to create a complex system, combining the advantages of its constituent parts to achieve a specific colour transition. This can also be utilised to other ends such as multi-responsive²²⁸ or multi-coloured devices.^{12,229}

Mixing TMOs that give complimentary coloured states is a way to improve the contrast between states. For example, a charge transfer from Ni to W oxide darkens both species, thus increasing the intensity of colour change, which is a benefit.³³ The opposite charge transfer bleaches both species.

A reported example of mixing involves two processes with MnO₂ and Mo-doped WO₃ at two electrodes. These processes produce dark colouration (Mn³⁺ → Mn⁴⁺ and W⁶⁺ → W⁵⁺) which mix brown and blue respectively,³⁹ Figure 1.15. Bleaching/discharging processes yield the reverse. Combination of two metal species introduces additional cost and complexity into the system, which a single component system does not incur. The high potentials needed for this device would also result in a higher cost of operation. A compromise between performance and cost of production and operation is likely to be made on a commercial scale and so it is important to look towards more cost efficient alternatives to metal oxides.

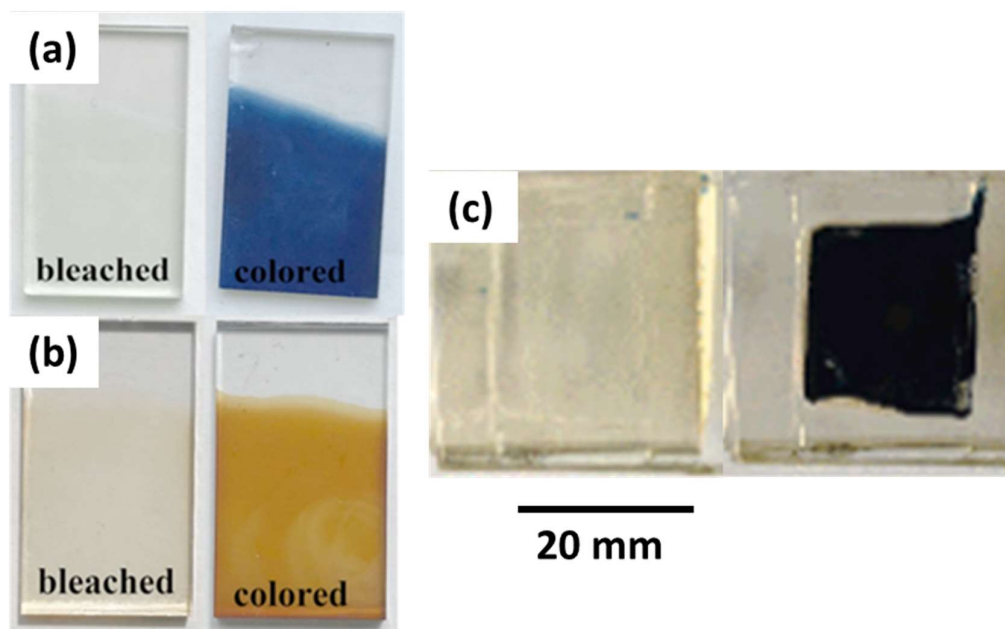


Figure 1.15. Colouration from MnO_2 (a) and Mo-doped WO_3 (b) separately and then combined (c) into a device on FTO glass with a Pt foil counter electrode. 2 V and -2 V vs Ag/AgCl reference applied to achieve the coloured and bleached state. Reproduced from Xie *et al.* (scale bar added).³⁹

Organic systems are sometimes mixed to achieve a black colour, for example, mixing anthracene and benzo {a} -pyrene. This system results in absorbance across the majority of the visible spectrum upon the application of -4 V, Figure 1.16.¹⁰⁵ This system uses tetrahydrofuran as its medium which is hazardous.²³⁰ Reported switching times are also not ideal (with dark colouration taking 5 minutes and reversal taking up to 40 minutes).¹⁰⁵ Similar to metal oxide mixing, the more components within a system, the more costly the production will be (depending upon the individual synthetic requirements of each component). Therefore, if systems are mixed, the benefit of mixing must outweigh this cost.

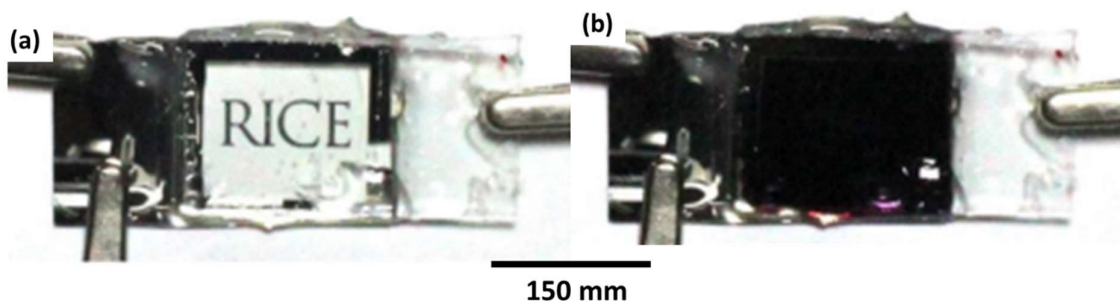


Figure 1.16. Colouration achieved in a device reported by Stec *et al.* (scale bar added)¹⁰⁵

Another example mixes an asymmetric viologen with a poly(2-isopropyl-2-oxazoline)-based molecule, utilising a combination of thermo- and electrochromic properties to achieve transmissive to black chromic changes.²³¹ This system achieved an intense black colour at 52 °C with application of 2 V. While an impressive transmittance change, the energy required to achieve this transformation is unlikely to be feasible and such high temperatures would not be conducive to use in a workplace.

Mixing organic and metal systems is another method to produce dark colouration. These systems can utilise MOFs and modified metal oxide films.^{70,173,174,212,232} However, there are issues with such hybrid devices, as some show poor cycle reversibility, lack of tuneability and low colouration.⁴⁷

A transparent to dark device using a MOF with an incorporated NDI was reported.²¹² The colour change speed was faster than comparable TMOs such as WO₃ (which sometimes need up to minutes to produce a colour change).^{52,233,234} The speeds were also comparable to polymeric electrochromic materials.^{233,234} This reversible colour change was found to yield the darkest reduced state with Ni and a 1:1 ratio of the NDI radical and dianionic species. MOFs are not commonly used within electrochromics due to difficulties with processing.²¹²

1.6.1 Mixing for other reasons

The mixing of components is not always for colour matching. Sometimes the physical properties of one component can be combined with a chromic system to yield a new device. For example, utilising the gelating, or film flexibility of a component whilst maintaining the chromic properties of another. A UV-crosslinked ethoxylated trimethylolpropane triacrylate polymer network is used to immobilize a heptyl and phenyl viologen.¹⁸⁶ This device can achieve green, marine, transparent and grey-blue colouration with switching times of between ~1 and 12 seconds.¹⁸⁶ Solutions of this system do not perform well due to π - π aggregation of the viologen radical.¹⁸⁶ Therefore, the solid state properties facilitated by the polymer network are a solution to this problem.

The nature of polymers means that two or more molecules can be combined, bringing positive properties from both into the new system. Polymer networks allow different organic molecules to be combined into one system in order to achieve multicoloured electrochromics.^{102,186}

Combination is not always beneficial. Polymer and TMOs are used in the form of films as electrodes in a combined inorganic and organic electrochromic device. This combination is not always successful if the processes of each electrode are not complimentary. Colouration efficiency has been reported for such devices as lesser than the constituent parts of the device.⁴⁸ Design of such devices is an additional challenge which could be time consuming.

Multi stimuli responsive materials that are both electro- and photo,- thermo- or hydro-chromic (a colour change in response to moisture, such as humidity) have been highlighted in a recent Smart Window review.²²⁸ Dual functionality was also highlighted in this review, using examples of windows that generate power through photovoltaics or are self-cleaning or air purifying, improving ease of use in an office type setting.²²⁸ Such devices used dyes and liquid crystals or a mix of metal oxide layers within one device. Electrochromic windows with multifunctional chromic and power charging properties have also been reported with the ability to self-colour and bleach without the need for external potential which would give additional environmental and financial benefits over a long term (but the initial cost a such a multicomponent system is higher than a singular system).²³⁵

1.7 Measuring the structures formed from small organic molecules

As discussed, the aggregation of self-assembling molecules is crucial to their properties.^{111,122,128,204,236-246} Differences in structure can be linked to various properties, such as viscosity, gelation, conductivity, colour and stability. To better understand these relationships, it is important to use a technique that gives insight into aggregation that can be linked to experimental data. SAS is a highly effective technique to assess non-crystalline aggregates of a 1-1000 nm size.^{144,247} We gain insight into structure types and properties (such as radius and flexibility) by fitting SAS data, obtained from the scattering of neutrons or X-rays by samples, to theoretical models.²⁴⁸ Larger structures scatter at a smaller angle of around 0.1-10°.¹⁴⁴ The scattering is elastic and coherent meaning there is no net loss of energy. Incoherent scattering arising from the solvent can be removed by background subtraction during data processing. When neutrons/X-rays are scattering from a sample, Figure 1.17, the intensity of scattering at different length scales is a result of molecular weight, size of object and concentration¹⁴⁴ and is measured with varying scattering angle. The scattering variable Q which intensity is plotted against, is resolved by Equation 1.1:

$$Q = \left(\frac{4\pi}{\lambda}\right) \sin\left(\frac{\theta}{2}\right) \quad \text{Equation 1.1}$$

where λ is the beam wavelength and θ is the scattering angle.

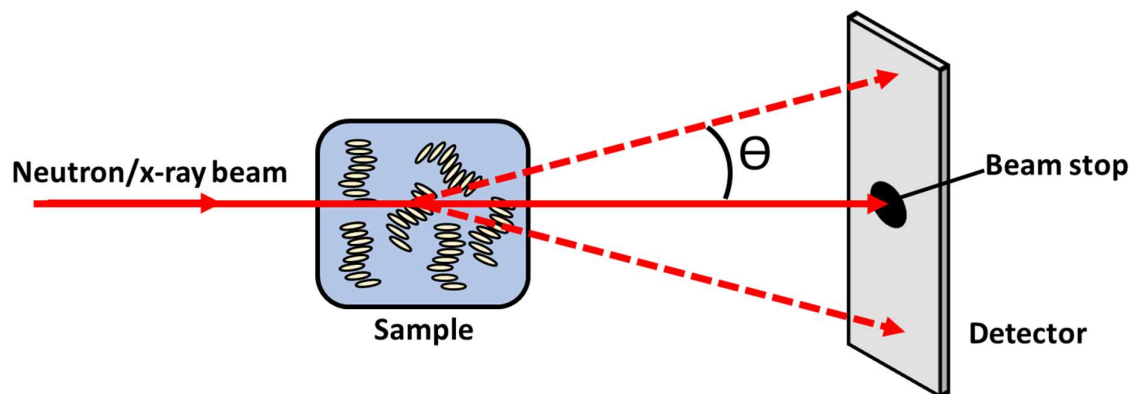


Figure 1.17. Cartoon representation of SAS. θ is the scattering angle of the beam from the sample.

Small angle neutron scattering (SANS) and small angle X-ray scattering (SAXS) have differences in sample preparations and various advantages and disadvantages. Neutrons interact with the nucleus (whereas X-rays interact with the electrons) of atoms²⁴⁷ but both techniques are comparable in terms of the Huygens-like description of wave propagation. SAS is a highly beneficial technique as it allows measurement of aggregates over a variety of length scales, allowing insight into network level and molecular level interactions and aggregates.^{149,161,249–252} The sensitivity of SAS makes it an attractive tool to measure self-assembling organic compounds. It is highly penetrating whilst not destroying the sample and gives insight into structures, crosslinking and distribution in space that we cannot gain from techniques that give more insight into local assemblies like packing (absorbance, and CD).^{144,161,247}

Another technique to study aggregates is using imaging, however imaging is not always suitable and will not always give a true representation of the sample as previously discussed.^{167,253} It is also a possibility that there is a difference in bulk and surface aggregation which leads to unrepresentative, incorrect or misleading characterisation.²⁵⁴ By penetrating into the bulk sample, SAS overcomes this issue.

The disadvantage of SAS is that it requires a neutron/X-ray beam (typically using advanced and physically large facilities). While some lab sized SAXS equipment is available, both SANS and SAXS typically requires application for measurement time at a specific location with facilities such as a spallation source (SANS).

1.7.1 SANS vs SAXS

There are various advantages and disadvantages of SANS and SAXS which depend on the specifics of a given experiment and its requirements. For example, while SAXS is not damaging, some biological molecules are more susceptible to damage from X-rays than neutrons.²⁵⁴ SANS requires contrast between the scattering length density of the solvent and the object being measured. This contrast is

achieved by using a deuterated solvent which will not scatter as much as hydrogenated objects. In SAXS this contrast comes from a difference in electron density.²⁴⁸ Due to this factor, SAXS can be performed using standard aqueous solutions (the same solutions used in experiments in a lab) which is advantageous if samples have different properties in D₂O than H₂O. For example, the hydrolysis of glucono-delta-lactone (a common gelation trigger²⁵⁵) is different in D₂O than H₂O²⁵⁶ which could lead to differences in gel properties.

Contrast matching can be used to make specific parts of the sample less 'visible' to neutron scattering.^{144,149,254,257} By deuterating parts of the molecule synthetically or by altering the mix of D₂O than H₂O to match the scattering length density of one of the components, this technique facilitates in-depth analysis of multicomponent systems or a method of following processes such as gelation¹⁴⁹ or elongation rate of fibrils.¹⁵⁰

An advantage of SAXS over SANS is that it has a high flux and can perform measurements within seconds, whereas neutron scattering, depending on the source, can take an hour for a well resolved measurement. This timescale depends on the number of neutrons available and how well the samples scatter. Therefore, if an experiment uses SAS to follow a short period of kinetics²⁵⁸ or if a large number of samples is required, SAXS is a more appropriate technique. SANS kinetic experiments are more suited to long term processes occurring overnight or over several hours.¹⁴⁸

In situ SANS or SAXS is a highly advantageous strategy to track changes in self-assembly, combining all the advantages of SAS for analysing self-assemblies of small organic molecules with those of *in situ* measurement (being able to measure and track changes in a property in real time, without the possibility of disturbing or transferring the sample). *In situ* SANS is reported when measuring the response to an initial stimulus such as a change in temperature, pH, or stress. This method can be used to follow phenomena such as dealloying,^{253,259} gelation,^{148,260,261} or response to applied shear^{136,261–263} but could be restricted by timescales and data quality.

A field in which this technique is not highly utilised is electrochemistry. The use of spectro-electrochemistry (an *in situ* electrochemical technique combining electrochemistry with absorption spectroscopy) is common but the use of *in situ* scattering alongside electrochemical processes is not. This phenomenon is largely due to complex experimental considerations, such as electrolyte reservoirs and cells within the beamline.^{147,253} It is challenging to perform electrochemistry in a beamline (usually needing custom made cells²⁶⁴) and electrochemically active species may not have stability if a potential is not applied, meaning a cell must be in use for the whole measurement. Irradiated samples have been used instead if samples are photo-and electrochemically active.²⁹ However, this method is not always possible, relies upon the stability of the irradiated species (which

may not be the length of a typical SAS measurement) and whether photo- and electrochemically triggered species are comparable. A combination of electrochemistry and SAS would be useful for the study of small organic electrochromic molecules.

1.8 Introduction to the work in this thesis

NDIs show a lot of potential for the application of Smart Windows, but they are not widely studied for this purpose. An NDI based hydrogelator has been reported with the intention for this application by the Draper group.²⁹ This system combines the benefits of an aqueous system, small organic molecules, and transmissive to dark colour change, Figure 1.18. Such NDIs (appended with simple amino acids or dipeptides) have many of the properties set out as requirements for Smart Windows in 1.2.1. They can exist as a neutral transmissive and an intensely coloured state, and the transition is reversible. This colour change occurs uniformly, quickly (within seconds for the reduction and within minutes for the oxidation) *via* the application of potentials less than 3 V.²⁹

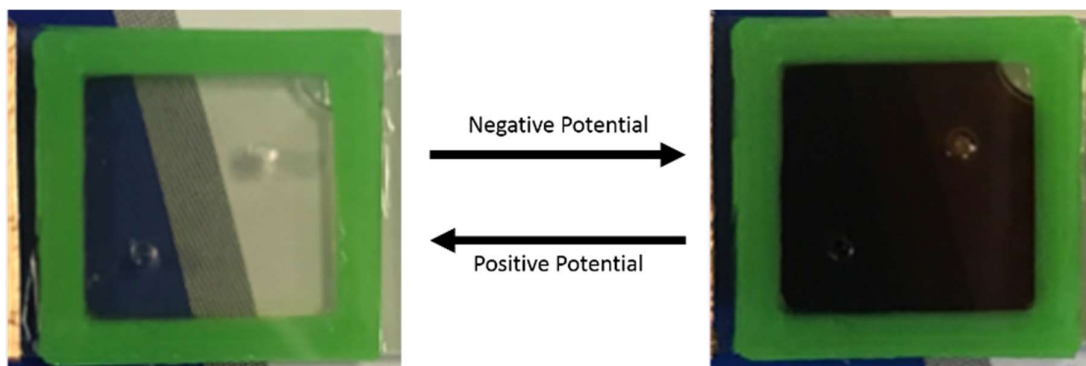


Figure 1.18. Transparent-to-dark colour change achieved hydrogel NDI based electrochromic device, reproduced from Gonzalez *et al.*²⁹

NDIs are also chemically robust, and so are likely to be stable within the operating temperatures of most buildings. NDI radicals have been found to be stable in aqueous solutions at high temperatures of 40-60 °C.²⁰⁰ The stability of the NDI radical means that an intense coloured state can be maintained without the requirement of constant application of potential and the simplicity of synthesis means that cost would be relatively low.²⁹ This factor is an advantage over aqueous viologens.

In order to compete with other Smart Window organic systems as well as TMO systems, on a commercial scale, NDIs need to prove that they can operate with the same or comparable colouration intensity, uniformity, switching times and cyclability.

As discussed, organic systems such as NDIs can self-assemble spontaneously into high-order organised structures. These assemblies are maintained by non-covalent interactions.^{265,266} These interactions are relatively weak and therefore structures can be influenced easily by factors such as pH (which creates

charge within a system) or adding different appended group to the molecule (that effect the attractive or steric forces that govern structure).²⁶⁶ The self-assembling nature of NDIs is of great interest as it has the potential to make these systems highly tuneable which is advantageous to Smart Window systems.¹⁹⁸

Continuing work from the reported system,²⁹ questions about tunability and durability can be investigated. Properties such as absorbance, stability, colour and efficiency of redox processes could all be affected by aggregation. NDI reduction has been notably affected by structure.^{211,267} No links have been made to colouration and aggregation, nor has tailoring or improvement of the set up and system been attempted. Other amino acid appended, water-soluble NDI systems not been investigated for this application to our knowledge.

The overall aim of this thesis is to evaluate how chemical structure and pH can be used to affect the chromic properties and/or stability of NDIs appended with amino acids/dipeptides (allowing water solubility). We believe these systems have great potential as a water-soluble organic alternative to TMOs and by understanding the relationship between aggregation and electrochromic properties, we can understand how to tune devices in terms of properties we would value in a Smart Window application.

1.9 References

- 1 J. W. Xu, M. H. Chua and K. W. Shah, Eds., *Electrochromic Smart Materials*, ed. J. Xu, M. Chua, K. Shah, Royal Society of Chemistry, Cambridge, 2019.
- 2 K. Ōtsuka and C. M. Wayman, *Shape memory materials*, ed. K. Otsuka and C. Wayman, Cambridge University Press, Cambridge, 1998.
- 3 S. R. Anton and H. A. Sodano, *Smart Mater. Struct.*, 2007, **16**, R1–R21.
- 4 P. R. Somani and S. Radhakrishnan, *Mater. Chem. Phys.*, 2002, **77**, 117–133.
- 5 M. Russo, US Pat., 0167989, 2002.
- 6 L. Aperfine, US Pat., 023716, 2004.
- 7 M. A. Invernale, Y. Ding and G. A. Sotzing, *Color. Technol.*, 2011, **127**, 167–172.
- 8 C. Ebejer, US Pat., 0313325, 2010.
- 9 L. Fuzhong, CN Pat., 203241171, 2013.
- 10 A. Vik, Michal, Periyasamy, *Micro. Nanosyst*, 2019, **11**, 154–164.
- 11 Y. Ke, C. Zhou, Y. Zhou, S. Wang, S. H. Chan and Y. Long, *Adv. Funct. Mater.*, 2018, **28**, 1800113.
- 12 R. Baetens, B. Petter Jelle and A. Gustavsen, *Sol. Energy Mater. Sol. Cells*, 2009, **94**, 87–105.
- 13 C. M. Lampert, *Sol. Energy Mater. Sol. Cells*, 1998, **52**, 207–221.
- 14 A. Donnadieu, *Mater. Sci. Eng., B*, 1989, **3**, 185–195.

- 15 M. V. Gandhi and B. S. Thompson, *Smart materials and structures*, Chapman & Hall, Bury St Edmunds, 1992.
- 16 R. J. Mortimer, *Annu. Rev. Mater. Res.*, 2011, **41**, 241-268.
- 17 C. G. Granqvist, *J. Eur. Ceram. Soc.*, 2005, **25**, 2907–2912.
- 18 P. Bonhôte, E. Gogniat, F. Campus, L. Walder and M. Grätzel, *Displays*, 1999, **20**, 137–144.
- 19 S. Hoseinzadeh, *Micro and Nanosystems*, 2019, **11**, 154–164.
- 20 C. G. Granqvist, *Eco-efficient Materials for Mitigating Building Cooling Needs: Design, Properties and Applications*, ed. F. Pacheco-Torgal, J. Labrincha, L. Cabeza, C. Granqvist, Elsevier Ltd, Cambridge, 2015, 442–471.
- 21 Ji, YX., Boman, M., Niklasson, G.A., Granqvist, *Nano and Biotech Based Materials for Energy Building Efficiency*, ed. F. Pacheco Torgal, Cinzia Buratti, Siva Kalaiselvam, Claes-Göran Granqvist, Volodymyr Ivanov, Springer, 1st edn, 2016, Thermochromics for Energy-Efficient Buildings: Thin Surface Coatings and Nanoparticle Composites, 71-96.
- 22 Y. Huang, B. Wang, F. Chen, Y. Han, W. Zhang, X. Wu, R. Li, Q. Jiang, X. Jia and R. Zhang, *Adv. Optical Mater.*, 2022, **10**, 2101783.
- 23 W. J. Hee, M. A. Alghoul, B. Bakhtyar, O. Elayeb, M. A. Shameri, M. S. Alrubaih and K. Sopian, *Renew. Sust. Energ. Rev.*, 2015, **42**, 323–343.
- 24 D. R. Rosseinsky and R. J. Mortimer, *Adv. Mater.*, 2001, **13**, 783–793.
- 25 N. DeForest, A. Shehabi, S. Selkowitz and D. J. Milliron, *Appl. Energy*, 2017, **192**, 95–109.
- 26 V. Torgal, F., Buratti, C., Kalaiselvam, S., Granquist, C., Ivanov, *Nano and Biotech Based Materials for Energy Building Efficiency*, Springer, eBook., 2016.
- 27 Y. Xu, C. Yan, S. Yan, H. Lui, Y. Pan, F. Zhu and Y. Jiang, *Energy*, 2022, **243**, 1222777.
- 28 N. Youngblood, C. Talagrand, B. Porter, C. G. Galante, S. Kneepkens, S. G. Sarwat, D. Yarmolich, R. S. Bonilla, P. Hosseini, R. Taylor and H. Bhaskaran, 2019, arxiv.org/abs/1911.02990.
- 29 L. Gonzalez, C. Liu, B. Dietrich, H. Su, S. Sproules, H. Cui, D. Honecker, D. J. Adams and E. R. Draper, *Comm. Chem.*, 2018, **1** (77), 1-8.
- 30 J. Pérez-Miqueo, A. Telleria, M. Muñoz-Olasagasti, A. Altube, E. García-Lecina, A. de Cózar and Z. Freixa, *Dalton Trans.*, 2015, **44**, 2075–2091.
- 31 E. S. Lee and D. L. Dibartolomeo, *Sol. Energy Mater. Sol. Cells*, 2002, **71**, 465–491.
- 32 Y. Alesanco, A. Viñuales, G. Cabañero, J. Rodriguez and R. Tena-Zaera, *Adv. Optical Mater.*, 2017, **5**, 1600989.
- 33 C. G. Granqvist, *J. Vac. Sci. Technol. B*, 2014, **32**, 060801.
- 34 R. D. Rauh, *Electrochimica Acta*, 1999, **44**, 3165–3176.
- 35 Y. Alesanco, A. Viñuales, J. Rodriguez and R. Tena-Zaera, *Materials*, 2018, **11**, 1–27.
- 36 T. A. Welsh and E. R. Draper, *RSC Adv.*, 2021, **11**, 5245–5264.
- 37 P. Shi, C. M. Amb, E. P. Knott, E. J. Thompson, D. Y. Liu, J. Mei, A. L. Dyer and J. R. Reynolds, *Adv. Mater.*, 2010, **22**, 4949–4953.

- 38 T. S. Hernandez, C. J. Barile, M. T. Strand, T. E. Dayrit, D. J. Slotcavage and M. D. McGehee, *ACS Energy Lett*, 2018, **3**, 24.
- 39 S. Xie, Y. Chen, Z. Bi, S. Jia, X. Guo, X. Gao and X. Li, *Chem. - Eur. J.*, 2019, **370**, 1459–1466.
- 40 Y. Alesanco, A. Viñ, J. J. J. Palenzuela, I. Odriozola, G. Germán, C. Ero, J. Rodriguez, R. Ramón, T.- Zaera, A. Viñuales, J. J. J. Palenzuela, I. Odriozola, G. Cabañero, J. Rodriguez and R. Tena-Zaera, *ACS Appl. Mater. Interfaces*, 2016, **8**, 14795–14801.
- 41 M. Li, O. A. Yassin, M. L. Baczkowski, X. Zhang, R. Daniels, A. A. Deshmukh, Y. Zhu, M. T. Otley and G. A. Sotzing, *Org. Electron.*, 2020, **84**, 105748.
- 42 Y. R. Huang and S. H. Hsiao, *Dyes Pigm.*, 2022, **199**, 110056.
- 43 Digital Imaging | Internet with a Brain, <http://www.web3.lu/digital-imaging/>, (accessed June 15, 2022).
- 44 Q. Zhao, W. Xu, H. Sun, J. Yang, K. Y. Zhang, S. Liu, Y. Ma and W. Huang, *Adv. Optical Mater.*, 2016, **4**, 1167–1173.
- 45 H. Sun, S. Liu, W. Lin, K. Y. Zhang, W. Lv, X. Huang, F. Huo, H. Yang, G. Jenkins, Q. Zhao and W. Huang, *Nat. Commun.*, 2014, **5**, 3601.
- 46 G. A. Niklasson and C. G. Granqvist, *J. Mater. Chem.*, 2006, **17**, 127–156.
- 47 P. Jittiarporn, S. Badilescu, M. N. al Sawafta, L. Sikong and V.-V. Truong, *J. Sci.: Adv. Mater. Devices*, 2017, **2**, 286–300.
- 48 S. S. Kalagi, S. S. Mali, D. S. Dalavi, A. I. Inamdar, H. Im and P. S. Patil, *Synth. Met.*, 2011, **161**, 1105–1112.
- 49 T. Gwang Yun, M. Park, S. Kim, D. Kim, J. Younh Cheong, J. Gook Bae, A. Min Han and I. Kim, *ACS Nano*, 2019, **13**, 3141–3150.
- 50 Y. Luo, H. Jin, Y. Lu, Z. Zhu, S. Dai, L. Huang, X. Zhuang, K. Liu and L. Huang, *ACS Energy Lett.*, 2022, **7**, 1880–1887.
- 51 W. Wei, Z. Li, Z. Guo, Y. Li, F. Hou, W. Guo and A. Wei, *Appl. Surf. Sci*, 2022, **571**, 151277.
- 52 D. R. Monk, P.M.S., Mortimer, R.J., and Rosseinsky, *Electrochromism and Electrochromic Devices*, Cambridge University Press, New York, 2007.
- 53 E. C. Barker, A. D. Martin, C. J. Garvey, C. Y. Goh, F. Jones, M. Mocerino, B. W. Skelton, M. I. Ogden and T. Becker, *Soft Matter*, 2017, **13**, 1006–1011.
- 54 M. Kamalisarvestani, R. Saidur, S. Mekhilef and F. S. Javadi, *Renewable and Sustainable Energy Rev.*, 2013, **26**, 353–364.
- 55 W. H. Nguyen, C. J. Barile and M. D. McGehee, *J. Phys. Chem. C*, 2016, **120**, 26336–26341.
- 56 K. Bodurov, G., Stefchev, P., Ivanova, T., Gesheva, *Mater. Lett.*, 2014, **117**, 270–272.
- 57 J.-L. Wang, Y.-R. Lu, H.-H. Li, J.-W. Liu and S.-H. Yu, *JACS*, 2017, **139**, 9921–9926.
- 58 S. Kiruthika, C. Sow and G. U. Kulkarni, *Small*, 2017, **13**, 1701906.
- 59 J. Xu, Y. Zhang, T.-T. Zhai, Z. Kuang, J. Li, Y. Wang, Z. Gao, Y.-Y. Song and X.-H. Xia, *ACS Nano*, 2018, **12**, 6895–6903.
- 60 H. T. J.L. Kahl, L.R. Faulkner, K. Dwarakanath, *J. Am. Chem. Soc.*, 1986, **108**, 5434.

- 61 I. S. K. P.N. Moskalev, *Opt. Spektrosk.*, 1970, **29**, 414.
- 62 P. M. Beaujuge, S. Ellinger and J. R. Reynolds, *Nat. Mater.*, 2008, **7**, 795–799.
- 63 J. Guo, X. Diao, M. Wang, Z. bin Zhang and Y. Xie, *ACS Appl. Mater. and Interfaces*, 2022, **14**, 10517–10525.
- 64 M. Guzel, E. Karataş and M. Ak, *Smart Mater. Struct.*, 2019, **28**, 025013.
- 65 K. Kanazawa and S. Uemura, *Eur. Polym. J.*, 2019, **119**, 322–326.
- 66 K. Perera, Z. Yi, L. You, Z. Ke and J. Mei, *Polym. Chem.*, 2020, **11**, 508–516.
- 67 P. Shi, C. M. Amb, A. L. Dyer and J. R. Reynolds, *ACS Appl. Mater. Interfaces*, 2012, **4**, 6512–6521.
- 68 P. M. Beaujuge, C. M. Amb and J. R. Reynolds, *Adv. Mater.*, 2010, **22**, 5383–5387.
- 69 F. A. R. Nogueira, A. J. C. da Silva, J. D. de Freitas, A. S. Tintino, A. P. L. A. Santos, I. N. Oliveira and A. S. Ribeiro, *J. Braz. Chem. Soc.*, 2019, **30**, 2702–2711.
- 70 S. V Vasilyeva, P. M. Beaujuge, S. Wang, J. E. Babiarz, V. W. Ballarotto and J. R. Reynolds, *ACS Appl. Mater. Interfaces*, 2011, **3**, 1022–1032.
- 71 A. A. Argun et al., *Chem. Mater.*, 2004, **16**, 4401–4412.
- 72 J. Kawahara, P. A. Ersman, I. Engquist and M. Berggren, *Org. Electron.*, 2012, **13**, 469–474.
- 73 D. Weng, Y. Shi, J. Zheng and C. Xu, *Org. Electron.*, 2016, **34**, 139–145.
- 74 B. Che, D. Zhou, H. Li, C. He, E. Liu and X. Lu, *Org. Electron.*, 2019, **66**, 86–93.
- 75 J. R. Welsh, D. M.; Kumar, A.; Meijer, E. W.; Reynolds, *Adv. Mater.*, 1999, **11**, 1379.
- 76 J. ; Sotzing, G. A.; Reddinger, J. L.; Katritzky, A. R.; Soloducho and J. R. . Musgrave, R.; Reynolds, *Chem. Mater.*, 1997, **9**, 1578.
- 77 J. P. Mudigonda, D. S. K.; Boehme, J. L.; Brotherson, I. D.; Meeker, D. L.; Ferraris, *Chem. Mater.*, 2000, **12**, 1508.
- 78 C. L. Gaupp, K. Zong, P. Schottland, B. C. Thompson, C. A. Thomas and J. R. Reynolds, *Macromolecules*, 2000, **33**, 1132–1133.
- 79 P. Schottland, K. Zong, C. L. Gaupp, B. C. Thompson, C. A. Thomas, I. Giurgiu, R. Hickman, K. A. Abboud and J. R. Reynolds, *Macromolecules*, 2000, **33**, 7051–7061.
- 80 G. Sönmez, I. Schwendeman, P. Schottland, K. Zong and J. R. Reynolds, *Macromolecules*, 2003, **36**, 639–647.
- 81 D. J. Irvin, C. J. DuBois and J. R. Reynolds, *Chem. Commun.*, 1999, **20**, 2121–2122.
- 82 C. J. DuBois and J. R. Reynolds, *Adv. Mater.*, 2002, **14**, 1844–1846.
- 83 H. Meng and F. Wudl, *Macromolecules*, 2001, **34**, 1810–1816.
- 84 G. Sonmez, H. Meng and F. Wudl, *Chem. Mater.*, 2003, **15**, 4923–4929.
- 85 F. Fungo, S. A. Jenekhe and A. J. Bard, *Chem. Mater*, 2003, **15**, 1264–1272.
- 86 G. A. Sotzing, J. R. Reynolds and P. J. Steel, *Chem. Mater*, 1996, **8**, 882–889.

- 87 J. A. Irvin, I. Schwendeman, Y. Lee, K. A. Abboud and J. R. Reynolds, *J. Polym. Sci., Part A: Polym. Chem.*, 2001, **39**, 2164–2178.
- 88 G. Sonmez, H. Meng, Q. Zhang and F. Wudl, *Adv. Funct. Mater.*, 2003, **13**, 726–731.
- 89 M. F. Pepitone, S. S. Hardaker and R. V. Gregory, *Chem. Mater.*, 2003, **15**, 557–563.
- 90 J. A. Irvin and J. R. Reynolds, *Polymer*, 1998, **39**, 2339–2347.
- 91 K. Lee and G. A. Sotzing, *Macromolecules*, 2001, **34**, 5746–5747.
- 92 G. A. Sotzing and K. Lee, *Macromolecules*, 2002, **35**, 7281–7286.
- 93 C. L. Gaupp and J. R. Reynolds, *Macromolecules*, 2003, **36**, 6305–6315.
- 94 X. Wang, K. Chen, L. Scalco De Vasconcelos, J. He, Y. C. Shin, J. Mei and K. Zhao, *Nat. Commun.*, 2020, **11**, 1–10.
- 95 M. Pan, Y. Ke, L. Ma, S. Zhao, N. Wu and D. Xiao, *Electrochim. Acta*, 2018, **266**, 395–403.
- 96 R. J. Mortimer, *Electrochim. Acta*, 1999, **44**, 2971–2981.
- 97 J.-L. Wang, M. Hassan, J.-W. Liu and S.-H. Yu, *Adv. Mater.*, 2018, **30**, 1803430.
- 98 H. C. Moon, C.-H. Kim, T. P. Lodge and C. Daniel Frisbie, *ACS Appl. Mater. Interfaces*, 2016, **8**, 6252–6260.
- 99 A. L. Eh, A. W. M. Tan, X. Cheng, S. Magdassi and P. S. Lee, *Energy Technol.*, 2018, **6**, 33–45.
- 100 É. Lèbre, M. Stringer, K. Svobodova, J. R. Owen, D. Kemp, C. Côte, A. Arratia-Solar and R. K. Valenta, *Nat. Commun.*, 2020, **11**, 4823.
- 101 S. Abraham, S. Mangalath, D. Sasikumar and J. Joseph, *Chem. Mater.*, 2017, **29**, 22.
- 102 H.-J. Yen, K.-Y. Lin and G.-S. Liou, *J. Mater. Chem.*, 2011, **21**, 6230–6237.
- 103 L. Beverina, G. A. Pagani and M. Sassi, *Chem. Commun.*, 2014, **50**, 5413–5430.
- 104 A. A. Argun, A. Cirpan and J. R. Reynolds, *Adv. Mater.*, 2003, **15**, 1338–1341.
- 105 Y. Tan and et al., *J. Mater. Chem.*, 2012, **22**, 17452–17455.
- 106 G. J. Stec, A. Lauchner, Y. Cui, P. Nordlander and N. J. Halas, *ACS Nano*, 2017, **11**, 3254–3261.
- 107 Z. Ji, S. K. Doorn and M. Sykora, *ACS Nano*, 2020, **9**, 4043–4049.
- 108 A. Lauchner, A. E. Schlather, A. Manjavacas, Y. Cui, M. J. McClain, G. J. Stec, F. Javier García de Abajo, P. Nordlander and N. J. Halas, *Nano Lett.*, 2015, **15**, 6208–6214.
- 109 K. AlKaabi, C. R. Wade and M. Dincă, *Chem*, 2016, **1**, 264–272.
- 110 J.-F. Penneau, B. J. Stallman and L. L. Kasai, Paul H, Miller, *Chem. Mater.*, 1991, **3**, 791–796.
- 111 R. Cinnsealach, G. Boschloo, S. N. Rao and D. Fitzmaurice, *Sol. Energy Mater. Sol. Cells*, 1998, **55**, 215–223.
- 112 H. C. Wentz and M. G. Campbell, *Polyhedron*, 2018, **154**, 309–313.
- 113 T. Li, X. M. Lu, M. R. Zhang, K. Hu and Z. Li, *Bioact. Mater.*, 2022, **11**, 268–282.
- 114 A. Nuthanakanti, M. B. Walunj, A. Torris, M. v Badiger and S. G. Srivatsan, *Nanoscale*, 2019, **11**, 11956–11966.

- 115 K. R. Miller, Larry L. Mann, *Acc. Chem. Res.*, 1996, **29**, 417–423.
- 116 E. R. Draper and D. J. Adams, *Chem*, 2017, **3**, 390–410.
- 117 K. Rajagopal, A. E. Bulent, O. Ae, D. J. Pochan and J. P. Schneider, *Eur. Biophys. J.*, 2006, **35**, 162–169.
- 118 J. Wang, K. Liu, R. Xing and X. Yan, *Chem. Soc. Rev.*, 2016, **45**, 5589–5604.
- 119 X. Zhao, F. Pan and J. R. Lu, *Prog. Nat. Sci.*, 2008, **18**, 653–660.
- 120 N. Kihal, A. Nazemi and S. Bourgault, *Nanomaterials*, 2022, **12**, 1223–1245.
- 121 A. Das and S. Ghosh, *Chem. Commun.*, 2016, **52**, 6860–6872.
- 122 H. Duan, F. Cao, M. Zhang, M. Gao and L. Cao, *Chin. Chem. Lett.*, 2022, **33**, 2459–2463.
- 123 R. G. Weiss, *J. Am. Chem. Soc.*, 2014, **136**, 7519–7530.
- 124 S. Ghosh, V. K. Praveen and A. Ajayaghosh, *Annu. Rev. Mater. Res.*, 2016, **46**, 235–262.
- 125 S. Ghosh, X. Q. Li, V. Stepanenko and F. Würthner, *Chem. - Eur. J.*, 2008, **14**, 11343–11357.
- 126 F. C. Spano, *Acc. Chem. Res.*, 2010, **43**, 429–439.
- 127 D. McDowall, B. J. Greeves, R. Clowes, K. McAulay, A. M. Fuentes-Caparrós, L. Thomson, N. Khunti, N. Cowieson, M. C. Nolan, M. Wallace, A. I. Cooper, E. R. Draper, A. J. Cowan and D. J. Adams, *Adv. Energy Mater.*, 2020, **10**, 1–10.
- 128 V. Adams, J. Cameron, M. Wallace and E. R. Draper, *Chem. Eur. J.*, 2020, **26**, 9879–9882.
- 129 E. Krieg, E. Shirman, H. Weissman, E. Shimoni, S. G. Wolf, I. Pinkas and B. Rybtchinski, *J. Am. Chem. Soc.*, 2009, **131**, 14365–14373.
- 130 J. Mizuguchi and K. Tojo, *J. Phys. Chem. B*, 2002, **106**, 767–772.
- 131 F. Würthner, T. E. Kaiser and C. R. Saha-Möllner, *Angew. Chem., Int. Ed.*, 2011, **50**, 3376–3410.
- 132 Y. Tian, V. Stepanenko, T. E. Kaiser, F. Würthner and I. G. Scheblykin, *Nanoscale*, 2011, **4**, 218–223.
- 133 E. R. Cross, S. Sproules, R. Schweins, E. R. Draper and D. J. Adams, *J. Am. Chem. Soc.*, 2018, **140**, 8667–8670.
- 134 J. G. Egan, G. Brodie, D. McDowall, A. J. Smith, C. J. C. Edwards-Gayle and E. R. Draper, *Mater. Adv.*, 2021, **2**, 5248.
- 135 J. Jeon, K. R. Thurber, R. Ghirlando, W. M. Yau and R. Tycko, *Proc. Natl. Acad. Sci. U. S. A.*, 2019, **116**, 16717–16722.
- 136 E. E. Cawood, T. K. Karamanos, A. J. Wilson and S. E. Radford, *Biophys. Chem*, 2021, **268**, 106505.
- 137 H. Fang, Y. Sun, X. Wang, M. Sharma, Z. Chen, X. Cao, M. Utz and Z. Tian, *Sci. China Chem.*, 2018, **61**, 1460–1464.
- 138 E. Y. Du, F. Ziaee, L. Wang, R. E. Nordon and Pall Thordarson, *Polym. J.*, 2020, **52**, 947–957.
- 139 S. M. Hashemnejad and S. Kundu, *Langmuir*, 2017, **33** (31), 7769–7779.
- 140 A. Dawn and H. Kumari, *Chem. - Eur. J.*, 2018, **24**.

- 141 M. Shibayama, H. Kawada, T. Kume, T. Matsunaga, H. Iwai, T. Sano, N. Osaka, S. Miyazaki, S. Okabe and H. Endo, *J. Chem. Phys.*, 2007, **127**, 184508.
- 142 K. McAulay, P. Agí Ucha, ab Han Wang, A. M. Fuentes-Caparró, L. Thomson, O. Maklad, N. Khunti, N. Cowieson, M. Wallace, H. Cui, R. J. Poole, A. Seddon gh and D. J. Adams, *Chem. Commun*, 2020, **56**, 4094.
- 143 L. Thomson, R. Schweins, E. R. Draper, D. J. Adams, L. Thomson, E. R. Draper, D. J. Adams and R. Schweins, *Macromol. Rapid Commun.*, 2020, **41**, 2000093.
- 144 U. K. Makhmanov, *J. Eng. Phys. Thermophys.*, 2022, **95**, 527–532.
- 145 E. S. A. Rashid, A. Gul, W. A. H. Yehya and N. M. Julkapli, *Heliyon*, 2021, **7**, e07267.
- 146 G. von Maltzahn, S. Vauthey, S. Santoso and S. Zhang, *Langmuir*, 2003, **19**, 4332–4337.
- 147 Y. Zhou, R. Yang, X. Fan, M. Sun and X. He, *J. Appl. Polym. Sci*, 2021, **138**, 49520.
- 148 Q. Song, J. Yue, Y. Zhao, J. Zhu, Y. Lin, Q. Zhang, C. Pan, S. Liu, Z. Yang, L. Quan and Y. Wang, *Polymer*, 2022, **245**, 124701.
- 149 D. McDowall, D. J. Adams and A. M. Seddon, *Soft Matter*, 2022, **18**, 1577–1590.
- 150 S. L. Gras and A. M. Squires, *Methods Mol. Biol.*, 2011, **752**, 147–163.
- 151 P. J. Mawer, T. A. Waigh, R. Harding, T. C. B. Mcleish, S. M. King, M. Bell and N. Boden, *Lab Chip*, 2003, 4940–4949.
- 152 C. J. Jafta, X. G. Sun, G. M. Veith, G. v. Jensen, S. M. Mahurin, M. P. Paranthaman, S. Dai and C. A. Bridges, *Energy Environ. Sci.*, 2019, **12**, 1866–1877.
- 153 K. Mcaulay, L. Thomson, L. Porcar, R. Schweins, N. Mahmoudi, D. J. Adams and E. R. Draper, *Org. Mater.*, 2020, **2**, 108–115.
- 154 E. R. Draper, B. Dietrich, K. McAulay, C. Brasnett, H. Abdizadeh, I. Patmanidis, S. J. Marrink, H. Su, H. Cui, R. Schweins, A. Seddon and D. J. Adams, *Matter*, 2020, **2**, 764–778.
- 155 B. J. Eves, J. J. Douth, A. E. Terry, H. Yin, M. Moulin, M. Haertlein, V. T. Forsyth, P. Flagmeier, T. P. J. Knowles, D. M. Dias, G. Lotze, A. M. Seddon and A. M. Squires, *RSC Chem. Biol.*, 2021, **2**, 1232–1238.
- 156 J. Gawron'ski, G. Gawron'ski, M. Brzostowska, K. Kacprzak, H. Kołbon and P. Skowronek, *Chirality*, 2000, **12**, 263-268.
- 157 G. Pescitelli, L. di Bari and N. Berova, *Chem. Soc. Rev.*, 2014, **43**, 5211–5233.
- 158 G. Gottarelli, S. Lena, S. Masiero, S. Pieraccini and G. P. Spada, *Chirality*, 2008, **20**, 471–485.
- 159 Y. Xue, N. Fehn, V. K. Brandt, M. Stasi, J. Boekhoven, U. Heiz and A. Kartouzian, *Chirality*, 2022, **34**, 550–558.
- 160 S.-J. Hu, X.-Q. Guo, L.-P. Zhou, D.-N. Yan, P.-M. Cheng, L.-X. Cai, X.-Z. Li and Q.-F. Sun, *J. Am. Chem. Soc.*, 2022, **144**, 4244–4253.
- 161 J. Zhang, Y. Huang, W. Liu, L. Xie, B. Wei, C. Xu, Y. Xu, M. Zheng and H. Wang, *New J. Chem.*, 2022, **46**, 9264.
- 162 J. Zhang, Y. Huang, W. Liu, L. Xie, B. Wei, C. Xu, Y. Xu, M. Zheng and H. Wang, *New J. Chem.*, 2022, **46**, 9264–9271.

- 163 C. Kuchi, N. G. Prakash, K. Prasad, Y. V. Manohara Reddy, B. Sravani, R. Mangiri and G. R. Reddy, *Mater Sci Semicond. Process*, 2022, **142**, 106453.
- 164 U. Narang, R. Gautam, K. K. Yadav, S. Bhattacharya, P. K. Sahu, A. K. Aggarwal and S. M. S. Chauhan, *Chem. Pap.*, 2022, **76**, 3759–3769.
- 165 A. Rizvi, J. T. Mulvey, B. P. Carpenter, R. Talosig and J. P. Patterson, *Chem. Rev.*, 2021, **121**, 14232–14280.
- 166 E. R. Draper and D. J. Adams, *Chem. Soc. Rev.*, 2018, **47**, 3395–3405.
- 167 T. S. Balaban, A. R. Holzwarth and K. Schaffner, *J. Mol. Struct.*, 1995, **349**, 183–186.
- 168 G. Gottarelli, S. Lena, S. Masiero, S. Pieraccini and G. P. Spada, *Chirality*, 2008, **20**, 471–485.
- 169 Y. Shindo, *Opt. Eng.*, 1995, **34**, 3369–3384.
- 170 E. R. Draper, H. Su, C. Brasnett, R. J. Poole, S. Rogers, H. Cui, A. Seddon and D. J. Adams, *Angew. Chem. Int. Ed.*, 2017, **56**, 10467–10470.
- 171 G. Pont, L. Chen, D. G. Spiller and D. J. Adams, *Soft Matter*, 2012, **8**, 7797–7802.
- 172 L. L. E Mears, E. R. Draper, A. M. Castilla, H. Su, B. Dietrich, M. C. Nolan, G. N. Smith, J. Douth, S. Rogers, R. Akhtar, H. Cui and D. J. Adams, *Biomacromolecules*, 2017, **18**, 3531–3540.
- 173 H. Shen and A. Eisenberg, *Angew. Chem. Int. Ed*, 2000, **39**, 3310–3312.
- 174 W. Iabs, J. P. Patterson, A. M. Sanchez, N. Petzetakis, T. P. Smart, T. H. Epps, I. Portman, N. R. Wilson and R. K. O, *Soft Matter*, 2012, **8**, 3267–3498.
- 175 N. Singh, C. Maity, K. Zhang, C. A. Angulo-Pachón, J. H. van Esch, R. Eelkema and B. Escuder, *Chem. Eur. J*, 2017, **23**, 2018–2021.
- 176 N. Singh, K. Zhang, C. A. Angulo-Pachón, E. Mendes, J. H. van Esch and B. Escuder, *Chem. Sci.*, 2016, **7**, 5568–5572.
- 177 J. R. Moffat and D. K. Smith, *Chem. Commun.*, 2009, 316–318.
- 178 A. Kavanagh, R. Copperwhite, M. Oubaha, J. Owens, C. McDonagh, D. Diamond and R. Byrne, *J. Mater. Chem.*, 2011, **21**, 8687–8693.
- 179 R. Cinnsealach, G. Boschloo, S. N. Rao and D. Fitzmaurice, *Sol. Energy Mater. Sol. Cells*, 1999, **57**, 107–125.
- 180 D. C. Bookbinder and M. S. Wrighton, *J. Electrochem. Soc.*, 1983, **130**, 1080.
- 181 L.-C. Cao, M. Mou and Y. Wang, *J. Mater. Chem.*, 2009, **19**, 3412–3418.
- 182 W. Shi, F. Xing, Y.-L. Bai, M. Hu, Y. Zhao, M.-X. Li and S. Zhu, *ACS Appl. Mater. Interfaces*, 2015, **7**, 1449–14500.
- 183 K. Madasamy, D. Velayutham, V. Suryanarayanan, M. Kathiresan and K.-C. Ho, *J. Mater. Chem.*, 2019, **4622**, 4622.
- 184 X. Marguerettaz, R. O'Neill and D. Fitzmaurice, *J. Am. Chem. Soc*, 1994, **116**, 2629–2630.
- 185 C. M. Lampert, *Sol. Energy Mater.*, 1984, **11**, 1–27.
- 186 Y. Alesanco, A. Viñ, J. J. Palenzuela, I. Odriozola, G. Germán, C. Ero, J. Rodriguez, R. Ramón and T. Zaera, *ACS Appl. Mater. Interfaces*, 2016, **8**, 14795–14801.

- 187 E. Hwang, S. Seo, S. Bak, H. Lee, M. Min and H. Lee, *Adv. Mater.*, 2014, **26**, 5129–5136.
- 188 K. Hoshino, R. Nakajima and M. Okuma, *Appl. Surf. Sci.*, 2014, **313**, 569–576.
- 189 T. H. Chang, H. C. Lu, M. H. Lee, S. Y. Kao and K. C. Ho, *Sol. Energy Mater. Sol. Cells*, 2018, **177**, 75–81.
- 190 S. Zhao, W. Huang, Z. Guan, B. Jin and D. Xiao, *Electrochimica Acta*, 2019, **298**, 533–540.
- 191 S. Xiao, Y. Zhang, L. Ma, S. Zhao, N. Wu and D. Xiao, *Dyes Pigm.*, 2020, **174**, 108055.
- 192 S.-Y. Kao, H.-C. Lu, C.-W. Kung, H.-W. Chen, T.-H. Chang and K.-C. Ho, *ACS Appl. Mater. Interfaces*, 2016, **8**, 4175–4184.
- 193 U. Bach, D. Corr, D., Lupo, F. Pichot M. Ryan, *Adv. Mater.*, 2002, **14**, 845–848.
- 194 J. P. Coleman, A. T. Lynch, P. Madhukar and J. H. Wagenknecht, *Sol. Energy Mater. Sol. Cells*, 1999, **56**, 395–418.
- 195 W. Kui, D. S. Guo, H. Q. Zhang, L. Dong, X. L. Zheng and L. Yu, *J. Med. Chem.*, 2009, **52**, 6402–6412.
- 196 J.-H. Ryu, M.-S. Park and K.-D. Suh, *Colloid Polym. Sci.*, 2007, **285**, 1675–1681.
- 197 P. M. S. Monk, *J. Electroanal. Chem.*, 1997, **432**, 175–179.
- 198 R. Sydam, A. Ghosh and M. Deepa, *Org. Electron.*, 2015, **17**, 33–43.
- 199 S. Y. Kao, C. W. Kung, H. W. Chen, C. W. Hu and K. C. Ho, *Sol. Energy Mater. Sol. Cells*, 2016, **145**, 61–68.
- 200 S. v. Bhosale, C. H. Jani and S. J. Langford, *Chem. Soc. Rev.*, 2008, **37**, 331–342.
- 201 M. al Kobaisi, S. v. Bhosale, K. Latham, A. M. Raynor and S. v. Bhosale, *Chem. Rev.*, 2016, **116**, 11685–11796.
- 202 G. Andric, A. F. John Boas, B. M. Alan Bond, D. D. Gary Fallon, A. P. Kenneth Ghiggino, C. F. Conor Hogan, A. A. James Hutchison, C. Marcia A-P Lee, A. J. Steven Langford, D. R. John Pilbrow, B. J. Gordon Troup and C. P. Woodward A, *Aust. J. Chem*, 2004, **57**, 1011–1019.
- 203 Q. Song, F. Li, Z. Wang and X. Zhang, *Chem. Sci.*, 2015, **6**, 3342–3346.
- 204 J. Zheng, W. Qiao, X. Wan, P. Jian, Gao and Z. Y. Wang, *Chem. Mater.*, 2008, **20**, 6163–6168.
- 205 M. Tomasulo, D. M. Naistat, A. J. P. White, D. J. Williams and F. M. Raymo, *Tetrahedron Lett.*, 2005, **46**, 5695–5698.
- 206 M. R. Molla and S. Ghosh, *Chem. - Eur. J.*, 2012, **18**, 9860–9869.
- 207 N. v. Ghule, D. D. La, R. S. Bhosale, M. al Kobaisi, A. M. Raynor, S. v. Bhosale and S. v. Bhosale, *Chemistry Open*, 2016, **5**, 157–163.
- 208 A. Das and S. Ghosh, *Chem. Commun.*, 2011, **47**, 8922–8924.
- 209 J. Zheng, W. Qiao, X. Wan, Jian, P. Gao and Z. Y. Wang, *Chem. Mater.*, 2008, **20**, 6163–6168.
- 210 X. Wu, K. Wang, J. Lin, D. Yan, Z. Guo and H. Zhan, *J. Colloid Interface Sci.*, 2021, **594**, 73–79.
- 211 J. Mater, F. Li, Z. Huang, Q. Zhou, M. Pan, Q. Tang and C. Gong, *J. Mater. Chem. C.*, 2020, **8**, 10031–10038.
- 212 S. Halder, S. Roy and C. Chakraborty, *Sol. Energy Mater. Sol. Cells*, 2022, **234**, 111429.

- 213 H. Shao and J. R. Parquette, *Chem. Comm.*, 2010, **46**, 4285–4287.
- 214 N. Nandi, S. Basak, S. Kirkham, I. W. Hamley and A. Banerjee, *Langmuir*, 2016, **32**, 13226–13233.
- 215 F. Wei, Y. Ye, W. Huang, Q. Lin, Z. Li, L. Liu, S. Chen, Z. Zhang and S. Xiang, *Inorg. Chem. Commun.*, 2018, **93**, 105–109.
- 216 G. Radha, S. Roy, C. Chakraborty, H. Aggarwal and R. Li, *Chem. Commun.*, 2022, **58**, 4024–4027.
- 217 T. C. Barros, S. Brochsztain, V. G. Toscano, P. B. Filho and M. J. Politi, *J. Photochem. Photobiol., A*, 1997, **111**, 97–104.
- 218 F. P. Byrne, S. Jin, G. Paggiola, T. H. M. Petchey, J. H. Clark, T. J. Farmer, A. J. Hunt, C. R. Mcelroy and J. Sherwood, *Sustain. Chem. Process.*, 2016, **4**, 7.
- 219 H. Shao, T. Nguyen, N. C. Romano, D. A. Modarelli and J. R. Parquette, *J. Am. Chem. Soc.*, 2009, **131**, 43.
- 220 L. Meunier, F. M. Kelly, C. Cochrane and V. Koncar, *Indian J. Fibre Text. Res.*, 2011, **36**, 429–435.
- 221 S. Kiruthika and G. U. Kulkarni, *Sol. Energy Mater. Sol. Cells*, 2017, **163**, 231–236.
- 222 K.-W. Kim, H. Oh, J. H. Bae, H. Kim, H. C. Moon and S. H. Kim, *ACS Appl. Mater. Interfaces*, 2017, **9**, 18994–19000.
- 223 C. J. Barile, D. J. Slotcavage, J. Hou, M. T. Strand, T. S. Hernandez and M. D. Mcgehee, *Joule*, 2017, **1**, 133–145.
- 224 Y. Huang, C. Yang, B. Deng, C. Wang, Q. Li, C. de Villenoisy Thibault, K. Huang, K. Huo and H. Wu, *Nano Energy*, 2019, **66**, 104200.
- 225 A. Håkansson, S. Han, S. Wang, J. Lu, S. Braun, M. Fahlman, M. Berggren, X. Crispin and S. Fabiano, *J. Polym. Sci., Part B: Polym. Phys.*, 2017, **55**, 814–820.
- 226 J. Žmija and M. J. Małachowski, *J. Achiev. Mater. Manuf. Eng.*, 2011, **48**, 14–23.
- 227 T. Jarosz, K. Gebka, A. Stolarczyk and W. Domagala, *Polymers*, 2019, **11**, 1–18.
- 228 P. M. Beaujuge and J. R. Reynolds, *Chem. Rev.*, 2009, **110**, 268–320.
- 229 D. T. Christiansen, A. L. Tomlinson and J. R. Reynolds, *J. Am. Chem. Soc.*, 2019, **141**, 3859–3862.
- 230 Y. J. Hwang, S. B. Pyun, M. J. Choi, J. H. Kim and E. C. Cho, *Chem. Nano. Mat.*, 2022, **8**, 1–13.
- 231 R. Lundy, E. R. Draper and J. J. Walsh, *New J. Chem.*, 2018, **42**, 19020–19025.
- 232 ThermoFisher, *Safety data sheet of Tetrahydrofuran (revision 7)*, 2022.
- 233 J. Pugan, P. Rathod, P. More and H. Kim, *Chem. Eng. J.*, 2022, **437**, 135157.
- 234 J. R. Beaujuge, P.M., Ellinger, S., and Reynolds, *Nat. Mater.*, 2008, **7**, 795.
- 235 Y. Hsu, P.-C., Wang, S., Narasimhan, V.K., Kong, D., Lee, H.R., and Cui, *Nat. Commun.*, 2013, **4**, 2522.
- 236 S. Zhao, X. Gao, L. Chen, W. Huang and Y. Liu, *Appl. Mater. Today*, 2022, **28**, 101543.

- 237 E. R. Draper, B. J. Greeves, M. Barrow, R. Schweins, M. A. Zwijnenburg and D. J. Adams, *Chem*, 2017, **2**, 716–731.
- 238 A. Z. Cardoso, L. L. E. Mears, B. N. Cattoz, P. C. Griffiths, R. Schweins and D. J. Adams, *Soft Matter*, 2016, **12**, 3612–3621.
- 239 L. Chen, K. Morris, A. Laybourn, D. Elias, M. R. Hicks, A. Rodger, L. Serpell and D. J. Adams, *Langmuir*, 2010, **26**, 5232–5242.
- 240 E. R. Draper, L. J. Archibald, M. C. Nolan, R. Schweins, M. A. Zwijnenburg, S. Sproules and D. J. Adams, *Chem. - Eur. J.*, 2018, **24**, 4006–4010.
- 241 H. Ann, M. Ardoñ, E. R. Draper, F. Citossi, M. Wallace, L. C. Serpell, D. J. Adams and J. D. Tovar, *J. Am. Chem. Soc.*, 2017, **139**, 8685–8692.
- 242 B. O. Okesola, Y. Wu, B. Derkus, S. Gani, D. Wu, D. Knani, D. K. Smith, D. J. Adams and A. Mata, *Chem. Mater.*, 2019, **31**, 7883–7897.
- 243 M. C. Nolan, J. J. Walsh, L. L. E. Mears, E. R. Draper, M. Wallace, M. Barrow, B. Dietrich, S. M. King, A. J. Cowan and D. J. Adams, *J. Mater. Chem. A*, 2017, **5**, 7555–7563.
- 244 L. Li, R. Sun and R. Zheng, *Mater. Des.*, 2021, **197**, 109209.
- 245 J. Mei, N. L. C. Leung, R. T. K. Kwok, J. W. Y. Lam and B. Z. Tang, *Chem. Rev.*, 2015, **115**, 11718–11940.
- 246 J. Jin, T. Iyoda, C. Cao, Y. Song, L. Jiang, T. Jin Li and D. ben Zhu, *Angew. Chem. Int. Ed.*, 2001, **40**, 2135–2138.
- 247 C. J. Gommès, S. Jaksch and H. Frielinghaus, *J. Appl. Crystallogr.*, 2021, **54**, 1832–1843.
- 248 Sasview, Version 4.2.2, www.sasview.org, (accessed January 2, 2020).
- 249 P. Terech, G. Clavier, H. Bouas-Laurent, J. P. Desvergne, B. Demé and J. L. Pozzo, *J. Colloid Interface Sci.*, 2006, **302**, 633–642.
- 250 J. K. Wychowaniec, A. M. Smith, C. Ligorio, O. O. Mykhaylyk, A. F. Miller and A. Saiani, *Biomacromolecules*, 2020, 2285–2297.
- 251 A. D. Martin, J. P. Wojciechowski, A. B. Robinson, C. Heu, C. J. Garvey, J. Ratcliffe, L. J. Waddington, J. Gardiner and P. Thordarson, *Sci. Rep.* **7**, 43947.
- 252 J. S. Pedersen and P. Schurtenberger, *Macromolecules*, 1996, **29**, 7602–7612.
- 253 S. G. Corcoran, D. G. Wiesler and K. Sieradzki, *Mat. Res. Soc. Symp. Proc.*, 1997, **451**, 93–98.
- 254 J.-B. Guilbaud and A. Saiani, *Chem. Soc. Rev.*, 2010, **40**, 1200–1210.
- 255 D. J. Adams, M. F. Butler, W. J. Frith, M. Kirkland, L. Mullen and P. Sanderson, *Soft Matter*, 2009, **5**, 1856–1862.
- 256 Y. Pocker, E. Green, A. F. Brodie, F. Lipmann, J. Biol Chem, H. C. Brown, J. H. Brewster, J. Amer, T. C. Bruice, P. G. Kury, D. M. McMahan and E. Green, *J. Am. Chem. Soc.*, 1975, **95**, 113–119.
- 257 H. Takahashi and K. Ito, *J. Phys.: Conf. Ser.*, 2007, **83**, 012022.
- 258 A. Milsom, A. M. Squires, B. Woden, N. J. Terrill, A. D. Ward and C. Pfrang, *Faraday Discuss.*, 2021, **226**, 364–381.

- 259 C. Dotzler, B. Ingam, B. Illy, M. Toney and M. P. Ryan, *ECS Meeting Abstracts*, 2010, **MA2010-01**, 1229.
- 260 N. Takahashi, T. Kanaya, K. Nishida, Y. Takahashi and M. Arai, *Physica B*, 2006, **385-386**, 810–813.
- 261 A. P. R. Eberle and L. Porcar, *Curr. Opin. Colloid Interface Sci.*, 2012, **17**, 33–43.
- 262 S. Rogers, J. Kohlbrecher and M. P. Lettinga, *Soft Matter*, 2012, **8**, 7831–7839.
- 263 M. Takeda, T. Kusano, T. Matsunaga, H. Endo, M. Shibayama and T. Shikata, *Langmuir*, 2011, **27**, 1731–1738.
- 264 S. J. Richardson, M. R. Burton, X. Luo, P. A. Staniec, I. S. Nandhakumar, N. J. Terrill, J. M. Elliott and A. M. Squires, *Nanoscale*, 2017, **9**, 10227.
- 265 L. A. Estroff and A. D. Hamilton, *Chem. Rev.*, 2004, **104**, 12001–1216.
- 266 T. Kato, H. Kihara, U. Kumar, T. Uryu, J. M. J. Fréchet, M. Muthukumar, C. K. Ober, E. L. Thomas and K Kanie, *J. Chem. Soc. Perkin Trans.*, 1994, **77**, 746.
- 267 M. Saha and S. Bandyopadhyay, *J. Phys. Chem. C*, 2021, **11**, 1.

CHAPTER TWO

Investigation into the effect of pH on solubility, colour, redox values, and reversibility of colour change

2.1 Introduction

As discussed in Chapter 1, electrochromic devices that utilise aqueous media are beneficial as they make use of a benign, cheap solvent but are often overlooked due to issues such as leakage.¹⁻⁵ On an industrial scale, such drawbacks could be minimised through engineering methods not accessible in most labs. For our ideal Smart Window, the system we aim to create must adhere to several parameters which we have set out below:

- solubility or dispersion in water
- fast reversible switching between a transmissive and a dark state
- a dark reduced state and a pale and transmissive neutral state
- a small potential needed to switch between states
- cyclability of at least 100 cycles without detriment of the above parameters (the ability to switch between states as many times as possible)
- stability (material should not degrade with use or age)

In this chapter we will be looking at the first four of these parameters as these can be used to quickly screen potential suitable candidates before any longer terms testing is done. This will ensure we are testing the best materials and therefore save time and resources.

To achieve these parameters, we looked at using naphthalene diimides (NDIs), a class of self-assembling small organic molecules which are promising candidates for Smart Windows. NDIs appended with simple amino acids or dipeptides form highly coloured reduced species photo- and electrochemically which can be reversed by oxidation¹, Figure 2.1. Due to the carboxylic acid present, these systems are water soluble with the addition of base. From previous studies using a dipeptide appended NDI at concentrations of 10 mg/mL, it was seen that the colouration is sufficiently dark to be of notable contrast while the neutral state appears colourless or very pale yellow¹ to the eye, especially in a thin gap of around 0.1-0.5 mm (such as is used throughout this work). This high level of contrast is particularly beneficial and highly sought after in this field and forms the basis of this work.⁶ It was found that these NDI systems are not conductive enough alone to form highly contrasting states when electrochemically reduced and so background electrolyte of NaCl was required, which is inexpensive.¹

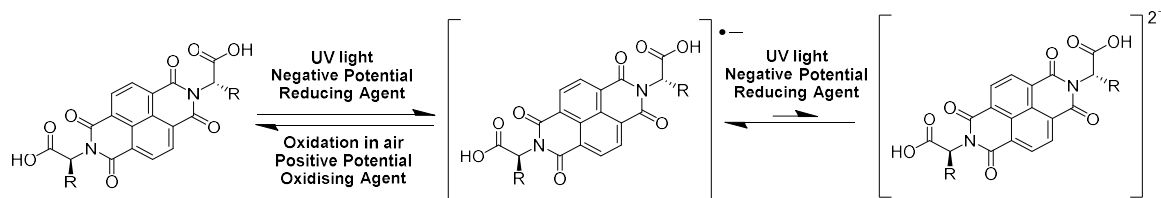


Figure 2.1. Reversible formation of the different reduced species of NDI-R.

NDIs can self-assemble, this assembly can be influenced easily by chemical structure or environment.^{1,7,8} These systems are known to form one-dimensional π dimers and stacks⁹ which then fold or assemble into larger aggregates¹⁰ such as spheres or cylinders. The structure has been reported to influence the radical anion production of NDI systems, for example, improved charge carrier transport upon formation of the radical anionic species when fibrous networks are present with increased hydrogen bonding.¹¹ A canopy structure between NDI molecules has also been associated with radical anion stability.¹² The self-assembly, and consequent properties such as photoconductivity and catalytic activity of related materials, has been reported to be heavily influenced by both chemical structure, packing and pH.^{13–18} We hypothesise that one or more of the parameters set out for our ideal system can be influenced by self-assembly.

In general, and from the literature, we would anticipate less defined aggregates and less self-assembly at high pH due to increased solubility, and more complex structures forming at lower pH due to reduced solubility,¹⁹ Figure 2.2. Some NDIs have the ability to form hydrogels from complex structures forming fibres and networks as the pH is lowered.^{1,20–22} As well as lower solubility, at lower pH the structures have less electrostatic repulsions between them. This reduction in charge can also lead to the formation of more stabilised or larger structures as molecules can move closer together and entangle. The chemical structure of the molecule will also have an influence in this respect. For example, bulky groups have the potential to sterically hinder certain structures from forming and can be more or less hydrophobic.

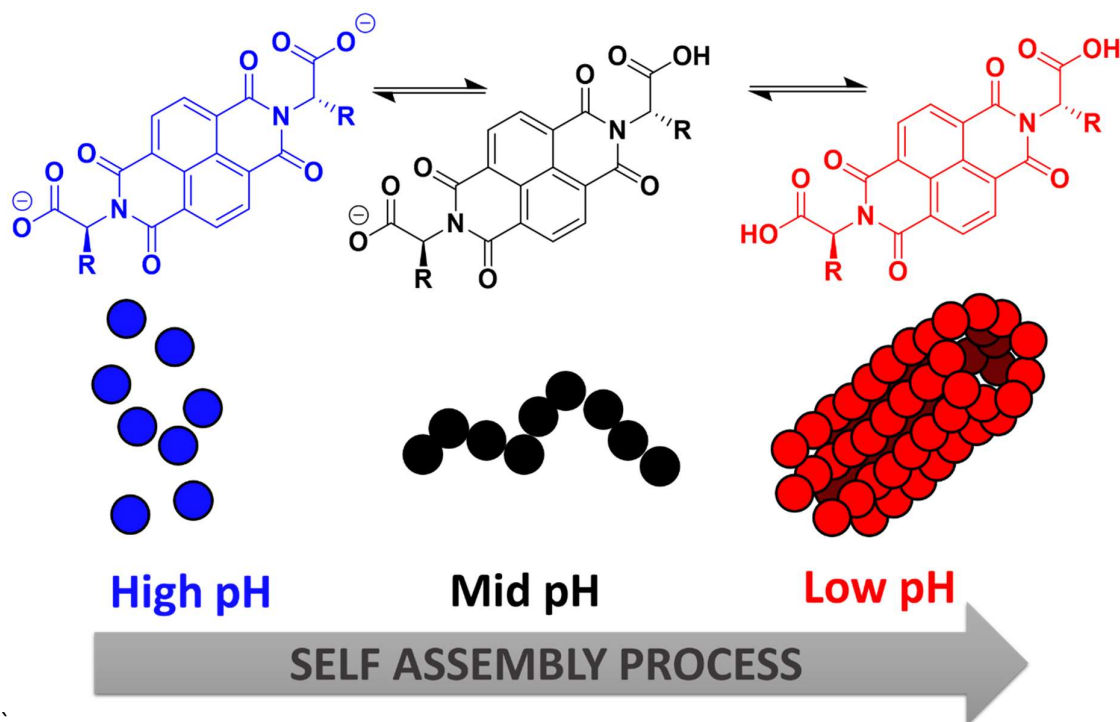


Figure 2.2. Cartoon showing NDI molecules forming different aggregation as pH changes and NDI-R is in various forms of deprotonation. A single amino acid R groups are assumed for simplicity.

As the amino acid appended NDIs have two free carboxylic acid moieties within their chemical structure, this will allow for different levels of protonation and therefore solubility, Figure 2.2. From previous studies on similar systems^{23,24} we anticipate two apparent pK_a values corresponding to the different carboxylic groups. These apparent pK_a values relate to a change in aggregation from a change in solubility rather than simply a carboxylic acid protonation (we would expect both carboxylic acid groups to have the same pK_a value at around pH 3-5 in unaggregated systems). Therefore, at each pK_a , we would expect the aggregation to change in the NDIs. This change may be subtle, but we anticipate that pH can potentially be used to tailor our systems to a particular aggregation above and below each pK_a . The value of the apparent pK_a will be influenced by chemical structure. By tailoring aggregation with pH, we will investigate whether consequent chromic properties can be influenced.

By understanding any relationship between aggregation and chromic performance, the advantages of these systems could be maximised for the application of Smart Windows. Many things can affect self-assembly such as pH,^{16,23,25-28} functionalisation/chemical structure,^{15,29-33} additional components or additives,³⁴⁻³⁹ solvent,^{33,40-43} counter ions and salts^{44,45} and temperature^{46,47} and so it is not likely to find one consistent overriding factor that corresponds to a state that fulfils all our criteria. More likely,

we hypothesise the influence of both pH and R group will be at play to influence an aggregation that can stabilise the coloured radical anion without detriment to the reversibility of the chromic properties of these systems. We are therefore going to investigate the effect of 'R' group in varying the amino acid in the imide position, and the effect of pH upon the depth on colour of neutral and reduced states, switching ability and reduction potentials.

2.2 Results and discussion

The NDIs used will be referred to as NDI-R, where R corresponds to the amino acid at the imide position, Figure 2.3. Full IUPAC names are (2S,3S)-2-{13-[(1S,2S)-1-carboxy-2-methylbutyl-5,7,12,14-tetraoxo-6,13-diazatetracyclohexadeca-1,3,8,10,15-pentaen-6-3-methylpentanoic acid (**NDI-I**), (2S)-2-{13-(1S)-1-carboxy-2-methylpropyl-5,7,12,14-tetraoxo-6,13-diazatetracyclohexadeca-1,3,8,10,15-pentaen-6-3-methylbutanoic acid (**NDI-V**), (2S)-2-{13-[(1S)-1-carboxy-2-phenylethyl-5,7,12,14-tetraoxo-6,13-diazatetracyclohexadeca-1,3,8,10,15-pentaen-6-3-phenylpropanoic acid (**NDI-F**), (2S)-2-{2-[13-(1S)-1-carboxy-2-phenylethylcarbamoylmethyl]-5,7,12,14-tetraoxo-6,13-diazatetracyclohexadeca-1,3,8,10,15-pentaen-6-acetamido}-3-phenylpropanoic acid (**NDI-GF**) and (2S)-2-[(2S)-2-{13-[(1S)-1-[(1S)-1-carboxy-2-phenylethyl]carbamoyl]-2-phenylethyl]-5,7,12,14-tetraoxo-6,13-diazatetracyclohexadeca-1,3,8,10,15-pentaen-6-3-henylpropanamido}-3-phenylpropanoic acid (**NDI-FF**).

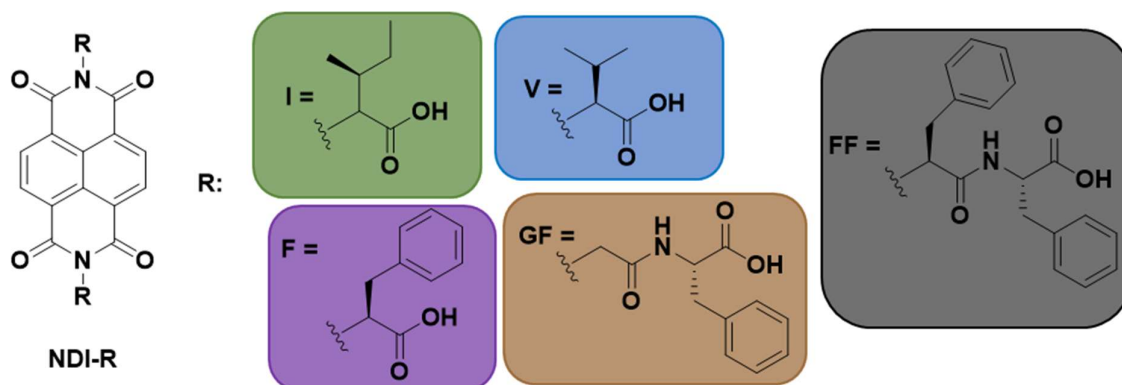


Figure 2.3. Chemical structures of **NDI-I**, **NDI-V**, **NDI-F**, **NDI-GF** and **NDI-FF**.

In order to assess the suitability of these systems by the parameters set out in the introduction to this chapter, initial investigations are undertaken. As pH will influence the protonation of the carboxylic acid groups within R, aggregation and solubility will ultimately be affected. We must determine the solubility limits of these systems and their apparent pK_a . The pK_a will indicate at what pH structures change. With this information we can investigate the structures formed above and below these pK_a

values. Using cyclic voltammetry (CV), we must also determine the redox potentials of these systems and investigate whether pH has a large effect upon their value.

2.2.1 Solubility

Solubility in water, a pale neutral state and dark coloured state were requirements for our systems set out in the introduction of this chapter. These properties must be evaluated, starting with solubility and neutral colour.

Solutions of the NDIs are soluble within water over approximately pH 6. Below this pH, solutions are turbid to the eye and the NDI starts to form precipitate. In a thin gap (0.1 mm) solutions are transmissive and in a standard Sterilin™ vial they appear a pale colour beige, yellow or brown, Figure 2.4.

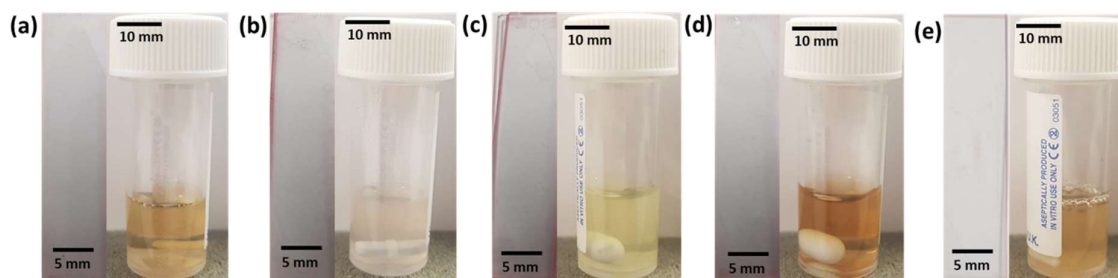


Figure 2.4. Images of solutions of (a) NDI-I, (b) NDI-V, (c) NDI-F, (d) NDI-GF and (e) NDI-FF in a thin gap of 0.1 mm (left) and in a vial (right) at 10 mg/mL, pH 9.

Solutions form suitably dark reduced states at a concentration of 10 mg/mL, however this concentration is too high to accurately measure the neutral state using absorbance spectroscopy. A concentration of 5 mg/mL was used for the measurement of the neutral state. A concentration series shows dilution has no influence on the spectra collected and the structures are diluted rather than changed, Figure 2.5. We can therefore assume the spectra at 10 mg/mL would be comparable to those at 5 mg/mL.

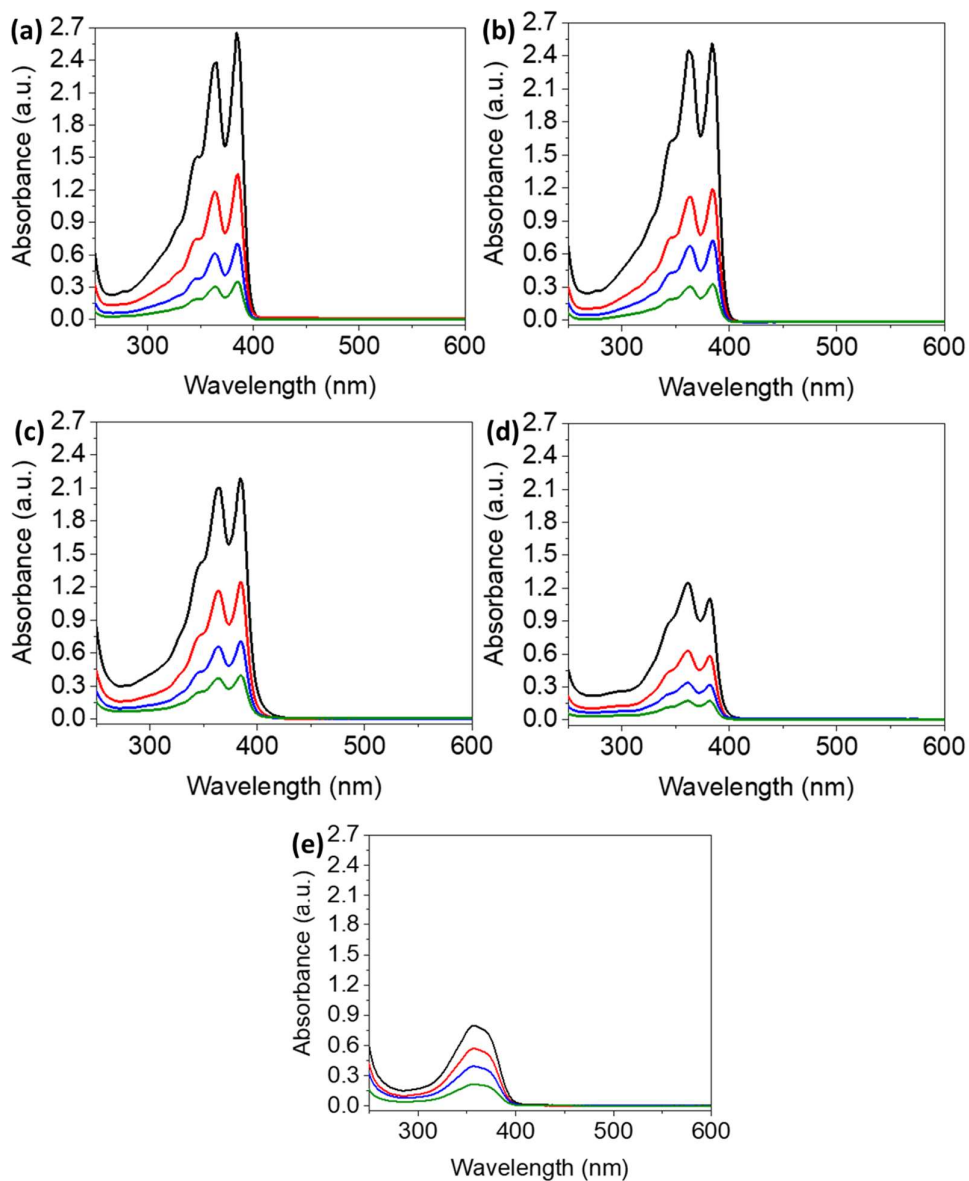


Figure 2.5. Absorption spectra of (a) **NDI-I**, (b) **NDI-V**, (c) **NDI-F**, (d) **NDI-GF** and (e) **NDI-FF** in neutral state at 5 (black), 2.5 (red), 1.25 (blue) and 0.625 (green) mg/mL at pH 9.

2.2.2 Apparent pK_a determination

We need to determine the apparent pK_a values of each system. Where pH is buffered during a pH titration will indicate a pH value at which structures change. Apparent pK_a titrations (Figures A.2.1-A.2.5, Appendix) are summarised in Table 2.1. Two pK_a values are found relating to each of the two ionisable carboxylic groups on each end of the molecule. Two apparent pK_a values are also reported in similar systems.²³ The difference in pK_a in different NDIs is not substantial. Two pK_a values were found at approximately 9.4 and 6.6.

Table 2.1. Tabulated pK_a values calculated from pH titrations of different NDIs.

NDI	First pK_a	Second pK_a
NDI-I	9.3	6.4
NDI-V	9.6	6.8
NDI-F	9.4	6.6
NDI-GF	9.2	6.5
NDI-FF	9.6	6.5

2.2.3 Neutral state colour

Next, we wanted to see the effect of pH on the neutral states, so we varied the pH between pH 6 and 12 and measured the neutral state of the NDI systems using absorbance spectroscopy. More detailed information about structure can be inferred from a combination of absorbance spectra and neutron or X-ray scattering measurements but the accessibility to the prior technique makes it suitable for initial investigation. Neutron scattering data is discussed in Chapter 3.

By eye, varying the pH does not affect the colouration of the neutral state for **NDI-F**, **NDI-GF** or **NDI-FF** (Figure 2.6(c-e)). The neutral state of **NDI-I** and **NDI-V** changes visually from a pale-yellow to a pink colour as pH increases, which could suggest a change in structures, Figure 2.6(a-b). After 30 minutes at pH 12, this pale-yellow colour is restored in **NDI-I**, Figure 2.6(a). This delayed change in colour is likely due to a change in aggregation that is not instantaneous. Changes in aggregation are not always instantaneous.⁴⁸ The colour change was noted to occur faster if the solution was shaken and so the delay may also be due to a diffusion of base through the whole solution. This change occurred whilst the sample was protected from UV light and so is not due to a photo-induced process. The neutral state spectrum is more equal in the absorbance intensity between 350 and 365 nm, Figure 2.7, after this colour change. This observation does not suggest significant changes to structure.

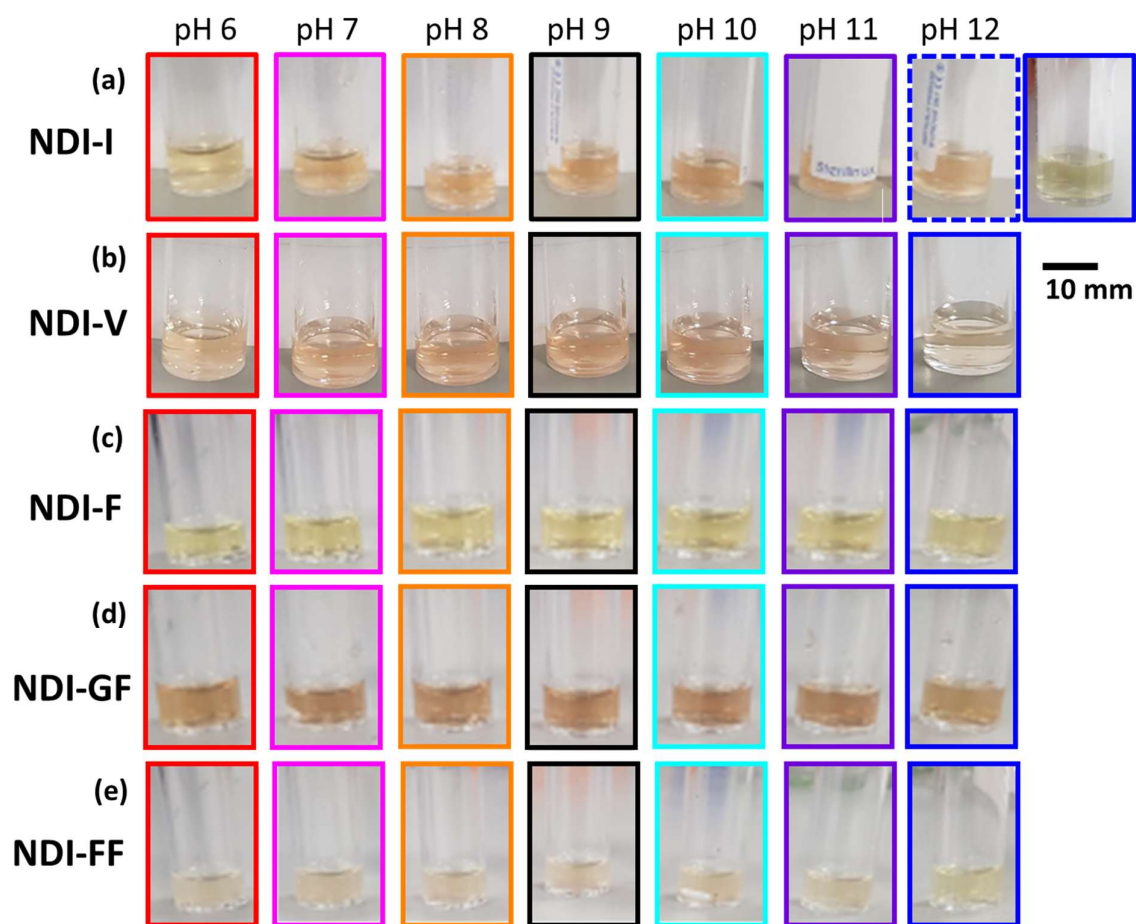


Figure 2.6. Photographs of neutral solutions of (a) NDI-I, (b) NDI-V, (c) NDI-F, (d) NDI-GF and (e) NDI-FF at 5 mg/mL at pH 6 (red), 7 (pink), 8 (orange), 9 (black), 10 (turquoise), 11 (purple) and 12 (blue dashed) and after (blue solid) sitting for 30 minutes.

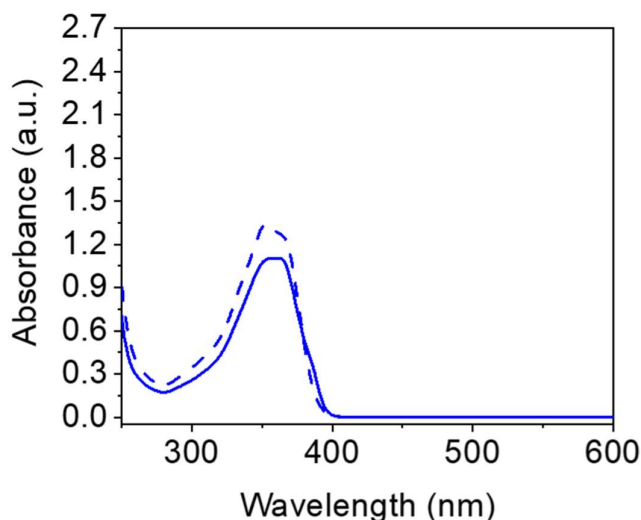


Figure 2.7. Absorbance spectra of **NDI-I** in neutral state at 5 mg/mL at pH 12. Measurements taken before (solid line) and after (dashed line) noted colour change of bulk solution.

A paler colour at pH 12 is also observed in **NDI-V**, Figure 2.6(b). This observation suggests that aggregation is altered at low and high pH. At high pH, we would expect these systems to be dispersed or forming very small or poorly defined aggregates⁴⁹ and so a change in aggregation is expected as pH is lowered. When placed in a thin gap of 0.1 mm, any difference in colouration of the neutral state of all NDIs can no longer be detected by eye, Figure 2.4.

The absorbance spectra of the neutral state of **NDI-I**, **NDI-V** and **NDI-F** show two distinct absorbances at 365 and 385 nm as well as a small shoulder at 345 nm, Figure 2.5(a-c) and Figure 2.8(a-f). These absorbances are observed in the spectra of **NDI-GF** at an approximately 5 nm shorter wavelength, Figure 2.5(d) and Figure 2.9(a-b). A difference in the ratios of 365 and 385 nm absorbances would suggest a difference in molecular packing of aggregates.^{13,15,50} We anticipate changes will occur around the pK_a of each system. Comparable absorbances at a longer wavelength in the neutral spectra of perylene bisimides (PBIs) have been attributed to one $\pi \rightarrow \pi^*$ electronic transition, coupled with vibrational transitions, corresponding to $S_0 \rightarrow S_1$ transitions.^{13,51,52} Absorbances at 380, 360 and 340 nm have been linked to vibrational transitions $0 \rightarrow 0$, $0 \rightarrow 1$ and $0 \rightarrow 2$ respectively in NDI systems.⁵³

No shifting in the wavelength of absorbances are observed as pH changes in any NDIs and so we infer no drastic changes in structure occur with pH. The relative ratio of absorbances at 365 and 385 nm changes as pH increases in both **NDI-I** and **NDI-V**, Figure 2.8(a-d). A decrease in intensity in the absorbance at 385 nm is observed at pH 10 and 11. At pH 12 one broad absorbance is observed instead of two distinct absorbances. This observation suggests that a subtle aggregation change in packing occur above the first pK_a and becomes more significant as pH increases.

NDI-F is less susceptible to aggregation changes between pH 6-11 than **NDI-I** and **NDI-V**, Figure 2.8(e-f). The aromatic groups could facilitate more rigid or less changeable structures due to inflexible nature of aromatic rings and their steric bulk^{54,55} (which could also affect packing¹⁶) or additional π - π interactions.⁵⁶ For **NDI-I** and **NDI-V**, as pH increases, first packing changes, then a larger change at pH 12 occurs. Spectra of **NDI-F** suggest that only the latter change occurs in this system which could suggest that the structures are less flexible than those formed by **NDI-I** and **NDI-V**.

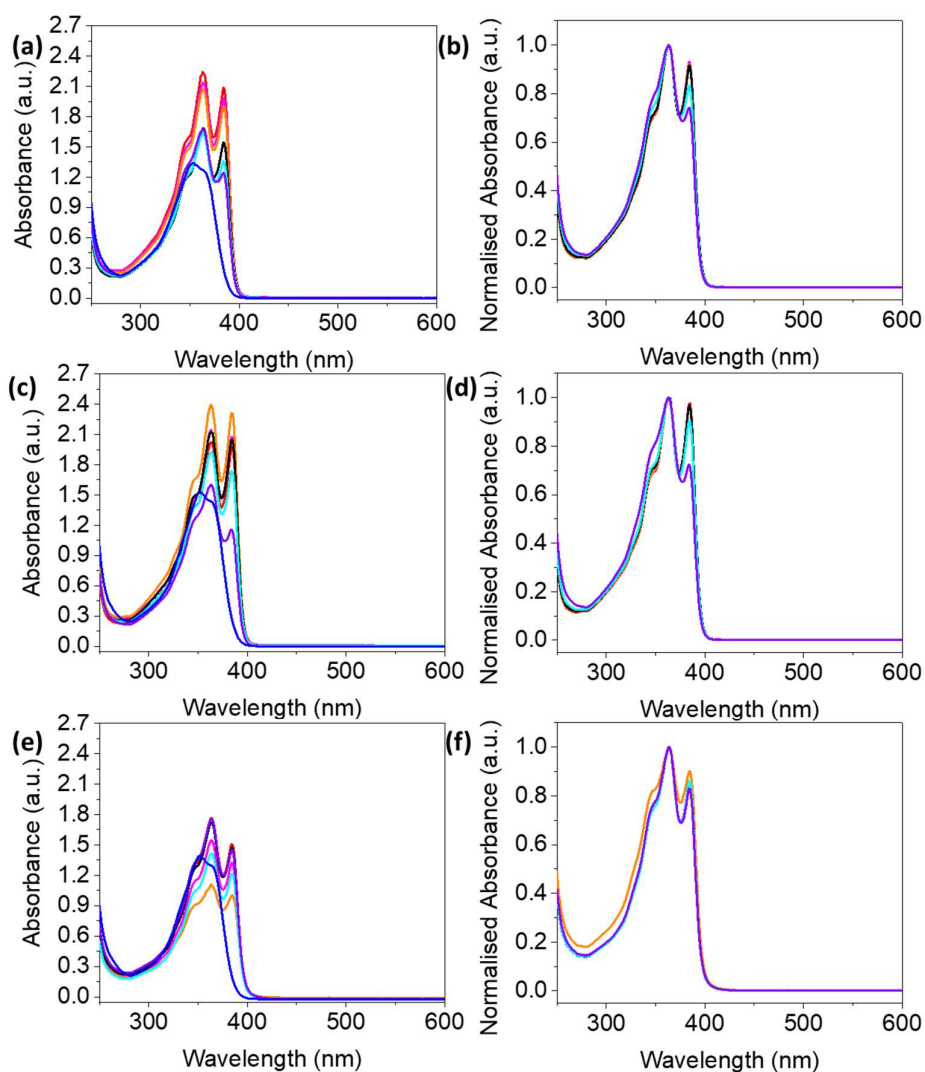


Figure 2.8. Absorbance of neutral solutions of (a-b) **NDI-I** and (c-d) **NDI-V** and (e-f) **NDI-F** at 5 mg/mL at pH 6 (red), 7 (pink), 8 (orange), 9 (black), 10 (turquoise), 11 (purple) and 12 (blue). (b), (d) and (f) show absorbance spectra of pH 6-11 between 250-600 nm normalised between 0 and 1.

We would expect dipeptide appended NDIs to be capable of forming larger aggregates than simple amino acid appended NDIs due to their increased size. The additional steric bulk of a second amino acid may also result in more crowded structures being formed. The neutral state of **NDI-GF** is the most influenced by pH compared to the simpler NDIs, however (similarly to **NDI-F**) **NDI-FF** is largely unaffected until high pH, Figure 2.9. This observation suggests that the role of the first amino acid in the dipeptide is important within aggregation. The glycine in **NDI-GF** could be providing more flexibility in the structure with freedom of movement and therefore allow the NDI to more freely change aggregation in response to pH.

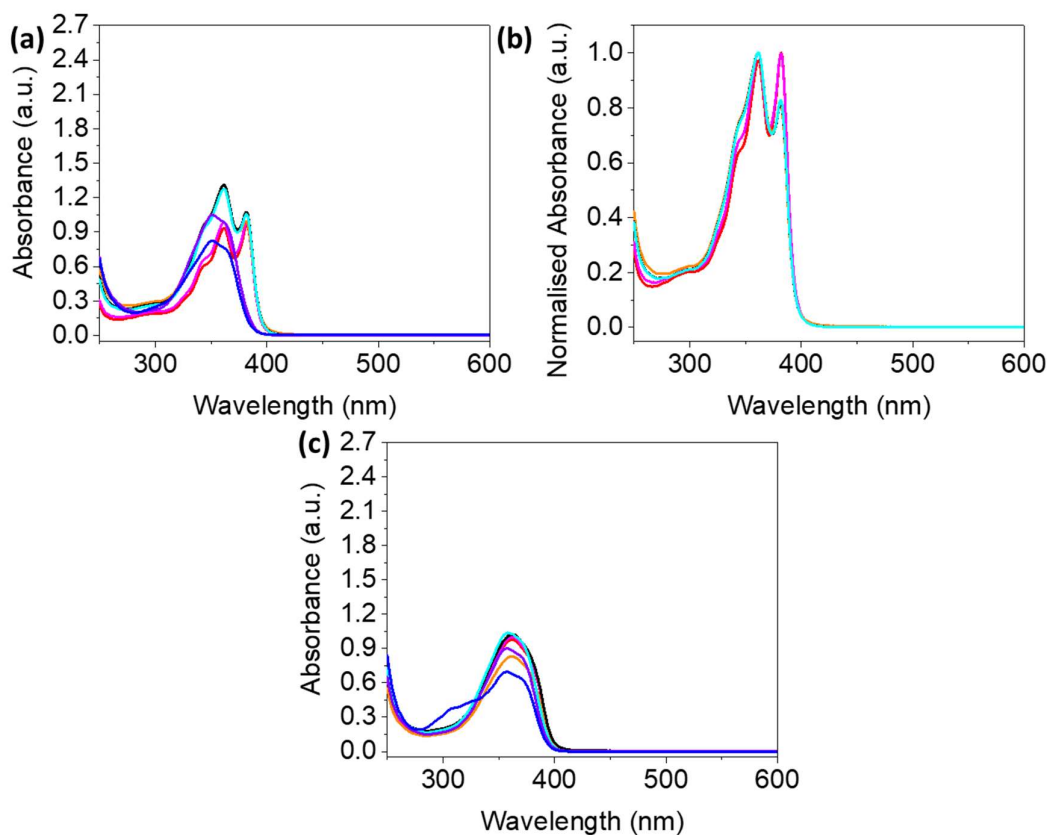


Figure 2.9. Absorbance of neutral solutions of (a-b) **NDI-GF** and (c) **NDI-FF** at 5 mg/mL at pH 6 (red), 7 (pink), 8 (orange), 9 (black), 10 (turquoise), 11 (purple) and 12 (blue). (b) show absorbance spectra of **NDI-GF** between pH 6-10 normalised between 0 and 1 for clarity.

Similarly to **NDI-I** and **NDI-V**, a change in the ratio of absorbances is observed in the spectra of **NDI-GF**, Figure 2.9(a-b). The absorbance at 380 nm decreases in relative intensity to that at 360 nm. This trend was observed around pH 10 in **NDI-I** and **NDI-V** but with **NDI-GF**, this phenomenon is observed from pH 8, Figure 2.9(b). The ratio of absorbances at pH 6 and 7 is comparable in absorbance intensity whereas at pH 8-10, the absorbances at 365 nm is larger. Changes to the packing of aggregates occurs

closer to the second pK_a than with other NDIs. A broad absorbance is observed at pH 11 whereas with the other NDIs this spectral change is only seen at pH 12, Figure 2.9(a). **NDI-GF** has the lowest first pK_a , which may be the reason changes occur at slightly lower pH values than the other NDIs. The added bulk of the dipeptide group may also cause changes in structure to occur at lower pH values.

NDI-FF has the most notably different neutral spectra to other NDIs investigated. One broad absorbance is observed centred around 365 nm, Figure 2.5(e) and Figure 2.9(c). This significant difference in spectra suggests a difference in the aggregation of this NDI compared to the other NDIs. This observation again suggests an importance in the first amino acid group of a dipeptide R group. At pH 12, a shoulder peak is now observed around 310-320 nm, Figure 2.9(b) which again, implies a change in aggregation. This behaviour is comparable with other NDIs as a change to the absorbance spectra is also noted at high pH. Only at pH 12 is there significant changes to the spectra, suggesting a consistent aggregation in this NDI through most pHs. This observation could suggest that this NDI does not form well defined aggregates.

2.2.4 Electrochromic response

NDIs can be reduced using photo- or electrochemistry to form the radical anion and dianion, in turn changing the colour of the system.¹ One of the criteria set out in the introduction was a dark coloured state. We hypothesise that the changes in aggregation of the neutral state discussed previously will influence the colouration of the reduced state of the NDIs. Firstly, we must investigate what the oxidation and reduction potentials are and whether they are pH dependent.

2.2.4.1 pH and redox potential values

Electrochemical reduction of the NDIs is achieved by application of a potential, which can be found by CV. In order to clearly see the colour change by eye, a two-electrode window cell as described in 2.4.2.8 is used. We intend to use this set-up for all measurements including spectro-electrochemistry for consistency. The diffusion rates within three-electrode spectro-electrochemistry cells may lead to data that is unrepresentative of the set-up we would use in real world applications (a window cell). CV of our systems performed in a two-electrode cell results in an asymmetric cyclic voltammogram. As a control, a 10 mg/mL hydroquinone solution was used as electrolyte in our two- and three-electrode set-ups, Table 2.2. and Figure A.2.6, Appendix. Oxidation and reduction peaks are shifted in the unreferenced set-up. Comparably to NDI systems, the reduction potentials are shifted to a greater extent than the oxidation potentials.

Table 2.2. Reduction and oxidation potentials taken from cyclic voltammograms of 10 mg/mL hydroquinone with 10 % 0.1 M NaCl. Cyclic voltammograms performed in referenced glassy carbon set-up (Ag/AgCl) or in a 1 x 1 FTO window set-up. The scan rate of the cyclic voltammograms was 0.5 V/s.

Set-up	Reduction Potential(s) (V)	Oxidation Potential (V)
Referenced glassy carbon	-0.2, -0.5	0.2
1 x 1 cm FTO window	-1.2, -1.9	0.9

CV carried out in a referenced set-up with our systems at pH 9 show more symmetrical peaks in the voltammograms, around ± 0.7 -1 V, Figures A.2.7-A.2.11, Appendix (this data is summarised in Table 2.3). Due to a small amount of reduction at the counter electrode (a colour change is observed by eye), a small shoulder at -0.3 V is observed in CVs. This peak is most pronounced in **NDI-I** and **NDI-V**, Figure 2.10. The large difference between oxidation and reduction potentials in a window cell is due to the unreferenced nature of the set-up and does not suggest an irreversible reduction.

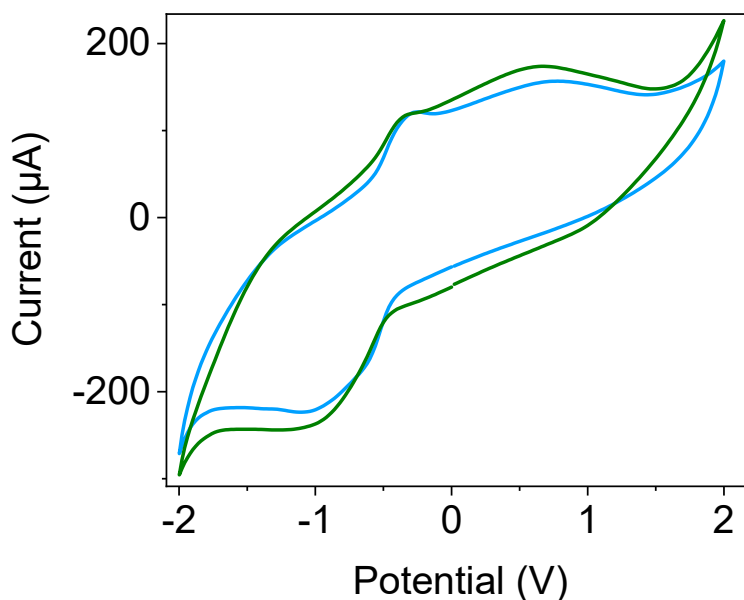


Figure 2.10. Cyclic voltammogram collected from 10 mg/mL solution of **NDI-I** (green) and **NDI-V** (blue) adjusted to pH 9. Voltammograms measured using a referenced glassy carbon set up (vs Ag/AgCl). The scan rate of the cyclic voltammograms was 0.2 V/s.

Table 2.3. Reduction and oxidation potentials taken from cyclic voltammograms of 10 mg/mL solutions of **NDI-I**, **NDI-V**, **NDI-F** and **NDI-GF** adjusted to pH 9. Cyclic voltammograms performed in referenced glassy carbon set-up (Ag/AgCl). The scan rate of the cyclic voltammograms was 0.2 V/s. The values for **NDI-GF** are shown at 0.2 and 0.5 V/s to see the oxidation potential.

	Reduction Potential(s) (V)	Oxidation Potential (V)
NDI-I pH 9	-1	0.7
NDI-V pH 9	-0.8	0.8
NDI-F pH 9	-1	0.7
NDI-GF pH 9 0.2 V/s	-0.9, -0.5	Unseen
NDI-GF pH 9 0.5 V/s	-1, -0.5	0.8
NDI-FF pH 9	-0.6, -1.3	1.6

CV was performed at different pH values to see whether the aggregates formed at different pHs as seen by UV-vis absorbance spectroscopy influenced the redox values, Figures A.2.12-A.2.16, Appendix. Data is summarised in Table 2.4-Table 2.8. An example of a voltammogram is shown in Figure 2.11.

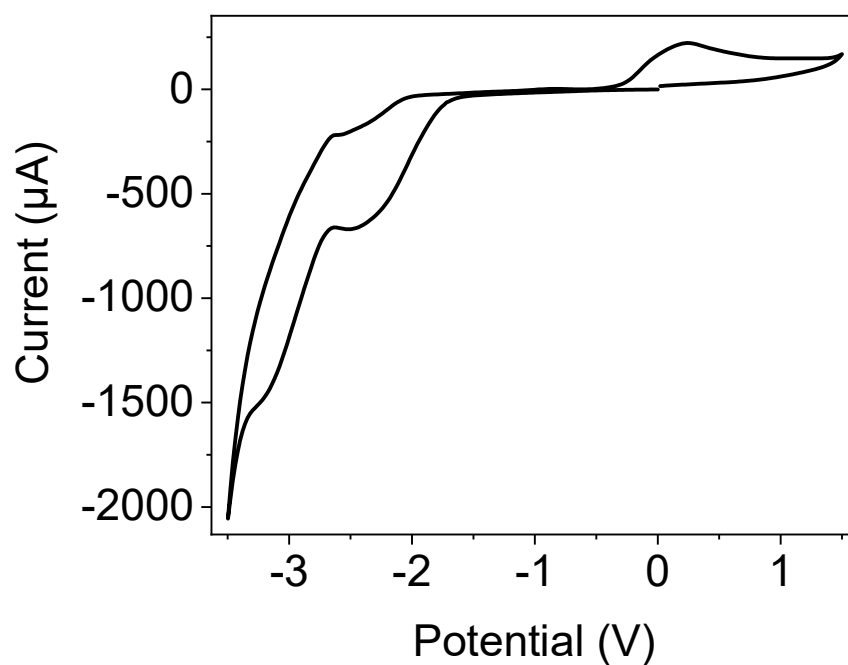


Figure 2.11. Cyclic voltammogram collected from 10 mg/mL solutions of **NDI-I** adjusted to pH 6 in a 1 x 1 FTO window cell. The scan rate of the cyclic voltammograms was 0.1 V/s.

As pH varies, we observe a small shift in reduction and oxidation potentials. The most significant difference in potential is observed at pH 12 compared with pH 6-11, Table 2.4-Table 2.8. This observation supports the evidence of absorbance spectroscopy, that a more significant aggregation change (which influences the redox potentials) occurs at pH 12 than between pH 6-11. Reduction potentials vary by roughly 0.7 V between pH 6 and 12 whilst oxidation potentials vary by 0.8, 0.8, 0.2, 0.4 and 0.5 V for **NDI-I**, **NDI-V**, **NDI-F**, **NDI-GF** and **NDI-FF** respectively.

Table 2.4. Reduction and oxidation potentials taken from cyclic voltammograms of 10 mg/mL solutions of **NDI-I** adjusted to different pH values. Cyclic voltammograms performed in FTO windows. The scan rate of the cyclic voltammograms was 0.1 V/s.

pH	Reduction Potential(s) (V)	Current at Reduction Potential(s) (μ A)	Oxidation Potential(s) (V)	Current at Oxidation Potential(s) (μ A)
6	-2.4, -3.2	-656, -1453	0.2	218
7	-2.6, -3.3	-981, 1459	0.3	309
8	-2.7	-956	0.3	275
9	-2.4, -3.3	-651, 1652	0.2	157
10	-2.7	-666	-0.1, 0.4	43, 71
11	-2.1, -2.7	-732, -1021	0.4	345
12	-2.0, -3.3	-507, -2363	0.1, 1.0	22, 308

Table 2.5. Reduction and oxidation potentials taken from cyclic voltammograms of 10 mg/mL solutions of **NDI-V** adjusted to different pH values. Cyclic voltammograms performed in FTO windows. The scan rate of the cyclic voltammograms was 0.1 V/s.

pH	Reduction Potential(s) (V)	Current at Reduction Potential(s) (μ A)	Oxidation Potential(s) (V)	Current at Oxidation Potential(s) (μ A)
6	-2.8	-289	0.3	144
7	-2.5	-1365	0.2	422
8	-2.5, -3.1	-1155, -1452	0.01, 0.9	649, 337
9	-2.7, -3.3	-1810, -1348	0.3	1053
10	-2.7, -3.3	-1668, -1418	0.3	830
11	-2.5, -3.2	-1053, -1567	0.1, 0.7	455, 371
12	-2.5, -3.1	-1274, -2139	0.2, 1	147, 105

The values of reduction and oxidation potentials are comparable across NDIs with the reduction around -2.5 V and the oxidation around 0.5 V. The reduction potential of **NDI-F** is found to be greater than other NDIs, Table 2.6. This observation suggests that R group influences redox potentials just as much as pH. The disparity with **NDI-F** is not significant, and an application of -2.5 V was found to result in a comparable colour to the other NDIs. Applying a more negative potential led to small amounts of water splitting in the 1 x 1 window cells which resulted in bubbles forming. For this reason, -2.5 V was chosen as the reduction potential for all NDIs at all pH values for consistency. This potential elicited a chromic response and was applied for 10 seconds. Spectra of the reduced states were observed using spectro-electrochemistry as described in 2.4.2.10.

Table 2.6. Reduction and oxidation potentials taken from cyclic voltammograms of 10 mg/mL solutions of **NDI-F** adjusted to different pH values. Cyclic voltammograms performed in FTO windows. The scan rate of the cyclic voltammograms was 0.1 V/s.

pH	Reduction Potential(s) (V)	Current at Reduction Potential(s) (μ A)	Oxidation Potential(s) (V)	Current at Oxidation Potential(s) (μ A)
6	-2.8	-1971	0.2	880
7	-2.8	-1307	0.2	365
8	-2.7	-2165	0.4	856
9	-2.9	-1777	0.2	798
10	-2.7	-1749	0.3	581
11	-2.1, -3.0	-545, -1856	0.2	752
12	-2.2, -3.0	-290, -456	0.2	149

We would expect two reduction and oxidation peaks, corresponding to the generation and oxidation of the radical anion and dianionic species. Both peaks are not always observed (especially the oxidation potentials) either because they are outside the range of the voltammogram in water or because both peaks are so close that they are overlapping or merged into one. Both reduction peaks are most clear in the voltammograms of **NDI-GF**, Table 2.7. In this set-up we cannot seem to selectively form one or the other reduced species specifically by choosing a specific potential, and there is no visible difference in colour observed by eye. This suggests perhaps our set-up is not suitable for this level of control, or something more complicated is occurring with the materials. For example, the dianionic species may not be stable.

Table 2.7. Reduction and oxidation potentials taken from cyclic voltammograms of 10 mg/mL solutions of **NDI-GF** adjusted to different pH values. Cyclic voltammograms performed in 1x1 cm FTO windows. The scan rate of the cyclic voltammograms was 0.1 V/s.

pH	Reduction Potential(s) (V)	Current at Reduction Potential(s) (μ A)	Oxidation Potential(s) (V)	Current at Oxidation Potential(s) (μ A)
6	-2.5, -3.1	-579, -1184	0.8	111
7	-2.4, -3.0	-614, -1203	0.8	143
8	-2.3, -2.9	-631, -1133	0.8	208
9	-2.3, -2.9	-717, -1168	0.7	234
10	-2.5, -3.2	-994, -1930	0.7	400
11	-2.0, -3.2	-588, -1966	0.04, 1.1	21, 286
12	-1.8, -2.6	-476, -1798	0.2, 1.1	18, 201

Table 2.8. Reduction and oxidation potentials taken from cyclic voltammograms of 10 mg/mL solutions of **NDI-FF** adjusted to different pH values. Cyclic voltammograms performed in FTO windows. The scan rate of the cyclic voltammograms was 0.1 V/s.

pH	Reduction Potential(s) (V)	Current at Reduction Potential(s) (μ A)	Oxidation Potential(s) (V)	Current at Oxidation Potential(s) (μ A)
6	-2.6	-492	0.6	60
7	-2.6	-489	0.4	175
8	-2.5	-359	0.7	112
9	-2.5	-357	0.6	124
10	-2.4	-465	0.5	86
11	-2.2, -3.2	-413, -1348	0.7	57
12	-1.9, -2.6	-326, -554	0.9	44

2.2.4.2 Electrochemically reduced colour

The radical anion can be generated in seconds by application of a reducing potential and is evidenced by a significant colour change as well as the appearance of absorbances in the visible/near-infrared (IR) region.^{1,44,57} In the reduced spectra, absorbances at long wavelength (>700 nm) have been attributed to $D_0 \rightarrow D_1$ transitions in comparable NDIs.⁵⁸ These transitions arise from the unpaired electron doublet state of the radical anionic species.⁵⁸ We would expect peaks arising from $\pi \rightarrow \pi^*$ and $n \rightarrow \pi^*$ transitions.⁵⁹ The darkest possible coloured state is a desirable quality for Smart Windows. Having confirmed pH does not significantly change the colour of the neutral states of the NDIs, we

must now investigate the coloured state. Having decided upon a reduction potential to be used across all experiments for consistency, we can now analyse whether electrochromic behaviour is affected by changes in aggregation triggered by pH.

Between pH 6-11, pH does not affect the position of absorbances related to the radical anion, but the absorbance intensity is affected, Figure 2.12-Figure 2.16. These observations imply that any difference in aggregation as pH changes does not affect the type of radical anion produced but does influence the amount of radical anion produced. Certain aggregations either facilitate electrochemical processes (through increased charge transfer, for example by π stacking) or can stabilise the radical anion once it is formed. Either factor will result in a higher concentration of radical anion and a darker colouration and higher absorbance intensity.

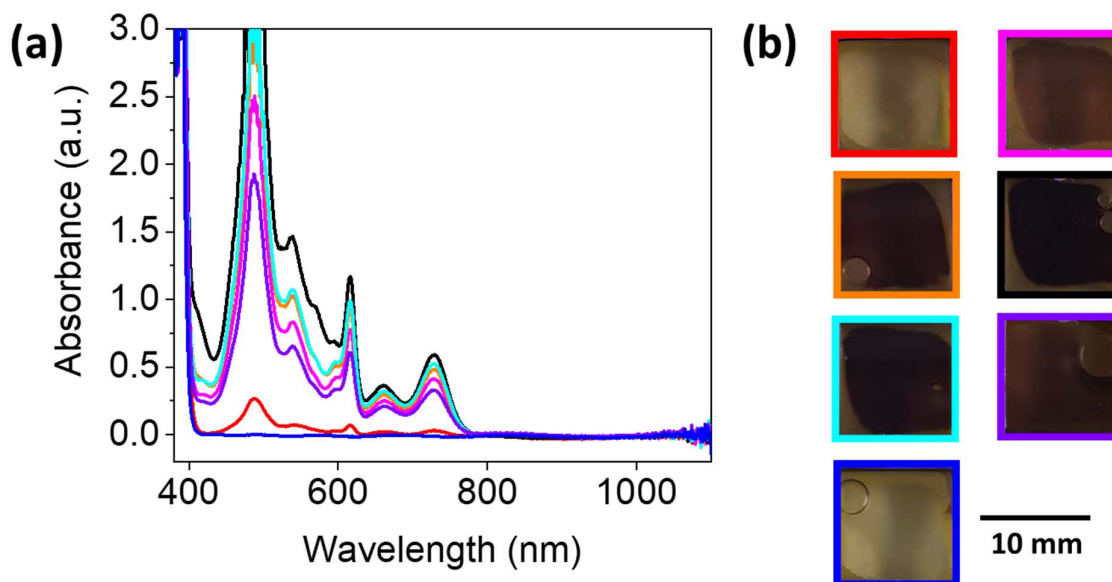


Figure 2.12. (a) Absorbance spectra of 10 mg/mL solutions of **NDI-I** after a 10 second application of -2.5 V. Solutions adjusted to pH 6 (red), 7 (pink), 8 (orange), 9 (black), 10 (turquoise), 11 (purple) and 12 (blue) (b) Images of the resulting colouration in FTO windows are shown. Any bubbles caused by loading.

There have been reports of mixes of both the radical and dianion (Figure 2.1) in solution but we assume the radical anion to be dominating in solution as the dianionic species relax to form the radical and the radical is formed readily.⁵⁷ This dianionic species is reported to be evidenced by an absorbance at approximately 410 nm.^{1,57} A purple colouration has been reported to be characteristic of the NDI dianionic species whilst the radical is brown.⁵⁷ However, other reported systems observed the dianion and radical anion as pink and orange respectively.⁶⁰ Colour alone is not an indication of the species present. While there may be some dianionic species in solution upon reduction, we expect it to be

minimal and relatively unstable compared to the radical anionic species. A strong electron paramagnetic resonance (EPR) signal is observed for NDI reduced states and so we assume little dianionic species are present.^{1,57} This data will be discussed further in Chapter 3.

The characteristic dianionic absorbance around 410-415 nm^{1,57} is observed very weakly in the reduced spectra of **NDI-I** and **NDI-V** at some pHs, Figure 2.12-Figure 2.13. This observation suggests that a small amount of dianion is present in solution but does not affect colouration. The dianionic absorbance is not observed in the spectra of **NDI-F** (Figure 2.14), but a consistent dark purple colouration is observed comparable with **NDI-I** and **NDI-V**, Figure 2.12-Figure 2.13.

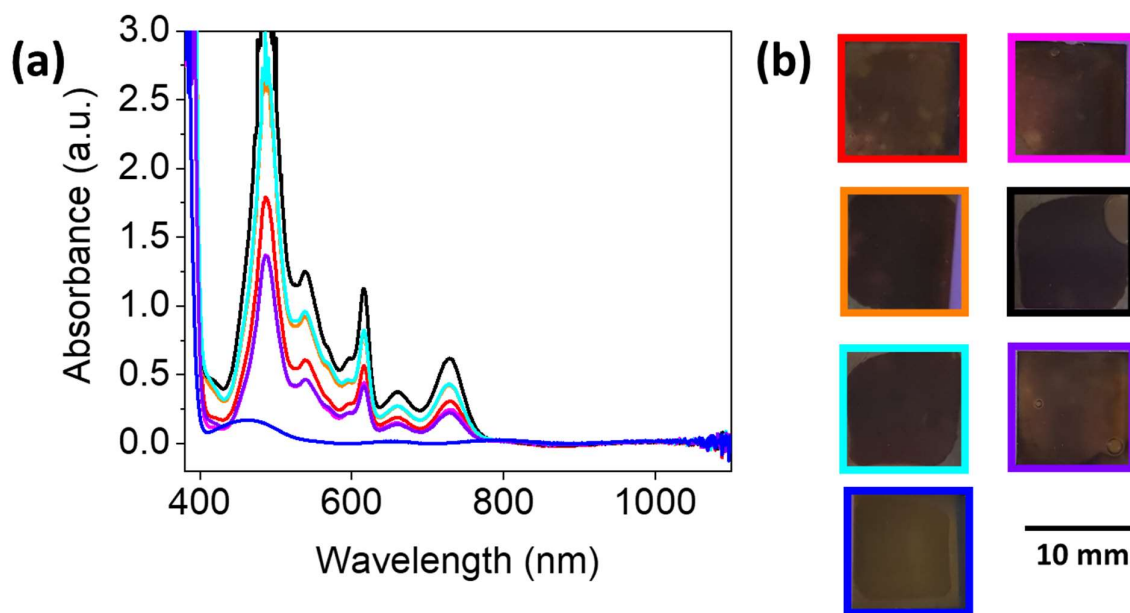


Figure 2.13. (a) Absorbance spectra of 10 mg/mL solutions of **NDI-V** after a 10 second application of -2.5 V. Solutions adjusted to pH 6 (red), 7 (pink), 8 (orange), 9 (black), 10 (turquoise), 11 (purple) and 12 (blue) (b) Images of the resulting colouration are shown. Any bubbles caused by loading.

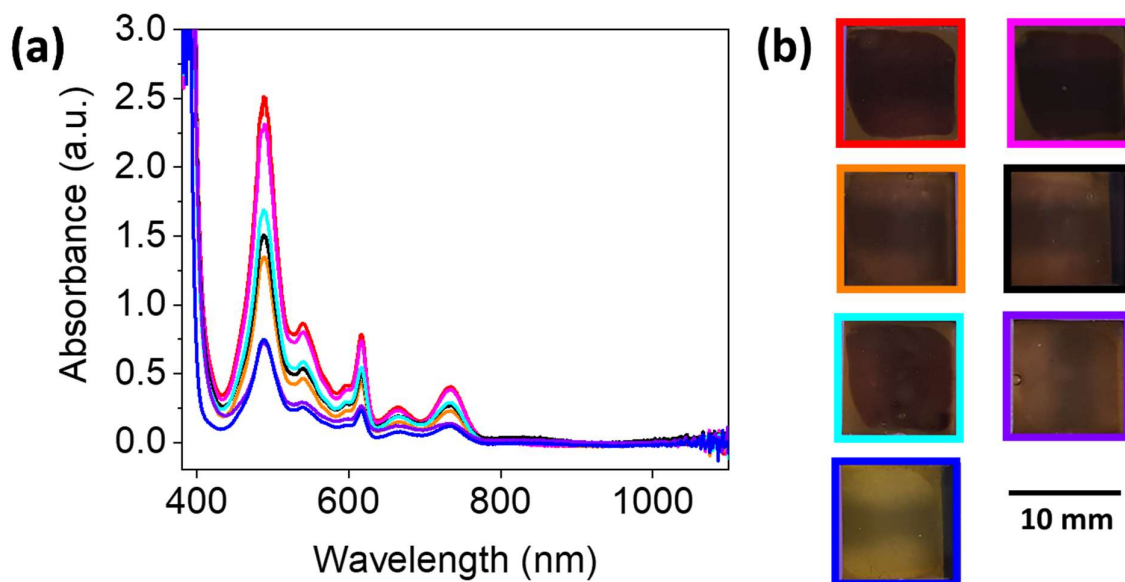


Figure 2.14. (a) Absorbance spectra of 10 mg/mL solutions of **NDI-F** after a 10 second application of -2.5 V. Solutions adjusted to pH 6 (red), 7 (pink), 8 (orange), 9 (black), 10 (turquoise), 11 (purple) and 12 (blue) (b) Images of the resulting colouration are shown. Any bubbles caused by loading.

Across all NDIs, solutions at pH 12 produce very little radical anion and any colouration is almost undetectable to the eye, Figure 2.12-Figure 2.16. This observation is consistent with the more significant change in aggregation observed across all NDIs in the neutral state (nonreduced) spectra.

With the exception of **NDI-I** and **NDI-FF** (Figure 2.12 and Figure 2.15), peaks are still observed in the visible/near IR region at pH 12 which suggests that a small amount of radical anion is produced. In **NDI-V** and **NDI-GF** spectra at pH 12 (Figure 2.13 and Figure 2.16), one broad absorbance around 500 nm is observed instead of more distinct absorbances seen in **NDI-F** at pH 12, Figure 2.14. This observation suggests that the absorbances are weak and poorly defined or else a difference in aggregation results in a different spectrum in some NDIs.

It is hypothesised that the consistent broad absorbance observed in all neutral NDIs at pH 12 is representative of an aggregation associated with poor electrochromic response. This type of spectra was observed at all pH values of **NDI-FF**, Figure 2.9(c). As a direct result, the electrochromic response across all pH values is also poor for **NDI-FF**, Figure 2.15. Compared to other NDIs investigated, the colour intensity was much weaker upon reduction. We hypothesise that the aggregation of this NDI does not significantly change as much as others with pH because that **NDI-FF** is incapable of forming comparable structures to other NDIs. As previously stated, the lack in freedom in structure can be linked to the chemical structure of **NDI-FF**.

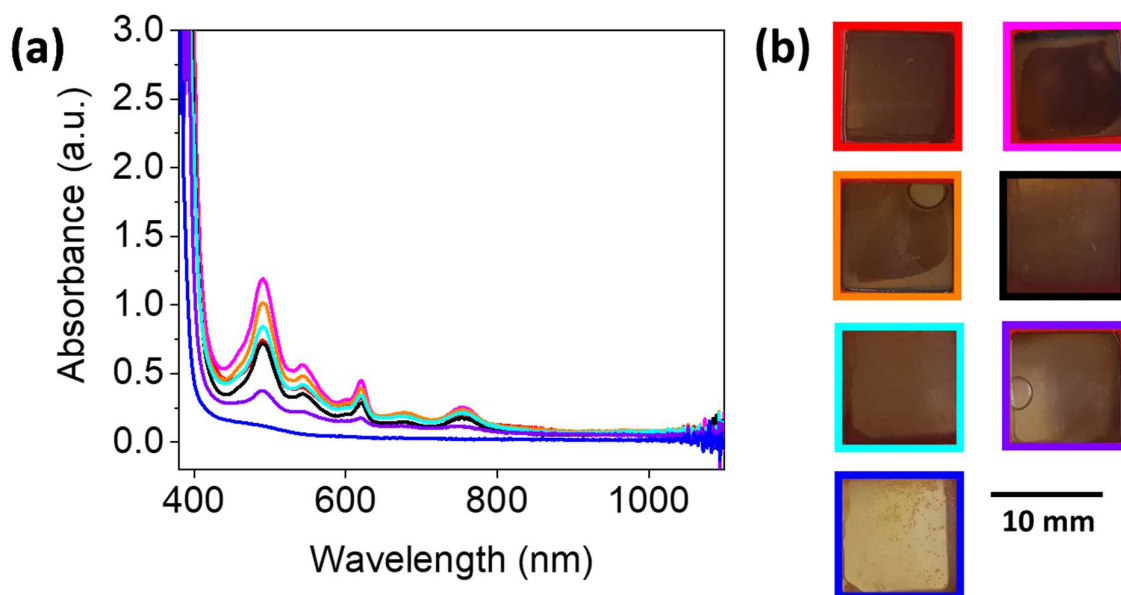


Figure 2.15. (a) Absorbance spectra of 10 mg/mL solutions of **NDI-FF** after a 10 second application of -2.5 V. Solutions adjusted to pH 6 (red), 7 (pink), 8 (orange), 9 (black), 10 (turquoise), 11 (purple) and 12 (blue) (b) Images of the resulting colouration are shown. Any bubbles caused by loading.

With the added flexibility of **NDI-GF** as discussed previously, we observe that this NDI can form darker reduced states than **NDI-FF**, Figure 2.16. This data supports our hypothesis that the aggregation of **NDI-FF** is responsible for its poor chromic behaviour. In the reduced solutions of **NDI-GF**, a broad absorption in the near IR region over 900 nm is associated with one-dimensional π -stacking of the radical anion.^{1,9,57} This observation suggests different packing or aggregation compared to the other NDIs and resulting in a brownish colour as opposed to a dark purple. As with the neutral states, absorbances are found at a slightly shorter wavelength compared to other NDIs.

In neutral spectra of **NDI-GF**, a broad absorbance was observed at pH 11 and pH 12, Figure 2.9(a). A very weak colouration is observed at both pH values, Figure 2.16. This observation supports the hypothesis that this aggregation type results in poor electrochemical reduction or else poor stabilisation of the radical anion.

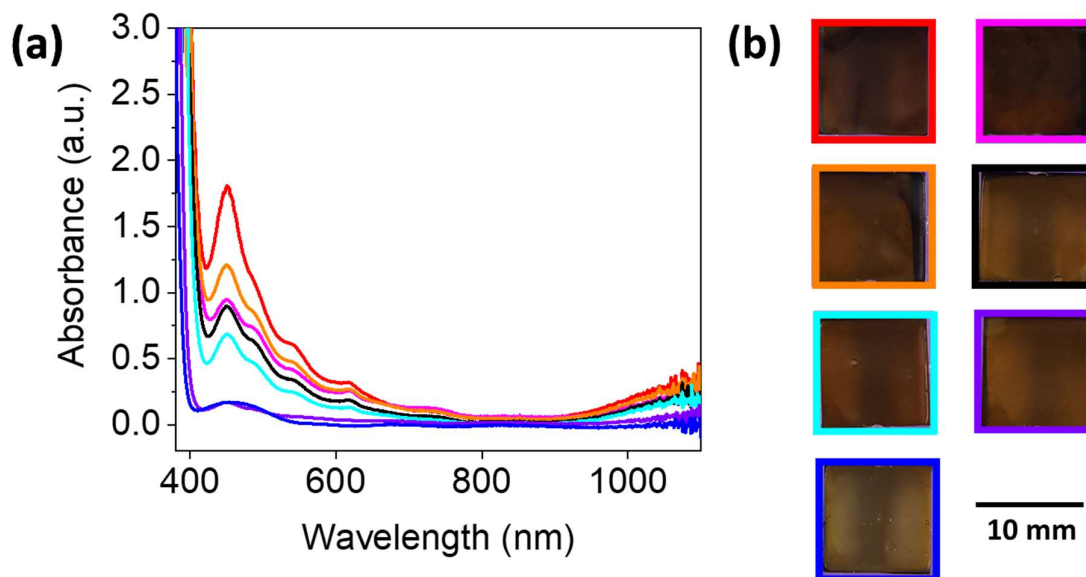


Figure 2.16. (a) Absorbance spectra of 10 mg/mL solutions of **NDI-GF** after a 10 second application of -2.5 V. Solutions adjusted to pH 6 (red), 7 (pink), 8 (orange), 9 (black), 10 (turquoise), 11 (purple) and 12 (blue) (b) Images of the resulting colouration are shown. Any bubbles caused by loading.

2.2.4.3 Ideal pH

It is quite clear from the data above that pH has an influence on the colour intensity of NDIs, therefore we can deduce that there is an ideal pH in order to satisfy the colour aspect of our stated criteria. We can compare the ideal pH of NDIs by monitoring the absorbance at 490 nm for **NDI-I**, **NDI-V**, **NDI-F**, and **NDI-FF** and 450 nm for **NDI-GF**. This absorbance, referred to as peak A, is characteristic for the radical anion in each species and is the λ_{max} of each spectra. Taking the series of values, the absorbance at peak A was normalised between 0 and 1 for clarity, with 0 being the pH at which the weakest absorbance intensity is recorded, and 1 the highest. By eye, we can see that the darkest colouration occurs at pH 9 for **NDI-I** and **NDI-V** whereas pH 6 gives darkest colour for **NDI-F** and **NDI-GF**. Although all the colouration in **NDI-FF** is weak, the darkest colour is seen at pH 7.

The shape of the plot in Figure 2.17(a) supports the assertion that aggregation changes occur around the pK_a values of these systems. Above the second pK_a of approximately pH 6.5, the production of radical anion decreases in **NDI-F** and increases in **NDI-I** and **NDI-V**. Between pH 8 and 11 (covering the range of the first pK_a of approximately 9.5) we observe changes in intensity across all three NDIs. **NDI-GF** and **NDI-FF** have generally more linear trends, Figure 2.17(b), than **NDI-I**, **NDI-V** and **NDI-F**. Fluctuations in the decrease in colouration intensity as pH increases in **NDI-F**, **NDI-GF** and **NDI-FF** are seen at pH 7 and pH 10 (more significantly at pH 10 in **NDI-FF** and **NDI-F**).

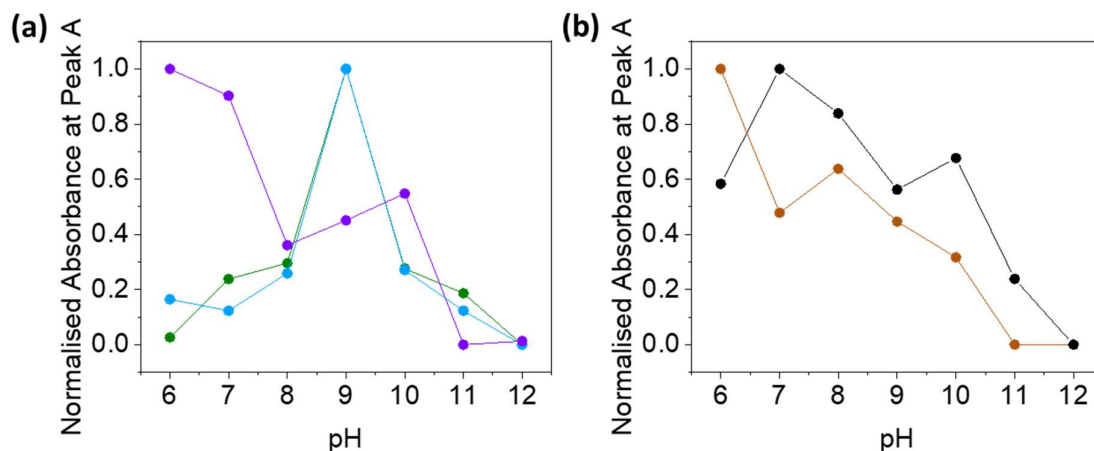


Figure 2.17. Absorbance normalised between 0 and 1 showing trend in absorbance (at 490 nm for **NDI-I**, **NDI-V**, **NDI-F**, and **NDI-FF** and 450 nm for **NDI-GF**) characteristic of the radical anionic species electrochemically generated between pH 6 and 12. Measurements taken from spectra of (a) **NDI-I** (green), **NDI-V** (blue) and **NDI-F** (purple) and (b) **NDI-GF** (brown) and **NDI-FF** (black) at 10 mg/mL.

These trends suggest a transition in aggregation between pH 6 and 10 and pH 10-12. Changes in this first region are consistent with the apparent pK_a values and the trends in packing of aggregates observed in the neutral states of **NDI-I**, **NDI-V** and **NDI-GF** between pH 6 and 11 or 10. Changes in the latter region are consistent with apparent pK_a values and the more significant trends in aggregation observed in the neutral states of all NDIs at pH 12. The trends in colouration of the reduced states are comparable between **NDI-I** and **NDI-V** and between **NDI-F**, **NDI-GF** and **NDI-FF**. We note these two groups of NDIs are similarly appended in terms of aliphatic or aromatic moieties. Within the groups, the NDIs have the same or comparable ideal pH. Without a larger library, we cannot make general comments about aliphatic and aromatic aggregates. Such a scale of library is outside of the scope of this investigation.

2.2.4.4 Switchability

While a dark colouration upon electrochemical reduction is of critical importance to the application of Smart Windows, the rate of electrochemical oxidation is also a property that should be maximised. As the efficiency of electrochemical reduction was found to be pH dependent, we hypothesised that the oxidation process will be similarly influenced. Solutions at pH 6, 9 and 12 were investigated. These three pHs will capture the systems within each state of aggregation, evaluating the NDIs above and below each pK_a value. Solutions were reduced for 20 seconds and the decrease in intensity at 540 nm is tracked. After 20 seconds even at pH 12, some characteristic radical anionic absorbances are observed in **NDI-I**, **NDI-V**, **NDI-F** and **NDI-GF**, Figure 2.18-Figure 2.19. NDIs that have darkest colouration (before a consistent oxidising potential of 0.5 V is applied) will likely take a longer time to

fully reverse the colour change because the concentration of radical anion to oxidise is higher. As the colouration of **NDI-FF** was so weak across all pH values (Figure 2.15) compared to other NDI systems and so did not meet our criteria, this system was not investigated for the application of Smart Windows further. Aggregation of this NDI is discussed in Chapter 3.

The oxidation process took longer than reduction. This observation is likely due to the stability of the radical anionic species.¹ In general, the initial loss in colouration is significant within the first minute of application of oxidising potential but then the rate decreases. Similar perylene bisimides (PBIs) have been shown to become more conductive when irradiated in films due to the production of the radical anion.^{16,29} While these PBIs are more conductive than our systems, it is likely that a higher concentration of radical anion in our system would also aid conductivity which is likely to contribute to a consequently initially fast electrochemical oxidation, dropping as radical concentration decreases.

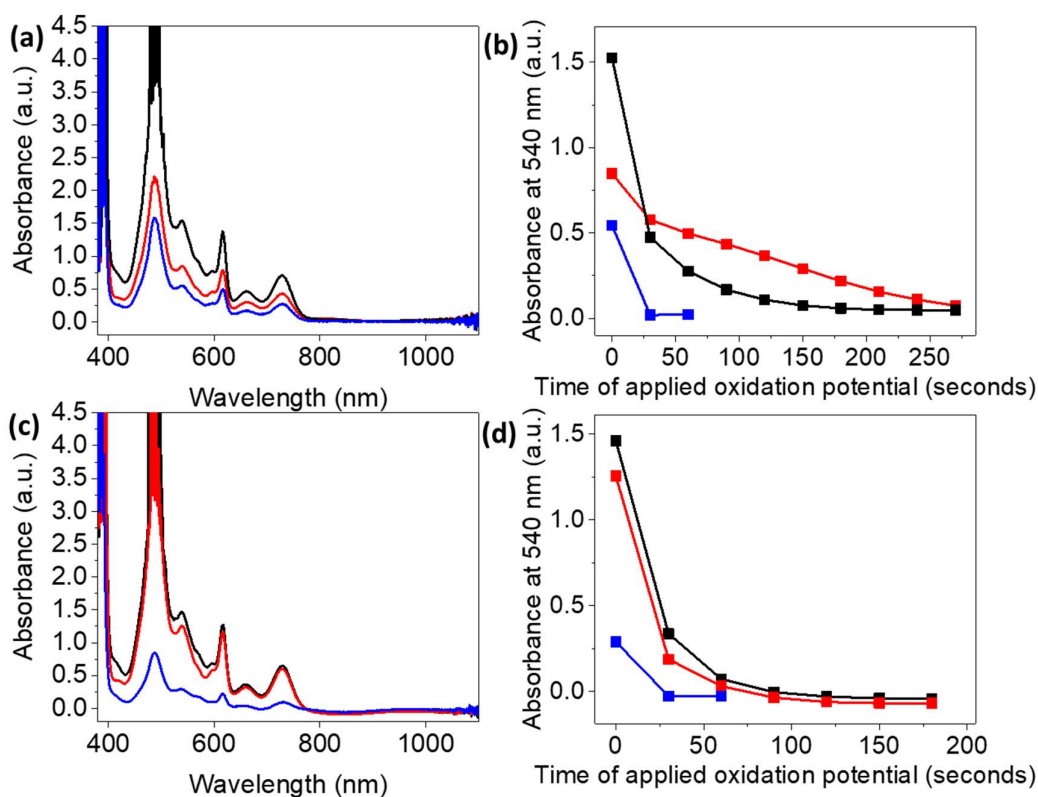


Figure 2.18. Absorbance spectra (lines) collected from electrochemically reduced solutions of (a) **NDI-I** and (c) **NDI-V** at 10 mg/mL after 20 second application of -2.5 V and a measure of absorbance at 540 nm (squares) taken every 30 seconds as oxidising potential of oxidation potential of 0.5 V was applied for 300 seconds to electrochemically reduced solutions of (b) **NDI-I** at and (d) **NDI-V** 10 mg/mL after 20 second application of -2.5 V. Solutions adjusted to pH 6 (red), 9 (black) and 12 (blue).

Because colouration is so weak at pH 12, the oxidation to a neutral state is very fast, Figure 2.18-Figure 2.19. Solutions of **NDI-I** demonstrate the fastest oxidation at pH 9, Figure 2.18(b) whereas oxidation at pH 9 and 6 are more comparable for **NDI-V**, Figure 2.18(d). The intensity of the reduced states are also more comparable at pH 6 and 9 for **NDI-V**. Oxidation is complete after approximately 150 and 90 seconds for **NDI-I** and **NDI-V** respectively. These NDIs form comparably intense states upon reduction at pH 9. For these NDIs, their ideal pH for reduction and oxidation are pH 9.

NDI-F and **NDI-GF** show similar trends to **NDI-V** in that the rate of oxidation is more comparable between pH 6 and 9 than observed in spectra of **NDI-I**, Figure 2.19(b and d). In both cases pH 6 shows a steeper rate of oxidation than pH 9, which is the same pH at which reduction was the most efficient (the same trend as demonstrated in **NDI-I** and **NDI-V**). Oxidation is completed in **NDI-F** and **NDI-GF** in 30 and 120 seconds respectively.

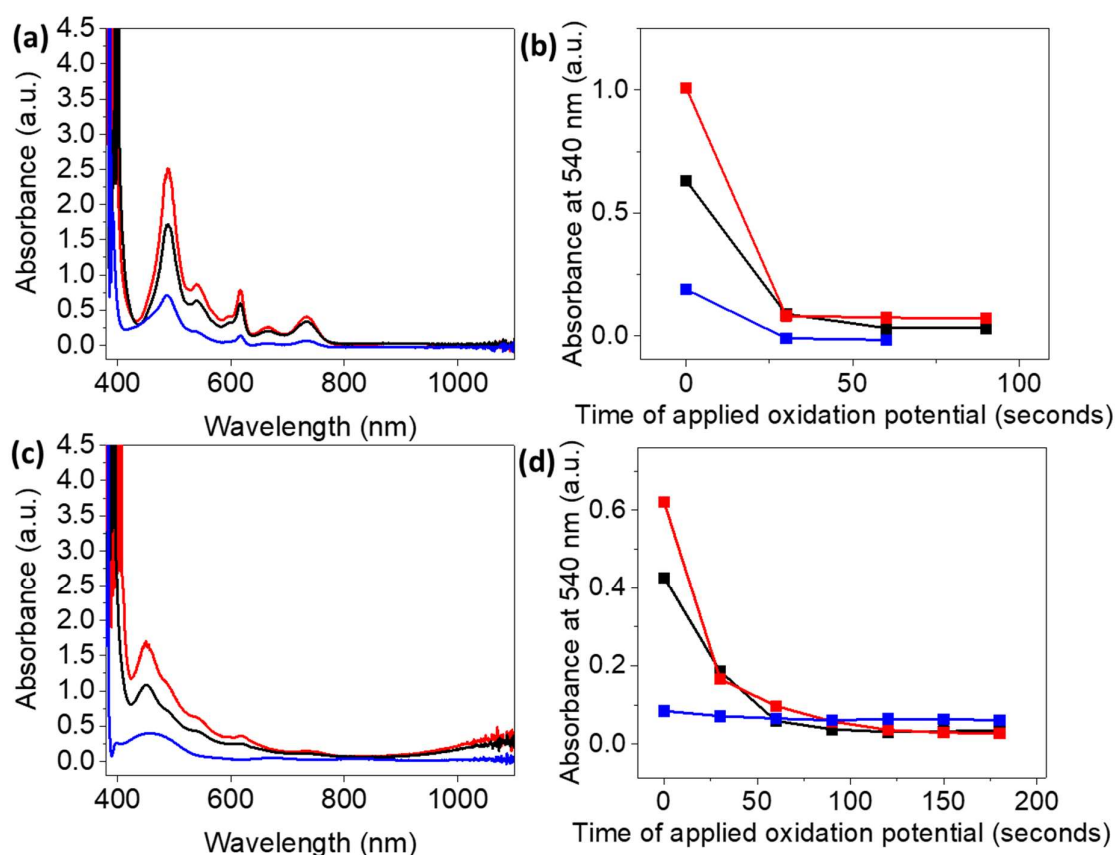


Figure 2.19. Absorbance spectra (lines) collected from electrochemically reduced solutions of (a) **NDI-F** and (c) **NDI-GF** at 10 mg/mL after 20 second application of -2.5 V and a measure of absorbance at 540 nm (squares) taken every 30 seconds as oxidising potential of oxidation potential of 0.5 V was applied for 300 seconds to electrochemically reduced solutions of (b) **NDI-F** at and (d) **NDI-GF** 10 mg/mL after 20 second application of -2.5 V. Solutions adjusted to pH 6 (red), 9 (black) and 12 (blue).

At their ideal pH of 9, **NDI-I** and **NDI-V** form the most intense coloured states and are comparable to each other. **NDI-GF** forms the least intense coloured state at its ideal pH of 6 compared to other NIDs at their ideal pH. The speed of oxidation is quickest in **NDI-F**. **NDI-V** demonstrates the next quickest oxidation, followed by **NDI-GF** and **NDI-I** is the slowest. While **NDI-F** has the quickest oxidation, it does not form the darkest reduced states. **NDI-V** seems the most promising, forming darkest coloured states and fully reversing colouration after 90 seconds.

2.3 Conclusions

Referring to our criteria for the application of Smart Windows, we can conclude at this stage that all NDIs investigated were able to be dispersed in water between pH 6 and 12. All NDIs were also a pale colour before reduction, especially when in a thin gap. **NDI-I**, **NDI-V**, **NDI-F** and **NDI-GF** can form dark coloured states within 10 seconds that are reversible. **NDI-FF** cannot form comparably dark states, most likely due to an aggregation which does not favour stabilisation of the radical anion. Due to the poor electrochemical performance of **NDI-FF**, it is not suitable to the application of Smart Windows.

We have found a pH for each of these NDIs at which electrochemical reduction and oxidation is maximised. Reduction occurs within a few seconds whereas oxidation can take several minutes. pH can be used to tune colouration intensity and 'switchability' by forming an aggregation that improves charge transfer through the system and /or stability of the radical anionic species, leading to efficient reduction and oxidation. Because the oxidation process takes longer than the reduction, we hypothesise that the aggregation stabilised the radical anion once formed. The final criteria of stability and cyclability will be assessed in Chapter 3. We can investigate the aggregates of each system at different pHs and infer more about what makes favourable or unfavourable structures with regards to electrochemical processes using more in-depth SAS techniques. The initial data supports our hypothesis that chemical structure and pH impact chromic properties and that this is likely linked to aggregation.

2.4 Experimental

2.4.1 Synthetic procedures

All chemicals and solvent were purchased from Merck Life Sciences, or Alfa Aesar and used as received except for naphthalenetetracarboxylic dianhydride (NTCDA). NTCDA was purchased from Flurochem, Alfa Aesar and Merck Life Sciences but impurities were found by nuclear magnetic resonance (NMR) spectroscopy in all batches. Following this, all NTCDA was purchased from Fluorchem and purified according to the procedure below. Deionised water was used throughout. Light was excluded using aluminium foil to reduce generating the radical anion which is hard to remove from solid material.

NMR spectra and high resolution mass spectrometry (HRMS) can be found in the Appendix (Figures A.2.17-A.2.54).

2.4.1.1 Purification of Isochromeno[6,5,4-def]isochromene-1,3,6,8-tetraone (NTCDA)

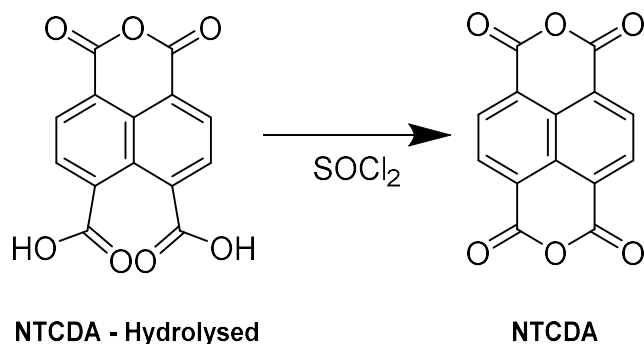


Figure 2.20. Reaction scheme of the purification of NTCDA.

More Information about this purification can be found in Appendix.

Impurities were removed by combining 32.1 g of impure material with 100 mL SOCl₂ and heating to 90 °C under reflux overnight. The reaction vessel was wrapped in aluminium foil to prevent light exposure. The SOCl₂ was then removed under vacuum and the product stirred in isoctane for 1 hour to remove any remaining SOCl₂. Isoctane was removed under vacuum and the product stirred in Et₂O for 1 hour. The mixture was filtered, and the product was dried under vacuum to remove trace solvents to yield a brown solid (30.2 g, 94%). This method successfully converted the impurity into NTCDA seen by ¹H NMR, Figures A.2.47-A.2.48, Appendix.

To remove the discolouration in the material 5.90 g of NTCDA was dissolved in 400 mL of dimethylformamide (DMF) and heated to 110 °C, then allowed to recrystallise in the freezer. The product was recovered and dried by suction filtration to yield NTCDA – Purified as a pale-yellow solid (4.42g, 75%). Both pure and impure material were not suitably soluble in DMSO-d₆ to produce a well-defined ¹³C NMR spectrum. No difference was observed by NMR in the pale-yellow and dark coloured NTCDA. The pale-yellow material was used throughout for the synthesis of the NDIs.

¹H NMR (400 MHz, DMSO-d₆) δ 8.71 (s, 4H, H-Ar).

2.4.1.2 Synthesis of (2*S*,3*S*)-2-{13-[(1*S*,2*S*)-1-carboxy-2-methylbutyl]-5,7,12,14-tetraoxo-6,13-diazatetracyclo[6.6.2.0^{4,16}.0^{11,15}]hexadeca-1,3,8,10,15-pentaen-6-yl}-3-methylpentanoic acid (**NDI-I**)

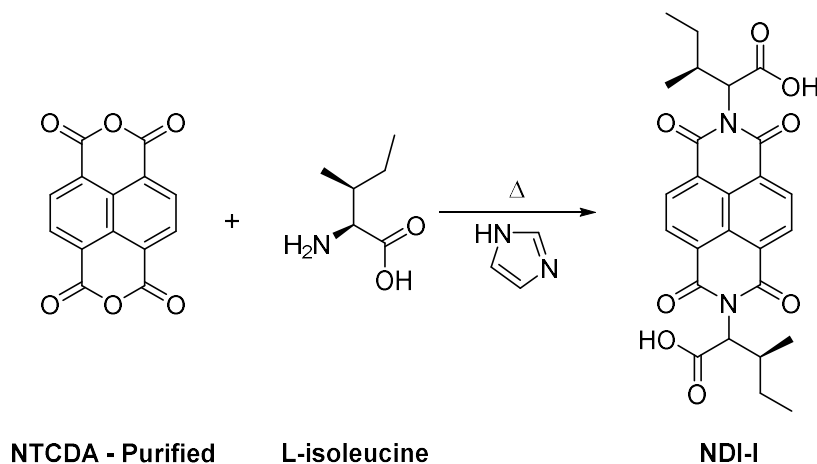


Figure 2.21. Synthesis of **NDI-I**.

NTCDA (2 g, 1 eq.), L-isoleucine (2 eq, 1.96 g), and imidazole (10 eq, 5.08 g) were added to a 250 mL Schlenk tube and sealed with a rubber septum. This was then degassed whilst vigorously stirring under argon atmosphere for 10 minutes. The temperature was set to 120 °C and the reactants allowed to stir for 5 hours. The temperature was then reduced to 90 °C. Water (50 mL) was added and stirring continued at 90 °C for a further hour, after which the mixture was allowed to cool to ambient temperature overnight in air. Insoluble materials were removed by filtration through filter paper and the filtrate was poured into hydrochloric acid (2M, 300 mL), and stirred for 30 minutes. This precipitate was collected by suction filtration, washed with lots of water, and transferred into another 300 mL portion of 1 M hydrochloric acid with 5 mL acetonitrile. This mixture was heated at 90 °C with stirring for 2 hours. The resulting solids were filtered while hot, washed with 1M HCl and then non-acidic water until the filtrate had an approximate pH of 6-7. The product was then dried by lyophilisation (after neutralisation) overnight to yield **NDI-I** as light beige solid (2.44 g, 66%). The solid was then characterised by ¹H and ¹³C NMR and HRMS.

¹H NMR (400 MHz, DMSO-*d*₆) δ 12.83 (br s, 2H, COOH), 8.78-8.74 (m, 4H, NDI-HAr), 5.26 (d, *J* = 9.0 Hz, 1H, NCH), 5.22 (d, *J* = 9.2 Hz, 1H, NCH), 2.48-2.41 (m, 2H, CH₃CH₂), 1.99-1.85 (m, 1H, CH₃CH), 1.35-1.23 (m, 2H, CH₃CH₂), 1.19 (d, *J* = 6.5 Hz, 3H, CH₃CH), 0.95 (t, *J* = 7.5 Hz, 3H, CH₃CH₂), 0.92-0.83 (m, 1H, CH₃CH), 0.74 (t, *J* = 7.3 Hz, 3H, CH₃CH₂), 0.69 (d, *J* = 6.9 Hz, 3H, CH₃CH). ¹³C NMR (100 MHz, DMSO-*d*₆) δ 170.70, 170.62, 162.99 and 162.97 (C=O), 131.99, 126.93, 126.28, 126.26, 126.25, 126.23 (CAr), 58.42 and 57.12 (NCH), 33.67 and 33.56 (CHCH₃), 28.18 and 25.18 (CH₂CH₃), 18.4 and 15.23 (CH₃),

11.52 and 11.34 (CH₃). HRMS (ESI) m/z: [M+Na]⁺ calculated for C₂₆H₂₆N₂O₈Na, 517.1581; found 517.1569.

2.4.1.3 Synthesis of (2S)-2-{13-[(1S)-1-carboxy-2-methylpropyl]-5,7,12,14-tetraoxo-6,13-diazatetracyclo[6.6.2.0^{4,16}.0^{11,15}]hexadeca-1,3,8,10,15-pentaen-6-yl}-3-methylbutanoic acid (**NDI-V**)

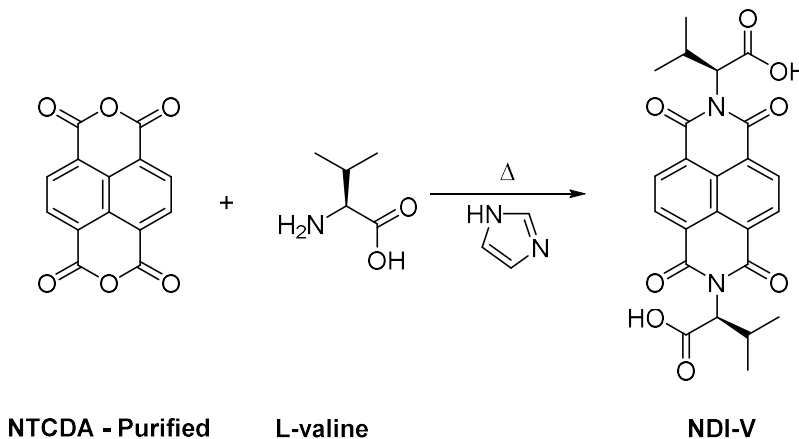


Figure 2.22. Synthesis of **NDI-V**.

The methodology of synthesis is identical to that described in 2.4.1.2, using L-valine (2 eq, 1.75 g), NTCDA (1 eq, 2 g) and imidazole (10 eq, 5.08 g). Synthesis was performed shielded from UV light and the solids degassed. The product **NDI-V** was collected as a light beige solid (2.53 g, 69 %). The solid was then characterised by ¹H and ¹³C NMR and HRMS.

¹H NMR (400 MHz, DMSO-d₆) δ 12.86 (br s, 2H, COOH), 8.78 (s, 4H, NDI-HAr), 5.18 (d, J = 9.1 Hz, 2H, NCH), 2.76–2.60 (m, 2H, CH(CH₃)₂), 1.24 (d, J = 6.5 Hz, 6H, CH(CH₃)(CH₃)), 0.74 (d, J = 6.9 Hz, 6H, CH(CH₃)(CH₃)). ¹³C NMR (100 MHz, DMSO-d₆) δ 170.62 and 162.95 (C=O), 131.99, 126.94, and 126.25 (CAr), 58.94 (NCH), 27.60 (CH(CH₃)₂), 22.54 and 19.46 (CH₃). HRMS (ESI) m/z: [M+Na]⁺ calculated for C₂₄H₂₂N₂O₈Na, 489.1268; found 489.1264.

2.4.1.4 Synthesis of (2S)-2-{13-[(1S)-1-carboxy-2-phenylethyl]-5,7,12,14-tetraoxo-6,13-diazatetracyclo[6.6.2.0^{4,16}.0^{11,15}]hexadeca-1,3,8,10,15-pentaen-6-yl}-3-phenylpropanoic acid (**NDI-F**)

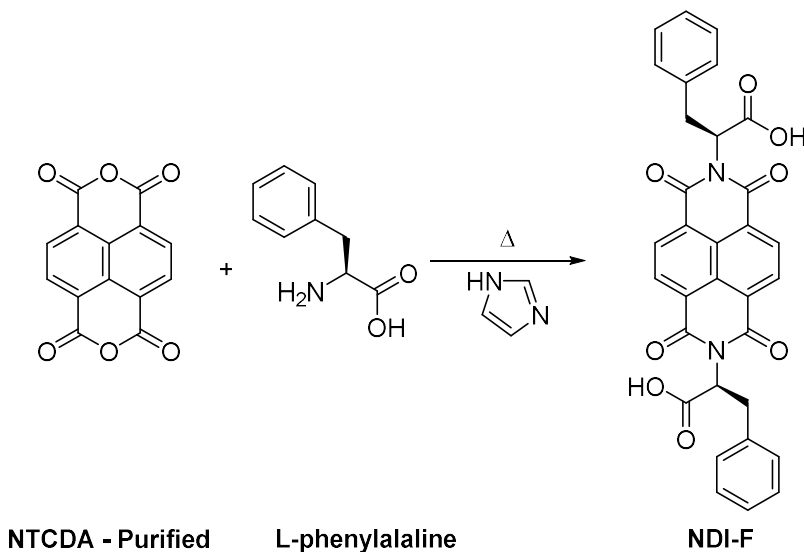


Figure 2.23. Synthesis of **NDI-F**.

The methodology of synthesis is identical to that described in 1.1, using L-phenylalanine (2 eq, 2.46 g), NTCDA (1 eq, 2 g), and imidazole (10 eq, 5.08 g). Synthesis was performed shielded from UV light and the solids degassed. The product **NDI-F** was collected as a light-yellow solid (3.06 g, 73%). The solid was then characterised by ¹H and ¹³C NMR and HRMS.

¹H NMR (400 MHz, DMSO-d₆ + TFA) δ 8.6 (br s, 4H, NDI-HAr), 7.2-6.9 (m, 10H, HAr), 5.9 (dd, J = 12.3, 5.5 Hz, 2H, NCH), 3.6 (dd, J = 14.0, 5.8 Hz, 2H, CHaHb) 3.3 (dd, J = 14.0, 9.5 Hz, 2H, CHaHb) ¹³C NMR (100 MHz, DMSO-d₆ + TFA) δ 170.7, 162.5 (C=O), 138.3, 131.6, 129.4, 128.6, 126.8, 126.6, 126.2 (CAr), 55.1 (NCH), 34.8 (CH₂Ph) HRMS (ESI) m/z: [M+Na]⁺ calculated for C₃₂H₂₂N₂O₈Na, 585.1268; found 585.1276.

2.4.1.5 Synthesis of (2S)-2-{2-[13-({[(1S)-1-carboxy-2-phenylethyl]carbamoyl)methyl]-5,7,12,14-tetraoxo-6,13-diazatetracyclo[6.6.2.0^{4,16}.0^{11,15}]hexadeca-1,3,8,10,15-pentaen-6yl]acetamido)-3-phenylpropanoic acid (**NDI-GF**)

2.4.1.5.1 Synthesis of tert-butyl (2S)-2-(2-[[tert-butoxy]carbonyl]amino)acetamido)-3-phenylpropanoate (**GF-Protected**)

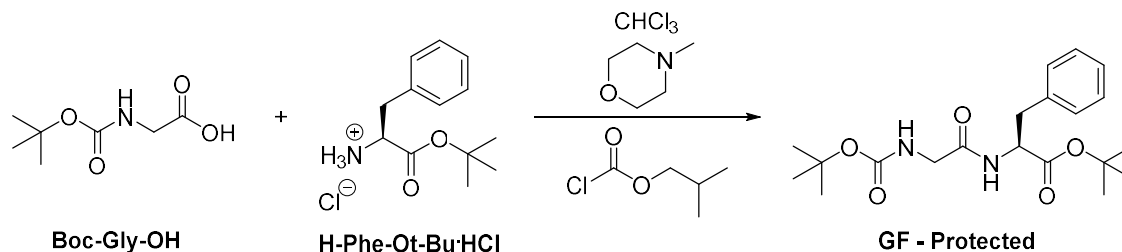


Figure 2.24. 1st step, synthesis of GF-Protected.

To a solution of Boc-glycine (1 eq, 3.75 g) in chloroform (125 mL) was added N-methylmorpholine (1 eq, 2.35 mL), followed by isobutyl chloroformate (1 eq, 2.78 mL) and the mixture was stirred over ice for 20 minutes. After this time, another portion of N-methylmorpholine (1 eq, 2.35 mL) and L-phenylalanine tert-butyl ester hydrochloride (1 eq, 5.52 g) were added and the reaction mixture was stirred overnight. After this time, the reaction mixture was diluted with chloroform, washed in turn with water, 1M hydrochloric acid, and water again, dried (MgSO₄), and evaporated to dryness under reduced pressure. The product GF- Protected was thus obtained as a pale yellow, viscous oil (5.52 g, 68%). The solid was then characterised by ¹H and ¹³C NMR. Impurities were removed in the next step of the synthesis.

¹H NMR (400 MHz, DMSO-d₆) δ 8.05 (d, J = 7.6 Hz, 1H, CHNH), 7.36 – 7.10 (m, 5H, HAr), 6.93 (t, J = 6.0 Hz, 1H, BocNH), 4.36 (t,d, J = 14.5, 7.4 Hz, 1H, CH), 3.53 (dd, J = 6.0, 2.7 Hz, 2H, NHCH₂), 3.08 – 2.74 (m, 2H, PhCH₂), 1.37 (s, 6H, C(CH₃)₃), 1.33 (s, 3H, C(CH₃)₃), 1.31 (s, 9H, C(CH₃)₃). ¹³C NMR (100 MHz, DMSO-d₆) δ 170.44, 169.26 and 155.70 (C=O), 137.03, 129.21, 128.14 and 126.48 (CAr), 80.73 and 77.96 (C(CH₃)₃), 53.95 (CH), 42.90 (NHCH₂), 37.06 (PhCH₂), 28.15 and 27.48 (C(CH₃)₃). HRMS (ESI) m/z: [M+Na]⁺ calculated for C₂₀H₃₀N₂NaO₅, 401.2047; found 401.2038.

2.4.1.5.2 Synthesis of (2S)-2-(2-Aminoacetamido)-3-phenylpropanoic acid trifluoroacetate (GF-Deprotected)

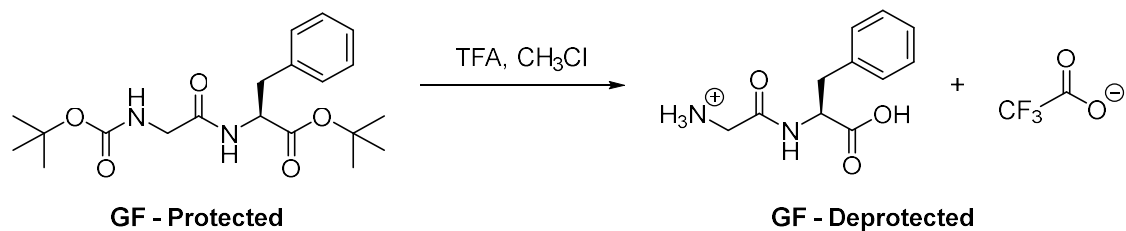
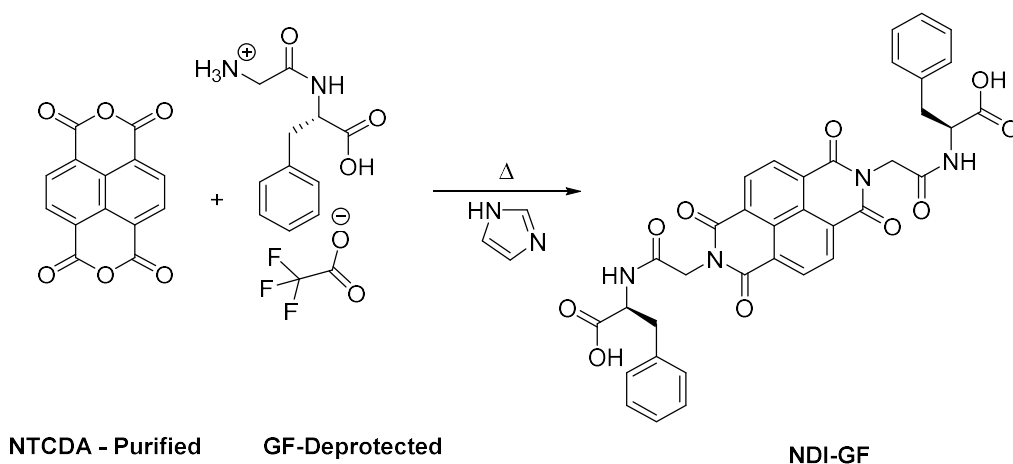


Figure 2.25. 2nd step, deprotection of GF-Protected.

To a solution of GF-Protected (1 eq, 5.52 g) in chloroform (50 mL) was added trifluoroacetic acid (TFA) (13 eq, ca. 15 mL) and the mixture was stirred overnight. The reaction mixture was then poured into diethyl ether (500 mL) and stirred for 30 minutes. The solids were filtered off, washed with diethyl ether in the filter and dried under vacuum. The product GF-Deprotected was obtained as a white solid (3.44 g, 70%). The solid was then characterised by ^1H and ^{13}C NMR and HRMS.

^1H NMR (400 MHz, DMSO- d_6) 8.75 (d, $J = 7.96$ Hz, 1H, NH), 7.34 – 7.13 (m, 5H, HAr), 4.51 (td, $J = 8.7, 4.9$ Hz, 1H, CH), 3.55 (q, $J = 17.92$ Hz, 2H, CH_2NH_3^+), 3.10 (dd, $J = 13.8, 4.9$ Hz, 1H, PhCH_aH_b), 2.89 (dd, $J = 13.8, 9.0$ Hz, 1H, PhCH_aH_b). ^{13}C NMR (100 MHz, DMSO- d_6) δ 172.84 and 166.32 (C=O), 158.42 (q, $J = 32.2$ Hz, $\text{F}_3\text{C-C=O}$), 137.65, 129.60, 128.69 and 126.96 (CAr), 54.22 (CH), 40.43 (CH_2NH_3^+), 37.28 (PhCH₂). HRMS (ESI) m/z : $[\text{M}]^+$ calculated for $\text{C}_{11}\text{H}_{15}\text{N}_2\text{O}_3$, 223.1077; found 223.1066

2.4.1.5.3 Synthesis of (2S)-2-{2-[13-({[(1S)-1-carboxy-2-phenylethyl]carbamoyl)methyl]-5,7,12,14-tetraoxo-6,13-diazatetracyclo[6.6.2.0.4,16.011,15]hexadeca-1,3,8,10,15-pentaen-6yl}acetamido)-3-phenylpropanoic acid (NDI-GF)

Figure 2.26. 3rd Step, synthesis of NDI-GF.

The methodology of synthesis is identical to that described in 2.4.1.2, using GF- Deprotected (2 eq, 2.50 g), NTCDA (1 eq, 1 g) and imidazole (10 eq, 2.54 g). Synthesis was performed shielded from UV light and the solids degassed. The product **NDI-GF** was collected as a beige solid (1.04 g, 41%). The solid was then characterised by ^1H and ^{13}C NMR and HRMS.

^1H NMR (400 MHz, DMSO- d_6) δ 12.84 (br s, 2H, COOH), 8.70 (s, 4H, NDI-HAr), 8.67 (d, $J = 8.03$ Hz, 2H, NH), 7.33 – 7.17 (m, 10H, HAR), 4.70 (br d, $J = 2.3$, 4H, NCH $_2$), 4.44 (dt, $J = 10.8$, 4.1 Hz, 2H, CH), 3.04 (dd, $J = 14.3$, 5.0 Hz, 2H, CHaHb), 2.90 (dd, $J = 13.6$, 8.9 Hz, 2H, CHaHb) ^{13}C NMR (100 MHz, DMSO- d_6) δ 173.09, 166.75 and 162.78 (C=O), 137.80, 131.19, 129.68, 128.68, 126.96 and 126.67 (CAr), 54.21 (CH), 42.93 (NCH $_2$), 37.20 (PhCH $_2$). HRMS (ESI) m/z : $[\text{M}+\text{H}]^+$ calculated for $\text{C}_{36}\text{H}_{29}\text{N}_4\text{O}_{10}$, 677.1878; found 677.1872, $[\text{M}+\text{Na}]^+$ calculated for $\text{C}_{36}\text{H}_{28}\text{N}_4\text{O}_{10}\text{Na}$, 699.1698; found 699.1671.

2.4.1.6 Synthesis of (2S)-2-[(2S)-2-{13-[(1S)-1-[(1S)-1-carboxy-2-phenylethyl]carbonyl]-2-phenylethyl]-5,7,12,14-tetraoxo-6,13-diazatetracyclo[6.6.2.0 4,16 .0 11,15]hexadeca-1,3,8,10,15-pentaen-6-yl]-3-henylpropanamido]-3-phenylpropanoic acid (**NDI-FF**)

2.4.1.6.1 Synthesis of tert-butyl (2S)-2-[(2S)-2-[(tert-butoxycarbonyl)amino]-3-phenylpropanamido]-3-phenylpropanoate (FF- Protected)

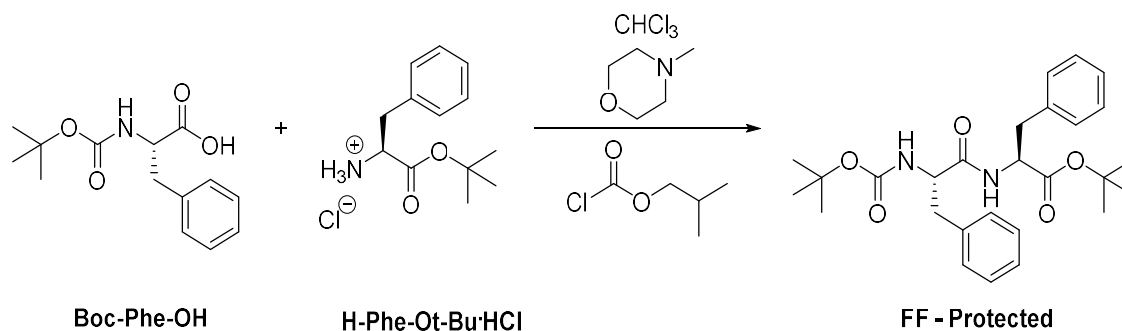


Figure 2.27. 1st step, synthesis of FF-Protected.

To a solution of Boc-phenylalanine (1 eq, 3.75 g) in chloroform (125 mL) was added N-methylmorpholine (1 eq, 1.55 mL), followed by isobutyl chloroformate (1 eq, 1.85 mL) and the mixture was stirred over ice for 20 minutes. After this time, another portion of N-methylmorpholine (1 eq, 1.55 mL) and L-phenylalanine tert-butyl ester hydrochloride (1 eq, 3.14 g) were added and the reaction mixture was stirred overnight. The remaining work up was as described in 2.4.1.5.1. The product FF- Protected was thus obtained as a pale orange-yellow, viscous oil (4.6 g, 69%). The solid was then characterised by ^1H and ^{13}C NMR. Impurities were removed in the next step of the synthesis.

^1H NMR (400 MHz, DMSO-d_6) δ 7.49 (d, $J = 8.1$ Hz, 1H, HAr), 7.33 – 7.14 (m, 9H, HAr), 4.13-4.03 (m, 1H, NHCH), 3.76-3.63 (m, 2H, CHCH₂), 2.96 (dd, $J = 13.6, 6.2$ Hz, 2H, CH₂Ph), 2.86 (dd, $J = 11.7, 9.5$ Hz, 2H, CH₂Ph), 1.83-1.73 (m, 1H, NHCH) 1.33 (s, 12H, C(CH₃)₃), 1.32 (s, 3H, C(CH₃)₃), 1.28 (s, 3H, C(CH₃)₃). ^{13}C NMR (100 MHz, DMSO-d_6) δ 171.00 156.21 and 155.08 (C=O), 138.03, 137.53, 137.04, 129.21, 129.08, 129.02, 128.10, 127.91, 126.45, 126.34, 126.24 and 126.13 (CAr), 80.63 and 80.50 (C(CH₃)₃), 77.97 and 69.77 (NCH), 54.10 and 55.89 (PhCH₂), 36.65, 28.08, 27.57, 27.49, 27.46, 18.76 (C(CH₃)₃). HRMS (ESI) m/z : [M+Na]⁺ calculated for C₂₇H₃₆N₂O₅Na, 491.2516; found 491.2512.

2.4.1.6.2 Synthesis of (2S)-2-[(2S)-2-ammonio-3-phenylpropanamido]-3-phenylpropanoic acid trifluoroacetate (FF- Deprotected)

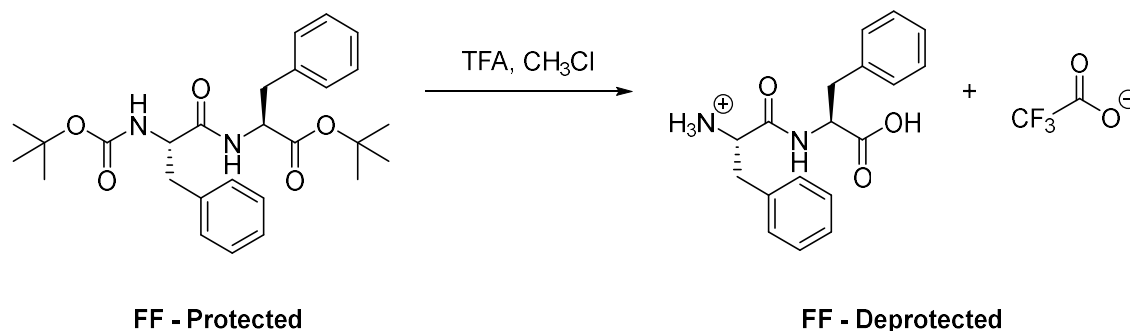


Figure 2.28. 2nd step, deprotection of FF-Protected.

Methodology of synthesis was identical to that described in 2.4.1.5.2 using a solution of FF-Protected (1 eq, 4.6 g) in chloroform (50 mL) and TFA (13 eq, ca. 15 mL). The product FF- Deprotected was obtained as a white solid (3.9 g, 93%). The solid was then characterised by ^1H and ^{13}C NMR and HRMS.

^1H NMR (400 MHz, DMSO-d_6) δ 13.0 (br s, 1H, OH), 8.9 (d, $J = 7.8$ Hz, 1 H, NH), 8.1 (br s, 3H, NH₃⁺), 7.4-7.2 (m, 10H, Har), 4.5 (td, $J = 5.3, 5.3, 8.2$ Hz, 1H, HNCO), 4.0 (dd, $J = 4.4, 8.5$ Hz, 1H, HNCH₂), 3.2-3.1 (m, 2 H, PhCHaHb), 3.0-2.9 (m, 2 H, PhCHaHb) ^{13}C NMR (100 MHz, DMSO-d_6) δ 172.87 and 168.30 (C=O), 158.60 (q, $J = 36.0$ Hz, F₃C-C=O), 137.55, 134.99, 129.96, 129.54, 128.93, 128.75, 127.59 and 127.16 (CAr), 116.90 (weak q, $J = 100.9$, CF₃), 54.02 (NCH), 53.61 (HCNH₃⁺), 37.59 and 37.37 (PhCH₂) HRMS (ESI) m/z : [M]⁺ calculated for C₁₈H₂₁N₂O₃, 313.1547; found 313.1550.

2.4.1.6.3 Synthesis of Synthesis of (2S)-2-[(2S)-2-{13-[(1S)-1-[(1S)-1-carboxy-2-phenylethyl]carbamoyl]-2-phenylethyl]-5,7,12,14-tetraoxo-6,13-diazatetracyclo[6.6.2.0^{4,16}.0^{11,15}]hexadeca-1,3,8,10,15-pentaen-6-yl]-3-phenylpropanamido]-3-phenylpropanoic acid (**NDI-FF**)

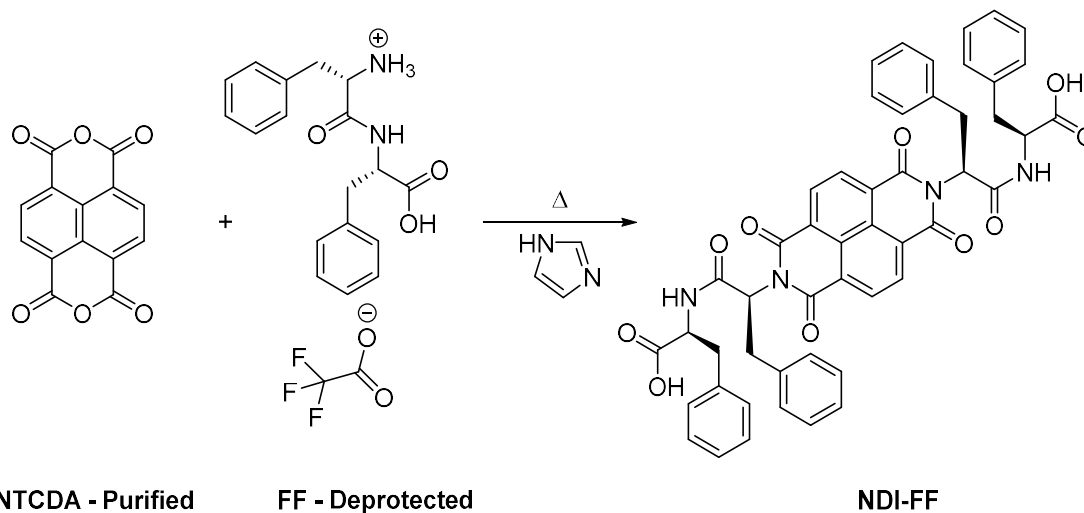


Figure 2.29. 3rd step, synthesis of **NDI-FF**.

The methodology of synthesis is identical to that described in 1.1, using FF- Deprotected (2 eq, 3.18 g), NTCDA (1 eq, 1 g) and imidazole (10 eq, 2.54 g). Synthesis was performed shielded from UV light and the solids degassed. The product **NDI-FF** was collected as a dark brown solid (1.1 g, 34%). The solid was then characterised by ¹H and ¹³C NMR and HRMS.

¹H NMR (400 MHz, DMSO-d₆ + TFA) δ 8.76 – 8.51 (m, 4H, NDI-HAr), 8.51 – 8.33 (m, 2H, NH), 7.31 – 6.95 (m, 20H, HAr), 5.80 – 5.64 (m, 2H, NCH), 4.56 – 4.34 (m, 2H, HNCH), 3.75 – 3.50 (m, 2H, PhCHaHb), 3.39 – 3.14 (m, 2H, PhCHaHb), 3.17 – 2.62 (m, 4H, PhCHaHb). ¹³C NMR (100 MHz, DMSO-d₆ + TFA) δ 173.65, 173.08, 168.88, 168.71, 168.33, 168.29, 162.68, 160.13 (C=O), 138.80, 138.61, 138.55, 138.40, 138.34, 138.13, 137.13, 132.19, 132.09, 131.05, 131.02, 130.96, 130.91, 130.90, 129.67, 129.65, 129.54, 129.53, 129.34, 129.33, 129.30, 128.59, 128.49, 128.43, 128.39, 126.83, 126.76, 126.74, 126.66, 126.64, 126.49, 126.44, 124.54, 124.48 (CAr), 55.61, 54.56 (NCH), 37.13, 36.64 (NHCH), 34.50, 34.44, 34.35, 27.98 (PhCH₂). HRMS (ESI) m/z: [M+Na]⁺ calculated for C₅₀H₄₀N₄O₁₀Na, 879.2637; found 879.2621.

2.4.2 Experimental protocols and equipment

2.4.2.1 Freeze-dryer

Synthetic products were dried by lyophilisation. Solids were neutralised by stirring for 30 minutes in water and filtering. This was repeated until the filtrate was no longer acidic (determined using

universal indicator paper (Merch Life Sciences)). Solids were then frozen using a freezer to approximately -18 °C. Water was removed using a LSCbasic freeze-dryer (Christ) at -85 °C and between 0.890 and 1.25 mBar.

2.4.2.2 Nuclear magnetic resonance (NMR) spectroscopy

For the characterisation after the synthesis of NDIs, NMR measurements were carried out on a Bruker 400 MHz spectrometer. Solids were dissolved in approximately DMSO-d₆. Approximately 2 µL trifluoroacetic acid was added in the case of **NDI-F** and **NDI-FF** to move the position of the residual water signal in the ¹H NMR spectrum which covered signals from the products. Spectrometer operated at 400 MHz for ¹H NMR and 101 MHz for ¹³C NMR spectroscopy.

2.4.2.3 High resolution mass spectroscopy (HRMS)

Measurements were carried out using a Bruker microTOFq mass spectrometer using electrospray ionisation (ESI) coupled to a time-of-flight analyser. The instrument is accurate to <5 ppm. Samples were run in ethanol by the University of Glasgow mass spectrometry service.

2.4.2.4 Preparation of solutions

Solutions were prepared at concentrations 10 mg/mL of NDI (unless otherwise stated). NDI solids were dissolved in 2 molar equivalents of aqueous NaOH (0.1 M) and 400 µL/mL of 0.1 M NaCl (to act as a background electrolyte). The remaining volume of solutions were made up with deionised water. Solutions were stirred overnight until all solids had dissolved. The pH of these solutions was adjusted using a FC200 pH probe. Solutions were adjusted between pH 6-12 in increments of 1. This concentration was chosen due to the intensity of colour produced upon electrochemical reduction.

2.4.2.5 pH measurements

pH was measured using a FC200 pH probe (HANNA instruments) with a 6 mm × 10 mm conical tip calibrated with buffers of pH 4, 7 and 10 (HANNA instruments). The stated accuracy of the pH measurements is ±0.1.

2.4.2.6 Absorption spectroscopy

Absorption spectra were collected using a Cary 60 UV-visible spectrophotometer from Agilent Technologies. Solutions were measured in a 0.1 mm pathlength quartz cuvette (Hellma Analytics) or spectro-electrochemical cells (BASi). Spectra were collected from 250-1100 nm at a scan rate of 2 nm/s unless stated otherwise.

2.4.2.6.1 Dilution series

Solutions were prepared at 10 mg/mL and diluted by half using a solution containing 0.4 mL/mL of 0.1 M NaCl to keep this ratio of background electrolyte consistent. Absorbance spectra were taken of the

neutral state of each NDI. Neutral solutions at 10 mg/mL were too concentrated to be reliably recorded by the spectrometer, resulting in noisy data and so the series is reported from 5 mg/mL onwards. Solutions were deposited (<0.2 mL) into a 0.1 mm quartz cuvette (Hellma Analytics) before measurement. Neutral states are recorded at 5 mg/mL under the assumption that aggregation is unchanged between 5 and 10 mg/mL.

2.4.2.7 Apparent pK_a titrations

All pK_a titrations were performed using 10 mg/mL solutions of each NDI pH adjusted to pH 12. 0.1 M HCl was added in 5-10 μ L portions. A portion was added, and the solution gently stirred before being allowed to sit for 5 minutes before a pH measurement was taken and another portion added. pH was measured using a FC200 pH probe (HANNA instruments) with a 6 mm \times 10 mm conical tip calibrated with buffers of pH 4, 7 and 10 (HANNA instruments). The stated accuracy of the pH measurements is ± 0.1 . pH was recorded by hand in a lab book. The temperature was maintained at 25 $^{\circ}$ C during the titration by using a circulating water bath. pK_a values were determined to be the pH at which a plateau is observed upon addition of HCl before the pH dropping again more steadily.

2.4.2.8 FTO windows

The windows used for the spectro-electrochemical experiments were prepared from fluorine-doped Sn oxide (FTO) coated glass (TEC 10 20 x 15 x 1.1 mm, surface resistivity $\sim 11 - 13 \Omega/\text{sq}$ from Ossila). The glass was sonicated in ethanol at 40 $^{\circ}$ C for 30 minutes prior to assembly and gloves were used throughout to prevent fingerprints on the glass. A 3D printed 1 mm thick spacer was secured onto the conductive side of the FTO glass using a 2-part epoxy resin. Solutions (0.5 mL) were deposited into this space and the second piece of glass placed on top and secured using a 3D printed holder, screwed into place. Excess solution was deposited to reduce the appearance of bubbles. This method was performed ensuring that the FTO layers were facing inside the cell (Figure 2.28). Pieces of copper tape were added to the edges of the cell to ensure good contact between the cell and the crocodile clips from the PalmSens4 potentiostat. While the FTO window will absorb light in a different range to quartz, only approximately 100 nm of the absorbance spectra between 250 and 350 nm is lost to absorbance of the FTO glass. As the absorbances corresponding to the radical anion are not found within this region, we concluded that this loss of the spectrum was a reasonable compromise.

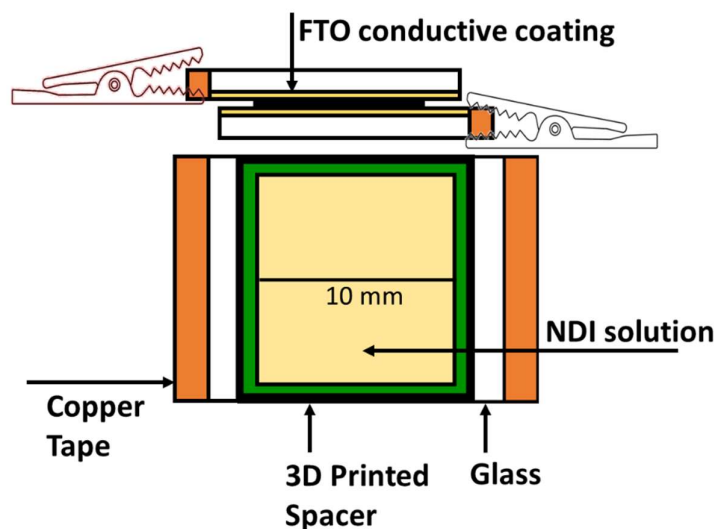


Figure 2.30. Schematic diagram of the FTO window set-up described above.

2.4.2.9 Cyclic voltammetry (CV)

Voltammograms were collected using a PalmSens4 potentiostat using a 2-electrode set-up. Solutions of (0.5-2 mL) depending upon the size of the glass used were deposited into FTO glass cells as described in 2.4.2.8.

All data were collected using a 2-electrode set-up without reference. Values cannot therefore be stated in reference to a known value. Cyclic voltammograms were carried out using a solution of 10 mg/mL hydroquinone dissolved in water with 10% 0.1 M NaCl. A comparison of the position of the peaks measured in the FTO (1 x 1 cm) window set-up are compared to the same solution measured in a referenced electrochemical set-up (CH Instruments and BASi), Figure 2.31. This data is tabulated in Table 2.2. Two reduction peaks are clear at a 0.5 V/s scan rate but the oxidation peak is more broad and not clearly defined as two separate processes. Solutions were deposited (5 mL) into a glass vial (CH Instruments) before electrodes were placed into solution. This set-up comprised of a glassy carbon working electrode, Pt counter electrode and an Ag/AgCl reference (BASi).

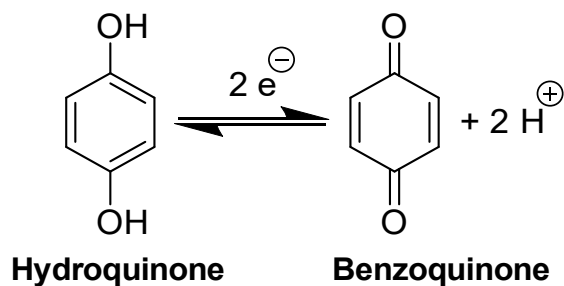


Figure 2.31. The redox reaction of hydroquinone/benzoquinone measured by CV as a control.

2.4.2.10 Spectroelectrochemistry

Spectra were collected using the spectrometer described in 2.4.2.6 while solutions (<0.2 mL) were deposited into a window cell (2.4.2.8) secured in place within the spectrometer using a 3D printed custom-built holder. A CAD (computer aided design) of the holder is shown below in Figure 2.30. Solution was retained in the cell by pressure from the holder using two screws.

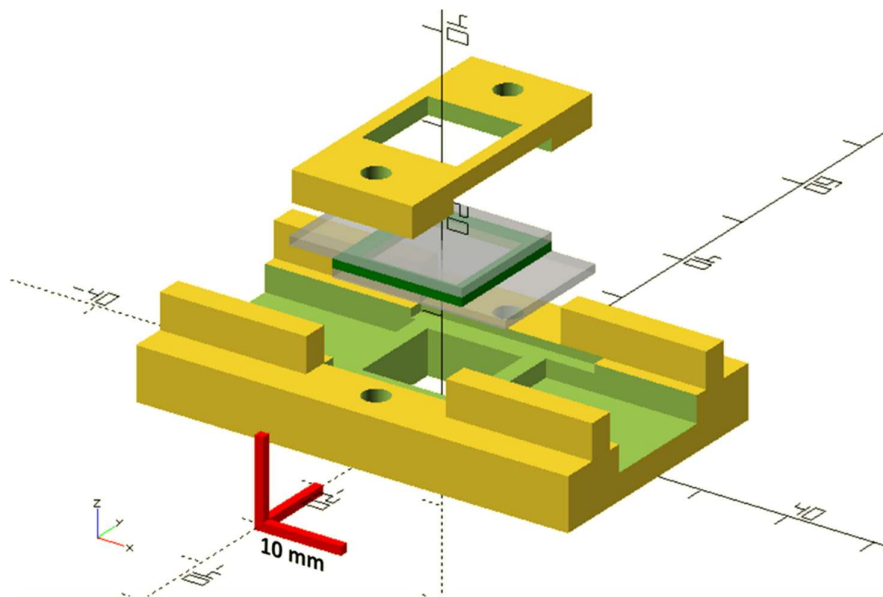


Figure 2.32. CAD image of 3D printed holder designed to secure a 10 x 10 mm window into the absorption spectrometer.

2.4.2.11 Electrochromic behaviour

Solutions at 10 mg/mL were deposited (<0.2 mL) and secured in FTO window cells (2.4.2.8) and a potential of -2.5 V applied for 10 seconds. The absorbance spectra were then collected immediately after reduction. Photographs were taken after a 10 second application of -2.5 V on a separate occasion with the cell outside of the spectrometer for ease.

2.4.2.11.1 Tracking electrochemical oxidation

Solutions were deposited into FTO cells and spectro-electrochemistry was performed as described in 2.4.2.10. The reduction potential of -2.5 V was applied for 20 seconds instead of 10 seconds in this instance to accentuate the difference in colouration between solutions at different pH values. An oxidising potential of 0.5 V was applied for 300 seconds. This potential was found to oxidise effectively and could be used consistently for all NDIs. The oxidation process was measured by collecting spectra every 30 seconds as an oxidising potential of 0.5 V was applied. The absorbance at 540 nm was recorded as this wavelength corresponded to an absorbance in the spectra of all reduced NDIs.

2.5 References

- 1 L. Gonzalez, C. Liu, B. Dietrich, H. Su, S. Sproules, H. Cui, D. Honecker, D. J. Adams and E. R. Draper, *Comm. Chem.*, 2018, **1** (77), 1-8.
- 2 T. Gwang Yun, M. Park, S. Kim, D. Kim, J. Younh Cheong, J. Gook Bae, A. Min Han and I. Kim, *ACS Nano*, 2019, **13**, 3141–3150.
- 3 R. Cinnsealach, G. Boschloo, S. N. Rao and D. Fitzmaurice, *Sol. Energy Mater. Sol. Cells*, 1998, **55**, 215–223.
- 4 S. Kiruthika and G. U. Kulkarni, *Sol. Energy Mater. Sol. Cells*, 2017, **163**, 231–236.
- 5 T. A. Welsh and E. R. Draper, *RSC Adv.*, 2021, **11**, 5245–5264.
- 6 T. Jarosz, K. Gebka, A. Stolarczyk and W. Domagala, *Polymers*, 2019, **11**, 1–18.
- 7 S. v. Bhosale, C. H. Jani and S. J. Langford, *Chem. Soc. Rev.*, 2008, **37**, 331–342.
- 8 M. al Kobaisi, S. v. Bhosale, K. Latham, A. M. Raynor and S. v. Bhosale, *Chem. Rev.*, 2016, **116**, 11685–11796.
- 9 K. R. Miller, Larry L., Mann, *Acc. Chem. Res.*, 1996, **29**, 417–423.
- 10 H. Kar, R. Molla and S. Ghosh, *Chem. Commun.*, 2013, **49**, 4220-4222.
- 11 N. Nandi, S. Basak, S. Kirkham, I. W. Hamley and A. Banerjee, *Langmuir*, 2016, **32**, 13226–13233.
- 12 M. Saha and S. Bandyopadhyay, *J. Phys. Chem. C*, 2021, **125** (11), 6427-6432.
- 13 E. R. Draper, L. J. Archibald, M. C. Nolan, R. Schweins, M. A. Zwijnenburg, S. Sproules and D. J. Adams, *Chem. - Eur. J.*, 2018, **24**, 4006–4010.
- 14 C. L. Smith, L. L. E. Mears, B. J. Greeves, E. R. Draper, J. Douth, D. J. Adams and A. J. Cowan, *Phys. Chem. Chem. Phys.*, 2019, **21**, 26466–26476.
- 15 D. McDowall, B. J. Greeves, R. Clowes, K. McAulay, A. M. Fuentes-Caparrós, L. Thomson, N. Khunti, N. Cowieson, M. C. Nolan, M. Wallace, A. I. Cooper, E. R. Draper, A. J. Cowan and D. J. Adams, *Adv. Energy Mater.*, 2020, **10**, 1–10.
- 16 E. R. Draper, B. J. Greeves, M. Barrow, R. Schweins, M. A. Zwijnenburg and D. J. Adams, *Chem*, 2017, **2**, 716–731.
- 17 Z. Chen, V. Stepanenko, V. Dehm, P. Prins, L. D. A. Siebbeles, J. Seibt, P. Marquetand, V. Engel and F. Würthner, *Chem. Eur. J.*, 2007, **13**, 436–449.
- 18 N. Sikdar, D. Dutta, R. Haldar, T. Ray, A. Hazra, A. J. Bhattacharyya and T. K. Maji, *J. Phys. Chem. C*, 2016, **120**, 13622–13629.
- 19 Y. Huang, Y. Yan, B. M. Smarsly, Z. Wei and C. F. J. Faul, *J. Mater. Chem.*, 2009, **19**, 2356–2362.
- 20 H. Shao and J. R. Parquette, *Chem. Commun.*, 2010, **46**, 4285–4287.
- 21 L.-H. Hsu, S.-M. Hsu, F.-Y. Wu, Y.-H. Liu, S. Rao Nelli, M.-Y. Yeh and H.-C. Lin, *RSC Adv.*, 2015, **5**, 20410–20413.
- 22 F.-K. Zhan, S.-M. Hsu, H. Cheng and H.-C. Lin, *RSC Adv.*, 2015, **5**, 48961–48964.
- 23 M. C. Nolan, J. J. Walsh, L. L. E. Mears, E. R. Draper, M. Wallace, M. Barrow, B. Dietrich, S. M. King, A. J. Cowan and D. J. Adams, *J. Mater. Chem. A*, 2017, **5**, 7555–7563.

- 24 L. Chen, S. Revel, K. Morris, L. C. Serpell and D. J. Adams, *Langmuir*, 2010, **26**, 13466–13471.
- 25 Y. Huang, C. Yang, B. Deng, C. Wang, Q. Li, C. de Villenoisy Thibault, K. Huang, K. Huo and H. Wu, *Nano Energy*, 2019, **66**, 104200.
- 26 A. Datar, K. Balakrishnan and L. Zang, *Chem. Commun*, 2013, **49**, 6894-6896.
- 27 E. R. Draper, L. L. E. E. Mears, A. M. Castilla, S. M. King, T. O. McDonald, R. Akhtar and D. J. Adams, *RSC Adv.*, 2015, **5**, 95369–95378.
- 28 K. P. Nandre, M. al Kobaisi, R. S. Bhosale, K. Latham, and S. Bhosale, *RSC Adv.*, 2014, **4**, 40381–40384.
- 29 V. Adams, J. Cameron, M. Wallace and E. R. Draper, *Chem. Eur. J.*, 2020, **26**, 9879–9882.
- 30 K. McAulay, B. Dietrich, H. Su, M. T. Scott, S. Rogers, Y. K. Al-Hilaly, H. Cui, L. C. Serpell, A. M. Seddon, E. R. Draper and D. J. Adams, *Chem. Sci.*, 2019, **10**, 7801–7806.
- 31 J. G. Egan, G. Brodie, D. McDowall, A. J. Smith, C. J. C. Edwards-Gayle and E. R. Draper, *Mater. Adv.*, 2021, **2**, 5248-5253.
- 32 A. D. Martin, J. P. Wojciechowski, A. B. Robinson, C. Heu, C. J. Garvey, J. Ratcliffe, L. J. Waddington, J. Gardiner and P. Thordarson, *Sci. Rep.*, 2017, **7**, 4397.
- 33 N. Ponnuswamy, G. D. Pantoş, M. M. J. Smulders and J. K. M. Sanders, *J. Am. Chem. Soc.*, 2012, **134**, 566–573.
- 34 E. R. Draper and D. J. Adams, *Chem. Soc. Rev.*, 2018, **47**, 3395–3405.
- 35 G. Pont, L. Chen, D. G. Spiller and D. J. Adams, *Soft Matter*, 2012, **8**, 7797–7802.
- 36 Y. J. Adhia, T. H. Schloemer, M. T. Perez and A. J. McNeil, *Soft Matter*, 2012, **8**, 430–434.
- 37 E. R. Cross, S. Sproules, R. Schweins, E. R. Draper and D. J. Adams, *J. Am. Chem. Soc.*, 2018, **140**, 8667–8670.
- 38 S. Panja and D. J. Adams, *Chem. Commun.*, 2019, **55**, 10154-10157.
- 39 Y. J. Adhia, T. H. Schloemer, M. T. Perez and A. J. McNeil, *Soft Matter*, 2012, **8**, 430–434.
- 40 E. R. Draper, B. Dietrich, K. McAulay, C. Brasnett, H. Abdizadeh, I. Patmanidis, S. J. Marrink, H. Su, H. Cui, R. Schweins, A. Seddon and D. J. Adams, *Matter*, 2020, **2**, 764–778.
- 41 Y. Lan, M. G. Corradini, R. G. Weiss, S. R. Raghavan and M. A. Rogers, *Chem. Soc. Rev.*, 2015, **44**, 6035–6058.
- 42 W. Shi, F. Xing, Y.-L. Bai, M. Hu, Y. Zhao, M.-X. Li and S. Zhu, *ACS Appl. Mater. Interfaces*, 2015, **7**, 1449–14500.
- 43 K. McAulay, H. Wang, A. M. Fuentes-Caparro, L. Thomson, N. Khunti, N. Cowieson, H. Cui, A. Seddon and D. J. Adams, *Langmuir*, 2020, **36**, 8626–8631.
- 44 J.-F. Penneau, B. J. Stallman and L. L. Kasai, Paul H, Miller, *Chem. Mater.*, 1991, **3**, 791–796.
- 45 K. McAulay, P. Agí Ucha, ab Han Wang, A. M. Fuentes-Caparró, L. Thomson, O. Maklad, N. Khunti, N. Cowieson, M. Wallace, H. Cui, R. J. Poole, A. Seddon and D. J. Adams, *Chem. Commun.*, 2020, **56**, 4094-4097.
- 46 E. R. Draper, H. Su, C. Brasnett, R. J. Poole, S. Rogers, H. Cui, A. Seddon and D. J. Adams, *Angew. Chem. Int. Ed.*, 2017, **56**, 10467–10470.

- 47 S. Panja and D. J. Adams, *Chem. Soc. Rev.*, 2021, **50**, 5165–5200.
- 48 R. Malfa and J. Steinhardt, *Biochem. Biophys. Res. Commun.*, 1974, **59**, 887–893.
- 49 E. R. Draper and D. J. Adams, *Chem*, 2017, **3**, 390–410.
- 50 D. Görl, X. Zhang and F. Würthner, *Angew. Chem. Int. Ed.*, 2012, **51**, 6328–6348.
- 51 E. Krieg, E. Shirman, H. Weissman, E. Shimoni, S. G. Wolf, I. Pinkas and B. Rybtchinski, *J. Am. Chem. Soc.*, 2009, **131**, 14365–14373.
- 52 J. Mizuguchi and K. Tojo, *J. Phys. Chem. B*, 2002, **106**, 767–772.
- 53 A. Kalita, N. V. v Subbarao and P. K. Iyer, *J. Phys. Chem. C*, 2015, **119**, 12772–12779.
- 54 J.-H. Ryu, D.-J. Hong and M. Lee, *Chem. Commun.*, 2008, 1043–1054.
- 55 K. M. Osten and P. Mehrkhodavandi, *Acc. Chem. Res.*, 2017, **50**, 2861–2869.
- 56 J. Jin, T. Iyoda, C. Cao, Y. Song, L. Jiang, T. Jin Li and D. Zhu, *Angew. Chem. Int. Ed.*, 2001, **40**, 2135–2138.
- 57 G. Andric, A. F. John Boas, B. M. Alan Bond, D. D. Gary Fallon, A. P. Kenneth Ghiggino, C. F. Conor Hogan, A. A. James Hutchison, C. Marcia A-P Lee, A. J. Steven Langford, D. R. John Pilbrow, B. J. Gordon Troup and C. P. Woodward, *Aust. J. Chem*, 2004, **57**, 1011–1019.
- 58 D. Gosztola, M. P. Niemczyk, W. Svec, A. S. Lukas and M. R. Wasielewski, *J. Phys. Chem.*, 2000, **104**, 6545–6551.
- 59 S. Alp, Ş. Erten, C. Karapire, B. Köz, A. O. Doroshenko and S. Içli, *J. Photochem. Photobiol., A*, 2000, **135**, 103–110.
- 60 S. Guha and S. Saha, *J. Am. Chem. Soc.*, 2010, **132**, 17674–17677.

CHAPTER THREE

Exploring stability and cyclability of NDI systems

3.1 Introduction

Self-assembling organic molecules such as the NDI systems discussed here are often highly influenced by external properties such as pH as well as more fundamental properties like chemical structure.¹⁻⁴ The ability of NDIs and similar molecules to produce radical anions both photo- or electrochemically is influenced by chemical structure (and consequent aggregation).⁵⁻⁸ These factors have been discussed in Chapter 2 for these systems and were found to greatly influence colouration and efficiency of electrochemical processes. However, there is only so much information about structure that can be gained from absorbance spectroscopy alone. This technique can give information about molecular packing in such systems^{1,2,4,6,9} but is not characteristic of the larger scale structures formed.

To infer a larger structure or morphology, scattering and imaging techniques are used. Techniques such as DLS assume spherical particles and calculate hydrodynamic radius and so can overestimate the size of our aggregates if light scatters from the side of a cylinder, assuming the length of the cylinder to be the radius for example, Figure 3.1. These systems are likely to assemble into large worm-like-micelles¹⁰⁻¹³ (due to their π -stacking capabilities), making this technique unsuitable. While imaging can give information about fibrous structures, as previously mentioned, the artefacts caused by drying (and the high salt concentration) also makes this technique unsuitable for our systems.^{14,15} SANS is a powerful technique to study the aggregates of self-assembling molecules over a variety of length scales.^{9,16-19} As discussed in Chapter 1, it has been widely reported to be used to probe hydrogelators and self-assembling organic molecules.^{9,14,16,18-21} The sensitivity and non-destructive nature of SANS makes it an attractive tool to measure our system and to understand the structures at low to high pH more clearly.

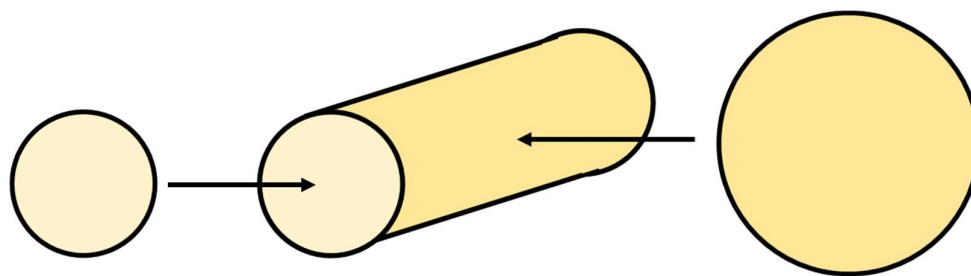


Figure 3.1. Cartoon representation of the overestimation of radius which may occur using DLS.

A desirable property of transmissive to dark electrochromic devices is not only that colour change is of a high contrast and occurs within a short period of time, but that these phenomena can be repeated many times over the lifetime of the device. Electrochromic devices reported

can achieve a widely varied range of cyclability between differently coloured states, from 10-20^{22,23} to hundreds^{5,24} to thousands.²⁵⁻³² The lifetime of a commercial device is estimated to be between 25,000,³³ 50,000³⁴ and 100,000 cycles³⁵ but will depend upon application. A common issue that can limit the number of cycles achieved in solution based devices is leaking^{5,29,36,37} or drying out of devices.⁵ While this factor is an issue in a research lab, when developed by an industrial partner, it is less likely to occur and so these systems should not be disregarded. The viability of a device is often reported in terms of the number of cycles it can achieve without detriment to colouration efficiency or contrast of colouration change. However, a discussion about how structure or aggregation is influenced by a lifetime of use is not as commonly discussed. As aggregation can influence electrochromic properties (Chapter 2) of these systems, this discussion is crucial in investigating their viability.

Whilst we assess the aggregation of our systems and how this factor varies with chemical structure and pH, we must also consider how electrochemical use may also influence aggregation which could influence the long-term use of our devices. It is likely that the absolute aggregates of the ideal states of each system will influence the number of cycles achieved. Some aggregates may also be more susceptible to change after electrochemical use. Assessing this property alongside measurements of cyclability will also allow an insight into the stability of the systems over time. We must also assess whether any degradation of the NDIs themselves takes place. It is important to know whether these systems degrade or become less efficient with use to assess suitability for application.

Spectro-electrochemistry has been used to assess the coloured states of our systems in Chapters 2 and facilitates *in situ* measurement during electrochemical reduction and oxidation. *In situ* SANS (as mentioned in Chapter 1) has been reported as a method to measure structure over a period of time after an initial stimulus, such as a variation in temperature or pH. However, electrochemical stimuli are less frequently reported alongside this technique, mostly due to additional experimental concerns and complexities.

Samples cannot be electrochemically reduced and oxidised in a standard quartz cuvette as used for SANS measurements without very specialist equipment. The pathlength of the cell is very thin and it is challenging to fit a cell inside that will be perfectly positioned in the beamline. Therefore, electrochemical processes may have to be performed *ex situ* before a measurement. Performing spectro-electrochemistry in the beamline itself would facilitate a more representative investigation of the way electrochemical processes may affect aggregation.

It has been stated that organic systems are not stable enough³⁸ for use in chromic materials due to secondary reactions,³⁹ degradation⁴⁰ or an inability to cycle between states.^{40,41} One of the reasons for such instability may be that the process of applying potential (or the formation of a radical) changes or destroys the aggregation of the system by the addition of charge. We have reported that subtle changes in aggregation with pH result in a direct impact upon electrochromic behaviour (Chapter 2). Changing pH will alter the charge in the molecules and in the solvent around them. It is therefore crucial to assess whether electrochemical use will have a similar impact to changing pH, and whether the reduced state has a different aggregation to the neutral state (using *in situ* methods).

The use of *in situ* electrochemical SANS (eSANS) combined with other *ex situ* techniques has been reported mostly in the evaluation of batteries.^{42–45} A cell is placed in the beamline and cycled through charge and discharge cycles.^{42,46} This technique has been used to assess the pore structure and host nature of electrodes^{43,44} and to give insight into mechanisms occurring within cells.⁴⁵ *In situ* SAXS has been reported using an electrochemical cell to track templated electrodeposition which required custom-made equipment.⁴⁷

In situ SANS focusing on redox reactions has been applied to the investigation of the irreversible change in size upon the reduction of ZnO nanoparticles⁴⁸, Figure 3.2, and to a measure of a porous structure during dealloying of $\text{Ag}_{0.7}\text{Au}_{0.3}$.⁴⁹ Often these reports involve addition set-up external to the beamline such as dialysis tubing⁵⁰ or large reservoirs of electrolyte.⁴⁹

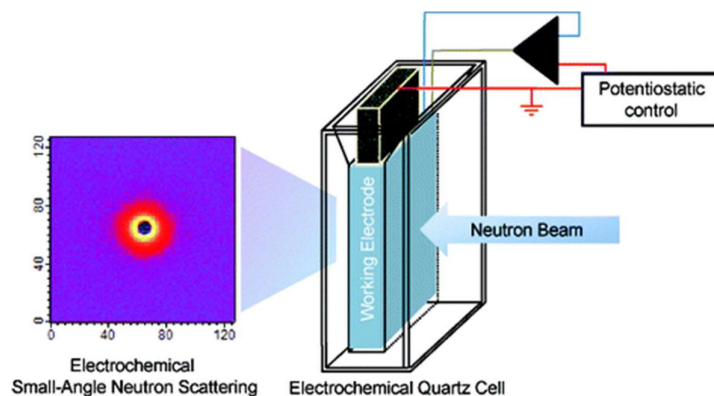


Figure 3.2. Set-up used for *in situ* SANS by Prabhu *et al.*⁴⁸

We report an easy-to-use methodology to perform *in situ* SANS combined with electrochemistry. Referring to the criteria we set out in Chapter 2, we have assessed solubility,

redox potentials and tuning of the speed and intensity of the transition to a dark coloured state from a transmissive neutral state. We can now use a mixture of *in situ* and *ex situ* SANS to understand more about the specific relationships between structure and intense (and also poorly) coloured states and evaluate the stability and cyclability of these systems in their 'ideal' states. The ability to perform *in situ* SANS will allow a measurement of the electrochemically reduced state and understand any influence of electrochemical reduction upon aggregation.

3.2 Results and discussion

Having assessed the influence of pH using absorbance spectroscopy, we concluded that each NDI had an ideal pH at which electrochemical processes were enhanced, Chapter 2. We refer to this as its 'ideal pH'. This chapter will focus first upon evaluating the aggregation of each NDI using SANS at high, mid and low pH/D and relating this to the trends in colouration observed in Chapter 2. We characterise these systems to better understand the relationship between aggregation and electrochromic behaviour. We can then assess the effect of the radical formation upon these structures. By cycling between states continuously we can gain insight into the long-term stability of these systems and whether aggregation and chemical structure influence this property.

As previously described in Figure 2.5, Chapter 2, we assume from their absorption, the structures dilute rather than change at lower concentration. The molar absorbance coefficient calculated from this concentration series suggests that this value has no impact upon colouration, with **NDI-FF** showing higher ϵ than **NDI-I** (Table 3.1) but demonstrating a significantly weaker electrochromic colouration (Chapter 2).

Table 3.1. Molar absorbance coefficient calculated from the gradient of a plot of concentration vs. absorbance at λ_{max} . Calculated from data shown in Figure 2.5 in main text of Chapter 2. Solutions adjusted to pH 9 and measured in their neutral state.

NDI	ϵ ($\text{M}^{-1}\text{cm}^{-1}$)
NDI-I	1379
NDI-V	1588
NDI-F	1808
NDI-GF	1809
NDI-FF	1501

3.2.1 Buffering

Having concluded that there is an ideal pH at which electrochemical reduction and oxidation is the most favourable, it is important to maintain these conditions that promote an ideal aggregation. The ideal pH of each solution is maintained using a buffer. Buffered solutions were prepared using two molar equivalents of NaOH and made up to volume with 0.1 M sodium carbonate-bicarbonate buffer adjusted to pH 9 (**NDI-I** and **NDI-V**) or 0.1 M sodium acetate, adjusted to pH 6 (**NDI-F** and **NDI-GF**). The concentration of salt in solutions is increased by buffering, which acts as an electrolyte in the system. We do not note any significant differences in the absorbance spectra of buffered and unbuffered NDIs to suggest a difference in aggregation, Figure 3.3. A minimal change in the ratio of absorbances at 365 and 384 nm (suggesting very subtle changes in packing) is observed in **NDI-GF** (Figure 3.3(d)).

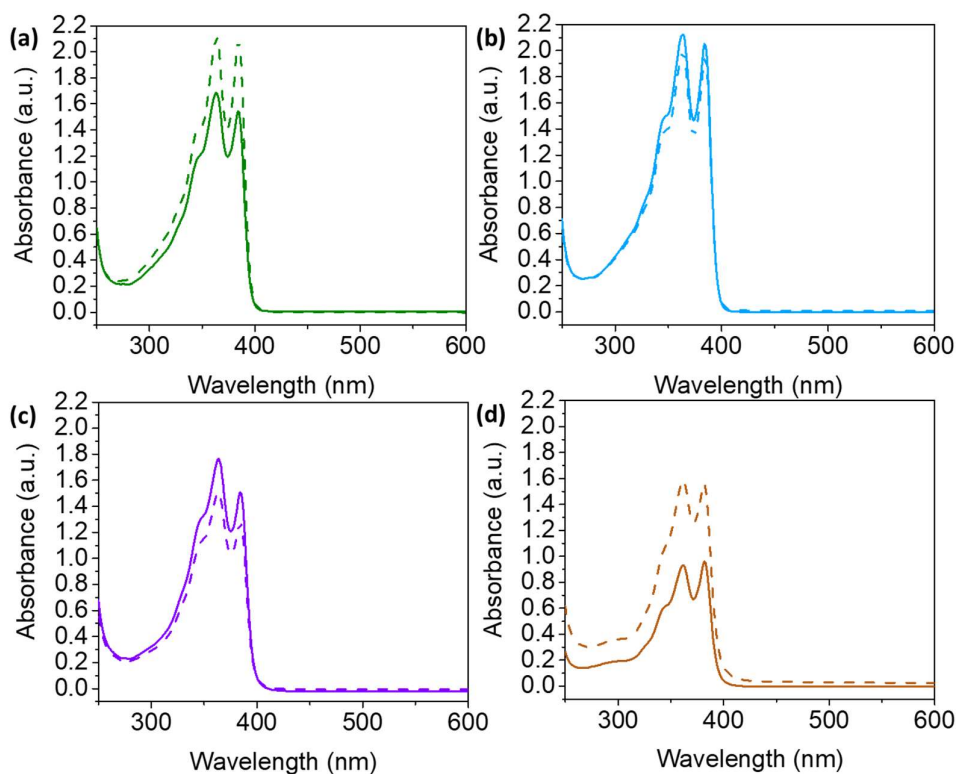


Figure 3.3. Absorbance spectra of the neutral state of 5 mg/mL buffered (dashed line) and unbuffered (solid line) of **NDI-I**, (b) **NDI-V**, (c) **NDI-F** and (d) **NDI-GF** adjusted to their respective ideal pH (pH 9 for **NDI-I** and **NDI-V** and pH 6 for **NDI-F** and **NDI-GF**).

There is minimal shifting (around 0.2 V at a maximum) observed in redox peaks upon buffering in both referenced and unreferenced set-ups, Table 3.2-Table 3.3 and Figures A.3.1-A.3.5, Appendix. In the case of **NDI-GF**, in non-buffered solutions, two reduction peaks are seen and in buffered solutions,

one is observed roughly between these two, Figure A.3.5(d), Appendix. This observation suggests that the two peaks have coalesced and are more distinct in non-buffered solutions which may be due to the subtle difference in molecular packing observed from absorbance spectra, (Figure 3.3(d)).

Table 3.2. Reduction and oxidation potentials taken from cyclic voltammograms of 10 mg/mL buffered and unbuffered solutions of **NDI-I**, **NDI-V**, **NDI-F** and **NDI-GF** adjusted to their respective ideal pH (pH 9 for **NDI-I** and **NDI-V** and pH 6 for **NDI-F** and **NDI-GF**). Cyclic voltammograms performed in referenced set up (Ag/AgCl) at 0.2 V/s.

Buffered System	Reduction Potential(s) (V)	Oxidation Potential (V)	Unbuffered System	Reduction Potential(s) (V)	Oxidation Potential (V)
NDI-I	-0.8	0.7	NDI-I	-1	0.7
NDI-V	-0.9	0.7	NDI-V	-0.8	0.8
NDI-F	-0.8, -1.4	0.8	NDI-F	-0.7	0.5
NDI-GF	-0.8	1	NDI-GF	-0.5, -1.3	0.8

Table 3.3. Reduction and oxidation potentials taken from cyclic voltammograms of 10 mg/mL buffered and unbuffered solutions of **NDI-I**, **NDI-V**, **NDI-F** and **NDI-GF** adjusted to their respective ideal pH (pH 9 for **NDI-I** and **NDI-V** and pH 6 for **NDI-F** and **NDI-GF**). Cyclic voltammograms performed in 1x1 FTO windows at 0.2 V/s.

Buffered System	Reduction Potential(s) (V)	Oxidation Potential (V)	Unbuffered System	Reduction Potential(s) (V)	Oxidation Potential (V)
NDI-I	-2.5	0.1	NDI-I	-2.6	0.2
NDI-V	-1.9, -2.6	0.2	NDI-V	-1.8, -2.5	0.2
NDI-F	-2.5	0.1	NDI-F	-2.6	0.1
NDI-GF	-2.3	0.4	NDI-GF	-2.3	0.4

Buffered solutions maintained their pH for at least 70 hours when left undisturbed, whereas unbuffered solutions do not maintain stable pH for more than a few hours, Figure 3.4. Future measurements will use buffered solutions to make sure pH, and consequent aggregation, is consistent. In **NDI-I** and **NDI-V**, buffering will have a significant impact as pH starts to drop from pH 9 within an hour, Figure 3.4(a). As the pH drops, aggregation also changes which will have an impact upon electrochemical behaviour. The drop in colouration intensity was most notable below and above pH

9 for both these systems, Figure 2.15, Chapter 2. In long term devices, **NDI-I** and **NDI-V** solutions would require buffering to be viable.

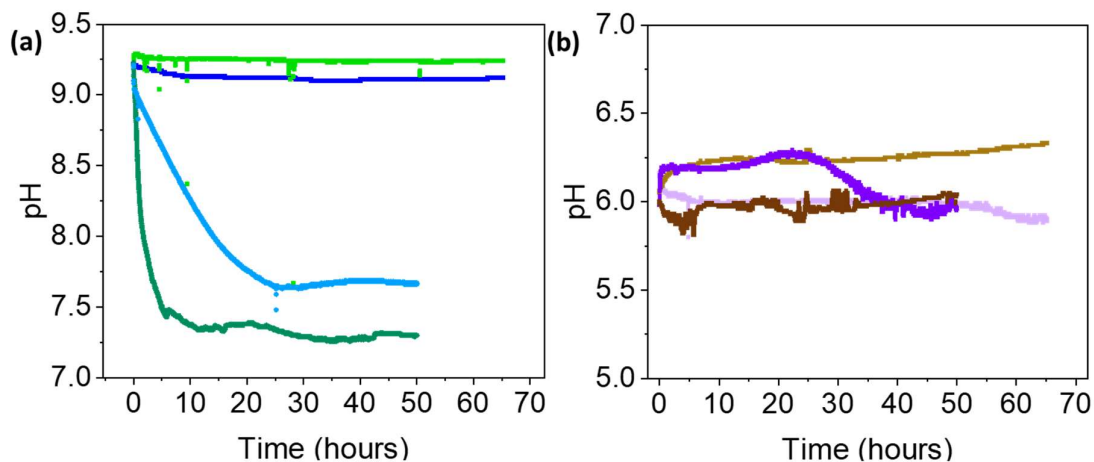


Figure 3.4. pH of 10 mg/mL buffered, and unbuffered solutions of **NDI-I** (green), **NDI-V** (blue), **NDI-F** (purple) and **NDI-GF** (brown) logged between 50-70 hours. Solutions were adjusted to their respective ideal pH (pH 9 for **NDI-I** and **NDI-V** and pH 6 for **NDI-F** and **NDI-GF**) at the start of the log. Buffered solutions are represented by **NDI-I** (light green), **NDI-V** (light blue), **NDI-F** (light purple) and **NDI-GF** (light brown).

The wavelength of peaks in the reduced absorbance spectra are unchanged by buffering but the intensity of colouration is affected, Table 3.4. The λ_{\max} of **NDI-I**, **NDI-V** and **NDI-F** are near the limits of the spectrometer and so absorbance at 540 nm is tabulated. The difference in colour intensity afforded by additional salt concentration is notable in the absorbance spectra of the reduced state but is less notable by eye, Figure 3.5.

Table 3.4. Tabulated absorbance at 540 nm for buffered and unbuffered solutions of NDI-R after a 10 second application of -2.5 V. Full data set available in Figure A.3.6, Appendix. 10 mg/mL solutions were adjusted to their respective ideal pH (pH 9 for **NDI-I** and **NDI-V** and pH 6 for **NDI-F** and **NDI-GF**).

Buffered System	Absorbance at 540 nm (a.u.)	Unbuffered System	Absorbance at 540 nm (a.u.)
NDI-I	1.93	NDI-I	1.52
NDI-V	1.81	NDI-V	1.45
NDI-F	1.40	NDI-F	0.86
NDI-GF	0.75	NDI-GF	0.62

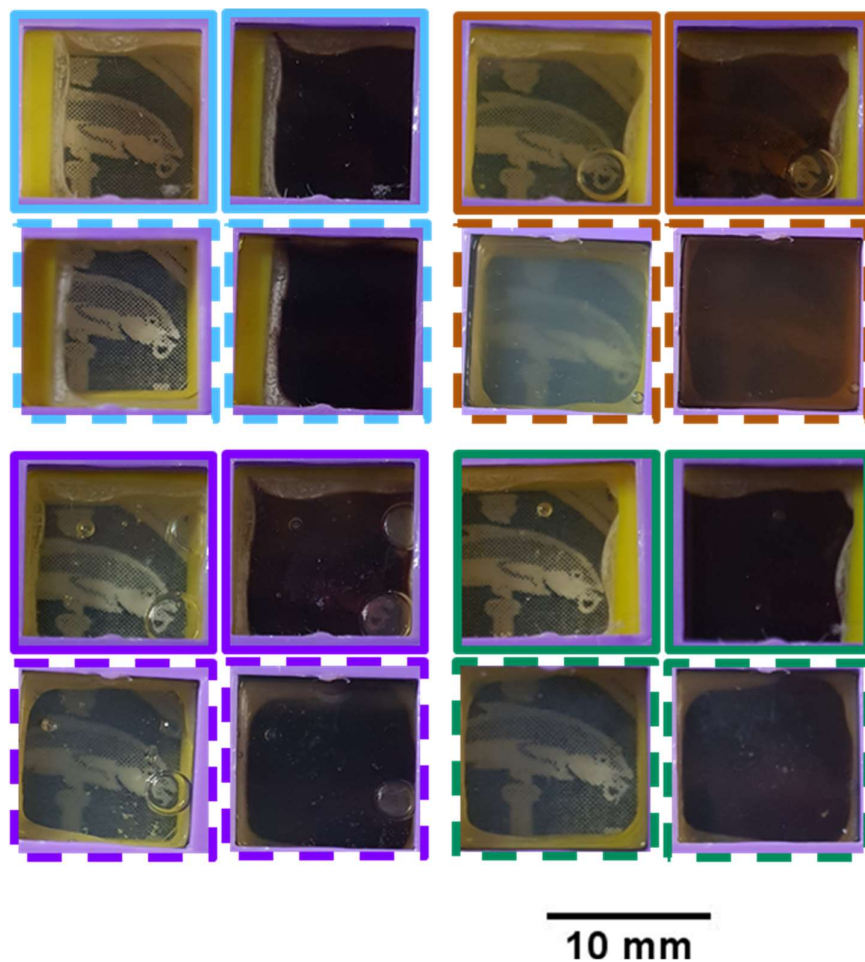


Figure 3.5. Photographs of neutral and electrochemically reduced buffered (dashed line) and unbuffered (solid line) solutions of **NDI-I** (green), **NDI-V** (blue), **NDI-F** (purple) and **NDI-GF** (brown) at 10 mg/mL and at their respective ideal pH (pH 9 for **NDI-I** and **NDI-V** and pH 6 for **NDI-F** and **NDI-GF**). Reduction was achieved by application of -2.5 V for 10 seconds. Any bubbles caused by loading.

The most significantly enhanced NDI was **NDI-F**, suggesting that the structures of this system may be less conductive than others and so are more significantly improved by additional salt concentration. The reversal of reduced colouration is comparable in buffered and unbuffered states, Figure 3.6

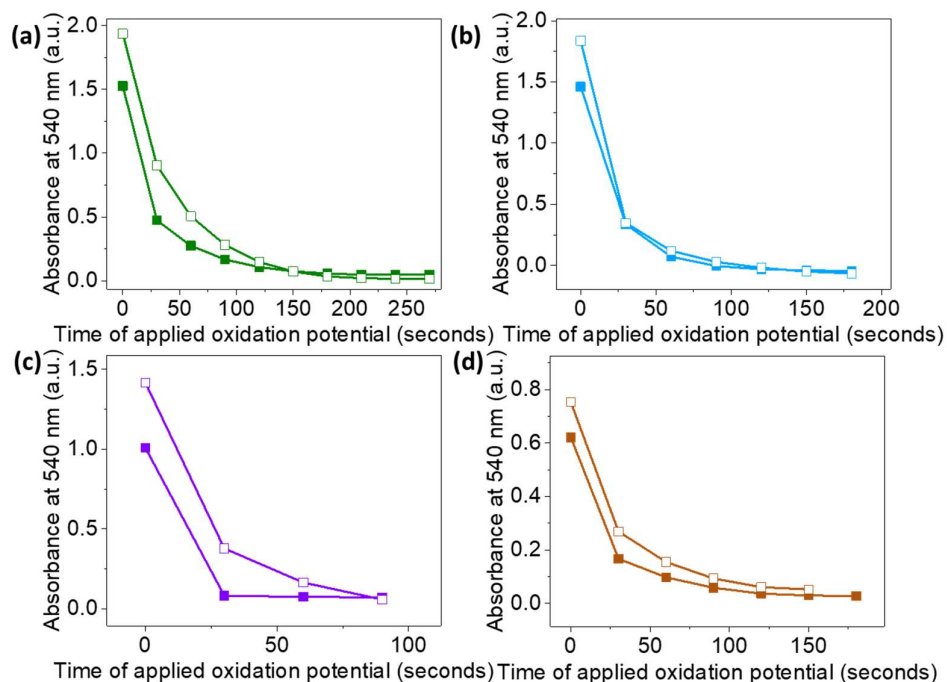


Figure 3.6. Absorbance at 540 nm taken every 30 seconds as oxidising potential of oxidation potential of 0.5 V was applied for 300 seconds to electrochemically reduced unbuffered (filled square) and buffered (open square) solutions of (a) **NDI-I**, (b) **NDI-V**, (c) **NDI-F** and (d) **NDI-GF** at 10 mg/mL after 20 second application of -2.5 V. Solutions adjusted to respective ideal pH (pH 9 for **NDI-I** and **NDI-V** and pH 6 for **NDI-F** and **NDI-GF**).

3.2.2 Comparing ideal states

From the absorbance spectra of the neutral state of each NDI at its ideal pH, there is no significant difference in molecular packing (apart from **NDI-F**, Figure 3.7(a)). The ratio of peaks at 365 and 385 nm is different in **NDI-F** compared to the other NDIs which indicates a different molecular packing.

Viscosity measurements give information about the bulk properties of these systems in their neutral state, Figure 3.7(b). At low shear, viscosity is measured at a higher value for buffered solutions of **NDI-GF** and **NDI-F** which suggests that larger aggregates are present, however, this region of shear has high error due to the low viscosity of the samples, as shown by error bars. Therefore, comparisons drawn here are not statistically significant. All NDIs show a small amount of shear thinning behaviour, which is characteristic of worm-like micelles being present in similar structures.^{11–13} As the viscosity of all NDI solutions are roughly comparable to water due to the low concentration used) we cannot gain a great deal of insight from viscosity measurements.

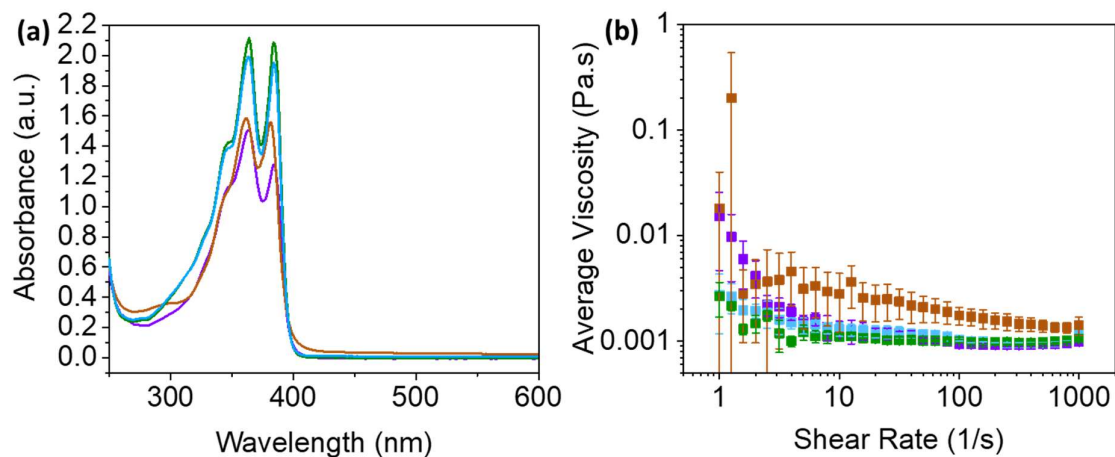


Figure 3.7. (a) Absorbance spectra of the neutral state of 5 mg/mL buffered **NDI-I** (green), **NDI-V** (blue) adjusted to pH 9, **NDI-F** (purple) and **NDI-GF** (brown) adjusted to pH 6 (b) Viscosity measurements under increasing shear rate for buffered solutions of **NDI-I** (green) and **NDI-V** (blue) at pH 9 and **NDI-F** (purple) and **NDI-GF** (brown) at pH 6 at 10 mg/mL. Measurements are taken as an average of triplicate measurements and error bars calculated from standard deviation.

There may be factors such as electron transfer efficiency that influence electrochemical processes, but aggregation is expected to be the most significant factor. For example, at high or low pH, we would anticipate higher conductivity than at pH 9 due to a higher concentration of charged ions. However, electrochemical processes are most efficient at pH 9 in the case of **NDI-I** and **NDI-V**, Chapter 2. This observation suggests that aggregation is an overriding factor. Therefore, to understand assembly further we use SANS. SANS also allows measurement over a wide Q range and long length scales to understand the primary structures of aggregates as well as any larger networks.

3.2.3 High pH

While we have observed differences in ‘ideal’ pH with R groups, pH 12 was consistently associated with almost no generation of the radical anion electrochemically. This observation corresponds to a change in aggregation which is suggested by significant changes in the absorbance spectra of the neutral state, as discussed in Chapter 2. Using SANS, we investigated this state further. SANS measurements require contrast between solvent and molecules and so NDIs are dissolved in D₂O (using deuterated base and acid to pD adjust). Therefore, we refer to pD in the following discussion. We do not expect a significant difference in aggregation in H₂O and D₂O.

SANS data for all NDIs measured at pD 12 can be fit to a flexible elliptical cylinder models combined with a power law. All fits have a radius of approximately 5 Å, a large ratio axis (Table 3.5) and scattering has similar intensity across all ranges of Q in all NDIs (with the exception of **NDI-FF**), Figure 3.8. **NDI-**

FF has a higher intensity at low Q which could suggest larger network interactions likely due to the two large aromatic groups of this dipeptide. The length of these systems is outside of the range that can be reliably modelled with SANS data.^{19,20,51} SANS experiment can resolve length scales of up to approximately 1000 Å.⁵² This structure type (large axis ratio flexible elliptical cylinder) could be attributed to poorly defined cylinders or planar tape-like structures (which have been reported to form in molecules with amide motifs capable of hydrogen bonding).⁵³ The dispersion of NDI molecules at this pH does not allow efficient π -stacking and the distance between NDI molecules is too large to effectively form the radical anion.^{54,55}

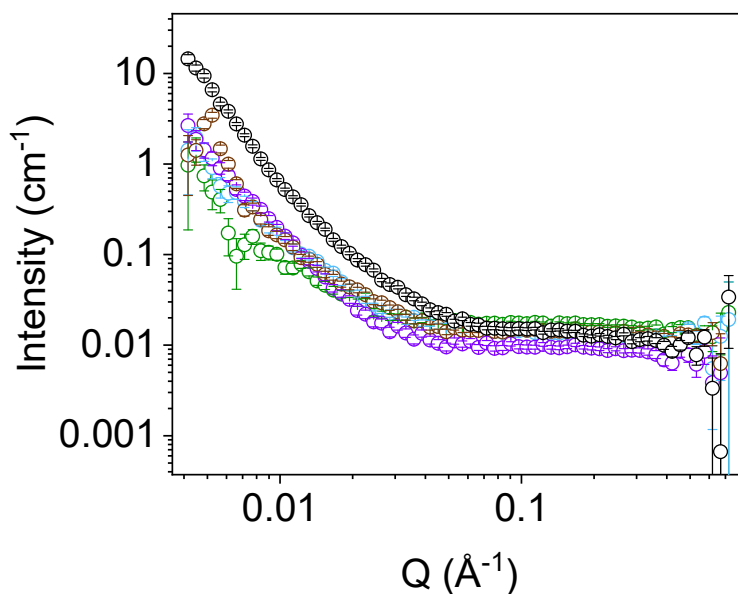


Figure 3.8. Small angle neutron scattering data (open circles) for 10 mg/mL solutions, in their neutral state, of **NDI-I** (green), **NDI-V** (blue), **NDI-F** (purple), **NDI-GF** (brown) and **NDI-FF** (black) at pD 12.

Table 3.5. Tabulated parameters from SANS model fits of systems at 10 mg/mL, pD 12. The parameters for **NDI-FF** at pD 7 are also shown. Full data sets available in Figures A.3.7-A.3.12 and Tables A.3.1-A.3.6, Appendix. Models using flexible, flexible elliptical and hollow cylinders combined with a power law.

System	Kuhn Length (Å)	Error	Radius (Å)	Error	Axis Ratio	Error
NDI-I	84.99	6.54	4.90	0.155	25.90	0.819
NDI-V	120.90	6.07	5.44	0.113	14.80	0.307
NDI-F	146.31	18.9	5.00	0.255	41.50	2.11
NDI-GF	46.79	2.58	4.93	0.0110	18.10	0.0405
NDI-FF pD 12	120.99	1.22	5.50	0.0883	19.82	0.0315
NDI-FF pD 7	133.99	9.65	10.04	0.0178	24.88	0.415

NDI-FF demonstrated poor electrochemical behaviour across all pH values (Chapter 2) and showed the same structure type (of tape-like cylinders with a high axis ratio) and scattering intensity at both pD 7 and 12, Table 3.5 and Figure 3.9. At lower pD, the radii increase, and the Kuhn length increases which suggests more rigid structures, however these changes are not significant. This observation suggests that this structure either disfavours the reductive process or cannot stabilise the radical anion and that **NDI-FF** does not form more defined structures as pD is lowered. The weak colour of the reduced state makes this system unsuitable as has already been noted (Chapter 2) and it should not be investigated for cyclability and stability.

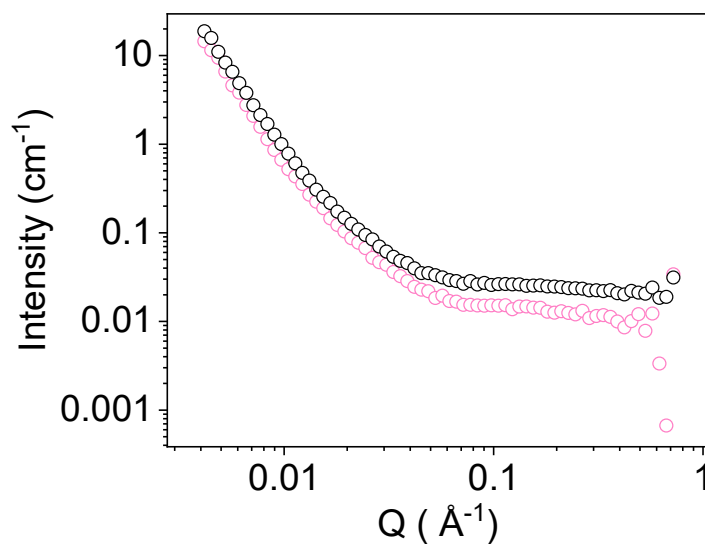


Figure 3.9. Small angle neutron scattering data for a neutral solution of **NDI-FF** at pD 7 (black) and pD 12 (pink).

It cannot be said with certainty what aspect of the tape-like aggregation disfavours production of the radical anion. In the case of **NDI-FF**, the lack of ability to form defined structures or stabilise the radical anion may be due to the steric bulk the aromatic rings, compromising π -stacking and influencing the efficiency of electron transfer along a π -stack.⁵⁶ These rings may also provide some form of shielding, preventing efficient electron transfer. A combination of factors is likely contributing to this observation.

3.2.4 Aggregation at pD 9 and 6

The ideal pH for each NDI was found to be in the region of one of two apparent pK_a values. As previously discussed, each pK_a is associated with a consequent change in aggregation. One consistent ideal pH was not found for all NDIs investigated. This observation suggests aggregation changes that occur at each pK_a either favour or disfavour electrochemical activity depending on amino acid 'R'

group. Having identified the structure type associated with very poor electrochromic behaviour, we can now investigate the structures at the lower pDs.

At pD 9 and 6, **NDI-I** fits to a flexible cylinder model combined with a power law. The length of these cylinders is, again, outside the range accessible by this technique,⁵² but the radius of these cylinders is approximately 5 Å at both pD, Table 3.6. The change in aggregation between pD 6 and 9 is mostly subtle (although statistically significant), as we hypothesised in Chapter 2. The most significant difference is a decrease in Kuhn length at pD 6, which suggests structures become more flexible, Table 3.6. The intensity at high Q is also lower at pD 6, suggesting smaller, or more solvated aggregates, Figure 3.10(a).

Table 3.6. Tabulated parameters from SANS model fits of neutral 10 mg/mL **NDI-I**. Full data sets available in Figures A.3.13-A.3.14 and Tables A.3.7-A.3.8, Appendix. Flexible cylinder and power law model used.

System	Kuhn Length (Å)	Error	Radius (Å)	Error
NDI-I pD 9	118.42	6.78	5.23	0.0727
NDI-I pD 6	89.94	8.14	5.02	0.128

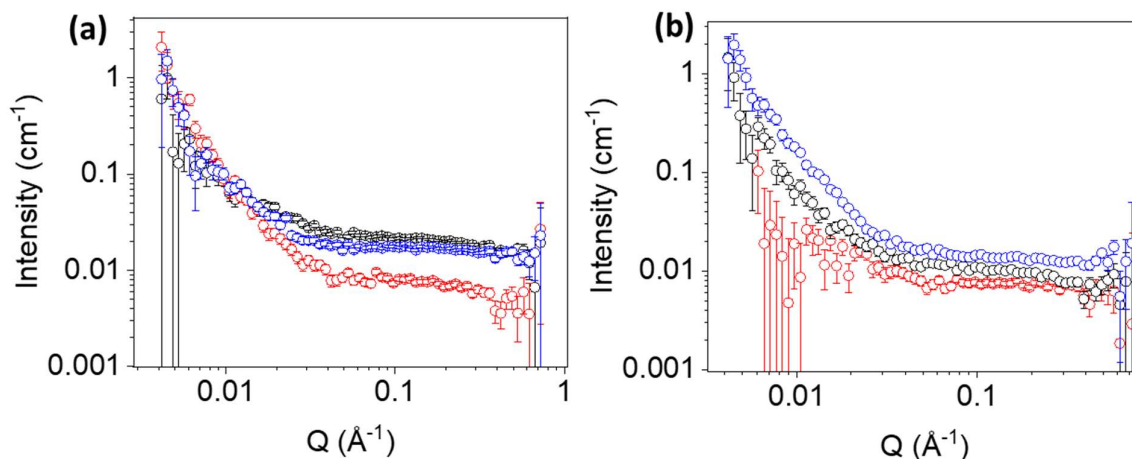


Figure 3.10. Small angle neutron scattering data for a 10 mg/mL neutral buffered solution of (a) **NDI-I** and (b) **NDI-V** at pD 6 (red), pD 12 (blue) and buffered at pD 9 (black).

NDI-V behaves very similarly to **NDI-I**, possibly due to their similar 'R' group. The trends of radii and Kuhn length are comparable (but the decrease in Kuhn length is more significant at pD 6 than in **NDI-I** suggesting this NDI forms more flexible structures), Table 3.7. Similarly, to **NDI-I**, scattering intensity is lower at pD 6 which suggests smaller aggregates, Figure 3.10(b).

. **Table 3.7.** Tabulated parameters from SANS model fits of neutral, 10 mg/mL **NDI-V**. Full data sets available in Figures A.3.15-A.3.16 and Tables A.3.9-A.3.10, Appendix. Flexible cylinder and power law model used.

System	Kuhn Length (Å)	Error	Radius (Å)	Error
NDI-V pD 9	111.38	8.13	5.18	0.125
NDI-V pD 6	41.85	7.89	5.00	0.253

Unlike **NDI-I** and **NDI-V**, **NDI-F** fits to a hollow cylinder model combined with a power law. This model implies significantly more rigid structures. This observation may be a result of the rigidity of the phenylalanine group of this NDI. **NDI-F** was also found to demonstrate different molecular packing to other NDIs (Figure 3.7(a)) which is likely because of this ability to form hollow cylinders. At pD 9, the hollow cylinders formed by **NDI-F** have much smaller radii (and thickness) than pD 6, which suggests that larger aggregates form as pD decreases, Table 3.8. As observed for **NDI-I** and **NDI-V**, there is a decrease in scattering intensity at high Q in **NDI-F** as pD decreases, Figure 3.11(a). As with **NDI-I** and **NDI-V**, the differences in parameters are statistically significant.

Table 3.8. Tabulated parameters from SANS model fits of neutral, 10 mg/mL **NDI-F**. Full data sets available in Figures A.3.17-A.3.18 and Tables A.3.11-A.3.12, Appendix. Hollow cylinder and power law model used.

System	Radius (Å)	Error	Thickness (Å)	Error
NDI-F pD 9	25.34	3.32	7.81	0.0782
NDI-F pD 6	52.33	2.17	11.76	0.624

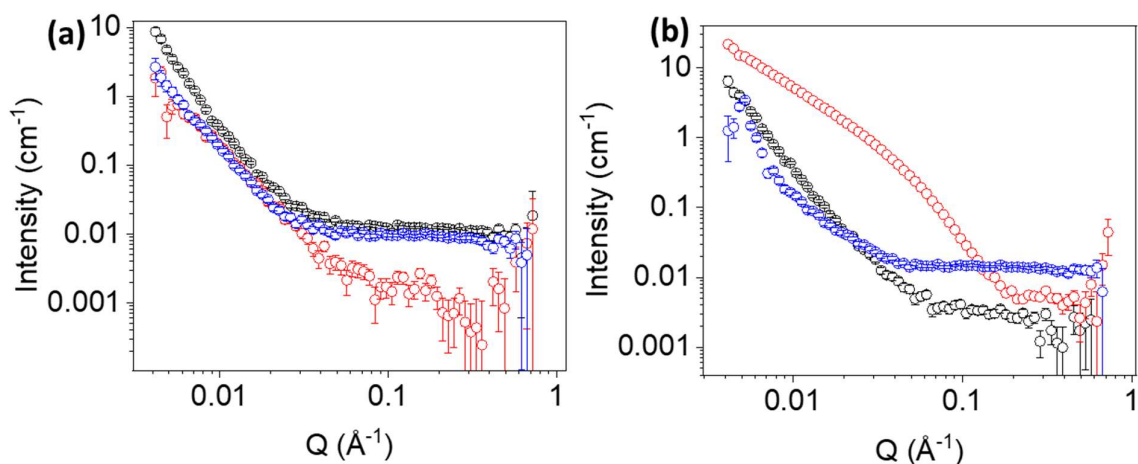


Figure 3.11. Small angle neutron scattering data for a 10 mg/mL neutral buffered solution of (a) **NDI-F** and (b) **NDI-GF** at pD 9 (black), pD 12 (blue) and buffered at pD 6 (red).

There is an obvious increase in intensity at low Q at pD 6 for **NDI-GF**, Figure 3.11(b). This phenomenon is the result of the gelating ability of this NDI. **NDI-GF** can form gels if pH is lowered slowly⁵ and this intensity at low Q suggests the formation of larger scale networks. While the solution does not form a gel when adjusted to pD 6 with acid by hand, it is likely that small networks or large aggregates similar to the start of gelation are formed at low pD. These more complex structures in solution at low pD may assist the electrochemical processes, making this **NDI-GF**'s ideal pD. Unlike other NDIs, there is a significant reduction in scattering intensity between pH 12 and 9 and high Q, Figure 3.11(b), which suggests that there are significant changes at each apparent pK_a of **NDI-GF**.

The scattering data for **NDI-GF** fit to a flexible elliptical cylinder model combined with a power law. The Kuhn length at pD 9 is larger than at pD 6 (comparable to **NDI-I** and **NDI-V**), Table 3.9. Changes are statistically significant. Between pD 12, 9 and 6, the axis ratio is observed to decrease as radius increases which suggests that cylinders become more defined as pD drops. However, this change in axis ratio is more gradual than observed in **NDI-I** and **NDI-V**, with axis ratio still being high at pD 9. This observation suggests that even at pH 9, structures of **NDI-GF** are either ill-defined or very elliptical. The bulky and electron rich nature of the dipeptide group may be responsible for lack of definition at pH 9. Steric or electrostatic repulsion could both contribute to difficulties forming structures at this pD, as the NDI molecules will be partially deprotonated.

Table 3.9. Tabulated parameters from SANS model fits of neutral, 10 mg/mL **NDI-GF**. Full data sets available in Figures A.3.19-A.3.20 and Tables A.3.13-A.3.14, Appendix. Flexible elliptical cylinder and power law model used.

System	Kuhn Length (Å)	Error	Radius (Å)	Error	Axis Ratio	Error
NDI-GF pD 9	126.55	9.41	7.26	0.146	10.35	0.206
NDI-GF pD 6	60.07	0.0232	19.51	0.00182	1.82	8.73E-04

The glycine in the dipeptide allows more freedom of movement within the molecule than other NDIs investigated. This added flexibility is reflected in the Kuhn length at pD 6 (lower than **NDI-I**, **NDI-V** and **NDI-FF**). **NDI-GF** was the only NDI in which a change in molecular packing between pH 6 and pH 9 was observed in absorbance spectra (suggested by a change in relative intensities of absorbances at 365 and 385 nm, Figure 3.12). This difference in packing suggests a local change in structure as larger aggregates form at pH 6.

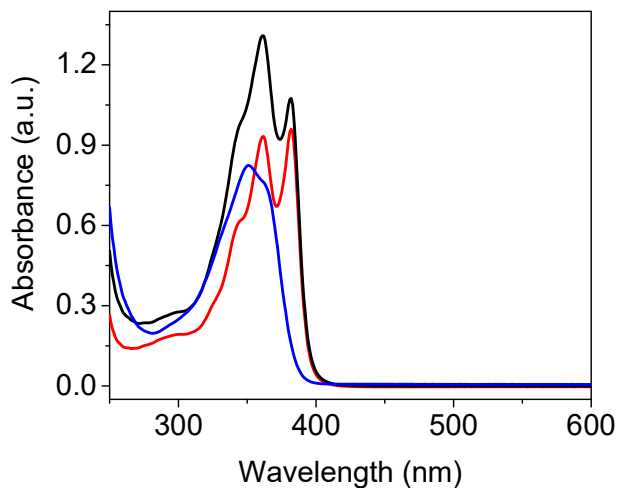


Figure 3.12. Absorbance spectra of **NDI-GF** containing NaCl in a neutral state at 5 mg/mL. Solutions recorded at pH 6 (red), 9 (black) and 12 (blue).

3.2.4.1 Comparison of NDIs

Comparing across NDIs at their ideal pD, Figure 3.13, **NDI-I** and **NDI-V** form very similar structures and have comparable scattering intensity, chromic behaviour and trends with pD. This observation suggests that these similarly appended NDIs have comparable aggregation, which is most favourable for their electrochromic performance at pD 9. The more rigid structures formed at pD 9 may be responsible for the difference in colouration intensity between pD 6 and 9 for these NDIs. We hypothesise that for these two systems, additional flexibility results in poorer colouration. The changes in structure are subtle for both NDIs between pD 9 and 6.

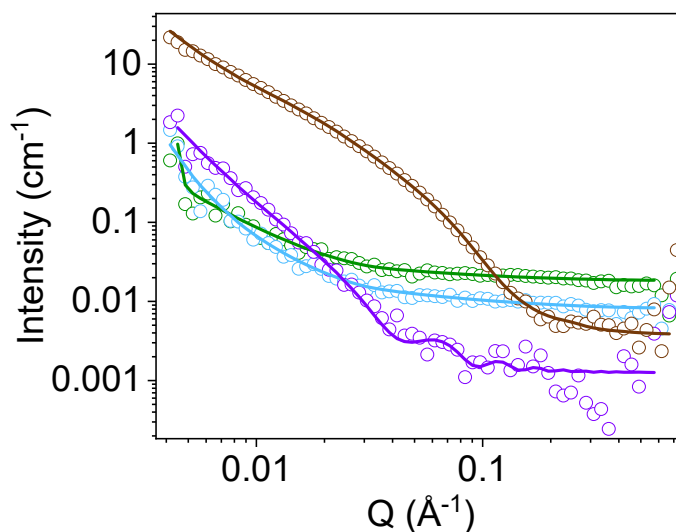


Figure 3.13. SANS (open circles) and fits (lines) for solutions of 10 mg/mL **NDI-I** (green), **NDI-V** (blue), **NDI-F** (purple), **NDI-GF** (brown) at their respective ideal pD (pD 9 for **NDI-I** and **NDI-V** and pD 6 for **NDI-F** and **NDI-GF**). Fits are to flexible cylinder, flexible cylinder, hollow cylinder and flexible elliptical cylinder (all combined with a power law) for **NDI-I** (green), **NDI-V** (blue), **NDI-F** (purple), **NDI-GF** (brown).

NDI-F has a lower scattering intensity than the other measured NDIs, which suggests that it is made up of smaller, or more solvated aggregates, Figure 3.13. **NDI-GF** has a large scattering intensity at low Q due to its gelling ability. **NDI-F** forms the most rigid structures as hollow cylinders (with no parameter to accommodate flexibility, such as Kuhn Length).

Both **NDI-F** and **NDI-GF** have larger radii than **NDI-I** and **NDI-V** which is likely a result of their larger aromatic groups. It is inferred from these data that these aromatically appended NDIs have more desirable chromic properties at pD 6 than pD 9 due the size of aggregates. Both systems demonstrate an increase in radii as pD lowers. As radii increase, perhaps these structures become less strained and more stable. At pD 6, we would expect molecules to be more likely to be fully protonated and less charged, reducing any electrostatic repulsion that may been influencing the aggregates at higher pD.

3.2.5 The reduced state at ideal pH

Having compared the ideal aggregation in a neutral state, we can now evaluate the reduced state. The “typical human eye” cannot distinguish a difference in a 5–10% change in transmittance and so in industry, an 85% of transmittance change is “standard”.⁵⁷ The values of %transmittance for the reduced and neutral state at λ_{\max} are tabulated in Table A.3.15, Appendix. These data were used to calculate colouration efficiency which is tabulated in Table 3.10. Colouration efficiency of these systems at their λ_{\max} is high compared to literature values of alternative systems.^{22,30,58–60} A viologen-

based device was reported to have a colouration efficiency of $120.8 \text{ cm}^2/\text{C}$,⁶¹ and a metal electrodeposition system has reported colouration efficiency between 19 and $132 \text{ cm}^2/\text{C}$, depending upon which metal was used.²⁷ Our systems have a colouration efficiency between approximately 95-250 cm^2/C . Due to the intense absorbance of **NDI-I** and **NDI-V** at their λ_{max} (near the limits of the spectrometer), data from a two second reduction as well as a ten second reduction was collected.

Table 3.10. Tabulated colouration efficiency calculated using transmittance taken at the λ_{max} of the reduced state of buffered **NDI-I**, **NDI-V**, **NDI-F**, and **NDI-GF** after application of -2.5 V. Colouration efficiency calculated using charge density in a 1 x 1 cm FTO window set-up.

Buffered System	Colouration Efficiency (cm^2/C)
NDI-I 10 mg/mL at pH 9	156.9 (10 second reduction)
	235.5 (2 second reduction)
NDI-V 10 mg/mL at pH 9	229.5 (10 second reduction)
	254.1 (2 second reduction)
NDI-F 10 mg/mL at pH 6	94.9 (10 second reduction)
NDI-GF 10 mg/mL at pH 6	154.2 (10 second reduction)

Absorbance spectra are compared while species are electrochemically reduced. Comparing between the differently appended NDIs at each ideal pH, **NDI-I** and **NDI-V** produce the strongest intensity colouration. These are the most promising candidates for Smart Windows at this stage.

The spectra and colouration by eye of electrochemically reduced solutions of **NDI-I**, **NDI-V** and **NDI-F** are comparable, but **NDI-GF** is notably different, Figure 3.14. In the spectra of reduced solutions of **NDI-GF**, a broad absorption in the near IR region over 900 nm is associated with one-dimensional π -stacking of the radical anion.^{5,56,62} This absorbance was strongest at low pH (Chapter 2). The λ_{max} is also found at an approximately 40 nm shorter wavelength than other NDIs, with peaks between 520-800 nm less intense and defined than other NDI spectra, Figure 3.14.

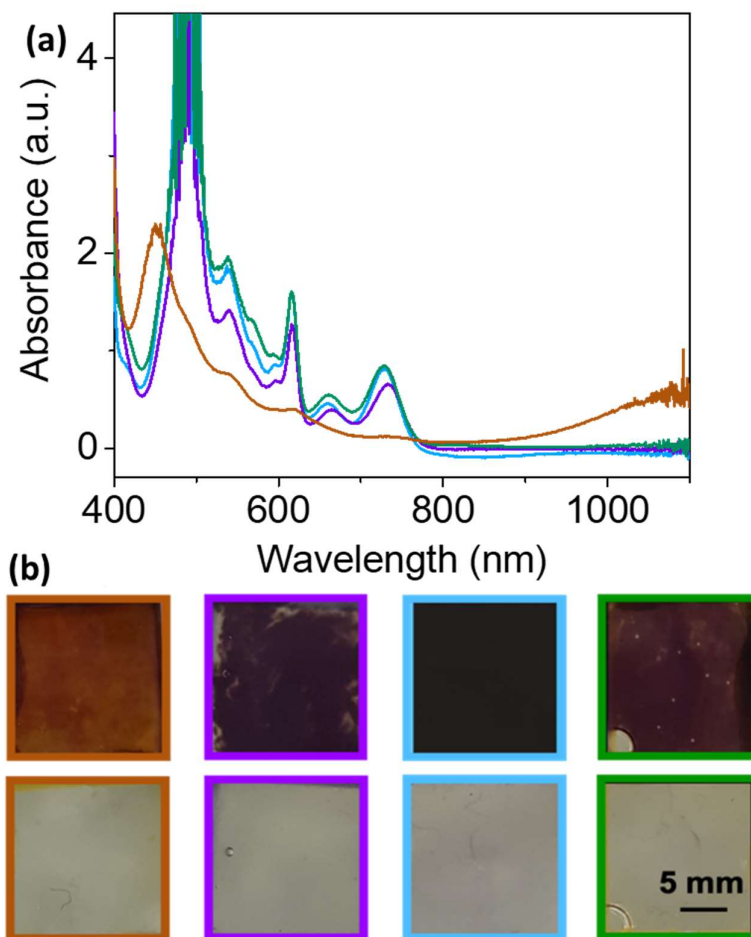


Figure 3.14. (a) Absorbance spectra of the reduced state of 10 mg/mL buffered **NDI-I** (green), **NDI-V** (blue) **NDI-F** (purple) and **NDI-GF** (brown) adjusted to their respective ideal pH (pH 9 for **NDI-I** and **NDI-V** and pH 6 for **NDI-F** and **NDI-GF**) after 20 seconds of application of -2.5 V, (b) Photographs of solutions of **NDI-I**, **NDI-V**, **NDI-F** and **NDI-GF** at their respective ideal pH in coloured (top) and neutral states (bottom). Coloured states achieved by application of -2.5 V for 20 seconds in 1 x 1 cm windows.

At a concentration of 10 mg/mL, there will be a small difference in molar concentration due to differences in molecular weight. When **NDI-GF** (the heaviest molecular weight NDI) solution was made up at an equal molar concentration to 10 mg/mL **NDI-V** (the lightest molecular weight NDI) there was no significant difference in electrochemical colouration upon reduction, Figure 3.15. We therefore attribute differences in colouration to aggregation of the NDI and not insignificant differences in molar concentration.

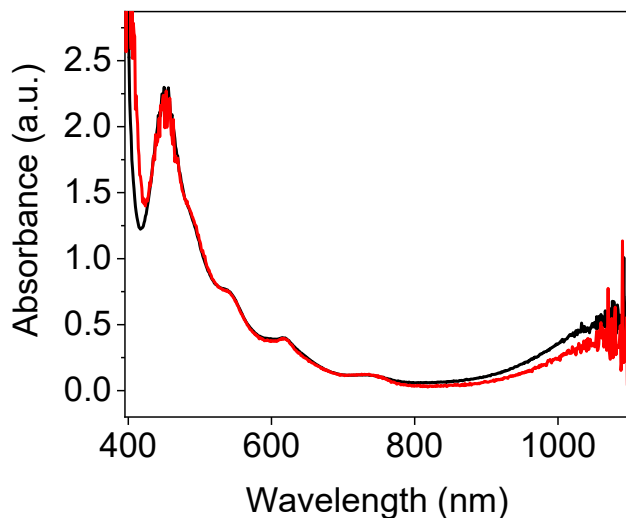


Figure 3.15. Absorbance spectra of the reduced state of 10 mg/mL buffered **NDI-GF** adjusted to pH 6 at 10 mg/mL (black) and 14.5 mg/mL (red). Spectra taken after 20 seconds of application of -2.5 V.

The added flexibility of glycine in **NDI-GF** may be responsible for its ability to form larger aggregated networks which results in a difference in the spectrum and a brown colouration by eye, Figure 3.14(b). The purple colouration of **NDI-I**, **NDI-V** and **NDI-F** cannot be associated with production of the dianionic species because the characteristic peak at 410 nm^{5,62} is not observed in the **NDI-F** spectrum and is very weakly observed in **NDI-I** and **NDI-V**, Figure 3.14(a).

To confirm that a difference in the radical anionic species itself is not the cause of the brown colour of the reduced state of **NDI-GF**, EPR spectroscopy was performed. The characteristic NDI signal has 13-line hyperfine splitting derived from the interaction of the unpaired electron with two ¹⁴N ($I = 1$) and four ¹H ($I = 1/2$) nuclei.⁶²

We observed that no further splitting is observed from the N-R groups, as the unpaired spin is confined to the NDI core unit,⁵⁴ Figure 3.16. The g -value of approximately 2 is typical of an NDI radical.⁶² While **NDI-I**, **NDI-V** and **NDI-F** produce similar signals to each other, there are subtle differences in hyperfine coupling which could be due to molecular motion rather than inherent electronic differences. No significant differences in the EPR spectra of each NDI radical are observed and therefore differences in colouration and colour intensity must be due to aggregation alone, Figure 3.16. The EPR signal produced by reduced solutions of **NDI-GF** has lower symmetry than that produced by other NDIs. The lower symmetry of **NDI-GF** suggests that the R groups on each side of the NDI core are inequivalent which is likely due to the flexibility of glycine within the dipeptide, allowing for more rotation about the bond. This data highlights the importance of aggregation upon electrochromic behaviour and agrees with our previously collected data and hypotheses.

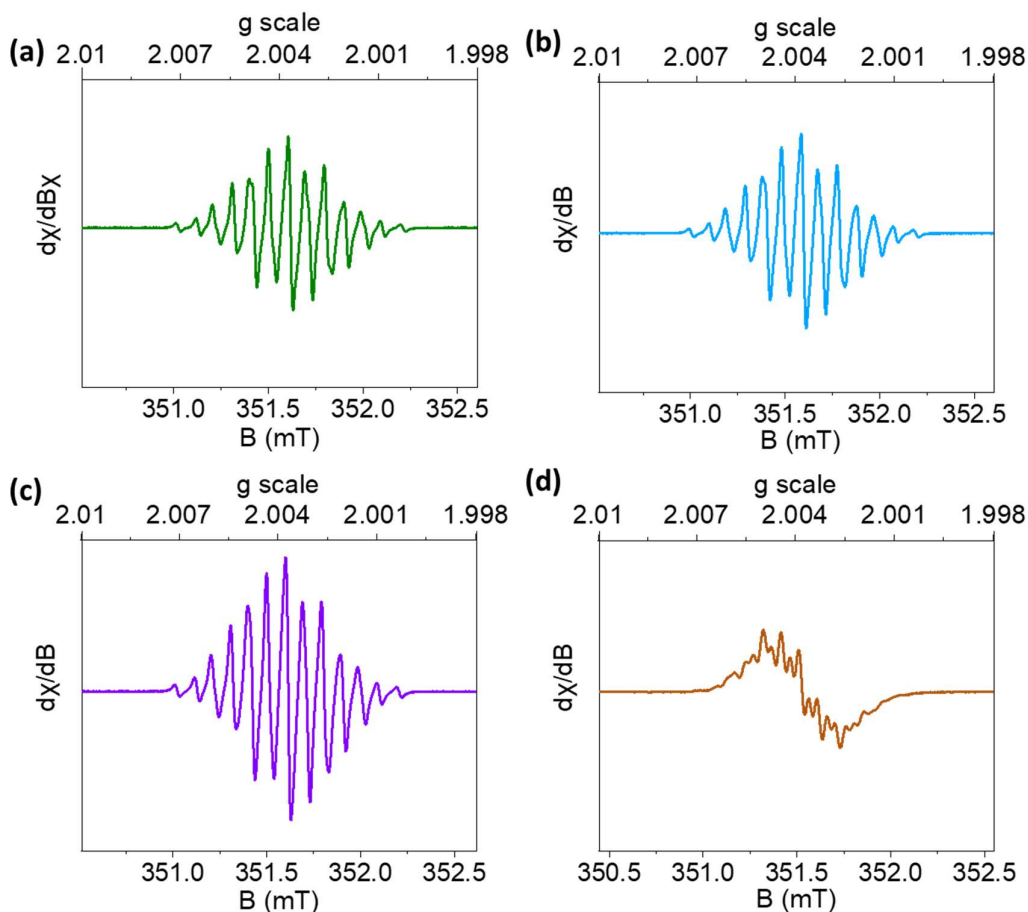


Figure 3.16. EPR signal measured for electrochemically reduced buffered solutions of 10 mg/mL (a) **NDI-I** (green), (b) **NDI-V** (blue), (c) **NDI-F** (purple) and (d) **NDI-GF** (brown) adjusted to their respective ideal pH (pH 9 for **NDI-I** and **NDI-V** and pH 6 for **NDI-F** and **NDI-GF**). Data collected by Dr Stephen Sproules.

3.2.6 Cyclability

3.2.6.1 Initial set-up

One of the most important features for the application of Smart Windows is cyclability because this will determine its stability over long term use. The system must be able to be switched from neutral to reduced state, not only on-demand, but consistently over a long period of use. To assess the cyclability (the ability to repeatedly switch between neutral and reduced states) of these systems, larger scale windows (5 x 5 cm) were used. The smaller scale windows (1 x 1 cm) used for spectro-electrochemistry were unsuitable as we experienced issues with sealing which made long time scale experiments challenging.

Using hydroquinone as a standard, as in Chapter 2, in a 1 x 1 and 5 x 5 cm FTO window set-up, it can be seen that the oxidation potential shifts to a lower potential and the two reduction peaks coalesce

into one broad peak roughly half way between the two seen in a 1 x 1 FTO window, Table 3.11. With the NDIs also, as the size of FTO glass increases, the redox potentials are slightly shifted relative to the potentials in the 1 x 1 cm windows, Table 3.12. This is most likely due to differences in resistivity and surface area of the FTO glass. The chemical structure does not greatly influence the position of reduction and oxidation peaks by CV, Table 3.12.

Table 3.11. Reduction and oxidation potentials taken from cyclic voltammograms of 10 mg/mL hydroquinone with 10 % 0.1 M NaCl. Cyclic voltammograms performed in a 1 x 1 and 5 x 5 FTO window set-up at 0.5 V/s. Data available in Figure A.3.21, Appendix.

Set-up	Reduction Potential(s) (V)	Oxidation Potential (V)
1 x 1 cm FTO window	-1.2, -1.9	0.9
5 x 5 cm FTO Window	-1.4	0.5

Table 3.12. Redox potentials collected from cyclic voltammograms of buffered **NDI-I**, **NDI-V**, **NDI-F** and **NDI-GF** collected at their ideal pH (pH 9 for **NDI-I** and **NDI-V** and pH 6 for **NDI-F** and **NDI-GF**) at 10 mg/mL within a 5 x 5 cm FTO window set-up. The scan rate of the cyclic voltammograms was 0.1 V/s. Full data available in Figure A.3.22, Appendix.

Buffered System	Reduction Potential(s) (V)	Oxidation Potential (V)
NDI-I	-2.51, -3.29	0.47
NDI-V	-2.44	0.55
NDI-F	-3.07	0.15
NDI-GF	-2.55, -3.24	0.50

NDI-F has a slightly more negative reduction potential (of approximately -3 V) and smaller oxidation potential (of 0.15 V) than other NDIs, the rest are mostly comparable at approximately -2.5 and 0.5 V for reduction and oxidation respectively, Table 3.12. Application of -2.7 V results in formation of the radical anion in all NDIs and so this potential was used consistently across all NDIs. It is possible that the difference in structures formed by **NDI-F** (hollow cylinders instead of flexible cylinders) influences diffusion rates within the cell and influences reduction and oxidation potentials. Application of more negative potentials than -2.7 V can result in a small amount of water splitting, which can cause bubble

formation within the cell so it was avoided. The colouration of each NDI can be seen in Figure 3.17. An application of 0.5 V resulted in oxidation of the reduced state across all NDIs, Figure 3.17.

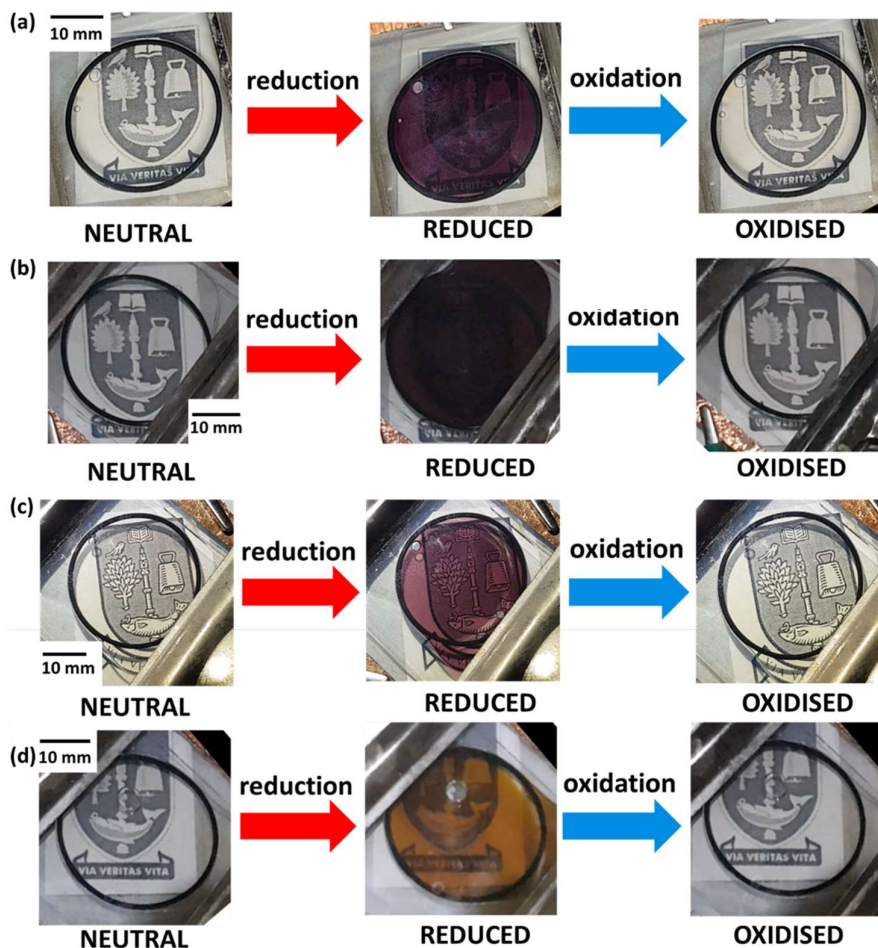


Figure 3.17. Images of the neutral and electrochemically reduced (10 seconds of -2.5 V) and oxidised (2 minutes of 0.5 V) states of buffered (a) **NDI-I**, (b) **NDI-V**, (c) **NDI-F** and (d) **NDI-GF** at their respective ideal pH (pH 9 for **NDI-I** and **NDI-V** and pH 6 for **NDI-F** and **NDI-GF**).

In real world applications, usage would be sporadic in terms of both frequency and length of use depending on the environment and exact application of any product these systems may be used in. On-off cycle tests are the best simulation of consistent usage but may be more wearing on the material than real-life scenarios would be. How reflective these lab tests are of real-world use is hard to ascertain without commercial prototypes, and such scrutiny is out of the scope of this investigation. **NDI-I** was chosen to perform initial tests to assess any issues within the set-up. Full discussion can be found in A.3.1, Figures A.3.22-A.3.29 Appendix.

3.2.7 Initial assessment of cyclability

Having improved the Smart Window set-up to a point which we believe we have achieved maximum efficiency; we could now assess the cyclability of each of the systems. Each system is assessed using a sweeping oxidation script and using a buffer to maintain their respective ideal pH. The cycling experiment was set-up in a dark room without natural light. For all the systems investigated, the reduced state maintains colouration intensity without detriment for at least 4-5 hours, the length of each cycling experiment, Figure 3.18 and Figure A.3.30, Appendix.

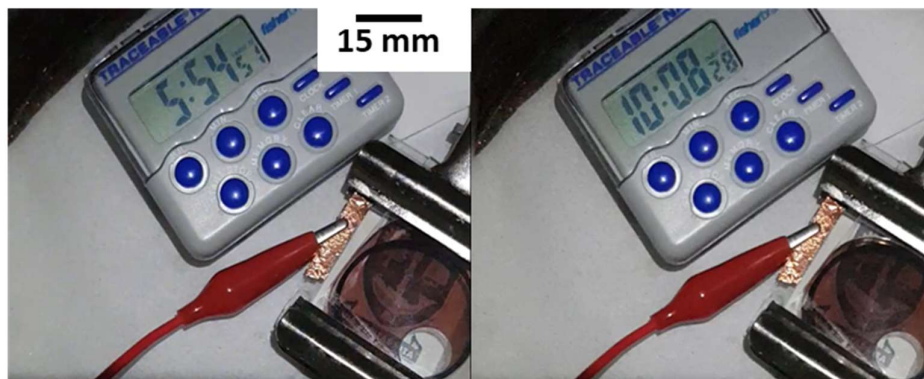


Figure 3.18. Images of the reduced state at the start (left) and end (right) of cycling experiments. Buffered solution of 10 mg/mL **NDI-I** adjusted to pH 9 is shown. The start time of (a) is offset as the stopwatch was not restarted at the beginning of this experiment in error. Images of other NDIs are available in Figure A.3.30, Appendix. Bubble in window caused by loading.

A discolouration of the neutral state occurs with cycling, Figure 3.19 (and Figure A.3.32-A.3.34, Appendix). When this was still observed at the end of an oxidising script, the experiment was stopped. It is hypothesised that this discolouration is due to a build-up of radical anion (caused by issues in the efficiency of electrochemical oxidation in this window set-up) over several cycles, rather than an irreversible chemical reduction. If the reduced species was not fully oxidised at the end of each cycle, then there would be a consequent build-up of a small amount of radical anion from each cycle, resulting in an eventual build-up of discolouration. Because the radical is so highly coloured, only a small amount would need to build up to be seen by the eye.

When removed from the window, the majority of colouration of the solution was removed with gentle shaking in air, Figure 3.19(e), demonstrating the solutions could still be oxidised and a permanent change in materials had not occurred. The change in colour is particularly notable in **NDI-V**, Figure 3.19(b). This observation could suggest a change in the aggregation of this NDI or a very small amount of highly coloured irreversible radical anionic species, resulting in discolouration of the originally pale

solution. Other organic electrochromic systems have produced a discoloured state with cycling.⁶³ In a thin gap, this discolouration is not as obvious as in a vial.

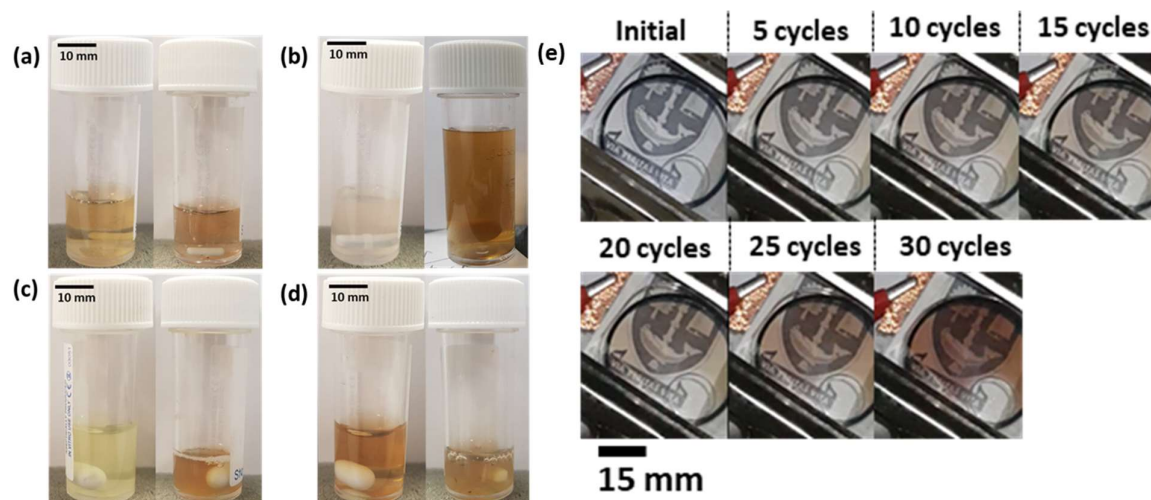


Figure 3.19. (a-d) Photographs of colouration of solutions before cycling experiment (left) and after being collected from window cells after excessive cycling (right). Solutions are at 10 mg/mL and buffered to their respective ideal pH (pH 9 for **NDI-I** and **NDI-V** and pH 6 for **NDI-F** and **NDI-GF**). Shown are (a) **NDI-I**, (b) **NDI-V**, (c) **NDI-F** and (d) **NDI-GF**. (e) Images of oxidised state after periods of cycling. Solution of buffered 10 mg/mL **NDI-I** at pH 9 used. Corresponding images for other NDIs are available in Figures A.3.32-A.3.34, Appendix. Bubble in window is caused by loading.

All systems oxidise within a comparable time frame for the first cycle (Figure 3.20) and so we hypothesise that any change in aggregation is the result of a repeated generation of the radical anion, subtly changing aggregation each cycle, resulting in an exponential effect in some systems.

NDI-I and **NDI-F** performed the best both in terms of number of cycles and oxidation time required to remove the radical (Figure 3.20). **NDI-I** was able to achieve the most cycles out all NDIs investigated. This NDI demonstrated the darkest colouration upon reduction of **NDI-I** and **NDI-F**, Figure 3.14, and is therefore the most promising system moving forward for the application of Smart Windows. **NDI-V** and **NDI-GF** showed a sharp increase in oxidation time and become discoloured after only a few cycles and so had poor cyclability.

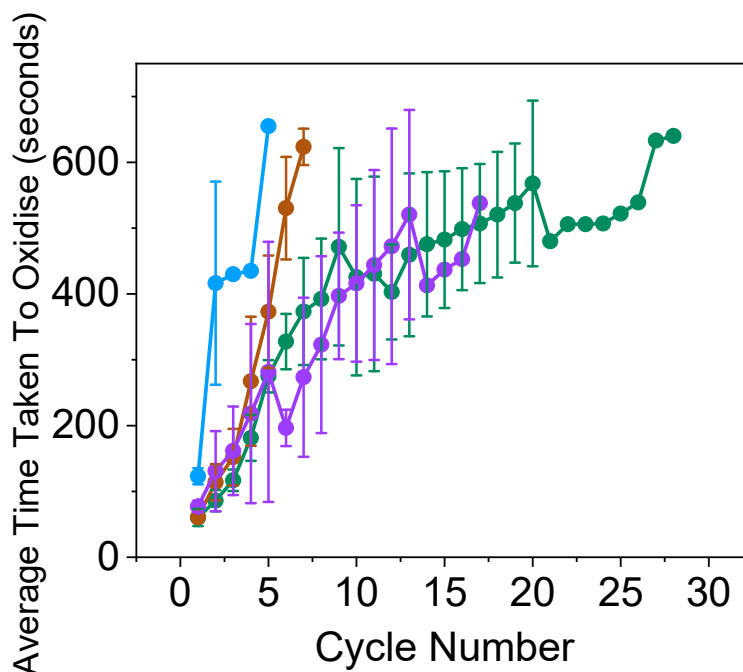


Figure 3.20. Plot showing how time to reach a state without colouration fluctuates with electrochemical cycling between a reduced and oxidised state. Measurements carried out using solutions of **NDI-I** (green), **NDI-V** (blue), **NDI-F** (purple) and **NDI-GF** (brown) at their respective ideal pH (pH 9 for **NDI-I** and **NDI-V** and pH 6 for **NDI-F** and **NDI-GF**). Measurements are taken as an average of triplicate measurements and error bars calculated from standard deviation.

NDI-I and **NDI-V** had comparable chromic properties and aggregation but perform very differently when cycled between neutral and reduced states. The darkened colour of **NDI-V** even after shaking in air could suggest a more significant aggregation change with cycling than **NDI-I**. This observation suggests that even subtle differences in the chemical structure influence long term efficiency. **NDI-I** and **NDI-F** do not form comparable structures at their ideal pH, nor do **NDI-GF** and **NDI-V**. This observation suggests that not one specific structure type is better or worse in terms of cyclability but perhaps that certain systems are more susceptible to changes in aggregation *via* the application of charge or generation of the radical anion more than others. Using a combination of absorbance and nuclear magnetic resonance (NMR) spectroscopy, CV, and SANS, we aim to gather as much information about the stability of these systems with electrochemical use.

3.2.8 Assessing aggregation after electrochemical use

We hypothesise that one of the factors affecting cyclability is the continued generation of the radical anionic species and an inefficiency in the oxidation process. A lack in oxidation efficiency could be affected by diffusion of the radical away from the working electrode surface, Figure 3.21. This issue

has been reported in short-alkyl chain viologens in aqueous electrolytes.^{38,64} After each cycle, the proportion of remaining radical species increases. This hypothesis was investigated further.

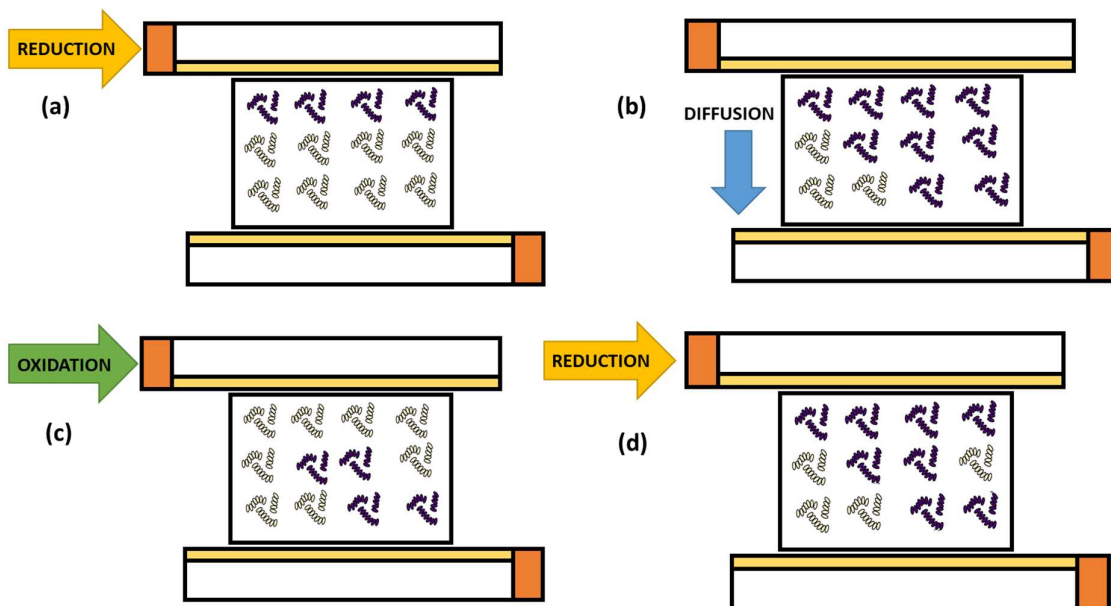


Figure 3.21. Cartoon showing show a build-up of radical anionic species could occur through a cycle of (a) reduction, (b) diffusion, (c) incomplete oxidation and (d) reduction.

3.2.8.1 Investigation with CV

Cyclic voltammograms were run at a scan rate of 0.5 V/s for 100 cycles to imitate cycling experiments whilst also measuring the position of redox peaks in the voltammograms. A faster scan rate was used to reproduce fast switching between states. Applying an oxidising potential for at least a minute is required to electrochemically oxidise the results of a few seconds of reduction (Chapter 2). Reduction occurs over a shorter time scale than oxidation, and so some reduced material will remain after a cyclic voltammogram scan. This method will replicate the hypothesis shown in Figure 3.21.

After 100 cyclic voltammograms, the current of the reduction peak reduced for all NDIs (Figure 3.22 and Figure A.3.35-A.3.38, Appendix.). The reduction in current for this process may be due to the increasing amount of radical anion present at the electrode surface with each scan and so the proportion of neutral species available to reduce decreases, and so the peak become less well defined. The largest change in reduction current is seen in **NDI-GF**, one of the most poorly performing NDIs in terms of cyclability, Figure 3.22 (d). A small peak around -0.5 V appears over time in **NDI-I**, **NDI-V**, and

NDI-F voltammograms, which we attribute to the presence of radical anionic species at the counter electrode surface, Figure 3.22(a-c). These data support our hypothesis of diffusion within the cell.

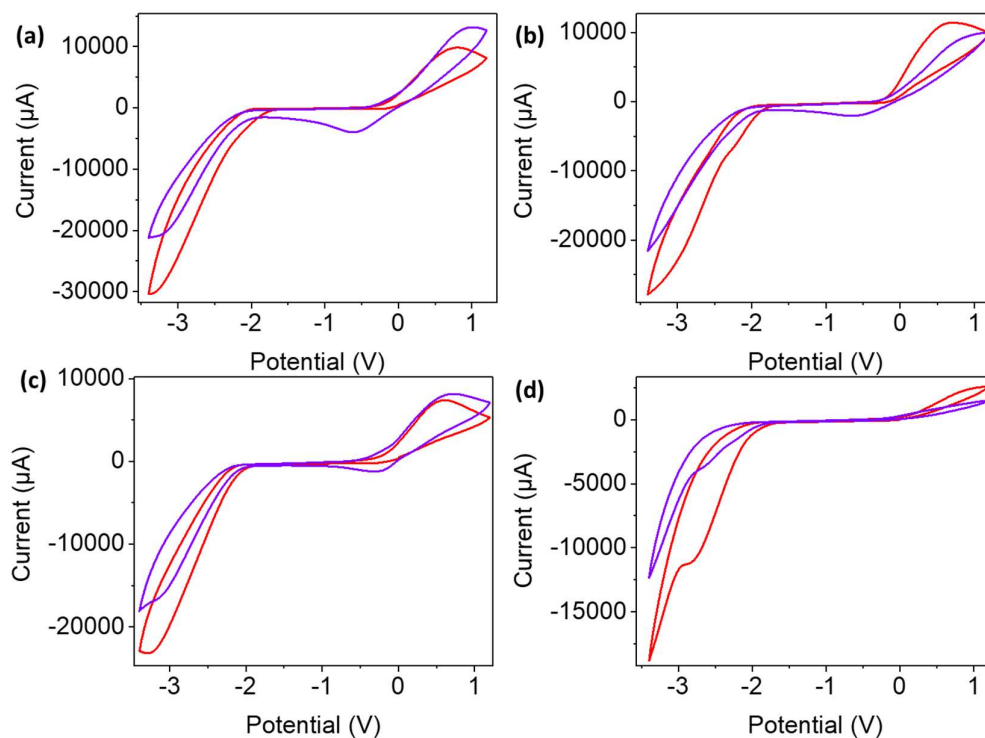


Figure 3.22. Cyclic voltammograms collected from neutral buffered 10 mg/mL solution of (a) **NDI-I**, (b) **NDI-V**, (c) **NDI-F** and (d) **NDI-GF** adjusted to their respective ideal pH (pH 9 for **NDI-I** and **NDI-V** and pH 6 for **NDI-F** and **NDI-GF**). Voltammograms measured using a 5 x 5 cm FTO window cell with a scan rate of 0.5 V/s. Measurements shown from scan number 1 (red) and 100 (purple). Full data sets are available in Figure A.3.35-A.3.38, Appendix.

The current of the oxidation peak of the voltammogram decreases for **NDI-V** and **NDI-GF** while increasing in **NDI-I** and remaining consistent in **NDI-F**, Figure 3.22. This observation suggests that resistivity is higher after 100 cycles in **NDI-V** and **NDI-GF** which makes oxidation less viable. The decrease in oxidation is most significant in **NDI-GF** (the peak itself becomes unseen over time, Figure 3.22(d)). The potentials of **NDI-V** shift the most over 100 cycles, Figure 3.22(b). All these factors could have implications for long term cyclability as **NDI-V** and **NDI-GF** had the poorest cyclability (and show the most significant changes to the oxidation potentials and currents). The reason for these observations cannot be purely due to set-up. We hypothesise that the differences in cyclability and the breakdown of electrochemical oxidation is likely (at least in part) due to a change in aggregation during cyclability experiments which causes a break down in electrochemical processes. Some NDIs appear to be more sensitive to this phenomenon than others.

3.2.8.2 Investigation with spectroscopy

To further assess our hypothesis about cycling changing aggregation, each NDI was cycled 50 times as described in a standard cycling test, 3.2.7. No distinct change is seen in the absorption spectra compared to pre-cycled measurements (Figure 3.23) and no EPR signal could be detected in solution. The sensitivity of this technique is high so we would expect to observe a signal if radical anionic species were present, therefore the discolouration is not due to radical anion remaining present. This observation suggests that the redox reaction is not irreversible, and that our systems can be used for long periods of time without changing the reversibility of the reduction.

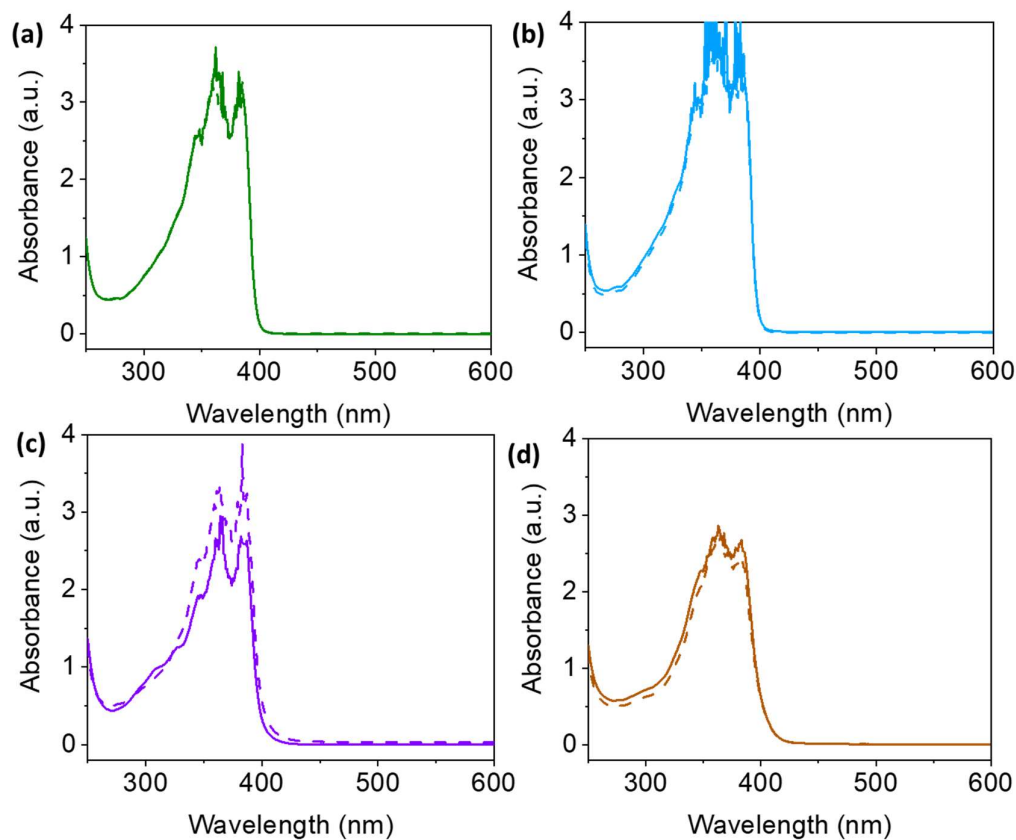


Figure 3.23. Absorbance spectra of the neutral state of 10 mg/mL buffered (a) **NDI-I**, (b) **NDI-V**, (c) **NDI-F** and (d) **NDI-GF**, adjusted to their respective ideal pH (pH 9 for **NDI-I** and **NDI-V** and pH 6 for **NDI-F** and **NDI-GF**), before (dashed lines) and after (solid lines) 50 electrochemical cycles. Spectra taken after a period of 24 hours of relaxation following cycling.

In the ^1H NMR spectra of pre- and post-cycled **NDI-F** and **NDI-GF** in D_2O , a second set of peaks are observed, which indicates a second set of environments arising from a structure with an inequivalent set of environments at the core of the NDI, Figure 3.24(a). The intensity of these peaks is pH dependent which suggests that this observation is a result of aggregation change in solvent rather than impurity.

The EPR spectra of **NDI-GF** also suggested an inequality of R groups in water, Figure 3.16. More explanation about the NMR spectra of **NDI-F** and **NDI-GF** is available in Appendix (A.3.2) and Figures A.3.39-A.3.57.

These additional peaks are most clear in the aromatic region where two doublets, as well as a singlet are observed in D₂O, Figure 3.24(b). These peaks are not seen in the same sample dissolved in d₆-DMSO, Chapter 2 Experimental. Dimerisation of NDIs is less likely to occur in less polar solvents like DMSO⁶⁵ and so this observation is likely a result of solvent dependent aggregation in these systems.

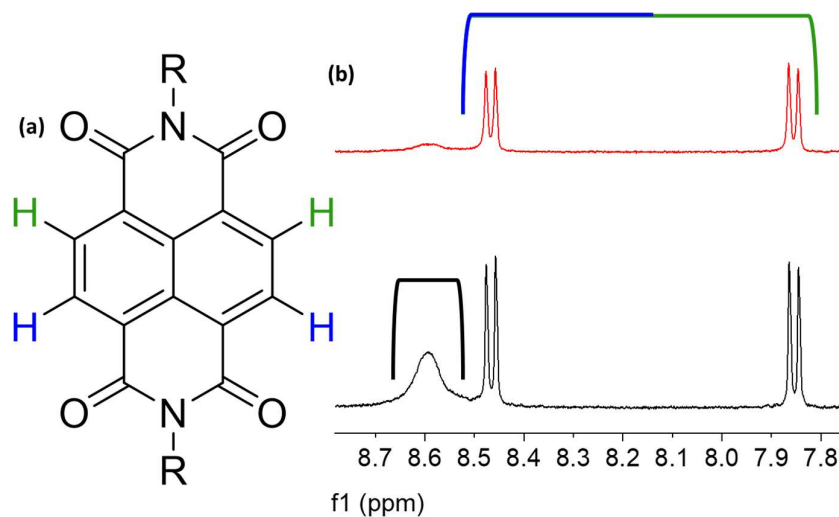


Figure 3.24. (a) Chemical structure of NDI-R showing two environments of the core protons (b) ¹H NMR spectra of the neutral state of 10 mg/mL buffered **NDI-GF** adjusted to pH 6 before (**black**) and after (**red**) excessive electrochemical cycling. Latter spectra taken after a period of 24 hours of relaxation following cycling. The peaks corresponding to a fully equivalent (**black**) and inequivalent (**green/blue**) core are marked in (b) as spanning lines.

The ratio of the two core environments alters after 50 cycles in the spectra of **NDI-GF**, Figure 3.24(b), which suggests a change in aggregation. As there is not a clear difference in the absorbance spectra (Figure 3.23(d)) it is assumed this change is subtle. There is no notable change in the NMR spectra of any other NDIs, Figures A.3.58-A.3.61, Appendix. No NMR spectra suggests any form of degradation.

3.2.8.3 Investigation with SANS

We next used SANS to probe the change in morphology or structure after cycling, in further detail. These data were collected after one and after 50 electrochemical cycles. Due to the restrictions of sample preparation and in-person access to facilities, these samples were electrochemically cycled and allowed to relax before measurement. Samples were then posted and stored for a few days before measurement.

Data sets after one and 50 cycles are comparable for **NDI-I** in terms of scattering intensity and model, implying little change to the size or shape of the aggregates in solution (Figure 3.25(a) and Figures A.3.62-A.3.63 and Table A.3.16, Appendix). The Kuhn length decreased upon cycling, Table 3.13. It was hypothesised that more rigid structures were associated with an ideal pD in **NDI-I** and **NDI-V** (3.2.4) so this factor could have some importance. The axis ratio of cylinders is unchanged by cycling and radii fluctuates slightly, Table 3.13.

Table 3.13. Tabulated parameters from SANS model fits of neutral, 10 mg/mL **NDI-I** after periods of cycling. Full data sets available in Figures A.3.62-A.3.63 and Table A.3.16, Appendix. Flexible cylinder and power law model used.

NDI-I Buffered pD	Kuhn Length (Å)	Error	Radius (Å)	Error
9				
Pre-cycled	118.42	6.78	5.23	0.0727
After 1 cycle	94.93	7.90	5.05	0.112
After 50 cycles	72.73	2.57	5.32	0.0706

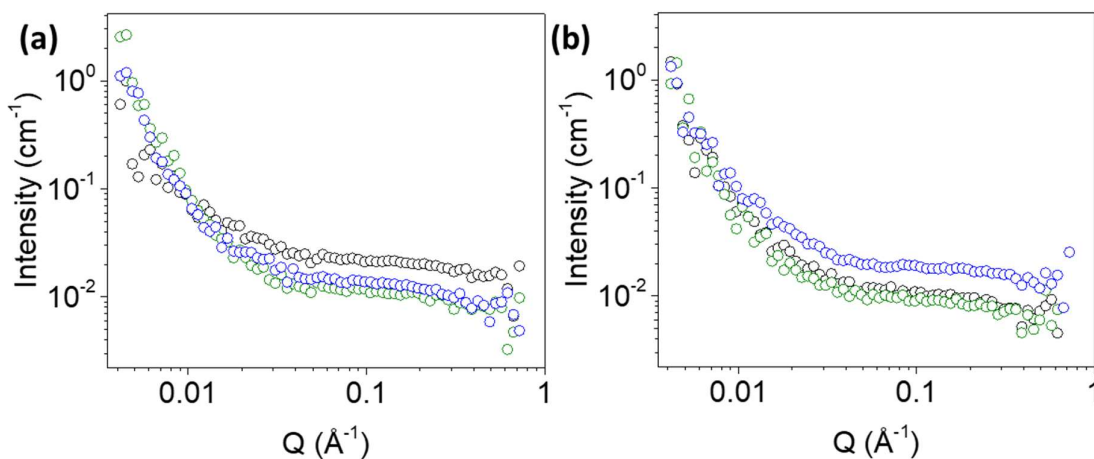


Figure 3.25. Small angle neutron scattering data for a neutral buffered 10 mg/mL solution of (a) **NDI-I** and (b) **NDI-V** at pD 9 (black), after relaxation following one electrochemical cycle (green) and after 50 electrochemical cycles (blue).

Similarly, to **NDI-I**, the SANS data for **NDI-V** is comparable after cycling, Figure 3.25(b) and Table 3.14. The trends in fit parameters are different, however. While radii fluctuate as with **NDI-I** and axis ratio remains constant, Kuhn length (a parameter that has been highlighted as important in this system) increases slightly after one cycle, then decreases significantly after 50. However, these changes within one cycle are not statistically significant as they are within the margin of error of the fit, Table 3.14.

Table 3.14. Tabulated parameters from SANS model fits of neutral, 10 mg/mL **NDI-V** after periods of cycling. Full data sets available in Figures A.3.64-A.3.65 and Table A.3.17, Appendix. Flexible cylinder and power law model used.

NDI-V pD 9	Buffered	Kuhn Length (Å)	Error	Radius (Å)	Error
	Pre-cycled	111.38	8.13	5.18	0.125
	After 1 cycle	115.62	11.5	5.15	0.127
	After 50 cycles	81.13	3.92	4.94	0.0715

The aggregated structures formed by **NDI-F** and **NDI-GF** are more significantly affected by electrochemical cycling (Figure 3.26) and Figures A.3.66-A.3.69 and Tables A.3.16-A.3.17, Appendix). The scattering intensity after one cycle is comparable to the uncycled state (Figure 3.26) but radii decrease (Table 3.15). After 50 cycles the SANS data collected will no longer fit to a hollow cylinder model and instead fits to a flexible cylinder model combined with a power law.

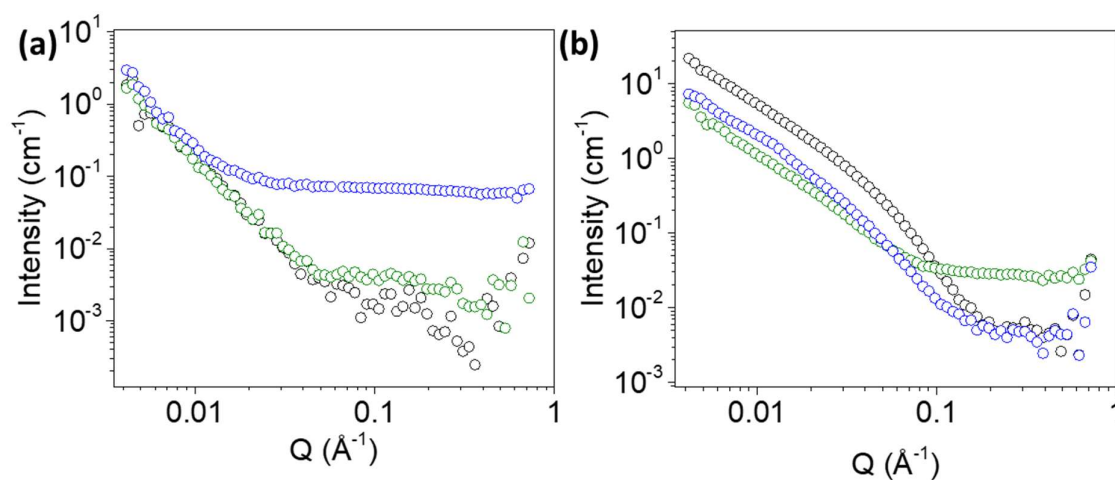


Figure 3.26. Small angle neutron scattering data for a neutral, 10 mg/mL buffered solution of (a) **NDI-F** and (b) **NDI-GF** at pD 6 (black), after relaxation following one electrochemical cycle (green) and after 50 electrochemical cycles (blue).

Table 3.15. Tabulated parameters from SANS model fits of neutral, 10 mg/mL **NDI-F** after periods of cycling. Full data sets available in Figures A.3.66-A.3.67 and Table A.3.18, Appendix. Hollow and flexible elliptical cylinder and power law models used.

NDI-F	Radius (Å)	Error	Thickness (Å)	Error	Kuhn Length (Å)	Error
Buffered pD 6						
Pre-cycled	52.33	2.17	11.76	0.624	N/A	N/A
After 1 cycle	41.80	2.18	10.55	0.553	N/A	N/A
After 50 cycles	6.40	0.0954	N/A	N/A	111.96	4.27

The difference in model suggests a large increase in flexibility of the cylindrical structures and a significant change in aggregation. The radius also decreases significantly, (Table 3.15). This change in radius is accompanied by a large increase in scattering intensity at high Q, Figure 3.26(a). Radii decreased so significantly, it is conceivable that a greater number of smaller structures are formed, leading to an increase in molecular-level interaction. As radii was highlighted as being maximised when colouration was darkest, such a significant loss in size would potentially result in poorer chromic behaviour.

After 50 cycles, **NDI-GF** scattering is more comparable to the uncycled state than after one cycle, Figure 3.26(b) which suggests either a breaking and recovery of the structures or ongoing changes with cycling. It could also indicate an error in the measurement. The intensity at low Q is lowest after one cycle, Figure 3.26(b).

As with all NDIs investigated, Kuhn length (or rigidity) decreases with cycling, Table 3.13-Table 3.16. A loss of rigidity of structure upon excessive electrochemical use may be linked to the eventual loss of oxidation efficiency. A reduction in Kuhn length is most notable for **NDI-GF**, Table 3.16. This increase in flexibility is facilitated by a glycine group which allows a greater degree of freedom around the N-CH₂-CO bond.

The change in Kuhn length is not comparable to differences in cyclability, however. The systems that have the biggest decrease in Kuhn length or biggest change in flexibility do not correspond to the worst cyclability performance. Therefore, we cannot directly compare rigidity and cyclability, but it could affect diffusion of the structures in solution. Similarly to **NDI-F**, **NDI-GF** loses radii size (significantly after only one cycle). The axis ratio also increases with cycling. Both factors are likely to affect redox processes as these NDIs preferred aggregates with larger radii and smaller axis ratio.

Table 3.16. Tabulated parameters from SANS model fits of neutral, 10 mg/mL **NDI-GF** after periods of cycling. Full data sets available in Figures A.3.68-A.3.69 and Table A.3.19, Appendix. Flexible elliptical cylinder and power law model used.

NDI-GF Buffered pD 6	Kuhn Length (Å)	Error	Radius (Å)	Error	Axis Ratio	Error
Pre-cycled	60.07	0.0232	19.51	0.00182	1.82	8.73E-04
After 1 cycle	45.64	0.358	7.17	0.0196	6.23	0.0169
After 50 cycles	15.26	0.0556	8.84	0.0132	4.72	6.99E-04

One possible explanation for the fluctuation of axis ratio of **NDI-GF** structures with cycling, is that the formation of the radical causes fibres to elongate (due to the charge of the radical anionic species, Figure 3.27(a)). Another explanation is that a reduced and neutral fibre are attracted together which gives the appearance of a more elliptical cylinder, Figure 3.27(b). The ability of **NDI-GF** to form large scale fibres (showing high scattering intensity at low Q, Figure 3.26(b)) may be the reason this NDI exhibits these trends. It is possible that the broad absorbance over 900 nm (Figure 3.14(a)) seen only in spectra of reduced **NDI-GF** is caused by charge transfer between fibres as in Figure 3.27(b).

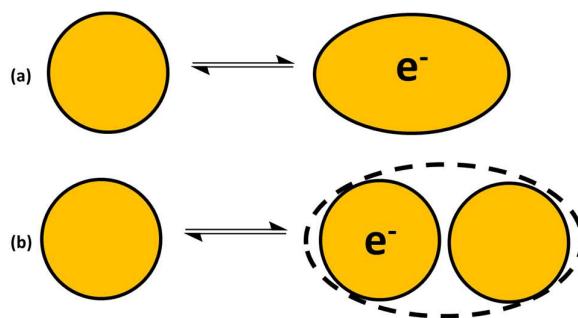


Figure 3.27. Cartoon representation of the hypothesised (a) elongation or (b) joining of fibres, leading to an increase in axis ratio of **NDI-GF** with cycling.

NDI-I and **NDI-F** have comparable cyclability but very different aggregated structures and different ideal pH. Therefore, we cannot directly link a particular structure to desirable performance. We also cannot link a change in structure during cycling to a loss in oxidation efficiency as **NDI-F**'s structure changed significantly, yet this NDI performed well in cyclability tests. These data suggest that the link between aggregation and performance is not straight forward and that many factors are at play. For example, diffusion rates within the set-up, which are affected by aggregation, packing and chemical structure.^{5,66-68} As time constraints only allowed measurement after one and 50 cycles, we are unable

to pinpoint when more significant changes in structure occur during cycling of **NDI-F** (did they occur after 10, 20 or 40 cycles?).

These data suggest to us that the formation of the radical anionic species does have an influence upon aggregation when repeatedly formed/oxidised in a short period of time. Each small change is likely to be incremental with each cycle and some NDIs appear more susceptible than others. From absorbance, EPR and NMR spectroscopy, we conclude that the NDI molecules themselves are not degrading with cycling and that the radical anionic species does not become irreversible. It is crucial to assess the formation of the radical anionic species *in situ*.

3.2.9 Using *in situ* SANS to assess aggregation

The changes in structure suggested by SANS data with cycling are not significant when compared to larger external changes such as pH (Chapter 2), suggesting electrochemical cycling causes subtle changes in aggregation. It is also a possibility that the process of removing solution from the FTO window cell and transferring to a cuvette, requiring the use of a pipette, may also impact aggregates, Figure 3.28. The application of shear or use of a pipette has been reported^{13,17,69} to influence structures in solution. Sample preparation TEM imaging involving agitation has also been noted to involve disentanglement of fibrous networks, resulting in “indirect information” rather than topological measurement.³⁸

It is also possible that, because samples were posted to the neutron facility in advance of measurement due to COVID restrictions, some aging and/or hydration of the D₂O occurred within the solutions in transit. The process of posting samples was not temperature controlled and although samples were packaged with plenty of protection, we cannot guarantee the systems were not disturbed by their journey as this delivery was performed by a third party. *In situ* real time measurements would be preferred. Unfortunately, due to time constraints, a full data set of **NDI-F** could not be collected and NDIs showing poor cyclability were given priority in measurement order.

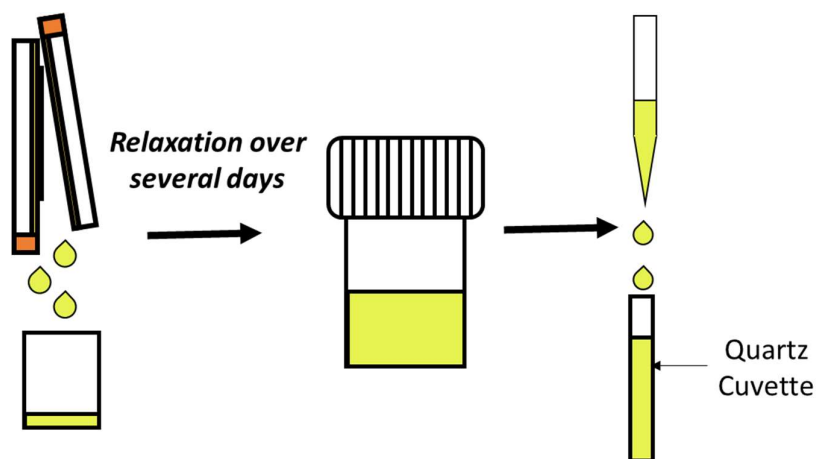


Figure 3.28. Diagram of the process of transferring solution from a FTO window cell to a cuvette for measurement with SANS.

NDI-GF showed the most significant change after one electrochemical cycle with a significant decrease in scattering intensity at low Q (Figure 3.25(d)). We identified this NDI as likely to be susceptible to agitation (which could break or destroy a network and increase the likelihood of any artefacts) due to the larger scale interactions suggested by intensity at low Q . If the process of reduction and oxidation combined with the physical agitation of sample preparation has an influence upon aggregation, the SANS measurements will be affected. We must consider sample preparation whilst looking at this data and assess whether any previous data contained artefacts. As **NDI-GF** is the most intensely scattering of all NDIs investigated, it is a good candidate to trial our new methodology of *in situ* SANS.

A spectro-electrochemical cell was used to electrochemically reduce and oxidise species in the beamline itself as SANS measurements were taken, Figure 3.29. To the best of our knowledge, this technique has not been reported in this context. Some custom-made equipment was required to modify an existing piece of equipment. Measurements were taken of the solution in its neutral, reduced and recovered neutral state. A self-contained cell allowed an advantageous and portable set-up which we could transport to the beamline with samples, Figure 3.29.

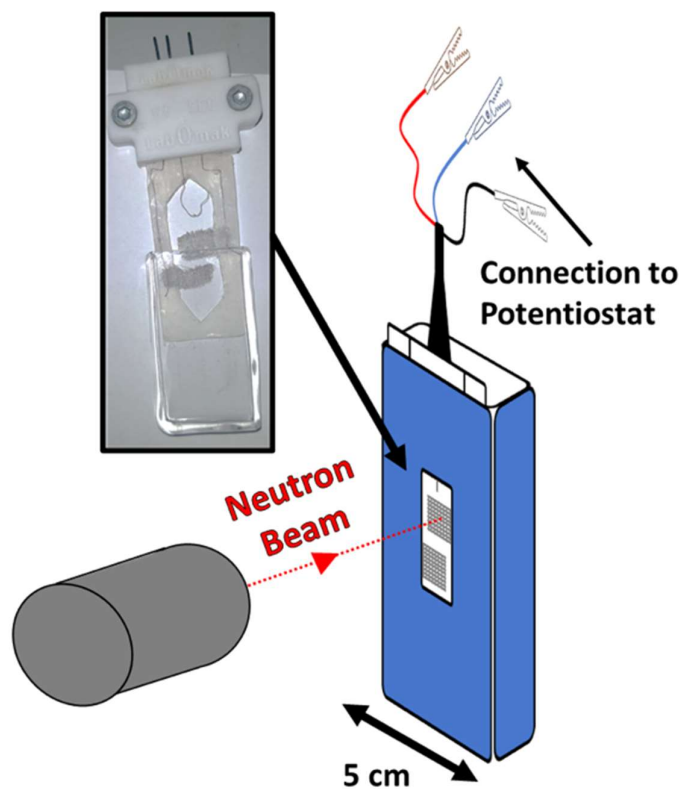


Figure 3.29. Diagram of the experimental set-up of spectro-electrochemical cell in the neutron beam.

The electrochemical reduction and oxidation occur at the working electrode of the cell (at which the neutron beam is aimed) and the cell can be controlled from outside the protective doors of the beamline, Figure 3.30. This methodology allows us to start and stop reduction and oxidation from outside of the beam.

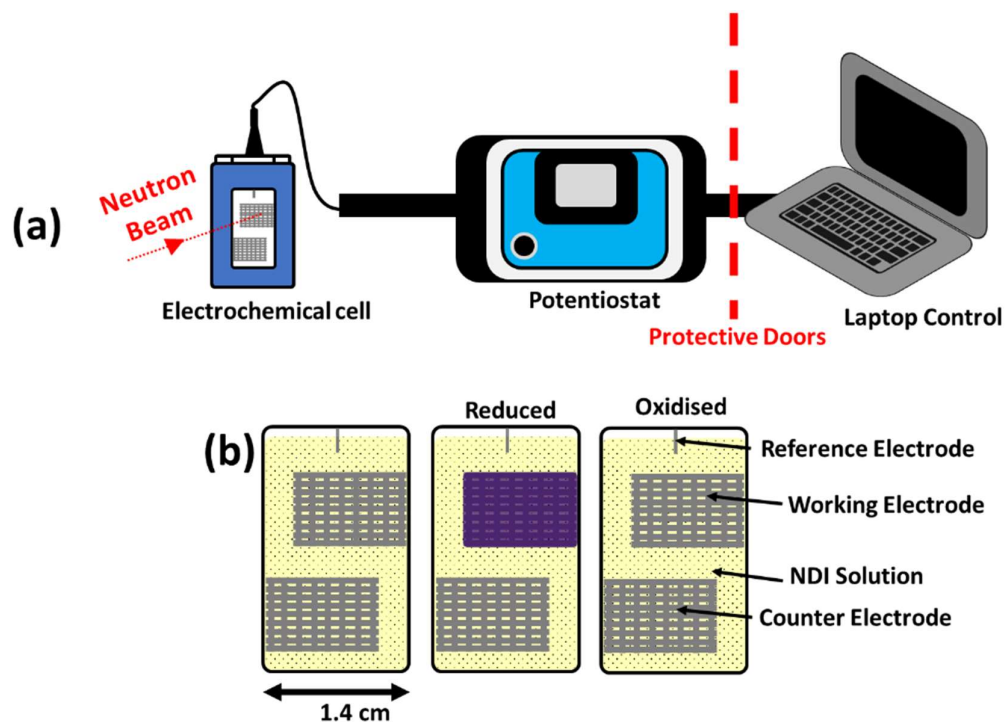


Figure 3.30. (a) Diagram of the experimental set-up control, (b) an expanded diagram of the electrochemical reduction and oxidation of NDI solution at the working electrode of the cell where the beam is positioned.

The redox potentials for this system within the used cell are tabulated in Table 3.17. A peak at approximately -0.47 V in the positive scan direction is attributed to some reduction at the counter electrode as it is present at the same potential in all NDIs investigated in this set-up, Figure A.3.70, Appendix.

Table 3.17. Redox potentials collected from cyclic voltammograms of neutral, 10 mg/mL **NDI-GF** collected within spectro-electrochemical cell set-up (referenced with Pt wire). The scan rate of the cyclic voltammograms was 0.2 V/s. Full data available in Figure A.3.70, Appendix.

	Reduction Potential(s) (V)	Oxidation Potential (V)
NDI-GF Buffered pH 6	-0.07, -0.61	0.75

To reduce the sample (for consistency across all NDIs) a potential of -0.7 V was applied whilst the measurement was being performed. To then oxidize the sample, a potential of $+0.7$ V was applied for 10-15 min until colour was removed and another measurement taken (Table 3.17-Table 3.19).

The initial scattering is comparable to the same solution in a standard quartz cuvette, Figure 3.31(a). There are some small discrepancies which is expected from the differences in the set-up. More discussion is available in the Appendix, A.3.3 and Figure A.3.71.

The change in scattering after one electrochemical cycle is significantly different depending on the procedure used, Figure 3.31. The scattering intensity is notably different across the whole Q range and the parameters of each fit are not comparable, Table 3.16 and Table 3.18. This data would suggest that the process of transferring the sample after electrochemical use or aging, or hydration of D_2O is the cause of at least some of the loss of intensity at low Q , rather than the electrochemical use itself. As this transfer was not an issue in the neutral state, we can also deduce that electrochemical use did have some subtle influence upon the aggregates, perhaps leaving them more susceptible to physical movement. However, we do not believe the changes in structure are wholly the result of this electrochemical use. Our *in situ* method not only allows measurement of the reduced state in real time, but has identified artefacts in previous measurements for **NDI-GF**.

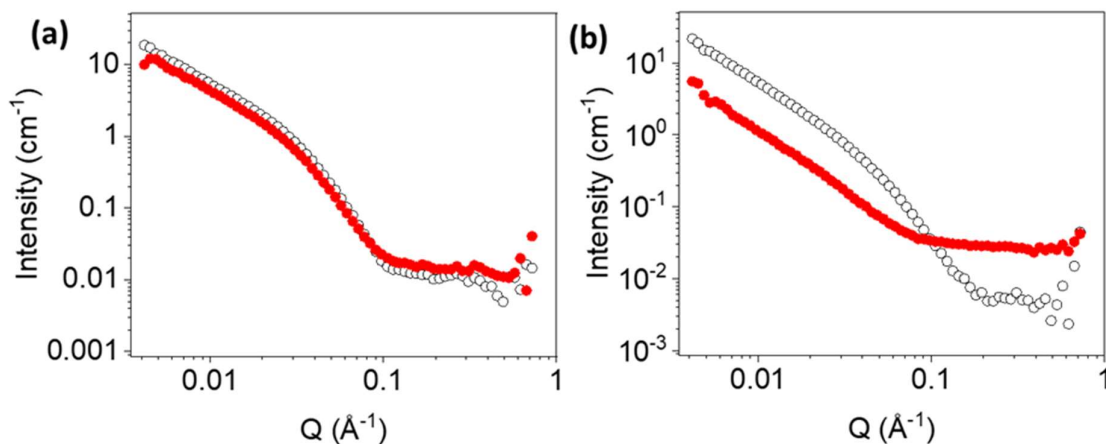


Figure 3.31. Small angle neutron scattering data for a 10 mg/mL buffered solution of **NDI-GF** at pH 6 in a neutral state before electrochemical reduction (open circles) and after one electrochemical reduction and oxidation (red filled circles). Measurements taken in (a) spectro-electrochemical cell and (b) in a standard quartz cuvette.

Table 3.18. Tabulated parameters from SANS model fits of 10 mg/mL **NDI-GF** taken from the electrochemical cell in various states of reduction and oxidation. Full data sets available in Figures A.3.72-A.3.74 and Table A.3.20, Appendix. Modelled with flexible elliptical cylinders.

NDI-GF Buffered pD 6	Kuhn Length (Å)	Error	Radius (Å)	Error	Axis Ratio	Error
Pre-cycled	40.95	0.113	24.13	0.0261	1.94	0.00188
Reduced	43.06	0.145	23.33	0.0288	2.18	0.00254
Oxidised	45.45	0.153	24.91	0.0303	2.04	0.00234

The measurement after one electrochemical cycle in the spectro-electrochemical cell is comparable to the initial neutral state, Figure 3.33. The process of both reduction and oxidation has minimal influence upon the fit parameters, Table 3.18. Kuhn length increases slightly upon reduction and again upon oxidation and radius fluctuates only by around 2 Å. Over the course of many cycles, the slight changes to parameters could continue to a more significant extent as is suggested by the data collected in standard cuvettes after 50 cycles. Time constraints did not allow us to perform 50 cycle measurements in this set-up. Changes are larger than the noted error of parameters within the fit and so are statistically significant, Table 3.18.

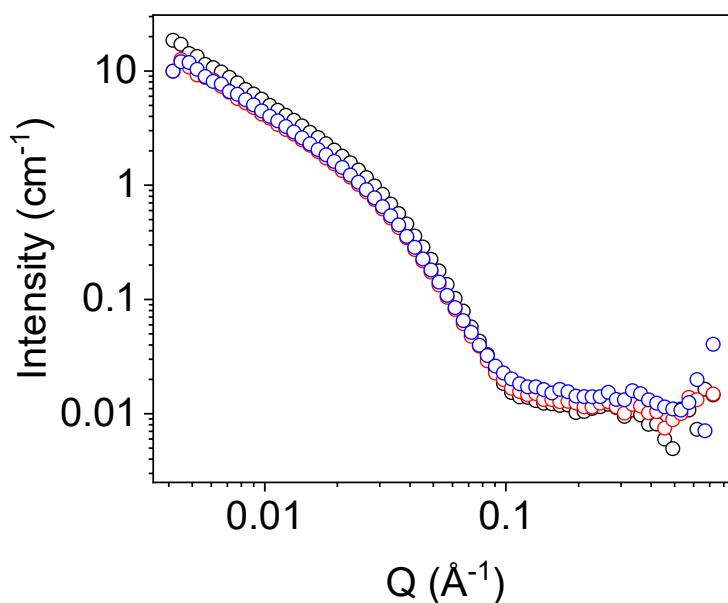


Figure 3.33. Small angle neutron scattering data for a 10 mg/mL buffered solution of **NDI-GF** at pD 6 (**black**), during reduction (**red**) and after electrochemical oxidation (**blue**) Data taken in spectro-electrochemical cell.

As previously observed (but to a far lesser extent), the axis ratio increases upon reduction, Table 3.18. Upon oxidation the ratio returns to almost its original value. This observation suggests that the radical anion causes fibres of **NDI-GF** to elongate or to join together which may lead to eventual changes in aggregation suggested by NMR (Figure 3.24) and consequent poor cyclability (Figure 3.20).

3.2.9.1 Using *in situ* SANS to assess the differences between **NDI-I** and **NDI-V**

As **NDI-I** and **NDI-V** have the same ideal pH, form similar structures and reduced states of comparable intensity but have different cyclabilities, further investigation was carried out using *in-situ* SANS. Both fits of **NDI-I** and **NDI-V** in the spectro-electrochemical cell are comparable to data collected in a cuvette, but are weakly scattering, Figure A.3.75-A.3.76, Appendix. The redox potentials for **NDI-I** and **NDI-V** are tabulated in Table 3.19. Measurements were performed identically to **NDI-GF**.

Table 3.19. Redox potentials collected from cyclic voltammograms of 10 mg/mL **NDI-I** and **NDI-V** collected within spectro-electrochemical cell set-up (referenced with Pt wire) in various states of reduction and oxidation. The scan rate of the cyclic voltammograms was 0.2 V/s. Full data available in Figure A.3.77, Appendix.

Buffered System pD 9	Reduction Potential(s) (V)	Oxidation Potential (V)
NDI-I	-0.18, -0.76	0.60
NDI-V	-0.18, -0.76	0.60

The scattering intensity after one electrochemical cycle is consistent between data collected in a cuvette and a spectro-electrochemical cell for both NDIs, Figures A.3.78-A.3.79, Appendix. Because **NDI-V** is so weakly scattering, some of the data at low Q was lost in the measurements taken within the electro-chemical cell. Therefore, these data were fit to a flexible cylinder model alone without the use of a power law. These NDIs do not form gels and are buffered at a higher pD than **NDI-GF**. At a higher pD, aggregates will be typically smaller due to higher solubility and less π stacking.^{70,71} We would hypothesise the agitation of transferring samples to cuvettes to be less impactful upon **NDI-I** and **NDI-V**, which appear to be the case.

There are minimal variances to measurements as samples are reduced and oxidised, Figure 3.34. All three NDIs measured with *in situ* SANS show a decrease in radius in their reduced state which does not change upon oxidation. However, this change is very minimal (around 1 Å) and so comes within a margin of error within the fit. Data collected in cuvettes for **NDI-I** and **NDI-V** after oxidation, showed no change in radius. This observation of reduced radii could support the hypothesis that fibres are

elongated by the charge of the radical anion and suggest that the radical anion can have some influence upon structures in solution.

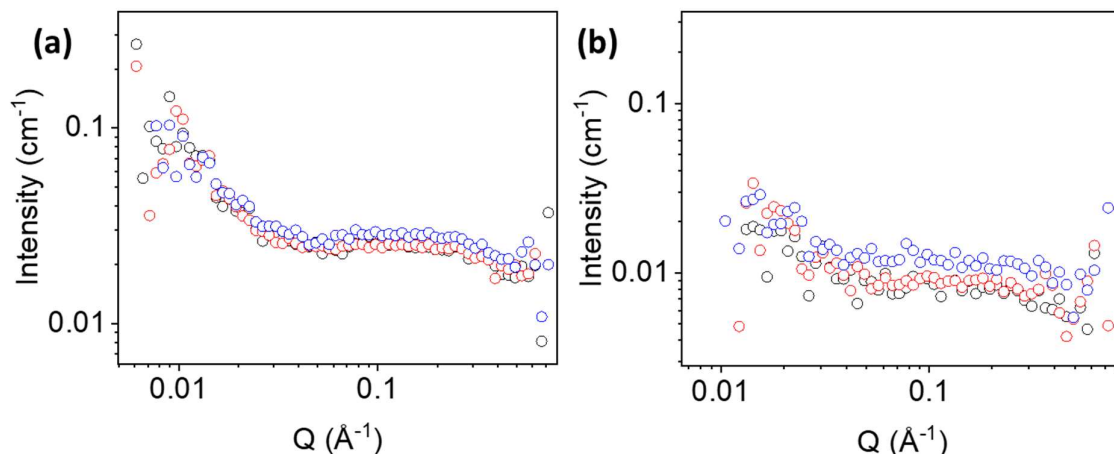


Figure 3.34. Small angle neutron scattering data for a buffered solution of (a) **NDI-I** and (b) **NDI-V** at pH 9 (black), during reduction (red) and after electrochemical oxidation (blue) Data taken in spectro-electrochemical cell.

When reduced, the Kuhn length of the fit to **NDI-I** and **NDI-V** decreases by approximately 5 and 11 Å respectively, Table 3.20. This parameter remains at this value after oxidation for **NDI-I** but increased to roughly the initial value for **NDI-V**. These trends are consistent with the cuvette data set which showed a decrease in Kuhn length for **NDI-I** and no significant change for **NDI-V** after one electrochemical cycle.

Table 3.20. Tabulated parameters from SANS model fits of 10 mg/mL **NDI-I** and **NDI-V** taken from the electrochemical cell in various states of reduction and oxidation. Full data sets available in Figures A.3.80-A.3.85 and Table A.3.21-A.3.22, Appendix. Modelled with flexible cylinder models.

Buffered System	Kuhn Length (Å)	Error	Radius (Å)	Error
pD 9				
NDI-I pre-cycled	84.56	0.145	6.12	0.313
NDI-I reduced	78.23	0.141	5.00	0.234
NDI-I oxidised	79.44	0.111	5.07	0.207
NDI-V pre-cycled	81.14	18.6	6.24	0.457
NDI-V reduced	70.01	12.2	5.09	0.266
NDI-V oxidised	80.47	11.6	5.10	0.229

Data from standard 2 mm quartz cuvettes, Figure 3.25(a)-(b), suggests that the structures after one and 50 cycles are comparable for **NDI-I** but not for **NDI-V**, suggesting that **NDI-V** shows a more significant change in structure after one cycle. Time constraints did not allow for measurement of 50 cycles within the spectro-electrochemical cell. **NDI-V** demonstrated a greater change in Kuhn length when in a reduced state than **NDI-I**, however, the changes are not statistically significant due to the larger error in these fits, Table 3.20. This error may be the result of the low scattering intensity of these data. It has already been hypothesised that more rigid structures are more favourable for electrochemical processes for **NDI-I** and **NDI-V** (3.2.4). If the reduced state of **NDI-V** has a lower Kuhn length than the reduced state of **NDI-I**, the efficiency of the electrochemical oxidation may be influenced by this difference in rigidity, which is likely to increase incrementally with cycling. It appears after an initial small change in aggregation, **NDI-I**'s structures are less susceptible to change over a larger number of cycles, resulting in better cyclability. The cumulative effect of this phenomenon may explain the difference in cyclability between these two similar systems.

The use of *in situ* SANS allowed insight into the reduced state of these systems in real time which is a great advantage. It is clear that for certain systems that have larger scale aggregates or networks, the process of performing electrochemical measurements in the beamline itself results in more accurate measurements than an *ex situ* set-up. Some of this error may have come from posting and aging samples. Our *in situ* methodology also allowed us insight into the electrochemically reduced state which has not been previously seen in the literature.

These data suggest that reduction does have a small impact upon the structures but that our systems are stable against degradation, and that some NDIs are more suitable than others for long term use. We anticipate diffusion is another issue within our set-up which may exacerbate the effect of the radical anion and affect the efficiency of electrochemical oxidation, Figure 3.21. Varying scan rate between 0.1 and 0.5 V/s suggests that the redox reactions are affected by diffusion. A small shifting of both reductive and oxidative peaks of around ± 0.1 V is observed as scan rate increases, (reduction potential shifting to more negative potential and oxidation potential shifting to a higher potential) Figure 3.35. This observation suggests that the reactions are diffusion controlled.⁷²

Diffusion could depend on the aggregation state and the ease of movement through the solution. Chemical structure, pH and aggregation all effect the chromic behaviour and long-term use of these NDI systems. The set-up used also has its own factors in the cyclability of the systems which we seek to improve in future work.

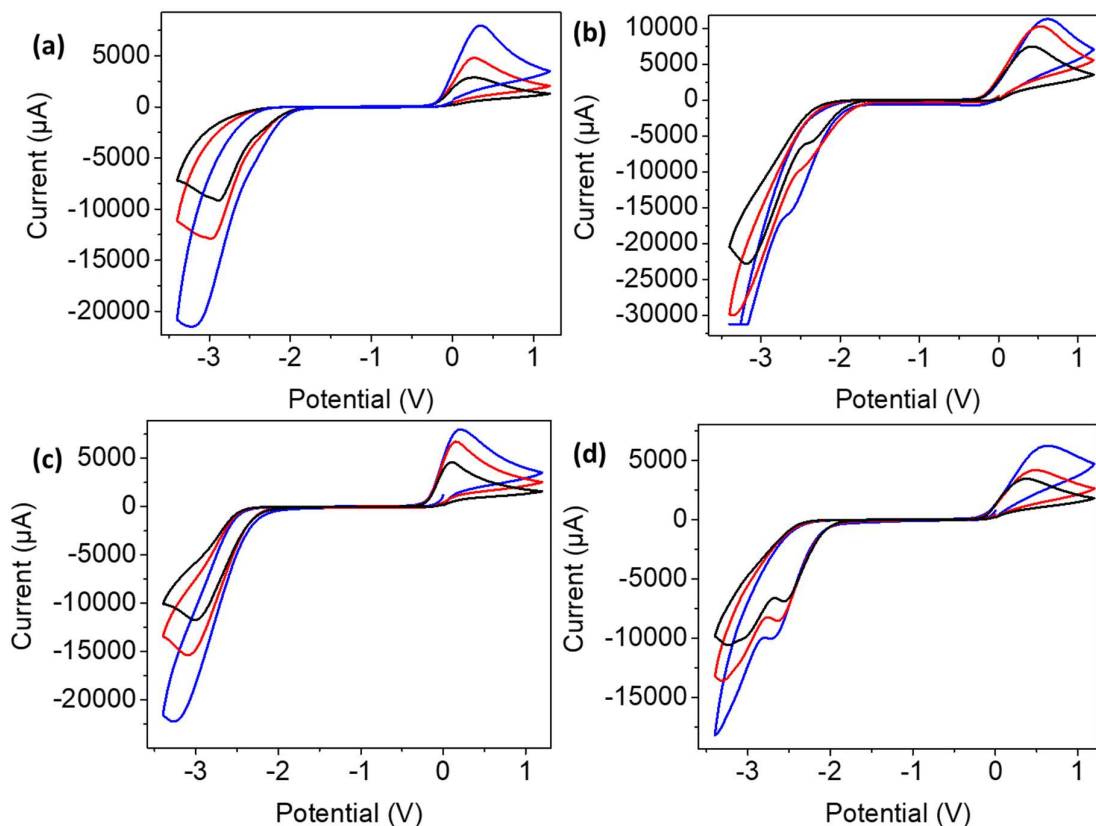


Figure 3.35. Cyclic voltammograms collected from 10 mg/mL solutions of buffered (a) **NDI-I**, (b) **NDI-V**, (c) **NDI-F** and (d) **NDI-GF** adjusted to their respective ideal pH (pH 9 for **NDI-I** and **NDI-V** and pH 6 for **NDI-F** and **NDI-GF**), using a scan rate of 0.1 (black), 0.2 (red) and 0.5 (blue) V/s. Voltammograms performed in 5 x 5 cm window cell (unreferenced).

3.3 Conclusions

Following an initial investigation into the effect of pH upon the absorbance spectra of neutral NDI species (as well as the intensity of their reduced state and oxidation rate), an ideal pH was selected. As absorbance spectroscopy does not allow great insight into the aggregates in solution and instead tells more about molecular packing, a more in-depth techniques was enlisted, SANS. The minimal affect of buffering solutions to an ideal pH was also investigated and found to improve conductivity and resulting radical concentration.

The aggregation of each system in its ideal and non-ideal state was assessed, the ideal state of **NDI-I**, **NDI-V**, **NDI-F** and **NDI-GF** were compared and cyclability and stability were investigated. The aggregation type of a flexible elliptical cylinder with a large axis ratio, suggesting poorly defined structures, was found to fit to data collected from all NDIs at pD 12 and **NDI-FF** at pD 7 and 12. This aggregation type is associated with poor electrochromic colouration upon reduction and so is

concluded to be unfavourable for production or stabilisation of the radical anion. The colouration of **NDI-FF** is poor because it is incapable of forming structure that stabilise the radical anionic species. We hypothesise the bulky, electron rich aromatic groups of this NDI are responsible.

Both chemical structure and pH affect aggregation as concluded by SANS measurements. NDIs with aromatic amino acid groups appear to produce more intense colour upon electrochemical reduction when their aggregates have larger radii and are perhaps less strained. When the number of aromatic amino acid groups increases, (as in **NDI-FF**) self-assembled structures do not form as readily and very little radical anionic species can be stabilised, even when radii is larger in these poorly defined structures. **NDI-I** and **NDI-V** have comparable aggregation and demonstrate the most desirable chromic properties when structures are more rigid. The EPR signal for radical anions produced by each NDI are comparable, suggesting that the type of radical produced is the same and therefore differences in colouration by eye are a result of aggregation alone.

Cyclability is also affected by chemical structure. The process of switching between states 50 times appears to impact aggregation, with **NDI-F** changing the most significantly over time. Cyclability has many contributing factors associated with it and so this issue is more complex. The aggregated state of the NDIs influences electrochemical behaviour, but physical factors of the set-up should also be considered. Diffusion issues may be exacerbating the influence of the radical anion upon structure.

We conclude that, for the data of **NDI-GF**, some of the changes in structure observed after cycling may be due to the transfer of solution into a cuvette or aging and more accurate data can be achieved by the use of our *in situ* SANS set-up. Data for **NDI-I** and **NDI-V** were comparable in a spectro-electrochemical cell and in quartz cuvettes. The larger scale aggregates of **NDI-GF** suggested by intensity at low Q when buffered at pD 6 make this system more susceptible to agitation during transfer. Both *in situ* and *ex situ* measurement suggested that the radical anionic species caused elongation or combination of fibres (characterised by an increase in axis ratio) of **NDI-GF**. After several cycles we hypothesise this phenomenon may result in an unfavourable change in aggregation which is why **NDI-GF** cannot be cycled for more than around five cycles. This trend in axis ratio is only observed in **NDI-GF**, but the radii decrease in the radical form for **NDI-I** and **NDI-V**, which could suggest elongation is less significant in these systems or harder to see due to weak scattering.

NDI-I and **NDI-F** have the best cyclability out of the four NDIs tested. Their oxidation rates are comparable to each other, but **NDI-I** has the darkest colouration of these two NDIs. These two are the most promising systems moving forward but do not have comparable aggregation or the same ideal pH. We therefore cannot link one absolute aggregation to desirable performance in a Smart

Window application at this stage. Further information could be gleaned by analysing a much larger library of NDIs which is outside of the scope of this investigation.

In terms of the list of properties set out in Chapter Two, cyclability is a criteria that should be improved further at this stage, with around 100-200 cycles being an aim to be comparable to alternative systems in the literature.^{5,24} The ultimate aim of this investigation is however to draw insight into the impact of different factors upon the aggregation of these NDI systems and so perfecting a set-up for commercial application is not necessary. Our hypothesis that aggregation and chromic properties are linked is further proven by these data and the impact of both chemical structure and pH upon aggregation appear to be slightly different for each system, allowing a high level of tunability.

We hypothesise that the addition of a more viscous component could localise the radical anion to the electrode surface by slowing diffusion rates. This could have a positive outcome of making oxidation more efficient which would result in either faster oxidation times, reduction in the amount of radical anion that may be left behind after each cycle (and subsequent aggregation changes) or both these results. It is also possible that such a multicomponent system could be less susceptible to changes in structure upon cycling if the secondary component formed more stable structures or strengthened the aggregates of the NDIs. We theorise that cyclability would be improved with the addition of a viscous component for these reasons and seek to investigate such systems in Chapter 4.

3.4 Experimental

3.4.1 Synthetic procedures

All synthetic procedures are described in Chapter 2.

3.4.2 Experimental protocols and equipment

3.4.2.1 Preparation of solutions

Solutions were prepared at concentrations 10 mg/mL of NDI. Unless otherwise stated, solutions were buffered to pH 9 (**NDI-I** and **NDI-V**) or pH 6 (**NDI-F** and **NDI-GF**) using 0.1 M buffers. The pH of solutions was adjusted using 0.1 M HCl and NaOH and pH of buffers adjusted with 1 M HCl and NaOH. The sodium carbonate-carbonate buffer was formulated by dissolving 3.822 g sodium bicarbonate and 0.477 g sodium carbonate in 500 mL water. The sodium acetate buffer was prepared by dissolving 1.64 g of sodium acetate in 200 mL water.

3.4.2.2 pH measurements

pH was measured using a FC200 pH probe as previously described in Chapter 2.

3.4.2.3 Absorption spectroscopy

Absorption spectra were collected using a Cary 60 UV-Visible spectrophotometer as in Chapter 2.

3.4.2.3.1 Dilution series

Solutions were prepared and dilution series collected as previously described. The absorbance at λ_{\max} was plotted against concentration for each NDI to calculate the molar extinction coefficient, Table 3.1.

3.4.2.4 pH logs

Buffered solutions were prepared, and their pH recorded for 50-70 hours using a FC200 pH probe. pH was logged using a custom-built pH logger. The vial containing solution was sealed with parafilm to prevent evaporation. The temperature was not maintained by a water bath to best accommodate for the temperature fluctuations that may occur during cycling tests and commercial use. A measurement was taken every 15 seconds.

3.4.2.5 Cyclic voltammetry (CV)

Voltammetry was measured as previously described in 1 x 1 and 5 x 5 cm FTO glass windows, Chapter 2. CV was performed in the spectro-electrochemical cell described in 3.4.5 before reduction and oxidation in the beamline. The scan rate is noted in the figure or table caption of the data.

3.4.2.6 Viscosity measurements

All viscosity measurements were performed using an Anton Paar Physica 301 rheometer using a cone and plate geometry (75 mm diameter, 1.0° angle, 50 μm) and a flat plate measuring system for all measurements. A gap of 0.05 mm was used. Measurements were recorded in triplicate. Buffered NDI solution, 3 mL, was deposited onto the plate and trimmed. All experiments were performed at 25 °C.

3.4.2.7 Small angle neutron scattering (SANS)

Solutions were prepared as previously described (3.4.2.1) using NaOD, NaCl and D₂O in the proportions consistent with prior aqueous samples. pD was adjusted using 0.1M NaOD and DCl.

The measurements were performed using the SANS2D instrument (STFC ISIS Pulsed Neutron Source, Oxfordshire, UK) by Dr Leide Cavalcanti. A multiple-slot sample changer with controlled temperature of 25 °C was used. The beamline set-up was 4 m sample-to-detector distance, beam size of 8 mm and a typical Q-range [$Q = 4\pi\sin(\theta/2)/\lambda$, where Q is the scattering angle] from 0.004 \AA^{-1} to 0.7 \AA^{-1} set by time-of-flight mode with incident wavelengths (λ) from 1.75 \AA to 16.5 \AA . Samples were placed in 2 mm quartz cuvettes and measured for ~60 minutes. The scattering data were normalised for the sample transmission and background corrected D₂O and data reduction was performed using Mantid framework⁷³ installed inside the ISIS virtual machines, IDAaaS. When buffered solutions were measured, the salts required were dissolved in D₂O and used to make sample solutions and as a background for these measurements. Scattering data were then fitted in the SasView software

(version 4.2.2).⁷⁴ The experiment number was 2010459. DOI: 10.5286/ISIS.E.RB2010459 can be accessed at <https://doi.org/10.5286/ISIS.E.RB2010459>.⁷⁵

The scattering length density (SLD) of each material was calculated using the national institute of standards and technology (NIST) neutron activation and scattering calculator⁷⁶ to be $6.39 \times 10^{-6} / \text{\AA}^2$. The SLDs of **NDI-I**, **NDI-V**, **NDI-F**, **NDI-GF** and **NDI-FF** were calculated to be 2.626, 2.85, 3.246, 3.174 and $3.031 \times 10^{-6} / \text{\AA}^2$ respectively. All data fitted best to a cylindrical model combined with a power law. The specific cylindrical model is described in the figure captions and tabulated parameters found in Appendix. The best fit was decided to be that which fit well to the data and had the lowest Chi^2 value.

3.4.2.8 FTO windows

FTO glass ($50 \times 50 \times 2.2$ mm, TEC 7, surface resistivity $\sim 7 \Omega/\text{sq}$, from Sigma Aldrich) was cleaned with ethanol by submerging in shallow trays for 30 minutes prior to assembly and gloves were used throughout to prevent fingerprints on the glass. FTO windows were prepared by pipetting solutions of (1-2 mL) onto a piece of glass containing a (0.1 mm) o-ring (30 mm diameter), then securing a second top piece by clamping with bulldog clips. Figure 3.36 shows a diagram of this set-up. Pieces of copper tape were added to the edges of the cell to ensure good contact between the cell and the crocodile clips from the PalmSens4 potentiostat.

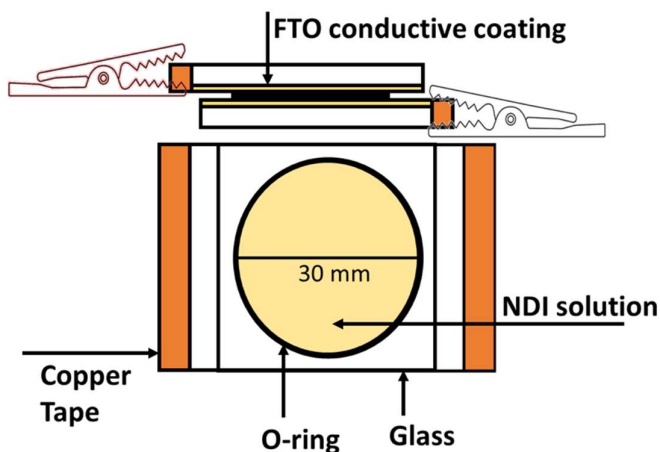


Figure 3.36. Schematic diagram of the FTO window set-up described above

3.4.2.9 Spectro-electrochemistry

Spectra were collected as previously described in Chapter 2 with a 1 x 1 cm sized window cell.

3.4.2.9.1 Transmittance

Solutions were prepared as previously described at 10 mg/mL using buffers and adjusting NDIs to their ideal pH. Solutions were deposited (< 0.2 mL) and secured in FTO window cells (1 x 1 cm) and a

potential of -2.5 V applied for 10 seconds. Transmittance was taken at λ_{\max} of 450 nm for **NDI-GF** and 490 nm for **NDI-I**, **NDI-V**, **NDI-F** and **NDI-FF**. The absorbance intensity of **NDI-I** and **NDI-V** after 10 seconds of application of -2.5 V was around the limits of the detector, Figure 3.14, To ensure this was not causing any errors in the transmittance data, another measurement was taken after 2 seconds, Table 3.10.

Colouration efficiency (CE) was calculated using Equation 3.1.⁷⁷

$$CE = \frac{\log\left(\frac{\text{Transmittance}_{\text{neutral state}}}{\text{Transmittance}_{\text{coloured state}}}\right) \lambda}{Q_d} \quad \text{Equation 3.1}$$

Where $\lambda = \lambda_{\max}$, Q_d = charge density over a 1 x 1 cm electrode surface area.

3.4.2.10 Electron paramagnetic resonance (EPR) spectroscopy

All EPR data were recorded at X-band frequency (9.67 GHz) on a Bruker ELEXSYS E500 spectrometer equipped with an ER 4102ST-O optical transmission resonator. All measurements were collected using 10 mg/mL buffered aqueous solutions prepared as described in 3.4.2.1. Solutions were transferred into soda glass capillary tubes with a 2 mm diameter. Capillary tubes were sealed at one end and samples filled 20 mm of the tube. Electrochemically reduced samples were reduced by application of -2.5 V in an unreferenceed SEC-C Thin Layer Quartz Glass Spectro-electrochemical Cell Kit (BASi) of 1 mm pathlength. The cell has a platinum gauze working and platinum counter electrode. A Palmsens4 potentiostat (Alvatek Ltd.) was used to control the voltage of the cell. Samples were reduced for 10 minutes then quickly transferred to a soda glass capillary tube using a degassed needle and syringe then measured immediately. Due to the weak intensity of the radical anionic species of **NDI-FF**, electrochemical reduction had to be performed by applying -2.5 V for 25 minutes. EPR measurements were performed by Dr Stephen Sproules.

3.4.2.11 Cycling tests

One cycle is defined as application of -2.7 V for 10 seconds to a 5 x 5 cm FTO window cell (containing 1 mL NDI solution at 10 mg/mL as electrolyte) followed by application of either the fixed oxidation potential of 0.5 V or a sweeping oxidation script for 10 minutes.

A sweeping script is defined as application of potential between 0.1 and 0.95 V increasing by 0.05 V every 5 seconds. This sweep is repeated for 10 minutes and was implemented to compensate for any shifting in oxidation potential over the course of the cycling experiment. A full explanation is available in A.3.1, Figures A.3.22-A.3.29 Appendix.

These cycles were repeated for 4-6 hours using an electrochemical scripting procedure in PS Trace (Version 5). Experiments were carried out in a darkened room using a torch covered with a UV light

filter to observe the cell. A stopwatch and time-lapse camera were used to record each test to observe the colouration of the solution within the cell, Figure 3.37. A PalmsSens4 potentiostat (Alvatek Ltd.) was used to control the voltage of the cell and methods were written using PS Trace (Version 5) software.



Figure 3.37. Photograph showing the set-up in which cycling test are run.

3.4.2.11.1 Tracking redox potential

Cyclic voltammograms were measured as described in Chapter 2, at a 0.2 V/s scan rate after every reduction or oxidation potential had been applied over the course of 50 ‘cycles’. An additional 5-minute rest period was added after the oxidation period to allow any reduced material remaining from the performance of the cyclic voltammogram to relax.

3.4.2.11.2 Temperature controlled cycling

Temperature controlled experiments were carried out in a crystallisation room with air conditioning allowing temperature to be maintained at 18 °C. Experiments were carried out with permission in Prof. Lee Cronin’s temperature controlled lab. Cycling tests were performed identically to those described in 3.4.2.12, using a reduction potential of -2.7 V for 10 seconds and a sweeping oxidation method. A 5 x 5 cm FTO window cell (with 1 mL buffered NDI solution at 10 mg/mL as electrolyte) was used. Potential was applied using a PalmsSens4 potentiostat (Alvatek Ltd.) controlled by PS Trace (Version 5). Experiments were carried out in darkness using a torch covered with a UV light filter, a

stopwatch and time-lapse camera to observe the cell. Temperature controlled experiments were undertaken to investigate the possibility of temperature fluctuation effecting cyclability and are discussed in A.3.E.1, Figures A.3.86-A.3.87, Appendix. These results suggests that small temperature fluctuation does not have significant impact and that these devices are suitable for use in a commercial environment (i.e. a room with people coming and going).

3.4.2.12 High temperature NMR Spectroscopy

Measurements were carried out on a Bruker 500 MHz spectrometer upon solutions at 5 mg/mL without buffer or background electrolyte, increasing the temperature inside the spectrometer to 50 and then 70 °C as required over the course of approximately 10 minutes.

3.4.2.13 Diffusion-ordered spectroscopy (DOSY)

Measurements were taken using a Bruker 400 MHz spectrometer. Pre-programmed parameters for DOSY experiment as provided by Bruker software ICON NMR were used.⁷⁸

3.4.2.14 SANS after cycling and electrochemistry in the beamline

Solutions were prepared as previously described using deuterated solvent and base. All solutions were prepared with deuterated buffers. pD was adjusted using 0.1M NaOD and DCl to their ideal pD. Solutions that were electrochemically used were transferred to and from FTO window cells to carry out electrochemical reduction and oxidation as described in 3.4.2.12. Solutions were then transferred to a quartz cuvette and measured approximately one week later. Solutions were prepared before arrival on site in advance due to the restrictions in place regarding COVID-19 and postal samples, Figure 3.38.

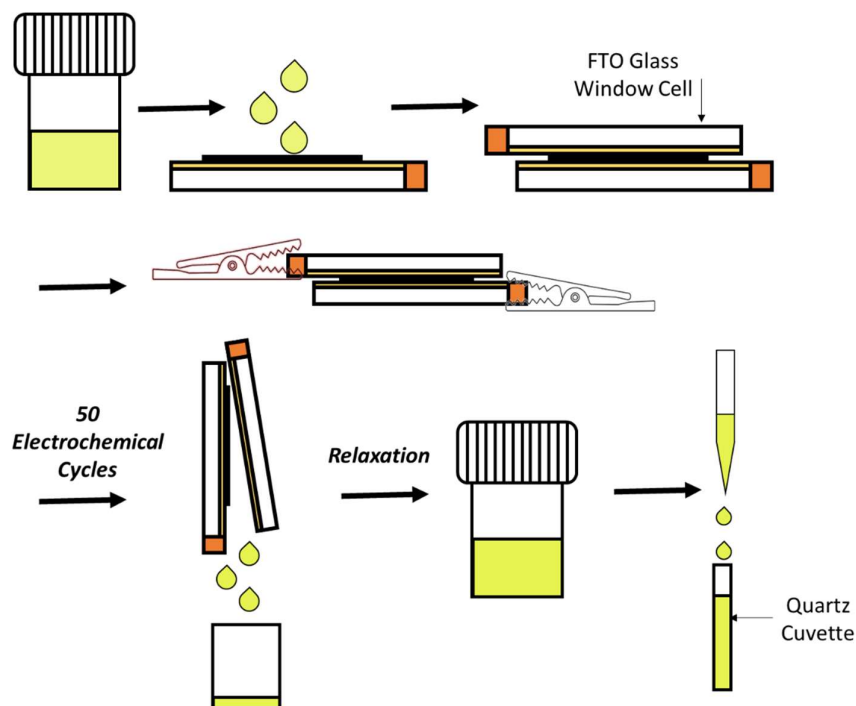


Figure 3.38. Schematic of how *ex situ* electrochemically used samples were transferred into cuvettes.

3.4.2.14.1 Electrochemistry in the beamline

Electrochemistry in the beamline was performed by myself on a separate visit to ISIS using the same beamline as used above. The position of the beam was set manually with the aid of a custom made plater (Figure 3.39) to hold the spectroelectrochemical cell. The cell was connected to a potentiostat *via* wires that were laid underneath the protective door to the beamline, Figure 3.40.

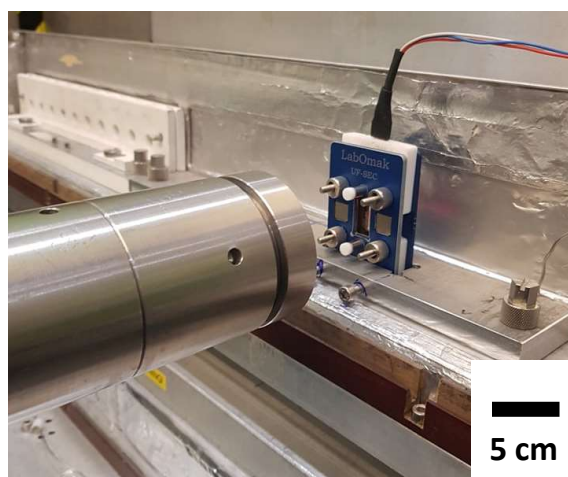


Figure 3.39. Image of manually setting the position of the beam on the rack at ISIS beamline.



Figure 3.40. Connection to PalmSense Potentiostat to cell in the beamline (covered by protective foil). Potentiostat is highlighted by red arrow.

A LabOmak UF-spectro-electrochemical cell was used, Figure 3.41. The cell has a platinum working and counter electrode. A Palmsens4 potentiostat (Alvatek Ltd.) was used to control the voltage of the cell. To reduce the sample a potential of -0.7 V was applied whilst the measurement was being performed. To then oxidize the sample, a potential of $+0.7\text{ V}$ was applied for 10-15 min and another measurement taken. Due to the small amount of Pt gauze in the cell, a radiation detector was used to determine whether it was safe to remove the cell after measurement. A quartz cuvette was custom made for the cell to be able perform SANS experiments.

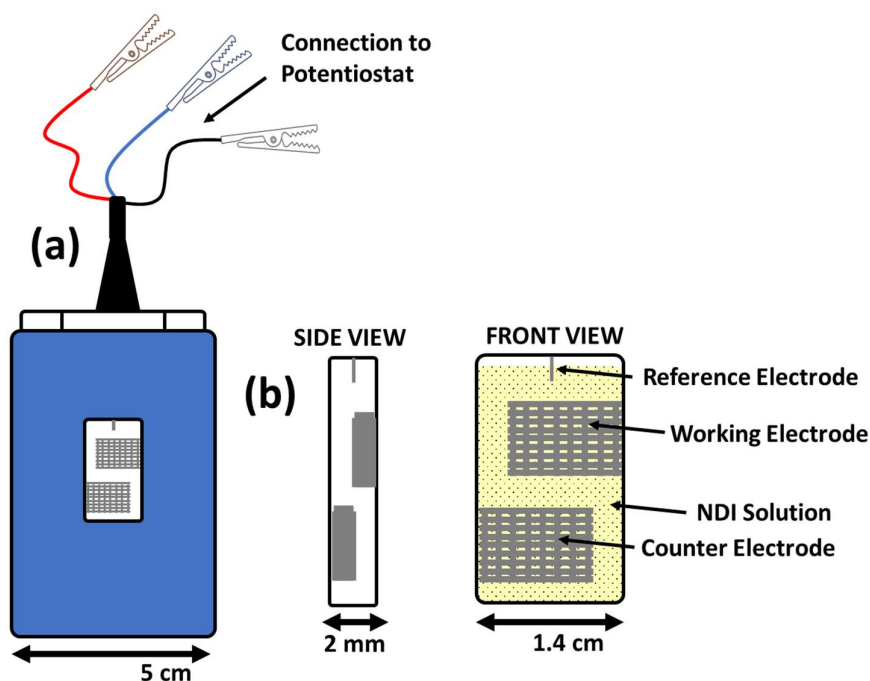


Figure 3.41. Schematic of spectro-electrochemical cell used in SANS experiments. Reference electrode is Pt wire.

3.5 References

- 1 E. R. Draper, B. J. Greeves, M. Barrow, R. Schweins, M. A. Zwijnenburg and D. J. Adams, *Chem*, 2017, **2**, 716–731.
- 2 E. R. Draper, L. J. Archibald, M. C. Nolan, R. Schweins, M. A. Zwijnenburg, S. Sproules and D. J. Adams, *Chem. Eur. J.*, 2018, **24**, 4006–4010.
- 3 C. L. Smith, L. L. E. Mears, B. J. Greeves, E. R. Draper, J. Douth, D. J. Adams and A. J. Cowan, *Phys. Chem. Chem. Phys.*, 2019, **21**, 26466–26476.
- 4 D. McDowall, B. J. Greeves, R. Clowes, K. McAulay, A. M. Fuentes-Caparrós, L. Thomson, N. Khunti, N. Cowieson, M. C. Nolan, M. Wallace, A. I. Cooper, E. R. Draper, A. J. Cowan and D. J. Adams, *Adv. Energy Mater.*, 2020, **10**, 1–10.
- 5 L. Gonzalez, C. Liu, B. Dietrich, H. Su, S. Sproules, H. Cui, D. Honecker, D. J. Adams and E. R. Draper, *Comm. Chem.*, 2018, **1** (77), 1–8.
- 6 V. Adams, J. Cameron, M. Wallace and E. R. Draper, *Chem. Eur. J.*, 2020, **26**, 9879–9882.
- 7 E. R. Draper, J. J. Walsh, T. O. McDonald, M. A. Zwijnenburg, P. J. Cameron, A. J. Cowan and D. J. Adams, *J. Mater. Chem. C*, 2014, **2**, 5570–5575.
- 8 M. C. Nolan, J. J. Walsh, L. L. E. Mears, E. R. Draper, M. Wallace, M. Barrow, B. Dietrich, S. M. King, A. J. Cowan and D. J. Adams, *J. Mater. Chem. A*, 2017, **5**, 7555–7563.
- 9 E. R. Draper and D. J. Adams, *Chem. Soc. Rev.*, 2018, **47**, 3395–3405.
- 10 S. Rogers, J. Kohlbrecher and M. P. Lettinga, *Soft Matter*, 2012, **8**, 7831–7839.

- 11 E. R. Draper, H. Su, C. Brasnett, R. J. Poole, S. Rogers, H. Cui, A. Seddon and D. J. Adams, *Angew. Chem. Int. Ed.*, 2017, **56**, 10467–10470.
- 12 J. J. Walsh, J. R. Lee, E. R. Draper, S. M. King, F. Jä, M. A. Zwijnenburg, D. J. Adams and A. J. Cowan, *J. Phys. Chem. C*, 2016, **120**, 18479–18486.
- 13 E. R. Draper, O. O. Mykhaylyk and D. J. Adams, *Chem. Commun.*, 2016, **52**, 6934–6937.
- 14 L. L. E Mears, E. R. Draper, A. M. Castilla, H. Su, B. Dietrich, M. C. Nolan, G. N. Smith, J. Douth, S. Rogers, R. Akhtar, H. Cui and D. J. Adams, *Biomacromolecules*, 2017, **18**, 3531–3540.
- 15 S. L. Gras and A. M. Squires, *Methods Mol. Biol.*, 2011, **752**, 147–163.
- 16 P. Terech, G. Clavier, H. Bouas-Laurent, J. P. Desvergne, B. Demé and J. L. Pozzo, *J. Colloid Interface Sci.*, 2006, **302**, 633–642.
- 17 J. K. Wychowaniec, A. M. Smith, C. Ligorio, O. O. Mykhaylyk, A. F. Miller and A. Saiani, *Biomacromolecules*, 2020, **21**, 2285–2297.
- 18 A. D. Martin, J. P. Wojciechowski, A. B. Robinson, C. Heu, C. J. Garvey, J. Ratcliffe, L. J. Waddington, J. Gardiner and P. Thordarson, *Sci. Rep.*, 2017, **7**, 43947.
- 19 E. R. Draper, B. Dietrich, K. McAulay, C. Brasnett, H. Abdizadeh, I. Patmanidis, S. J. Marrink, H. Su, H. Cui, R. Schweins, A. Seddon and D. J. Adams, *Matter*, 2020, **2**, 764–778.
- 20 K. McAulay, L. Thomson, L. Porcar, R. Schweins, N. Mahmoudi, D. J. Adams and E. R. Draper, *Org. Mater.*, 2020, **2**, 108-115.
- 21 A. Z. Cardoso, L. L. E. Mears, B. N. Cattoz, P. C. Griffiths, R. Schweins and D. J. Adams, *Soft Matter*, 2016, **12**, 3612.
- 22 K. AlKaabi, C. R. Wade and M. Dincă, *Chem*, 2016, **1**, 264–272.
- 23 B. A. Johnson, A. Bhunia, H. Fei, S. M. Cohen and S. Ott, *J. Am. Chem. Soc.*, 2018, **140**, 2985–2994.
- 24 T. Jarosz, K. Gebka, A. Stolarczyk and W. Domagala, *Polymers (Basel)*, 2019, **11**, 1–18.
- 25 S. Abraham, S. Mangalath, D. Sasikumar and J. Joseph, *Chem. Mater.*, 2017, **29**, 9877-9881.
- 26 Y. Alesanco, A. Viñuales, J. Rodriguez and R. Tena-Zaera, *Materials*, 2018, **11**, 1–27.
- 27 C. J. Barile, D. J. Slotcavage, J. Hou, M. T. Strand, T. S. Hernandez and M. D. McGehee, *Joule*, 2017, **1**, 133–145.
- 28 G. A. Niklasson and C. G. Granqvist, *J. Mater. Chem.*, 2006, **17**, 127–156.
- 29 R. Cinnsealach, G. Boschloo, S. N. Rao and D. Fitzmaurice, *Sol. Energy Mater. Sol. Cells*, 1998, **55**, 215–223.
- 30 S. Xie, Y. Chen, Z. Bi, S. Jia, X. Guo, X. Gao and X. Li, *Chem. Eur. J.*, 2019, **370**, 1459–1466.
- 31 E. S. Lee and D. L. Dibartolomeo, *Sol. Energy Mater. Sol. Cells*, 2002, **71**, 465–491.
- 32 S. V Vasilyeva, P. M. Beaujuge, S. Wang, J. E. Babiarz, V. W. Ballarotto and J. R. Reynolds, *ACS Appl. Mater. Interfaces*, 2011, **3**, 1022–1032.
- 33 J. N. C.M. Lampert, A. Agrawal, C. Baertlien, *Sol. Energy Mater. Sol. Cells*, 1999, **56**, 449.
- 34 A. W. Czanderna, D. K. Benson, G. J. Jorgensen, J. G. Zhang, C. E. Tracy and S. K. Deb, *Sol. Energy Mater. Sol. Cells*, 1999, **56**, 419–436.

- 35 Å. Stefan, *J. New Mater. Electrochem. Syst.*, 2001, **4**, 173–179.
- 36 S. Kiruthika and G. U. Kulkarni, *Sol. Energy Mater. Sol. Cells*, 2017, **163**, 231–236.
- 37 T. Gwang Yun, M. Park, S. Kim, D. Kim, J. Younh Cheong, J. Gook Bae, A. Min Han and I. Kim, *ACS Nano*, 2019, **13**, 3141–3150.
- 38 R. J. Mortimer, *Electrochim. Acta*, 1999, **44**, 2971–2981.
- 39 S.-Y. Kao, H.-C. Lu, C.-W. Kung, H.-W. Chen, T.-H. Chang and K.-C. Ho, *ACS Appl. Mater. Interfaces*, 2016, **8**, 4175–4184.
- 40 L. Beverina, G. A. Pagani and M. Sassi, *Chem. Commun.*, 2014, **50**, 5413–5430.
- 41 K. Hoshino, R. Nakajima and M. Okuma, *Appl. Surf. Sci.*, 2014, **313**, 569–576.
- 42 G. Möhl, E., E. Metwalli, R. Bouchet, T. N. T. Phan, R. Cubitt and P. Müller-Buschbaum, *ACS Energy Lett.*, 2018, **3**, 1–6.
- 43 S. Risse, E. Härk, B. Kent and M. Ballauff, *ACS Nano*, 2019, **13**, 10233–10241.
- 44 A. Djire, P. Pande, A. Deb, J. B. Siegel, O. T. Ajenifujah, L. He, A. E. Sleightholme, P. G. Rasmussen and L. T. Thompson, *Nano Energy*, 2019, **60**, 72–81.
- 45 C. J. Jafta, X. G. Sun, G. M. Veith, G. v. Jensen, S. M. Mahurin, M. P. Paranthaman, S. Dai and C. A. Bridges, *Energy Environ. Sci.*, 2019, **12**, 1866–1877.
- 46 X. He, R. Wang, M. C. Stan, E. Paillard, J. Wang, H. Frielinghaus and J. Li, *Adv. Mater. Interfaces*, 2017, **4**, 1601047.
- 47 S. J. Richardson, M. R. Burton, X. Luo, P. A. Staniec, I. S. Nandhakumar, N. J. Terrill, J. M. Elliott and A. M. Squires, *Nanoscale*, 2017, **9**, 10227.
- 48 V. M. Prabhu and V. Reipa, *J. Phys. Chem. Lett.*, 2012, **3**, 646–650.
- 49 S. G. Corcoran, D. G. Wiesler and Karl Sieradzki, *Mat. Res. Soc. Symp. Proc.*, 1997, **451**, 93–98.
- 50 V. M. Prabhu, V. Reipa, A. J. Rondinone, E. Formo and P. V. Bonnesen, *ECS Trans*, 2016, **72**, 179–188.
- 51 K. McAulay, H. Wang, A. M. Fuentes-Caparro, L. Thomson, N. Khunti, N. Cowieson, H. Cui, A. Seddon and D. J. Adams, *Langmuir*, 2020, **36**, 8626–8631.
- 52 B. J. Eves, J. J. Douth, A. E. Terry, H. Yin, M. Moulin, M. Haertlein, V. T. Forsyth, P. Flagmeier, T. P. J. Knowles, D. M. Dias, G. Lotze, A. M. Seddon and A. M. Squires, *RSC Chem. Biol*, 2021, **2**, 1232–1238.
- 53 J. C. MacDonald and G. M. Whitesides, *Chem. Rev.*, 1994, **94**, 2383–2420.
- 54 S. v. Bhosale, C. H. Jani and S. J. Langford, *Chem. Soc. Rev.*, 2008, **37**, 331–342.
- 55 Y. Matsunaga, K. Goto, K. Kubono, K. Sako and T. Shinmyozu, *Chem. Eur. J.*, 2014, **20**, 7309–7316.
- 56 K. R. Miller, Larry L., Mann, *Acc. Chem. Res.*, 1996, **29**, 417–423.
- 57 T. A. Welsh and E. R. Draper, *RSC Adv.*, 2021, **11**, 5245–5264.
- 58 P. Jittiarporn, S. Badilescu, M. N. al Sawafta, L. Sikong and V.-V. Truong, *J. Sci.: Adv. Mater. Devices*, 2017, **2**, 286–300.

- 59 J.-L. Wang, Y.-R. Lu, H.-H. Li, J.-W. Liu and S.-H. Yu, *JACS*, 2017, **139**, 9921–9926.
- 60 C. Fu, C. Foo and P. S. Lee, *Electrochim. Acta*, 2014, **117**, 139–144.
- 61 K. Madasamy, D. Velayutham, V. Suryanarayanan, M. Kathiresan and K.-C. Ho, *J. Mater. Chem.*, 2019, **4622**, 4622.
- 62 G. Andric, A. F. John Boas, B. M. Alan Bond, D. D. Gary Fallon, A. P. Kenneth Ghiggino, C. F. Conor Hogan, A. A. James Hutchison, C. Marcia A-P Lee, A. J. Steven Langford, D. R. John Pilbrow, B. J. Gordon Troup and C. P. Woodward A, *Aust. J. Chem*, 2004, **57**, 1011–1019.
- 63 Y. Alesanco, J. Palenzuela, A. Viñuales, G. Cabañero, H. J. Grande and I. Odriozola, *ChemElectroChem*, 2015, **2**, 218–223.
- 64 J. Žmija and M. J. Małachowski, *J. Achiev. Mater. Manuf. Eng.*, 2011, **48**, 14–23.
- 65 Z. Chen, A. Lohr, C. R. Saha-Möller and F. Würthner, *Chem. Soc. Rev.*, 2009, **38**, 564–584.
- 66 J. M. Lim, P. Kim, M. C. Yoon, J. Sung, V. Dehm, Z. Chen, F. Würthner and D. Kim, *Chem. Sci.*, 2012, **4**, 388–397.
- 67 H. Marciniak, X. Q. Li, F. Würthner and S. Lochbrunner, *J. Phys. Chem. A*, 2011, **115**, 648–654.
- 68 Y. Tian, V. Stepanenko, T. E. Kaiser, F. Würthner and I. G. Scheblykin, *Nanoscale*, 2011, **4**, 218–223.
- 69 D. McDowall, M. Walker, M. Vassalli, M. Cantini, N. Khunti, C. Edwards-Gayle, N. Cowieson and D. J. Adams, *Chem. Comm.*, 2021, **57**, 8782–8785.
- 70 E. R. Draper and D. J. Adams, *Chem*, 2017, **3**, 390–410.
- 71 Y. Huang, Y. Yan, B. M. Smarsly, Z. Wei and C. F. J. Faul, *J. Mater. Chem.*, 2009, **19**, 2356–2362.
- 72 J. Xie, N. Imanishi, T. Matsumura, A. Hirano, Y. Takeda and O. Yamamoto, *Solid State Ion.*, 2008, **179**, 362–370.
- 73 J. Z. O. Arnold, J. C. Bilheux, J. M. Borreguero, A. Buts, S. I. Campbell, L. Chapon, M. Doucet, N. Draper, R. Ferraz Leal, M. A. Gigg, V. E. Lynch, A. Markvardsen, D. J. Mikkelsen, R. L. Mikkelsen, R. Miller, K. Palmen, P. Parker, G. Passos, T. G. Perring, P., *Nucl. Instrum.*, 2014, **764**, 156–166.
- 74 Sasview, Version 4.2.2, www.sasview.org, (accessed January 2, 2020).
- 75 E. Draper et al.; (2020): Investigating the effect of pH and functionalisation upon the self-assembly of NDIs, STFC ISIS Neutron and Muon Source, <https://doi.org/10.5286/ISIS.E.RB2010459>.
- 76 <https://www.ncnr.nist.gov/resources/activation/>, (accessed October 9, 2019).
- 77 G. G. W. M. Fabretto, T. Vaithianathan, C. Hall, P. Murphy, P.C. Innis, J. Mazurkiewicz, *Electrochem. Commun.*, 2007, **9**, 2032.
- 78 Automation Software | Automated Acquisition | Bruker, <https://www.bruker.com/en/products-and-solutions/mr/nmr-software/icon-nmr.html>, (accessed January 10, 2022).

CHAPTER FOUR

Improving Cyclability with Multicomponent
Electrochromic Systems

4.1 Introduction

In Chapter 3, it was concluded that the ideal aggregation for each system is found at a specific pH where certain properties such as flexibility or radius size promote the formation or stabilisation of the radical anionic species. This ideal state can be maintained using a buffer, and electrochemical protocol can be tuned, to yield the highest number of cycles. Referring to our initial criteria in Chapter 2, the cyclability of the systems requires development. Diffusion is still an issue within the window set-up which may contribute to incomplete oxidation, thus causing changes in aggregation *via* the prolonged presence of the radical anion. We hypothesise this is the cause of less efficient cyclability.

Diffusion is influenced by temperature, aggregation and viscosity. It was hypothesised that the addition of a transmissive, viscous component could result in a lower rate of diffusion which would immobilise the reduced species at the working electrode surface, Figure 4.1. It is important that this component is colourless to the eye so as not to influence chromic properties. It is also important that this component does not interact with the NDI species in a way that will disrupt the aggregates in an unfavourable way. This factor is incredibly difficult to calculate as we cannot reliably predict how any two species will interact.¹⁻⁵

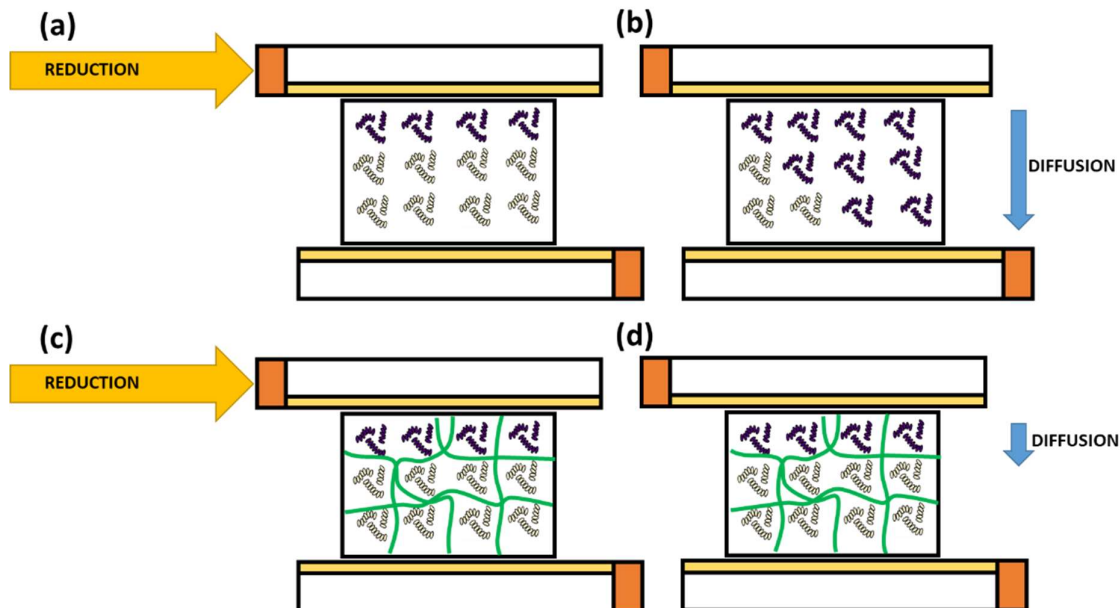


Figure 4.1. Cartoon representation of (a/c) reduction and diffusion (b/d) away from the electrode surface within the cell. (a-b) shows the current set-up and (c-d) shows what may occur with the addition of a viscous component.

Adding in components such as metal organic frameworks (MOFs)⁶⁻¹² or a conductive gel¹³ that are not themselves electrochromic has been reported. Metal components allow multiple colours due to the utilisation of their own variable oxidative states in addition to colour changes of an organic chromophore.¹¹ Some electrochromic devices are reported using a polyol-borax “slime” electrolyte (combining solid and liquid like properties) to improve wettability, contact to electrodes, ionic conductivity and charge transmission, Figure 4.2.^{14,15} Such devices will have different diffusion rates than solution based devices.

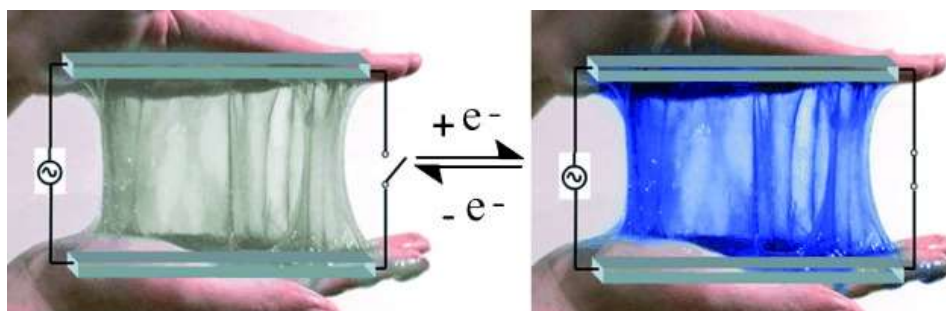


Figure 4.2. Image reported by Alesanco *et al.* showing a “slime” based electrolyte.¹⁵

Multicomponent systems have many advantages as, in theory, you can combine the desirable properties of each component.^{1,3,16-23} There are reports of multicomponent gelating systems combining a strong gelator with a weaker but electronically active gelator or combining p-type gelators with n-type to create a heterojunction.^{4,17} Not all multicomponent systems result in this ‘best of both worlds’ result as some can have poor tunability or colouration.²⁴

It is important to consider the way in which components may interact.^{1,5,25} Whether components are self-sorted or co-assembled (either randomly or ordered) on a molecular level is one question, Figure 4.3. Next, whether fibres and larger assemblies will assemble into homo- (self-sorted) or hetero-aggregates (co-assembled). On a larger scale, various microstructures are then possible.^{1,5,25} This question has added complexity when gelating components are considered as networks will be larger and more complex. The interaction of large-scale gel networks may also be stronger than smaller aggregates. **NDI-GF** can form gels and although this study does not focus upon the gelled state of these systems, this investigation could be undertaken in the future and the ability of gelators should be considered when understanding these multicomponent systems. Understanding both the primary and larger scale structures and whether components interact with each other is important, and so a variety of techniques should be used to understand a variety of length scales.

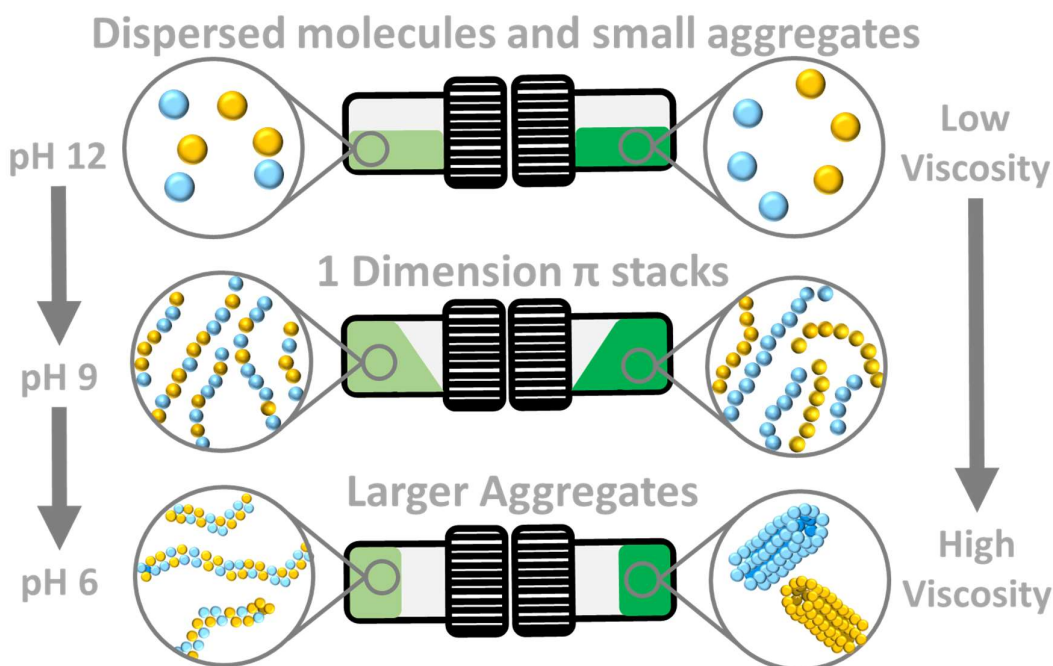


Figure 4.3. Cartoon representation of hetero- (left) and homo- (right) type aggregates forming as pH is lowered in theoretical multicomponent systems.

Relating this theory to our systems, we have observed poor chromic behaviour at pH 12 which has been linked to poorly defined structures (Chapter 3). It is conceivable that if structures co-assembled, either specifically or randomly, the NDI π stacking could be disrupted. This phenomenon could impact the efficiency of reduction and oxidation, or just what kind of structure forms, Figure 4.3. It is also possible that a second component could stabilise π stacking and improve electrochromic processes. Fibrous networks can aid electron transfer and improve efficiency of redox reactions.²⁶

Assembly into fibres leads to entanglement and immobilising of solvent in some systems, forming a gel.^{1,27-30} The addition of a gelating component could also open up the potential to form gel-based devices for the NDIs that cannot form gels. Gel electrolytes have advantages over solutions as they are less likely to leak or produce bubbles.³¹ Gel systems also give smooth colour changes (due to less mixing by diffusion) than solutions.³² Gel electrolytes also have advantages over solid electrolytes, which have slow switching times and non-deformability (which could limit contact with electrodes).³¹ This area of investigation is outside of the scope of this work but could be pursued if such multicomponent systems show promise.

This chapter will focus upon investigating whether diffusion issues can be improved by addition of a viscous component and understand if and how the components interact with each other. It is

important to understand if and how such interaction would impact chromic properties within our devices.

4.2 Results and discussion

4.2.1 Proof of concept showing diffusion influence

We have noted that diffusion may have some impact upon the efficiency of electrochemical oxidation within our set-up, Figure 4.1. This is our hypothesis and so as a proof of concept, cycling tests were carried out as previously described with a speaker playing bass heavy music directly underneath the window cell.³³ The vibration from the speaker gently shook the cell whilst the experiment was run, similar to low power sonicating, increasing the diffusion rate within the cell. The result was a reduction in cyclability, and an increase in the time taken for oxidation to take place, Figure 4.4. This observation suggested to us that diffusion rates within the cell could be resulting in lower cyclability than these systems are capable of.

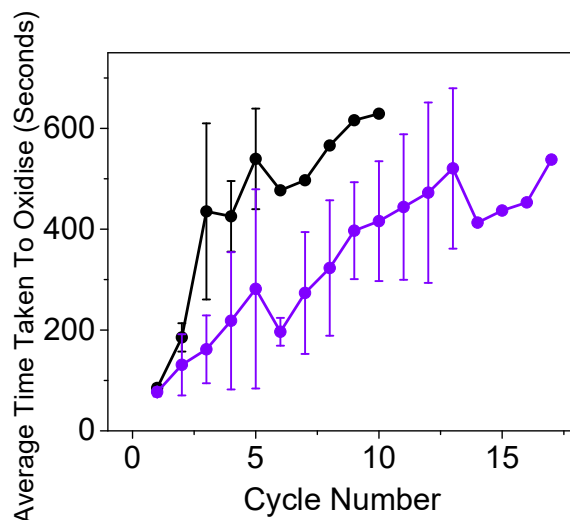


Figure 4.4. Plot showing how time to reach a state without colouration fluctuates with electrochemical cycling between a reduced and oxidised state. Measurements carried out using solutions of buffered **NDI-F** at 10 mg/mL and adjusted to pH 6 (purple). The same experiment was repeated whilst heavy bass music played (black) at pH 6. Measurements are taken as an average of triplicate measurements and error bars calculated from standard deviation.

4.2.2 Screening trends in multicomponent systems

Because the properties of multicomponent systems are not always predictable, we first undertook a broad screening of a variety of ratios of components and pH. If these systems are to have real world application, it is important to determine how much of a second component is required (for example, if only 3 mg/mL is needed, then it would be wasteful to use 5 mg/mL on a large scale. We also wanted

to maximise cyclability and so investigated our best performing systems. **NDI-I** and **NDI-F** were found to have the best cyclability (Chapter 3) of the four NDIs investigated. **NDI-GF** was found to have the worst cyclability, but also exhibited interesting trends in axis ratio upon reduction (Chapter 3). These three NDIs were taken forward into this new investigation to see the impact of adding 2-{2-[2-(naphthalen-1-yloxy)acetamido]-3-phenylpropanamido}-3-phenylpropanoic acid (**1-NapFF**), Figure 4.5(a).

1-NapFF is a widely reported hydrogelator^{34–36} that can form viscous solutions at a comparable concentration to the NDI solutions previously discussed. As a gelator, **NDI-GF** may have different interactions with **1-NapFF** than other NDIs and so was of interest to investigate. For brevity, **NDI-I** data is excluded from this discussion as the results showed little change in behaviour. **1-NapFF** and similar materials can also undergo an increased viscosity when heat-cooled³⁷ which would be beneficial if required. **1-NapFF** is also colourless to the eye, Figure 4.5(b), which means it is unlikely to detrimentally discolour the pale neutral state of the NDIs.

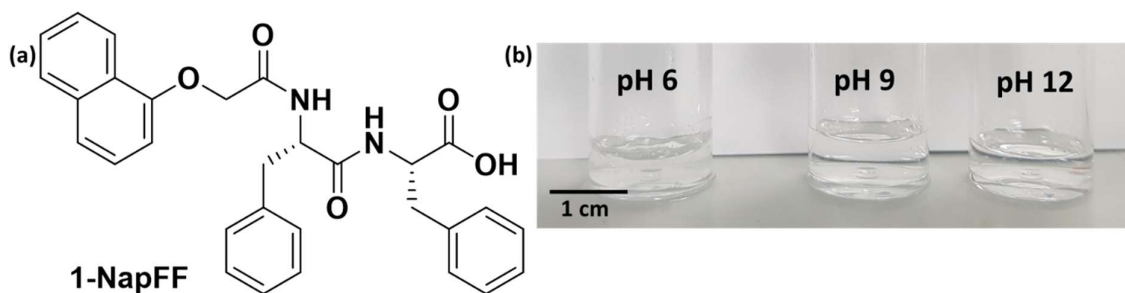


Figure 4.5. (a) Chemical structure of **1-NapFF** (b) colour by eye of 5 mg/mL solutions at pH 6, 9 and 12.

If the addition of a viscous component had no influence upon structure, we would expect comparable behaviour or linear relationships across both NDIs. It is possible that the components will interact with each other and that this will have an influence upon self-assembly and consequent electrochromic properties of these systems.

As an initial screening process, **NDI-F** and **NDI-GF** were prepared and mixed with **1-NapFF** in 5:0, 5:0.625, 5:1.25, 5:2.5 and 5:5 mg/mL ratios. Each mixture was adjusted to pH 6, 9 and 12 as these pH values were previously used to chart the changes in structure in NDIs (Chapter 3). A lower concentration of NDI was used to perform a high volume of screening measurements without using excessive material (as previously reported in Chapter 2, we see from absorption measurements that structures dilute rather than change at lower concentration). A higher percentage of 0.1 M NaCl was used in order to aid conductivity due to the addition of a non-conductive component. 50% of the total

solution was made up of 0.1 M NaCl instead of 40%. A measurement of viscosity, absorbance (of neutral and electrochemically reduced species), CV and SAXS was measured for each of these mixtures at each pH to understand the bulk behaviour, the molecular packing, electrochemical properties and the aggregation of each multicomponent system.

4.2.3 pK_a

Two apparent pK_a values were previously reported in Chapter 2 for NDI systems. Similarly, two apparent pK_a values have been reported for comparable systems to **1-NapFF** that correspond to the expected protonation/deprotonation of the carboxylic acid group of phenylalanine and to a further change in structure.³⁷ We could therefore expect four apparent pK_a values for each multicomponent system if the system was self-sorting. If we observe significant shifting or absence of apparent pK_a , we may infer that there are significant changes to the structure of one or both components, or co-assembly is happening.

In Table 4.1, it can be observed that the apparent pK_a of the multicomponent systems does not greatly shift compared to the single components, with any shifting within 0.4 (but most variation in the region of 0.2) pH units. This is not significant when the stated accuracy of the pH probe is ± 0.1 . Overall concentration will also affect pK_a (with multicomponent systems being 10 mg/mL overall). The largest change observed is the 2nd apparent pK_a of both NDIs in multicomponent systems is found at a lower pH, possibly due to the interaction of larger aggregates at low pH. It is possible that the high viscosity of the multicomponent systems at low pH affects the measurement due to the slow diffusion of H^+ . Gentle stirring and five-minute intervals between measurements were employed to compensate for this. These data suggest that the pH at which aggregation changes in components is not significantly altered but that there may be some interaction at low pH.

Table 4.1. Tabulated data from apparent pK_a titrations of 50 % 0.1 M NaCl solution showing pH at which buffering occurs from raw data in Figure A.4.1-A.4.5, Appendix.

NDI-F 5 mg/mL	NDI-GF 5 mg/mL	1-NapFF 5 mg/mL	NDI-F:1-NapFF 5:5 mg/mL	NDI-GF:1-NapFF 5:5 mg/mL
9.7	9.7		9.5	9.5
		7.5	7.7	7.7
6.9	6.7		6.6	6.3
		6.1	6.2/6.1	6.0

4.2.4 Trends in viscosity

Higher viscosity systems will have slower diffusion rates. The viscosity of multicomponent systems is important to characterise in order to ascertain whether there is a linear relationship between viscosity and cyclability. Bulk properties can also give indication of component interaction.

The viscosity of **1-NapFF** is pH dependent, Table 4.3. Viscosity at 5 mg/mL is comparable at pH 12 and 9 then increases at pH 6 (Table 4.2) due to the formation of large aggregates and fibres forming. This observation is due to the strong gelling ability of **1-NapFF**. At lower pH we expect structures similar to those present in gels (or at the early formation stage of gelation). As concentration decreases, viscosity decreases as expected (Table 4.2). Significant changes of viscosity are statistically significant but smaller differences (for example between **NDI-F** and **NDI-GF** at pH 6 and 9, or **1-NapFF** between pH 9 and 12) at low shear are within error. Refer to individual error bars for each data set in the Appendix for more information.

Table 4.2. Tabulated average apparent viscosity at a shear rate of 1 s^{-1} for **1-NapFF** and NDI-R systems containing 50% 0.1 M NaCl as single components at different pH. Full data sets available in Figure A.4.6-A.4.8, Appendix.

System (mg/mL)	Average apparent viscosity at 1 s^{-1} shear at pH 6 (Pa·s)	Average apparent viscosity at 1 s^{-1} shear at pH 9 (Pa·s)	Average apparent viscosity at 1 s^{-1} shear at pH 12 (Pa·s)
NDI-F (5)	0.001	0.001	0.001
NDI-GF (5)	0.006	0.010	0.001
1-NapFF (5)	50.867	0.219	0.126
1-NapFF (2.5)	8.387	0.063	0.039
1-NapFF (1.25)	0.122	0.010	0.032
1-NapFF (0.625)	0.022	0.005	0.015

Initially NDIs are mixed with **1-NapFF** to create a 5:5 mg/mL ratio. We see an immediate change to the trends in viscosity, Table 4.3 and Figure A.4.9. While solutions at pH 6 are always the most viscous, the viscosity at pH 12 is notably increased (and comparable with that at pH 6 when **NDI-F** is used, Table 4.3). The viscosity is more comparable across all pHs in **NDI-GF:1-NapFF** mixes but viscosity at pH 12 is higher than at pH 9, Table 4.3. Compared to 5 mg/mL **1-NapFF**, mixes of NDI-R:**1-NapFF** are comparable in viscosity at pH 9 and lower at pH 6 (Figure 4.6(a-b)). This observation suggests that at pH 6, the NDI molecules are disrupting the large aggregates of **1-NapFF**.

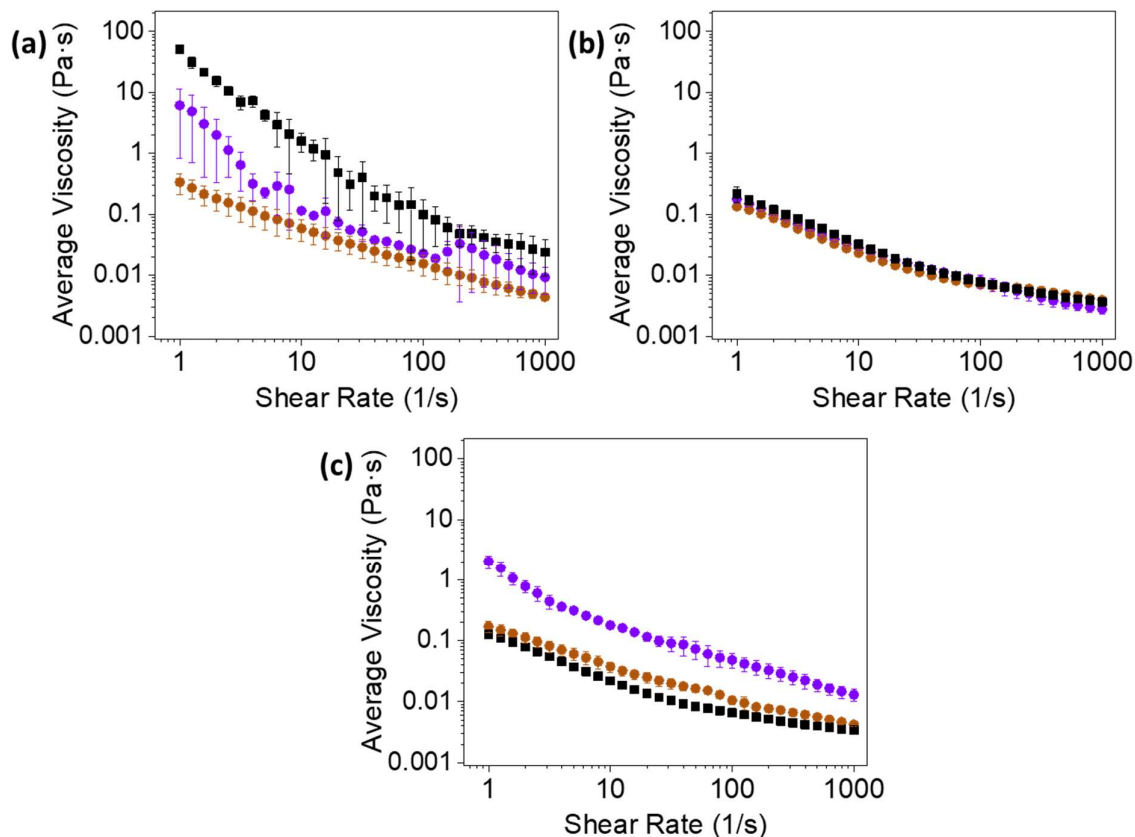


Figure 4.6. Viscosity measurements of 5 mg/mL **1-NapFF** (black) and 5:5 mg/mL, **NDI-F:1-NapFF** (purple), and **NDI-GF:1-NapFF** (brown) at (a) pH 6, (b) 9 and (c) 12 containing 50% 0.1 M NaCl. Measurements are taken as an average of triplicate measurements and error bars calculated from standard deviation.

At high pH, we observed that **NDI-R:1-NapFF** mixes have higher viscosity than **1-NapFF** at 5 mg/mL, Figure 4.6(c). This observation is unexpected, as at high pH we would expect molecules to be more dispersed and less likely to interact with one another. **NDI-F:1-NapFF** mixes are the most viscous across all pHs (particularly at pH 12, Figure 4.6). This observation suggests that chemical structure has some impact on the way the two components are interacting but that the NDI core may also be involved as trends are fairly comparable across mixes. **NDI-F** was seen to form more rigid structures (Chapter 3) and so this may be a key factor.

These trends are mostly consistent through all ratios and suggests that the greatest degree of interaction between component occurs at low and high pH, and so may be influenced by electrostatic forces and the charge of the NDI molecules, Table 4.3.

Table 4.3. Tabulated average apparent viscosity at a shear rate of 1 s^{-1} for NDI-R:1-NapFF containing 50 % 0.1 M NaCl at different ratios and pH. Full data sets available in Figure A.4.7-A.4.9, Appendix.

System (mg/mL)	Average apparent viscosity at 1 s^{-1} shear at pH 6 (Pa·s)	Average apparent viscosity at 1 s^{-1} shear at pH 9 (Pa·s)	Average apparent viscosity at 1 s^{-1} shear at pH 12 (Pa·s)
NDI-F:1-NapFF (5:5)	6.144	0.180	2.023
NDI-GF:1-NapFF (5:5)	0.337	0.133	0.170
NDI-F:1-NapFF (5:2.5)	7.323	0.067	2.452
NDI-GF:1-NapFF (5:2.5)	0.094	0.044	0.040
NDI-F:1-NapFF (5:1.25)	0.107	0.048	0.198
NDI-GF:1-NapFF (5:1.25)	0.085	0.010	0.062
NDI-F:1-NapFF (5:0.625)	0.021	0.001	0.093
NDI-GF:1-NapFF (5:0.625)	0.008	0.045	0.004

As the concentration of **1-NapFF** in mixes is reduced, the viscosity of the mix generally decreases (Table 4.3) although this trend is not as linear as with **1-NapFF** alone. For example, at pH 6 and 12, 5:5 and 5:2.5 mg/mL **NDI-F:1-NapFF** are comparable, Table 4.3. These observations suggest that not only does chemical structure, but ratio of components and pH all have an influence upon bulk viscosity of mixes. It is likely that the structures in solution are therefore also influenced by these factors. The overall viscosity of all mixes at 5:1.25, 5:2.5 and 5:5 mg/mL is significantly higher than NDIs alone (Table 4.3) which means these systems are likely to have slower diffusion rates, which will theoretically aid cyclability. As aggregation has such a crucial influence upon electrochromic behaviour of the NDI systems (Chapter 2 and 3), we must investigate whether aggregation, and consequent electrochromic behaviour, is significantly influenced by **1-NapFF**.

4.2.5 Trends in neutral state

Having investigated the trends in bulk viscosity of these multicomponent systems and concluded there may be some interaction between components that influences aggregation, we must investigate this hypothesis. Absorbance spectra of each ratio at pH 6, 9 and 12 were collected to give insight into significant changes to aggregation and subtle changes in molecular packing. In self sorting systems, we would expect the spectra to be comparable to the overlaid spectra of each component.⁵

The colour of both NDIs is influenced upon the addition of **1-NapFF**, Figure 4.7. When 0.625 mg/mL is added, a yellowish colour is apparent in both systems which only becomes darker as the concentration of **1-NapFF** increases. This observation may indicate charge transfer between components. This colouration is weakest at pH 12, especially in **NDI-GF:1NapFF**, Figure 4.7(b), which suggests that there

is less charge transfer between components due to less defined and dispersed aggregates at this pH. The change in colouration is most notable in **NDI-GF**, Figure 4.7(b). The dark colour of the multicomponent system is disadvantageous for the application of Smart Windows which require a pale neutral state.

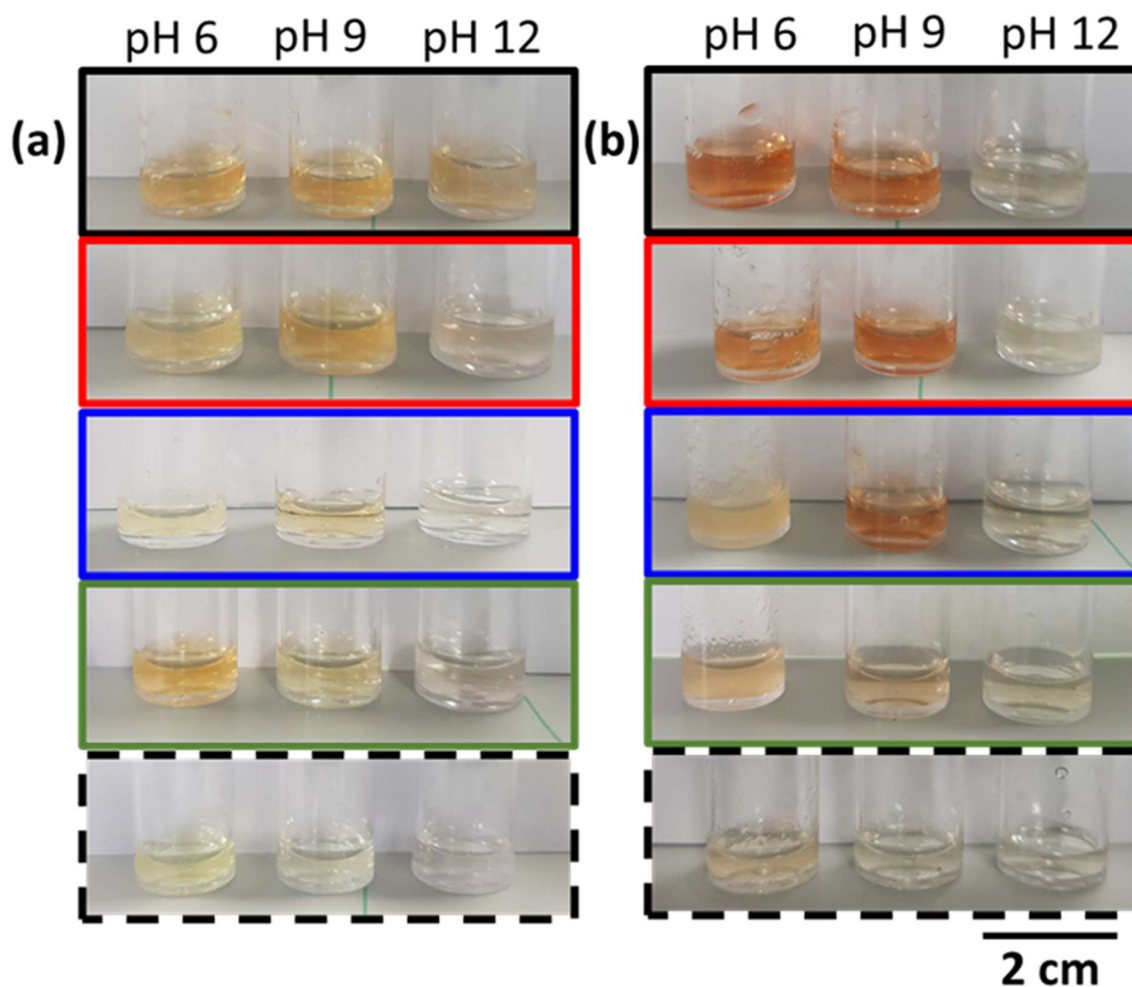


Figure 4.7. Images of (a) **NDI-F:1-NapFF** and (b) **NDI-GF:1-NapFF** neutral solutions containing 50% 0.1 M NaCl at pH 6, 9 and 12 at 5:5 (black), 5:2.5 (red), 5:1.25 (blue), 5:0.625 (green) and 5:0 (dashed line) mg/mL.

The absorbance spectra of **1-NapFF** are unchanged by pH (Figure 4.8(a)) and are observed as an undefined broad absorbance around 290 nm. This wavelength is close to the region at which quartz absorbs so is not as reliable to measure as the NDI components.

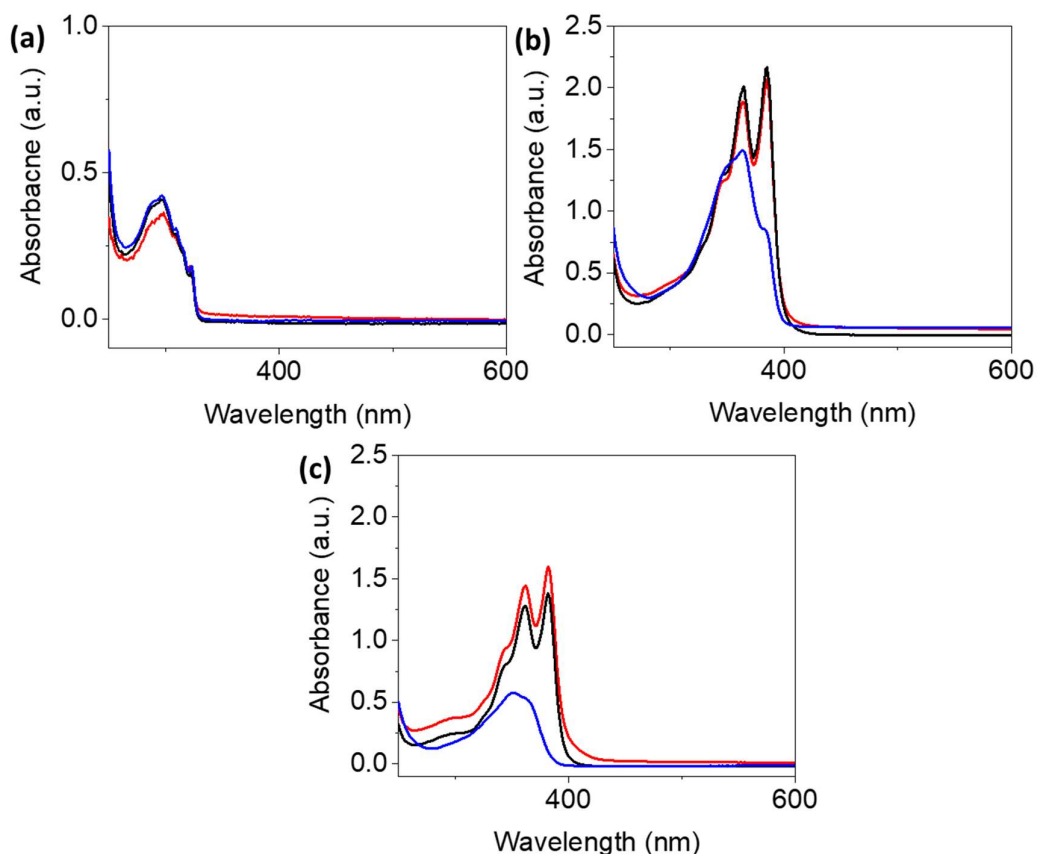


Figure 4.8. Absorbance spectra of neutral single components at 5 mg/mL of (a) **1-NapFF** and (b) **NDI-F**, (c) **NDI-GF** at pH 6 (red), 9 (black) and 12 (blue) containing 50% 0.1 M NaCl.

The higher concentration electrolyte has some influence upon the molecular packing of the NDI systems compared to the results discussed in Chapter 2. The ratio of absorbances at 365 and 385 nm are unchanged between pH 6 and 9 in both NDIs, Figure 4.8(b-c) (whereas a change was observed previously in **NDI-GF**, Chapter 2). The ratio of absorbances at pH 6 and 9 also appears slightly different which indicates a subtle change in packing with additional salt for **NDI-F**.³⁸⁻⁴⁰ The absorbance at 385 nm is higher compared to 365 nm at pH 6 and 9 (not previously observed), Figure 4.8(b). The higher concentration of 0.1 M NaCl may result in charge screening causing a change in packing. The behaviour at pH 12 (showing only a broad absorbance at 360 nm) is consistent with previous discussion for all NDIs, although a small shoulder is observed in **NDI-F** at 385 nm, (Figure 4.8(b)).

Despite a colour difference by eye in **NDI-F:1-NapFF** and **NDI-GF:1-NapFF** (Figure 4.7), at a 5:5 mg/mL **NDI-R:1-NapFF** ratio, the ratio of absorbances of the NDI component are unchanged compared to single component equivalents, Figure 4.9. There may be some changes in aggregation that cannot be fully characterised by absorbance spectroscopy. The spectra appear as an overlap of the two components, which suggests a self-sorting system.

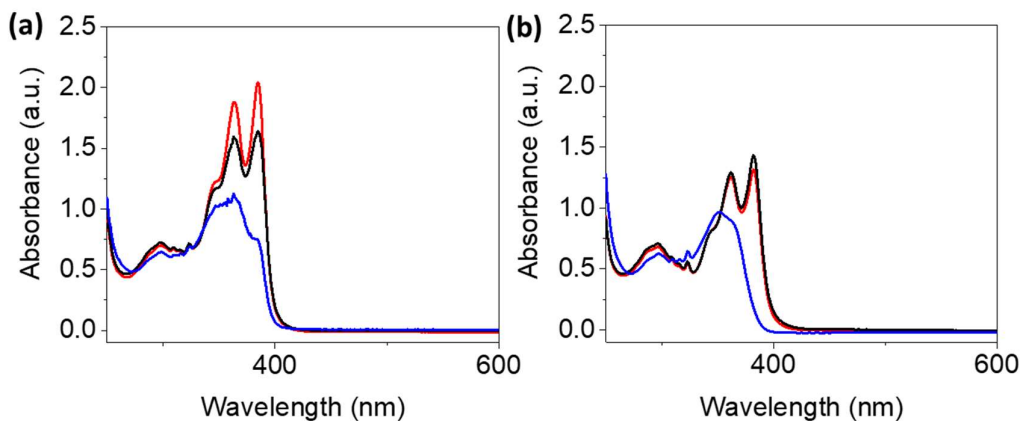


Figure 4.9. Absorbance spectra of neutral 5:5 mg/mL (a) **NDI-F:1-NapFF**, (b) **NDI-GF:1-NapFF** at pH 6 (red), 9 (black) and 12 (blue) containing 50% 0.1 M NaCl.

When the concentration of **1-NapFF** is decreased, no significant change is observed in the spectra of mixes, Figure A.4.10-A.4.11, Appendix. The shoulder at 385 nm in spectra of **NDI-F** at pH 12 is less defined in mixes 5:2.5 and 5:0.625 mg/mL and not visible in the 5:1.25 mg/mL mix, Figure A.4.10, Appendix. We do not think this suggests a significant difference in aggregation but could be the result of interactions at high pH (suggested by rheology). However, at high pH, spectra are broad and poorly defined and so shoulders are more difficult to observe.

4.2.6 The reduced state

Having investigated the neutral state of single and multicomponent systems, we now investigate the electrochemically reduced states. As with the initial investigations in Chapter 2, cyclic voltammograms are performed to ascertain whether the addition of another component has changed the position of reduction and oxidation potentials. Next, the colouration intensity of the electrochemically reduced state and the speed of electrochemical oxidation can be evaluated.

4.2.6.1 Trends in CV

CV was undertaken as previously described in FTO windows cells. In multicomponent systems, at pH 6 and 9, the current of the redox peaks is generally increased by the presence of **1-NapFF** (Figures A.4.12-A.4.13, Appendix). This suggests that the resistivity of the device is lowered, possibly by localisation of the active material at the surface. Data is tabulated in Table 4.4-Table 4.9. Multicomponent system **NDI-F:1-NapFF** demonstrates little variation in redox potentials. We see most variance in the oxidation potential, but no changes are significant.

Table 4.4. Tabulated reduction and oxidation potentials found by CV of solutions of **NDI-F:1-NapFF** containing 50% 0.1 M NaCl at various ratios at pH 6. Scan rate 0.2 V/s. Full data set found in Figure A.4.12, Appendix. CV performed in 1 x 1 FTO window cells.

Ratio of NDI-F:1-NapFF (mg/mL)	Reduction Potential(s) (V)	Current (μ A)	Oxidation Potential(s) (V)	Current (μ A)
5:5	-2.7, -3.2	-706, -818	0.4	256
5:2.5	-2.9	-1220	0.6	401
5:1.25	-2.6	-472	0.5	292
5:0.625	-2.8	-996	0.3	292
5:0	-2.7	-443	0.6	85

Table 4.5. Tabulated reduction and oxidation potentials found by CV of solutions of **NDI-F:1-NapFF** containing 50% 0.1 M NaCl at various ratios at pH 9. Scan rate 0.2 V/s. Full data set found in Figure A.4.12, Appendix. CV performed in 1 x 1 FTO window cells.

Ratio of NDI-F:1-NapFF (mg/mL)	Reduction Potential(s) (V)	Current (μ A)	Oxidation Potential(s) (V)	Current (μ A)
5:5	-2.8	-578	0.5	223
5:2.5	-2.8	-1243	0.6	259
5:1.25	-2.4	-614	0.4	338
5:0.625	-2.6	-400	0.4	124
5:0	-2.8	-765	0.6	190

Table 4.6. Tabulated reduction and oxidation potentials found by CV of solutions of **NDI-F:1-NapFF** containing 50% 0.1 M NaCl at various ratios at pH 12. Scan rate 0.2 V/s. Full data set found in Figure A.4.12, Appendix. CV performed in 1 x 1 FTO window cells.

Ratio of NDI-F:1-NapFF (mg/mL)	Reduction Potential(s) (V)	Current (μ A)	Oxidation Potential(s) (V)	Current (μ A)
5:5	-1.9, -2.6	-296, -781	0.3	85
5:2.5	-1.8, -3.0	-519, -2120	0.9	104
5:1.25	-1.7, -2.6	-237, -873	1.1	138
5:0.625	-2.0, -2.8	-394, -886	1.2	111
5:0	-1.9, -3.1	-552, -1457	0.8	92

The oxidation potentials of **NDI-GF** and **NDI-GF:1-NapFF** systems are not well defined at any pH, Figure A.4.13, Appendix and Table 4.7-Table 4.9. As with **NDI-F**, the changes in redox potentials with the addition of **1-NapFF** are not significant. When only one reduction peak is observed at 5:2.5 and 5:5 mg/mL at pH 6, the value is between the two reduction peaks observed at other ratios as has been previously noted (Chapter 2/3), Table 4.7.

Table 4.7. Tabulated reduction and oxidation potentials found by CV of solutions of **NDI-GF:1-NapFF** containing 50% 0.1 M NaCl at various ratios at pH 6. Scan rate 0.2 V/s. Full data set found in Figure A.4.13, Appendix. CV performed in 1 x 1 FTO window cells.

Ratio of NDI-GF:1-NapFF (mg/mL)	Reduction Potential(s) (V)	Current (μ A)	Oxidation Potential(s) (V)	Current (μ A)
5:5	-2.7	-664	0.4	97
5:2.5	-2.6	-579	0.6	112
5:1.25	-2.5, -3.1	-545, -988	0.8	104
5:0.625	-2.5, -3.1	-526, -797	0.7	93
5:0	-2.4, -3.1	-499, -877	0.8	97

Table 4.8. Tabulated reduction and oxidation potentials found by CV of solutions of **NDI-GF:1-NapFF** containing 50% 0.1 M NaCl at various ratios at pH 9. Scan rate 0.2 V/s. Full data set found in Figure A.4.13, Appendix. CV performed in 1 x 1 FTO window cells.

Ratio of NDI-GF:1-NapFF (mg/mL)	Reduction Potential(s) (V)	Current (μ A)	Oxidation Potential(s) (V)	Current (μ A)
5:5	-2.5	-550	0.4	107
5:2.5	-2.5, -3.1	-447, -1060	0.6	85
5:1.25	-2.5, -3.2	-600, -1137	0.7	129
5:0.625	-2.4, -3.1	-515, -939	0.7	129
5:0	-2.3, -3.1	-569, -1163	0.8	192

Table 4.9. Tabulated reduction and oxidation potentials found by CV of solutions of **NDI-GF:1-NapFF** containing 50% 0.1 M NaCl at various ratios at pH 12. Scan rate 0.2 V/s. Full data set found in Figure A.4.13, Appendix. CV performed in 1 x 1 FTO window cells.

Ratio of NDI-GF:1-NapFF (mg/mL)	Reduction Potential(s) (V)	Current (μ A)	Oxidation Potential(s) (V)	Current (μ A)
5:5	-1.7, -2.4	-342, -961	1.2	258
5:2.5	-1.8, -2.4	-384, -1209	1.1	195
5:1.25	-1.8, -2.4	-321, -899	1.1	278
5:0.625	-1.8, -2.4	-362, -858	1.1	133
5:0	-1.9, -2.6	-672, -1663	1.0	236

From these data we can conclude that reduction and oxidation potentials used in Chapter 2 can be carried through to this investigation. The intensity of the reduced state can now be assessed. This investigation will confirm whether the addition of **1-NapFF** has an influence upon the chromic properties of the NDIs, and whether that is positive or negative in terms of our criteria.

4.2.6.2 Trends in reduced state colouration

As previously observed, **NDI-F** alone shows darkest colouration at pH 6, Table 4.10. At pH 12 there is comparable colouration to **NDI-F** (alone at pH 6) at ratios 5:5 and 5:0.625 mg/mL, Table 4.10. This observation is particularly interesting as radical anion concentration at pH 12 is typically very low for these systems and the second component appears to have improved chromic behaviour.

Table 4.10. Tabulated absorbance intensity at λ_{\max} (after 10 seconds of application of -2.5 V) for **NDI-F:1-NapFF** containing 50% 0.1 M NaCl at different ratios and pH. Full data sets available in Figure A.4.14, Appendix. CV performed in 1 x 1 FTO window cells.

System (mg/mL)	Absorbance at λ_{\max} at pH 6 (a.u.)	Absorbance at λ_{\max} at pH 9 (a.u.)	Absorbance at λ_{\max} at pH 12 (a.u.)
NDI-F (5)	0.740	0.532	0.156
NDI-F:1-NapFF (5:5)	1.596	0.977	0.521
NDI-F:1-NapFF (5:2.5)	0.862	0.494	0.117
NDI-F:1-NapFF (5:1.25)	1.640	1.839	0.146
NDI-F:1-NapFF (5:0.625)	0.795	0.742	0.589

At pH 6 and 9, we observed a significant enhancement of colouration at certain ratios of **NDI-F:1-NapFF**. At pH 9, 5:0.625, 5:5 and 5:1.25 mg/mL produced darker colouration than **NDI-F** alone, Table 4.10. The intensity of colour at 5:1.25 mg/mL is particularly significant as it is darker than any ratio at pH 6 (which was the ideal pH for this NDI as discussed in Chapter 2). This observation suggests that at this ratio there is a change in structure which results in better stabilisation of the radical anion. The bulk viscosity for this ratio was comparable to 5:2.5 mg/mL at pH 9 (Figure A.4.14, Appendix) which shows a weaker colouration than **NDI-F** alone, Figure 4.10 and Table 4.10. This observation suggests that differences in aggregation rather than diffusion rates are responsible for this colour intensity.

At pH 6, every ratio of **NDI-F:1-NapFF** enhances the colouration compared to **NDI-F**, Figure 4.10(a) and Table 4.10. The most significant increase in colour intensity is observed at 1.25:5 and 5:5 mg/mL ratios. There is no linear relationship between colour intensity and concentration of **1-NapFF**, however, across all pHs, 5:2.5 mg/mL **NDI-F:1-NapFF** performed poorly, Figure 4.10. The ratio of components has influence, perhaps due to the size of **1-NapFF** aggregates compared to **NDI-F**. Viscosity is likely also having some influence as well. It is hard to separate out the factors contributing to aggregation.

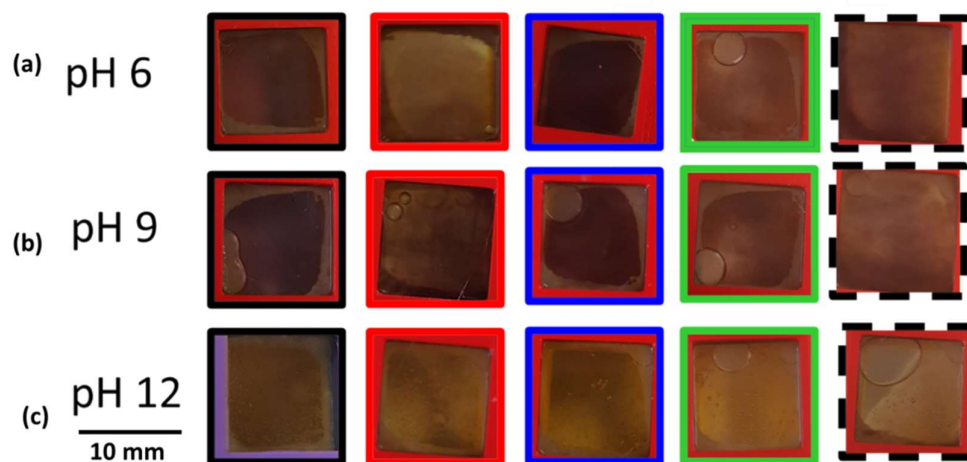


Figure 4.10. Images of **NDI-F:1-NapFF** 5:5 (black), 5:2.5 (red), 5:1.25 (blue), 5:0.625 (green) and 5:0 (dashed line) mg/mL at pH 6 (a), 9 (b) and 12 (c) following application of -2.5 V for 10 seconds. Any bubbles are a result of loading. Solutions contain 50% 0.1 M NaCl.

As previously observed, the highest colouration intensity of **NDI-GF** is at pH 6, Table 4.11. At pH 12 and 9, there is no significant change in colouration upon addition of **1-NapFF**, (although significantly less radical is formed at 5:1.25 mg/mL) Table 4.11. This observation suggests that there is little interaction between components (supported by viscosity being comparable to **1-NapFF** at these pHs, Figure 4.6(b-c)). At pH 6, all ratios of **NDI-GF:1-NapFF** result in a decrease in colouration intensity,

Table 4.11 and Figure 4.11(a). At higher concentrations of **1-NapFF**, colour intensity is reduced, Table 4.11. Large structures present at low pH may be unfavourably interacting resulting in a disruption of the 1-dimensional π stacking of **NDI-GF**, which in turn results in either a destabilisation of the radical anion, or in a lack of charge transfer through the electrochromic active species within the multicomponent system. Most significant changes in coloration occur at low pH for both NDIs, where aggregates are larger (Chapter 3).

Table 4.11. Tabulated absorbance intensity at λ_{\max} (after 10 seconds of application of -2.5 V) for **NDI-GF:1-NapFF** containing 50% 0.1 M NaCl at different ratios and pH. Full data sets available in Figure A.4.15, Appendix. CV performed in 1 x 1 FTO window cells.

System (mg/mL)	Absorbance at λ_{\max} at pH 6 (a.u.)	Absorbance at λ_{\max} at pH 9 (a.u.)	Absorbance at λ_{\max} at pH 12 (a.u.)
NDI-GF (5)	0.730	0.592	0.107
NDI-GF:1-NapFF (5:5)	0.286	0.427	0.074
NDI-GF:1-NapFF (5:2.5)	0.212	0.379	0.080
NDI-GF:1-NapFF (5:1.25)	0.452	0.476	0.001
NDI-GF:1-NapFF (5:0.625)	0.436	0.450	0.090

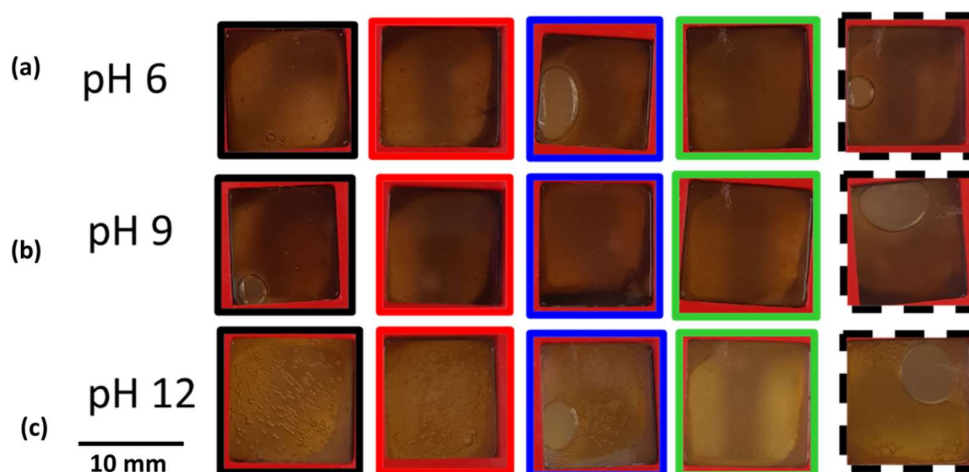


Figure 4.11. Images of **NDI-GF:1-NapFF** 5:5 (black), 5:2.5 (red), 5:1.25 (blue), 5:0.625 (green) and 5:0 (dashed line) mg/mL at pH 6 (a), 9 (b) and 12 (c) following application of -2.5 V for 10 seconds. Any bubbles are a result of loading. Solutions contain 50% 0.1 M NaCl.

4.2.6.3 Trends in oxidation rate

The rates of oxidation in **NDI-F:1-NapFF** systems are enhanced (the gradient of the plot is steeper) in 5:1.25 and 5:5 at pH 6 and 9, Figure 4.12(a-b). These ratios showed significant enhancement of colour intensity. As previously discussed, the radical anion species is likely to be more conductive than the neutral species.^{39,41} A higher concentration of radical is likely to correspond with a faster oxidation rate due to slightly higher conductivity. Both these ratios should be investigated further. After 20 seconds of reduction, the 5:5 mg/mL ratio is darker than 5:1.25 mg/mL at pH 6 (Figure 4.12(a)) and so this ratio will be taken forward as the best performing ratio at pH 6.

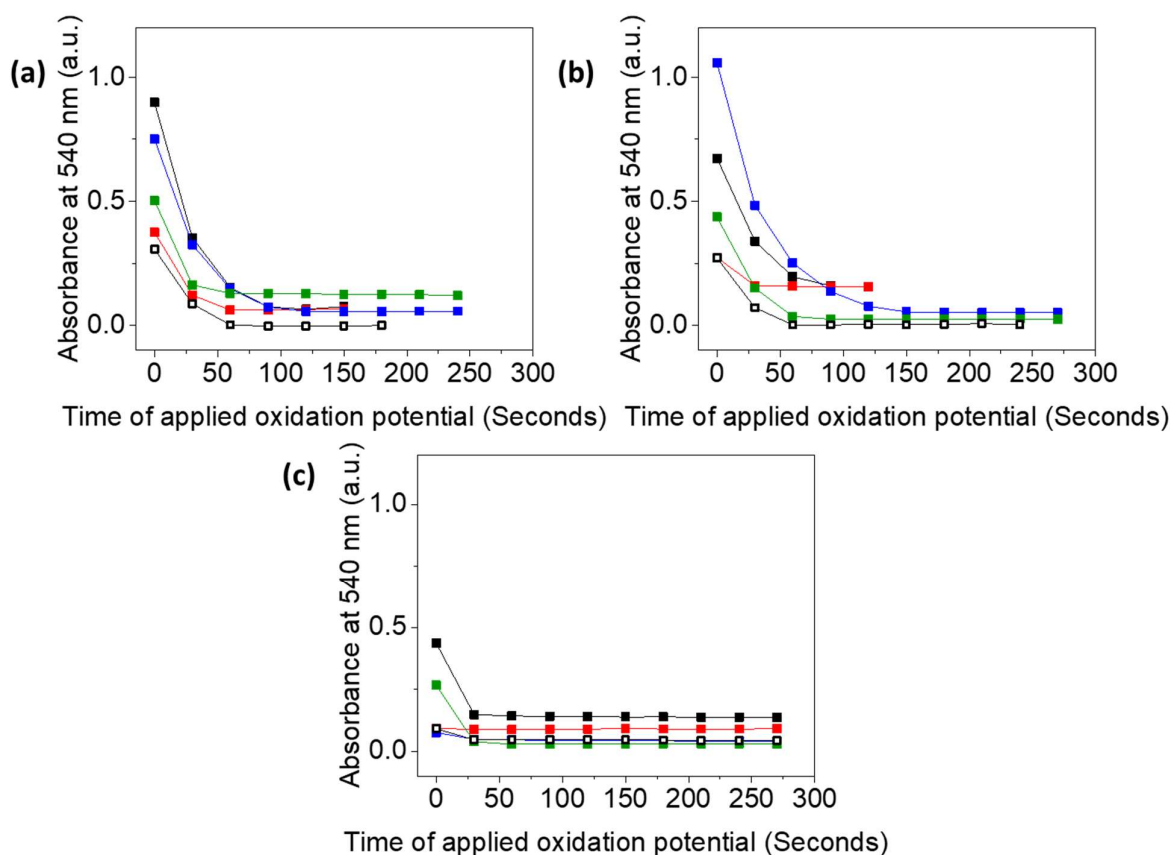


Figure 4.12. Measurement of absorbance at 540 nm as an oxidising potential of 0.5 V was applied for 5 minutes after 20 seconds of reduction with -2.5 V. Solutions of **NDI-F:1-NapFF** at 5:5 (black), 5:2.5 (red), 5:1.25 (blue), 5:0.625 (green) and 5:0 (open square) mg/mL at pH 6 (a), 9 (b) and 12 (c) were used.

The rates of oxidation for **NDI-GF:1-NapFF** at all ratios are comparable, Figure 4.13. At pH 6 and 9, the fastest rate of electrochemical oxidation occurred in systems without **1-NapFF**, Figure 4.13(a-b), which suggests that the addition of **1-NapFF** results in a weakening in colour intensity upon reduction as well

as a slowing of oxidation rate. Both factors suggest that **NDI-GF** and **1-NapFF** interact unfavourably in a way that disrupts the NDI network.

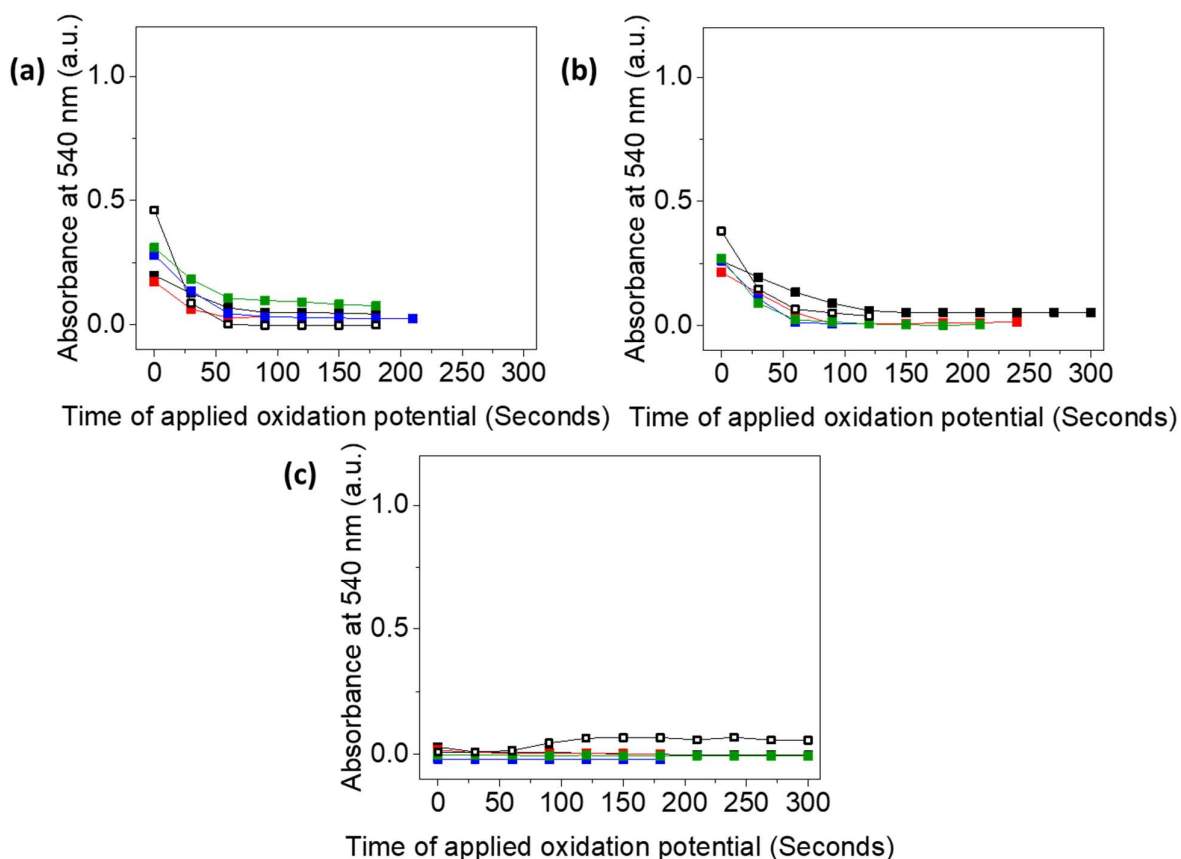


Figure 4.13. Measurement of absorbance at 540 nm as an oxidising potential of 0.5 V was applied for 5 minutes after 20 seconds of reduction with -2.5 V. Solutions of **NDI-GF:1-NapFF** at 5:5 (black), 5:2.5 (red), 5:1.25 (blue), 5:0.625 (green) and 5:0 (open square) mg/mL at pH 6 (a), 9 (b) and 12 (c) were used.

4.2.7 Trends in SAXS data

Having investigated trends in the bulk viscosity, the electrochromic behaviour and aggregation through absorbance spectroscopy, we can now investigate aggregation in more detail using SAXS. This technique will give us more detailed insight into the structures and interactions between components and whether we can link this information to the electrochemical behaviour of the systems we have investigated. While we have previously used SANS to investigate these systems, the length of time required to perform a SANS measurement (approximately one hour) is too long to measure the different combinations of components at different ratios and pHs. SAXS has a high flux and can perform measurements within seconds. Therefore, SAXS is the preferred technique. SAXS

measurements are run in H₂O instead of D₂O, and due to the lack of contrast between solvent and molecules, hollow cylinders are often poorly defined and data instead fits to a flexible cylinder model with a high Kuhn length.^{42,43} This has been observed with similar molecules to **1-NapFF** which form hollow cylinders.^{42,44,45} At 5 mg/mL the NDIs are weakly scattering compared to **1-NapFF**. We therefore anticipate that **1-NapFF** scattering may dominate the measurements.

4.2.7.1 Individual components

There are no significant differences in the scattering intensity of **NDI-F** as pH changes, Figure 4.14(b). This observation is comparable in **NDI-GF** at pH 12 and 9 but at pH 6, large aggregates are formed Figure 4.14(c). These trends (and trends in model fits) are consistent with those discussed in Chapter 3 (Table 4.12), however due to the weaker concentration of NDI, there are less significant differences in intensity than observed at 10 mg/mL. At 5 mg/mL and high pH, a sphere model is used, which is consistent with similar systems at high pH at 5 mg/mL.³⁸ Differences from Chapter 3 are likely an effect of lowering the concentration of NDI at high pH. At high pH, molecules are more likely to be dissociated,²⁷ especially at lower concentrations, and so modelling is more challenging.

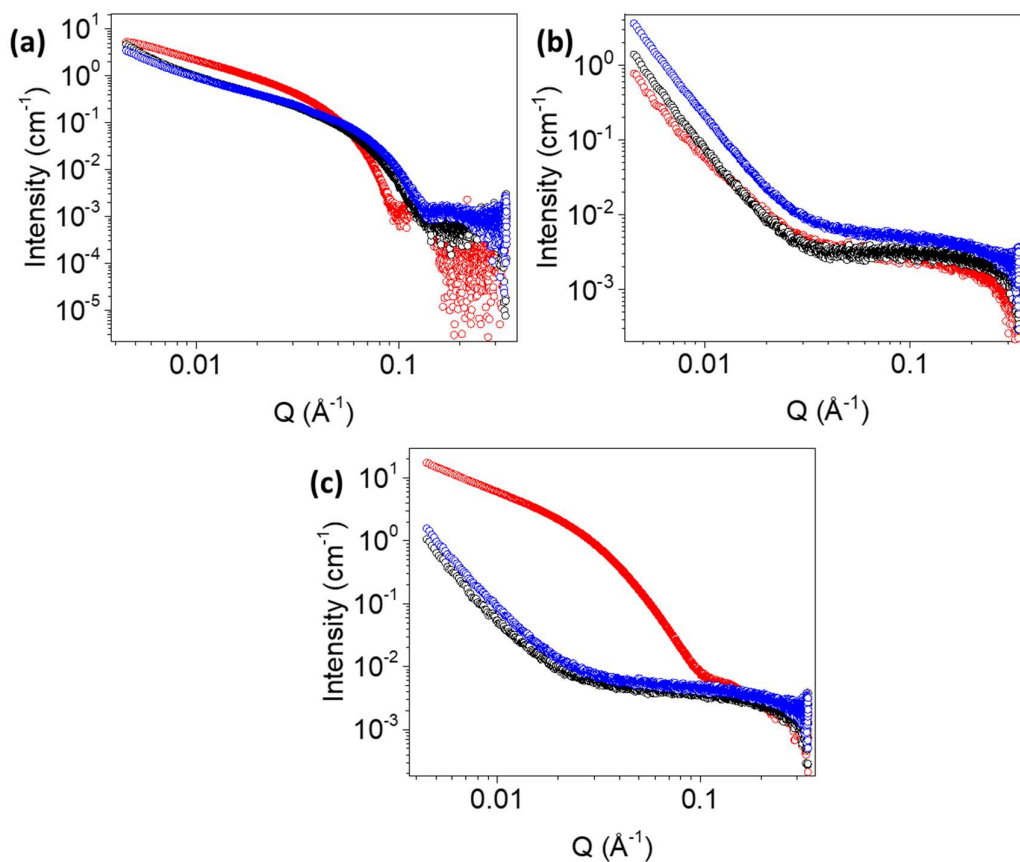


Figure 4.14. SAXS measurements of (a) **1-NapFF**, (b) **NDI-F** and (c) **NDI-GF** at 5 mg/mL. Solutions adjusted to pH 6 (red), 9 (black) and 12 (blue). Solutions contain 50% 0.1 M NaCl.

Table 4.12. Tabulated parameters from fits to SAXS data from single component systems. Full data set available in Figures A.4.16-A.4.25 and Tables A.4.1-A.4.9, Appendix. Modelled using various cylinders (see Appendix).

System (5 mg/mL)	Length (Å)	Error	Kuhn length (Å)	Error		
NDI-F pH 6	20.51	0.0943	N/A	N/A		
NDI-F pH 9	14.10	1.40	N/A	N/A		
NDI-F pH 12	N/A	N/A	N/A	N/A		
NDI-GF pH 6	423.94	0.110	70.99	0.0148		
NDI-GF pH 9	1.34E+58	1.52E+50	114.96	0.812		
NDI-GF pH 12	N/A	N/A	N/A	N/A		
1-NapFF pH 6	310.63	0.0308	310.32	0.973		
1-NapFF pH 9	9.85E+03	51.4	420.78	0.419		
1-NapFF pH 12	382.26	0.708	491.36	8.37		
System (5 mg/mL)	Radius (Å)	Error	Thickness (Å)	Error	Axis Ratio	Error
NDI-F pH 6	4.74	0.0339	5.08	0.0155	N/A	N/A
NDI-F pH 9	6.26	1.08	4.00	0.320	N/A	N/A
NDI-F pH 12	9.10	0.00550	N/A	N/A	N/A	N/A
NDI-GF pH 6	32.55	0.00215	N/A	N/A	2.04	1.24E-04
NDI-GF pH 9	6.03	0.0169	N/A	N/A	6.64	0.0185
NDI-GF pH 12	8.65	0.00468	N/A	N/A	N/A	N/A
1-NapFF pH 6	36.89	0.00367	N/A	N/A	1.30	1.21E-04
1-NapFF pH 9	23.75	0.00189	N/A	N/A	1.74	1.32E-04
1-NapFF pH 12	23.39	0.00197	N/A	N/A	1.38	1.08E-04

The scattering intensity of **1-NapFF** does not significantly change between pH 12 and 9, and there is an increase in intensity at low Q at pH 6 as with **NDI-GF**, Figure 4.14(a). At pH 9 and 12, **1-NapFF** is still above its first apparent pK_a and at pH 6 it will be on the border of its second (Table 4.1). We would therefore expect fewer differences between pH 9 and 12 than in NDI species. However, this investigation focuses upon the NDI species and so we stick to these three pH values for consistency. The similarity between length and Kuhn length is another indication that the flexible cylinders are actually hollow cylinders (but that the inner core is poorly defined due to low contrast between the molecules and the solvent).^{42,44,45} The length of a flexible cylinder is made up of locally stiff sections⁴⁶ (related to Kuhn length, Figure 4.15) and we would expect length to be larger than Kuhn length.

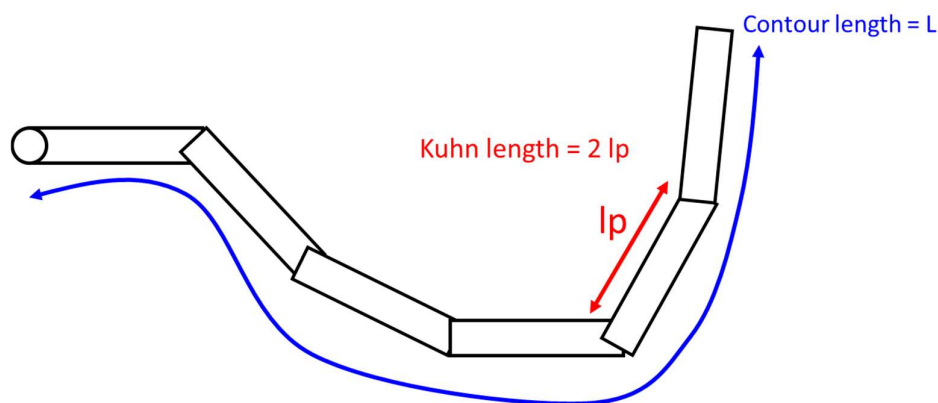


Figure 4.15. Cartoon representation of a flexible cylinder and Kuhn length.

As pH is lowered, aggregates become more flexible and larger (Kuhn length decreases and radii increases, Table 4.12) and the axis ratio increases and decreases again between pH 9 and 6 (Table 4.12). This observation suggests that the cylinders are elongating as pH drops and moving together to appear less or more spherical. The changes to **1-NapFF** are less significant than **NDI-GF** as pH drops, Figure 4.14(a and c), suggesting defined structures are present even at high pH. The ability to form structures at high pH could allow more interaction at high pH than two dispersed systems.

4.2.7.2 Multicomponent systems

Having assessed the single component systems, we can compare the scattering of the multicomponent systems. Some measurements contained kinks due to shear aligning of the sample in the thin SAXS capillaries.^{47,48} Form factor fitting described here assumes that structures in solution are randomly oriented and so aligned samples may lead to small errors in fitting, but we do not believe the shear is significant enough to cause large error. The 2D scattering plots do not show an extreme ‘bow-tie’ shape as has been reported under large shear.⁴⁸ An example of this is shown in Figure 4.16. In cases of shear alignment, the 2D scattering plots are shown with the data in the Appendix to indicate the unsymmetrical shape of the anisotropic 2D scattering. This phenomenon also occurs in the data of **1-NapFF** at pH 12, and scattering plots are shown for this data in Figure A.4.25, Appendix. These kinks (and sometimes large error at high Q) lead to a slightly higher value of χ^2 . For significant kinks, this section of the data is cut out to aid fitting. Residuals of fits are shown if a small kink in the data causes a particularly high χ^2 despite a good fit in the rest of the data. This data demonstrates that the kink is the reason for the poorer fit. A control 2D scattering plot of a measurement with no kink and of water is shown for comparison, Figures A.4.26-A.4.27, Appendix.

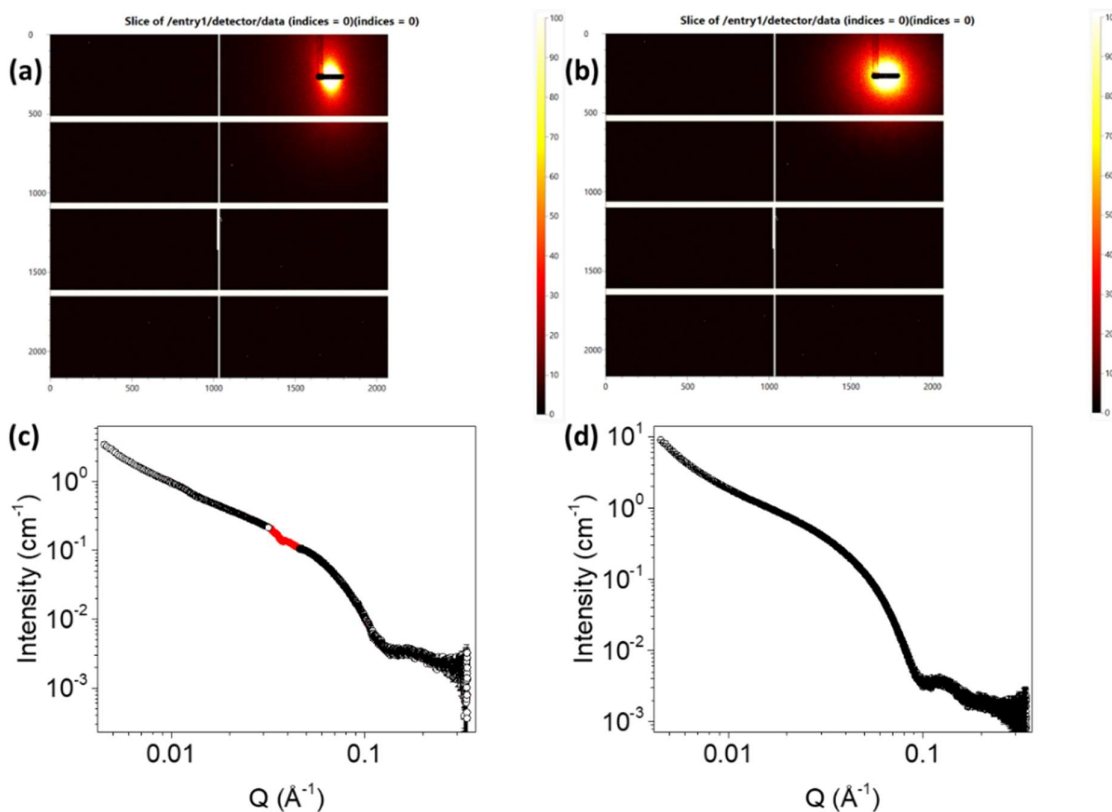


Figure 4.16. Raw detector data of 2D scattering plots of measurement taken from for a solution of **NDI-F:1-NapFF** 5:5 mg/mL adjusted to pH 9 (a) and 6 (b). Histogram plots are shown at a range of 0 to 100. Small angle X-ray scattering data for a solution of the same system at pH 9 (c) and 6 (d). (a) and (c) shows alignment causing a kink (red) highlighted in (c).

At all pH values, the scattering profile of the multicomponent systems are comparable to **1-NapFF** below $Q = 0.1 \text{ \AA}^{-1}$ (Figure 4.17). The influence of **NDI-F** and **NDI-GF** is apparent because the scattering of the multicomponent systems is not identical to the data of **1-NapFF**. All data fits to various cylindrical or spherical models, sometimes combined with power law where appropriate.

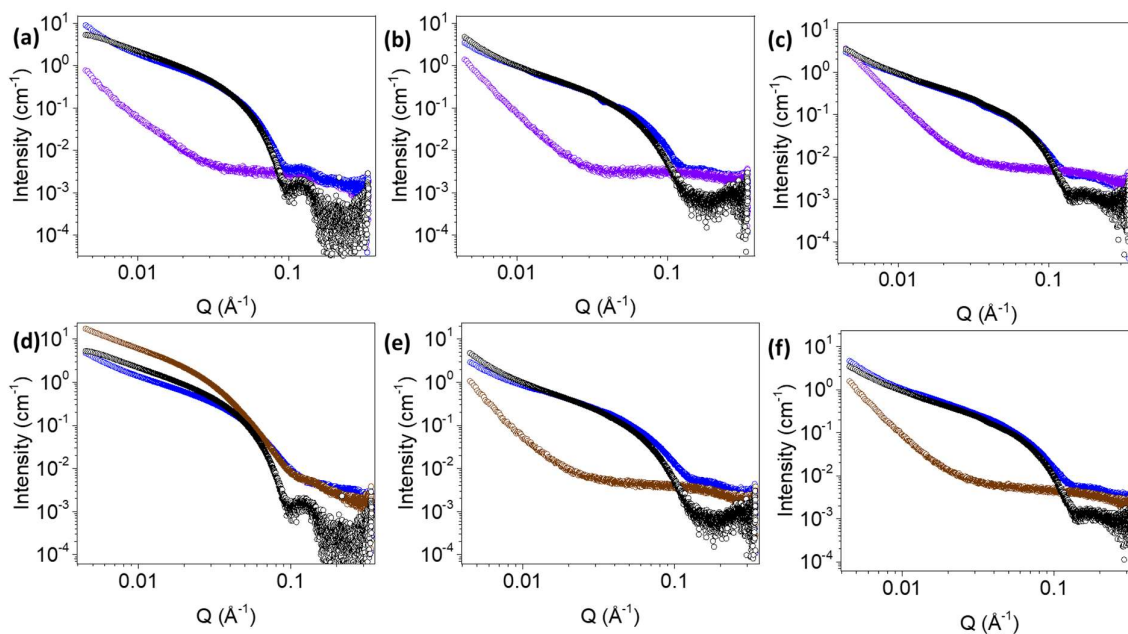


Figure 4.17. SAXS measurements of neutral **NDI-F** (purple) and **NDI-GF** (brown) at 5 mg/mL, **1-NapFF** (5mg/mL, black), and **NDI-R:1-NapFF** (5:5 mg/mL, blue) at pH 6 (a,d), 9 (b,e) and 12 (c,f). Multicomponent systems contain **NDI-F** (a-c), and **NDI-F** (d-f). Solutions contain 50% 0.1 M NaCl.

4.2.7.3 **NDI-GF:1-NapFF**

Data for **NDI-GF:1-NapFF** structures fit mostly to a flexible elliptical cylinder model combined with a power law. At certain ratios (5:2.5 mg/mL pH 6 and 5:5 and 5:1.25 mg/mL pH 9), an additional cylinder component is required, Table 4.13. At high pH, data fits to a flexible elliptical cylinder combined with a sphere (or cylinder at 5:1.25 mg/mL), Table 4.13. With the exception of 5:5 mg/mL **NDI-GF:1-NapFF** at pH 6, the Kuhn length of all ratios and pHs of this multicomponent system are lower than of **1-NapFF** alone, Table 4.12 and Table 4.13. These data suggest that both component structures are disrupted, but most significantly the **NDI-GF** structures as the shape of the scattering plot is closest to **1-NapFF**. This data suggests that the components are not co-assembling, but that some influence upon each other is likely.

Table 4.13. Tabulated parameters from fits to SAXS data from **NDI-GF:1-NapFF** systems. Full data set available in Figures A.4.28-A.4.40 and Tables A.4.10-A.4.21, Appendix. Data modelled as various cylinders (see Appendix).

System (mg/mL)	Kuhn length (Å)	Error	Radius (Å)	Error	Axis Ratio	Error	Radius B (Å)	Error
NDI-GF:1-NapFF (5:5) pH 6	349.11	1.19	26.33	0.00279	1.73	1.67E-04	N/A	N/A
NDI-GF:1-NapFF (5:5) pH 9	113.68	0.0732	14.58	0.00379	3.59	8.93E-04	30.38	0.00403
NDI-GF:1-NapFF (5:5) pH 12	244.22	0.537	22.90	0.00182	1.46	1.08E-04	6.97	0.00319
NDI-GF:1-NapFF (5:2.5) pH 6	202.70	0.446	31.16	0.00339	1.61	1.60E-04	N/A	N/A
NDI-GF:1-NapFF (5:2.5) pH 9	40.95	0.0271	36.88	0.00648	N/A	N/A	N/A	N/A
NDI-GF:1-NapFF (5:2.5) pH 12	250.75	0.313	22.43	0.00273	1.47	1.67E-04	6.84	0.00328
NDI-GF:1-NapFF (5:1.25) pH 6	59.58	0.0174	35.57	0.00331	1.87	1.60E-04	N/A	N/A
NDI-GF:1-NapFF (5:1.25) pH 9	50.17	0.237	84.21	0.622	3.00	0.0143	12.25	0.0181
NDI-GF:1-NapFF (5:1.25) pH 12	136.97	0.212	29.26	0.0230	2.90	0.00207	5.00	0.00292
NDI-GF:1-NapFF (5:0.625) pH 6	76.84	5.95E-05	34.96	0.00625	1.37	2.08E-04	4.90	0.00278
NDI-GF:1-NapFF (5:0.625) pH 9	207.73	1.01	31.44	0.0149	1.59	1.28E-04	N/A	N/A
NDI-GF:1-NapFF (5:0.625) pH 12	211.42	0.365	23.91	0.00363	1.35	1.89E-04	12.24	0.0128

Intensity of scattering is comparable across all ratios at pH 6, Figure 4.18(a). At pH 9 and 12, there is a significant reduction in scattering intensity at low-mid Q at 5:1.25 mg/mL ratio, Figure 4.18(b-c). In

these conditions, a second cylindrical component is required in modelling (Table 4.13). This observation suggests that larger networks of **1-NapFF** are significantly disrupted or broken (allowing **NDI-GF** structures to be better modelled). At this ratio, the parameters of fits are varying, showing significantly reduced Kuhn length, varying radii and very small cylinders in the second component, Table 4.13. Because **NDI-GF** is also highly scattering at pH 6, it is more likely to dominate scattering measurement as the concentration of **1-NapFF** decreases, which may be why at 5:1.25 and 5:0.625 mg/mL, the Kuhn length is more comparable to **NDI-GF** alone, Table 4.12 and Table 4.13. The parameters of the fits of **NDI-GF:1-NapFF** do not show clear trends that can be linked to the chronic properties observed, Table 4.13.

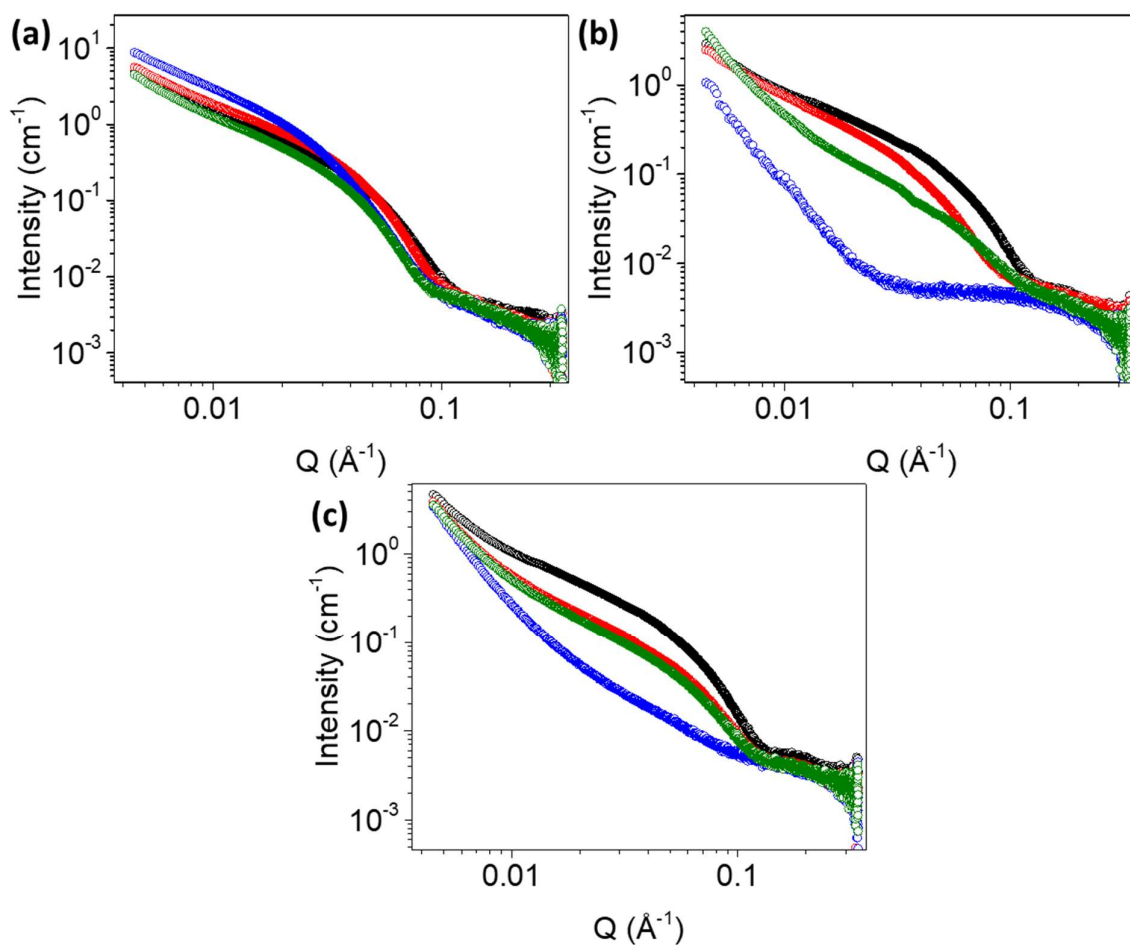


Figure 4.18. SAXS measurement of **NDI-GF:1-NapFF** at 5:5 (black), 5:2.5 (red), 5:1.25 (blue) and 5:0.625 (green) mg/mL at pH 6 (a), 9 (b) and 12 (c).

4.2.7.4 *NDI-F:1-NapFF*

Structures of **NDI-F** appear to have more influence within the multicomponent systems than **NDI-GF**. A hollow cylinder, cylinder or sphere component must be added to the model at all pH values, Table 4.14. In general, the Kuhn length of the **1-NapFF** component is comparable when **NDI-F** is added at pH 6, but slightly lower at pH 9 and 12, Table 4.12 and Table 4.14. Radii are also comparable, Table 4.12 and Table 4.14. These data suggests that well defined structures of both components exist heterogeneously. Based on previous observations, these structures may then interact further.

Table 4.14. Tabulated parameters from fits to SAXS data from **NDI-F:1-NapFF** systems. Full data set available in Figures A.4.41-A.4.55 and Tables A.4.22-A.4.33, Appendix. Modelled using various cylinders (see Appendix).

System (mg/mL)	Kuhn length (Å)	Error	Radius (Å)	Error	Axis Ratio	Error
NDI-F:1-NapFF (5:5) pH 6	317.28	0.487	32.97	0.00244	1.42	9.77E-05
NDI-F:1-NapFF (5:5) pH 9	242.53	0.468	19.30	0.00469	1.38	3.31E-04
NDI-F:1-NapFF (5:5) pH 12	302.58	0.289	24.78	0.00256	N/A	N/A
NDI-F:1-NapFF (5:2.5) pH 6	162.02	0.117	34.10	0.00581	1.64	2.53E-04
NDI-F:1-NapFF (5:2.5) pH 9	193.59	0.571	19.22	0.0105	2.39	0.00125
NDI-F:1-NapFF (5:2.5) pH 12	171.02	0.405	21.40	0.0101	7.17	0.00374
NDI-F:1-NapFF (5:1.25) pH 6	330.09	1.28	34.88	0.00517	1.48	1.99E-04
NDI-F:1-NapFF (5:1.25) pH 9	286.86	0.737	15.67	0.00428	N/A	N/A
NDI-F:1-NapFF (5:1.25) pH 12	208.48	0.288	22.38	0.00313	1.44	1.87E-04
NDI-F:1-NapFF (5:0.625) pH 6	240.99	0.286	35.81	0.00586	1.34	1.96E-04
NDI-F:1-NapFF (5:0.625) pH 9	228.08	0.367	26.51	0.00575	1.31	2.59E-04
NDI-F:1-NapFF (5:0.625) pH 12	344.68	1.22	28.22	0.00500	1.17	1.90E-04
System (mg/mL)	Radius B (Å)	Error	Thickness B (Å)	Error		
NDI-F:1-NapFF (5:5) pH 6	6.66	0.148	5.06	0.0583		
NDI-F:1-NapFF (5:5) pH 9	5.91	0.00493	23.42	0.00416		
NDI-F:1-NapFF (5:5) pH 12	14.29	0.0134	16.42	0.00784		
NDI-F:1-NapFF (5:2.5) pH 6	6.52	0.00741	N/A	N/A		
NDI-F:1-NapFF (5:2.5) pH 9	6.96	0.00421	N/A	N/A		
NDI-F:1-NapFF (5:2.5) pH 12	1.74	7.79E-04	N/A	N/A		
NDI-F:1-NapFF (5:1.25) pH 6	5.02	0.0439	5.05	0.0195		
NDI-F:1-NapFF (5:1.25) pH 9	12.94	0.0311	17.05	0.0172		
NDI-F:1-NapFF (5:1.25) pH 12	6.10	0.00324	N/A	N/A		
NDI-F:1-NapFF (5:0.625) pH 6	9.26	0.133	N/A	N/A		
NDI-F:1-NapFF (5:0.625) pH 9	10.07	0.00991	N/A	N/A		
NDI-F:1-NapFF (5:0.625) pH 12	12.72	0.0110	N/A	N/A		

The scattering intensities for all ratios and pHs are comparable (Figure 4.19), but at 5:2.5 mg/mL. The scattering intensity is weakest in mid Q at pH 9 and 12, Figure 4.19(a-c). At this ratio electrochemical colouration and Kuhn length is lower than other ratios across all pHs, Figure 4.19(d). At pH 6 and 9,

ratios 5:5 and 5:1.25 mg/mL, Kuhn length is higher than at other ratios (Figure 4.19(d)) and electrochemical colouration is most intense, Table 4.10. This observation suggests that the rigidity of **1-NapFF** structures is linked to electrochromic properties. At pH 9, 5:1.25 mg/mL (where unexpected high colouration intensity is observed, Table 4.10) the radii of **1-NapFF** decreases significantly and the radii of hollow cylinders increases, Table 4.14. This observation could suggest that the **1-NapFF** network is affected, allowing larger aggregates of **NDI-F** to form. Larger radii of this NDI have been linked to better electrochromic colouration (Chapter 3).

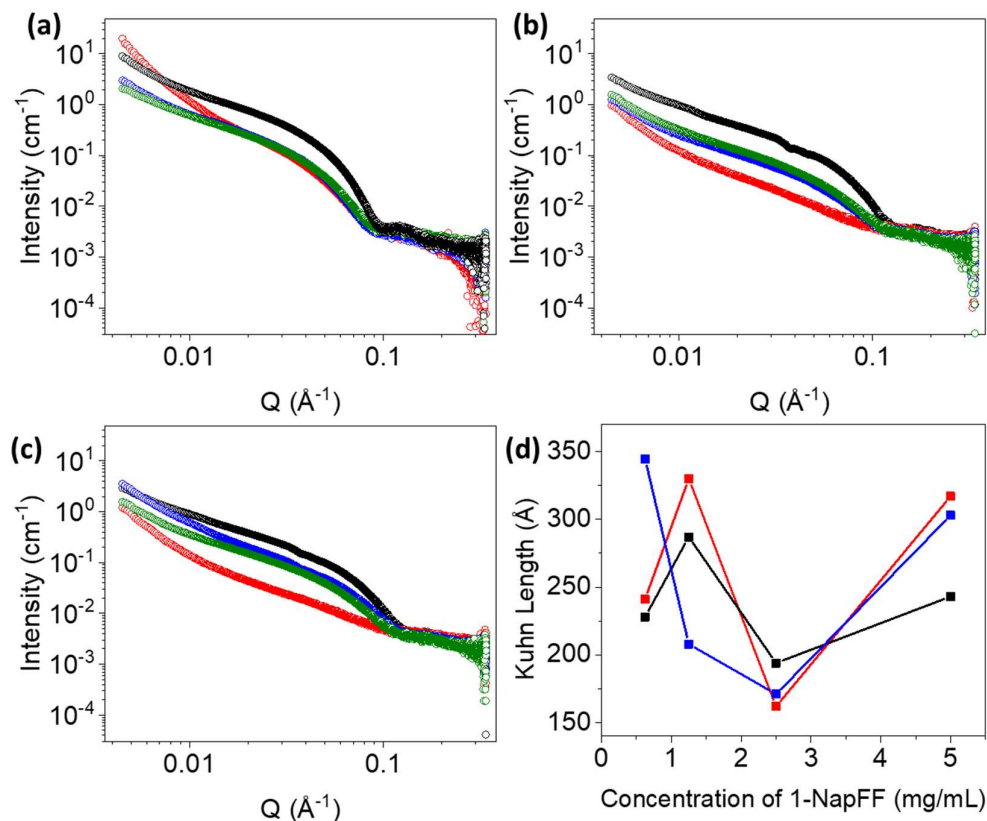


Figure 4.19. SAXS measurement of **NDI-F:1-NapFF** at 5:5 (black), 5:2.5 (red), 5:1.25 (blue) and 5:0.625 (green) mg/mL at pH 6 (a), 9 (b) and 12 (c). (d) plot showing how Kuhn length of model fits varies with concentration of **1-NapFF** in **NDI-F:1-NapFF** systems at pH 6 (red), 9 (black) and 12 (blue).

At pH 6 and 9, lower electrochemical colouration intensity was observed at 5:2.5 and 5:0.625 mg/mL compared to other multicomponent ratios, Table 4.10. Under these conditions, the NDI hollow cylinders are less well defined, and a cylinder or sphere (pH 9, 5:2.5 mg/mL) component is used in modelling instead, Table 4.14. The radii of these components are much lower than other ratios at pH 9 and more comparable with **NDI-F** alone at this pH, Figure 4.20(a). This observation could suggest that **NDI-F** forms larger structures with certain concentrations of **1-NapFF**, in conditions where **1-**

NapFF structures are most rigid, Table 4.14. This observation again is supported by previous findings relating larger radii to colour intensity in **NDI-F** (Chapter 3).

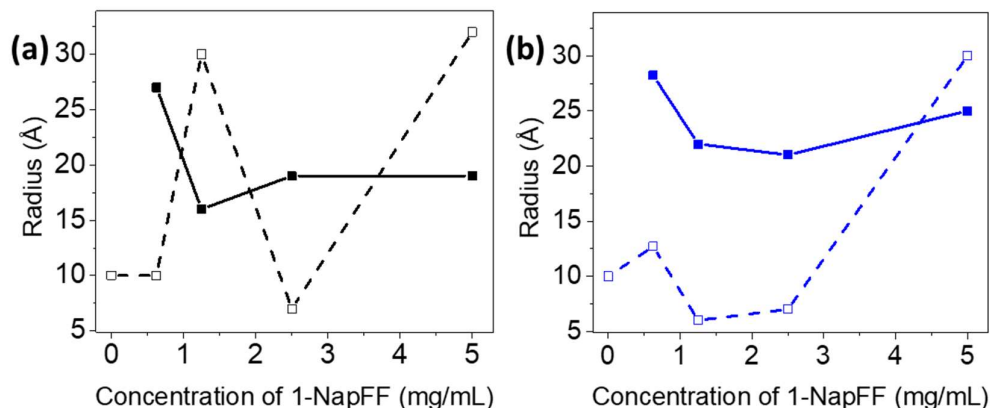


Figure 4.20. Plot showing how radii of **1-NapFF** (filled squares) and **NDI-F** (open squares) components fluctuates in models with concentration of **1-NapFF** in **NDI-F:1-NapFF** systems at pH 9 (a) and 12 (b).

At pH 12 ratios 5:5 and 5:0.625 mg/mL in **NDI-F:1-NapFF** systems produce spectra that when reduced are more comparable than at pH 9 and 6. Instead of a broad absorbance, defined peaks are observed, Figure 4.21. At these ratios, SAXS data fits to a flexible cylinder combined with a hollow cylinder or cylinder rather than a sphere (Table 4.14). Kuhn length of the **1-NapFF** component and radii of the **NDI-F** component are also largest at these ratios, Figure 4.19(d) and Figure 4.20(b). This observation is consistent with the trends of size and rigidity supporting radical formation (Chapter 3) and that when **NDI-F** is more defined by the model, we observe darker colouration. It is of note that radical production was enhanced at the poorest performing at pH of 12 (Chapter 2 and 3).

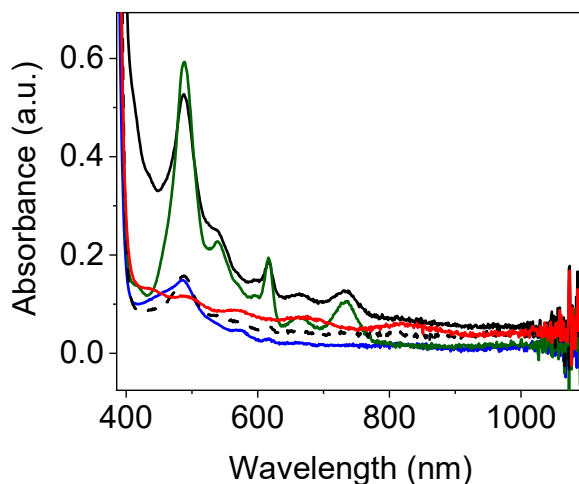


Figure 4.21. Absorbance spectra of solutions of reduced **NDI-F:1-NapFF** at pH 12 at ratios of 5:5 (black), 5:2.5 (red), 5:1.25 (blue), 5:0.625 (green) and 5:0 (dashed line) mg/mL. Spectra taken after 10 seconds of -2.5 V application.

4.2.7.5 Comparisons

The more defined two-cylinder model for the SAXS data and the increased electrochemical colouration suggest that **NDI-F** interacts more favourably with **1-NapFF** than **NDI-GF**. As **NDI-GF** can form gels, there may be some entanglement of fibres at low pH leading to disruption of NDI π stacking (leading to a decrease in electrochemical colouration as **1-NapFF** concentration increases, Table 4.11). Scattering intensity is fairly comparable in the multicomponent systems, A.4.56-A.4.58, Appendix. In general, **NDI-GF** systems have higher scattering intensity (because of the higher scattering of **NDI-GF** most likely) but at some ratios and pH, there are more significant differences when structures in one component appears to become disrupted, for example in **NDI-GF:1-NapFF** (5:1.25 mg/mL at pH 9, Figure A.4.57(c), Appendix) and **NDI-F:1-NapFF** (5:2.5 mg/mL at pH 12, Figure A.4.58(b), Appendix). The ratio of components, chemical structure of NDI and pH all influence aggregation, making these systems difficult to fully understand in detail.

NDI-F appears to have the strongest interaction with **1-NapFF** (even at high pH) which may be due to a matching of size and chemical structure (for example, the phenylalanine of **NDI-F** may be able to π -stack with **1-NapFF** in a way that does not compromise the π -stacking of the NDIs). Or there could be interaction because both systems form hollow cylinders. As a result, the colouration of **NDI-F** is enhanced at several ratios. As **NDI-GF** colouration was diminished by the addition of **1-NapFF**, these systems were not investigated further in this chapter.

4.2.8 Effect of second component upon cyclability

Based on the intensity of reduced colouration and the efficiency of electrochemical oxidation **NDI-F** systems were found to have one or two “ideal” pH and ratios of **NDI-F:1-NapFF** to test in cyclability experiments. We expected more viscous systems to have better diffusion rates and therefore better cyclability, and so these experiments will test this hypothesis as well as evaluate the long-term use of our best performing multicomponent systems. We used a 5 x 5 FTO window cell for this testing and found that reduction and oxidation potentials are not significantly shifted in larger cell, Table 4.15.

Table 4.15. Tabulated data from cyclic voltammograms of tabulated systems performed in 5 x 5 FTO window cell at 0.2 V/s scan rate. Full data available in Figure A.5.59, Appendix.

System (NDI-F:1-NapFF mg/mL)	Reduction Potential (V)	Oxidation Potential (V)
NDI-F (5:0) pH 6	-2.4	(undefined) approximately 0.9 V
NDI-F (5:5) pH 6	-2.3	(undefined) approximately 1 V
NDI-F (5:1.25) pH 9	-2.3	(undefined) approximately 1 V

NDI-F:1-NapFF systems became significantly darker than **NDI-F** systems upon reduction (at 5:5 mg/mL pH 6 and 5:1.25 mg/mL pH 9, Figure 4.10(a-b)). Both ratios demonstrated an improvement in the number of cycles achieved, Figure 4.22(a). The 5:5 mg/mL ratio at pH 6 was able to achieve a larger number of cycles, a quicker average oxidation time between 6 and 10 cycles and a more gradual increase in oxidation time with cycling than the 5:1.25 mg/mL ratio at pH 9, Figure 4.22(a). For this reason, 5:5 mg/mL at pH 6 was identified as this system’s ideal conditions. These data suggest that aggregation is a more dominating factor than diffusion (based on no linear trend between colouration and viscosity). Our original hypothesis is supported, and the use of a second component shows some improvement to cyclability. Aggregation will also affect diffusion however, and so it is difficult to directly separate these variables.

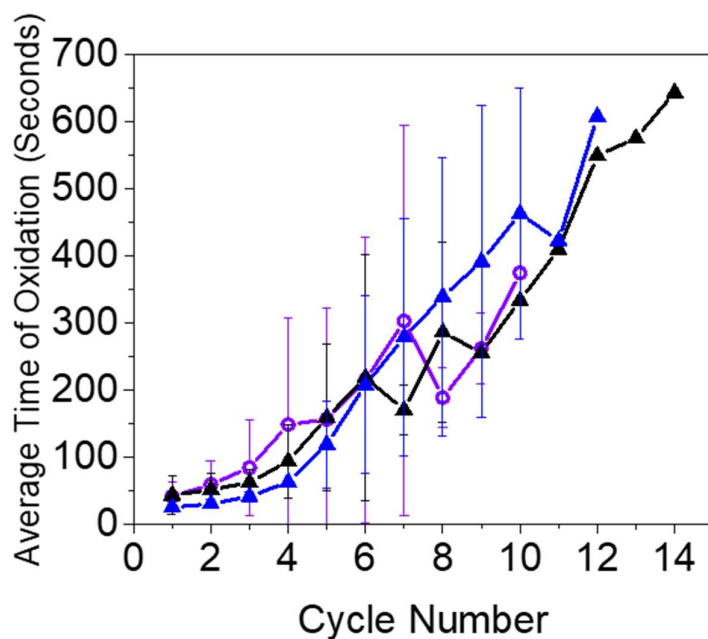


Figure 4.22. Plot showing how time to reach a state without colouration fluctuates with electrochemical cycling between a reduced and oxidised state. Measurements carried out using solutions of 5 mg/mL of **NDI-F** (purple) and mixes of 5:5 mg/mL **NDI-F:1-NapFF** at pH 6 (black), 5:1.25 mg/mL **NDI-F:1-NapFF** at pH 9 (blue). Measurements are taken as an average of triplicate measurements and error bars calculated from standard deviation.

4.2.8.1.1 Buffering

As for the single component systems (Chapter 3), the best performing multicomponent system was buffered to an ideal pH. Before moving forward, the effect of buffering must be investigated. We found that buffering decreases viscosity of **1-NapFF** containing systems, Table 4.16. This observation may be due to an element of charge or charge shielding from the higher salt concentration disrupting structures.

Table 4.16. Tabulated average apparent viscosity at a shear rate of 1 s^{-1} for single and multicomponent systems buffered and unbuffered. All solutions adjusted to pH 6. Full data set in Figure A.4.60, Appendix.

System (mg/mL)	Average apparent viscosity at 1 s^{-1} shear at pH 6 (Pa·s)	Average apparent viscosity at 1 s^{-1} shear buffered to pH 6 (Pa·s)
NDI-F:1-NapFF (5:5)	6.144	1.318
1-NapFF (5)	50.867	4.424
NDI-F (5)	0.001	0.008

The absorbance spectrum of **1-NapFF** is not significantly affected by buffering, Figure 4.23(a). In terms of scattering, the ‘hump’ at high Q is less well defined in buffered solutions, Figure 4.23(b), but otherwise scattering profiles are comparable upon using a buffer.

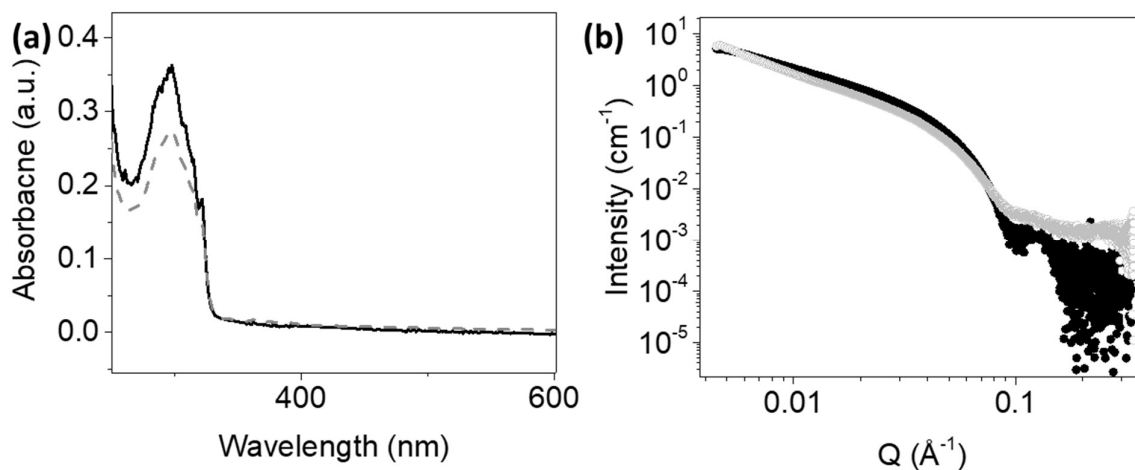


Figure 4.23. (a) Absorbance spectra (b) SAXS measurement of **1-NapFF** 5 mg/mL at pH 6. Solutions are buffered (grey) and unbuffered (black).

The fit parameters are also comparable, Table 4.17. The shorter length of cylinders may be the reason for decreased viscosity, Table 4.16-Table 4.17. In buffered systems, the radii decrease slightly, and the axis ratio increases, which suggests that fibres are more elliptical, mostly likely due to increased salt concentration leading to higher ionic strength of solution. These observations are not significant but should be considered.

Table 4.17. Tabulated parameters from fits to SAXS data from **1-NapFF** at 5 mg/mL buffered and unbuffered at pH 6. Full data set available in Figures A.4.22 and A.4.61 and Tables A.4.7 and A.4.34, Appendix. Flexible elliptical cylindrical models used.

1-NapFF mg/mL pH 6	5	Length (Å)	Error	Kuhn length (Å)	Error	Radius (Å)	Error	Axis Ratio	Error
Unbuffered		310.63	0.0308	310.32	0.973	36.89	0.00367	N/A	N/A
Buffered		250.95	0.237	308.02	1.01	32.95	0.00318	1.60	1.43E-03

4.2.8.1.1.1 NDI-F containing systems

When buffered, the molecular packing of **NDI-F** changes, both as a single and multicomponent system, Figure 4.24. The absorbance at 385 nm decreases relevant to the absorbance at 365 nm, which is a

spectrum comparable with buffered **NDI-F** discussed in Chapter 3. These data suggest this NDI is sensitive to salt concentration.

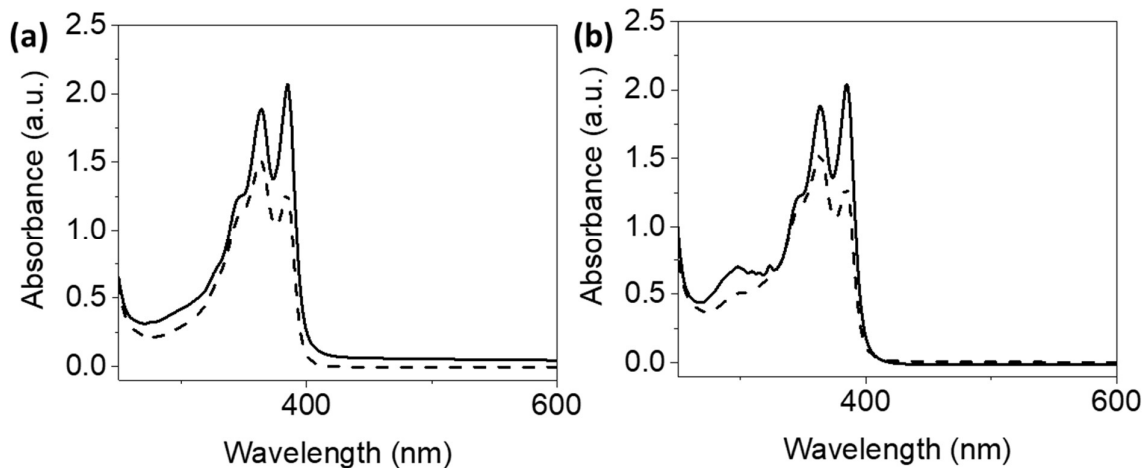


Figure 4.24. Absorbance spectra of neutral state of buffered (dashed line) and unbuffered (solid line) (a) **NDI-F** 5 mg/mL and (b) **NDI-F:1-NapFF** 5:5 mg/mL adjusted to pH 6.

In terms of the redox potentials, the redox peaks shift to a less negative and larger positive potential upon buffering, Table 4.18. The shifts are in the order of approximately 0.4-0.5 V and in both sizes of FTO glass. The second reduction peak of **NDI-F** can be seen in buffered solutions, suggesting it has shifted from a range outside of the voltammogram in unbuffered solutions. Similar trends are observed in 5:5 mg/mL and 5 mg/mL, Table 4.18.

Table 4.18. Tabulated data of redox potentials taken from cyclic voltammograms taken at 0.2 V/s of **NDI-F** 5 mg/mL and **NDI-F:1-NapFF** 5:5 mg/mL, buffered and unbuffered at pH 6 in different sizes of FTO window cell. Full data sets available in Figure A.4.62, Appendix.

System (mg/mL)	Reduction Potential(s) (V)	Current (μ A)	Oxidation Potential(s) (V)	Current (μ A)
NDI-F (5) buffered in 1 x 1 FTO window cell	-2.3, -2.9	-791, -859	0.01	275
NDI-F (5) unbuffered in 1 x 1 FTO window cell	-2.7	-443	0.6	85
NDI-F (5) buffered in 5 x 5 FTO window cell	-2.7, -3.2	-7022, -8151	0.5	2092
NDI-F (5) unbuffered in 5 x 5 FTO window cell	-2.4	-2.4	(undefined) approximately 0.9 V	414
NDI-F:1-NapFF (5:5) buffered in 1 x 1 FTO window cell	-2.3, -2.9	-589, -809	0.1	401
NDI-F:1-NapFF (5:5) unbuffered in 1 x 1 FTO window cell	-2.7, -3.2	-706, -818	0.4	256
NDI-F:1-NapFF (5:5) buffered in 5 x 5 FTO window cell	-2.9	-9128	0.77	1733
NDI-F:1-NapFF (5:5) unbuffered in 5 x 5 FTO window cell	-2.3	-1647	(undefined) approximately 1 V	752

The redox potentials used for cycling are kept consistent for the measurements, and as previously described in Chapter 3, we observe an increase in colouration intensity and electrochemical oxidation in buffered **NDI-F** systems, Figure 4.25(a and c). However, there is no significant difference when 5:5 mg/mL multicomponent systems are buffered, Figure 4.25(b and d).

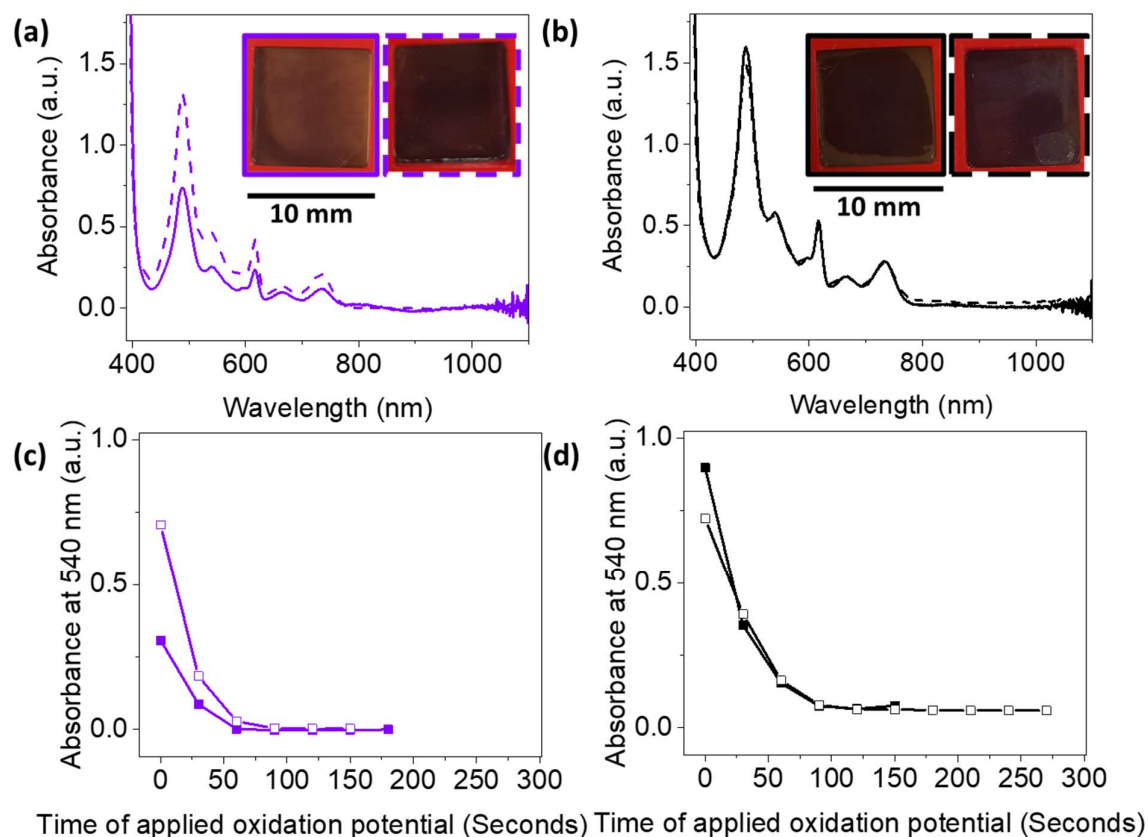


Figure 4.25. (a-b) Absorbance spectra of reduced state after application of -2.5 V for 10 seconds (c-d) Measurement of absorbance at 540 nm as an oxidising potential of 0.5 V was applied for 5 minutes after 20 seconds of reduction with -2.5 V. Solutions of buffered (dashed line/open square) and unbuffered (solid line/filled square) (a/c) **NDI-F** 5 mg/mL and (b/d) **NDI-F:1-NapFF** 5:5 mg/mL all adjusted to pH 6 were used. Images showing colouration by eye after reduction are included as insets of (a-b).

As previously observed for **NDI-I** (Chapter 3), buffering has the effect of improving cyclability of **NDI-F** by maintaining the ideal pH of the system, Figure 4.26(a). This trend is also observed in the multicomponent system, Figure 4.26(b). Comparing buffered systems, **NDI-F** as a single component system is more cyclable and demonstrates faster electrochemical oxidation than the multicomponent system, Figure 4.26(c). The additional viscous component does not improve cyclability, however, the multicomponent system does improve the colouration of the electrochemical reduction, Figure 4.25(a-b) and so the additional component does have advantages. These data suggests that the addition of the **1-NapFF** to change diffusion rates and viscosity does not fully solve our cyclability issues.

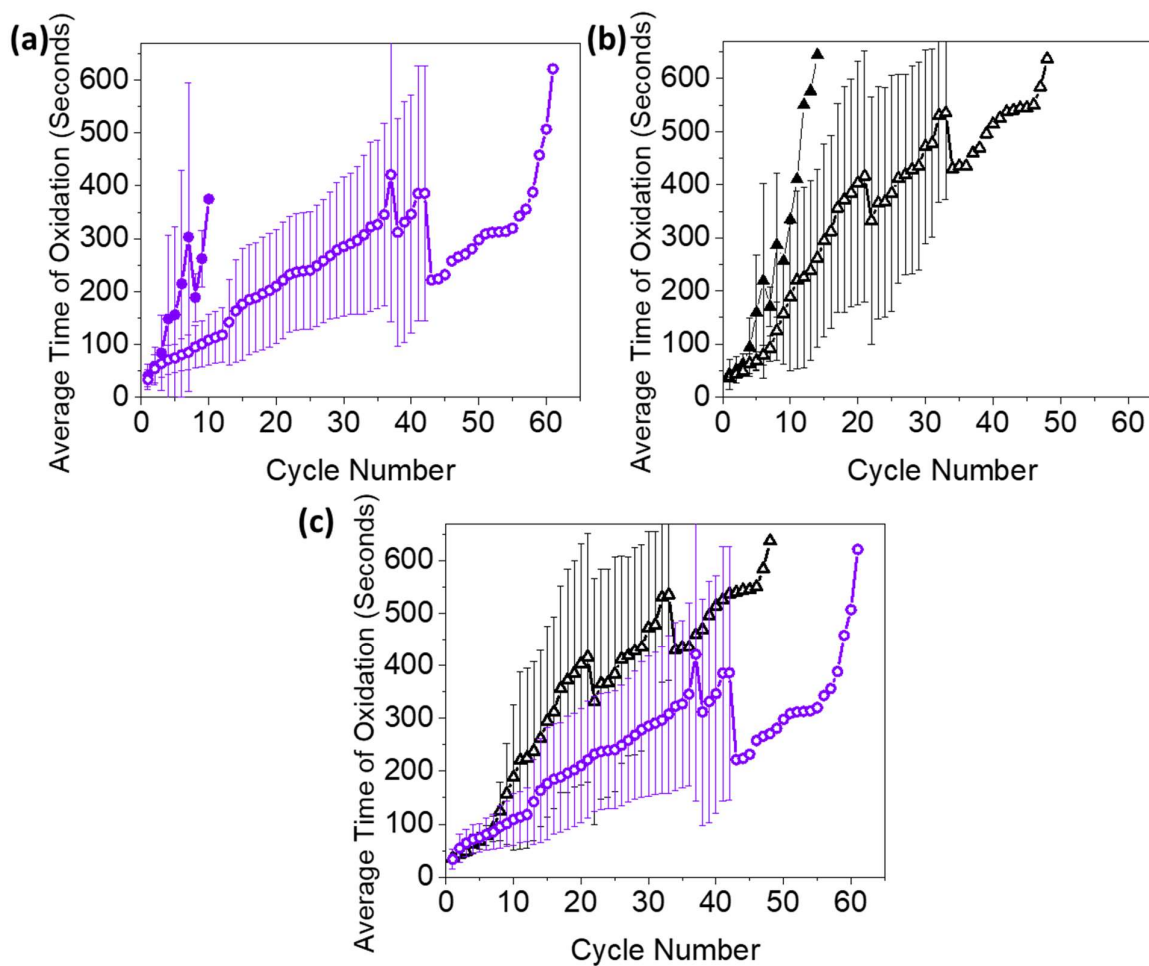


Figure 4.26. Plots showing how time to reach a state without colouration fluctuates with electrochemical cycling between a reduced and oxidised state. Measurements of buffered (open shape) and unbuffered (filled shape) **NDI-F** 5 mg/mL (purple) and **NDI-F:1-NapFF** 5:5 mg/mL (black) adjusted to pH 6. Measurements are taken as an average of triplicate measurements and error bars calculated from standard deviation.

In terms of aggregation, the use of a buffer results in lower scattering intensity for **NDI-F** and **NDI-F:1-NapFF** at low Q (Figure 4.27) and higher scattering intensity at high Q in **NDI-F:1-NapFF**, Figure 4.27(b). As with **1-NapFF** (Figure 4.23) the ‘bump’ at high Q is less defined in buffered solutions, Figure 4.27(b).

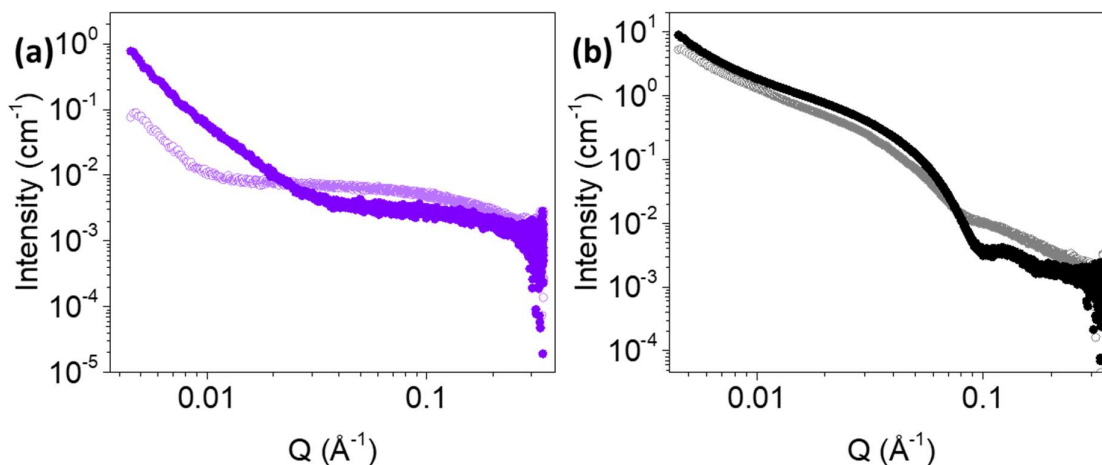


Figure 4.27. SAXS measurement of neutral (a) **NDI-F** 5 mg/mL and (b) **NDI-F:1-NapFF** 5:5 mg/mL at pH 6. Solutions are buffered (light lilac and grey) and unbuffered (purple and black colour).

Trends of a larger axis ratio and a reduction in Kuhn length comparable to **1-NapFF** are observed (Table 4.17 and Table 4.19) upon buffering multicomponent systems. While the radii of **NDI-F** are slightly larger upon buffering, the radii of **NDI-F** in the multicomponent systems remain comparable, Table 4.19. This observation may explain why colouration is not improved in the multicomponent buffered system. None of these changes are significant so we assume changes to aggregation are subtle and that a change in molecular packing has the most significant affect.

Table 4.19. Tabulated parameters from fits to SAXS data from **NDI-F** and **NDI-F:1-NapFF** systems. Full data set available in Figures A.4.16, A.4.41 and A.4.63-A.4.64 and Tables A.4.1, A.4.22 and A.4.35-A.4.36, Appendix. Modelled using various cylinders (see Appendix).

System (mg/mL) pH 6	Kuhn length (Å)	Error	Radius (Å)	Error	Axis Ratio	Error
NDI-F (5) unbuffered	N/A	N/A	N/A	N/A	N/A	N/A
NDI-F (5) buffered	N/A	N/A	N/A	N/A	N/A	N/A
NDI-F:1-NapFF (5:5) unbuffered	317.28	0.487	32.97	0.00244	1.42	9.77E-05
NDI-F:1-NapFF (5:5) buffered	304.54	0.573	32.90	0.00319	1.72	1.54E-04
System (mg/mL) pH 6	Radius B (Å)	Error	Thickness B (Å)	Error		
NDI-F (5) unbuffered	4.74	0.0338	5.08	0.0155		
NDI-F (5) buffered	9.12	0.106	5.27	0.0359		
NDI-F:1-NapFF (5:5) unbuffered	6.66	0.148	5.06	0.0583		
NDI-F:1-NapFF (5:5) buffered	4.84	0.0108	6.34	0.00562		

4.2.9 Effect of use upon aggregation

In Chapter 3, we analysed the stability of our systems in terms of aggregation after periods of cycling. This method is repeated to ascertain whether the same trends are observed in multicomponent systems and whether **1-NapFF** has any stabilising influence over the aggregates of **NDI-F**.

Due to the weak scattering of **NDI-F** at 5 mg/mL, fits to the data collected may not be fully representative. The scattering intensity is comparable upon cycling, increasing slightly over time at low Q, Figure 4.28(b). This trend is also observed in the multicomponent system with cycling, Figure 4.28(a). The parameters of **NDI-F** and the multicomponent system do not significantly change with cycling, Table 4.20. The radius increases slightly, and axis ratio decreases after 50 cycles, Table 4.20. This data suggests that cycling has minimal influence upon aggregation which is a positive result in terms of the long-term stability of these systems. The multicomponent system did not improve cyclability which suggests that the complexities of the multicomponent system have added in other factors besides diffusion. As the systems do not seem to be degrading or breaking down, the observed lack of long-term cyclability may be due to the inherent inefficiency of the oxidation process in this set-up, possibly due to the lower potential and current of this process compared to reduction.

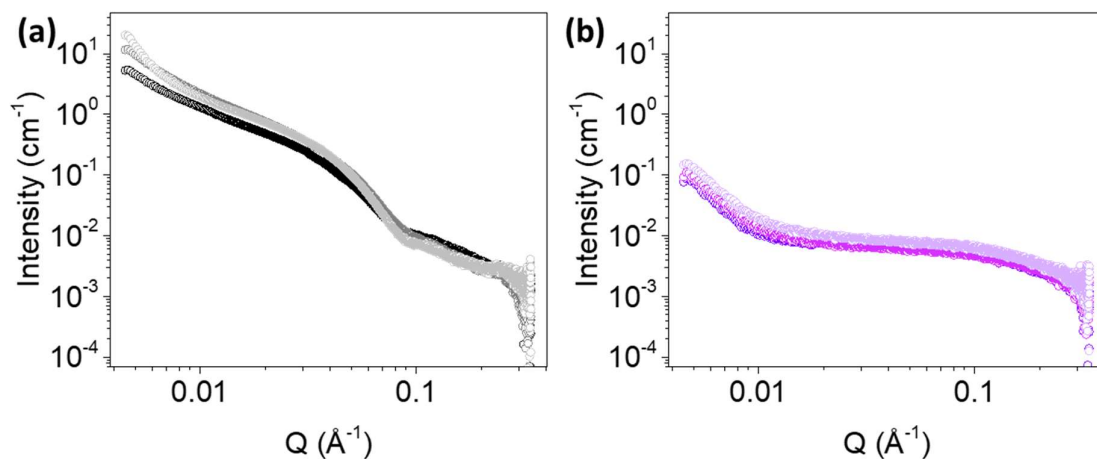


Figure 4.28. SAXS measurement of relaxed buffered (a) **NDI-F:1-NapFF** 5:1.5 mg/mL and (b) **NDI-F** 5 mg/mL at pH 6. Solutions are measured after 0 (black/purple), 1 (grey/lilac) and 50 (light grey/light lilac) electrochemical cycles.

Table 4.20. Tabulated parameters from fits to SAXS data from **NDI-F** and **NDI-F:1-NapFF** systems. Full data set available in Figures A.4.16, A.4.41 and A.4.65-A.4.68 and Tables A.4.1, A.4.22 and A.4.37-A.4.40, Appendix. Modelled using various cylinders (see Appendix).

Buffered System (mg/mL)	Kuhn length (Å)	Error	Radius (Å)	Error	Axis Ratio	Error
NDI-F (5) pre-cycled	N/A	N/A	N/A	N/A	N/A	N/A
NDI-F (5) after 1 cycle	N/A	N/A	N/A	N/A	N/A	N/A
NDI-F (5) after 50 cycles	N/A	N/A	N/A	N/A	N/A	N/A
NDI-F:1-NapFF (5:5) pre-cycled	304.54	0.573	32.90	0.00319	1.72	1.54E-04
NDI-F:1-NapFF (5:5) after 1 cycle	298.49	0.217	32.00	0.00222	1.68	1.09-04
NDI-F:1-NapFF (5:5) after 50 cycles	307.39	0.153	34.87	0.00229	1.52	9.44E-05
Buffered System (mg/mL)	Radius B (Å)	Error	Thickness B (Å)	Error		
NDI-F (5) pre-cycled	9.12	0.106	5.27	0.0359		
NDI-F (5) after 1 cycle	5.06	0.113	3.91	0.0326		
NDI-F (5) after 50 cycles	9.54	0.0711	5.26	0.0243		
NDI-F:1-NapFF (5:5) pre-cycled	4.84	0.0108	6.34	0.00562		
NDI-F:1-NapFF (5:5) after 1 cycle	4.87	0.0137	6.53	0.00722		
NDI-F:1-NapFF (5:5) after 50 cycles	4.74	0.0225	7.46	0.0127		

4.2.10 Heat-cooling **NDI-F** containing systems

In very similar systems to **1-NapFF**, the process of heating to 40 °C and allowing to cool results in a significantly increased viscosity above approximately 5 mg/mL and at pH 9.48.³⁷ This change does not occur until solutions have been allowed to cool and is attributed to a partial dehydration of the core resulting in an extension of fibre length, a decrease in radius and flexibility and a change in packing.³⁷ The result is that solutions become self-supporting liquids. From this report we would expect increased viscosity at pH 12 for **1-NapFF** but we do not know the effect heat-cooling will have upon **NDI-F**, nor do we know if the mixed multicomponent will have differing reactions to heat-cooling than **1-NapFF**. Our systems contain salt, so this factor may also trigger a difference in the heat-cool response to previous reports. If an increase in viscosity is observed, it may improve cyclability. For this reason, we took the best performing system (**NDI-F:1-NapFF**) forward and investigated the effects of heat-cooling upon viscosity, electrochromic behaviour and cyclability. Worm-like micelles are thought to be present in **1-NapFF** from around 1 mg/mL and so we expect most (if not all) ratios in multicomponent systems could potentially respond to heat-cooling processing. If not cyclability, then maybe a further improvement in radical formation could be observed. By adding heat into the system, we may overcome an energy barrier and allow different aggregation of components.

Viscosity measurements were carried out on the plate of the rheometer to minimise transfer and stress upon the sample, which may affect aggregates. **NDI-F** has increased viscosity across all pH values but as this value is so low initially, so the new viscosity is still comparable to water, Table 4.21. Across all pH values at 2.5 mg/mL and lower (and across all concentrations at pH 9 and 12), **1-NapFF** systems demonstrated an increase in viscosity upon heat-cooling, Table 4.21 The increased viscosity is most significant at pH 12 which is expected as it is the only pH we investigated above pH 9.48.³⁷ At pH 6 at 5 mg/mL there is a significant drop in viscosity, Table 4.21. We would anticipate this system to be the most 'crowded' as it contains the highest concentration and because aggregates are typically larger or more complex at lower pH.^{27,49} Therefore, the structures may not have enough space to extend as they do at higher pH or lower concentrations. Despite this decrease, this concentration and pH system is still the most viscous compared to heat-cooled **1-NapFF** at other pH and concentrations.

Table 4.21. Tabulated average apparent viscosity at a shear rate of 1 s^{-1} for **NDI-F** 5 mg/mL and **1-NapFF** and **NDI-F:1-NapFF** at different ratios and pH after heating to $40 \text{ }^\circ\text{C}$ and allowing to cool for 30 minutes. Full data sets of available in Figures A.4.6 and A.4.69-A.4.70, Appendix. Heat-cooled data is shown as red text. All solutions contain 50% 0.1 M NaCl.

System (mg/mL)	Apparent viscosity at 1 s^{-1} shear at pH 6 (Pa·s)	Apparent viscosity at 1 s^{-1} shear at pH 6 after heat cool (Pa·s)	Apparent viscosity at 1 s^{-1} shear at pH 9 (Pa·s)	Apparent viscosity at 1 s^{-1} shear at pH 9 after heat cool (Pa·s)	Apparent viscosity at 1 s^{-1} shear at pH 12 (Pa·s)	Apparent viscosity at 1 s^{-1} shear at pH 12 after heat cool (Pa·s)
NDI-F (5)	0.001	0.005	0.001	0.002	0.001	0.005
1-NapFF (5)	50.867	9.880	0.219	0.796	0.126	1.533
1-NapFF (2.5)	8.387	9.470	0.063	0.241	0.039	0.488
1-NapFF (1.25)	0.122	0.500	0.010	0.124	0.032	0.216
1-NapFF (0.625)	0.022	0.182	0.005	0.045	0.015	0.134
NDI-F:1-NapFF (5:5)	6.144	2.212	0.180	1.425	2.023	0.799
NDI-F:1-NapFF (5:2.5)	7.323	0.072	0.067	0.063	2.452	0.590
NDI-F:1-NapFF (5:1.25)	0.107	0.470	0.048	0.055	0.198	0.133
NDI-F:1-NapFF (5:0.625)	0.021	0.158	0.001	0.032	0.093	0.040

In multicomponent systems, we see a significant difference in trends with heat-cooling. At every ratio at pH 12, there is a decrease in viscosity, Table 4.21, the opposite trend to single component **1-NapFF**. At pH 9, viscosity increases at 5:5 and 5:0.625 mg/mL but is comparable at 5:2.5 and 5:1.25 mg/mL. At pH 6 we observed a decrease in viscosity at 5:5 and 5:2.5 mg/mL but an increase at 5:1.25 and 5:0.625 mg/mL. At 5:2.5 mg/mL, pH 6, the most significant decrease in viscosity is observed (Table 4.21). This ratio showed the weakest scattering at pH 9 and 12 and had a much lower Kuhn length than other ratios at pH 6 pre heat-cooling (suggesting the **1-NapFF** structures are significantly less rigid), Table 4.14. These observations coupled with the trends in viscosity suggests that aggregates are less stable at this ratio and are perhaps broken apart by heat-cooling.

Compared to single component **1-NapFF**, all multicomponent systems across all pHs (with the exception of 5:5 mg/mL at pH 9 and 5:2.5 mg/mL at pH 12) have a lower viscosity (which is not observed in solutions before heat-cooling). This observation suggests that heat-cooling leads to a change in the physical properties of mixes of **NDI-F:1-NapFF**, and further supports our hypothesis that components are interacting with each other, influencing the properties of **NDI-F**. Further investigation into the structures and chromic properties of these systems upon heat-cooling was carried out.

4.2.10.1.1 Aggregation and heat-cooling

We must now establish whether heat cooling has any impact upon the aggregation of the systems (both as single and multicomponent). As the physical property of viscosity changes, we expect some changes to aggregation, but we do not expect these to be significant.³⁷ Firstly we assess the molecular packing using absorbance spectroscopy.

When heat-cooled, the absorbance spectra of **NDI-F,1-NapFF** and **NDI-F:1-NapFF** does not greatly alter, Figure A.4.71, Appendix. There are some spectra which show a subtle change in molecular packing as suggested by a change in the ratios of the **NDI-F** absorbances previously discussed. **NDI-F** at all ratios of **NDI-F:1-NapFF** (except for 5:1.25 mg/mL) at pH 12 show a loss of the small shoulder at 385 nm, Figure 4.29. This is most significant at 5:0 and 5:5 mg/mL ratios, Figure 4.29(a-b). Heat-cooling has most affect upon the absorbance at pH 12 (under which conditions, absorbances are broad and undefined and molecules are more dispersed). This observation (coupled with the loss of viscosity at high pH) suggests that heat-cooling could be disrupting or changing the interaction between components at high pH.

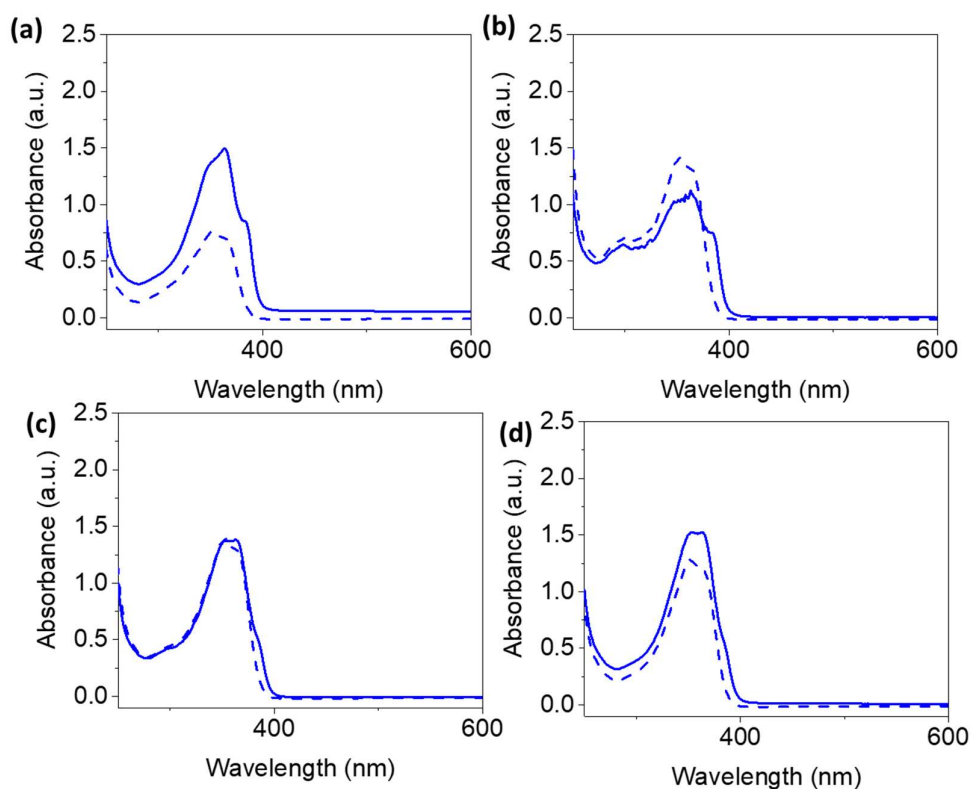


Figure 4.29. Absorbance spectra of neutral **NDI-F:1-NapFF** at pH 12 before (solid line) and after (dashed line) a heat-cool transition (heating to 40 °C and allowing to cool for 30 minutes) at (a) 5:0, (b) 5:5, (c) 5:2.5, (d) 5:0.625 mg/mL.

At pH 6, ratios of 5:1.25 and 5:0.625 mg/mL show a subtle change in the ratio of absorbances, Figure 4.30, which suggests small changes to molecular packing. At these ratios at pH 6, viscosity increased upon heat-cooling, Table 4.21. SAXS will give us further insight into the structures themselves. The trends in packing changes are not consistent. At lower concentration of **1-NapFF** at pH 6, the absorbance at 385 nm becomes smaller with heat-cooling, making the ratio at 365 and 385 nm become closer to 1:1. At 5:1.25 mg/mL, the absorbance at 385 nm gets larger from a ratio more comparable with 1:1. This observation shows how subtle changes to the multicomponent system ratio affect the reaction to heat-cooling.

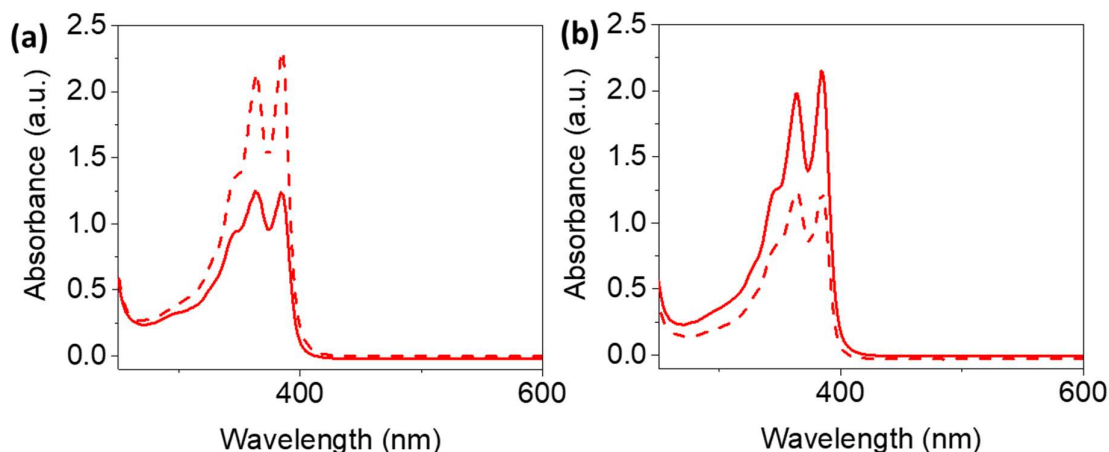


Figure 4.30. Absorbance spectra of neutral **NDI-F:1-NapFF** at pH 6 before (solid line) and after (dashed line) a heat-cool transition (heating to 40 °C and allowing to cool for 30 minutes) at (a) 5:1.25 and (b) 5:0.625 mg/mL.

4.2.10.1.2 The reduced state

Having identified some changes at certain ratios of **NDI-F:1-NapFF** to absorbance spectra after heat-cooling, we must next assess any changes to the electrochemical properties of these systems. In terms of the position of the reduction and oxidation potentials, some shifting of peaks is observed at certain ratios and pH, Table 4.22-Table 4.24. These shifts are mostly small, and the majority of the ratios and pH combinations do not significantly differ upon heat-cooling.

At pH 6 and 9, the reduction occurs at a more negative potential, and oxidation at a less positive potential at 5:1.25 mg/mL (this latter trend is also observed at 5:0.625 mg/mL at pH 6 and 5:0 mg/mL at pH 9), Table 4.22-Table 4.23.

Table 4.22. Tabulated reduction and oxidation potentials found by CV of solutions of **NDI-F:1-NapFF** at various ratios at pH 6 after heat-cooling (heating to 40 °C and allowing to cool for 30 minutes). Scan rate 0.2 V/s. Full dataset available in Figure A.4.72, Appendix. CV performed in 1 x 1 FTO window cells.

Ratio of NDI-F:1-NapFF (mg/mL)	Reduction Potential(s) (V)	Current (μ A)	Oxidation Potential(s) (V)	Current (μ A)
5:5	-2.8	-1392	0.5	446
5:2.5	-2.7	-817	0.4	236
5:1.25	-3.2	-641	0.2	232
5:0.625	-2.6	-695	0.1	300
5:0	-2.6	-509	0.1	310

Table 4.23. Tabulated reduction and oxidation potentials found by CV of solutions of **NDI-F:1-NapFF** at various ratios at pH 9 after heat-cooling (heating to 40 °C and allowing to cool for 30 minutes). Scan rate 0.2 V/s. Full dataset available in Figure A.4.72, Appendix. CV performed in 1 x 1 FTO window cells.

Ratio of NDI-F:1-NapFF (mg/mL)	Reduction Potential(s) (V)	Current (μ A)	Oxidation Potential(s) (V)	Current (μ A)
5:5	-2.8	-2027	0.6	734
5:2.5	-2.8	-843	0.7	202
5:1.25	-3.1	-781	0.2	340
5:0.625	-2.6	-1081	0.4	427
5:0	-2.6	-655	0.3	152

At pH 12, differences are more prevalent, especially in the reduction potentials, Table 4.24. At 5:5 mg/mL all potentials are shifted to a larger (more positive or more neagative) value. At 5:2.5 mg/mL the first reduction peak is found at a more negative potential whereas at 5:0.625 and 5:0 mg/mL the second reduction peak is found at a less negative potential, Table 4.24. This observation suggests that more significant changes occur at pH 12 (consistent with viscosity and absorbance data) and that the ratio of components is important. The range of potentials is not significantly changed and so we anticipate that the same potentials can be used in spectro-electrochemical assessment as previously described for consistency.

Table 4.24. Tabulated reduction and oxidation potentials found by CV of solutions of **NDI-F:1-NapFF** at various ratios at pH 12 after heat-cooling (heating to 40 °C and allowing to cool for 30 minutes). Scan rate 0.2 V/s. Full dataset available in Figure A.4.72, Appendix. CV performed in 1 x 1 FTO window cells.

Ratio of NDI-F:1-NapFF (mg/mL)	Reduction Potential(s) (V)	Current (μ A)	Oxidation Potential(s) (V)	Current (μ A)
5:5	-2.4, -3.3	-2009, -5185	1.1	291
5:2.5	-2.4, -3.1	-1241, -3579	1.2	365
5:1.25	-1.8, -2.5	-342, -1142	1.0	234
5:0.625	-1.8, -2.4	-519, -1297	1.0	478
5:0	-1.8, -2.5	-631, -1585	1.1	257

The absorbance intensities are tabulated in Table 4.25 and the colour by eye can be seen in Figure 4.31. In general, heat-cooling results in an increase in colour intensity. All ratios and pH are enhanced with the exception of 5:5 and 5:0.625 mg/mL at pH 12 and 5:1.25 mg/mL at pH 6 and 9, Table 4.25. Across all pH, single component **NDI-F** has improved colouration after heat-cooling. This observation suggests that heat-cooling has some impact upon structures of **NDI-F** even without **1-NapFF**, resulting in more efficient electrochemical reduction.

Table 4.25. Tabulated absorbance intensity at λ_{\max} (after 10 seconds of application of -2.5 V) for **NDI-F:1-NapFF** at different ratios and pH before and after heat-cooling (heating to 40 °C and allowing to cool for 30 minutes). Full data sets available in Figure A.4.73, Appendix. Heat-cooled data is shown as red text.

System (mg/mL)	Absorbance at λ_{\max} at pH 6 (a.u.)	Absorbance at λ_{\max} at pH 9 (a.u.)	Absorbance at λ_{\max} at pH 12 (a.u.)
NDI-F (5)	0.740	0.532	0.156
NDI-F (5) heat-cooled	1.416	1.019	0.243
NDI-F:1-NapFF (5:5)	1.596	0.977	0.521
NDI-F:1-NapFF (5:5) heat-cooled	1.955	1.900	0.462
NDI-F:1-NapFF (5:2.5)	0.862	0.494	0.117
NDI-F:1-NapFF (5:2.5) heat-cooled	1.048	0.645	0.487
NDI-F:1-NapFF (5:1.25)	1.640	1.839	0.146
NDI-F:1-NapFF (5:1.25) heat-cooled	0.222	1.408	0.179
NDI-F:1-NapFF (5:0.625)	0.795	0.742	0.589
NDI-F:1-NapFF (5:0.625) heat-cooled	2.213	2.135	0.185

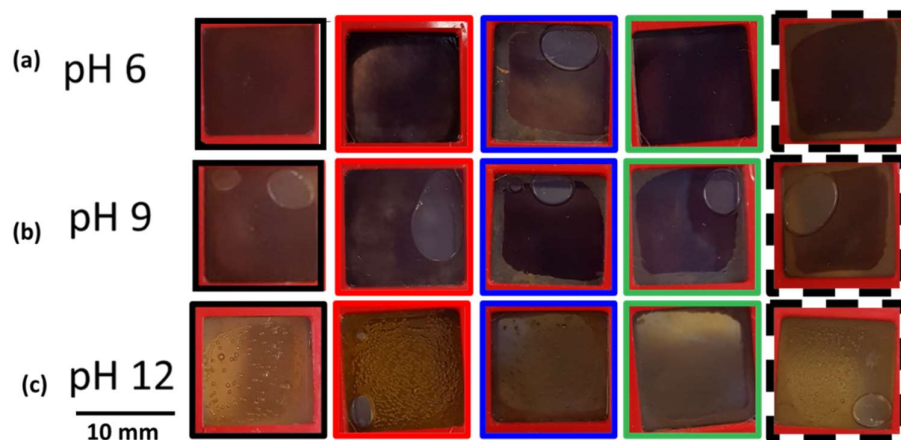


Figure 4.31. Images of **NDI-F:1-NapFF** 5:5 (black), 5:2.5 (red), 5:1.25 (blue), 5:0.625 (green) and 5:0 (dashed line) mg/mL after heat-cooling (heating to 40 °C and allowing to cool for 30 minutes) at pH 6 (a), 9 (b) and 12 (c) following application of -2.5 V for 10 seconds. Any bubbles are a result of loading.

There are significant reductions in colour intensity at pH 6 at 5:1.25 mg/mL (corresponding with a change in molecular packing, Figure 4.30). At 5:0.625 mg/mL there is a significant increase in colouration intensity at both pH 6 and 9 which is of particular interest as this is the lowest concentration of **1-NapFF**, Table 4.25. At pH 6 there is also a change in molecular packing opposite to that at 5:1.25 (corresponding with poorer colouration), Figure 4.30. The increase in viscosity upon heat-cooling is also more significant at these lower concentrations, Table 4.21. This trend is not consistent with an increase in colour intensity and so it is likely aggregation is a more significant factor than viscosity.

These observations suggest that, at lower concentrations of **1-NapFF** and at high pH, there are more significant changes to colouration, even if this is a negative impact. Heat-cooling may add energy into the system, breaking intercomponent interactions or redistributing structures or aligning fibres, resulting in more efficient electron transfer or stabilisation of the radical anionic species in some cases. It is of interest that systems that performed well before heat-cooling and gave enhanced colouration at the non-ideal pH of **NDI-F** (5:1.25 mg/mL pH 9 and 5:5 and 5:0.625 mg/mL at pH 12) show a reduction in colouration after heat-cooling. This factor could be of concern as use in an everyday setting could involve temperature fluctuation (although perhaps not to such high temperatures).

4.2.10.1.3 Oxidation rates

Similar to the enhancement of colour, at 5:0.625 mg/mL, the oxidation rate is also enhanced, Figure 4.32. As previously discussed, the larger concentration of radical anionic species likely aids the conductivity of the system and improves the efficiency of oxidation in the initial 30-60 seconds after

reduction. Compared to pre- heat-cooling there is not a significant improvement in oxidation rate and this property is relatively consistent.

Based on this investigation, the best performing systems after heat-cooling was **NDI-F:1NapFF** at a ratio of 5:0.625 mg/mL at pH 6 and 9. These two systems gave the darkest colouration upon reduction. After a more thorough investigation of aggregation and the effect of heat-cooling, we can compare this system to **NDI-F** at 5 mg/mL ratio at pH 6 and to the non-heat cooled systems previously used, to compare their cyclability and stability.

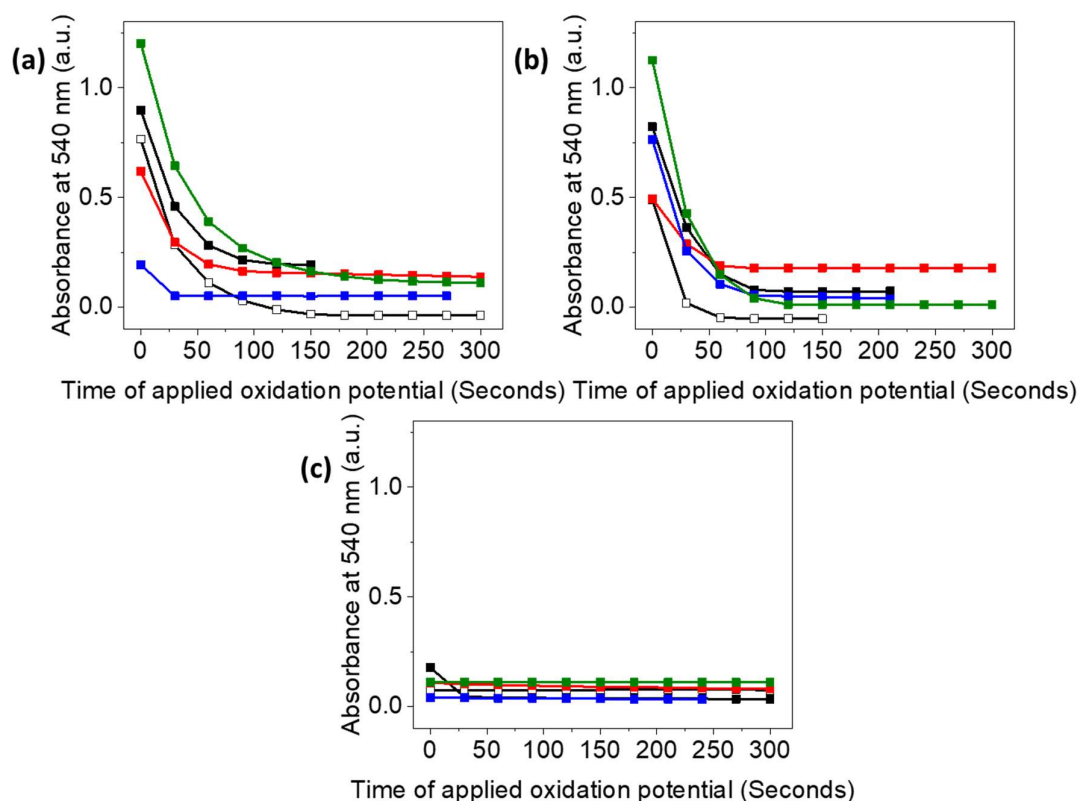


Figure 4.32. Measurement of absorbance at 540 nm as an oxidising potential of 0.5 V was applied for 5 minutes after 20 seconds of reduction with -2.5 V. Solutions of **NDI-F:1NapFF** after heat-cooling (heating to 40 °C and allowing to cool for 30 minutes) at 5:5 (black), 5:2.5 (red), 5:1.25 (blue), 5:0.625 (green) and 5:0 (open square) mg/mL at pH 6 (a), 9 (b) and 12 (c) were used.

4.2.11 SAXS analysis

To gain more detailed insight into how structures are affected by the heat-cool process, we use SAXS, firstly focusing upon the single components, Figure 4.33 and Table 4.26. Trends in **1-NapFF** at high pH are comparable with the literature.³⁷ Flexibility and radii decreases (consistent with elongation of structures during heat-cooling). Changes to Kuhn length at high pH are not statistically significant. At pH 6, Kuhn length and radii decrease and at pH 9 the Kuhn length and radii increase, Table 4.26,

suggesting structures at different pH have a different response to heat-cooling. It should be noted that these systems contain salt which may have subtle impact upon aggregation.

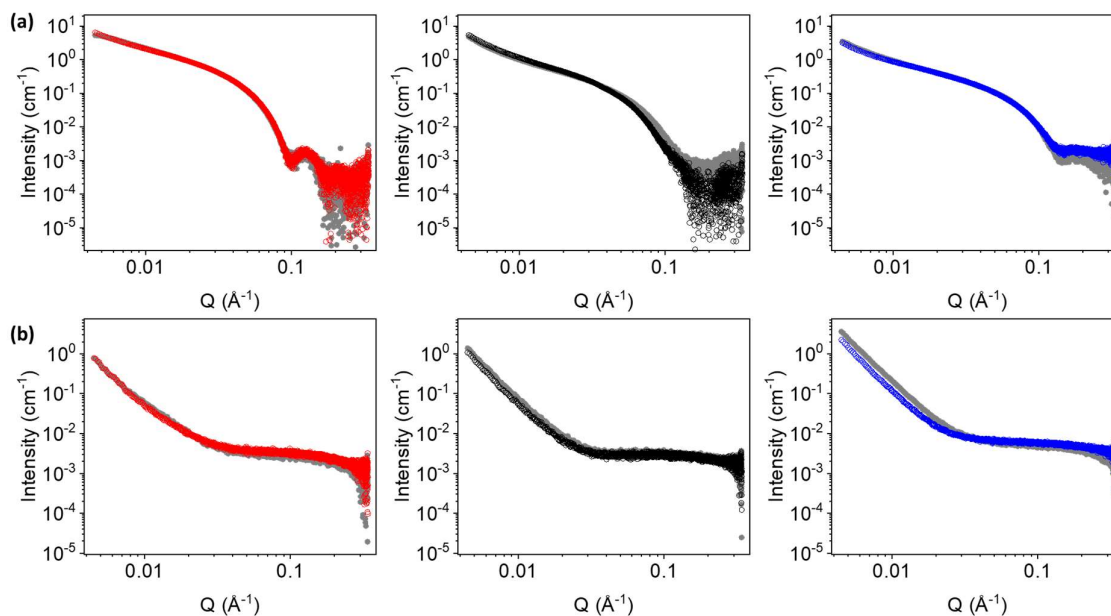


Figure 4.33. SAXS data of 5 mg/mL (a) **1-NapFF** and (b) **NDI-F** before (grey) and after (open circles) a heat-cool transition (heating to 40 °C and allowing to cool for 30 minutes) at pH 6 (red), 9 (black) and 12 (blue).

Table 4.26. Tabulated parameters from fits to SAXS data from single component systems after heat-cooling (heating to 40 °C and allowing to cool for 30 minutes). Full data set available in Figures A.4.74-A.4.79 and Tables A.4.41-A.4.46, Appendix. Modelled using various cylinders (see Appendix).

System (mg/mL)	Kuhn length (Å)	Error	Radius (Å)	Error	Thickness (Å)	Error	Axis Ratio	Error
NDI-F (5) pH 6	N/A	N/A	4.67	0.0273	5.05	0.0126	N/A	N/A
NDI-F (5) pH 9	N/A	N/A	5.55	0.101	4.94	0.162	N/A	N/A
NDI-F (5) pH 12	N/A	N/A	10.74	0.00946	N/A	N/A	N/A	N/A
1-NapFF (5) pH 6	307	137	35.75	0.00324	N/A	N/A	1.30	1.09E-04
1-NapFF (5) pH 9	427.05	0.565	27.79	0.00249	N/A	N/A	1.75	1.47E-04
1-NapFF (5) pH 12	548	248	22.92	0.00171	N/A	N/A	1.45	1.03E-04

4.2.11.1.1 Heat-cooling multicomponent systems

In multicomponent systems, there are more pronounced differences in the scattering profile upon heat-cooling than in single components. In general, we observe a small increase in scattering intensity

at low Q (more prevalent at the lower concentrations of **1-NapFF**, Figure A.4.80, Appendix). These lower concentrations also showed more significant changes in packing and electrochemical colouration, 4.2.10.1-4.2.10.2.

At high pH and high **1-NapFF** concentration, we observe an increase in rigidity in the system after heat-cooling. As this concentration is lowered however, we see an increase in flexibility, as Kuhn length decreases after heat-cooling, Table 4.27. This observation suggests that the response to heat-cooling is changed when **NDI-F** is the more dominating structure.

In two cases (5:2.5 mg/mL pH 6 and 9) there is a large decrease in scattering intensity across the Q range as well as a change in the shape of the profile. These observations suggest a significant loss in network level aggregation, Figure 4.34. This ratio has the most extreme reaction to heat-cooling and at pH 6, a significant decrease in viscosity is observed (Table 4.21). The consequent improvement in colouration, Table 4.25, may be due to disruption of **1-NapFF** structures, allowing more freedom to **NDI-F** to π -stack and form structures that stabilise the radical anion. However, while improvements in colour intensity are observed upon heat-cooling, these systems do not achieve better colouration than single component **NDI-F**, Table 4.25.

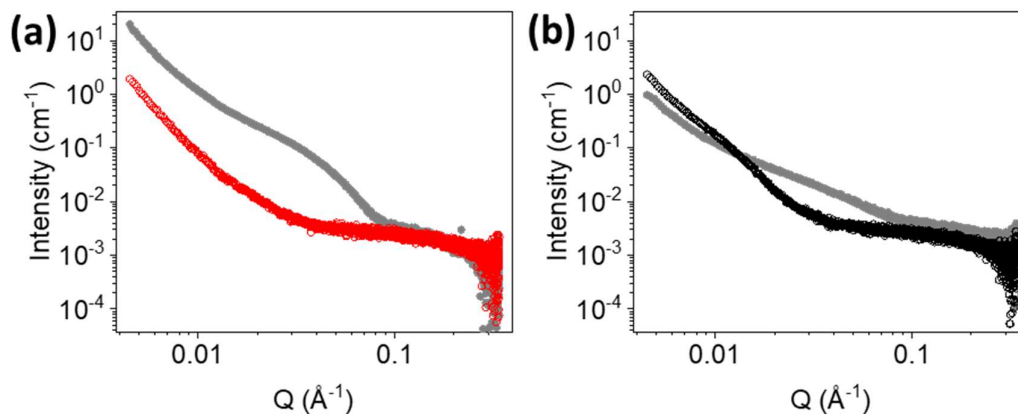


Figure 4.34. SAXS data of **NDI-F:1-NapFF** before (filled circles) and after (open circles) a heat-cool transition (heating to 40 °C and allowing to cool for 30 minutes) at 5:2.5 mg/mL (a) pH 6 and (b) 9.

Table 4.27. Tabulated fit parameters data from **NDI-F:1-NapFF** systems after heat-cooling (heating to 40 °C and allowing to cool for 30 minutes). Full data of heat-cooled measurements available in Figures A.4.81-A.4.92 and Tables A.4.47-A.4.58, Appendix. Heat-cooled data is shown as red text. Modelled using various cylinders (see Appendix).

System (mg/mL)	Kuhn length (Å)	Error	Radius (Å)	Error	Axis Ratio	Error	Radius B (Å)	Error	Thickness B (Å)	Error
NDI-F:1-NapFF (5:5) pH 6	317.28	0.487	32.97	0.00244	1.42	9.77E-05	6.66	0.148	5.06	0.0583
NDI-F:1-NapFF (5:5) pH 6 heat-cooled	215.71	0.128	34.06	0.00281	1.38	1.05E-04	4.55	0.0579	6.63	0.0313
NDI-F:1-NapFF (5:5) pH 9	242.53	0.468	19.30	0.00469	1.38	3.31E-04	5.91	0.00493	23.42	0.00416
NDI-F:1-NapFF (5:5) pH 9 heat-cooled	343.64	1.07	21.13	0.00242	1.75	0.00190	9.94	0.0190	20.90	0.0136
NDI-F:1-NapFF (5:5) pH 12	302.58	0.289	24.78	0.00256	N/A	N/A	14.29	0.0134	16.42	0.00784
NDI-F:1-NapFF (5:5) pH 12 heat-cooled	384.05	0.554	24.84	0.00183	1.28	8.87E-05	11.56	0.0128	N/A	N/A
NDI-F:1-NapFF (5:2.5) pH 6	162.02	0.117	34.10	0.00581	1.64	2.53E-04	6.52	0.00741	N/A	N/A
NDI-F:1-NapFF (5:2.5) pH 6 heat-cooled	62.82	0.295	50.43	0.258	10.8	0.0369	12.70	0.0313	N/A	N/A
NDI-F:1-NapFF (5:2.5) pH 9	193.59	0.571	19.22	0.0105	2.39	0.00125	6.96	0.00421	N/A	N/A
NDI-F:1-NapFF (5:2.5) pH 9 heat-cooled	157.15	0.222	83.32	0.126	6.72	0.00734	12.31	0.0159	N/A	N/A
NDI-F:1-NapFF (5:2.5) pH 12	171.02	0.405	21.40	0.0101	7.17	0.00374	1.74	7.79E-04	N/A	N/A
NDI-F:1-NapFF (5:2.5) pH 12 heat-cooled	237.49	0.567	8.96	0.00311	4.13	0.00141	N/A	N/A	N/A	N/A
NDI-F:1-NapFF (5:1.25) pH 6	330.09	1.28	34.88	0.00517	1.48	1.99E-04	5.02	0.0439	5.05	0.0195
NDI-F:1-NapFF (5:1.25) pH 6 heat-cooled	393.71	0.658	37.00	0.00559	1.40	1.94E-04	N/A	N/A	N/A	N/A
NDI-F:1-NapFF (5:1.25) pH 9	286.86	0.737	15.67	0.00428	N/A	N/A	12.94	0.0311	17.05	0.0172
NDI-F:1-NapFF (5:1.25) pH 9 heat-cooled	130.22	0.180	10.45	0.00348	N/A	N/A	11.76	0.0215	16.36	0.0120
NDI-F:1-NapFF (5:1.25) pH 12	208.48	0.288	22.38	0.00313	1.44	1.87E-04	6.10	0.00324	N/A	N/A

NDI-F:1-NapFF (5:1.25) pH 12 heat-cooled	138.49	0.122	21.72	0.00433	1.58	2.95E-04	8.55	0.00695	N/A	N/A
NDI-F:1-NapFF (5:0.625) pH 6	240.99	0.286	35.81	0.00586	1.34	1.96E-04	9.26	0.133	N/A	N/A
NDI-F:1-NapFF (5:0.625) pH 6 heat-cooled	236.34	0.210	8.04	0.0237	1.30	1.95E-04	36.26	0.00608	N/A	N/A
NDI-F:1-NapFF (5:0.625) pH 9	228.08	0.367	26.51	0.00575	1.31	2.59E-04	10.07	0.00991	N/A	N/A
NDI-F:1-NapFF (5:0.625) pH 9 heat-cooled	242.51	0.290	30.10	0.00540	1.04	1.68E-04	8.66	0.00364	N/A	N/A
NDI-F:1-NapFF (5:0.625) pH 12	344.68	1.22	28.22	0.00500	1.17	1.90E-04	12.72	0.0110	N/A	N/A
NDI-F:1-NapFF (5:0.625) pH 12 heat- cooled	193.67	0.279	24.49	0.00478	1.28	2.33E-04	12.07	0.0142	N/A	N/A

As two components are present, we expect there may be some inaccuracies in the fits due to the additional complexity of the multicomponent system. Thinking critically about these data, some parameters (for example length, which is already potentially unreliably estimated by fitting software at this length scale) may be subject to larger errors. It is likely that a cylinder model is more appropriate (Figure 4.15), but the use of an inflexible flexible cylinder allows us to assess any smaller changes in flexibility within **1-NapFF** more easily and so is used.

4.2.11.1.2 Trends in heat-cooled multicomponent systems

Some trends between the parameters of heat-cooled systems and their chromic behaviour were observed. For example, axis ratio peaks at a ratio of 5:2.5 mg/mL at all pHs, Figure 4.35. This increase is significant at pH 6 and 9 and corresponds with a loss of scattering intensity at low-mid Q, Figure 4.34. This observation suggests that structures are more elliptical and strained, resulting in disruption of large scale **1-NapFF** networks at this specific ratio of components (most significantly at pH 6, where more larger aggregates or networks are present). This data highlights the impact of component ratio.

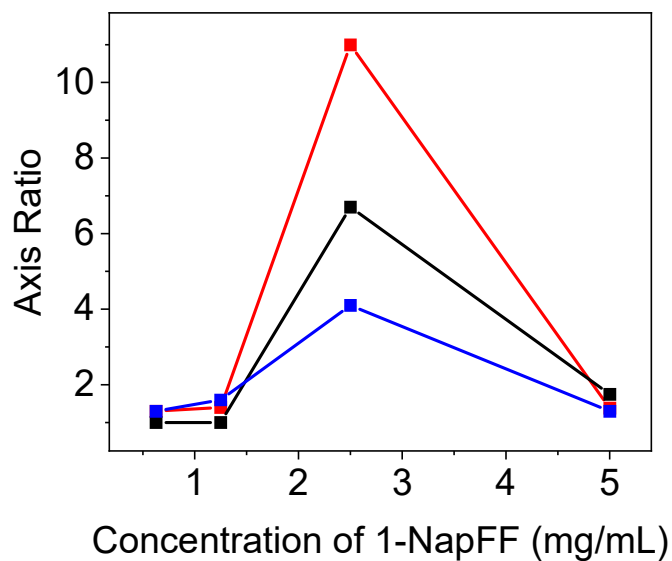


Figure 4.35. Plot showing how axis ratio of cylindrical model fits varies with concentration of **1-NapFF** in **NDI-F:1-NapFF** systems at pH 6 (red), 9 (black) and 12 (blue) after heat-cooling (heating to 40 °C and allowing to cool for 30 minutes). **NDI-F** kept at a constant concentration of 5 mg/mL.

The trends of flexibility fluctuating with increasing concentration of **1-NapFF** is comparable to pre-heat-cooling at pH 6, Figure 4.19(d) and Figure 4.36. Colouration compared to **NDI-F** alone is enhanced at 5:5 and 5:0.625 mg/mL ratios at pH 6, Table 4.25 (where Kuhn length is comparable), while at 5:2.5 and 5:1.25 mg/mL there is a reduction in colour intensity (especially at 5:1.25 mg/mL). When colour is detrimentally affected, Kuhn length is much lower or higher than 200 Å. This observation suggests that structures of **1-NapFF** that are too rigid or too flexible will affect **NDI-F** aggregates and result in poor electrochromic colouration. A region of approximately 200 Å appears to be an ideal Kuhn length. Before heat-cooling, the ratio and pH combination showing large colour enhancements also had a Kuhn length in this area in their model fits (5:5 mg/mL pH 6 and 5:1.25 mg/mL pH 9), Table 4.27. This observation suggests that a region of flexibility of **1-NapFF** supports **NDI** radical formation or stabilises/influences the structures of **NDI-F** to do so.

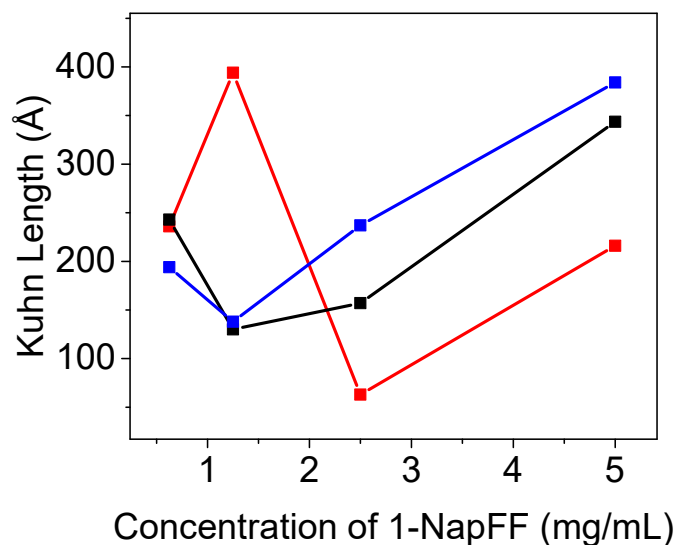


Figure 4.36. Plot showing how Kuhn length of **1-NapFF** component fluctuates in cylindrical models with concentration of **1-NapFF** in heat-cooled **NDI-F:1-NapFF** systems at pH 6 (red), 9 (black) and 12 (blue). Data after heat-cooling (heating to 40 °C and allowing to cool for 30 minutes). **NDI-F** kept at a constant concentration of 5 mg/mL.

At pH 9 and 12 the trends in flexibility are not consistent with pre-heat-cooling, Figure 4.19(d) and Figure 4.36, but are consistent with each other, Figure 4.36. These trends do not correspond with trends in colouration nor with the trends at pH 6. Low pH systems seem to have the most favourable response to heat-cooling which may be due to the larger size of aggregate at low pH. Heat-cooling may put enough energy into the system to subtly redistribute aggregates and relive some unfavourable interaction between components or steric strain.

At pH 9, the trends in radii of the **NDI-F** and **1-NapFF** component are comparable to pre-heat-cooling, Figure 4.20(a) and Figure 4.37. The increase in radii size at 5:2.5 mg/mL in **1-NapFF** is more significant after heat-cooling, Figure 4.37(b). However, the larger scale networks were observed to be disrupted, shown by a reduction in scattering intensity at low Q, Figure 4.34. This observation suggests that **1-NapFF** structure may have broken into shorter fibres with larger radii and is consistent with trends in colouration before heat-cooling. While there is improvement of colouration compared to pre heat-cooling, compared to **NDI-F** alone, there is a reduction in colour intensity at this ratio. Interplanar distances between NDI molecules must not be too large as this will not facilitate effective π electron delocalisation to form the radical anion.^{50,51} Consistent with Chapter 2, the radius size of **NDI-F** is a critical factor for stabilisation of the radical.

At pH 6 in ratio 5:1.25 mg/mL, colouration is significantly reduced, Table 4.25, and this corresponds with the NDI component becoming less defined within the model (i.e. a single cylinder model is used that has parameters consistent with **1-NapFF**), Table 4.27. This observation suggests that the NDI component is forming smaller or less defined structures, resulting in poor electrochromic behaviour. The radii of the NDI component is larger at 5:0.625 and much smaller at 5:2.5 mg/mL, which could suggest that at 5:1.25 mg/mL there is a transition structure which cannot be defined by the model, Figure 4.37(a). The best colouration was found at 5:0.625 mg/mL at pH 6, corresponding to the largest radii of **NDI-F** at this pH, Figure 4.37(a).

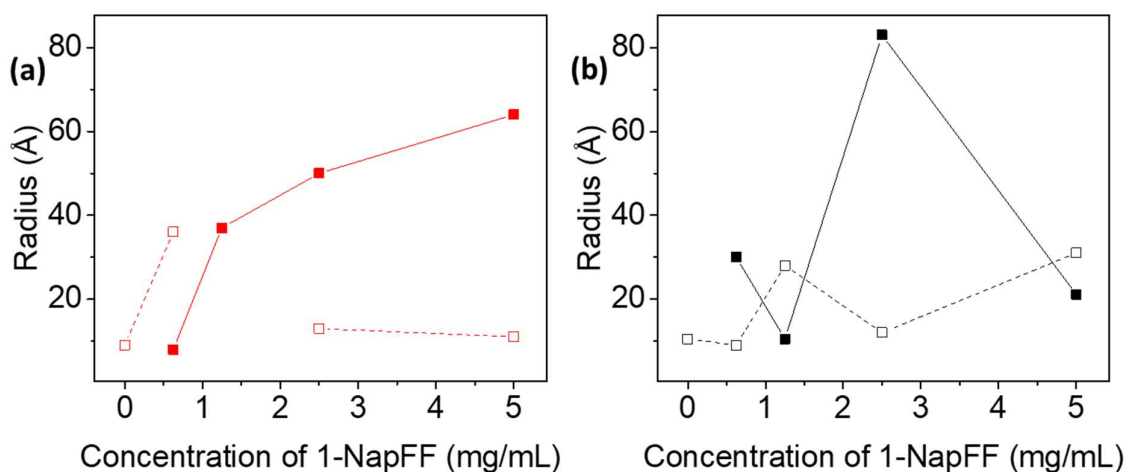


Figure 4.37. Plot showing how radii of **1-NapFF** (filled squares) and **NDI-F** (empty squares) components fluctuates in cylindrical models with concentration of **1-NapFF** in heat-cooled (heating to 40 °C and allowing to cool for 30 minutes). **NDI-F:1-NapFF** systems at (a) pH 6 and (b) 9. Where data is missing, no NDI component was used in the model. **NDI-F** kept at a constant concentration of 5 mg/mL.

Exact parameters cannot be directly linked to better electrochromic properties. A compromise of the size of **1-NapFF** components compared to **NDI-F** as well as pH, component interaction and overall viscosity must be found to maximise electrochromic behaviour in these systems. Colouration is also enhanced at 5:0.625 mg/mL at pH 6 and 9 which may be due to the flexibility of **1-NapFF** cylinders being within the ideal region of around 200 Å, Figure 4.36.

4.2.12 Cyclability

Having identified **NDI-F:1-NapFF** at a ratio of 5:0.625 mg/mL at pH 6 and 9 as our best multicomponent heat-cooled systems, we compared these pHs in terms of their cyclability as previously described. This system performed better, in terms of the oxidation rate and the number of cycles achieved, at pH 6

(Figure 4.38). At this pH, the aggregates of **NDI-F** in solutions were larger in terms of radius, Table 4.27. This ratio is now buffered at pH 6 and compared to **NDI-F** heat-cooled as a single component system.

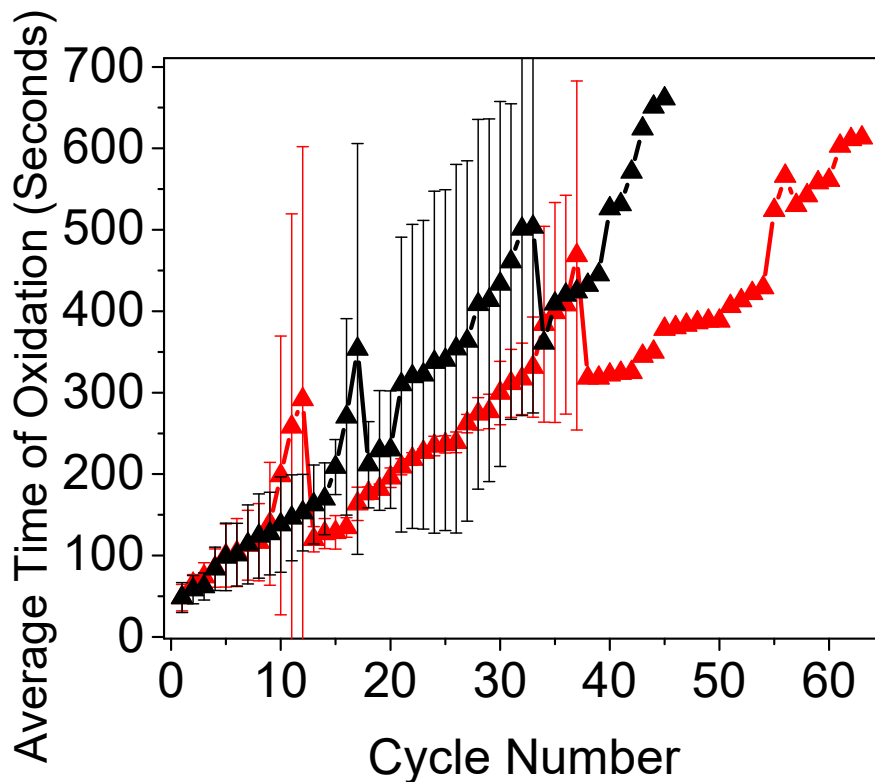


Figure 4.38. Plot showing how time to reach a state without colouration fluctuates with electrochemical cycling between a reduced and oxidised state. Measurements carried out using solutions of heat-cooled (heating to 40 °C and allowing to cool for 30 minutes) 5:0.625 mg/mL **NDI-F:1-NapFF** at pH 6 (red) and 9 (black). Measurements are taken as an average of triplicate measurements and error bars calculated from standard deviation.

When buffered, both **NDI-F** and **NDI-F:1-NapFF** systems become slightly more viscous, Table 4.28, but have comparable molecular packing to the unbuffered state, Figure 4.39(a and c). The SAXS data suggests there are some differences in the aggregation upon buffering, Figure 4.39(b and d). There is a higher scattering intensity at mid to low Q (which suggests larger aggregates) in the multicomponent system, and a larger intensity at high Q in the single component system (which indicates less solvated aggregates).

Table 4.28. Tabulated average apparent viscosity at a shear rate of 1 s^{-1} for heat-cooled (heating to $40 \text{ }^\circ\text{C}$ and allowing to cool for 30 minutes) single and multicomponent systems buffered and unbuffered. All solutions adjusted to pH 6. Full data set available in Figure A.4.94, Appendix.

System (mg/mL)	Average apparent viscosity at 1 s^{-1} shear at pH 6 (Pa·s)	Average apparent viscosity at 1 s^{-1} shear buffered to pH 6 (Pa·s)
NDI-F:1-NapFF (5:0.625)	0.158	0.390
NDI-F (5)	0.005	0.010

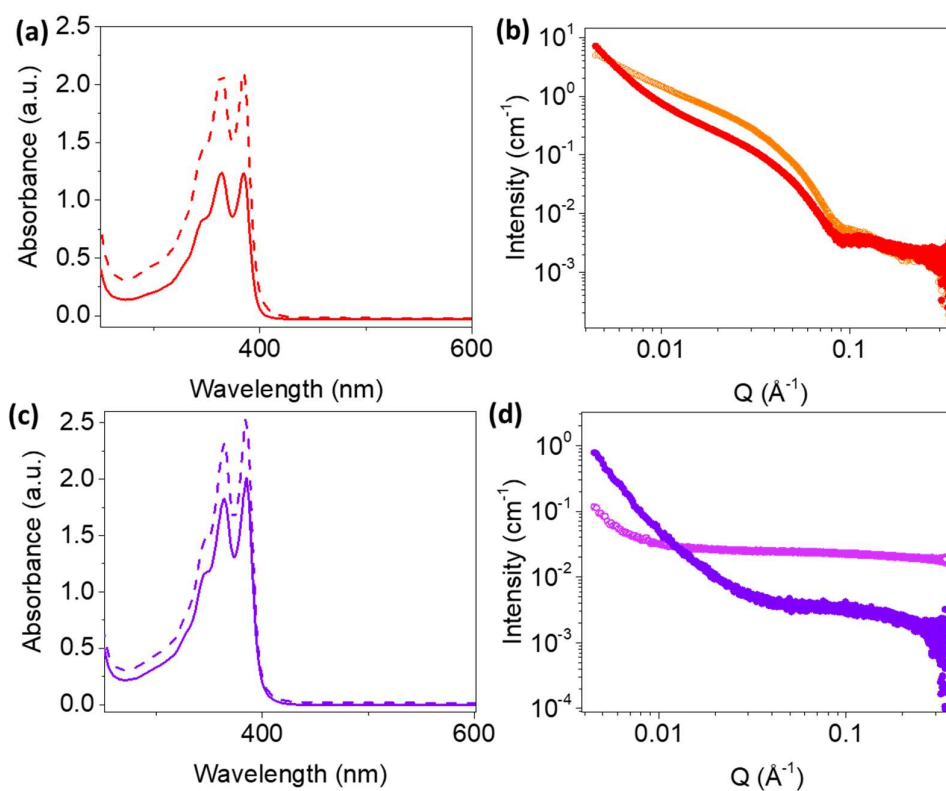


Figure 4.39. (a and c) Absorbance spectra of neutral state, (b and d) SAXS measurements at pH 6. Solutions of heat-cooled (heating to $40 \text{ }^\circ\text{C}$ and allowing to cool for 30 minutes) (a-b) **NDI-F:1-NapFF** 5:0.625 mg/mL and (c-d) **NDI-F** 5 mg/mL are buffered (dashed line or a lighter colour of orange and lilac) and unbuffered (solid line or a darker colour of red and purple).

Table 4.29. Tabulated fit parameters of SAXS data from for heat-cooled (heating to 40 °C and allowing to cool for 30 minutes) single and multicomponent systems buffered and unbuffered. All solutions adjusted to pH 6. Full data set of buffered data found in Figures A.4.95-A.4.96 and Tables A.4.59-A.5.60, Appendix. Modelled to various cylinders (see Appendix).

Heat-cooled system (mg/mL) pH 6, heat-cooled	Length (Å)	Error	Kuhn length (Å)	Error	Radius (Å)	Error	Axis Ratio	Error
NDI-F:1-NapFF (5:0.625) unbuffered	502.61	1.11	236.34	0.210	8.035	0.0237	1.30	1.95E-04
NDI-F:1-NapFF (5:0.625) buffered	303.56	0.802	201.23	0.403	16.41	0.00833	5.12	0.00235
NDI-F (5) unbuffered	N/A	N/A	N/A	N/A	N/A	N/A	N/A	N/A
NDI-F (5) buffered	N/A	N/A	N/A	N/A	N/A	N/A	N/A	N/A
Heat-cooled system (mg/mL) pH 6, heat-cooled	Length B (Å)	Error	Radius B (Å)	Error	Thickness B (Å)	Error		
NDI-F:1-NapFF (5:0.625) unbuffered	5.41E+03	110	36.26	0.00608	N/A	N/A		
NDI-F:1-NapFF (5:0.625) buffered	1.04E+04	7.04	43.14	0.00561	N/A	N/A		
NDI-F (5) unbuffered	16.812	0.0587	4.67	0.0273	5.05	0.0126		
NDI-F (5) buffered	19.72	0.101	6.77	0.0618	7.21	0.113		

When parameters are compared, Table 4.29, the **NDI-F** component is longer and has a larger radius in buffered solutions. This data is consistent with previous findings, Table 4.19. More significant changes occur to the **1-NapFF** component of **NDI-F:1-NapFF**. Comparably to the buffering of **1-NapFF** at 5 mg/mL (Table 4.17), length and Kuhn length decrease and axis ratio increases (Table 4.29). There are more significant changes to radius and axis ratio at this lower **1-NapFF** concentration, which suggests that more dilute aggregates are more susceptible to high salt concentrations, resulting in a more elliptical cylindrical aggregate, possibly due to charge interactions.

The **NDI-F** component does not appear to be significantly affected by buffering as the redox potentials are comparable (slightly more shifting in 5 x 5 FTO window set-up), Table 4.30.

Table 4.30. Tabulated data of redox potentials taken from cyclic voltammograms taken at 0.2 V/s of heat-cooled (heating to 40 °C and allowing to cool for 30 minutes) **NDI-F:1-NapFF** 5:0.625 mg/mL and **NDI-F** 5 mg/mL, buffered and unbuffered at pH 6 in different sizes of FTO window cell. Full data sets available in Figure A.4.97, Appendix.

Heat-cooled system (mg/mL)	Reduction Potential(s) (V)	Current (μ A)	Oxidation Potential(s) (V)	Current (μ A)
NDI-F:1-NapFF (5:0.625) buffered in 1 x 1 FTO window cell	-2.7	-712	0.2	226
NDI-F:1-NapFF (5:0.625) unbuffered in 1 x 1 FTO window cell	-2.6	-695	0.1	300
NDI-F:1-NapFF (5:0.625) buffered in 5 x 5 FTO window cell	-2.8	-8488	0.9	1686
NDI-F:1-NapFF (5:0.625) unbuffered in 5 x 5 FTO window cell	-2.5	-2676	0.7	2485
NDI-F (5) buffered in 1 x 1 FTO window cell	-2.5	-1007	0.3	303
NDI-F (5) unbuffered in 1 x 1 FTO window cell	-2.6	-509	0.1	310
NDI-F (5) buffered in 5 x 5 FTO window cell	-2.7	-5283	0.5	1514
NDI-F (5) unbuffered in 5 x 5 FTO window cell	-2.4	-1754	0.8	426

The oxidation rate is improved by the additional salt concentration (Figure 4.40(b and d)) but colouration intensity is only enhanced in the single component system (Figure 4.40(a and c)). This trend agrees with previous findings for non-heat-cooled systems, Figure 4.25.

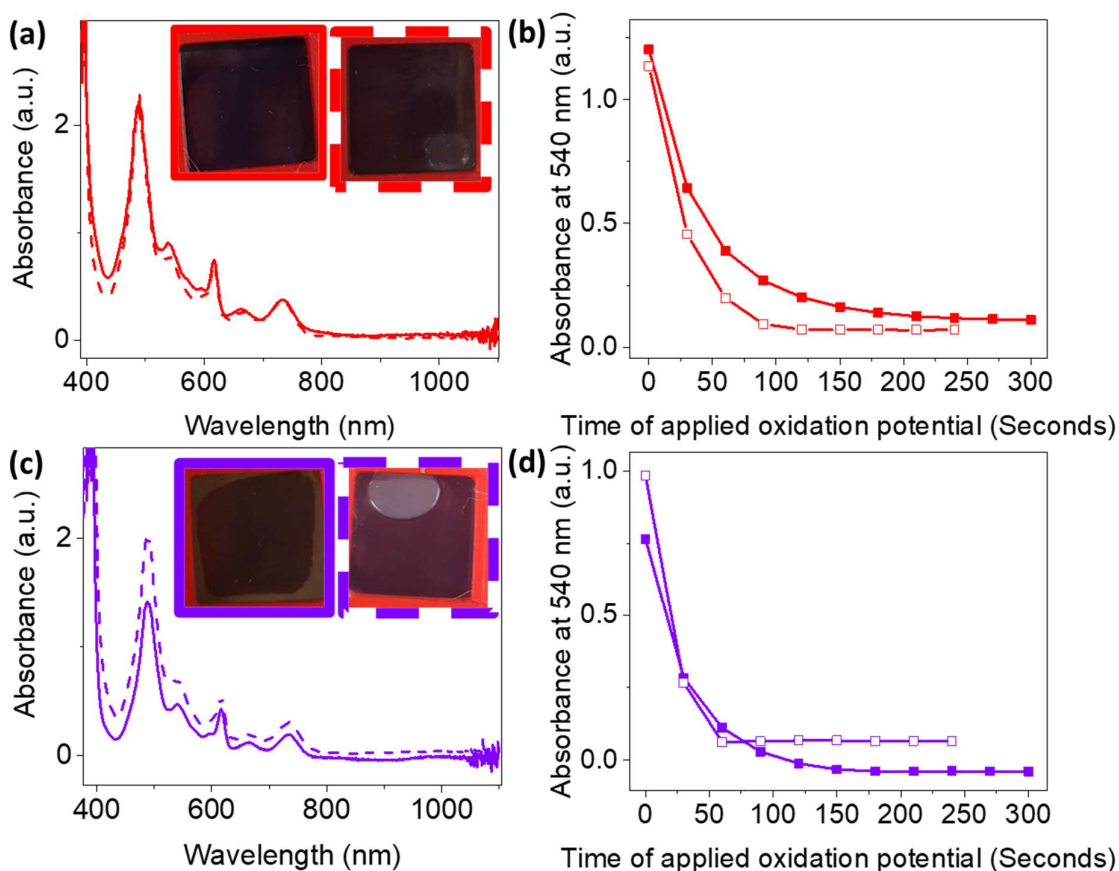


Figure 4.40. (a/c) Absorbance spectra of reduced state after application of -2.5 V for 10 seconds, (b/d) measurement of absorbance at 540 nm as an oxidising potential of 0.5 V was applied for 5 minutes after 20 seconds of reduction with -2.5 V. Solutions of heat-cooled (heating to 40 °C and allowing to cool for 30 minutes) (a-b) **NDI-F:1-NapFF** 5:0.625 mg/mL and (c-d) **NDI-F** 5 mg/mL are buffered (dashed line or open squares) and unbuffered (solid line or filled squares).

As previously found, an improvement in cyclability is also observed upon buffering as the ideal pH and aggregation is maintained through the experiment, Figure 4.41 (although this is less significant in the multicomponent system, Figure 4.41(b)). This observation suggests that the **1-NapFF** component (in small concentrations) act as a support for the **NDI-F** aggregation when heat-cooled, aiding cyclability even before buffering.

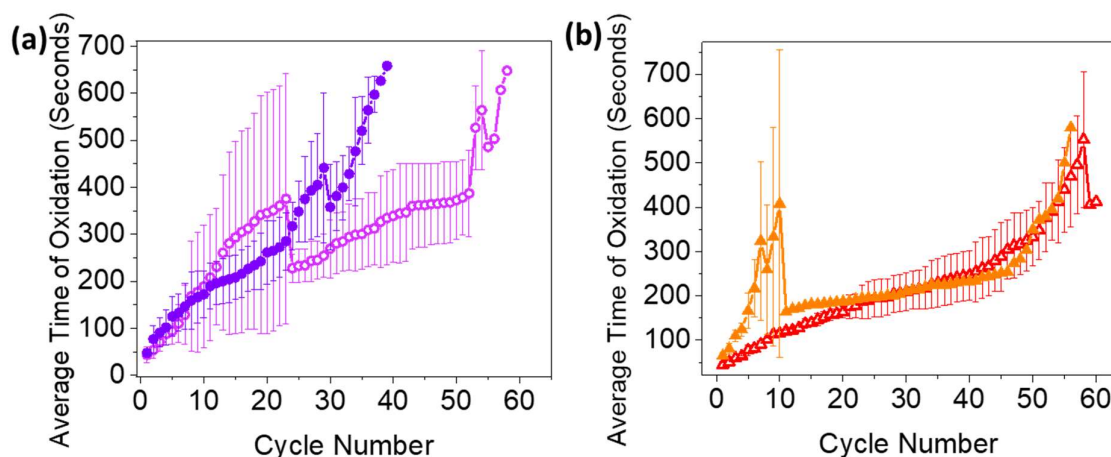


Figure 4.41. Plot showing how much time is needed to reach a transmissive state fluctuates with electrochemical cycling between a reduced and oxidised state. Measurements carried out using solutions of heat-cooled (heating to 40 °C and allowing to cool for 30 minutes) (a) **NDI-F** 5 mg/mL and (b) **NDI-F:1-NapFF** 5:0.625 mg/mL at pH 6 buffered (open shapes, lilac and red) and unbuffered (filled shapes, purple and orange). Measurements are taken as an average of triplicate measurements and error bars calculated from standard deviation.

NDI-F:1-NapFF 5:0.625 mg/mL has better cyclability than **NDI-F** 5 mg/mL. This is significant as non-heat-cooled multicomponent systems did not improve cyclability, only colouration intensity. This heat-cooled system improves both.

Despite an improvement in cyclability, the network scale structures of **NDI-F:1-NapFF** 5:0.625 mg/mL heat-cooled appear to be significantly affected by cycling, suggested by a significant reduction in low Q scattering intensity after only one cycle, Figure 4.42. The models after one and 50 cycles also do not require a power law. However, due to the *ex situ* nature of the measurements, it is possible that the transfer and/or mailing process has resulted in the weakening and breaking apart of these larger structures as suggested in Chapter 3 in **NDI-GF** systems. As the concentration of **1-NapFF** is low, we would expect structures to be weaker and more susceptible to handling artefacts. Structures become more flexible with cycling which has been previously observed in NDI systems (Chapter 3), Table 4.31. This observation could be a product of models no longer including a different cylinder type for **NDI-F**.

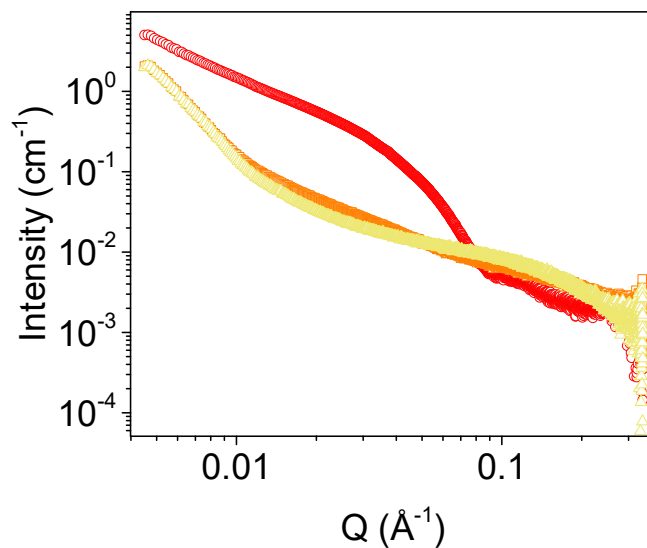


Figure 4.42. SAXS measurement of relaxed buffered (a) **NDI-F:1-NapFF** 5:0.625 mg/mL heat-cooled (heating to 40 °C and allowing to cool for 30 minutes) and buffered at pH 6. Solutions are measured after 0 (red), 1 (orange) and 50 (yellow) electrochemical cycles.

Table 4.31. Tabulated parameters from fits to SAXS data from buffered **NDI-F:1-NapFF** systems after heat-cooling (heating to 40 °C and allowing to cool for 30 minutes) at pH 6. Full data set available in Figures A.4.49 and A.4.98-A.4.99 and Tables A.4.59 and A.4.61-A.4.62, Appendix. Various cylindrical models used (see Appendix).

Buffered heat-cooled system (mg/mL)	Kuhn length (Å)	Error	Radius (Å)	Error	Axis Ratio	Error	Radius B (Å)	Error
NDI-F:1-NapFF (5:0.625) pre-cycled	201.23	0.403	16.41	0.00833	5.12	0.00235	43.14	0.00561
NDI-F:1-NapFF (5:0.625) after 1 cycle	98.88	0.1335	5.00	8.93E-04	N/A	N/A	N/A	N/A
NDI-F:1-NapFF (5:0.625) after 50 cycles	112.73	0.145	6.86	0.00209	N/A	N/A	N/A	N/A

Having identified ideal heat-cooled and non-heat-cooled systems, it is of interest to compare the influence of heat-cooling upon **NDI-F** as a single component system to identify whether **1-NapFF** is even required to yield comparable results.

Comparing buffered systems of **NDI-F** pre- and post- heat-cooling, colour intensity is improved by heat-cooling, however, oxidation time and cyclability are not significantly improved, Figure 4.43. Non-heat-cooled **NDI-F** has smaller variation in oxidation time and achieves two further cycles. It is of interest that heat-cooling results in enhanced colouration in single component systems as heating to this temperature would be a simple processing step in a commercial production.

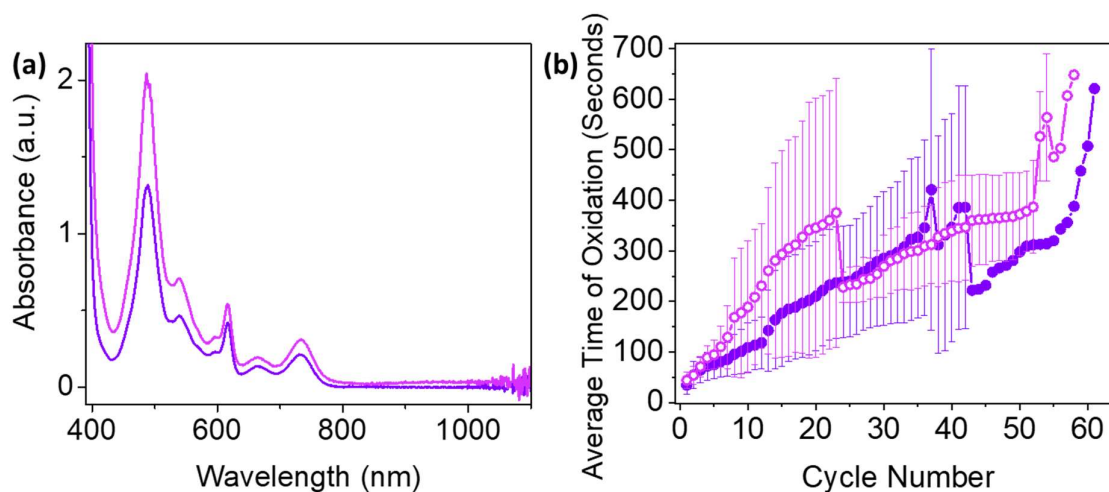


Figure 4.43. (a) Absorbance spectra after 10 second application of -2.5 V and (b) plot showing how time to reach a state without colouration fluctuates with electrochemical cycling between a reduced and oxidised state. Measurements carried out using solutions of 5 mg/mL **NDI-F** buffered to pH 6 before (light purple) and after heat-cooling (heating to 40 °C and allowing to cool for 30 minutes) (purple). Measurements are taken as an average of triplicate measurements and error bars calculated from standard deviation.

Heat-cooled structures have higher scattering intensity, which indicates larger aggregates, although the parameters of the cylinders themselves are comparable, Table 4.32 and Figure 4.44(a). Absorbance spectra (Figure 4.44(b)) suggests that the molecular packing differs in heat-cooled systems as the ratio of peaks at 365 and 385 nm are notably different. This packing change may be responsible for the formation of larger aggregates and better stability of the radical anionic species.

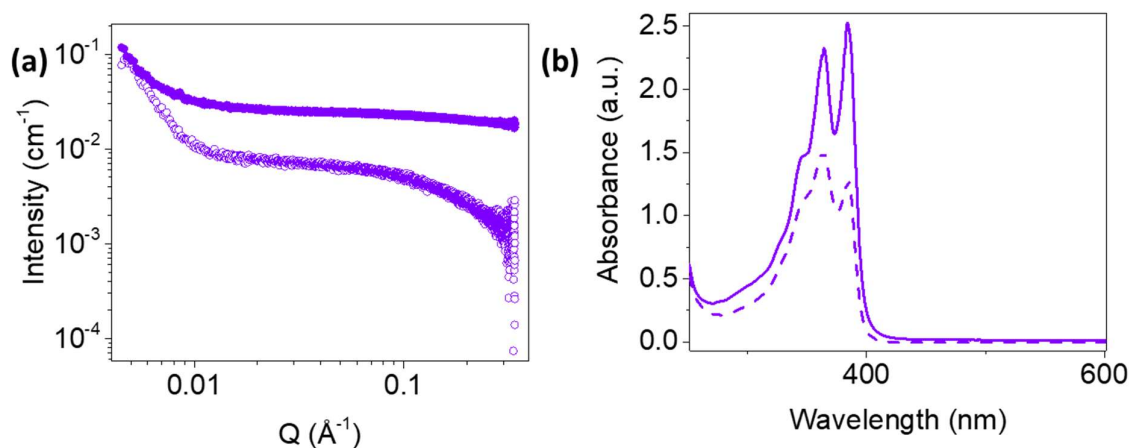


Figure 4.44. (a) SAXS measurement and (b) absorbance spectra of neutral buffered **NDI-F** 5 mg/mL pre- (open circles and dashed lines) and post- (filled circles and solid lines) heat-cooling (heating to 40 °C and allowing to cool for 30 minutes).

Table 4.32. Tabulated parameters from fits to SAXS data from for heat-cooled (heating to 40 °C and allowing to cool for 30 minutes) systems buffered and unbuffered. All solutions adjusted to pH 6. Full data set available in Figures A.4.63 and A.4.96 and Tables A.4.35 and A.4.60, Appendix. Hollow cylindrical models used.

Buffered System (5 mg/mL)	Radius(Å)	Error	Thickness (Å)	Error
NDI-F heat-cooled	6.77	0.0618	7.21	0.113
NDI-F	9.12	0.106	5.27	0.0359

Aggregation does not significantly change with cycling in buffered heat-cooled **NDI-F**, Figure 4.45 and Table 4.33. While radius and thickness subtly fluctuate, the overall radius size remains consistent. There is a loss of intensity after 50 cycles, which suggests smaller or more solvated aggregates and is consistent with the trends observed in **NDI-F** at 10 mg/mL in Chapter 3.

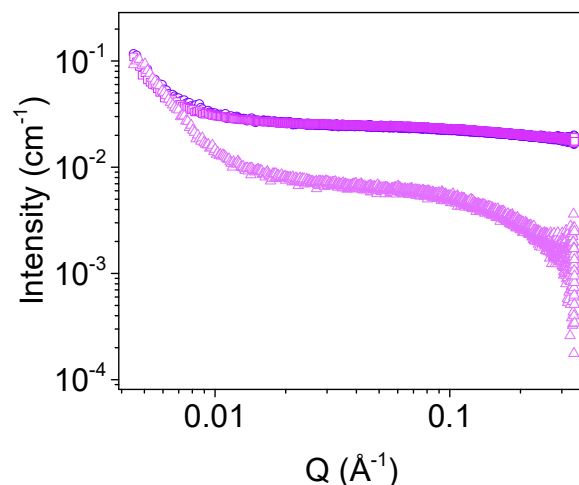


Figure 4.45. SAXS measurement of buffered relaxed **NDI-F** 5 mg/mL heat-cooled (heating to 40 °C and allowing to cool for 30 minutes) and buffered at pH 6. Solutions are measured after 0 (purple), 1 (lilac) and 50 (light lilac) electrochemical cycles.

Table 4.33. Tabulated parameters from fits to SAXS data from relaxed **NDI-F** systems at 5 mg/mL after heat-cooling (heating to 40 °C and allowing to cool for 30 minutes). Solutions buffered at pH 6. Full data set available in Figures A.4.50 and A.4.100-A.4.101 and Tables A.4.60 and A.4.63-A.4.64, Appendix. Hollow cylindrical models used.

NDI-F buffered, and heat cooled	Radius (Å)	Error	Thickness (Å)	Error
Pre-cycled	6.77	0.0618	7.21	0.113
After 1 cycle	4.99	0.0190	8.15	0.0574
After 50 cycles	8.88	0.135	5.22	0.0322

4.2.13 Comparing our best performing systems

Now that we know our best performing single and multicomponent systems (heat-cooled and non-heat-cooled) we can compare across our entire investigation. Firstly, assessing the neutral state, Figure 4.46. The heat-cooled systems are more comparable to each other but still have a slightly differing ratio of absorbances at 365 and 385 nm between single and multicomponent systems. While the non-heat-cooled systems are comparable to each other, the ratio of absorbances is different to the heat-cooled systems. This data suggests that heat-cooling influences molecular packing of **NDI-F** in single and multicomponent systems.

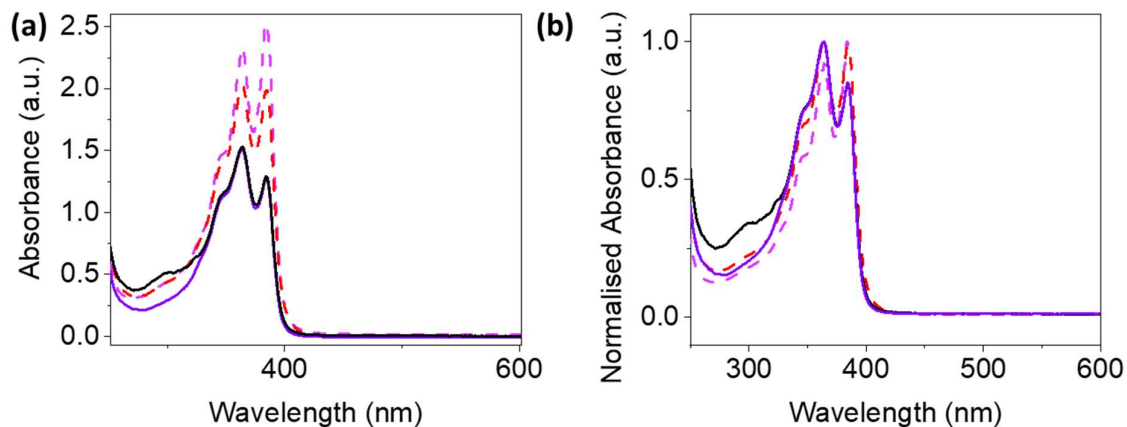


Figure 4.46. (a) Absorbance and (b) normalised absorbance spectra of the neutral state of **NDI-F** 5 mg/mL (purple), **NDI-F:1-NapFF** 5:0.625 mg/mL (red) and **NDI-F:1-NapFF** 5:5 mg/mL (black). All solutions buffered to pH 6. Dashed lines indicate heat-cooling (heating to 40 °C and allowing to cool for 30 minutes).

Next, we can compare the reduced state. Both heat-cooled systems have higher colouration intensity and are comparable to each other (the multicomponent system has slightly higher absorbance), Figure 4.47(a). The single component systems have a faster oxidation rate than the multicomponent systems, Figure 4.47(b). The heat-cooled single component system reaches full oxidation approximately 30 seconds earlier, but this difference (in terms of colour intensity during oxidation) is negligible to the eye. The improvement in colouration in both heat-cooled systems may be the result of the change in molecular packing observed in absorbance spectra.

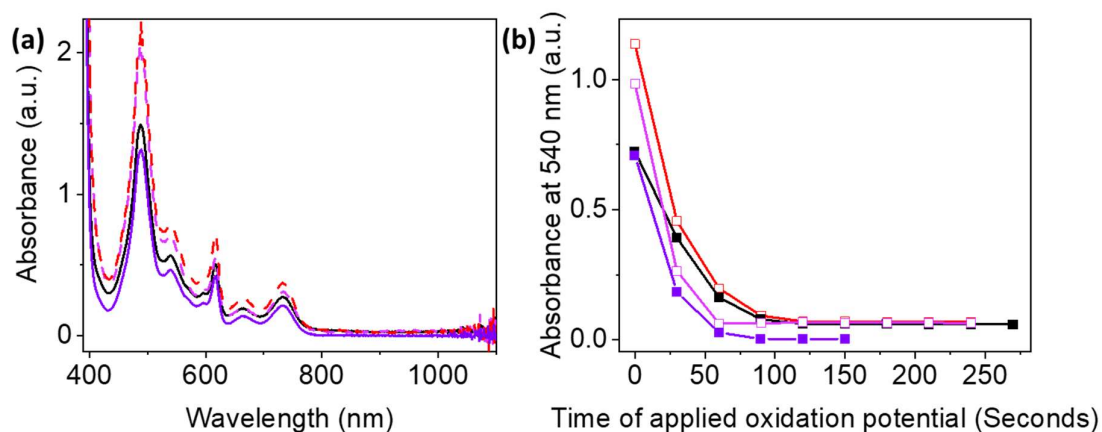


Figure 4.47. (a) Absorbance spectra of reduced state after application of -2.5 V for 10 seconds and (b) measurement of absorbance at 540 nm as an oxidising potential of 0.5 V was applied for 5 minutes after 20 seconds of reduction with -2.5 V. Spectra taken with **NDI-F** 5 mg/mL (purple), **NDI-F:1-NapFF** 5:0.625 mg/mL (red) and **NDI-F:1-NapFF** 5:5 mg/mL (black). All solutions buffered to pH 6. Dashed lines and open squares indicate heat-cooling (heating to 40 °C and allowing to cool for 30 minutes).

The viscosity of systems with higher concentrations of **1-NapFF** is higher, as expected, Figure 4.48(a). There is not a linear relationship between cyclability and viscosity however, as the multicomponent system with higher **1-NapFF** concentration does not show the best performance (Figure 4.48(b)). Interestingly, heat-cooled **NDI-F** shows a far less significant shear thinning behaviour than non-heat-cooled **NDI-F** and has a higher viscosity through shearing, Figure 4.48(a). This suggests that aggregates are larger or more stable which is likely what stabilised the formation of the radical anionic species.

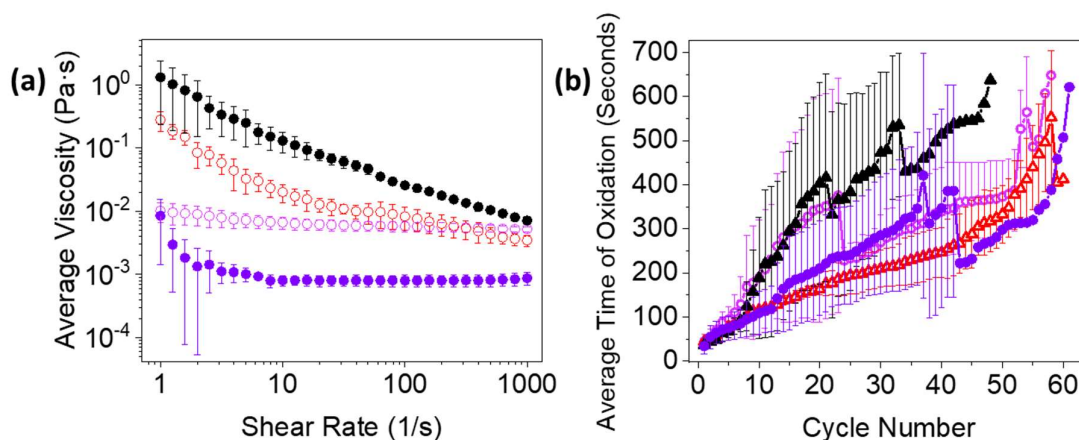


Figure 4.48. (a) Viscosity measurements and (b) plot showing how time to reach a state without colouration fluctuates with electrochemical cycling between a reduced and oxidised state. Measurements taken with **NDI-F** 5 mg/mL (purple), **NDI-F:1-NapFF** 5:5 mg/mL (black), heat-cooled **NDI-F** 5 mg/mL (lilac) and heat-cooled **NDI-F:1-NapFF** 5:0.625 mg/mL (red). All solutions buffered to pH 6. Heat-cooled systems (heating to 40 °C and allowing to cool for 30 minutes) are shown as open shapes. Measurements are taken as an average of triplicate measurements and error bars calculated from standard deviation.

Heat-cooled systems are fairly comparable in terms of their oxidation times and cyclability but the multicomponent **NDI-F:1-NapFF** 5:0.625 mg/mL performs better on both accounts, Figure 4.49. The error bars for this system are also smaller than **NDI-F** alone, which indicates more reproducible performance. Non-heat-cooled **NDI-F** can perform one more cycle than **NDI-F:1-NapFF** 5:0.625 mg/mL but overall, the oxidation time is shorter, and the error bars are smaller in the multicomponent system. This system also has the better colouration.

These data suggests that diffusion issues within our devices are occurring, but that our solution was not as straightforward as we anticipated. However, we have discovered some interesting interactions between these components that result in enhancement of colour as well as cyclability and discovered more about the effect of heat-cooling these systems. Multicomponent systems could be investigated further to form gels, which could have application in patterning.

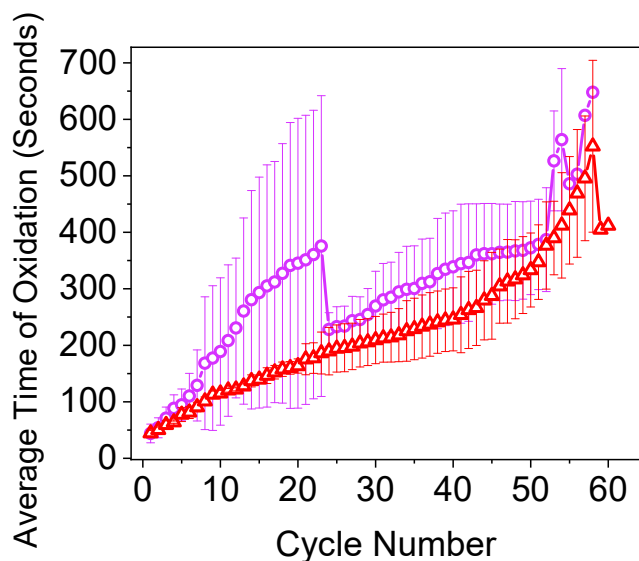


Figure 4.49. Plot showing how time to reach a state without colouration fluctuates with electrochemical cycling between a reduced and oxidised state. Measurements taken with heat-cooled (heating to 40 °C and allowing to cool for 30 minutes) **NDI-F** 5 mg/mL (lilac) and **NDI-F:1-NapFF** 5:0.625 mg/mL (red). All solutions buffered to pH 6. Measurements are taken as an average of triplicate measurements and error bars calculated from standard deviation.

The 5:5 mg/mL non-heat-cooled system contains longer, more rigid and less elliptical cylinders of **1-NapFF** with larger radii than 5:0.625 mg/mL heat-cooled systems, Table 4.34. The **NDI-F** component has a larger length and radius in this heat-cooled multicomponent system than the 5:0 and 5:5 mg/mL systems, Table 4.34. This data suggests that the **1-NapFF** structures have been affected and the **NDI-F** structures have become larger (a trait which supports radical formation). The increased cyclability of the multicomponent system may be due to these factors as well as an increased viscosity and lower diffusion rates. It is likely that both diffusion and aggregation contribute to cyclability.

Table 4.34. Tabulated parameters from fits to SAXS data from single and multicomponent systems. Some systems are heat-cooled (heating to 40 °C and allowing to cool for 30 minutes). All are buffered at pH 6. Various cylindrical models used (see Appendix).

Buffered System at pH 6 (mg/mL)	Length (Å)	Error	Kuhn length (Å)	Error	Radius (Å)	Error	Axis Ratio	Error
NDI-F:1-NapFF (5:0.625) heat-cooled	303.56	0.802	201.23	0.403	16.41	0.00833	5.12	0.00235
NDI-F (5) heat-cooled	N/A	N/A	N/A	N/A	N/A	N/A	N/A	N/A
NDI-F:1-NapFF (5:5)	9.61E+03	1.11E+03	304.54	0.573	32.90	0.00319	1.72	1.54E-04
NDI-F (5)	N/A	N/A	N/A	N/A	N/A	N/A	N/A	N/A
Buffered System at pH 6 (mg/mL)	Length B (Å)	Error	Radius B (Å)	Error	Thickness B (Å)	Error		
NDI-F:1-NapFF (5:0.625) heat-cooled	1.04E+04	7.04	43.14	0.00561	N/A	N/A		
NDI-F (5) heat-cooled	19.72	0.101	6.77	0.0618	7.21	0.113		
NDI-F:1-NapFF (5:5)	40.32	0.0791	4.84	0.0108	6.34	0.00562		
NDI-F (5)	21.92	0.168	9.12	0.1064	5.27	0.0359		

Due to suspected artefacts in our SAXS data for cycles 5:0.625 mg/mL heat-cooled **NDI-F:1-NapFF**, we cannot directly compare the impact of cyclability upon aggregation in our best performing systems. After 50 cycles, the 5:5 mg/mL system is most comparable to its pre-cycled states but has the worst cyclability, 4.2.9 and 4.2.10.4. Taking this into consideration we find that a multicomponent system of **NDI-F:1-NapFF** at a 5:0.625 mg/mL ratio, at pH 6 and heat-cooled, gives the best performance in our devices. Colouration is not significantly enhanced by the **1-NapFF** component compared to heat-cooled **NDI-F**, but long term cyclability, oxidation times and reproducibility are.

4.3 Conclusions

Thus far, using absorbance spectroscopy and SAS, the aggregated state of five different NDIs at different pH has been assessed and preferences for each systems linked to improved chromic properties. For example, larger radii of aromatic NDIs and more rigidity in aliphatic NDIs. *In situ* techniques have also shown that the production of the radical does not have great impact upon aggregation but that there may be some attraction of a charged and uncharged fibre which could

subtly impact aggregation. This finding could have some significance if the radical was allowed to build up over cycling. Using NMR spectroscopy, SANS and absorbance spectroscopy, we cannot detect any evidence of degradation with use in our systems. These systems still have great promise and our hypothesis that they are suitable for long term use is supported by evidence in Chapter 3.

This investigation set out to test a hypothesis that a viscous component will aid cyclability. What we discovered was that this hypothesis was not a simple matter of increased viscosity leading to improved properties. We suspect an interaction of components but that ultimately, the components are still self-sorted structures. This interaction is particularly notable at high and low pH. We found that chemical structure, ratio of components, pH and the process of heat-cooling affect both the physical and electrochemical properties of multicomponent systems. From an initial discussion of 24 multicomponent systems, we selected one that demonstrated the best performance. We next investigated the effect of heat-cooling upon 15 electrochemically active systems and selected a further two systems, both of which showed improved performance. This investigation allowed us some insight into complex systems and confirmed some of our earlier findings about single component NDI aggregation.

NDI-GF:1-NapFF systems were not better performing than **NDI-GF**. At low pH we believe the two gelating systems to be interacting in a detrimental way. The higher the concentration of **1-NapFF**, the worse colouration became at low pH in these systems. We attribute this behaviour to the size or high flexibility of **NDI-GF** aggregates. At low pH, two fibrous networks are formed and can entangle or disrupt each other. The interplanar distance between NDI molecules must be small enough to allow effective π electron delocalisation to efficiently form the radical anion.^{50,51}

NDI-F:1-NapFF systems were actively improved by the addition of **1-NapFF** at specific pH and ratios of component. There was even improvement at non-ideal pHs of **NDI-F**. At high pH we saw evidence of unexpected interaction of components, resulting in increases viscosity and improved colouration at certain ratios. At low pH we also suspect there to be a higher level of interaction between components. **NDI-F** forms hollow cylinders (as does **1-NapFF**^{42,44,45}) and so this may lead to favourable interaction between components. **NDI-F**'s amino acid is also smaller than **NDI-GF** and **1-NapFF** as so may be able to partially co-assemble or interact favourably with **1-NapFF** structures. We suspect the aggregates are homogeneous but that larger structures could be less so.

Heat-cooling was also investigated and found to improve colouration upon reduction, which we believe is linked to larger aggregates and different packing. Enhancement of colour was observed in many (but not all) multicomponent systems upon heat-cooling, and again rigidity of **1-NapFF** and size of **NDI-F** aggregates are linked to more intense electrochromic colouration. These factors are

consistent with non-heat-cooled **NDI-F** systems. Cyclability is not improved by heat-cooling in **NDI-F** alone.

Overall, heat-cooled **NDI-F:1-NapFF** 5:0.625 mg/mL at pH 6 showed best cyclability, colouration intensity, oxidation time during cycling experiments, and reproducibility. Packing of aggregates was identified as an important factor as well as the size of **NDI-F** aggregates and the process of heat-cooling (as this ratio did not show great colouration before heat-cooling).

In our best performing system (heat cooled 5:0.625 mg/mL **NDI-F:1-NapFF** buffered at pH 6), viscosity was higher than **NDI-F** but lower than other systems investigated. The increased viscosity and decrease in diffusion rates could still be improving cyclability compared to single component **NDI-F**. Both diffusion and component interactions are factors. At higher concentration of **1-NapFF**, we believe that the more dominant structures of **1-NapFF** were limiting the NDI π stacking or aggregates, resulting in poorer colouration than other systems.

We have identified how **1-NapFF** can improve our systems in a way we did not originally anticipate and understand more about the factors that may influence such multicomponent systems. The overall improvement is not significant in terms of the number of cycles, but other properties such as reproducibility and colour intensity are improved from Chapter 3.

The ideal pH of **NDI-F** found in Chapter 2 is consistently the best performing, which suggests that aggregates are comparable in single and multicomponent structures and highlights the importance of pH upon the chromic ability of NDI systems.

4.4 Experimental

4.4.1 Synthetic procedures

All synthetic procedures and product identical to those described in Chapter 2. **1-NapFF** has been reported previously.^{34–36} All chemicals and solvent were purchased from Merck Life Sciences, or Alfa Aesar and used as received. Deionised water was used throughout. NMR spectra and HRMS can be found in the Appendix (Figures A.4.101-A.4.117).

4.4.1.1 Synthesis of 2-{2-[2-(naphthalen-1-yloxy)acetamido]-3-phenylpropanamido]-3-phenylpropanoic acid (1-NapFF)

4.4.1.1.1 Synthesis of ethyl 2-(2-[[tert-butoxy]carbonyl]amino)-3-phenylpropanamido)-3-phenylpropanoate (FF-OEt – Protected)

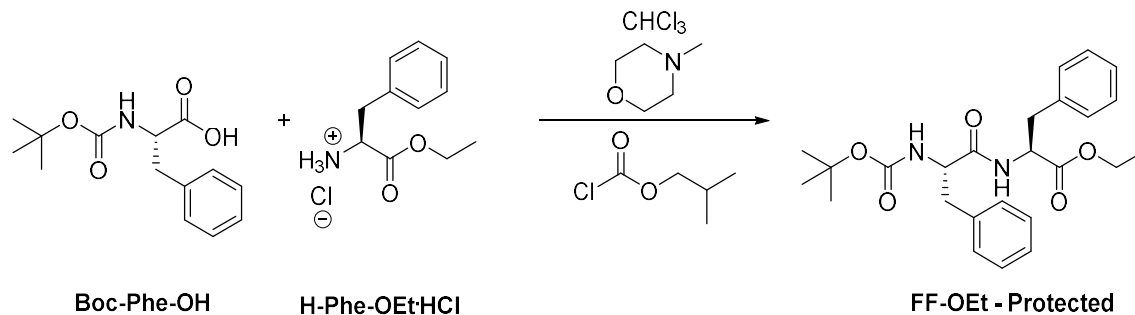
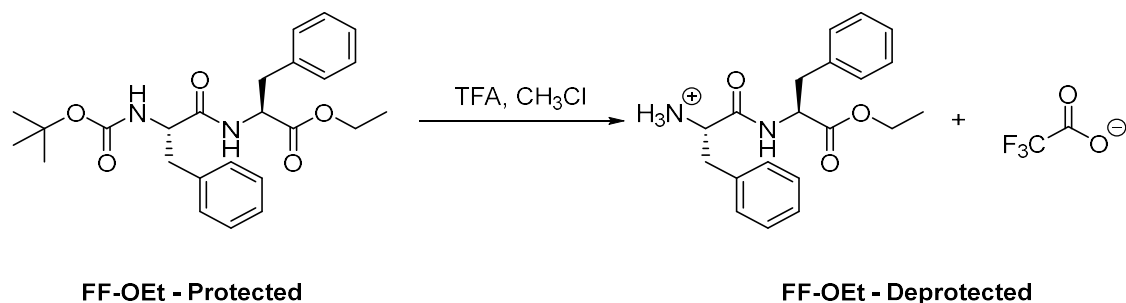


Figure 4.50. 1st step, synthesis of FF-OEt – Protected.

To a solution of Boc-phenylalanine (1 eq, 21.22 g) in chloroform (180 mL) was added N-methylmorpholine (1 eq, 8.78 mL), followed by isobutyl chloroformate (1 eq, 10.38 mL) and the mixture was stirred over ice for 20 minutes. After this time, another portion of N-methylmorpholine (1 eq, 8.78 mL) and L-phenylalanine tert-butyl ester hydrochloride (1 eq, 18.38 g) were added, and the reaction mixture was stirred overnight. After this time reaction mixture was diluted with chloroform, washed in turn with water, 1M hydrochloric acid, and water again, dried (MgSO_4), and evaporated to dryness under reduced pressure. The product FF-OEt - Protected was thus obtained as a pale yellow, viscous oil (10.6 g, 30%). The solid was then characterised by ^1H and ^{13}C NMR. Impurities were removed in the next step of the synthesis.

FF-OEt-Protected: ^1H NMR (400 MHz, DMSO-d_6) δ 8.45 (d, 8.0 Hz, 1H, NHCOOC), 7.34-7.12 (m, 10 H, HAr), 6.78 (d, Hz, 1H, 8.8 NH), 4.53-4.44 (m, 1H, CH), 4.24-4.16 (m, 1H, CH), 4.09 (q, 7.1 Hz, 2H, CH_2CH_3), 3.05 (dd, 5.5, 14.0 Hz, 1H, CH_2Ph), 2.90 (dd, 9.3, 13.6 Hz, 1H, CH_2Ph), 2.69 (dd, 3.9, 13.7 Hz, 1H, CH_2Ph), 2.55 (m, 1H, CH_2Ph), 1.29 (s, 7H, $\text{C}(\text{CH}_3)_3$), 1.21 (s, 2H, $\text{C}(\text{CH}_3)_3$), 1.15 (t, 7.1 Hz, 3H, CH_2CH_3), ^{13}C NMR (100 MHz, DMSO-d_6) δ 172.19 and 171.85 and 155.61 (C=O), 138.50, 137.53, 129.68, 129.63, 128.66, 128.37, 127.04 and 126.56 (CAr), 78.44 (CCH_3), 61.06 (CH_2CH_3), 55.83 and 53.99 (NHCH), 37.97 and 37.43 (CH_2Ph), 28.57 ($\text{C}(\text{CH}_3)_3$), 14.44 (CH_2CH_3), HRMS (ESI) m/z: $[\text{M}+\text{Na}]^+$ calculated for $\text{C}_{25}\text{H}_{32}\text{N}_2\text{O}_5\text{Na}$, 463.2197; found 463.2203.

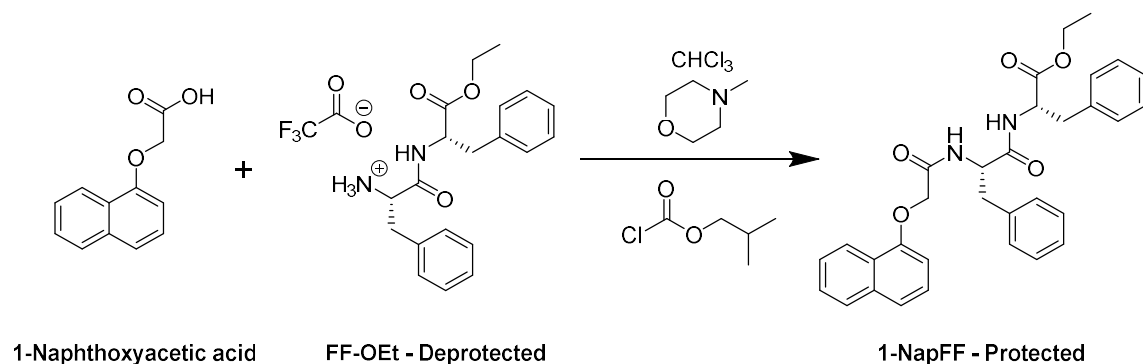
4.4.1.1.2 Synthesis of ethyl 2-(2-azaniumyl-3-phenylpropanamido)-3-Phenylpropanoate (FF-OEt – Deprotected)

Figure 4.51. 2nd step, deprotection of FF-OEt – Protected.

To a solution of FF-OEt - Protected (1 eq, 10.6 g) in chloroform (100 mL) was added trifluoroacetic acid (13 eq, ca. 25 mL) and the mixture was stirred overnight. The reaction mixture was then poured into diethyl ether (500 mL) and stirred for 30 minutes. The solids were filtered off, washed with diethyl ether in the filter and dried under vacuum. The product FF-OEt - Deprotected was obtained as a white solid (10.33 g, 94%). The solid was then characterised by ¹H and ¹³C NMR and HRMS.

FF-OEt-Deprotected: ¹H NMR (400 MHz, DMSO-*d*₆) δ 9.11 (d, 7.5 Hz, 1H, NH), 8.3, (br s, 3H, NH₃⁺), 7.39-7.16 (m, 10 H, HAR), 4.56 (dd, 7.0, 21.9 Hz, 1H, NHCH), 4.11 (br s, 1 H, NH₃⁺CH), 4.06 (q, 7.0, 21.2 Hz, 2H, CH₂CH₃), 3.20-2.93 (m, 4 H, CH₂Ph), 1.11 (t, 7.1 Hz, 3H, CH₂CH₃) ¹³C NMR (100 MHz, DMSO-*d*₆) δ 171.14 and 168.71 (C=O), 158.92 (q, 32.8 Hz, F₃C-C=O), 137.26, 135.26, 130.03, 129.6, 128.94, 128.80, 127.60 and 127.21 (CAr), 117.25 (q, 927 Hz, CF₃), 61.23 (CH₂CH₃), 54.42 and 53.65 (NHCH), 37.35 and 37.25 (CH₂Ph), 14.37 (CH₃), HRMS (ESI) *m/z*: [M]⁺ calculated for C₂₀H₂₅N₂O₃Na, 341.19; found 341.1860.

4.4.1.1.3 Synthesis of ethyl 2-[2-[2-(naphthalen-1-yloxy)acetamido]-3-phenylpropanamido]-3-phenylpropanoate (1-NapFF – Protected)

Figure 4.52. 3rd step, synthesis of 1-NapFF – Protected.

To a solution of FF-OEt - Deprotected (1 eq, 8.30 g) in chloroform (125, 1.87 mL) was added N-methylmorpholine (1 eq, 2.49 mL), followed by isobutyl chloroformate (1 eq, 2.94 mL) and the mixture was stirred at on ice for 20 minutes. After this time, another portion of N-methylmorpholine (1 eq, 1.87 mL) and 1-Naphthoxyacetic acid (1 eq, 3.70 g) were added and the reaction mixture was stirred overnight. After this time reaction mixture was diluted with chloroform, washed in turn with water, 1M hydrochloric acid, and water again, dried (MgSO₄), and evaporated to dryness under reduced pressure. The product **1-NapFF - Protected** was obtained as a pale pink/orange solid (6.00 g, 76%). The solid was then characterised by ¹H and ¹³C NMR. Trace Impurities were removed in the next step of the synthesis.

1-NapFF-Protected: ¹H NMR (400 MHz, DMSO-d₆) δ 8.6 (d, 7.5 Hz, 1H, H_{Ar}), 8.1 (t, 7.3 Hz, 2H, H_{Ar}), 7.9, (dd, 1.9, 9.3 Hz, 1H, H_{Ar}), 7.6-7.5 (m, 3H, H_{Ar}), 7.3 (t, 7.9 Hz, 1H, NH), 7.3-7.2 (m, 10 H, Ph), 6.7 (d, 7.5 Hz, 1 H, NH), 4.8-4.7 (m, 1 H, CH), 4.7-4.6 (m, 2H, OCH₂), 4.6-4.5 (m, 1H, CH), 4.1-4.0 (q, 2H, CH₂CH₃), 3.1-2.8 (m, 4H, CH₂Ph), 1.1 (t, 7.1 Hz, 3H, CH₂CH₃), ¹³C NMR (100 MHz, DMSO-d₆) δ 171.76, 171.32 and 167.53 (C=O), 153.35, 137.81, 137.47, 134.53, 129.74, 129.59, 129.55, 128.73, 128.55, 128.52, 128.47, 127.91, 127.05, 127.00, 126.83, 126.83, 126.47, 125.84, 125.19, 122.14, 121.08 and 106.18 (C_{Ar}), 67.80 (OCH₂), 61.00 (CH₂CH₃), 54.35 and 53.59 (NHCH), 37.99 and 37.19 (CH₂Ph), 14.41 (CH₂CH₃), HRMS (ESI) m/z: [M+Na]⁺ calculated for C₃₂H₃₂N₂O₅Na, 547.2197; found 547.2203.

4.4.1.1.4 Synthesis of 2-[2-[2-(naphthalen-1-yloxy)acetamido]-3-phenylpropanamido]-3-phenylpropanoic acid (**1-NapFF**)

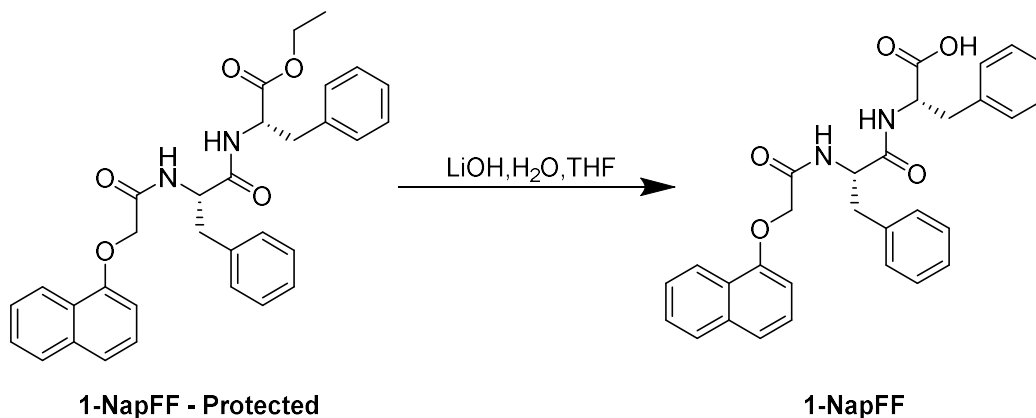


Figure 4.53. 4th step, deprotection of **1-NapFF** – Protected.

1-NapFF – Protected (1 eq, 4.94 g) was dissolved in minimal THF (ca. 10 mL). Dilute lithium hydroxide (4 eq, 0.9 g) in water (ca. 100 mL) was added to the solution was stirred for 6-7 hours. After this time HCl (0.1 M) was added in excess (ca. 400 mL). The resulting white precipitate was allowed to stir overnight. Solids were collected by filtration and washed well with water and petroleum ether before

being dried under vacuum to give **1-NapFF** as a white solid (3.70 g, 79%). The solid was then characterised by ^1H and ^{13}C NMR.

1-NapFF: ^1H NMR (400 MHz, DMSO- d_6) δ 12.9 (br s, 1H, OH), 8.5 (d, 7.9 Hz, 1H, HAr), 8.1 (m, 2H, HAr), 7.9 (dd, 1.9, 3.1 Hz, 1H, HAr), 7.6-7.5 (m, 3H, HAr), 7.3 (t, 8.0 Hz, 1H, NH), 7.3-7.2 (m, 10H, Ph), 6.7 (d, 7.5 Hz, 1H, NH), 4.8-4.7 (m, 1H, CH), 4.6 (m, 2H, OCH $_2$), 4.5 (m, 1H, CH), 3.2-3.0 (m, 2H, CH $_2$ Ph) 3.0-2.8 (m, 2H, CH $_2$ Ph). ^{13}C NMR (100 MHz, DMSO- d_6) δ 173.21, 171.25 and 167.60 (C=O), 153.55, 137.94, 134.51, 129.85, 129.68, 128.69, 128.53, 127.93, 127.00, 126.94, 126.80, 126.48, 125.83, 125.17, 122.14, 121.09 and 106.15 (CAr), 67.58 (OCH $_2$), 53.98 and 53.52 (NHCH), 38.01 and 37.23 (PhCH $_2$) HRMS (ESI) m/z: [M] $^+$ calculated for C $_{30}$ H $_{29}$ N $_2$ O $_5$, 497.2100; found 497.2071

4.4.2 Experimental protocols and equipment

4.4.2.1 Nuclear magnetic resonance (NMR) spectroscopy

For the characterisation after the synthesis of NDIs, NMR measurements were carried out on a Bruker 400 MHz spectrometer as previously described in Chapter 2.

4.4.2.2 Preparation of solutions

Solutions were prepared at 5 or 10 mg/mL of NDIs as previously described in Chapter 2. Solutions were prepared using two molar equivalents of 0.1 M NaOH and 0.5 mL/mL of 0.1 NaCl to help conductivity. Solutions of **1-NapFF** only require one molar equivalents of 0.1 M NaOH. Multicomponent solutions were prepared by mixing together a solution of 10 mg/mL NDI and a solution of **1-NapFF** at double the required concentration. For example, for a 5:2.5 ratio, equal volumes of 10 mg/mL NDI and 5 mg/mL **1-NapFF** were combined and gently shaken to mix. The pH of all solutions was adjusted as previously described. When buffered, solutions were prepared as previously described.

4.4.2.3 Cycling tests

Cycling tests were performed exactly as described in Chapter 3. As a proof of concept to show diffusion influenced cyclability, an identical experiment was undertaken whilst bass heavy music³³ played from a speaker directly underneath the cell.

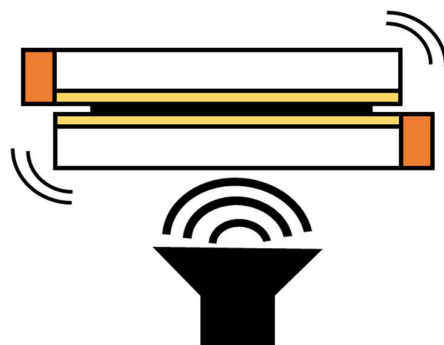


Figure 4.4.54 Cartoon representation of cycling test set-up with the vibration of music.

When solutions were heat cooled the sample was heated in an oil bath at 40 °C for 30 minutes and transferred into the FTO window whilst still hot by pouring so as not to disturb the structures with shear. The window was sealed and left undisturbed for a further 30 minutes before performing electrochemistry.

4.4.2.4 Apparent pK_a titrations

All pK_a titrations were performed as previously described in Chapter 2.

4.4.2.5 Absorption spectroscopy

Absorption spectra were collected using a Cary 60 UV-Visible spectrophotometer as previously described in Chapter 2.

4.4.2.6 Viscosity measurements

All viscosity measurements were performed using an Anton Paar Physica 301 rheometer using a cone and plate geometry (75 mm diameter, 1.0° angle, 50 μm) and a flat plate measuring system for all measurements as previously described. When heat cooled, samples were heated on the plate to 40 °C over the course of 30 seconds. After this 40 °C was maintained for 2 minutes. The sample was then cooled to 25 °C over the course of 30 minutes and left at this final temperature for 5 minutes. Viscosity measurements were undertaken as previously described after this time has elapsed. Samples were sealed using a small amount of oil around the edge of the geometry to prevent drying out.

4.4.2.7 FTO windows

FTO glass (50 × 50 × 2.2 mm, TEC 7, surface resistivity $\sim 7 \Omega/\text{sq}$, from Sigma Aldrich) was used as previously described in Chapter 3.

4.4.2.8 Spectro-electrochemistry

Spectra were collected using the spectrometer as previously described in Chapter 2 In **NDI-F** containing systems, λ_{max} is taken at 485 nm (pH 6 and 9) and 460 nm (pH 12). In **NDI-GF** containing

systems, λ_{max} is taken at 450 nm (pH 6 and 9) and 460 nm (pH 12). When solutions were heat cooled the sample was heated in an oil bath at 40 °C for 30 minutes and transferred into the FTO window whilst still hot by pouring so as not to shear align the structures. The window was sealed and left undisturbed for a further 30 minutes before performing electrochemistry.

4.4.2.9 Cyclic voltammetry (CV)

CV was performed as previously described in 1 x 1 or 5 x 5 FTO glass window cells. Set-up and scan rate is described in figure captions and tables as previously described.

4.4.2.10 Small angle X-ray scattering (SAXS)

Scattering data was collected at B21, Diamond Light Source under experiment number SM27906-2, SM27906-3 and SM27906-4 using a beam energy of 12.4 keV and a sample to detector distance of 5.647 m calibrated using a standard sample of silver behenate. Data was collected as a single frame of 1 s duration and reduced to a 1^d dataset using the DAWN software package and standard pipelines.⁵² Samples were prepared in advance as described in 4.4.2.2 and run by Charlotte Edwards-Gayle due to COVID-19 restrictions. High viscosity systems were run in capillary tubes and where possible low viscosity samples were run from well plates using an autosampler. Samples were pH adjusted before being loaded into capillaries and heat cooled samples were heated within the capillaries using a water bath set at 40 °C for 30 minutes before being allowed to cool for a further 30 minutes.

Data was fitted using SasView (Version 4.2.2)⁵³ as previously described. The SLD of each material was calculated using the NIST neutron activation and scattering calculator.⁵⁴ Where multicomponent systems are used, an average of the two components relative to their proportion is used. SLD of water is 9.469. SLD of **NDI-F**, **NDI-GF** and **1-NapFF** were 13.705, 13.736 and 13.927 respectively.

When electrochemistry was performed upon solutions, as previously described, this was done *ex situ* and samples were left to relax before posting.

4.4.2.10.1 Dawn analysis of scattering data

In data sets where kinks were seen, raw detector data of two-dimensional (2D) scattering plots are shown in the appendix to prove alignment of samples. Histogram plots are shown at a range of 0 to 10, 20, 50 and 100.

4.5 References

- 1 L. E. Buerkle and S. J. Rowan, *Chem. Soc. Rev.*, 2012, **41**, 6089–6102.
- 2 V. M. P. Vieira, L. L. Hay and D. K. Smith, *Chem. Sci.*, **8** (10), 6981-6990.
- 3 H. Kar, M. R. Molla and S. Ghosh, *Chem. Commun.*, 2013, **49**, 4220–4222.

- 4 E. R. Cross, S. Sproules, R. Schweins, E. R. Draper and D. J. Adams, *J. Am. Chem. Soc.*, 2018, **140**, 8667–8670.
- 5 E. R. Draper and D. J. Adams, *Chem. Soc. Rev.*, 2018, **47**, 3395–3405.
- 6 K. AlKaabi, C. R. Wade and M. Dincă, *Chem*, 2016, **1**, 264–272.
- 7 J. F. Penneau, B. J. Stallman and L. L. Kasai, P. H., Miller, *Chem. Mater.*, 1991, **3** (5), 791–796.
- 8 R. Cinnsealach, G. Boschloo, S. N. Rao and D. Fitzmaurice, *Sol. Energy Mater. Sol. Cells*, 1998, **55**, 215–223.
- 9 H. C. Wentz and M. G. Campbell, *Polyhedron*, 2018, **154**, 309–313.
- 10 A. A. Argun *et al.*, *Chem. Mater.*, 2004, **16**, 4401–4412.
- 11 O. Oms, K. Hakouk, R. R. Dessapt, P. Deniard, S. S. Jobic, A. Dolbecq, T. Palacin, L. Nadjjo, B. Keita, J. Jero, J. Marrot and P. Mialane, *Chem. Commun.*, 2012, **48**, 12103–12105.
- 12 M. al Kobaisi, S. v. Bhosale, K. Latham, A. M. Raynor and S. v. Bhosale, *Chem. Rev.*, 2016, **116**, 11685–11796.
- 13 S. Xiao, Y. Zhang, L. Ma, S. Zhao, N. Wu and D. Xiao, *Dyes Pigm.*, 2020, **174**, 108055.
- 14 Y. Alesanco, A. Viñ, J. J. Palenzuela, I. Odriozola, G. Germán, C. Ero, J. Rodriguez, R. Ramón and T.- Zaera, *ACS Appl. Mater. Interfaces*, 2016, **8**, 14795–14801.
- 15 Y. Alesanco, J. Palenzuela, A. Viñuales, G. Cabañero, H. J. Grande and I. Odriozola, *ChemElectroChem*, 2015, **2**, 218–223.
- 16 K. J. Nagy, M. C. Giano, A. Jin, D. J. Pochan and J. P. Schneider, *J. Am. Chem. Soc.*, 2011, **133**, 14975–14977.
- 17 K. Sugiyasu, S. Kawano, N. Fujita and S. Shinkai, *Chem. Mater.*, 2008, **20**, 2863–2865.
- 18 T. A. Welsh, O. Matsarskaia, R. Schweins and E. R. Draper, *New J. Chem*, 2021, **45**, 14005–14013.
- 19 D. J. Cornwell, O. J. Daubney and D. K. Smith, *J. Am. Chem. Soc.*, 2015, **137**, 15486–15492.
- 20 J. Raeburn, B. Alston, J. Kroeger, T. O. McDonald, J. R. Howse, P. J. Cameron and D. J. Adams, *Mater. Horiz.*, 2014, **1**, 241–246.
- 21 K. Fan, H. Kong, X. Wang, X. Yang and J. Song, *RSC Adv.*, 2016, **6**, 80934–80938
- 22 H. Kar, R. Molla and S. Ghosh, *Chem. Commun.*, 2013, **49**, 4220–4222.
- 23 B. V. K. J. Schmidt, *Macromol. Rapid. Commun.*, 2022, **43**, 1–32.
- 24 P. Jittiarporn, S. Badilescu, M. N. al Sawafta, L. Sikong and V.-V. Truong, *J. Sci.: Adv. Mater. Devices*, 2017, **2**, 286–300.
- 25 J. M. Dodda, M. G. Azar and R. Sadiku, *Macromol. Biosci.*, 2021, **21**, 2100232–2100232.
- 26 S. Ghosh, X. Q. Li, V. Stepanenko and F. Würthner, *Chem. Eur. J.*, 2008, **14**, 11343–11357.
- 27 E. R. Draper and D. J. Adams, *Chem*, 2017, **3**, 390–410.
- 28 D. J. Cornwell and D. K. Smith, *Mater. Horiz.*, 2015, **2**, 279–293.
- 29 S. Ghosh, V. K. Praveen and A. Ajayaghosh, *Annu. Rev. Mater. Res.*, 2016, **46**, 235–262.
- 30 P. Terech and R. G. Weiss, *Chem. Rev.*, 1997, **97**, 3133–3159.

- 31 Y. Alesanco, A. Viñuales, J. Rodriguez and R. Tena-Zaera, *Materials*, 2018, **11**, 1–27.
- 32 L. Gonzalez, C. Liu, B. Dietrich, H. Su, S. Sproules, H. Cui, D. Honecker, D. J. Adams and E. R. Draper, *Comm. Chem.*, 2018, **1** (77), 1-8.
- 33 SLAPPING the BASS for 5 HOURS STRAIGHT - YouTube, <https://www.youtube.com/watch?v=oRzyceprYYQ>, (accessed March 7, 2022).
- 34 L. Chen, S. Revel, K. Morris, L. C. Serpell and D. J. Adams, *Langmuir*, 2010, **26**, 13466–13471.
- 35 L. Chen, K. Morris, A. Laybourn, D. Elias, M. R. Hicks, A. Rodger, L. Serpell and D. J. Adams, *Langmuir*, 2010, **26**, 5232–5242.
- 36 G. Pont, L. Chen, D. G. Spiller and D. J. Adams, *Soft Matter*, 2012, **8**, 7797–7802.
- 37 E. R. Draper, H. Su, C. Brasnett, R. J. Poole, S. Rogers, H. Cui, A. Seddon and D. J. Adams, *Angew. Chem. Int. Ed.*, 2017, **56**, 10467–10470.
- 38 D. McDowall, B. J. Greeves, R. Clowes, K. McAulay, A. M. Fuentes-Caparrós, L. Thomson, N. Khunti, N. Cowieson, M. C. Nolan, M. Wallace, A. I. Cooper, E. R. Draper, A. J. Cowan and D. J. Adams, *Adv. Energy Mater.*, 2020, **10**, 1–10.
- 39 E. R. Draper, L. J. Archibald, M. C. Nolan, R. Schweins, M. A. Zwijnenburg, S. Sproules and D. J. Adams, *Chem. Eur. J.*, 2018, **24**, 4006–4010.
- 40 D. Görl, X. Zhang and F. Würthner, *Angew. Chem. Int. Ed.*, 2012, **51**, 6328–6348.
- 41 E. R. Draper, B. J. Greeves, M. Barrow, R. Schweins, M. A. Zwijnenburg and D. J. Adams, *Chem*, 2017, **2**, 716–731.
- 42 E. R. Draper, B. Dietrich, K. McAulay, C. Brasnett, H. Abdizadeh, I. Patmanidis, S. J. Marrink, H. Su, H. Cui, R. Schweins, A. Seddon and D. J. Adams, *Matter*, 2020, **2**, 764–778.
- 43 D. McDowall, D. J. Adams and A. M. Seddon, *Soft Matter*, 2022, **18**, 1577–1590.
- 44 A. Z. Cardoso, L. L. E. Mears, B. N. Cattoz, P. C. Griffiths, R. Schweins and D. J. Adams, *Soft Matter*, 2016, **12**, 3612–3621.
- 45 K. McAulay, B. Dietrich, H. Su, M. T. Scott, S. Rogers, Y. K. Al-Hilaly, H. Cui, L. C. Serpell, A. M. Seddon, E. R. Draper and D. J. Adams, *Chem. Sci.*, 2019, **10**, 7801–7806.
- 46 flexible_cylinder — SasView 5.0.4 documentation, https://www.sasview.org/docs/user/models/flexible_cylinder.html, (accessed May 12, 2022).
- 47 D. McDowall, M. Walker, M. Vassalli, M. Cantini, N. Khunti, C. Edwards-Gayle, N. Cowieson and D. J. Adams, *Chem. Comm.*, 2021, **57**, 8782–8785.
- 48 R. P. Murphy, Z. W. Riedel, M. A. Nakatani, P. F. Salipante, J. S. Weston, S. D. Hudson and K. M. Weigandt, *Soft Matter*, 2020, **16**, 6285–6293.
- 49 Y. Huang, Y. Yan, B. M. Smarsly, Z. Wei and C. F. J. Faul, *J. Mater. Chem.*, 2009, **19**, 2356–2362.
- 50 S. V. Bhosale, C. H. Jani and S. J. Langford, *Chem. Soc. Rev.*, 2008, **37**, 331–342.
- 51 Y. Matsunaga, K. Goto, K. Kubono, K. Sako and T. Shinmyozu, *Chem. Eur. J.*, 2014, **20**, 7309–7316.
- 52 L. J. Marshall, O. Matsarskaia, R. Schweins and D. J. Adams, *Soft Matter*, 2021, **17**, 8459–8464.
- 53 <https://dawnsi.org/>, <https://dawnsi.org/>, (accessed March 28, 2022).

- 54 Sasview, Version 4.2.2, www.sasview.org, (accessed January 2, 2020).
- 55 <https://www.ncnr.nist.gov/resources/activation/>, (accessed October 9, 2019).

CHAPTER FIVE

Summary, Conclusions and Future Work

This thesis set out to understand the relationship between aggregation of amino acid and dipeptide appended NDIs and their electrochromic properties. These tuneable systems have great potential as an organic alternative to transition metal oxide and conductive polymer systems for application as Smart Window devices, as they can achieve intense colour, fast switching times and do not require mining or extensive processing. The self-assembling nature of these NDI systems allows their tunability with pH and chemical structure.

We set out criteria of properties for an ideal system:

- solubility or dispersion in water
- fast reversible switching between a transmissive and a dark state
- a dark reduced state and a pale and transmissive neutral state
- a small potential needed to switch between states
- cyclability of at least 100 cycles without detriment of the above parameters (the ability to switch between states as many times as possible)
- stability (material should not degrade with use or age)

These systems are soluble in water, capable of forming a dark reduced state from a pale and transmissive state in a short period of time using a small potential. The intensity of the colour change upon reduction, and the speed of oxidation can be tailored using aggregation.

By investigating five differently appended NDIs, we identified that both chemical structure and pH have a significant impact upon aggregation, and consequently chromic behaviour. Aggregation influences the efficiency of electrochemical processes and cyclability, with certain properties supporting the formation or stability of the NDI radical anionic species. Each system with different chemical structure has different preferences in terms of their ideal aggregation, with size and flexibility being noted as key parameters. pH is a very easy factor to change and to maintain (using a buffer), meaning that the ideal aggregation for each NDI can be kept stable. This ease of maintaining an ideal state is another advantage alongside the easily tunability of these systems.

We identified that particularly rigid or large dipeptides prevent the efficient formation of cylindrical aggregates and consequently, have poor chromic performance. These findings allow a more intelligent approach to design moving forward with these systems. While we cannot conclude conclusively about what aggregates or properties would be favoured for every amino acid or dipeptide, this thesis lays the groundwork for a larger library to be explored in the future and critically highlights the importance of aggregation. It would be of interest to look specifically at dipeptides and investigate the role of the first amino acid, for example **NDI-FG**, **NDI-AF**, **NDI-IF**, **NDI-VF** etc (Figure 5.1). Is the colouration poor

if anything other than hydrogen is appended the first amino acid group? This line of investigation would be of interest to test the hypothesis that **NDI-FF** has poor chromic properties due to its steric bulk and at what size of group this becomes an issue. Tripeptides or longer chains could also be investigated which may gain insight into if and when length of the peptide R group becomes an issue for chromic properties. Alternatively, the effect of larger aromatic groups upon singular amino acids could be investigated, such as **NDI-W**. The use of groups to further improve solubility (such as **NDI-D**, **NDI-E** or **NDI-S** and **NDI-T**) could also be investigated, Figure 5.1.

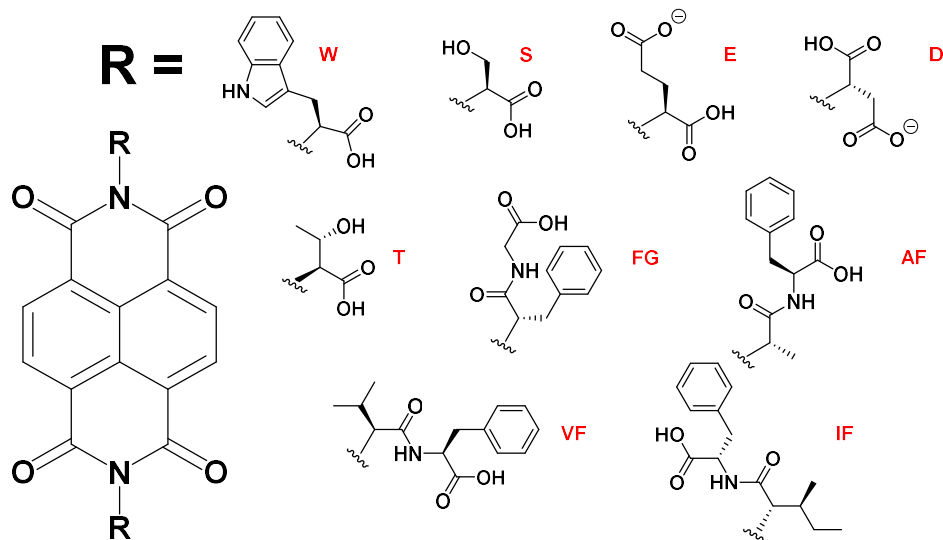


Figure 5.1. Chemical structure of NDIs that could be investigated in future work.

Investigating the long-term stability and cyclability of these NDI systems lead us to develop a methodology, combining the benefits of SANS with *in situ* electrochemistry. This method yields more representative data with accurate insight into electrochemically reduced states and has potential for use in electrochemical kinetics studies such as the growing of gels. We conclude that our materials do not degrade with use and their chromic properties do not change with cycling. Their potential for long term use is high. We attribute some issues in our set-up causing radical anionic species to accumulate, potentially altering aggregation. The formation of the radical anion does not become irreversible, nor is there a change to the NMR spectra to suggest ageing or degradation.

The final chapter of this thesis highlighted the possibility of improving cyclability with a second component. It was found that the secondary component interacts with the NDI, in both detrimental and positive ways depending upon chemical structure, pH and ratio of components. This insight is useful as it was an unexpected result and allowed investigation into a complex multicomponent system. In future work, a component could be used that does not react in any way with NDI, but still

alters diffusion. This scenario is unlikely as the aggregation of these systems are so sensitive and it is incredibly difficult to predict the behaviour of multicomponent interactions based on theory alone. For this reason, perhaps a larger unit rather than a small organic molecular system, such as a polymer, could be used to eliminate the possibility of any co-assembly.

Using a water-soluble polymer (trying to keep to non-toxic components) could also allow the formation of films instead of solution based devices. Polymers have been seen to align PBI fibres and improve conductivity in flexible films in our group and could be a promising candidate if it aligned NDI fibres too. The use of films could mean fitting a product to existing windows could be viable, rather than replacement of the whole window. This feature in itself would be a big advantage for Smart Window technology.

We also identified the use of heat-cooling as a method of influencing aggregation and interaction of these components and ultimately, their chromic properties and cyclability. Again, this investigation highlights the impact of aggregation upon properties and how sensitive aggregation is to small changes in the NDI itself, as well as changes to the environment/solution. Heat-cooling could be looked at in future work to ascertain whether it could improve cyclability in different NDIs.

Up to approximately 60 cycles were achieved in our best performing systems. This is under what we set out in our initial criteria, and below reports of chromic systems in the literature but we believe this is a limitation of the set-up rather than the NDIs themselves. We found improvements to cyclability through buffering, electrochemical scripting and adding additional components. In future work perhaps NDI films would perform better in terms of cyclability.

Overall, we have fulfilled many of our criteria and showed the potential for NDIs as electrochromic devices with a high contrast, reversible transmissive to dark colour changes. The cyclability is the main point that could be improved upon, and we have set out a potential strategy to combat this drawback. It is our hope that either investigating further multicomponent systems, or potentially changing the form from solution to gel or film based devices could alleviate the diffusion issues we suspect in our set-up. Such system could further improve cyclability to a standard that is comparable with the literature. Differing diffusion rates by use of a film or gel could not only improve cyclability but also open possibilities such as photo- and electrochemically patterning.

Appendix

TABLE OF CONTENTS

A.2 Chapter 2 appendices	1
A.2.E. Chapter 2 experimental appendices.....	15
A.3 Chapter 3 appendices	54
A.3.1 Development of cyclability testing	75
A.3.2 The influence of electrochemical script.....	79
A.3.2 Explanation of NMR	89
A.3.3 <i>In situ</i> measurement.....	119
A.3.E Chapter 3 experimental appendices.....	134
A.3.E.1 The influence of temperature.....	134
A.4 Chapter 4 appendices	136
A.4.E Chapter 4 experimental appendices.....	232
References	248

TABLE OF FIGURES

Figures

Figure A.2.1. pH titration data taken for 10 mg/mL NDI-I with background electrolyte (a). The area of the plot with both pK_a values with x axis on a logarithmic scale is also shown (b).	1
Figure A.2.2. pH titration data taken for 10 mg/mL NDI-V with background electrolyte (a). The area of the plot with both pK_a values with x axis on a logarithmic scale is also shown (b).	2
Figure A.2.3. pH titration data taken for 10 mg/mL NDI-F with background electrolyte (a). The area of the plot with both pK_a values with x axis on a logarithmic scale is also shown (b).	3
Figure A.2.4. pH titration data taken for 10 mg/mL NDI-GF with background electrolyte (a). The area of the plot with both pK_a values with x axis on a logarithmic scale is also shown (b).	4
Figure A.2.5. pH titration data taken for 10 mg/mL NDI-FF with background electrolyte (a). The area of the plot with both pK_a values with x axis on a logarithmic scale is also shown (b).	5
Figure A.2.6. Cyclic voltammogram collected from a 10 mg/mL hydroquinone solution with 10 % 0.1 M NaCl. Voltammograms collected in (a) a referenced glassy carbon set up (vs Ag/AgCl) and (b) a 1 x 1 cm FTO window cell set up. The scan rate was 0.2 V/s.	6
Figure A.2.7. Cyclic voltammogram collected from 10 mg/mL solution of NDI-I adjusted to pH 9. Voltammograms measured using a referenced glassy carbon set up (vs Ag/AgCl). The scan rate of the cyclic voltammograms was 0.2 V/s.	6

Figure A.2.8. Cyclic voltammogram collected from 10 mg/mL solution of NDI-V adjusted to pH 9. Voltammograms measured using a referenced glassy carbon set up (vs Ag/AgCl). The scan rate of the cyclic voltammograms was 0.2 V/s.	7
Figure A.2.9. Cyclic voltammogram collected from 10 mg/mL solution of NDI-F adjusted to pH 9. Voltammograms measured using a referenced glassy carbon set up (vs Ag/AgCl). The scan rate of the cyclic voltammograms was 0.2 V/s.	7
Figure A.2.10. Cyclic voltammogram collected from 10 mg/mL solution of NDI-GF adjusted to pH 9. Voltammograms measured using a referenced glassy carbon set up (vs Ag/AgCl). The scan rate of the cyclic voltammograms was (a) 0.2 and (b) 0.5 V/s.	8
Figure A.2.11. Cyclic voltammogram collected from 10 mg/mL solution of NDI-FF adjusted to pH 9. Voltammograms measured using a referenced glassy carbon set up (vs Ag/AgCl). The scan rate of the cyclic voltammograms was 0.2 V/s.	9
Figure A.2.12. Cyclic voltammograms collected from 10 mg/mL solutions of NDI-I adjusted to pH 6 (red), 7 (pink), 8 (orange), 9 (black), 10 (turquoise), 11 (purple) and 12 (blue). The scan rate of the cyclic voltammograms was 0.1 V/s.	10
Figure A.2.13. Cyclic voltammograms collected from 10 mg/mL solutions of NDI-V adjusted to pH 6 (red), 7 (pink), 8 (orange), 9 (black), 10 (turquoise), 11 (purple) and 12 (blue). The scan rate of the cyclic voltammograms was 0.1 V/s.	11
Figure A.2.14. Cyclic voltammograms collected from 10 mg/mL solutions of NDI-F adjusted to pH 6 (red), 7 (pink), 8 (orange), 9 (black), 10 (turquoise), 11 (purple) and 12 (blue). The scan rate of the cyclic voltammograms was 0.1 V/s.	12
Figure A.2.15. Cyclic voltammograms collected from 10 mg/mL solutions of NDI-GF adjusted to pH 6 (red), 7 (pink), 8 (orange), 9 (black), 10 (turquoise), 11 (purple) and 12 (blue). The scan rate of the cyclic voltammograms was 0.1 V/s. (b) shows data from solutions at pH 6 (red), 7 (pink), 8 (orange), 9 (black), 10 (turquoise), and 11 (purple) and on a smaller scale for clarity.	13
Figure A.2.16. Cyclic voltammograms collected from 10 mg/mL solutions of NDI-FF adjusted to pH 6 (red), 7 (pink), 8 (orange), 9 (black), 10 (turquoise), 11 (purple) and 12 (blue). The scan rate of the cyclic voltammograms was 0.1 V/s. (b) shows data from solutions at pH 6 (red), 7 (pink), 8 (orange), 9 (black) and 10 (turquoise) on a smaller scale for clarity.	14
Figure A.2.17. Annotated ¹ H NMR spectrum (400 MHz, DMSO-d ₆) of impure starting material as received.	15
Figure A.2.18. Overlaid annotated ¹ H NMR spectra (400 MHz, DMSO-d ₆) of impure starting material (black) and purified product (red).	16
Figure A.2.19. Annotated ¹ H NMR spectrum (400 MHz, DMSO-d ₆) of NDI-I (a) full spectra with insert of area between 5.2-5.3 ppm (b) enhanced section of spectra shown between 2.5-0 ppm.	17
Figure A.2.20. ¹ H NMR spectrum showing intergration (400 MHz, DMSO-d ₆) of NDI-I (a) full spectra with insert of area at 5.2 ppm (b) enhanced section of spectra shown between 2.5-0.5 ppm.	19
Figure A.2.21. Annotated ¹³ C NMR spectrum (100 MHz, DMSO-d ₆) of NDI-I	20
Figure A.2.22. HRMS report of NDI-I in ethanol.	21
Figure A.2.23. Annotated ¹ H NMR spectrum (400 MHz, DMSO-d ₆) of NDI-V	22
Figure A.2.24. ¹ H NMR spectrum showing intergration (400 MHz, DMSO-d ₆) of NDI-V	23
Figure A.2.25. Annotated ¹³ C NMR spectrum (100 MHz, DMSO-d ₆) of NDI-V	24
Figure A.2.26. HRMS report of NDI-V in ethanol.	25
Figure A.2.27. Annotated ¹ H NMR spectrum (400 MHz) of NDI-F in DMSO-d ₆ + TFA.	26
Figure A.2.28. ¹ H NMR spectrum showing integration (400 MHz, DMSO-d ₆) of NDI-F	27
Figure A.2.29. Annotated ¹³ C NMR spectrum (100 MHz, DMSO-d ₆ + TFA) of NDI-F (a) full spectra (b) enhanced section marked Ar showing the aromatic carbon environments.	28
Figure A.2.30. HRMS report of NDI-F in ethanol.	29
Figure A.2.31. Annotated ¹ H NMR spectrum (400 MHz, DMSO-d ₆) of GF-Protected.	30

Figure A.2.32. ^1H NMR spectrum showing integration (400 MHz, DMSO-d_6) of GF-Protected with enhanced section of spectra shown around 3.35 ppm.	31
Figure A.2.33. Annotated ^{13}C NMR spectrum (100 MHz, DMSO-d_6) of GF-Protected.	32
Figure A.2.34. HRMS report of GF-Protected.	33
Figure A.2.35. Annotated ^1H NMR spectrum (400 MHz, DMSO-d_6) of GF-Deprotected.	34
Figure A.2.36. Annotated ^1H NMR spectrum showing integration (400 MHz, DMSO-d_6) of GF-Deprotected.	35
Figure A.2.37. Annotated ^{13}C NMR spectrum (100 MHz, DMSO-d_6) of GF-Deprotected. Environment 12 is too weak to be well defined.	36
Figure A.2.38. HRMS report of GF-Deprotected in ethanol.	37
Figure A.2.39. Annotated ^1H NMR spectrum (400 MHz, DMSO-d_6) of NDI-GF	38
Figure A.2.40. ^1H NMR spectrum showing integration (400 MHz, DMSO-d_6) of NDI-GF with enhanced section of spectra shown around 8.6-8.7 ppm.	39
Figure A.2.41. Annotated ^{13}C NMR spectrum (100 MHz, DMSO-d_6) of NDI-GF (a) full spectra (b) enhanced section marked Ar showing the aromatic carbon environments.	40
Figure A.2.42. HRMS report of NDI-GF in ethanol.	41
Figure A.2.43. Annotated ^1H NMR spectrum (400 MHz, DMSO-d_6) of FF-Protected.	42
Figure A.2.44. ^1H NMR spectrum showing integration (400 MHz, DMSO-d_6) of FF-Protected with enhanced section of spectra shown around 0.85 ppm.	43
Figure A.2.45. Annotated ^{13}C NMR spectrum (100 MHz, DMSO-d_6) of FF-Protected.	44
Figure A.2.46. HRMS report of FF-Protected in ethanol.	45
Figure A.2.47. Annotated ^1H NMR spectrum (400 MHz, DMSO-d_6) of FF-Deprotected.	46
Figure A.2.48. ^1H NMR spectrum showing integration (400 MHz, DMSO-d_6) of FF-Deprotected.	47
Figure A.2.49. Annotated ^{13}C NMR spectrum (100 MHz, DMSO-d_6) of FF-Deprotected (a) full spectra with expanded 55-53 ppm (b) enhanced section marked Ar showing the aromatic carbon environments.	48
Figure A.2.50. HRMS report of FF-Deprotected in ethanol.	49
Figure A.2.51. Annotated ^1H NMR spectrum (400 MHz, DMSO-d_6 + TFA) of NDI-FF	50
Figure A.2.52. ^1H NMR spectrum showing integration (400 MHz, DMSO-d_6) of NDI-FF	51
Figure A.2.53. Annotated ^{13}C NMR spectrum (100 MHz, DMSO-d_6 + TFA) of NDI-FF	52
Figure A.2.54. HRMS report of NDI-FF in ethanol.	53
Figure A.3.1. Cyclic voltammograms collected from buffered (dashed line) and unbuffered (solid line) 10 mg/mL solutions of NDI-I adjusted to pH 9 and pH 9 respectively. Voltammograms measured using a 1x 1 FTO glass window cell. The scan rate of the cyclic voltammograms was 0.1 V/s.	54
Figure A.3.2. Cyclic voltammograms collected from buffered (dashed line) and unbuffered (solid line) 10 mg/mL solutions of NDI-V adjusted to pH 9 and pH 9 respectively. Voltammograms measured using a 1x 1 FTO glass window cell. The scan rate of the cyclic voltammograms was 0.1 V/s.	55
Figure A.3.3. Cyclic voltammograms collected from buffered (dashed line) and unbuffered (solid line) 10 mg/mL solutions of NDI-F adjusted to pH 6. Voltammograms measured using a 1x 1 FTO glass window cell. The scan rate of the cyclic voltammograms was 0.1 V/s.	55
Figure A.3.4. Cyclic voltammograms collected from buffered (dashed line) and unbuffered (solid line) 10 mg/mL solutions of NDI-GF adjusted to pH 6. Voltammograms measured using a 1x 1 FTO glass window cell. The scan rate of the cyclic voltammograms was 0.1 V/s.	56
Figure A.3.5. Cyclic voltammogram collected from buffered (dashed line) and buffered (solid line) 10 mg/mL solution of (a) NDI-I , (b) NDI-V pH 9, (c) NDI-F , (d) NDI-GF pH 6. Voltammograms measured using a referenced classy carbon set up (vs Ag/AgCl). The scan rate of the cyclic voltammograms was 0.2 V/s.	57
Figure A.3.6. Absorbance spectra collected from buffered (dashed line) and buffered (solid line) 10 mg/mL solution of (a) NDI-I , (b) NDI-V pH 9, (c) NDI-F , (d) NDI-GF pH 6 after a 10 second application of -2.5 V.	58

Figure A.3.7. Small angle neutron scattering data for a neutral solution of 10 mg/mL NDI-I at pD 12 (open circles) fitted to a flexible elliptical cylinder model combined with power law (red). Fit parameters can be found in Table A.3.1.....	59
Figure A.3.8. Small angle neutron scattering data for a neutral solution of 10 mg/mL NDI-V at pD 12 (open circles) fitted to a flexible elliptical cylinder model combined with power law (red). Fit parameters can be found in Table A.3.2.....	60
Figure A.3.9. Small angle neutron scattering data for a neutral solution of 10 mg/mL NDI-F at pD 12 (open circles) fitted to a flexible elliptical cylinder model combined with power law (red). Fit parameters can be found in Table A.3.3.....	61
Figure A.3.10. Small angle neutron scattering data for a neutral solution of 10 mg/mL NDI-GF at pD 12 (open circles) fitted to a flexible elliptical cylinder model combined with power law (red). Fit parameters can be found in Table A.3.4.....	62
Figure A.3.11. Small angle neutron scattering data for a neutral solution of 10 mg/mL NDI-FF at pD 12 (open circles) fitted to a flexible elliptical cylinder model combined with power law (red). The fit parameters can be found in Table A.3.5.....	63
Figure A.3.12. Small angle neutron scattering data for a neutral buffered solution of 10 mg/mL NDI-FF at pD 7 (open circles) fitted to a flexible elliptical cylinder model combined with power law (red). The fit parameters can be found in Table A.3.5.	64
Figure A.3.13. Small angle neutron scattering data for a neutral buffered solution of 10 mg/mL NDI-I at pD 9 (open circles) fitted to a flexible cylinder model combined with power law (red). Fit parameters can be found in Table A.3.7.	65
Figure A.3.14. Small angle neutron scattering data for a neutral solution of 10 mg/mL NDI-I at pD 6 (open circles) fitted to a flexible elliptical cylinder model combined with power law (red). Fit parameters can be found in Table A.3.8.....	66
Figure A.3.15. Small angle neutron scattering data for a neutral buffered solution of 10 mg/mL NDI-V at pD 9 (open circles) fitted to a flexible cylinder model combined with power law (red). Fit parameters can be found in Table A.3.9.	67
Figure A.3.16. Small angle neutron scattering data for a neutral solution of 10 mg/mL NDI-V at pD 6 (open circles) fitted to a flexible elliptical cylinder model combined with power law (red). Fit parameters can be found in Table A.3.10.....	68
Figure A.3.17. Small angle neutron scattering data for a neutral solution of 10 mg/mL NDI-F at pD 9 (open circles) fitted to a hollow cylinder model combined with power law (red). Fit parameters can be found in Table A.3.11.	69
Figure A.3.18. Small angle neutron scattering data for a neutral buffered solution of 10 mg/mL NDI-F at pD 6 (open circles) fitted to a hollow cylinder model combined with power law (red). Fit parameters can be found in Table A.3.12.	70
Figure A.3.19. Small angle neutron scattering data for a neutral solution of 10 mg/mL NDI-GF at pD 9 (open circles) fitted to a flexible elliptical cylinder model combined with power law (red). Fit parameters can be found in Table A.3.13.....	71
Figure A.3.20. Small angle neutron scattering data for a neutral buffered solution of 10 mg/mL NDI-GF at pD 6 (open circles) fitted to a flexible elliptical cylinder model combined with power law (red). Fit parameters can be found in Table A.3.14.....	72
Figure A.3.21. Cyclic voltammogram showing Reduction and oxidation potentials taken from cyclic voltammograms of 10 mg/mL hydroquinone with 10 % 0.1 M NaCl. Measurements performed in 5 x 5 FTO window set up. The scan rate of the cyclic voltammograms was 0.5 V/s.....	74
Figure A.3.22. Cyclic voltammograms collected from buffered 10 mg/mL solutions of NDI-I (green), NDI-V (blue), NDI-F (purple) and NDI-GF (brown) adjusted to their respective ideal pH (pH 9 for NDI-I and NDI-V and pH 6 for NDI-F and NDI-GF). Voltammograms measured using a 5 x 5 FTO glass window cell at 0.1 V/s scan rate.	74
Figure A.3.23. Images of FTO windows filled with NDI-I at 10 mg/mL exposed to natural daylight without (A) and with (B) UV filter protective film. A1 and B1 represent the solution at the start of the	

experiments and images following were taken every 30 minutes of exposure to natural light, starting with A1 and B2 until A7 and B7 (images after 3 hours 30 minutes).....	75
Figure A.3.24. (a) Images of FTO glass window filled with NDI-I at 10 mg/mL and buffered at pH 9 during one of the triplicated runs of this cycling experiment. Images captured before the experiment (I) and at the point of full reduction (R) and oxidation (O) for each cycle. (b) Plot showing how time to reach a state of full oxidation (i.e. without discolouration of the neutral state) fluctuates with cycling for buffered (open squares) and unbuffered (filled squares) solutions of 10 mg/mL NDI-I . Measurements are taken as an average of triplicate measurements and error bars calculated from standard deviation.	76
Figure A.3.25. Cyclic voltammograms performed before (black) and during a cycling experiment using unbuffered 10 mg/mL solutions of NDI-I at pH 9. Cyclic voltammograms were taken after the reduction process (a) and the oxidation process (b) had completed. Measurements taken during cycle 1 (purple), 2 (blue), 3 (green), 4 (red) and 5 (pink).....	77
Figure A.3.26. Cyclic voltammograms performed before (black) and during a cycling experiment using buffered 10 mg/mL solutions of NDI-I at pH 9. Cyclic voltammograms were taken after the reduction process (a) and the oxidation process (b) had completed. Measurements taken during cycle 1 (purple), 2 (blue), 3 (green), 4 (red) and 5 (pink).....	78
Figure A.3.27. Plot showing the shifting of the (a) reduction potential and (b) oxidation potential with cycling based on cyclic voltammetry measurements taken after each cycle. Measurements carried out using buffered (open squares) and non-buffered (filled squares) 10 mg/mL NDI-I	79
Figure A.3.28. Simplified schematic representation of the electrochemical procedure containing a fixed potential (a) and sweep potential (b) oxidation method. Potential axis is not to scale. (c) Plot showing how time to reach a state of full oxidation (i.e. without discolouration of the neutral state) fluctuates with cycling of 10 mg/mL buffered NDI-I with a fixed potential (open squares) and sweep potential (filled circles) methods. Measurements are taken as an average of triplicate measurements and error bars calculated from standard deviation.	80
Figure A.3.29. Schematic showing how after reduction (a) diffusion away from the electrode surface (b) may compromise the efficiency of electrochemical oxidation when oxidising potential is applied (c).	81
Figure A.3.30. Simplified schematic representation of the electrochemical oxidation procedure defined as (a) the sweep method, (b) a short flicker method and (c) a long flicker method. Potential axis is not to scale. (d) Plot showing how time to reach a state of full oxidation (i.e. without discolouration of the neutral state) fluctuates with cycling of 10 mg/mL buffered NDI-I with a sweep potential (red circles), short (pink open triangles) and long (purple filled triangles) flicker methods. Measurements are taken as an average of triplicate measurements and error bars calculated from standard deviation.	82
Figure A.3.31. Images of the reduced state at the start (left) and end (right) of cycling experiments. Buffered solutions of 10 mg/mL NDI-V (a), NDI-F (b) and NDI-GF (c) were used adjusted to their respective ideal pH (pH 9 for NDI-V and pH 6 for NDI-F and NDI-GF). The time at the start and end of the experiment is shown on a stopwatch.....	83
Figure A.3.32. Images of oxidised state after periods of cycling. Solution of buffered 10 mg/mL NDI-V at pH 9 used.	84
Figure A.3.33. Images of oxidised state after periods of cycling. Solution of buffered 10 mg/mL NDI-F at pH 6 used.	84
Figure A.3.34. Images of oxidised state after periods of cycling. Solution of buffered 10 mg/mL NDI-GF at pH 6 used.	85
Figure A.3.35. Cyclic voltammogram collected from buffered 10 mg/mL solution of NDI-I adjusted to pH 9. Voltammograms measured using a 5 x 5 cm FTO window cell with a scan rate of 0.5 V/s. Measurements shown from scan number 1 (red), 5 (orange), 10 (yellow), 30 (green), 50 (blue), 80 (lilac) and 100 (purple).....	85

Figure A.3.36. Cyclic voltammogram collected from buffered 10 mg/mL solution of NDI-V adjusted to pH 9. Voltammograms measured using a 5 x 5 cm FTO window cell with a scan rate of 0.5 V/s. Measurements shown from scan number 1 (red), 5 (orange), 10 (yellow), 30 (green), 50 (blue), 80 (lilac) and 100 (purple).....	86
Figure A.3.37. Cyclic voltammogram collected from buffered 10 mg/mL solution of NDI-F adjusted to pH 6. Voltammograms measured using a 5 x 5 cm FTO window cell with a scan rate of 0.5 V/s. Measurements shown from scan number 1 (red), 5 (orange), 10 (yellow), 30 (green), 50 (blue), 80 (lilac) and 100 (purple).....	87
Figure A.3.38. Cyclic voltammogram collected from buffered 10 mg/mL solution of NDI-GF adjusted to pH 6. Voltammograms measured using a 5 x 5 cm FTO window cell with a scan rate of 0.5 V/s. Measurements shown from scan number 1 (red), 5 (orange), 10 (yellow), 30 (green), 50 (blue), 80 (lilac) and 100 (purple).....	88
Figure A.3.39. Enlarged section of ¹ H NMR spectra of 5 mg/mL NDI-F in D ₂ O at (a) pD 11 and (b) pD 6. Signals corresponding to different proton environments for aggregate A and B are highlighted alongside their assignation.	90
Figure A.3.40. Enlarged section of ¹ H NMR spectra of 5 mg/mL NDI-F in D ₂ O at (a) pD 11 and (b) pD 6. Signals corresponding to different proton environments for aggregate A and B are highlighted alongside their assignment.....	91
Figure A.3.41. ¹ H NMR spectra of 5 mg/mL NDI-F in D ₂ O at pD 11 showing integration of aggregate A.	92
Figure A.3.42. ¹ H NMR spectra of 5 mg/mL NDI-F in D ₂ O at pD 11 showing integration of aggregate B.	93
Figure A.3.43. Enlarged section of ¹ H NMR spectra of 5 mg/mL NDI-GF in D ₂ O at (a) pD 11 and (b) pD 6. Due to low intensity of peaks at pD 6, a rescaled plot is shown (c). Signals corresponding to different proton environments for aggregate A and B are highlighted alongside their assignation.....	95
Figure A.3.44. Enlarged section of ¹ H NMR spectra of 5 mg/mL NDI-GF in D ₂ O at (a) pD 11 and (b) pD 6. Signals corresponding to different proton environments for aggregate A and B are highlighted alongside their assignation.	96
Figure A.3.45. Enlarged section of ¹ H NMR spectra of 5 mg/mL NDI-GF in D ₂ O at 70 °C showing CH proton environments of each aggregate (and their relative integration) shifted from below the water peak.....	97
Figure A.3.46. Enlarged section of ¹ H NMR spectra of 5 mg/mL NDI-GF in D ₂ O at (a) pD 11 and (b) pD 6. Signals corresponding to different proton environments for aggregate A and B are highlighted alongside their assignation.	98
Figure A.3.47. ¹ H NMR spectra of 5 mg/mL NDI-GF in D ₂ O at pD 11 showing integration.	99
Figure A.3.48. ¹ H NMR spectra of 5 mg/mL NDI-F (a) NDI-GF (b) in D ₂ O at (a) pD as temperature of the sample was increased.	101
Figure A.3.49. DOSY spectra of 5 mg/mL NDI-F in D ₂ O at pD 11.	102
Figure A.3.50. Enlarged region of DOSY spectra of 5 mg/mL NDI-F in D ₂ O at pD 11.	102
Figure A.3.51. Enlarged region of DOSY spectra of 5 mg/mL NDI-F in D ₂ O at pD 11.	103
Figure A.3.52. Enlarged region of DOSY spectra of 5 mg/mL NDI-F in D ₂ O at pD 11.	103
Figure A.3.53. DOSY spectra of 5 mg/mL NDI-GF in D ₂ O at pD 11.....	104
Figure A.3.54. Enlarged region of DOSY spectra of 5 mg/mL NDI-GF in D ₂ O at pD 11.....	104
Figure A.3.55. Enlarged region of DOSY spectra of 5 mg/mL NDI-GF in D ₂ O at pD 11.....	105
Figure A.3.56. Enlarged region of DOSY spectra of 5 mg/mL NDI-GF in D ₂ O at pD 11.....	105
Figure A.3.57. ¹ H NMR spectra of D ₂ O used in these experiments.	106
Figure A.3.58. ¹ H NMR spectra of the neutral state of 10 mg/mL buffered NDI-I adjusted to pH 9 before (black) and after (red) excessive electrochemical cycling. Spectra taken after a period of 24 hours of relaxation following cycling.	107

Figure A.3.59. ^1H NMR spectra of the neutral state of 10 mg/mL buffered NDI-V adjusted to pH 9 before (black) and after (red) excessive electrochemical cycling. Spectra taken after a period of 24 hours of relaxation following cycling.	108
Figure A.3.60. ^1H NMR spectra of the neutral state of 10 mg/mL buffered NDI-F adjusted to pH 6 before (black) and after (red) excessive electrochemical cycling. Spectra taken after a period of 24 hours of relaxation following cycling.	109
Figure A.3.61. ^1H NMR spectra of the neutral state of 10 mg/mL buffered NDI-GF adjusted to pH 6 before (black) and after (red) excessive electrochemical cycling. Spectra taken after a period of 24 hours of relaxation following cycling.	110
Figure A.3.62. Small angle neutron scattering data for a neutral buffered solution of 10 mg/mL NDI-I at pD 9 after one electrochemical cycle and relaxation for several days for several days (open circles) fitted to a flexible cylinder model combined with power law (red). Fit parameters can be found in Table A.3.16.	111
Figure A.3.63. Small angle neutron scattering data for a neutral buffered solution of 10 mg/mL NDI-I at pD 9 after 50 electrochemical cycles applying -2.7 V for 10 seconds and a sweeping oxidation potential between 0.1 and 0.95 V in order to switch between a neutral and reduced state followed by a relaxation period of several days (open circles) fitted to a flexible cylinder model combined with power law (red). Fit parameters can be found in Table A.3.16.	111
Figure A.3.64. Small angle neutron scattering data for a neutral buffered solution of 10 mg/mL NDI-V at pD 9 after one electrochemical cycle and relaxation for several days (open circles) fitted to a flexible cylinder model combined with power law (red). Fit parameters can be found in Table A.3.17.	113
Figure A.3.65. Small angle neutron scattering data for a neutral buffered solution of 10 mg/mL NDI-V at pD 9 after 50 electrochemical cycles applying -2.7 V for 10 seconds and a sweeping oxidation potential between 0.1 and 0.95 V in order to switch between a neutral and reduced state followed by a relaxation period of several days (open circles) fitted to a flexible cylinder model combined with power law (red). Fit parameters can be found in Table A.3.17.	113
Figure A.3.66. Small angle neutron scattering data for a neutral buffered solution of 10 mg/mL NDI-F at pD 6 after application of -2.7 V for 5 minutes and relaxing for several days (open circles) fitted to a hollow cylinder model combined with power law (red). Fit parameters can be found in Table A.3.18.	115
Figure A.3.67. Small angle neutron scattering data for a neutral buffered solution of 10 mg/mL NDI-F at pD 6 after 50 electrochemical cycles applying -2.7 V for 10 seconds and a sweeping oxidation potential between 0.1 and 0.95 V in order to switch between a neutral and reduced state followed by a relaxation period of several days (open circles) fitted to a flexible cylinder model combined with power law (red). Fit parameters can be found in Table A.3.18.	115
Figure A.3.68. Small angle neutron scattering data for a neutral buffered solution of 10 mg/mL NDI-GF at pD after one electrochemical cycle and relaxation for several days for several days (open circles) fitted to a flexible elliptical cylinder model combined with power law (red). Fit parameters can be found in Table A.3.19.	117
Figure A.3.69. Small angle neutron scattering data for a neutral buffered solution of 10 mg/mL NDI-GF at pD 6 after 50 electrochemical cycles applying -2.7 V for 10 seconds and a sweeping oxidation potential between 0.1 and 0.95 V in order to switch between a neutral and reduced state followed by a relaxation period of several days (open circles) fitted to a flexible elliptical cylinder model combined with power law (red). Fit parameters can be found in Table A.3.19.	117
Figure A.3.70. Cyclic voltammogram of buffered NDI-GF collected at pH 6 at 10 mg/mL within spectro-electrochemical cell setup (vs Pt). The scan rate of the cyclic voltammograms was 0.2 V/s.	119
Figure A.3.71. Small angle neutron scattering data for a neutral buffered solution of 10 mg/mL NDI-GF at pD 6 in a spectro-electrochemical cell (black) and in a standard quartz cuvette (red) performed on the exact same solution in the same ISIS visit.	120

Figure A.3.72. Small angle neutron scattering data for a neutral buffered solution of 10 mg/mL NDI-GF at pD 6 (open circles) fitted to a flexible elliptical cylinder model combined with power law (red). Data taken in spectro-electrochemical cell. Fit parameters can be found in Table A.3.20.....	121
Figure A.3.73. Small angle neutron scattering data for a buffered reduced solution of 10 mg/mL NDI-GF at pD 6 (open circles) fitted to a flexible elliptical cylinder model combined with power law (red). Data taken in spectro-electrochemical cell. Fit parameters can be found in Table A.3.20.....	121
Figure A.3.74. Small angle neutron scattering data for a buffered electrochemically oxidised solution of 10 mg/mL NDI-GF at pD 6 (open circles) fitted to a flexible elliptical cylinder model combined with power law (red). Data taken in spectro-electrochemical cell. Data taken in spectro-electrochemical cell. Fit parameters can be found in Table A.3.20.	122
Figure A.3.75. Small angle neutron scattering data for a neutral buffered solution of 10 mg/mL NDI-I at pD 9 in a spectro-electrochemical cell (black) and in a standard quartz cuvette (red).....	124
Figure A.3.76. Small angle neutron scattering data for a neutral buffered solution of 10 mg/mL NDI-V at pD 9 in a spectro-electrochemical cell (black) and in a standard quartz cuvette (red).....	124
Figure A.3.77. Cyclic voltammograms of buffered 10 mg/mL NDI-I and NDI-V collected at pH 9 at 10 mg/mL within spectro-electrochemical cell setup (vs Pt). The scan rate of the cyclic voltammograms was 0.2 V/s.....	125
Figure A.3.78. Small angle neutron scattering data for a buffered solution of 10 mg/mL NDI-I at pD 9 in a neutral state before electrochemical reduction (black) and after one electrochemical reduction and oxidation (red). Measurements taken in (a) spectro-electrochemical cell and (b) in a standard quartz cuvette.	126
Figure A.3.79. Small angle neutron scattering data for a buffered solution of 10 mg/mL NDI-V at pD 9 in a neutral state before electrochemical reduction (black) and after one electrochemical reduction and oxidation (red). Measurements taken in (a) spectro-electrochemical cell and (b) in a standard quartz cuvette.....	127
Figure A.3.80. Small angle neutron scattering data for a neutral buffered solution of 10 mg/mL NDI-I at pD 9 (open circles) fitted to a flexible elliptical cylinder model combined with power law (red). Data taken in spectro-electrochemical cell. Data taken in spectro-electrochemical cell. Fit parameters can be found in Table A.3.21.	128
Figure A.3.81. Small angle neutron scattering data for a buffered reduced solution of 10 mg/mL NDI-I at pD 9 (open circles) fitted to a flexible elliptical cylinder model combined with power law (red). Data taken in spectro-electrochemical cell. Fit parameters can be found in Table A.3.21.	128
Figure A.3.82. Small angle neutron scattering data for a buffered electrochemically oxidised solution of 10 mg/mL NDI-I at pD 9 (open circles) fitted to a flexible elliptical cylinder model combined with power law (red). Data taken in spectro-electrochemical cell. Fit parameters can be found in Table A.3.21.	129
Figure A.3.83. Small angle neutron scattering data for a neutral buffered solution of 10 mg/mL NDI-V at pD 9 (open circles) fitted to a flexible elliptical cylinder model (red). Data taken in spectro-electrochemical cell. Fit parameters can be found in Table A.3.22.....	131
Figure A.3.84. Small angle neutron scattering data for a buffered reduced solution of 10 mg/mL NDI-V at pD 9 (open circles) fitted to a flexible elliptical cylinder model (red). Data taken in spectro-electrochemical cell. Fit parameters can be found in Table A.3.22.....	131
Figure A.3.85. Small angle neutron scattering data for a buffered electrochemically oxidised solution of 10 mg/mL NDI-V at pD 9 (open circles) fitted to a flexible elliptical cylinder model (red). Data taken in spectro-electrochemical cell. Fit parameters can be found in Table A.3.22.	132
Figure A.3.86. Plot showing the fluctuation in of the room temperature of the lab over the course of weekdays (red, blue, beige, pink) and weekends (black, grey).	134
Figure A.3.87. Plot showing how time to reach a state of full oxidation (i.e., without discolouration of the neutral state) fluctuates with cycling from neutral to reduced state and back in standard (filled triangles) and temperature-controlled experiments (open triangles). Experiments undertaken using 10 mg/mL buffered solutions of (a) NDI-I , (b) NDI-V , (c) NDI-F and (d) NDI-GF at their respective 'idea'	

pH. Measurements are taken as an average of triplicate measurements and error bars calculated from standard deviation. Reduced state is achieved by applying -2.7 V for 10 seconds and oxidation achieved by applying a potential sweep between 0.1 and 0.95 V in 0.05 V increments every 5 seconds.

.....	135
Figure A.4.1. pH titration data taken of 5 mg/mL 1-NapFF with background electrolyte.....	136
Figure A.4.2. pH titration data taken of 5 mg/mL NDI-F with background electrolyte.....	136
Figure A.4.3. pH titration data taken of 5 mg/mL NDI-GF with background electrolyte.....	137
Figure A.4.4. pH titration data taken of 5:5 mg/mL NDI-F:1-NapFF with background electrolyte.	138
Figure A.4.5. pH titration data taken of 5:5 mg/mL NDI-GF:1-NapFF with background electrolyte..	139
Figure A.4.6. Viscosity measurements of 1-NapFF at 5 (black), 2.5 (red), 1.25 (blue) and 0.625 (green) mg/mL at pH 6 (a), 9 (b) and 12 (c). Measurements are taken as an average of triplicate measurements and error bars calculated from standard deviation. Background electrolyte present.	140
Figure A.4.7. Viscosity measurements of NDI-F:1-NapFF at 5:5 (black), 5:2.5 (red), 5:1.25 (blue), 5:0.625 (green) and 5:0 (open circles) mg/mL at pH 6 (a), 9 (b) and 12 (c). Measurements are taken as an average of triplicate measurements and error bars calculated from standard deviation. Background electrolyte present.....	141
Figure A.4.8. Viscosity measurements of NDI-GF:1-NapFF at 5:5 (black), 5:2.5 (red), 5:1.25 (blue), 5:0.625 (green) and 5:0 (open circles) mg/mL at pH 6 (a), 9 (b) and 12 (c). Measurements are taken as an average of triplicate measurements and error bars calculated from standard deviation. Background electrolyte present.....	142
Figure A.4.9. Viscosity measurements of (a) 5 mg/mL 1-NapFF and 5:5 mg/mL (b) NDI-F:1-NapFF and (c) NDI-GF:1-NapFF at pH 6 (red), 9 (black) and 12 (blue). Measurements are taken as an average of triplicate measurements and error bars calculated from standard deviation. Background electrolyte present.....	143
Figure A.4.10. Absorbance spectra of neutral NDI-F:1-NapFF at 5:5 (black), 5:2.5 (red), 5:1.25 (blue), 5:0.625 (green) and 5:0 (dashed line) mg/mL at pH 6 (a), 9 (b) and 12 (c). Background electrolyte present.....	144
Figure A.4.11. Absorbance spectra of neutral NDI-GF:1-NapFF at 5:5 (black), 5:2.5 (red), 5:1.25 (blue), 5:0.625 (green) and 5:0 (dashed line) mg/mL at pH 6 (a), 9 (b) and 12 (c). Background electrolyte present.....	145
Figure A.4.12. Cyclic voltammograms of NDI-F:1-NapFF at 5:5 (black), 5:2.5 (red), 5:1.25 (blue), 5:0.625 (green) and 5:0 (dashed line) mg/mL at pH 6 (a), 9 (b) and 12 (c). Scan rate used was 0.2 V/s. Performed in 1 x 1 FTO window cells.....	146
Figure A.4.13. Cyclic voltammograms of NDI-GF:1-NapFF at 5:5 (black), 5:2.5 (red), 5:1.25 (blue), 5:0.625 (green) and 5:0 (dashed line) mg/mL at pH 6 (a), 9 (b) and 12 (c). Scan rate used was 0.2 V/s. Performed in 1 x 1 FTO window cells.....	147
Figure A.4.14. Absorbance spectra of reduced solutions of NDI-F:1-NapFF at 5:5 (black), 5:2.5 (red), 5:1.25 (blue), 5:0.625 (green) and 5:0 (dashed line) mg/mL at pH 6 (a), 9 (b) and 12 (c). Spectra taken after 10 second application of -2.5 V. Solutions contain background electrolyte.....	148
Figure A.4.15. Absorbance spectra of reduced solutions of NDI-GF:1-NapFF at 5:5 (black), 5:2.5 (red), 5:1.25 (blue), 5:0.625 (green) and 5:0 (dashed line) mg/mL at pH 6 (a), 9 (b) and 12 (c). Spectra taken after 10 second application of -2.5 V. Solutions contain background electrolyte.....	149
Figure A.4.16. Small angle X-ray scattering data for a solution of 5 mg/mL NDI-F at pH 6 (open circles) fitted to a hollow cylinder model combined with power law (red). Fit parameters can be found in Table A.4.1.	150
Figure A.4.17. Small angle X-ray scattering data for a solution of 5 mg/mL NDI-F at pH 9 (open circles) fitted to a hollow cylinder model combined with power law (red). Fit parameters can be found in Table A.4.2.	151
Figure A.4.18. Small angle X-ray scattering data for a solution of 5 mg/mL NDI-F at pH 12 (open circles) fitted to a sphere model combined with power law (red). Fit parameters can be found in Table A.4.3.	152

Figure A.4.19. Small angle X-ray scattering data for a solution of 5 mg/mL NDI-GF at pH 6 (open circles) fitted to a flexible elliptical cylinder model combined with power law (red). Fit parameters can be found in Table A.4.4.	153
Figure A.4.20. Small angle X-ray scattering data for a solution of 5 mg/mL NDI-GF at pH 9 (open circles) fitted to a flexible elliptical cylinder model combined with power law (red). Fit parameters can be found in Table A.4.5.	154
Figure A.4.21. Small angle X-ray scattering data for a solution of 5 mg/mL NDI-GF at pH 12 (open circles) fitted to a sphere model combined with power law (red). Fit parameters can be found in Table A.4.6.	155
Figure A.4.22. Small angle X-ray scattering data for a solution of 5 mg/mL 1-NapFF at pH 6 (open circles) fitted to a flexible elliptical cylinder model combined with power law (red). Fit parameters can be found in Table A.4.7.	156
Figure A.4.23. Small angle X-ray scattering data for a solution of 5 mg/mL 1-NapFF at pH 9 (open circles) fitted to a flexible elliptical cylinder model combined with power law (red). Fit parameters can be found in Table A.4.8.	157
Figure A.4.24. Small angle X-ray scattering data for a solution of 5 mg/mL 1-NapFF at pH 12 (open circles) fitted to a flexible elliptical cylinder model combined with power law (red). Fit parameters can be found in Table A.4.9. Shear alignment causing elliptical scattering plot and kink in data is evidenced in Figure A.4.25.	158
Figure A.4.25. Raw detector data of 2D scattering plots of measurement taken from for a solution of 5 mg/mL 1-NapFF at pH 12. Histogram plots are shown at a range of 0 to (a) 100, (b) 50, (c) 20 and (d) 10.	159
Figure A.4.26. Raw detector data of 2D scattering plots of measurement taken from for a solution of H ₂ O containing 50% 0.1 M NaCl. Histogram plots are shown at a range of 0 to (a) 100, (b) 50, (c) 20 and (d) 10. This data has no kinks and are shown as a control for no shear aligned sample.....	160
Figure A.4.27. Raw detector data of 2D scattering plots of measurement taken from for a solution of NDI-F:1-NapFF 5:5 mg/mL adjusted to pH 6. Histogram plots are shown at a range of 0 to (a) 100, (b) 50, (c) 20 and (d) 10. This data has no kinks and are shown as a control for no shear aligned sample.	161
Figure A.4.28. Small angle X-ray scattering data for a solution of NDI-GF:1-NapFF 5:5 mg/mL at pH 6 (open circles) fitted to a flexible elliptical cylinder model combined with power law (red). Fit parameters can be found in Table A.4.10.....	162
Figure A.4.29. Small angle X-ray scattering data for a solution of NDI-GF:1-NapFF 5:5 mg/mL at pH 9 (open circles) fitted to a flexible elliptical cylinder model combined with cylinder (red). Fit parameters can be found in Table A.4.11.	163
Figure A.4.30. Small angle X-ray scattering data for a solution of NDI-GF:1-NapFF 5:5 mg/mL at pH 12 (open circles) fitted to a flexible elliptical cylinder model combined with sphere (red). Fit parameters can be found in Table A.4.12.	164
Figure A.4.31. Small angle X-ray scattering data for a solution of NDI-GF:1-NapFF 5:2.5 mg/mL at pH 6 (open circles) fitted to a flexible elliptical cylinder model combined with power law (red). Fit parameters can be found in Table A.4.13.....	165
Figure A.4.32. Small angle X-ray scattering data for a solution of NDI-GF:1-NapFF 5:2.5 mg/mL at pH 9 (open circles) fitted to a flexible cylinder model combined with power law (red). Fit parameters can be found in Table A.4.14.	166
Figure A.4.33. Small angle X-ray scattering data for a solution of NDI-GF:1-NapFF 5:2.5 mg/mL at pH 12 (open circles) fitted to a flexible elliptical cylinder model combined with sphere (red). Fit parameters can be found in Table A.4.15.....	167
Figure A.4.34. Small angle X-ray scattering data for a solution of NDI-GF:1-NapFF 5:1.25 mg/mL at pH 6 (open circles) fitted to a flexible elliptical cylinder model combined with power law (red). Fit parameters can be found in Table A.4.16.....	168

Figure A.4.35. Small angle X-ray scattering data for a solution of NDI-GF:1-NapFF 5:1.25 mg/mL at pH 9 (open circles) fitted to a flexible elliptical cylinder model combined with cylinder (red). Fit parameters can be found in Table A.4.17.....	169
Figure A.4.36. Small angle X-ray scattering data for a solution of NDI-GF:1-NapFF 5:1.25 mg/mL at pH 12 (open circles) fitted to a flexible elliptical cylinder model combined with cylinder (red). Fit parameters can be found in Table A.4.18.....	170
Figure A.4.37. Small angle X-ray scattering data for a solution of NDI-GF:1-NapFF 5:0.625 mg/mL at pH 6 (open circles) fitted to a flexible elliptical cylinder model combined with cylinder (red). Fit parameters can be found in Table A.4.19.....	171
Figure A.4.38. Small angle X-ray scattering data for a solution of NDI-GF:1-NapFF 5:0.625 mg/mL at pH 9 (open circles) fitted to a flexible cylinder model combined with power law (red). Fit parameters can be found in Table A.4.20. Shear alignment causing elliptical scattering plot and kink in data is evidenced in Figure A.4.39.....	172
Figure A.4.39. Raw detector data of 2D scattering plots of measurement taken from for a solution of NDI-GF:1-NapFF 5:0.625 mg/mL adjusted to pH 9. Histogram plots are shown at a range of 0 to (a) 100, (b) 50, (c) 20 and (d) 10.....	173
Figure A.4.40. Small angle X-ray scattering data for a solution of NDI-GF:1-NapFF 5:0.625 mg/mL at pH 12 (open circles) fitted to a flexible cylinder model combined with sphere (red). Fit parameters can be found in Table A.4.21.....	174
Figure A.4.41. Small angle X-ray scattering data for a solution of NDI-F:1-NapFF 5:5 mg/mL at pH 6 (open circles) fitted to a flexible elliptical cylinder model combined with hollow cylinder (red). Fit parameters can be found in Table A.4.22.....	175
Figure A.4.42. Small angle X-ray scattering data for a solution of NDI-F:1-NapFF 5:5 mg/mL at pH 9 (open circles) fitted to a flexible elliptical cylinder model combined with hollow cylinder (red). Part of the data has been cut out (grey) due to a large kink. Fit parameters can be found in Table A.4.23. Shear alignment causing elliptical scattering plot and kink in data is evidenced in Figure A.4.43.....	176
Figure A.4.43. Raw detector data of 2D scattering plots of measurement taken from for a solution of NDI-F:1-NapFF 5:5 mg/mL adjusted to pH 9. Histogram plots are shown at a range of 0 to (a) 100, (b) 50, (c) 20 and (d) 10.	177
Figure A.4.44. Small angle X-ray scattering data for a solution of NDI-F:1-NapFF 5:5 mg/mL at pH 12 (open circles) fitted to a flexible cylinder model combined with hollow cylinder (red). A small kink results in a higher χ^2 value shown by (b) the residuals of the fit (open triangles). Fit parameters can be found in Table A.4.24. Shear alignment causing elliptical scattering plot and kink in data is evidenced in Figure A.4.45.....	177
Figure A.4.45. Raw detector data of 2D scattering plots of measurement taken from for a solution of NDI-F:1-NapFF 5:5 mg/mL adjusted to pH 12. Histogram plots are shown at a range of 0 to (a) 100, (b) 50, (c) 20 and (d) 10.	178
Figure A.4.46. Small angle X-ray scattering data for a solution of NDI-F:1-NapFF 5:2.5 mg/mL at pH 6 (open circles) fitted to a flexible elliptical cylinder model combined with cylinder (red). Fit parameters can be found in Table A.4.25.	179
Figure A.4.47. Small angle X-ray scattering data for a solution of NDI-F:1-NapFF 5:2.5 mg/mL at pH 9 (open circles) fitted to a flexible elliptical cylinder model combined with sphere (red). Fit parameters can be found in Table A.4.26.	180
Figure A.4.48. Small angle X-ray scattering data for a solution of NDI-F:1-NapFF 5:2.5 mg/mL at pH 12 (open circles) fitted to a flexible elliptical cylinder model combined with sphere (red). Fit parameters can be found in Table A.4.27.	181
Figure A.4.49. Small angle X-ray scattering data for a solution of NDI-F:1-NapFF 5:1.25 mg/mL at pH 6 (open circles) fitted to a flexible elliptical cylinder model combined with hollow cylinder (red). Fit parameters can be found in Table A.4.28.....	182

Figure A.4.50. Small angle X-ray scattering data for a solution of NDI-F:1-NapFF 5:1.25 mg/mL at pH 9 (open circles) fitted to a flexible cylinder model combined with hollow cylinder (red). Fit parameters can be found in Table A.4.29.	183
Figure A.4.51. Small angle X-ray scattering data for a solution of NDI-F:1-NapFF 5:1.25 mg/mL at pH 12 (open circles) fitted to a flexible elliptical cylinder model combined with sphere (red). Fit parameters can be found in Table A.4.30. Shear alignment causing elliptical scattering plot and kink in data is evidenced in Figure A.4.52.	184
Figure A.4.52. Raw detector data of 2D scattering plots of measurement taken from for a solution of NDI-F:1-NapFF 5:1.25 mg/mL adjusted to pH 12. Histogram plots are shown at a range of 0 to (a) 100, (b) 50, (c) 20 and (d) 10.	185
Figure A.4.53. Small angle X-ray scattering data for a solution of NDI-F:1-NapFF 5:0.625 mg/mL at pH 6 (open circles) fitted to a flexible elliptical cylinder model combined with cylinder (red). Fit parameters can be found in Table A.4.31.	186
Figure A.4.54. Small angle X-ray scattering data for a solution of NDI-F:1-NapFF 5:0.625 mg/mL at pH 9 (open circles) fitted to a flexible elliptical cylinder model combined with cylinder (red). Fit parameters can be found in Table A.4.31.	187
Figure A.4.55. Small angle X-ray scattering data for a solution of NDI-F:1-NapFF 5:0.625 mg/mL at pH 12 (open circles) fitted to a flexible elliptical cylinder model combined with hollow cylinder (red). Fit parameters can be found in Table A.4.33.	188
Figure A.4.56. SAXS data of NDI-F:1-NapFF (purple) and NDI-GF:1-NapFF (brown) at (a) 5:5, (b) 5:2.5, (c) 5:1.25 and (d) 5:0.625 mg/mL ratios. Solutions at pH 6.	189
Figure A.4.57. SAXS data of NDI-F:1-NapFF (purple) and NDI-GF:1-NapFF (brown) at (a) 5:5, (b) 5:2.5, (c) 5:1.25 and (d) 5:0.625 mg/mL ratios. Solutions at pH 9.	190
Figure A.4.58. SAXS data of NDI-F:1-NapFF (purple) and NDI-GF:1-NapFF (brown) at (a) 5:5, (b) 5:2.5, (c) 5:1.25 and (d) 5:0.625 mg/mL ratios. Solutions at pH 12.	191
Figure A.4.59. Cyclic voltammograms of NDI-F (purple) and NDI-F:1-NapFF (black) at a 5 and 5:5 mg/mL concentration respectively at pH 6. NDI-F:1-NapFF at 5:1.25 mg/mL at pH 9 is also shown (blue). Voltammograms performed in 5 x 5 FTO window cell at 0.2 V/s scan rate. (a) full voltammogram and (b) expanded between 0-1 V is shown for clarity.	191
Figure A.4.60. Viscosity measurements of NDI-F:1-NapFF at 5:5 mg/mL (black), NDI-F at 5 mg/mL (purple) and 1-NapFF at 5 mg/mL (grey). All solutions buffered at pH 6. Measurements are taken as an average of triplicate measurements and error bars calculated from standard deviation.	192
Figure A.4.61. Small angle X-ray scattering data for a solution of 5 mg/mL buffered 1-NapFF at pH 6 (open circles) fitted to a flexible elliptical cylinder model combined with power law (red). Fit parameters can be found in Table A.4.34.	192
Figure A.4.62. Cyclic voltammograms taken at 0.2 V/s of (a/d) NDI-F 5 mg/mL and (a/c) NDI-F:1-NapFF 5:5 mg/mL buffered (dashed line) and unbuffered (solid line) at pH 6 in (a-b) 1 x 1 and (c-d) 5 x 5 FTO window cells.	193
Figure A.4.63. Small angle X-ray scattering data for a solution of 5 mg/mL NDI-F buffered at pH 6 (open circles) fitted to a hollow cylinder model combined with power law (red). Fit parameters can be found in Table A.4.35.	194
Figure A.4.64. Small angle X-ray scattering data for a solution of NDI-F:1-NapFF 5:5 mg/mL buffered at pH 6 (open circles) fitted to a flexible elliptical cylinder model combined with hollow cylinder (red). Fit parameters can be found in Table A.4.36.	195
Figure A.4.65. Small angle X-ray scattering data for a solution of NDI-F 5 mg/mL buffered at pH 6 and electrochemically cycles once (open circles) fitted to a flexible elliptical cylinder model combined with power law (red). Solutions were relaxed for several days prior to measurement. Fit parameters can be found in Table A.4.37.	196
Figure A.4.66. Small angle X-ray scattering data for a solution of NDI-F 5 mg/mL buffered at pH 6 and electrochemically cycles 50 times (open circles) fitted to a flexible elliptical cylinder model combined	

with power law (red). Solutions were relaxed for several days prior to measurement. Fit parameters can be found in Table A.4.38.	197
Figure A.4.67. Small angle X-ray scattering data for a solution of NDI-F:1-NapFF 5:5 mg/mL buffered at pH 6 and electrochemically cycles once (open circles) fitted to a flexible elliptical cylinder model combined with hollow cylinder (red). Solutions were relaxed for several days prior to measurement. Fit parameters can be found in Table A.4.39.....	198
Figure A.4.68. Small angle X-ray scattering data for a solution of NDI-F:1-NapFF 5:5 mg/mL buffered at pH 6 and electrochemically cycles 50 times (open circles) fitted to a flexible elliptical cylinder model combined with hollow cylinder (red). Solutions were relaxed for several days prior to measurement. Fit parameters can be found in Table A.4.40.....	199
Figure A.4.69. Viscosity measurements 1-NapFF after heat cooling at 40 °C at (a) pH 6, (b) 9 and (c) 12. Solutions at 5 (black), 2.5 (red), 1.25 (blue), 0.625 (green) and 5:0 (open circles) mg/mL. Measurements are taken as an average of triplicate measurements and error bars calculated from standard deviation.	200
Figure A.4.70. Viscosity measurements NDI-F:1-NapFF after heat cooling at 40 °C at (a) pH 6, (b) 9 and (c) 12. Solutions at 5:5 (black), 5:2.5 (red), 5:1.25 (blue), 5:0.625 (green) and 5:0 (open circles) mg/mL. Measurements are taken as an average of triplicate measurements and error bars calculated from standard deviation.	201
Figure A.4.71. Absorbance spectra of neutral NDI-F:1-NapFF before (solid line) and after (dashed line) heat-cooling at 40 °C at (a) 0:5, (b) 5:0, (c) 5:5, (d) 5:2.5, (e) 5:1.25 and (f) 5:0.625 mg/mL at pH 6 (red), 9 (black) and 12 (blue).	202
Figure A.4.72. Cyclic voltammograms of NDI-F:1-NapFF at 5:5 (black), 5:2.5 (red), 5:1.25 (blue), 5:0.625 (green) and 5:0 (dashed line) mg/mL at pH 6 (a), 9 (b) and 12 (c) after heat-cooling at 40 °C. Scan rate used was 0.2 V/s. Performed in 1 x 1 FTO window cells.	203
Figure A.4.73. Absorbance spectra of reduced solutions (heat-cooled at 40 °C) of NDI-F:1-NapFF at 5:5 (black), 5:2.5 (red), 5:1.25 (blue), 5:0.625 (green) and 5:0 (dashed line) mg/mL at pH 6 (a), 9 (b) and 12 (c). Spectra taken after 10 second application of -2.5 V.....	204
Figure A.4.74. Small angle X-ray scattering data for a solution of NDI-F 5 mg/mL at pH 6 after heat-cooling (heated to 40 °C and allowed to cool) (open circles) fitted to a hollow cylinder model combined with power law (red). Fit parameters can be found in Table A.4.41.	205
Figure A.4.75. Small angle X-ray scattering data for a solution of NDI-F 5 mg/mL at pH 9 after heat-cooling (heated to 40 °C and allowed to cool) (open circles) fitted to a hollow cylinder model combined with power law (red). Fit parameters can be found in Table A.4.42.	206
Figure A.4.76. Small angle X-ray scattering data for a solution of NDI-F 5 mg/mL at pH 12 after heat-cooling (heated to 40 °C and allowed to cool) (open circles) fitted to a hollow cylinder model combined with power law (red). Fit parameters can be found in Table A.4.43.....	207
Figure A.4.77. Small angle X-ray scattering data for a solution of 1-NapFF 5 mg/mL at pH 6 after heat-cooling (heated to 40 °C and allowed to cool) (open circles) fitted to a hollow cylinder model combined with power law (red). Fit parameters can be found in Table A.4.44.....	208
Figure A.4.78. Small angle X-ray scattering data for a solution of 1-NapFF 5 mg/mL at pH 9 after heat-cooling (heated to 40 °C and allowed to cool) (open circles) fitted to a hollow cylinder model combined with power law (red). Fit parameters can be found in Table A.4.45.	209
Figure A.4.79. Small angle X-ray scattering data for a solution of 1-NapFF 5 mg/mL at pH 12 after heat-cooling (heated to 40 °C and allowed to cool) (open circles) fitted to a hollow cylinder model combined with power law (red). Fit parameters can be found in Table A.4.46.....	210
Figure A.4.80. SAXS data of NDI-F:1-NapFF before (grey) and after (open circles) a heat-cool transition (heated to 40 °C and allowed to cool) at pH 6 (red), 9 (black) and 12 (blue) at (a) 5:5, (b) 5:2.5, (c) 5:1.25 and (d) 5:0.625 mg/mL.	211
Figure A.4.81. Small angle X-ray scattering data for a solution of NDI-F:1-NapFF 5:5 mg/mL at pH 6 after heat-cooling (heated to 40 °C and allowed to cool) (open circles) fitted to a flexible elliptical model combined with hollow cylinder (red). Fit parameters can be found in Table A.4.47.	212

Figure A.4.82. Small angle X-ray scattering data for a solution of NDI-F:1-NapFF 5:5 mg/mL at pH 9 after heat-cooling (heated to 40 °C and allowed to cool) (open circles) fitted to a flexible elliptical model combined with hollow cylinder (red). Fit parameters can be found in Table A.4.48.	213
Figure A.4.83. Small angle X-ray scattering data for a solution of NDI-F:1-NapFF 5:5 mg/mL at pH 12 after heat-cooling (heated to 40 °C and allowed to cool) (open circles) fitted to a flexible elliptical model combined with cylinder (red). Fit parameters can be found in Table A.4.49.	214
Figure A.4.84. Small angle X-ray scattering data for a solution of NDI-F:1-NapFF 5:2.5 mg/mL at pH 6 after heat-cooling (heated to 40 °C and allowed to cool) (open circles) fitted to a flexible elliptical model combined with cylinder (red). Fit parameters can be found in Table A.4.50.	215
Figure A.4.85. Small angle X-ray scattering data for a solution of NDI-F:1-NapFF 5:2.5 mg/mL at pH 9 after heat-cooling (heated to 40 °C and allowed to cool) (open circles) fitted to a flexible elliptical model combined with sphere (red). Fit parameters can be found in Table A.4.51.	216
Figure A.4.86. Small angle X-ray scattering data for a solution of NDI-F:1-NapFF 5:2.5 mg/mL at pH 12 after heat-cooling (heated to 40 °C and allowed to cool) (open circles) fitted to a flexible elliptical model combined with power law (red). Fit parameters can be found in Table A.4.52.	217
Figure A.4.87. Small angle X-ray scattering data for a solution of NDI-F:1-NapFF 5:1.25 mg/mL at pH 6 after heat-cooling (heated to 40 °C and allowed to cool) (open circles) fitted to a flexible elliptical model combined with power law (red). Fit parameters can be found in Table A.4.53.	218
Figure A.4.88. Small angle X-ray scattering data for a solution of NDI-F:1-NapFF 5:1.25 mg/mL at pH 9 after heat-cooling (heated to 40 °C and allowed to cool) (open circles) fitted to a flexible elliptical model combined with hollow cylinder (red). Fit parameters can be found in Table A.4.54.	219
Figure A.4.89. Small angle X-ray scattering data for a solution of NDI-F:1-NapFF 5:1.25 mg/mL at pH 12 after heat-cooling (heated to 40 °C and allowed to cool) (open circles) fitted to a flexible elliptical model combined with sphere (red). Fit parameters can be found in Table A.4.55.	220
Figure A.4.90. Small angle X-ray scattering data for a solution of NDI-F:1-NapFF 5:0.625 mg/mL at pH 6 after heat-cooling (heated to 40 °C and allowed to cool) (open circles) fitted to a flexible elliptical model combined with cylinder (red). Fit parameters can be found in Table A.4.56.	221
Figure A.4.91. Small angle X-ray scattering data for a solution of NDI-F:1-NapFF 5:0.625 mg/mL at pH 9 after heat-cooling (heated to 40 °C and allowed to cool) (open circles) fitted to a flexible elliptical model combined with cylinder (red). Fit parameters can be found in Table A.4.57.	222
Figure A.4.92. Small angle X-ray scattering data for a solution of NDI-F:1-NapFF 5:0.625 mg/mL at pH 12 after heat-cooling (heated to 40 °C and allowed to cool) (open circles) fitted to a flexible elliptical model combined with sphere (red). Fit parameters can be found in Table A.4.58.	223
Figure A.4.93. SAXS data of NDI-F:1-NapFF after heat-cooling (heated to 40 °C and allowed to cool) at 5:5 (black), 5:2.5 (red), 5:1.25 (blue) and 5:0.625 (green) mg/mL at pH 6 (a), 9 (b) and 12 (c).	224
Figure A.4.94. Viscosity measurements (a) NDI-F:1-NapFF 5:0.625 mg/mL and (b) NDI-F 5 mg/mL after heat cooling at 40 °C. Solutions at pH 6 buffered (open circles) and unbuffered (filled circles). Measurements are taken as an average of triplicate measurements and error bars calculated from standard deviation.	224
Figure A.4.95. Small angle X-ray scattering data for a solution of NDI-F:1-NapFF 5:0.625 mg/mL at buffered at pH 6 after heat-cooling (heated to 40 °C and allowed to cool) (open circles) fitted to a flexible elliptical model combined with cylinder (red). Fit parameters can be found in Table A.4.59.	225
Figure A.4.96. Small angle X-ray scattering data for a solution of NDI-F 5 mg/mL at buffered at pH 6 after heat-cooling (heated to 40 °C and allowed to cool) (open circles) fitted to a hollow cylinder model combined with power law (red). Fit parameters can be found in Table A.4.60.	226
Figure A.4.97. Cyclic voltammograms taken at 0.2 V/s of heat-cooled (heated to 40 °C and allowed to cool) (a-b) NDI-F:1-NapFF 5:0.625 mg/mL and (b-c) NDI-F 5 mg/mL buffered (dashed line) and unbuffered (solid line) at pH 6 in (a/c) 1 x 1 and (b/d) 5 x 5 FTO window cells.	227
Figure A.4.98. Small angle X-ray scattering data for a solution of NDI-F:1-NapFF 5:0.625 mg/mL buffered at pH 6, heat-cooled (heated to 40 °C and allowed to cool) and electrochemically cycles once	

(open circles) fitted to a flexible cylinder model (red). Solutions were relaxed for several days prior to measurement. Fit parameters can be found in Table A.4.61.	228
Figure A.4.99. Small angle X-ray scattering data for a solution of NDI-F:1-NapFF 5:0.625 mg/mL buffered at pH 6, heat-cooled (heated to 40 °C and allowed to cool) and electrochemically cycles 50 times (open circles) fitted to a flexible cylinder model combined (red). Solutions were relaxed for several days prior to measurement. Fit parameters can be found in Table A.4.62.	229
Figure A.4.100. Small angle X-ray scattering data for a solution of NDI-F 5 mg/mL buffered at pH 6, heat-cooled (heated to 40 °C and allowed to cool) and electrochemically cycles once (open circles) fitted to a hollow cylinder model combined with power law (red). Solutions were relaxed for several days prior to measurement. Fit parameters can be found in Table A.4.63.	230
Figure A.4.101. Small angle X-ray scattering data for a solution of NDI-F 5 mg/mL buffered at pH 6, heat-cooled (heated to 40 °C and allowed to cool) and electrochemically cycles 50 times (open circles) fitted to a flexible elliptical cylinder model combined with cylinder (red). Solutions were relaxed for several days prior to measurement. Fit parameters can be found in Table A.4.64.	231
Figure A.4.102. Annotated ¹ H NMR spectrum (400 MHz, DMSO-d ₆) of FF-OEt – Protected.....	232
Figure A.4.103. ¹ H NMR spectrum showing integrals (400 MHz, DMSO-d ₆) of FF-OEt – Protected...	233
Figure A.4.104. Annotated ¹³ C NMR spectrum (100 MHz, DMSO-d ₆) of FF-OEt - Protected. (a) full spectra (b) enhanced section marked Ar showing the aromatic carbon environments.	234
Figure A.4.105. HRMS report of FF-OEt – Protected in ethanol.	235
Figure A.4.106. Annotated ¹ H NMR spectrum (400 MHz, DMSO-d ₆) of FF-OEt – Deprotected with expanded 4.3-3.9 ppm.	236
Figure A.4.107. ¹ H NMR spectrum showing integrals (400 MHz, DMSO-d ₆) of FF-OEt – Deprotected.	237
Figure A.4.108. Annotated ¹³ C NMR spectrum (100 MHz, DMSO-d ₆) of FF-OEt - Deprotected. (a) full spectra (b) enhanced section marked Ar showing the aromatic carbon environments.	238
Figure A.4.109. HRMS report of FF-OEt – Deprotected in ethanol.....	239
Figure A.4.110. Annotated ¹ H NMR spectrum (400 MHz, DMSO-d ₆) of 1-NapFF - Protected.....	240
Figure A.4.111. ¹ H NMR spectrum showing integrals (400 MHz, DMSO-d ₆) of 1-NapFF - Protected.	241
Figure A.4.112. Annotated ¹³ C NMR spectrum (100 MHz, DMSO-d ₆) of 1-NapFF - Protected. (a) full spectra (b) enhanced section marked Ar showing the aromatic carbon environments.	242
Figure A.4.113. HRMS report of 1-NapFF – Protected in ethanol.	243
Figure A.4.114. Annotated ¹ H NMR spectrum (400 MHz, DMSO-d ₆) of 1-NapFF	244
Figure A.4.115. ¹ H NMR spectrum showing integrals (400 MHz, DMSO-d ₆) of 1-NapFF	245
Figure A.4.116. Annotated ¹³ C NMR spectrum (100 MHz, DMSO-d ₆) of 1-NapFF (a) full spectra (b) enhanced section marked Ar showing the aromatic carbon environments.	246
Figure A.4.117. HRSM report of 1-NapFF in ethanol.	247

Tables

Table A.3.1. Parameters of SANS model fit seen in Figure A.3.7.....	59
Table A.3.2. Parameters of SANS model fit seen in Figure A.3.8.....	60
Table A.3.3. Parameters of SANS model fit seen in Figure A.3.9.....	61
Table A.3.4. Parameters of SANS model fit seen in Figure A.3.10.....	62
Table A.3.5. Parameters of SANS model fit in Figure A.3.11.	63
Table A.3.6. Parameters of SANS model fit in Figure A.3.12.	64
Table A.3.7. Parameters of SANS model fit seen in Figure A.3.13.....	65
Table A.3.8. Parameters of SANS model fit seen in Figure A.3.14.....	66
Table A.3.9. Parameters of SANS model fit seen in Figure A.3.15.....	67

Appendix

Table A.3.10. Parameters of SANS model fit seen in Figure A.3.16.....	68
Table A.3.11. Parameters of SANS model fit seen in Figure A.3.17.....	69
Table A.3.12. Parameters of SANS model fit seen in Figure A.3.18.....	70
Table A.3.13. Parameters of SANS model fit seen in Figure A.3.19.....	71
Table A.3.14. Parameters of SANS model fit seen in Figure A.3.20.....	72
Table A.3.15. Tabulated transmittance taken at the λ_{max} of the reduced state for buffered 10 mg/mL NDI-GF , NDI-I , NDI-V , NDI-F and NDI-FF after 10 seconds of application of -2.5 V unless stated otherwise. Data collected in a 1 x 1 cm FTO window set up.	73
Table A.3.16. Parameters of SANS model fits seen in Figure A.3.62 and Figure A.3.63.....	112
Table A.3.17. Parameters of SANS model fits seen in Figure A.3.64 and Figure A.3.65.....	114
Table A.3.18. Parameters of SANS model fits seen in Figure A.3.66 and Figure A.3.67.....	116
Table A.3.19. Parameters of SANS model fits seen in Figure A.3.68-Figure A.3.69.....	118
Table A.3.20. Parameters of SANS model fits seen in Figure A.3.72-Figure A.3.74.....	123
Table A.3.21. Parameters of SANS model fits shown in Figure A.3.80-Figure A.3.82.....	130
Table A.3.22. Parameters of SANS model fits shown in Figure A.3.83-Figure A.3.85.....	133
Table A.4.1. Parameters of SAXS model fit seen in Figure A.4.16.	150
Table A.4.2. Parameters of SAXS model fit seen in Figure A.4.17.	151
Table A.4.3. Parameters of SAXS model fit seen in Figure A.4.18.	152
Table A.4.4. Parameters of SAXS model fit seen in Figure A.4.19.	153
Table A.4.5. Parameters of SAXS model fit seen in Figure A.4.20.	154
Table A.4.6. Parameters of SAXS model fit seen in Figure A.4.21.	155
Table A.4.7. Parameters of SAXS model fit seen in Figure A.4.22.	156
Table A.4.8. Parameters of SAXS model fit seen in Figure A.4.23.	157
Table A.4.9. Parameters of SAXS model fit seen in Figure A.4.24.	158
Table A.4.10. Parameters of SAXS model fit seen in Figure A.4.28.	162
Table A.4.11. Parameters of SAXS model fit seen in Figure A.4.29.	163
Table A.4.12. Parameters of SAXS model fit seen in Figure A.4.30.	164
Table A.4.13. Parameters of SAXS model fit seen in Figure A.4.31.	165
Table A.4.14. Parameters of SAXS model fit seen in Figure A.4.32.	166
Table A.4.15. Parameters of SAXS model fit seen in Figure A.4.33.	167
Table A.4.16. Parameters of SAXS model fit seen in Figure A.4.34.	168
Table A.4.17. Parameters of SAXS model fit seen in Figure A.4.35.	169
Table A.4.18. Parameters of SAXS model fit seen in Figure A.4.36.	170
Table A.4.19. Parameters of SAXS model fit seen in Figure A.4.37.	171
Table A.4.20. Parameters of SAXS model fit seen in Figure A.4.37.	172
Table A.4.21. Parameters of SAXS model fit seen in Figure A.4.40.	174
Table A.4.22. Parameters of SAXS model fit seen in Figure A.4.41.	175
Table A.4.23. Parameters of SAXS model fit seen in Figure A.4.42.	176
Table A.4.24. Parameters of SAXS model fit seen in Figure A.4.44.	178
Table A.4.25. Parameters of SAXS model fit seen in Figure A.4.46.	179
Table A.4.26. Parameters of SAXS model fit seen in Figure A.4.47.	180
Table A.4.27. Parameters of SAXS model fit seen in Figure A.4.48.	181
Table A.4.28. Parameters of SAXS model fit seen in Figure A.4.49.	182
Table A.4.29. Parameters of SAXS model fit seen in Figure A.4.50.	183
Table A.4.30. Parameters of SAXS model fit seen in Figure A.4.51.	184
Table A.4.31. Parameters of SAXS model fit seen in Figure A.4.53.	186
Table A.4.32. Parameters of SAXS model fit seen in Figure A.4.53.	187
Table A.4.33. Parameters of SAXS model fit seen in Figure A.4.55.	188
Table A.4.34. Parameters of SAXS model fit seen in Figure A.4.61.	193
Table A.4.35. Parameters of SAXS model fit seen in Figure A.4.63.	194
Table A.4.36. Parameters of SAXS model fit seen in Figure A.4.64.	195

Appendix

Table A.4.37. Parameters of SAXS model fit seen in Figure A.4.65. 196

Table A.4.38. Parameters of SAXS model fit seen in Figure A.4.66. 197

Table A.4.39. Parameters of SAXS model fit seen in Figure A.4.67. 198

Table A.4.40. Parameters of SAXS model fit seen in Figure A.4.68. 199

Table A.4.41. Parameters of SAXS model fit seen in Figure A.4.74. 205

Table A.4.42. Parameters of SAXS model fit seen in Figure A.4.75. 206

Table A.4.43. Parameters of SAXS model fit seen in Figure A.4.76. 207

Table A.4.44. Parameters of SAXS model fit seen in Figure A.4.77. 208

Table A.4.45. Parameters of SAXS model fit seen in Figure A.4.78. Chi² is higher for this fit likely due to noisy data at high Q (Figure A.4.78) leading to a poor fit of the model over approximately 0.1 Å⁻¹. 209

Table A.4.46. Parameters of SAXS model fit seen in Figure A.4.79. 210

Table A.4.47. Parameters of SAXS model fit seen in Figure A.4.81. 212

Table A.4.48. Parameters of SAXS model fit seen in Figure A.4.82. 213

Table A.4.49. Parameters of SAXS model fit seen in Figure A.4.83. 214

Table A.4.50. Parameters of SAXS model fit seen in Figure A.4.84. 215

Table A.4.51. Parameters of SAXS model fit seen in Figure A.4.85. 216

Table A.4.52. Parameters of SAXS model fit seen in Figure A.4.86. 217

Table A.4.53. Parameters of SAXS model fit seen in Figure A.4.87. 218

Table A.4.54. Parameters of SAXS model fit seen in Figure A.4.88. 219

Table A.4.55. Parameters of SAXS model fit seen in Figure A.4.89. 220

Table A.4.56. Parameters of SAXS model fit seen in Figure A.4.90. 221

Table A.4.57. Parameters of SAXS model fit seen in Figure A.4.91. 222

Table A.4.58. Parameters of SAXS model fit seen in Figure A.4.92. 223

Table A.4.59. Parameters of SAXS model fit seen in Figure A.4.95. 225

Table A.4.60. Parameters of SAXS model fit seen in Figure A.4.96. 226

Table A.4.61. Parameters of SAXS model fit seen in Figure A.4.98. 228

Table A.4.62. Parameters of SAXS model fit seen in Figure A.4.99. 229

Table A.4.63. Parameters of SAXS model fit seen in Figure A.4.100. 230

Table A.4.64. Parameters of SAXS model fit seen in Figure A.4.101. 231

A.2 Chapter 2 appendices

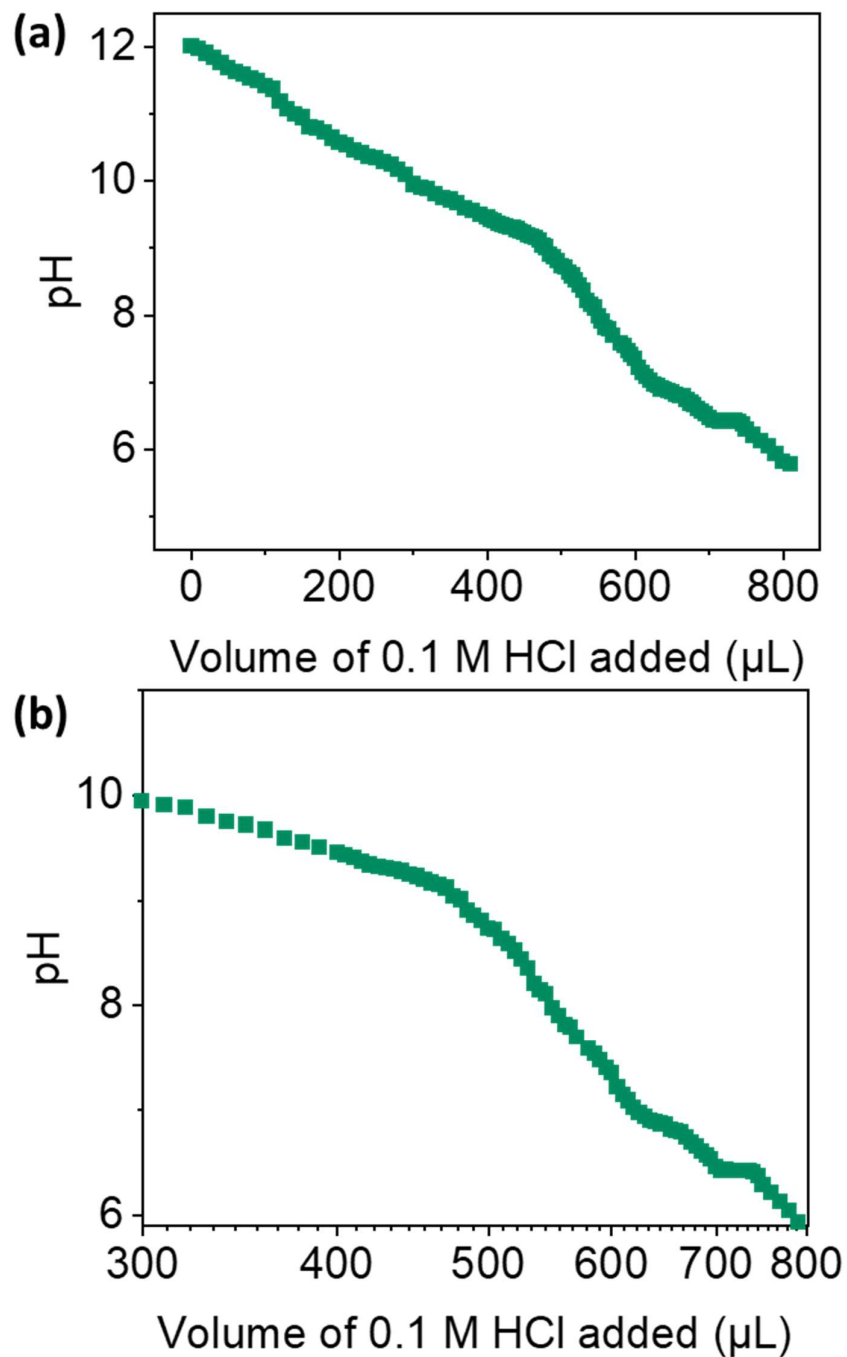


Figure A.2.1. pH titration data taken for 10 mg/mL NDI-I with background electrolyte (a). The area of the plot with both pK_a values with x axis on a logarithmic scale is also shown (b).

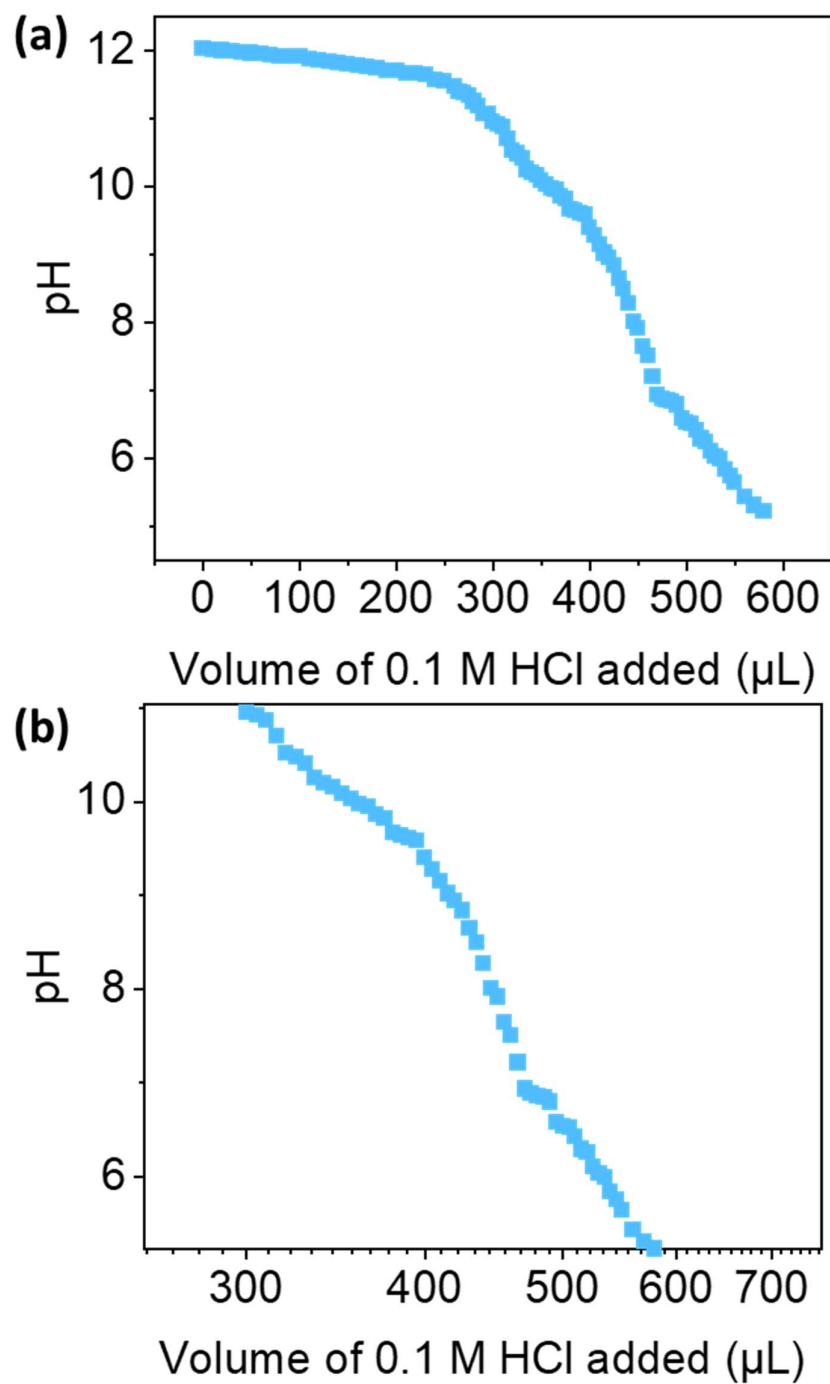


Figure A.2.2. pH titration data taken for 10 mg/mL NDI-V with background electrolyte (a). The area of the plot with both pK_a values with x axis on a logarithmic scale is also shown (b).

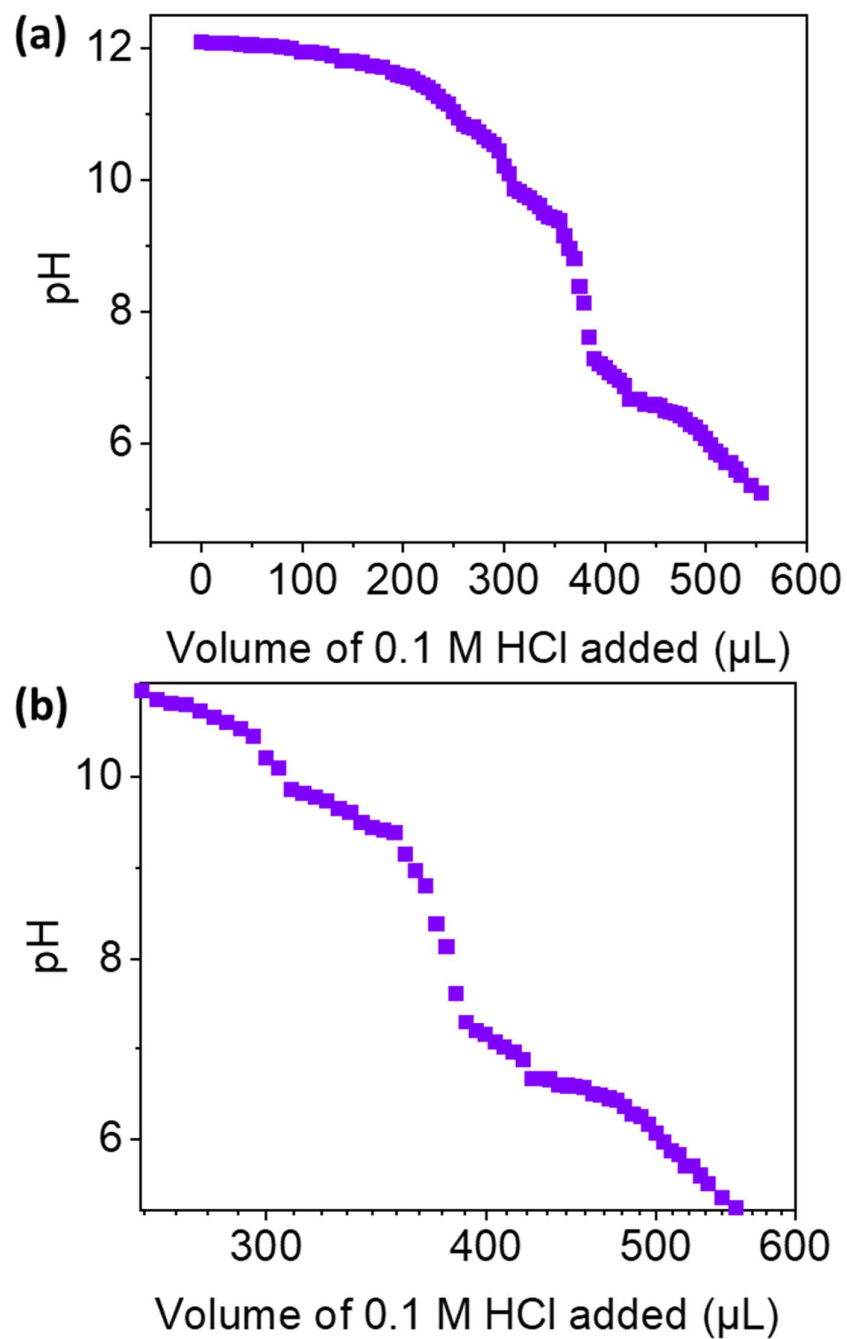


Figure A.2.3. pH titration data taken for 10 mg/mL NDI-F with background electrolyte (a). The area of the plot with both pK_a values with x axis on a logarithmic scale is also shown (b).

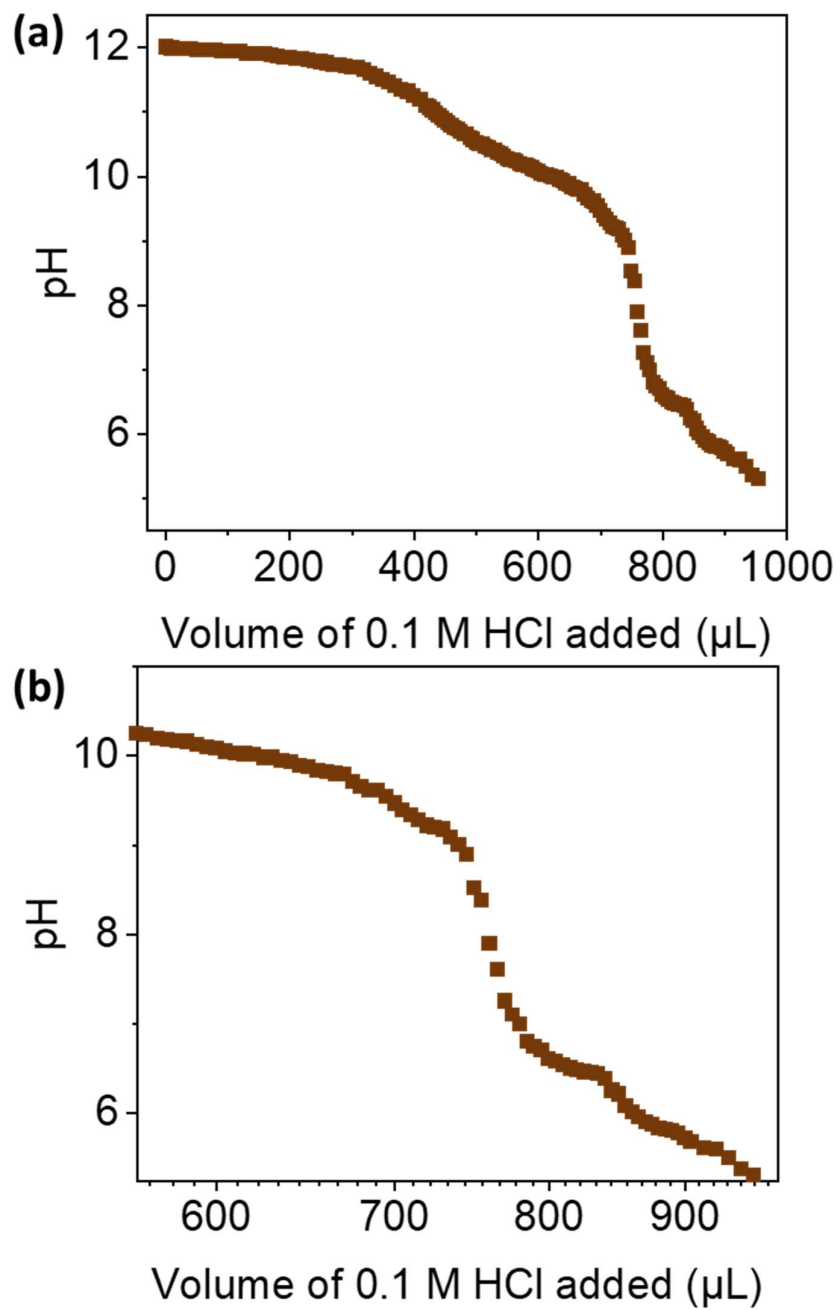


Figure A.2.4. pH titration data taken for 10 mg/mL NDI-GF with background electrolyte (a). The area of the plot with both pK_a values with x axis on a logarithmic scale is also shown (b).

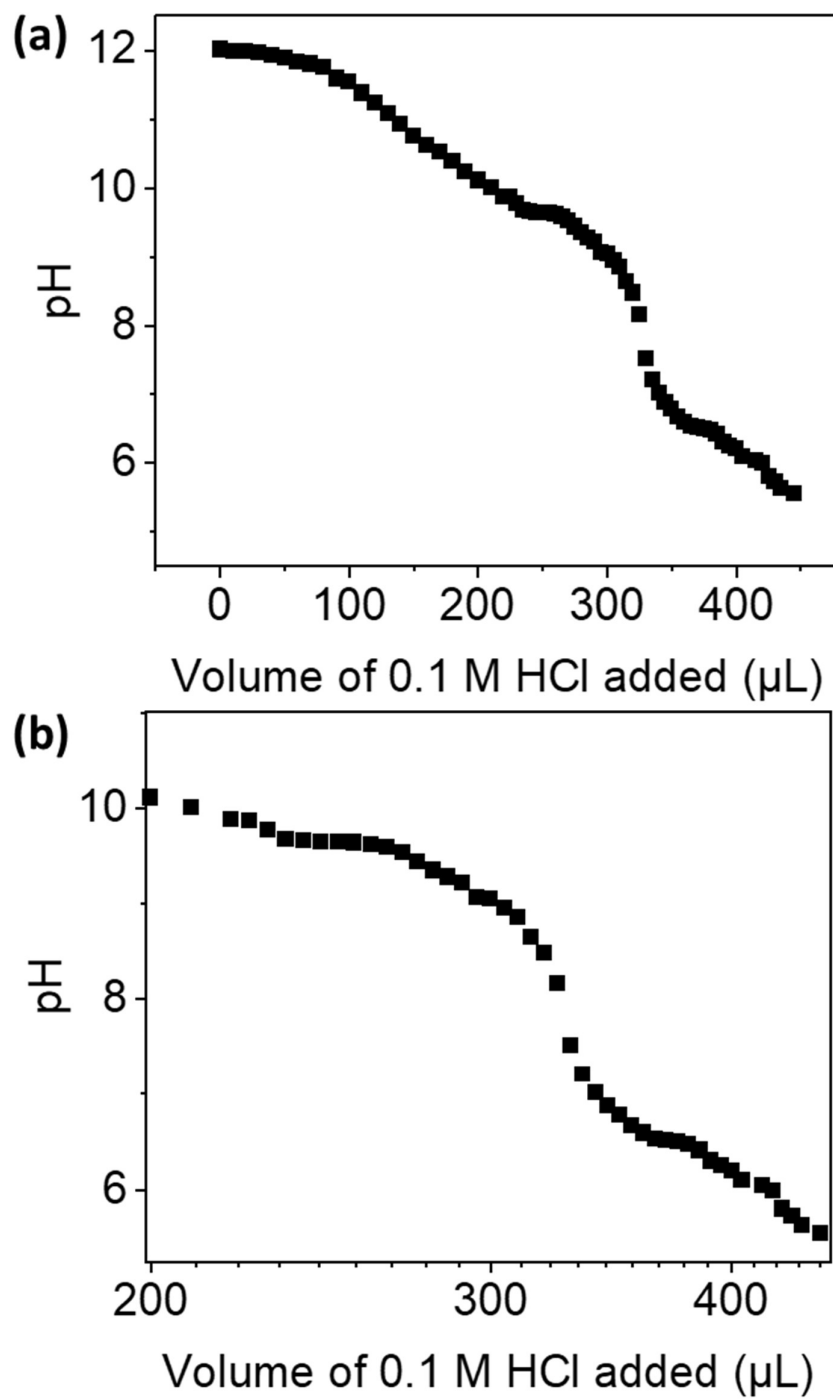


Figure A.2.5. pH titration data taken for 10 mg/mL NDI-FF with background electrolyte (a). The area of the plot with both pK_a values with x axis on a logarithmic scale is also shown (b).

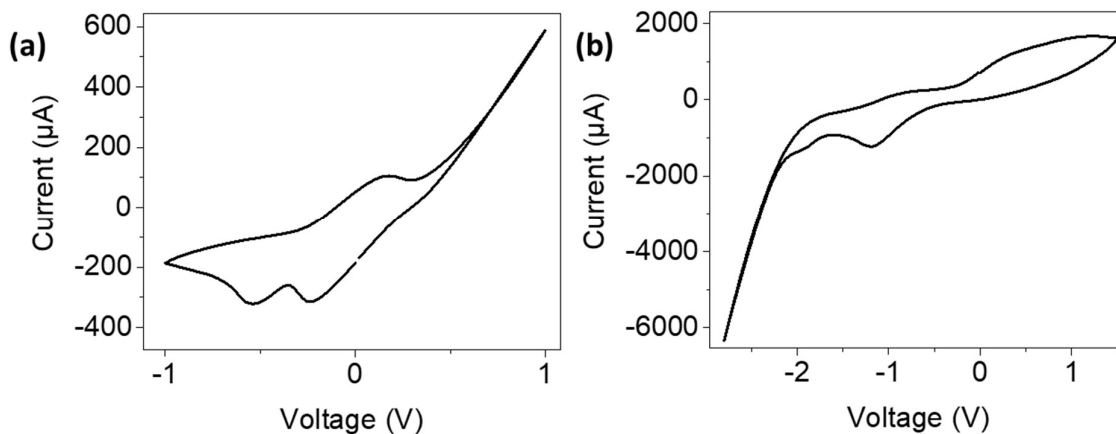


Figure A.2.6. Cyclic voltammogram collected from a 10 mg/mL hydroquinone solution with 10 % 0.1 M NaCl. Voltammograms collected in (a) a referenced glassy carbon set up (vs Ag/AgCl) and (b) a 1 x 1 cm FTO window cell set up. The scan rate was 0.2 V/s.

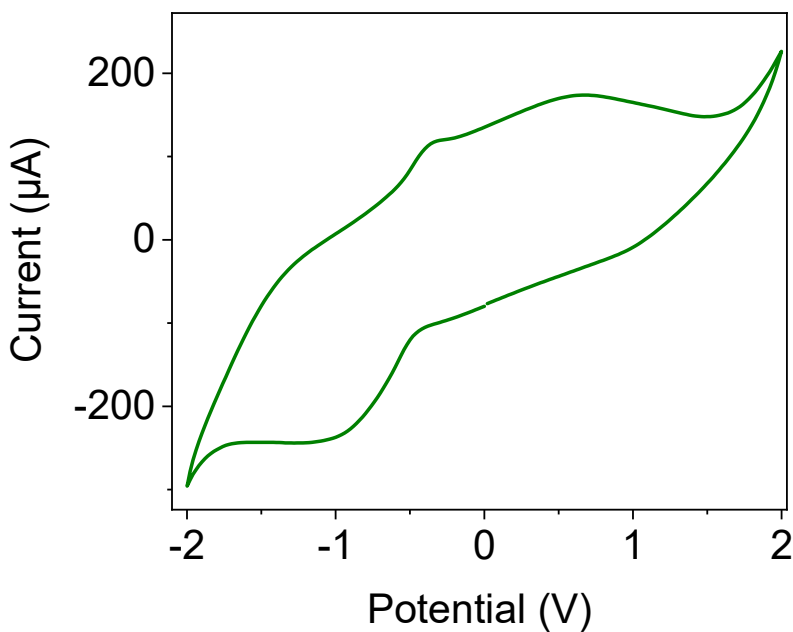


Figure A.2.7. Cyclic voltammogram collected from 10 mg/mL solution of **NDI-I** adjusted to pH 9. Voltammograms measured using a referenced glassy carbon set up (vs Ag/AgCl). The scan rate of the cyclic voltammograms was 0.2 V/s.

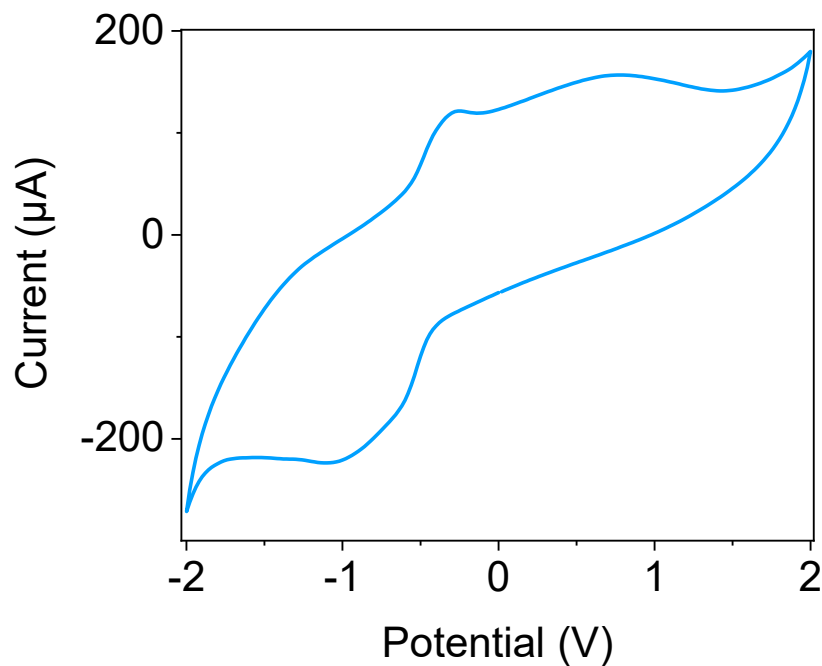


Figure A.2.8. Cyclic voltammogram collected from 10 mg/mL solution of **NDI-V** adjusted to pH 9. Voltammograms measured using a referenced glassy carbon set up (vs Ag/AgCl). The scan rate of the cyclic voltammograms was 0.2 V/s.

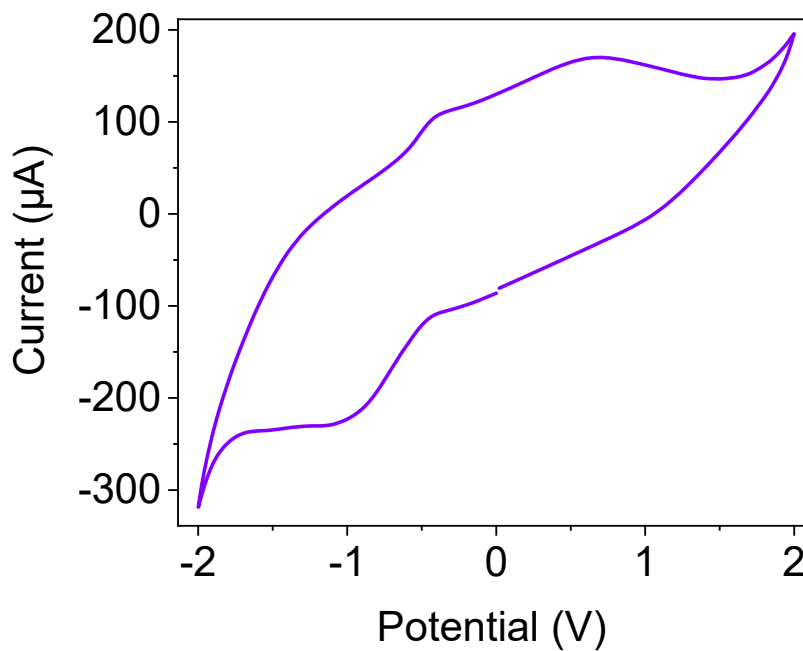


Figure A.2.9. Cyclic voltammogram collected from 10 mg/mL solution of **NDI-F** adjusted to pH 9. Voltammograms measured using a referenced glassy carbon set up (vs Ag/AgCl). The scan rate of the cyclic voltammograms was 0.2 V/s.

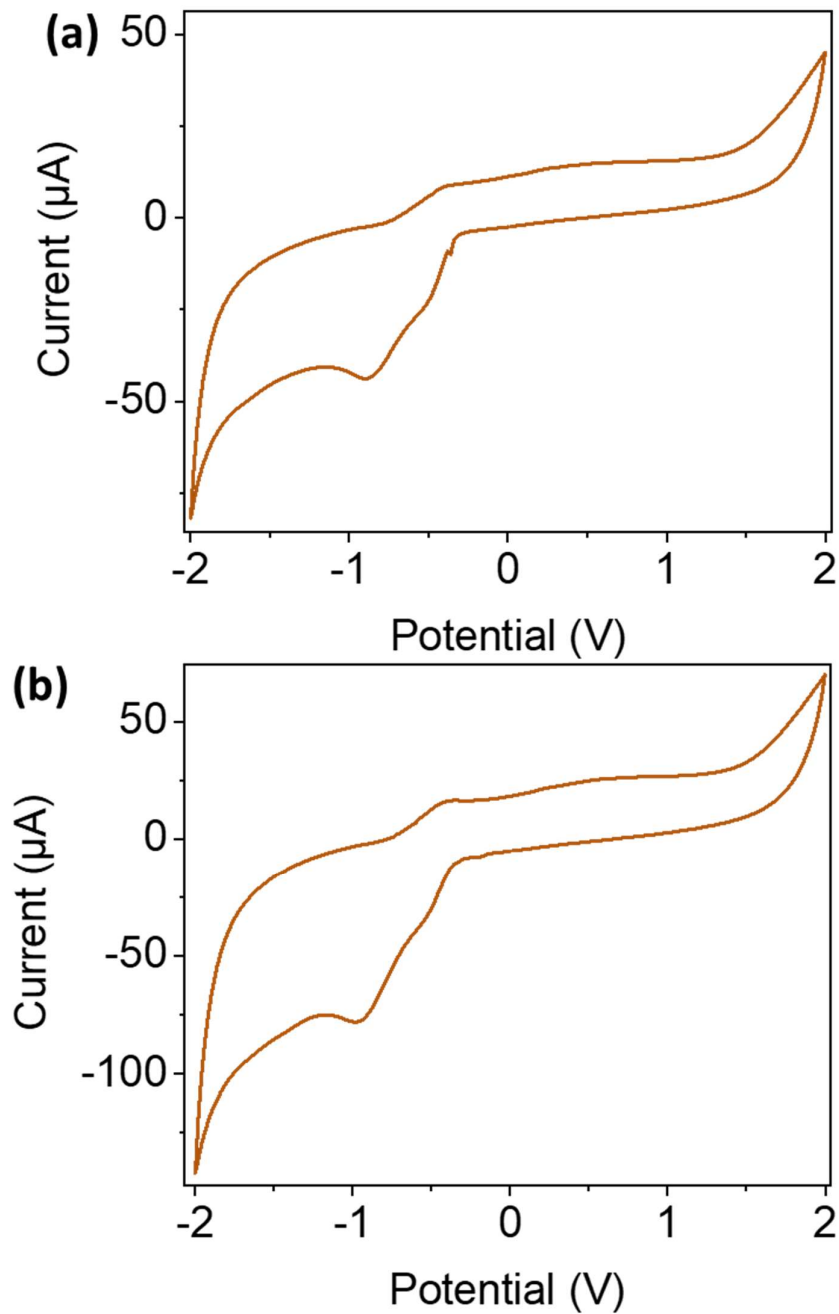


Figure A.2.10. Cyclic voltammogram collected from 10 mg/mL solution of **NDI-GF** adjusted to pH 9. Voltammograms measured using a referenced glassy carbon set up (vs Ag/AgCl). The scan rate of the cyclic voltammograms was (a) 0.2 and (b) 0.5 V/s.

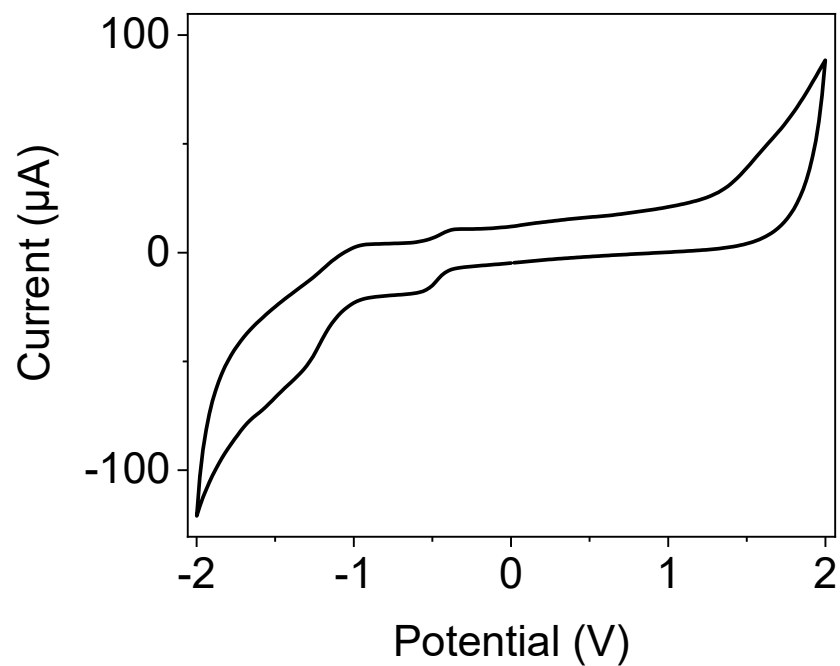


Figure A.2.11. Cyclic voltammogram collected from 10 mg/mL solution of **NDI-FF** adjusted to pH 9. Voltammograms measured using a referenced glassy carbon set up (vs Ag/AgCl). The scan rate of the cyclic voltammograms was 0.2 V/s.

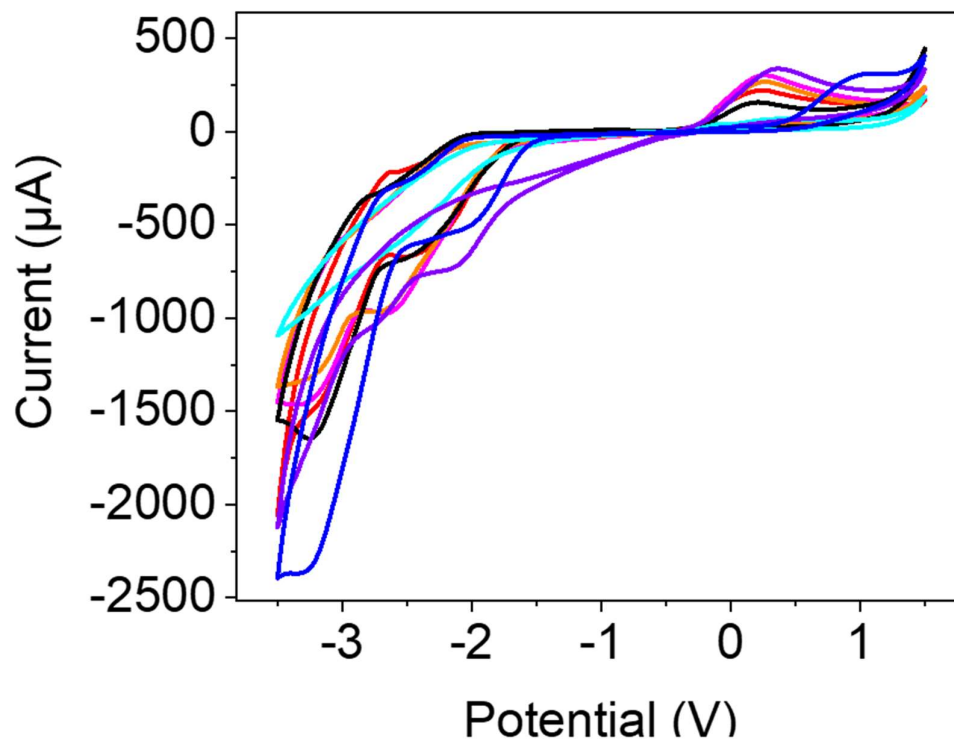


Figure A.2.12. Cyclic voltammograms collected from 10 mg/mL solutions of **NDI-I** adjusted to pH 6 (red), 7 (pink), 8 (orange), 9 (black), 10 (turquoise), 11 (purple) and 12 (blue). The scan rate of the cyclic voltammograms was 0.1 V/s.

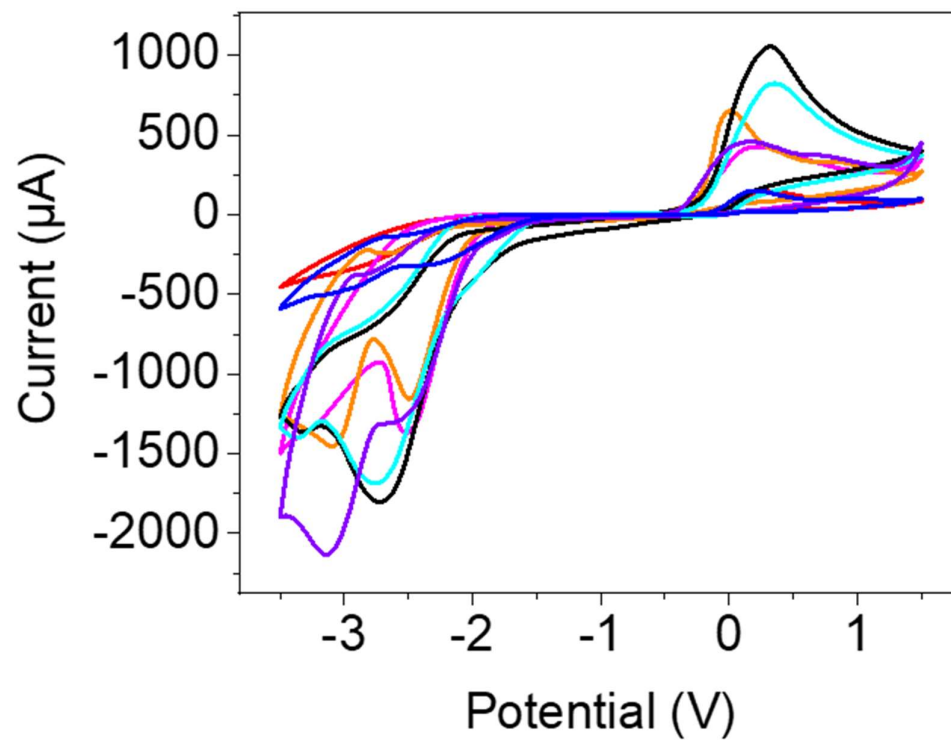


Figure A.2.13. Cyclic voltammograms collected from 10 mg/mL solutions of **NDI-V** adjusted to pH 6 (red), 7 (pink), 8 (orange), 9 (black), 10 (turquoise), 11 (purple) and 12 (blue). The scan rate of the cyclic voltammograms was 0.1 V/s. The scan rate of the cyclic voltammograms was 0.1 V/s.

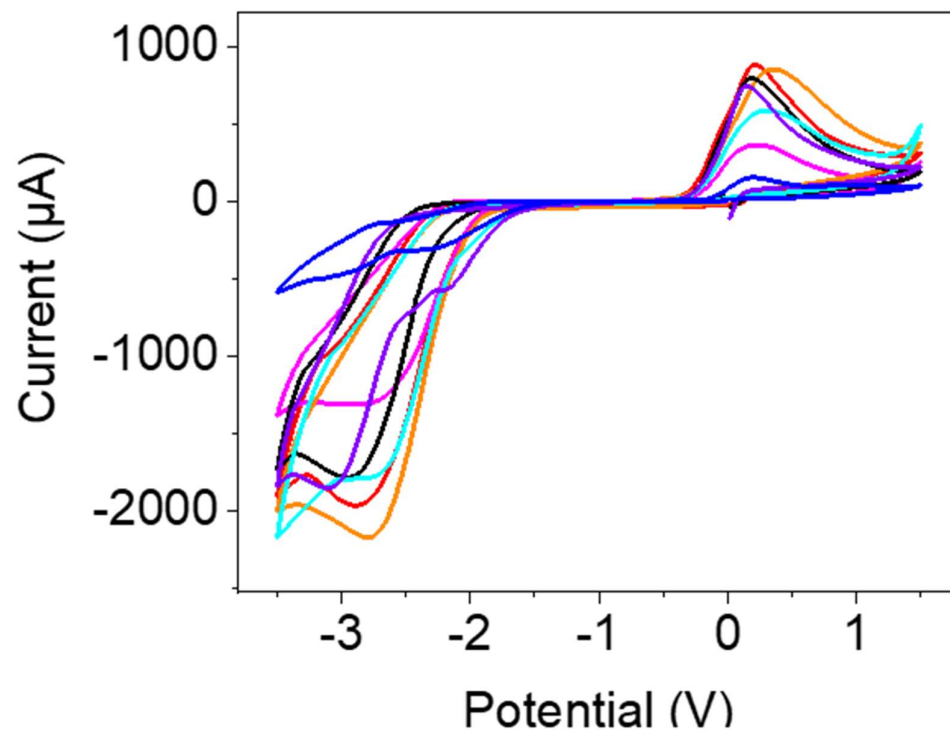


Figure A.2.14. Cyclic voltammograms collected from 10 mg/mL solutions of **NDI-F** adjusted to pH 6 (red), 7 (pink), 8 (orange), 9 (black), 10 (turquoise), 11 (purple) and 12 (blue). The scan rate of the cyclic voltammograms was 0.1 V/s.

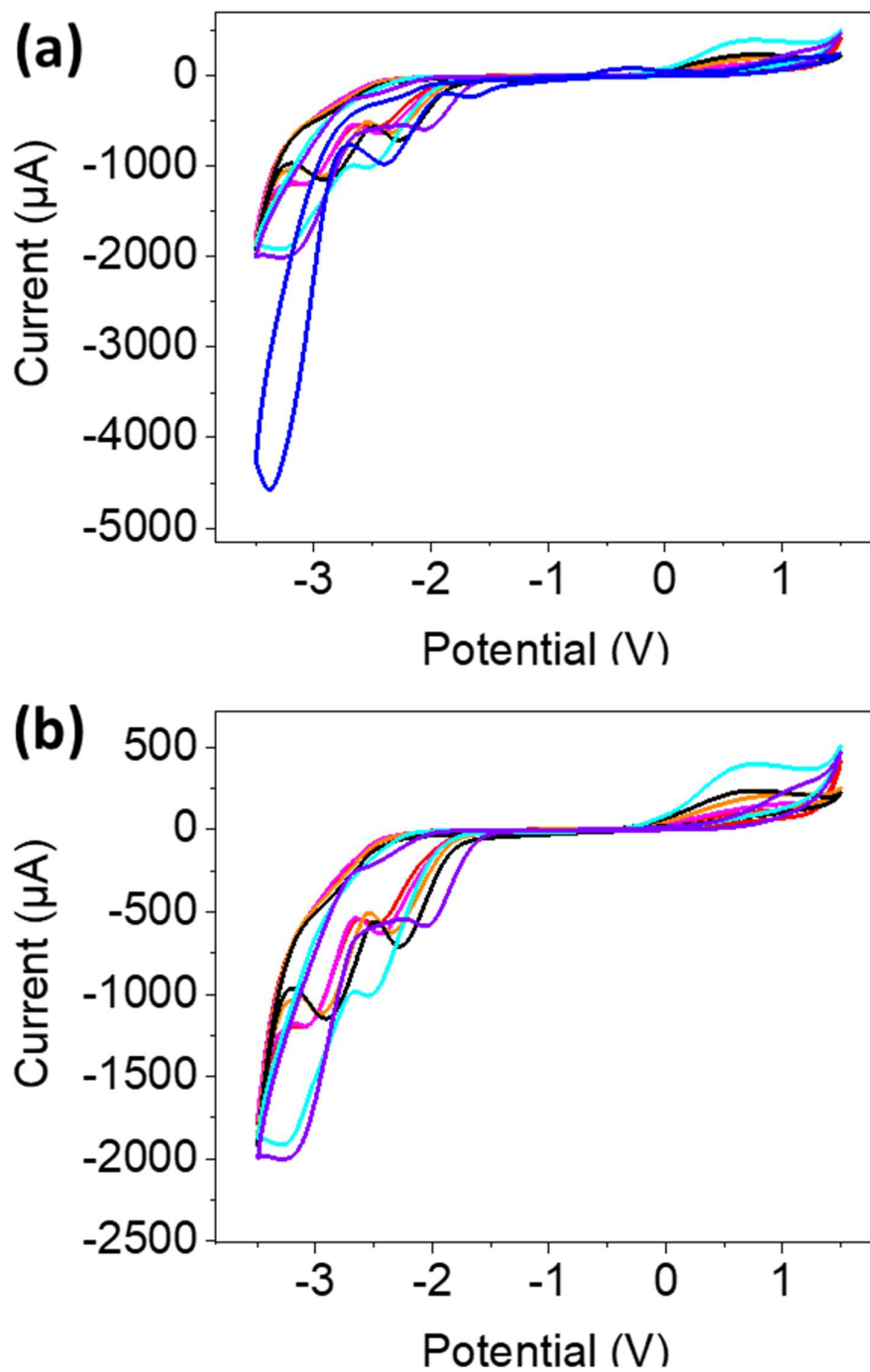


Figure A.2.15. Cyclic voltammograms collected from 10 mg/mL solutions of NDI-GF adjusted to pH 6 (red), 7 (pink), 8 (orange), 9 (black), 10 (turquoise), 11 (purple) and 12 (blue). The scan rate of the cyclic voltammograms was 0.1 V/s. (b) shows data from solutions at pH 6 (red), 7 (pink), 8 (orange), 9 (black), 10 (turquoise), and 11 (purple) and on a smaller scale for clarity.

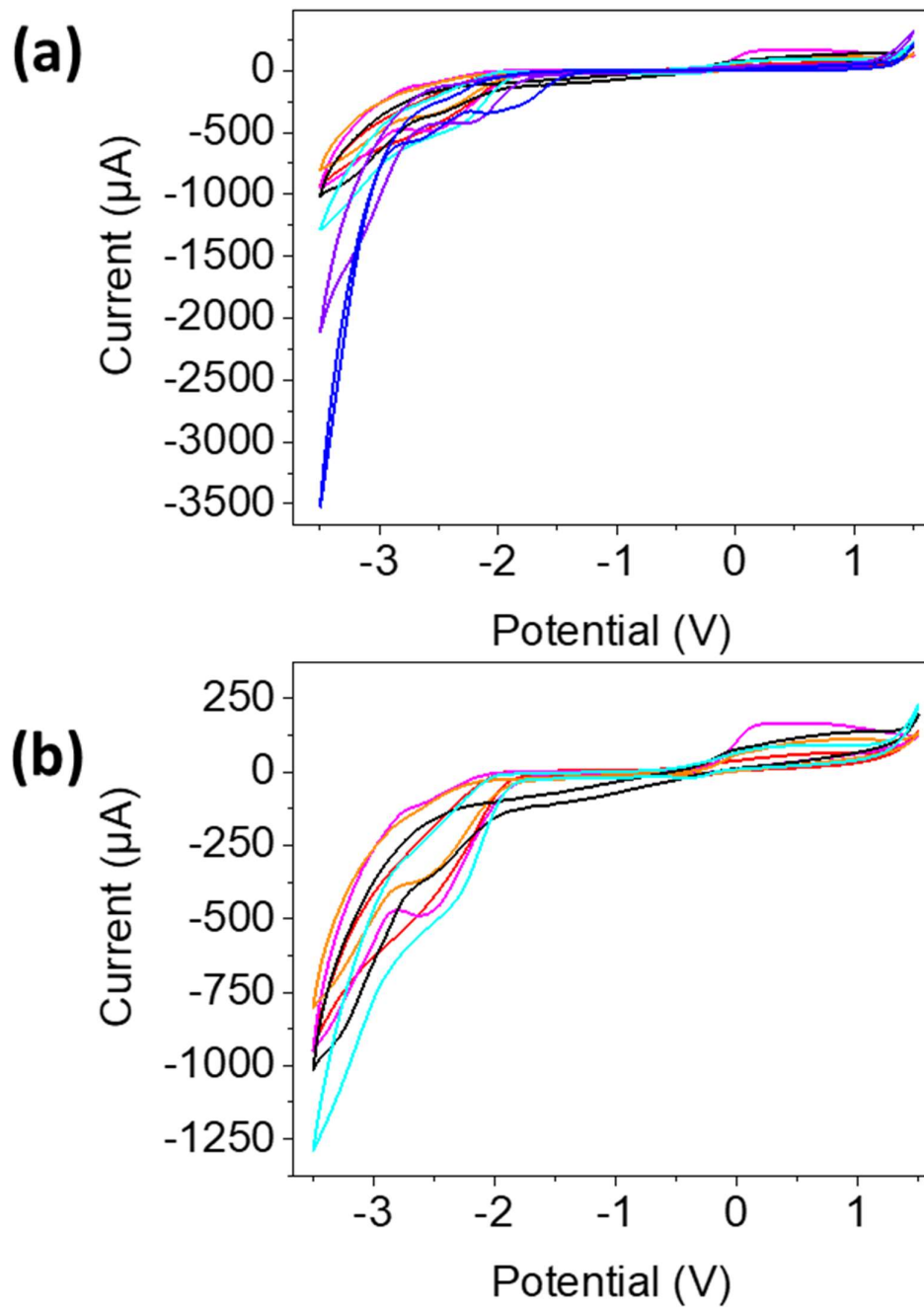


Figure A.2.16. Cyclic voltammograms collected from 10 mg/mL solutions of NDI-FF adjusted to pH 6 (red), 7 (pink), 8 (orange), 9 (black), 10 (turquoise), 11 (purple) and 12 (blue). The scan rate of the cyclic voltammograms was 0.1 V/s. (b) shows data from solutions at pH 6 (red), 7 (pink), 8 (orange), 9 (black) and 10 (turquoise) on a smaller scale for clarity.

A.2.E. Chapter 2 experimental appendices

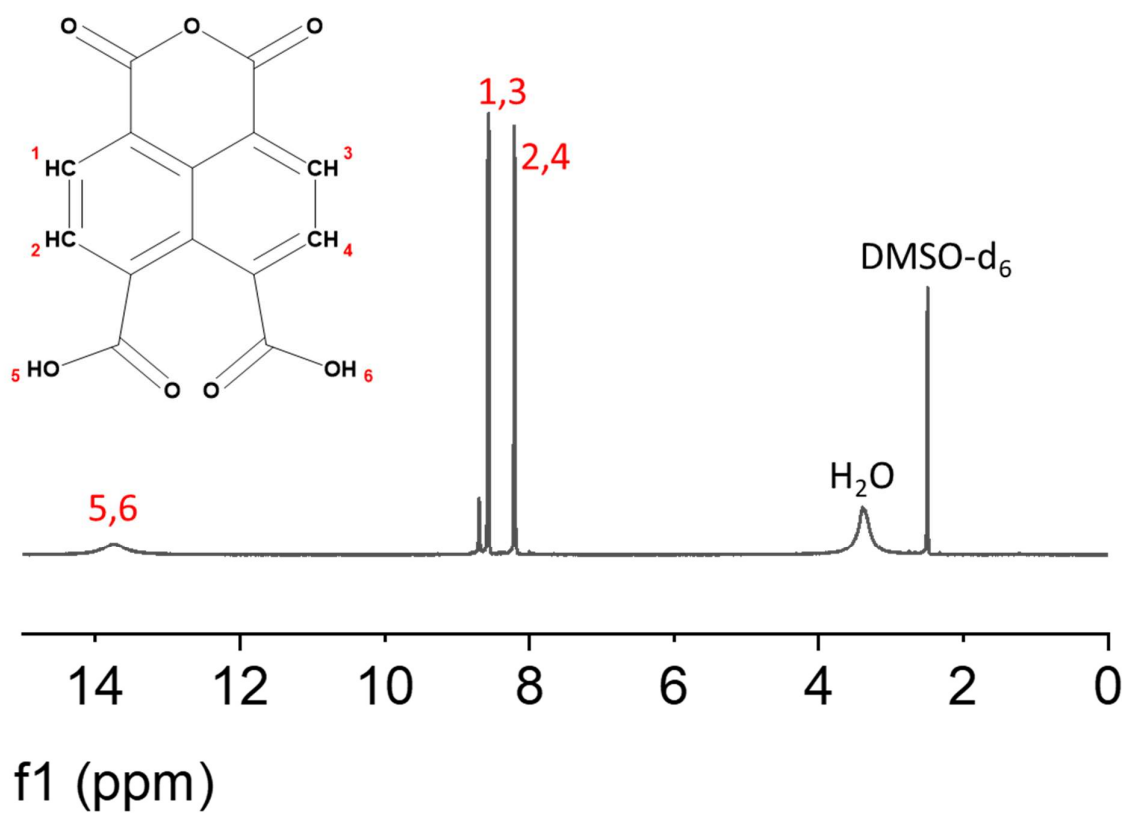


Figure A.2.17. Annotated ^1H NMR spectrum (400 MHz, DMSO-d_6) of impure starting material as received.

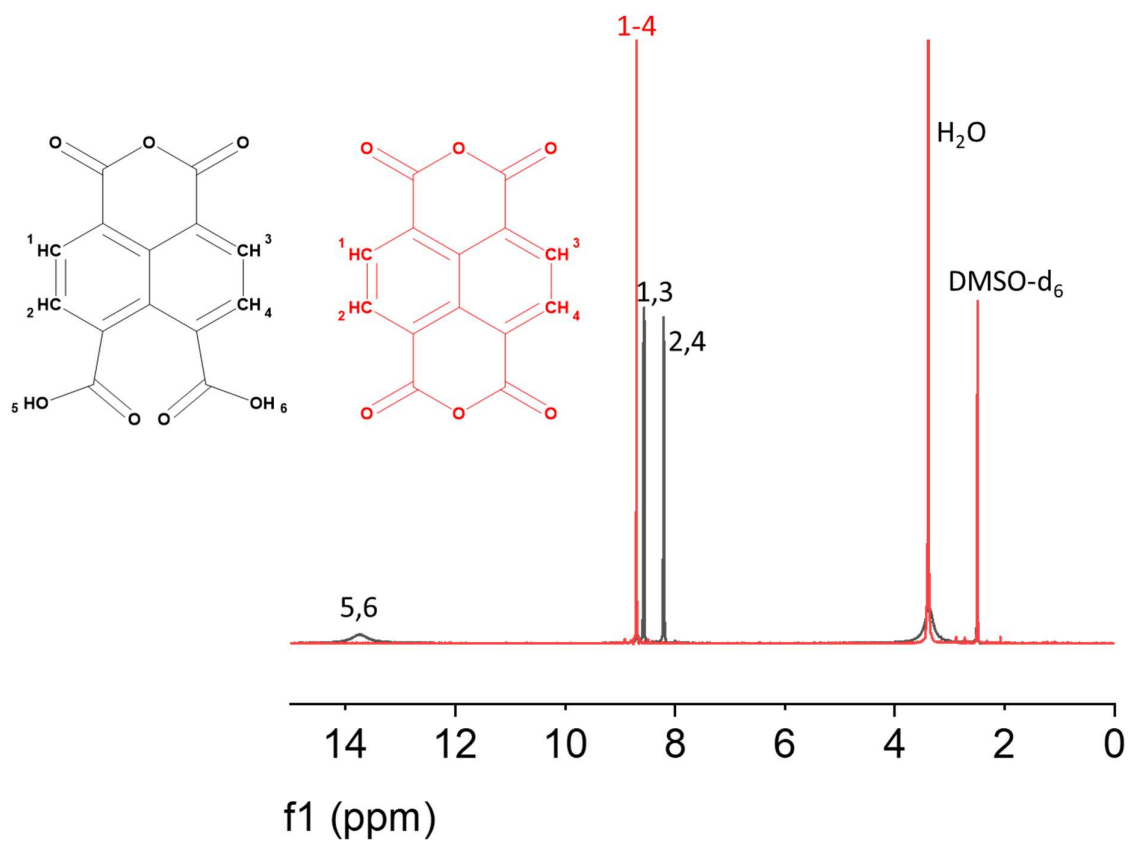


Figure A.2.18. Overlaid annotated ^1H NMR spectra (400 MHz, DMSO-d_6) of impure starting material (black) and purified product (red).

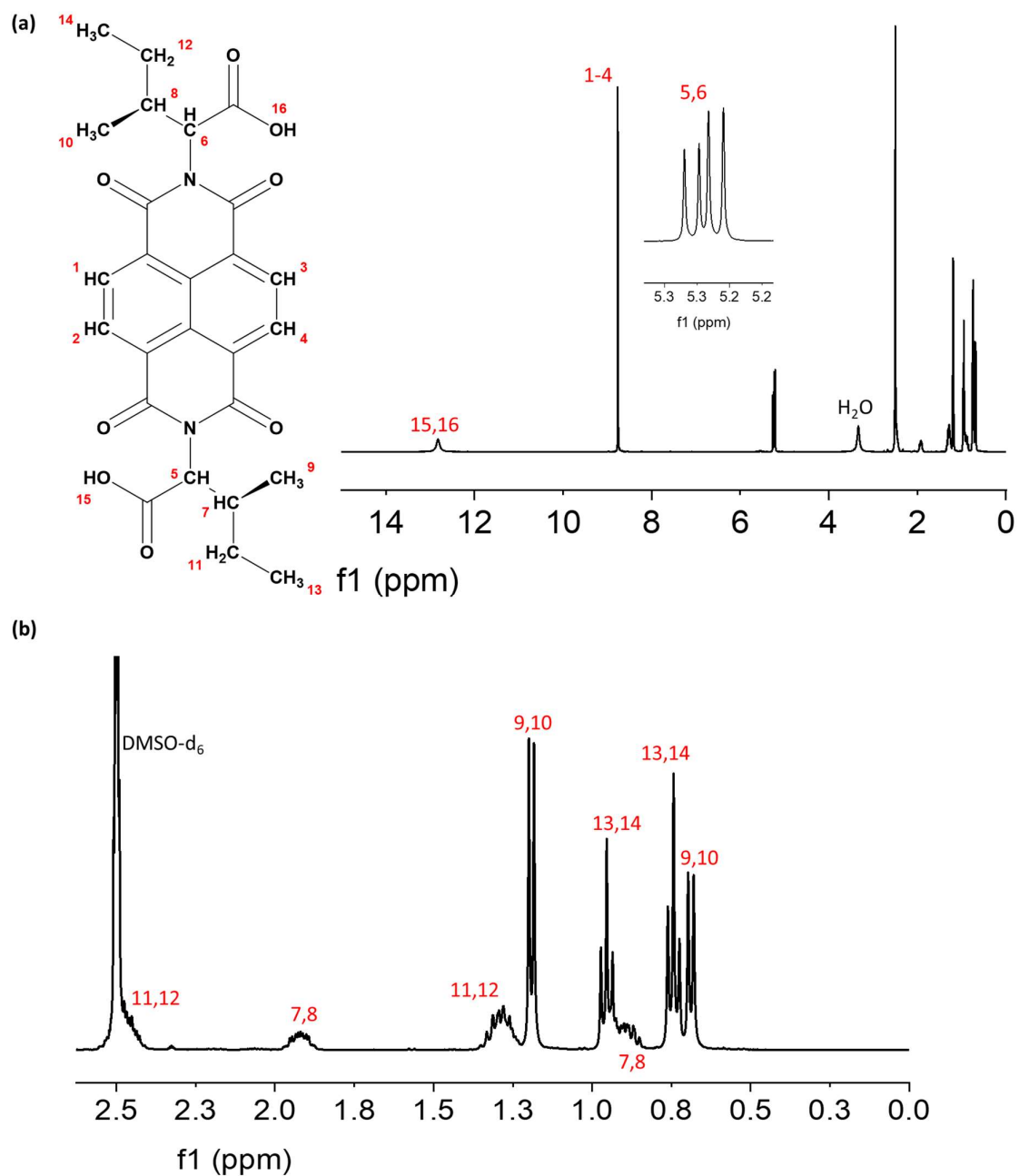
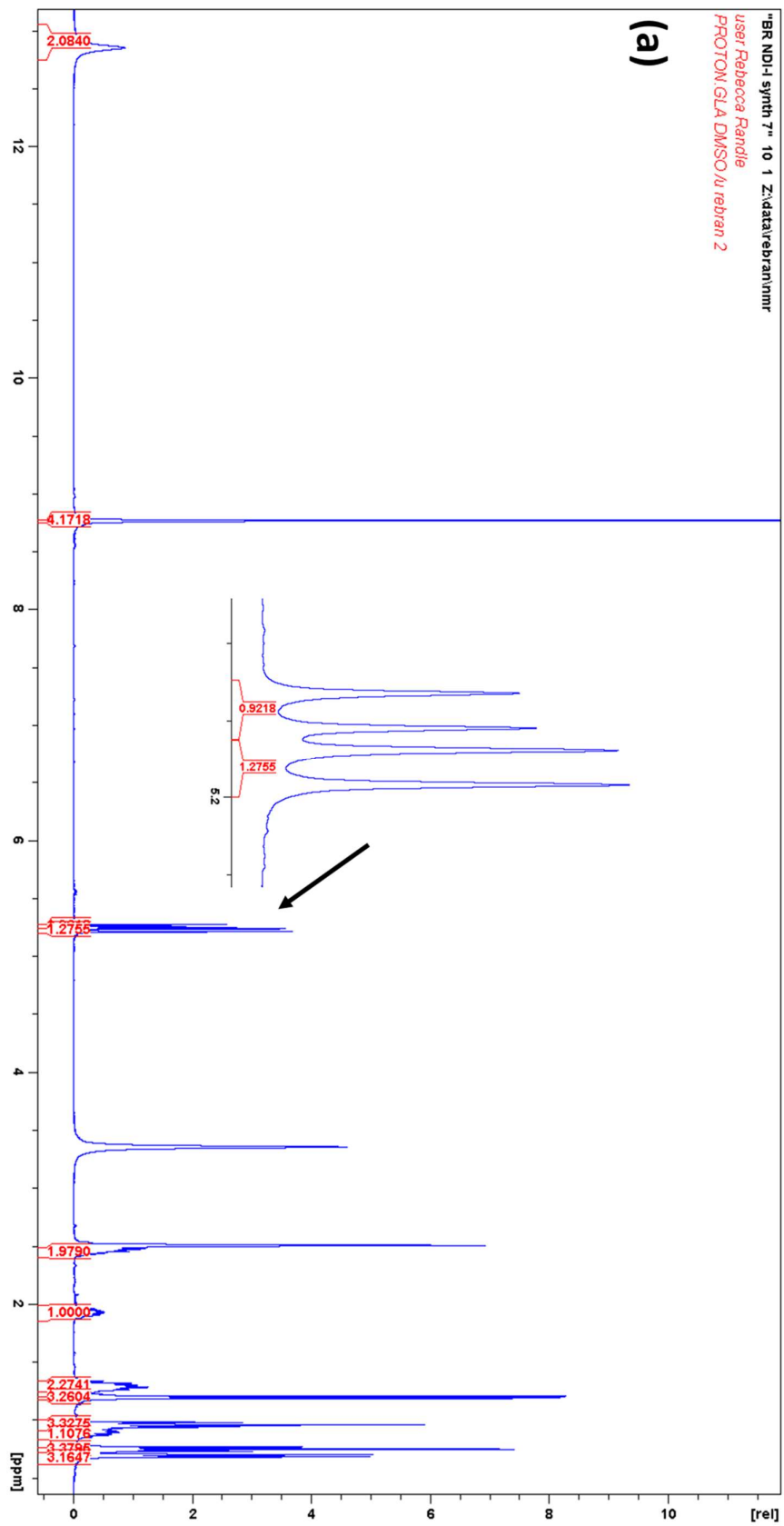


Figure A.2.19. Annotated ^1H NMR spectrum (400 MHz, DMSO-d_6) of **NDI-I** (a) full spectra with insert of area between 5.2-5.3 ppm (b) enhanced section of spectra shown between 2.5-0 ppm.



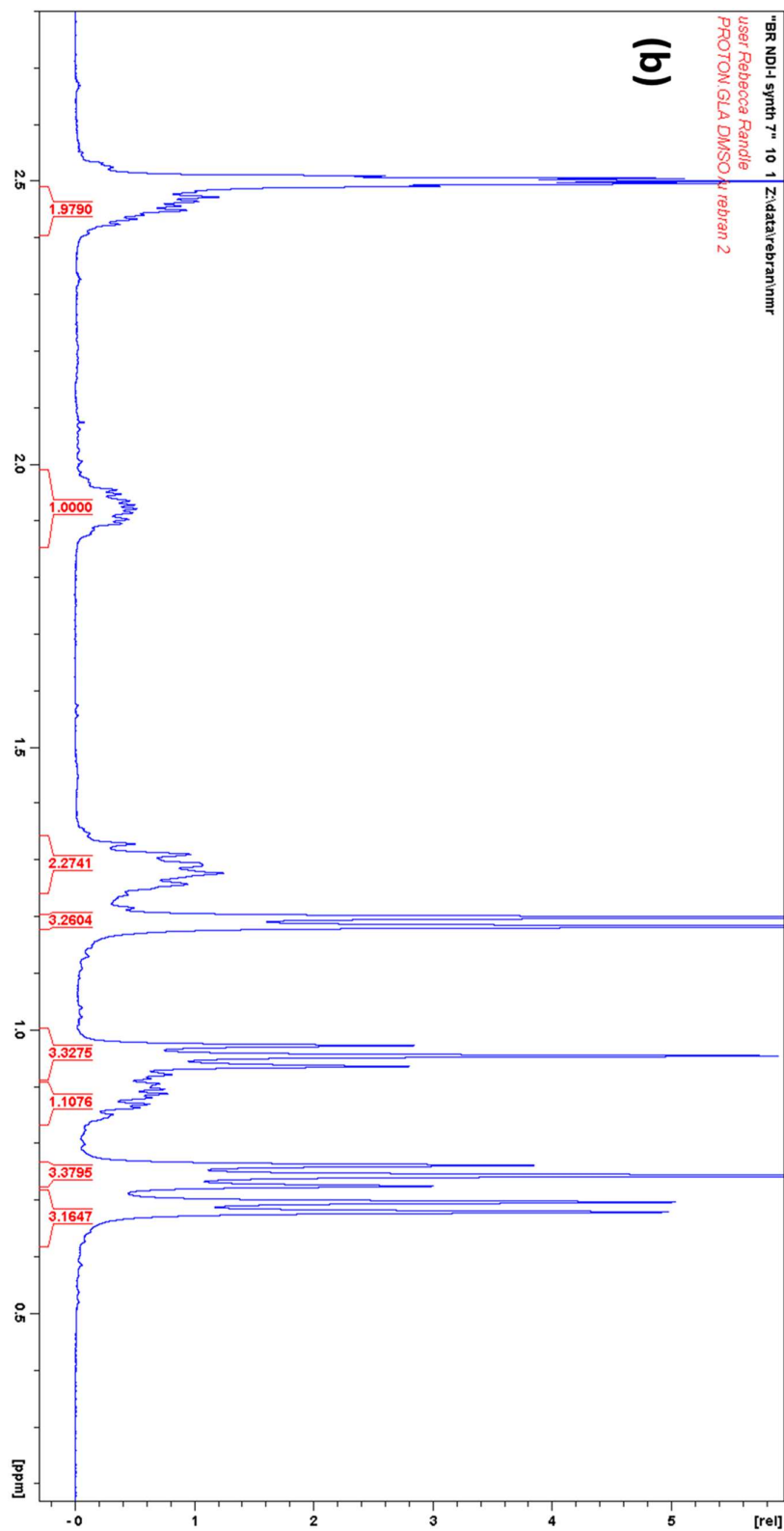


Figure A.2.20. ^1H NMR spectrum showing integration (400 MHz, DMSO- d_6) of ND-I (a) full spectra with insert of area at 5.2 ppm (b) enhanced section of spectra shown between 2.5-0.5 ppm.

Appendix

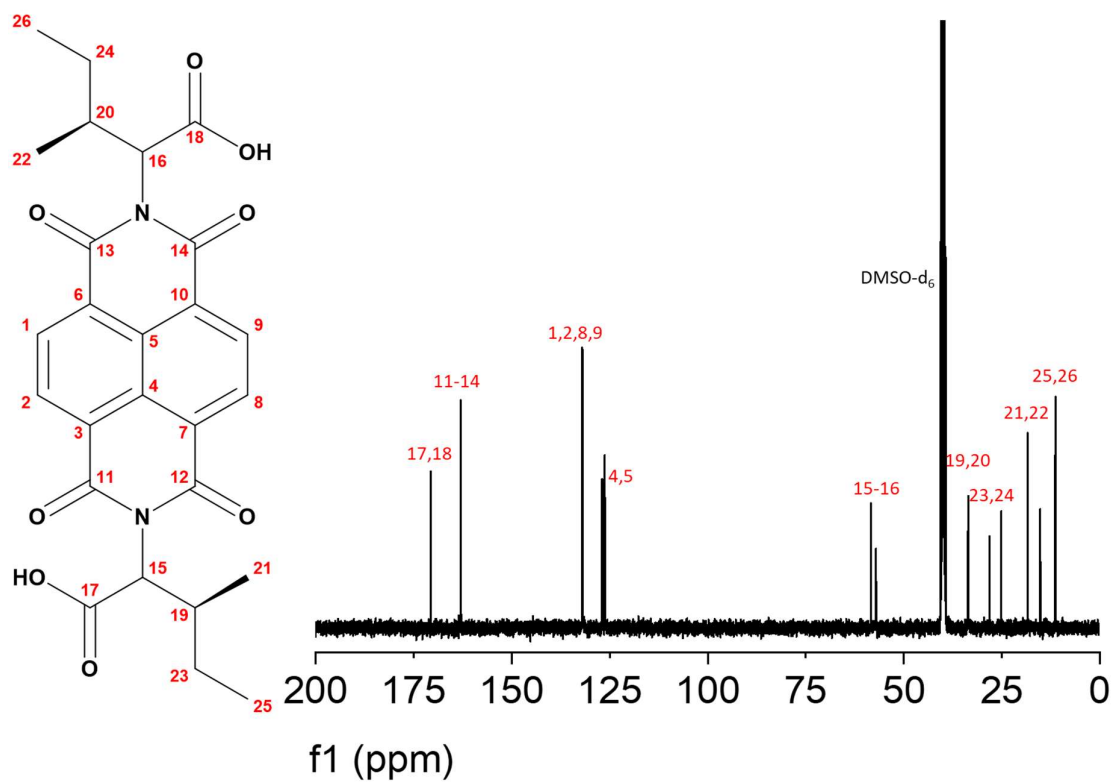
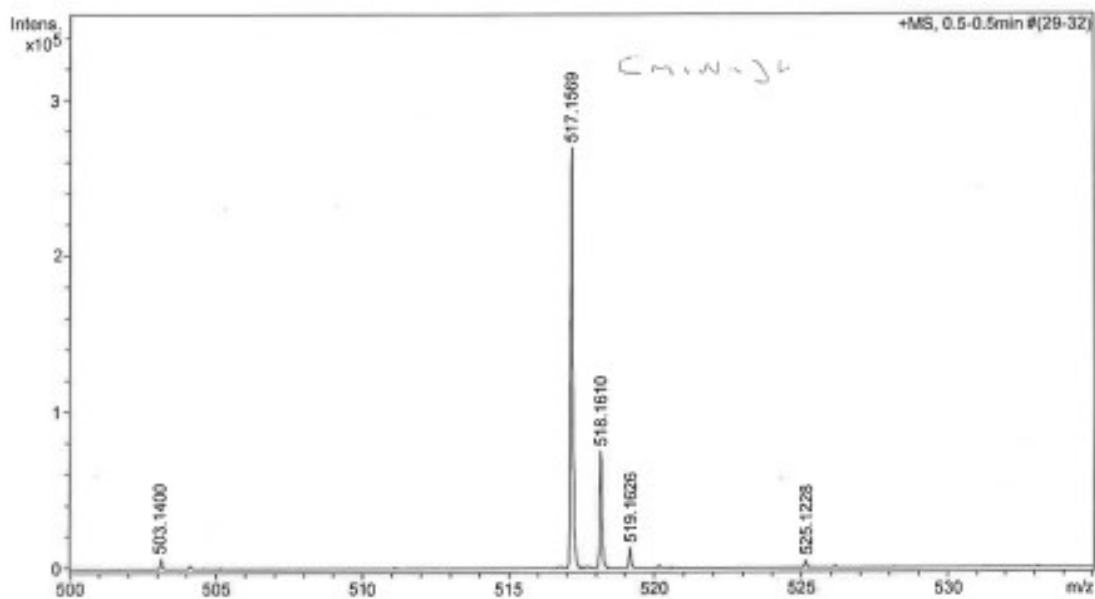


Figure A.2.21. Annotated ^{13}C NMR spectrum (100 MHz, DMSO-d_6) of NDI-I.

Mass Spectrum SmartFormula Report

Analysis Info		Acquisition Date	1/9/2020 8:19:47 AM
Analysis Name	D:\Data\Mass Spectrometry Service\74842-000001.d	Operator	user
Method	LM MS 50 to 1100 KIM 071215.m	Instrument / Ser#	micrOTOF-Q 74
Sample Name	dietrich-BR ND1-I		
Comment			

Acquisition Parameter			
Source Type	ESI	Ion Polarity	Positive
Scan Begin	50 m/z		
Scan End	1100 m/z		



Formula	z	m/z	Meas. m/z	err [ppm]	err [mDa]
C ₂₆ H ₂₆ N ₂ NaO ₈	1+	517.1581	517.1569	2.3	1.2

Figure A.2.22. HRMS report of NDI-I in ethanol.

Appendix

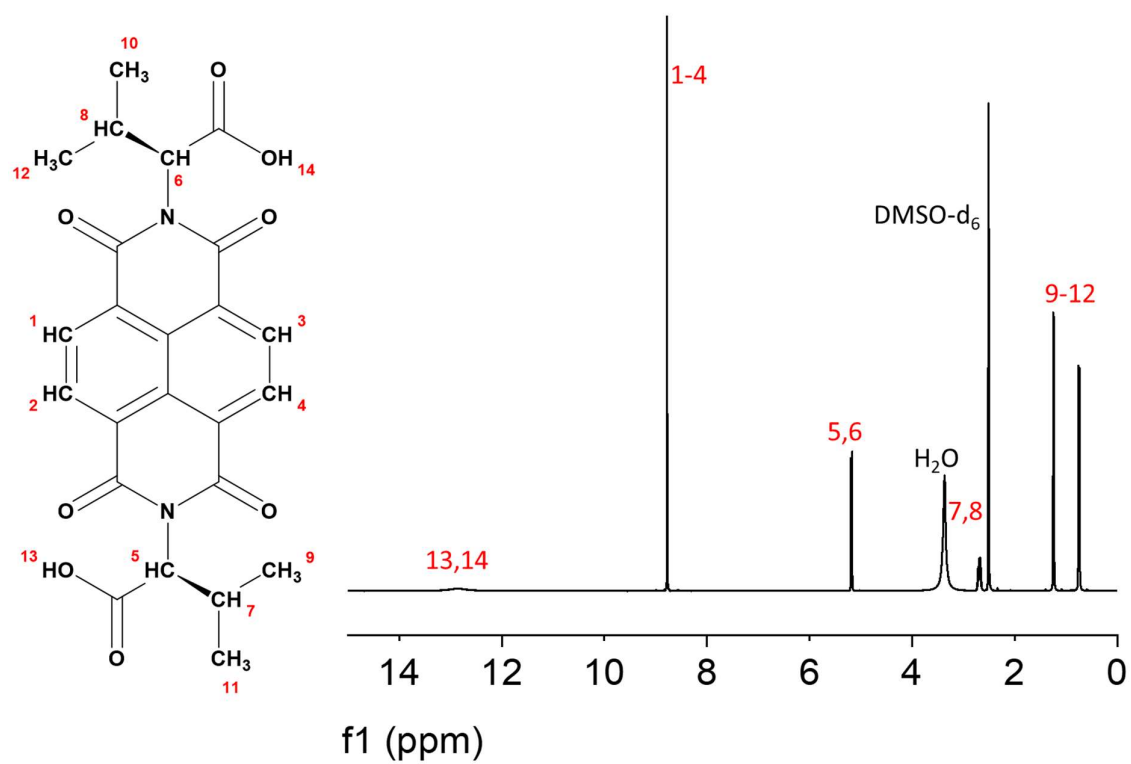


Figure A.2.23. Annotated ¹H NMR spectrum (400 MHz, DMSO-d₆) of NDI-V.

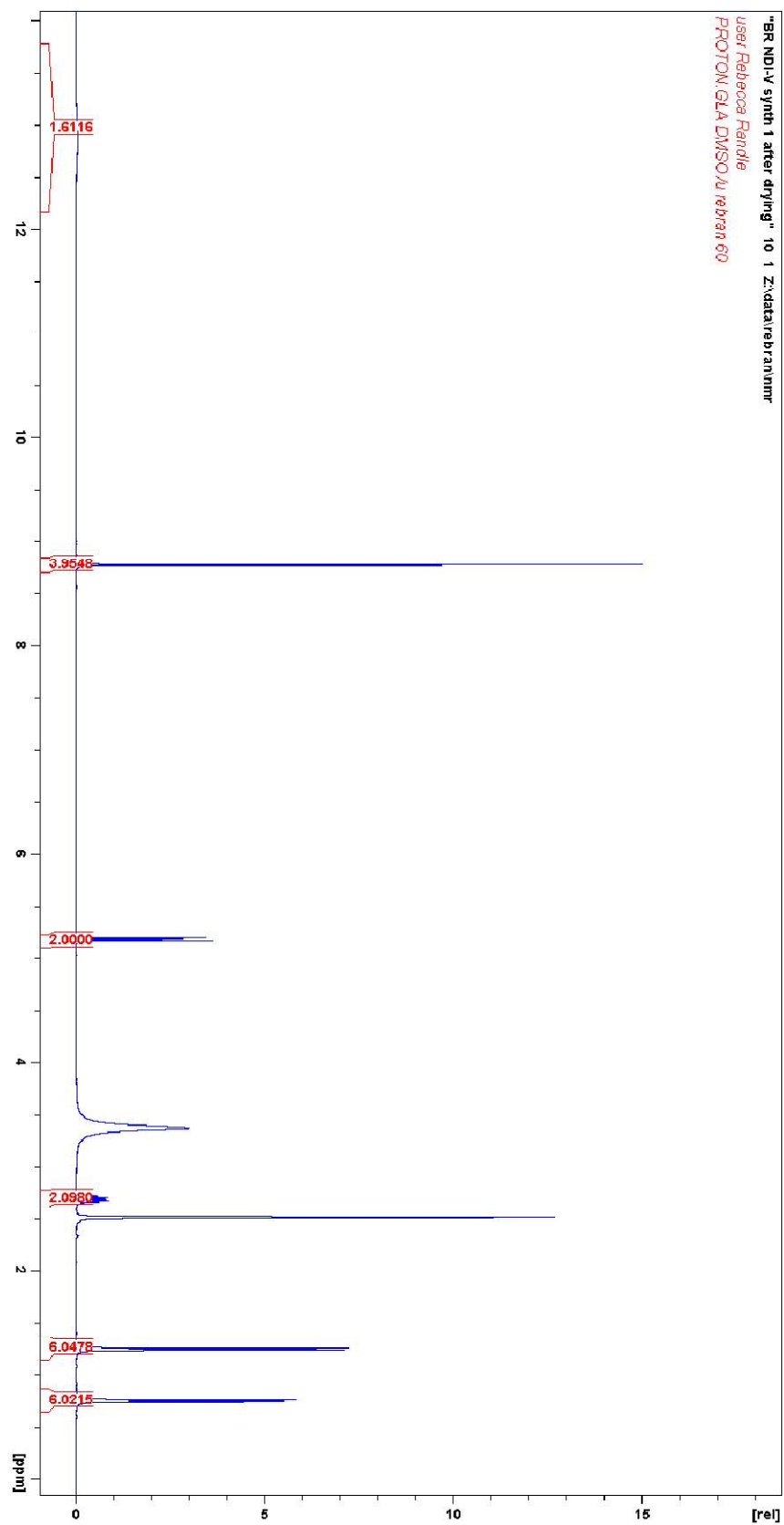


Figure A.2.24. ¹H NMR spectrum showing intergration (400 MHz, DMSO-d₆) of NDI-V.

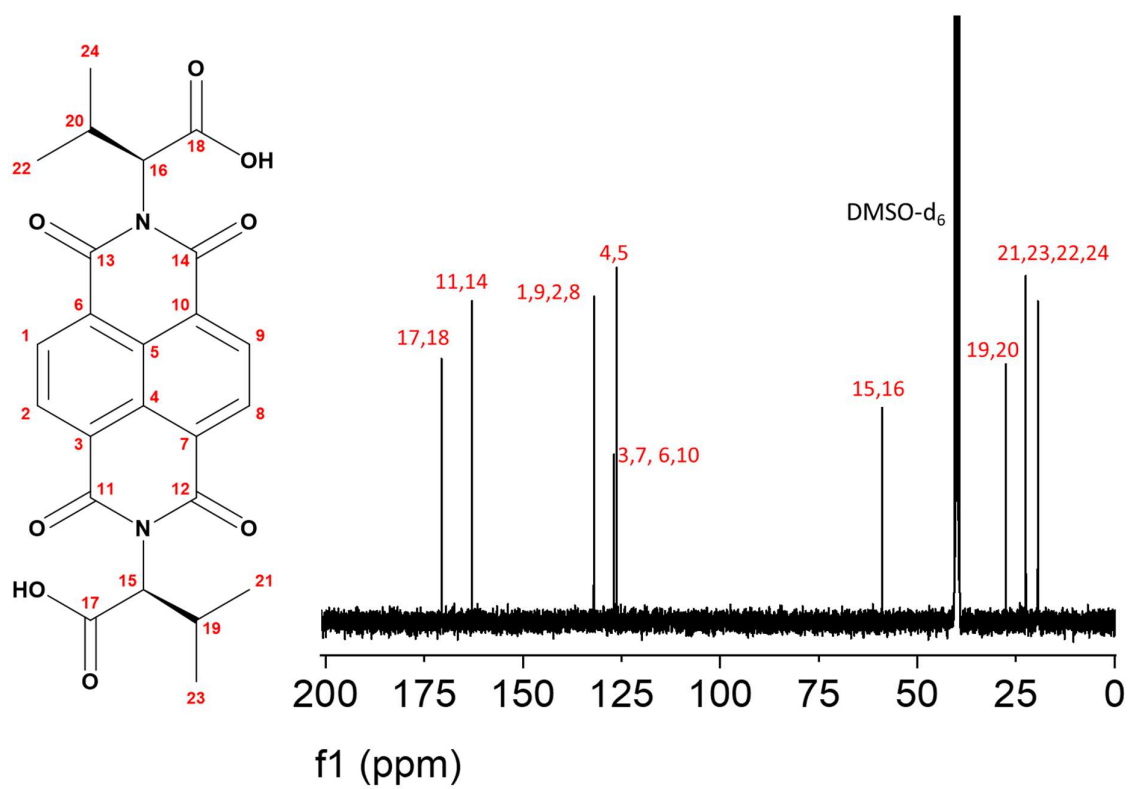


Figure A.2.25. Annotated ^{13}C NMR spectrum (100 MHz, DMSO-d_6) of NDI-V.

Mass Spectrum SmartFormula Report

Analysis Info

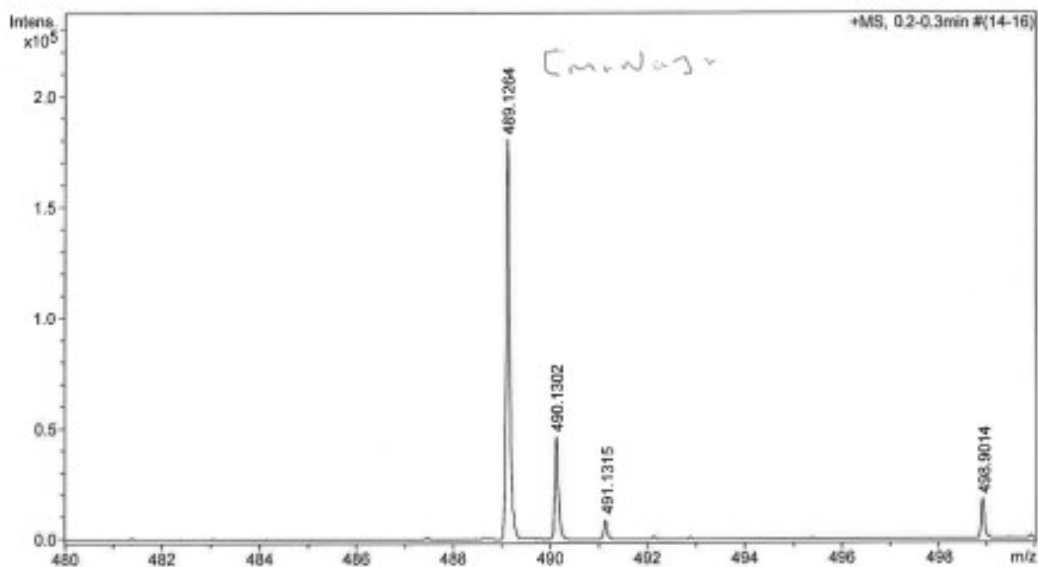
Analysis Name D:\Data\Mass Spectrometry Service\74897-000001.d
Method LM MS 50 to 1100 KIM 071215.m
Sample Name Dietrich-BR ND1-V
Comment

Acquisition Date 1/16/2020 8:10:59 AM

Operator user
Instrument / Ser# microTOF-Q 74

Acquisition Parameter

Source Type ESI Ion Polarity Positive
Scan Begin 50 m/z
Scan End 1100 m/z



Formula	z	m/z	Meas. m/z	err [ppm]	err [mDa]
C 24 H 22 N 2 Na O 8	1+	489.1268	489.1264	0.8	0.4

Figure A.2.26. HRMS report of NDI-V in ethanol.

Appendix

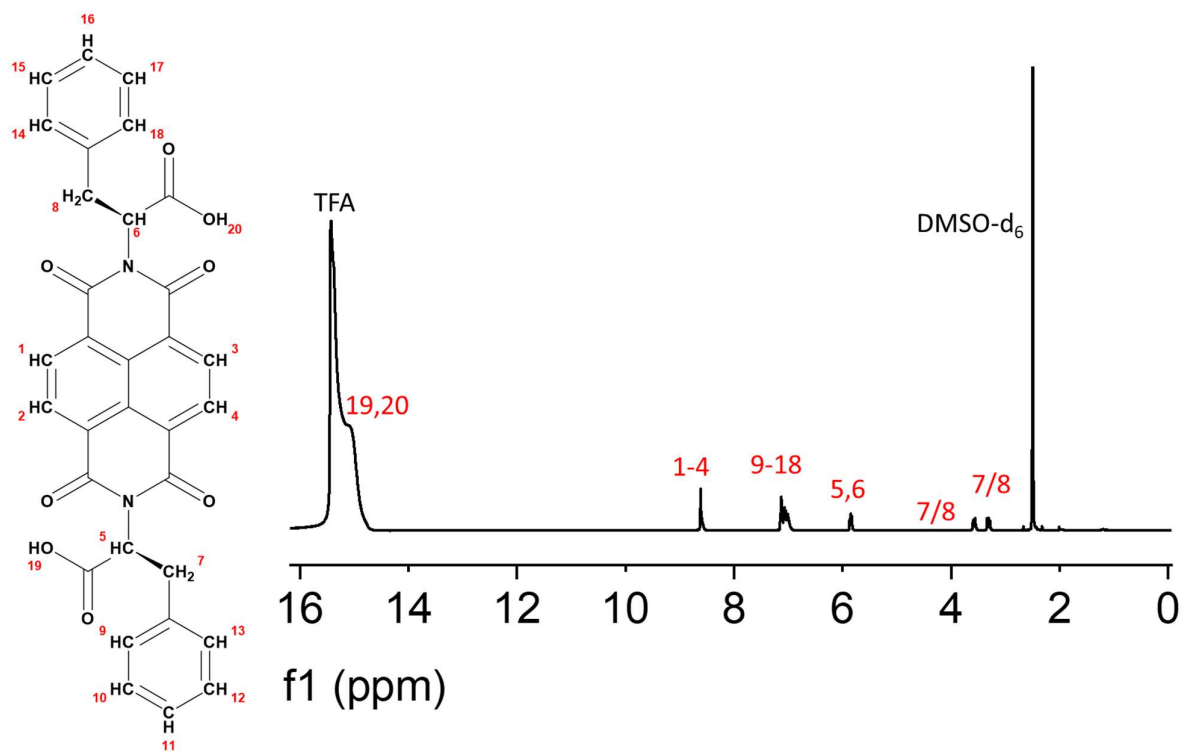


Figure A.2.27. Annotated ¹H NMR spectrum (400 MHz) of NDI-F in DMSO-d₆ + TFA.

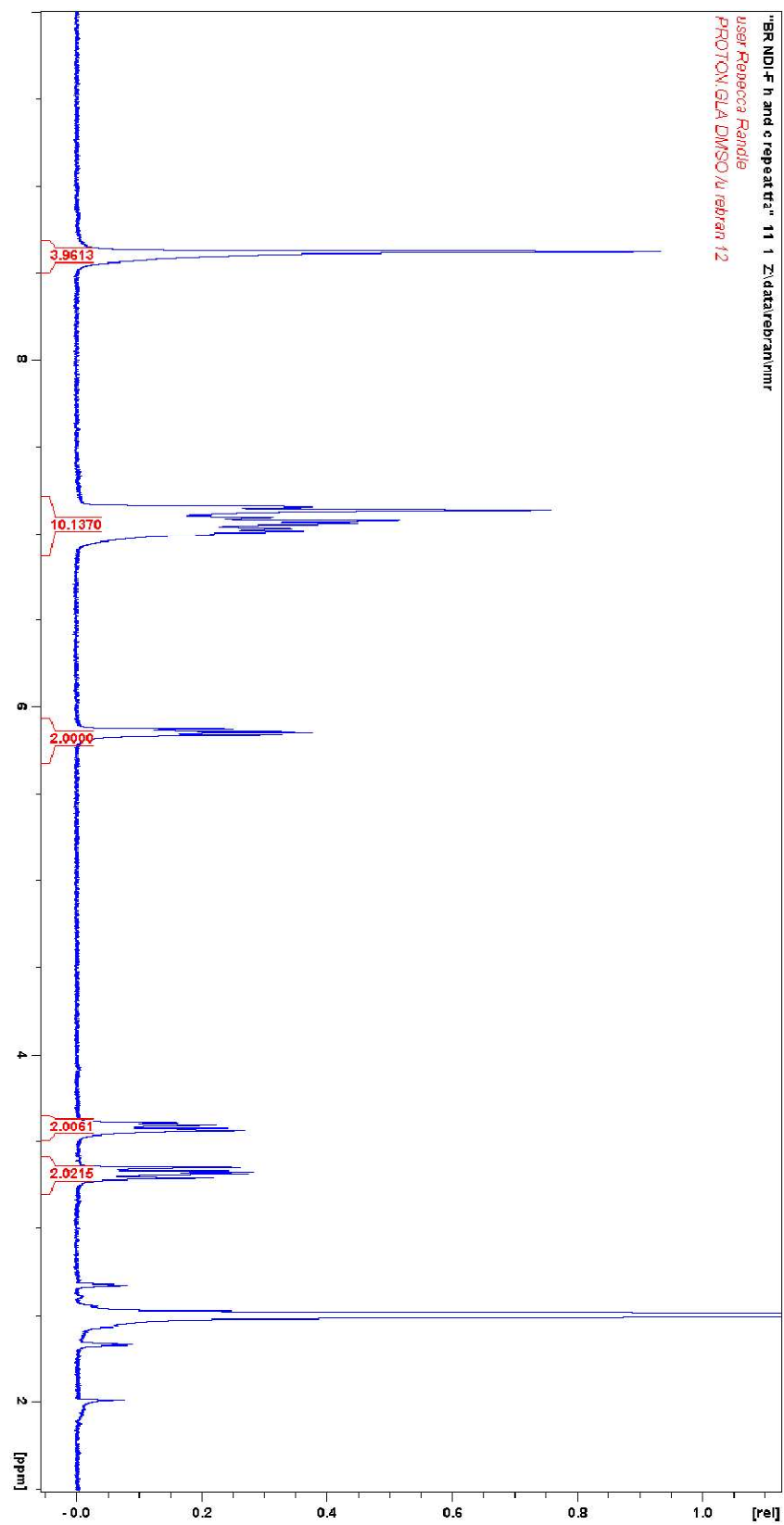
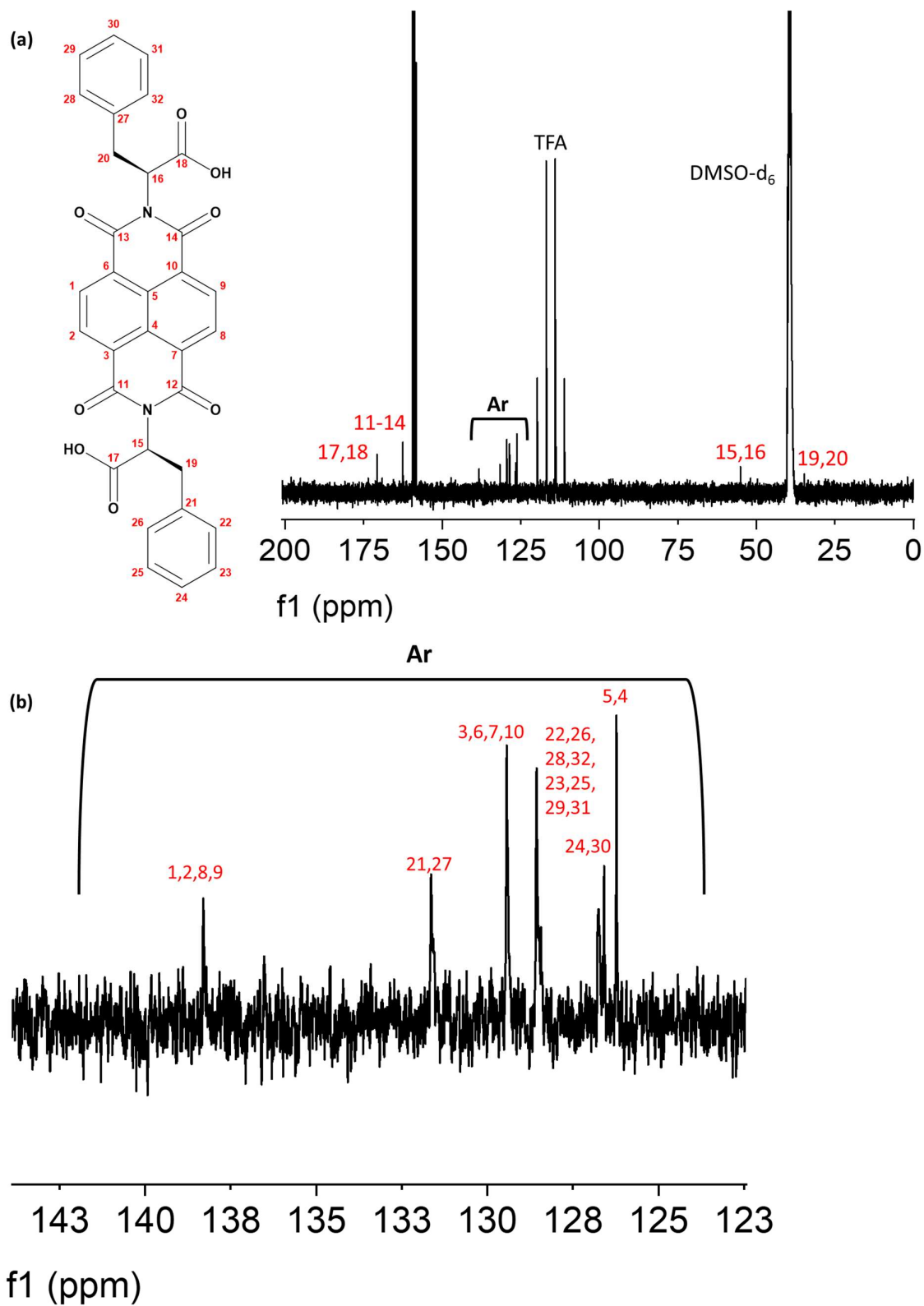


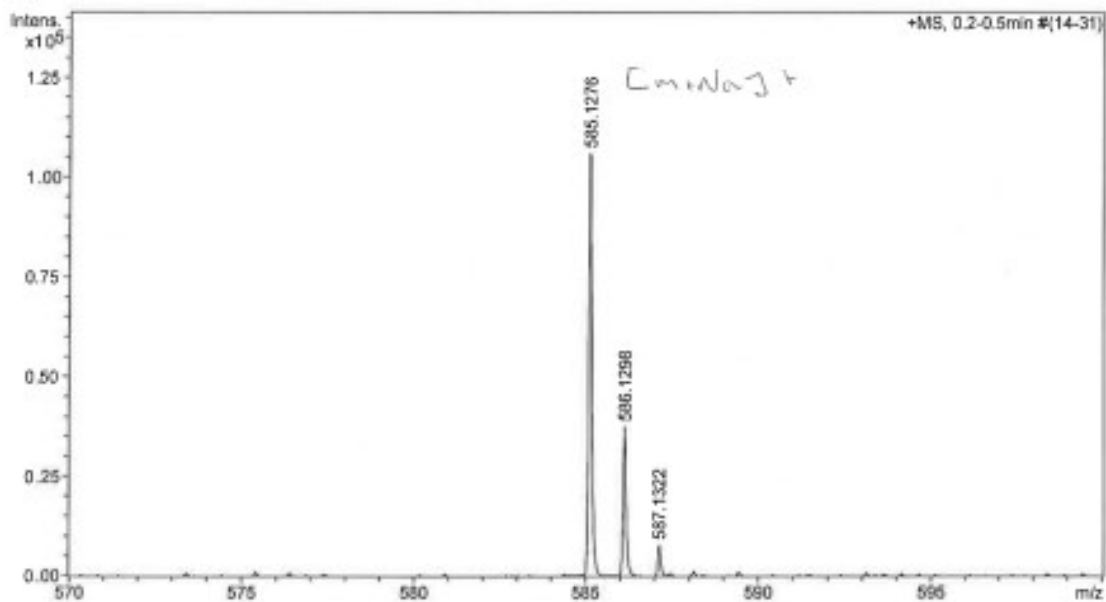
Figure A.2.28. ^1H NMR spectrum showing integration (400 MHz, DMSO-d_6) of NDI-F.



Mass Spectrum SmartFormula Report

Analysis Info		Acquisition Date	1/9/2020 8:13:49 AM
Analysis Name	D:\Data\Mass Spectrometry Service\74841-000001.d	Operator	user
Method	LM MS 50 to 1100 KIM 071215.m	Instrument / Ser#	micrOTOF-Q 74
Sample Name	dietrich-BR ND1-F		
Comment			

Acquisition Parameter			
Source Type	ESI	Ion Polarity	Positive
ScanBegin	50 m/z		
ScanEnd	1100 m/z		



Formula	z	m/z	Meas. m/z	err [ppm]	err [mDa]
C 32 H 22 N 2 Na O 8	1+	585.1268	585.1276	-1.2	-0.7

Figure A.2.30. HRMS report of NDI-F in ethanol.

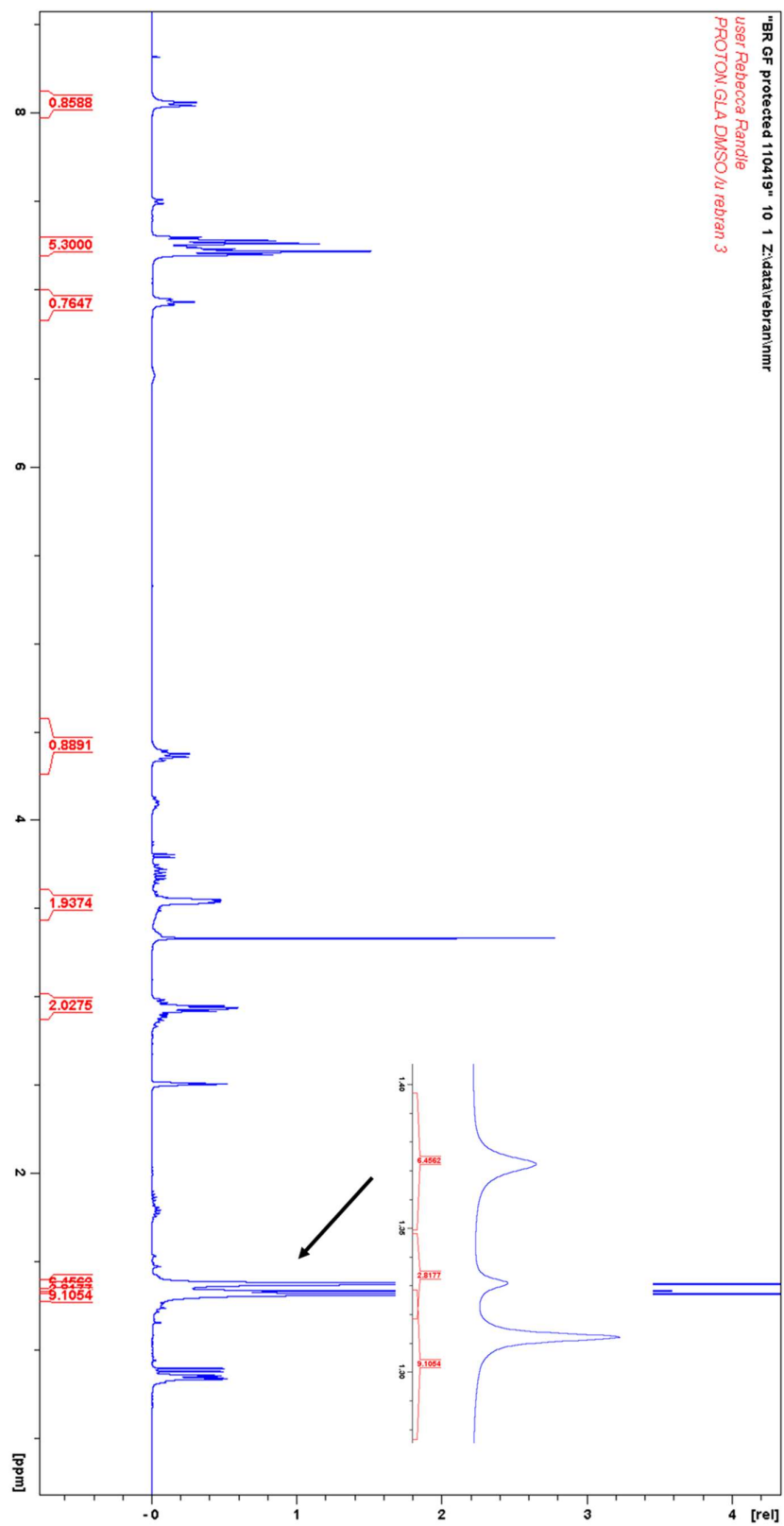


Figure A.2.32. ^1H NMR spectrum showing integration (400 MHz, DMSO- d_6) of GF-Protected with enhanced section of spectra shown around 3.35 ppm.

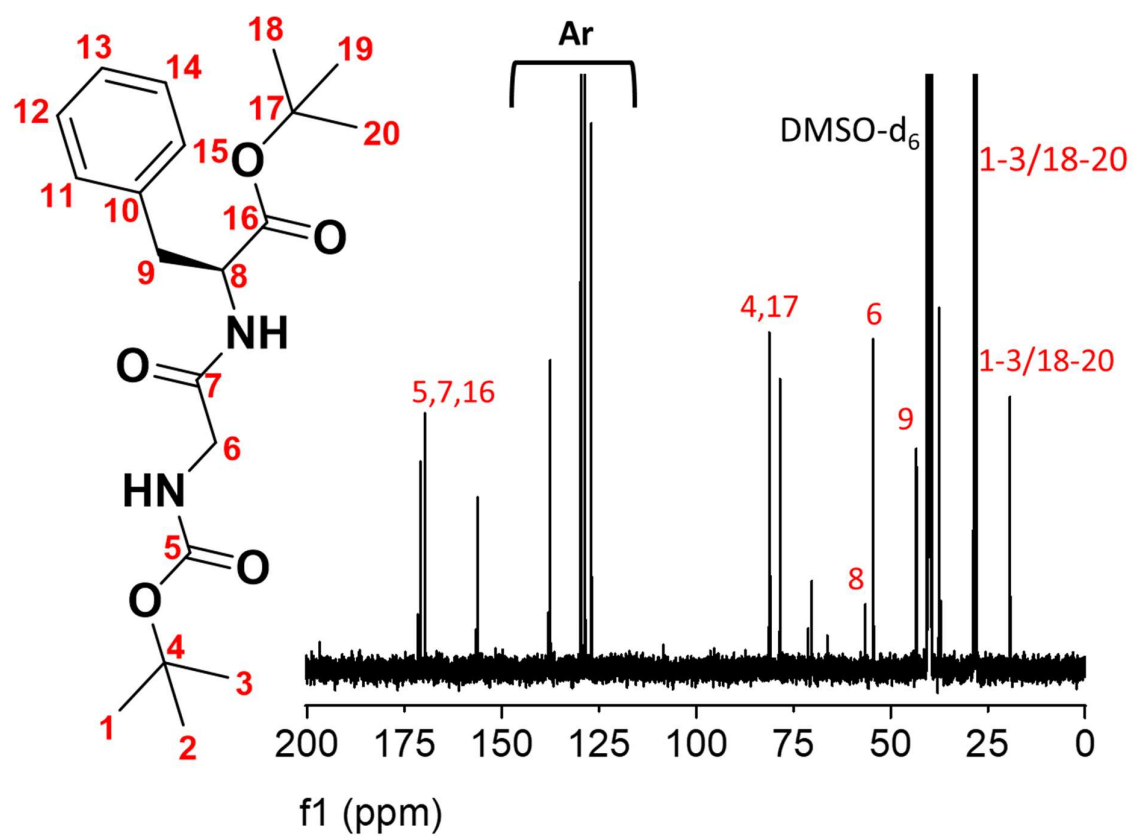


Figure A.2.33. Annotated ^{13}C NMR spectrum (100 MHz, DMSO-d_6) of GF-Protected.

Mass Spectrum SmartFormula Report

Analysis Info

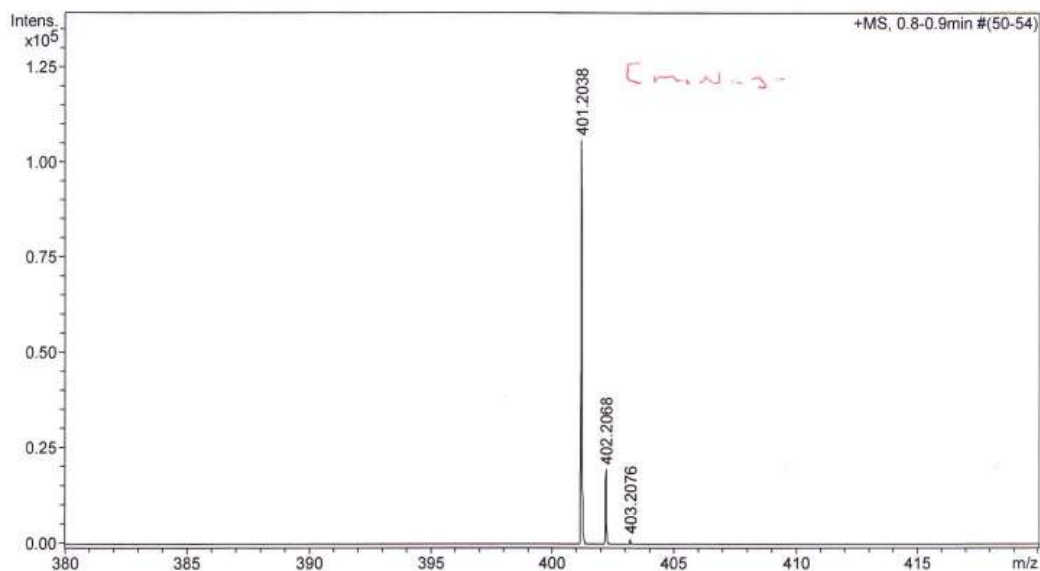
Analysis Name D:\Data\Mass Spectrometry Service\72426-000001.d
Method LM MS 50 to 1100.m
Sample Name Dietrich-BR GFP
Comment

Acquisition Date 4/15/2019 9:32:18 AM

Operator user
Instrument / Ser# micrOTOF-Q 74

Acquisition Parameter

Source Type ESI Ion Polarity Positive
Scan Begin 50 m/z
Scan End 1100 m/z



Formula	z	m/z	Meas. m/z	err [ppm]	err [mDa]
C ₂₀ H ₃₀ N ₂ O ₅	1+	401.2047	401.2038	2.3	0.9

Figure A.2.34. HRMS report of GF-Protected.

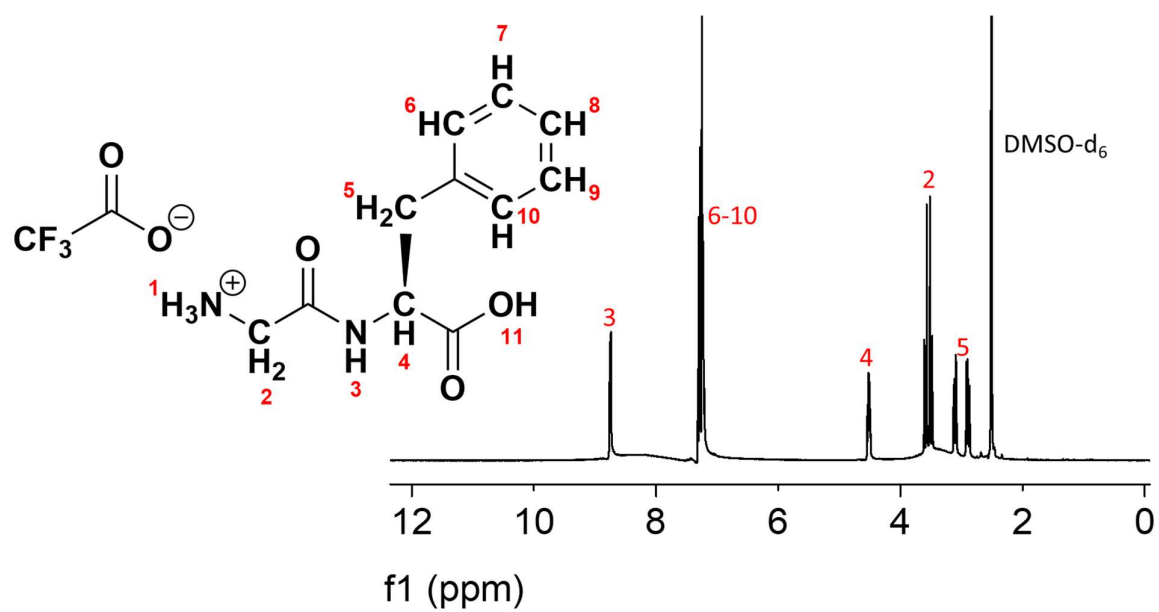


Figure A.2.35. Annotated ^1H NMR spectrum (400 MHz, DMSO-d_6) of GF-Deprotected.

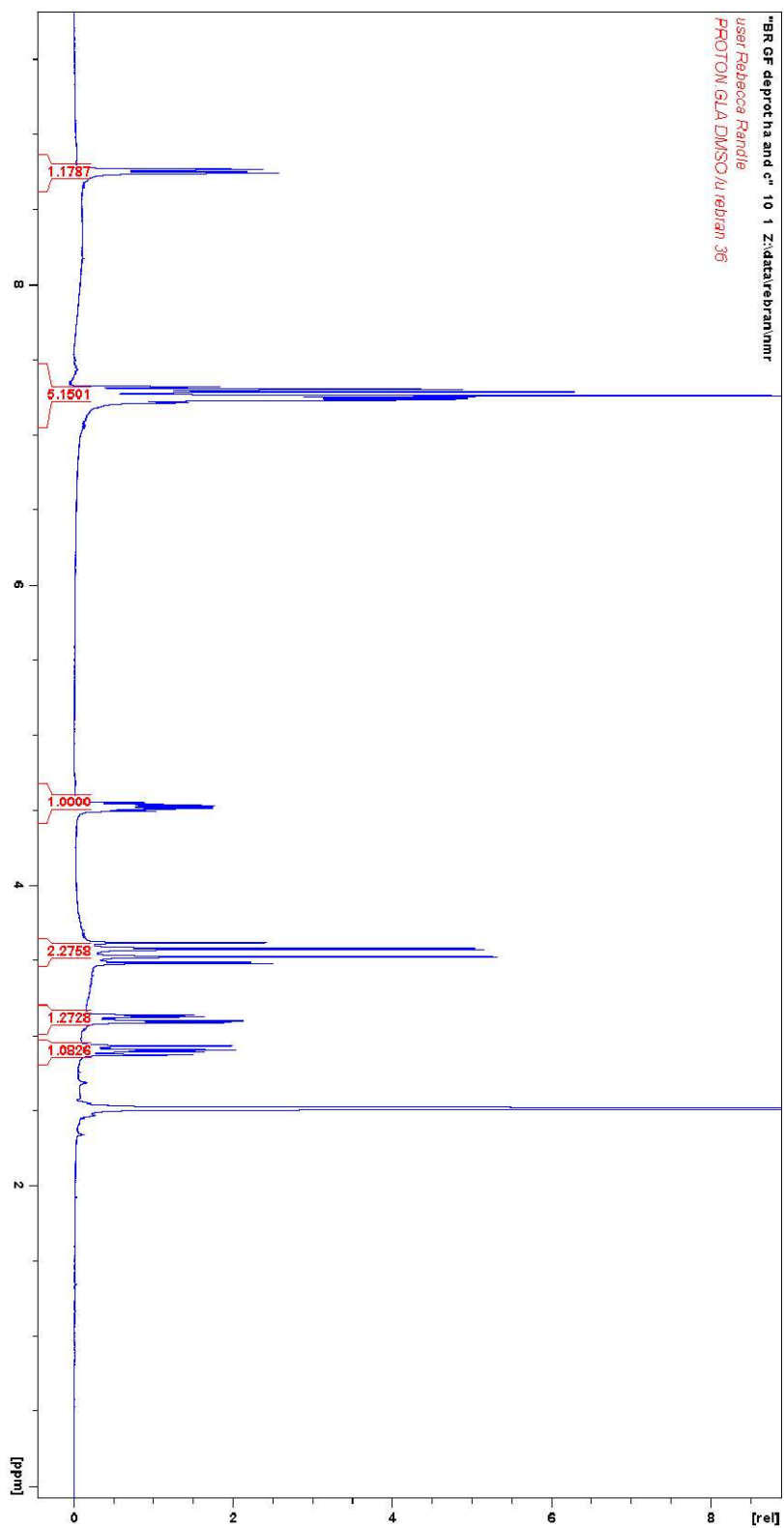


Figure A.2.36. Annotated ^1H NMR spectrum showing integration (400 MHz, DMSO-d_6) of GF-Deprotected.

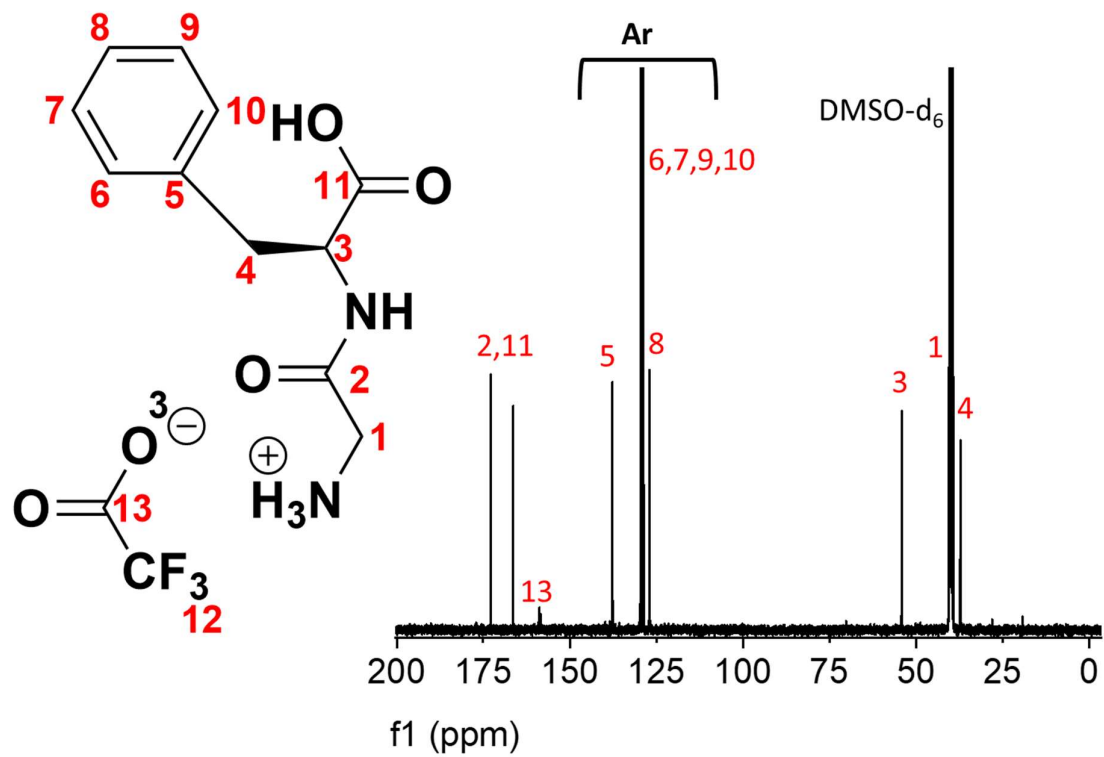
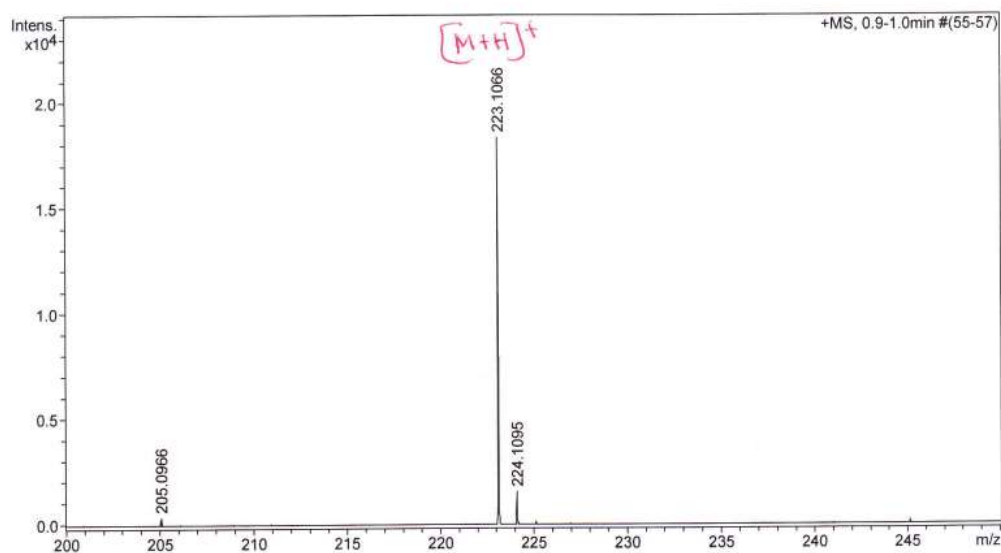


Figure A.2.37. Annotated ^{13}C NMR spectrum (100 MHz, DMSO- d_6) of GF-Deprotected. Environment 12 is too weak to be well defined.

Mass Spectrum SmartFormula Report

Analysis Info
Analysis Name D:\Data\Mass Spectrometry Service\72412-000001.d
Method SM MS 50 to 600.m
Sample Name Dietrich-BR GFDP
Comment
Acquisition Date 4/12/2019 8:48:51 AM
Operator user
Instrument / Ser# micrOTOF-Q 74

Acquisition Parameter
Source Type ESI Ion Polarity Positive
Scan Begin 50 m/z
Scan End 600 m/z



Formula	z	m/z	Meas. m/z	err [ppm]	err [mDa]
C 11 H 15 N 2 O 3	1+	223.1077	223.1066	5.0	1.1

Figure A.2.38. HRMS report of GF-Deprotected in ethanol.

Appendix

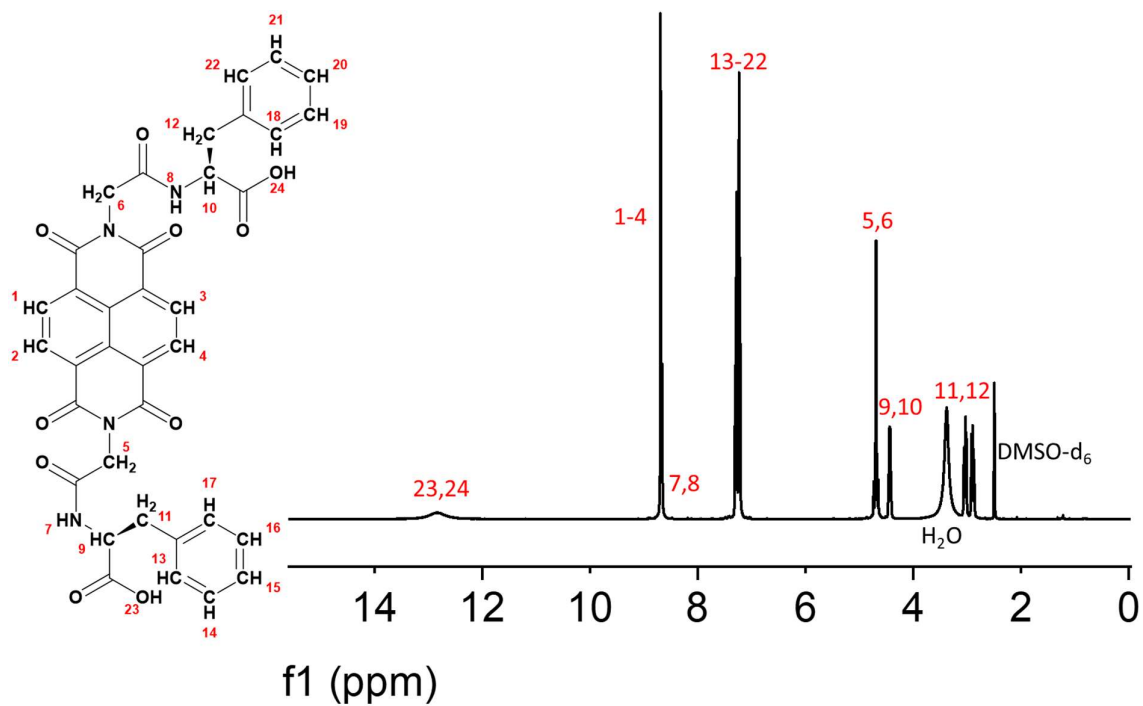


Figure A.2.39. Annotated ¹H NMR spectrum (400 MHz, DMSO-d₆) of NDI-GF.

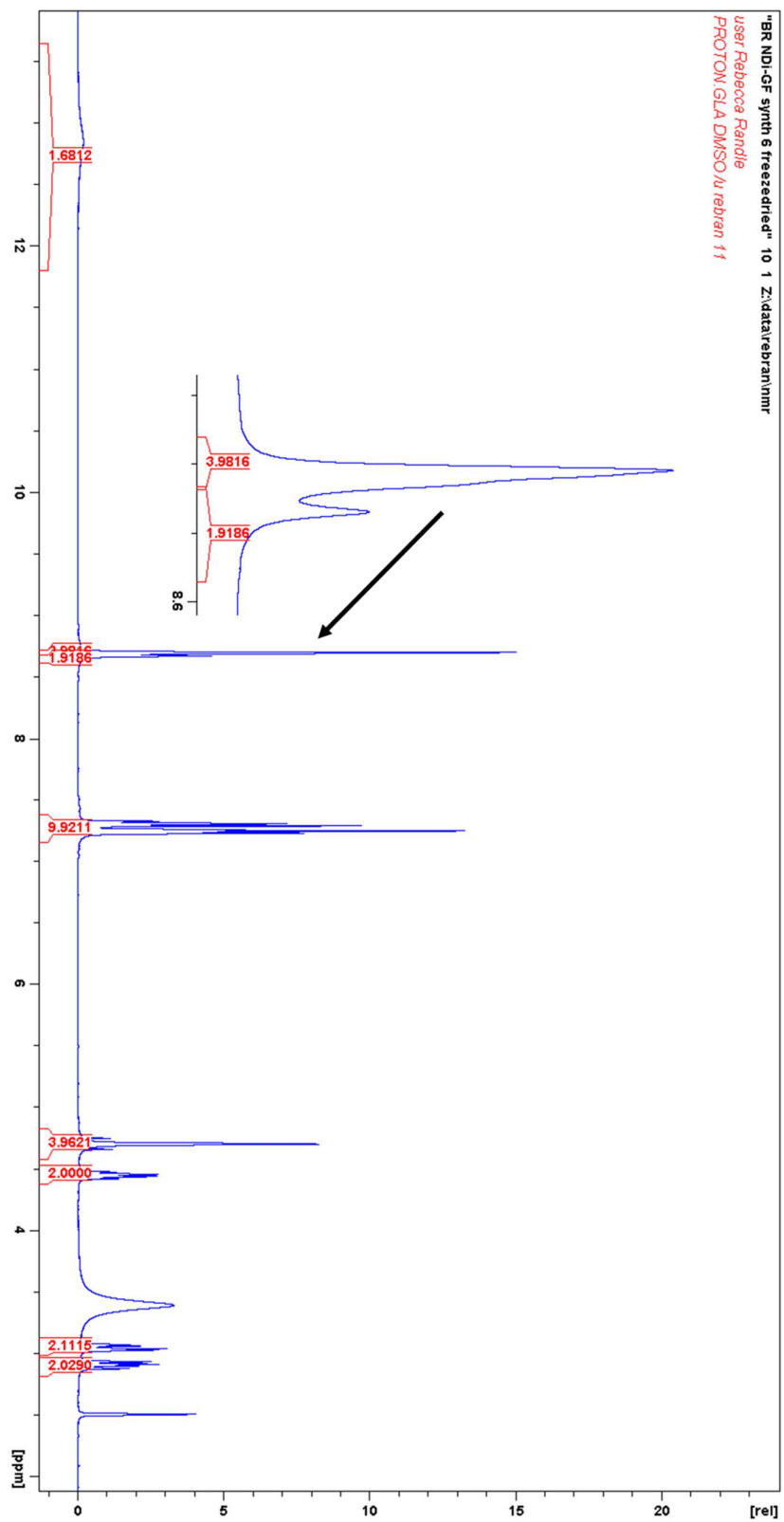
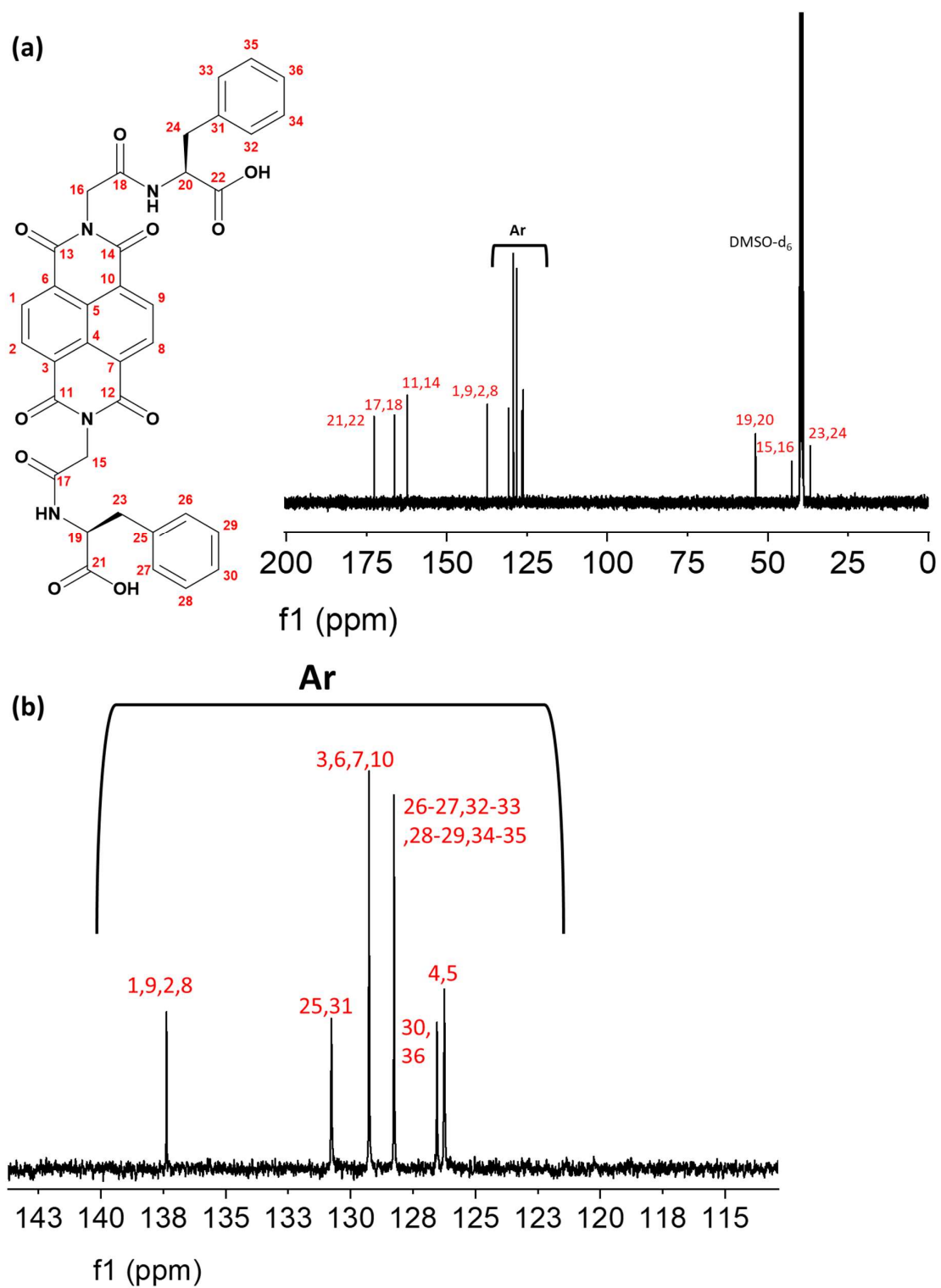


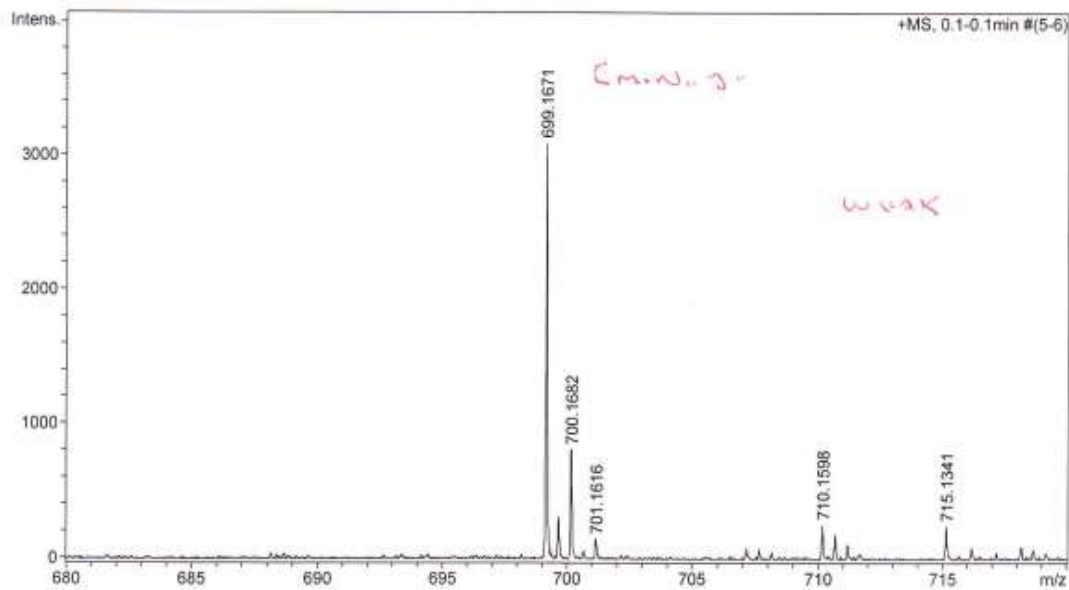
Figure A.2.40. ¹H NMR spectrum showing integration (400 MHz, DMSO-d₆) of **NDI-GF** with enhanced section of spectra shown around 8.6-8.7 ppm.



Mass Spectrum SmartFormula Report

Analysis Info
Analysis Name D:\Data\Mass Spectrometry Service\72532-000001.d
Method LM MS 50 to 2500.m
Sample Name Dietrich-BR008 GF
Comment
Acquisition Date 4/29/2019 4:35:27 PM
Operator user
Instrument / Ser# micrOTOF-Q 74

Acquisition Parameter
Source Type ESI Ion Polarity Positive
Scan Begin 50 m/z
Scan End 2500 m/z



Formula	z	m/z	Meas. m/z	err [ppm]	err [mDa]
C 36 H 28 N 4 Na O 10	1+	699.1698	699.1671	3.8	2.7

Figure A.2.42. HRMS report of NDI-GF in ethanol.

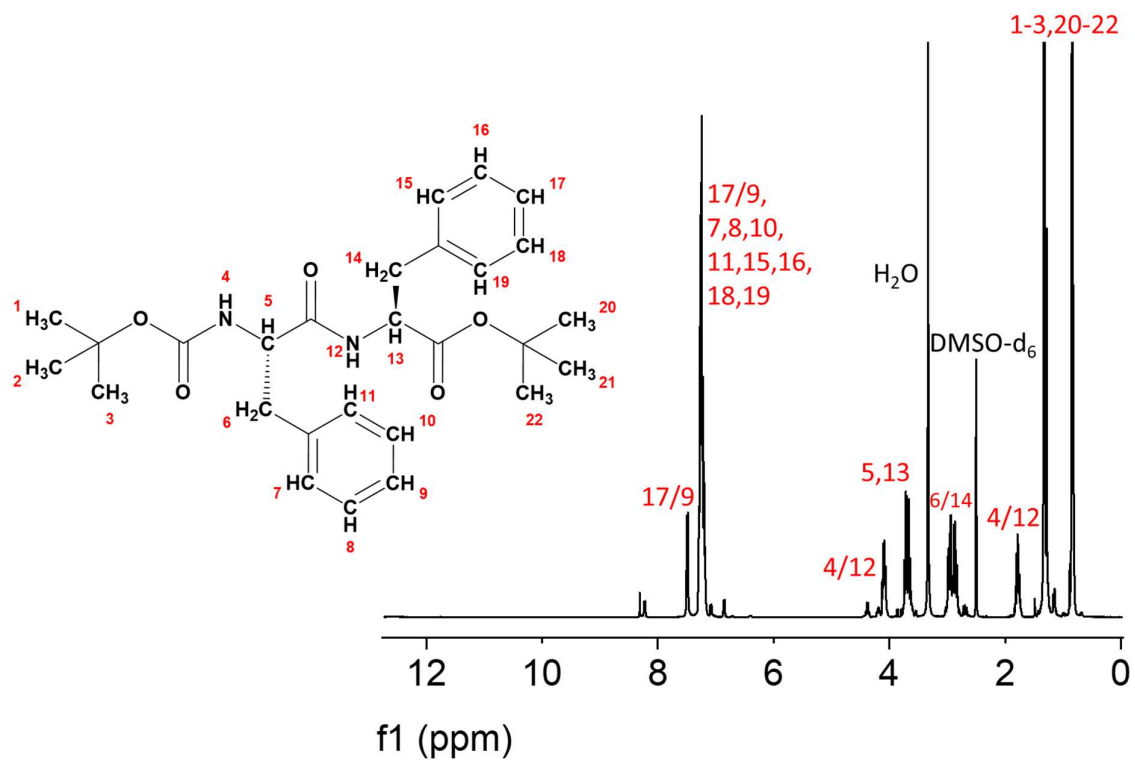


Figure A.2.43. Annotated ¹H NMR spectrum (400 MHz, DMSO-d₆) of FF-Protected.

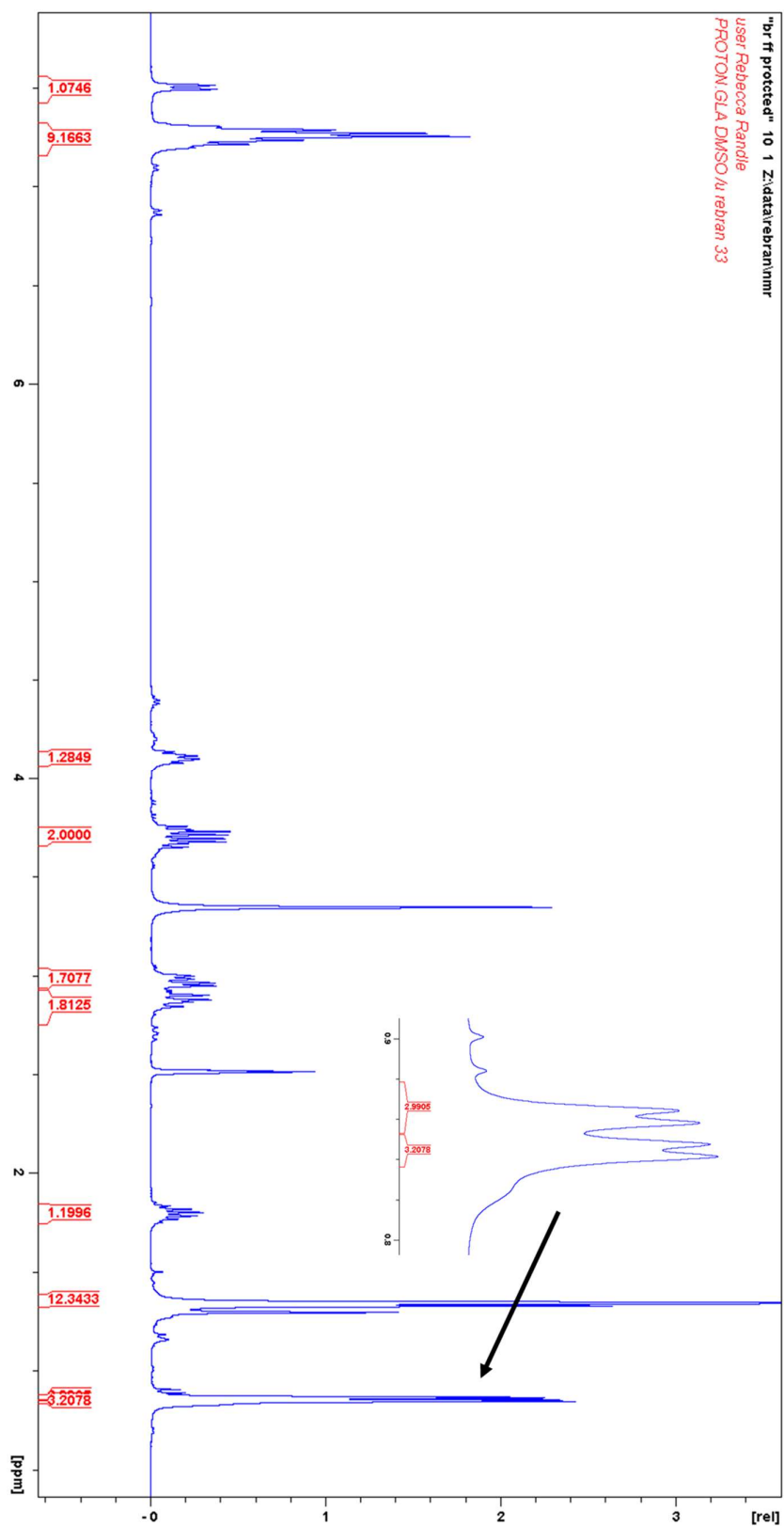


Figure A.2.44. ^1H NMR spectrum showing integration (400 MHz, DMSO-d_6) of FF-Protected with enhanced section of spectra shown around 0.85 ppm.

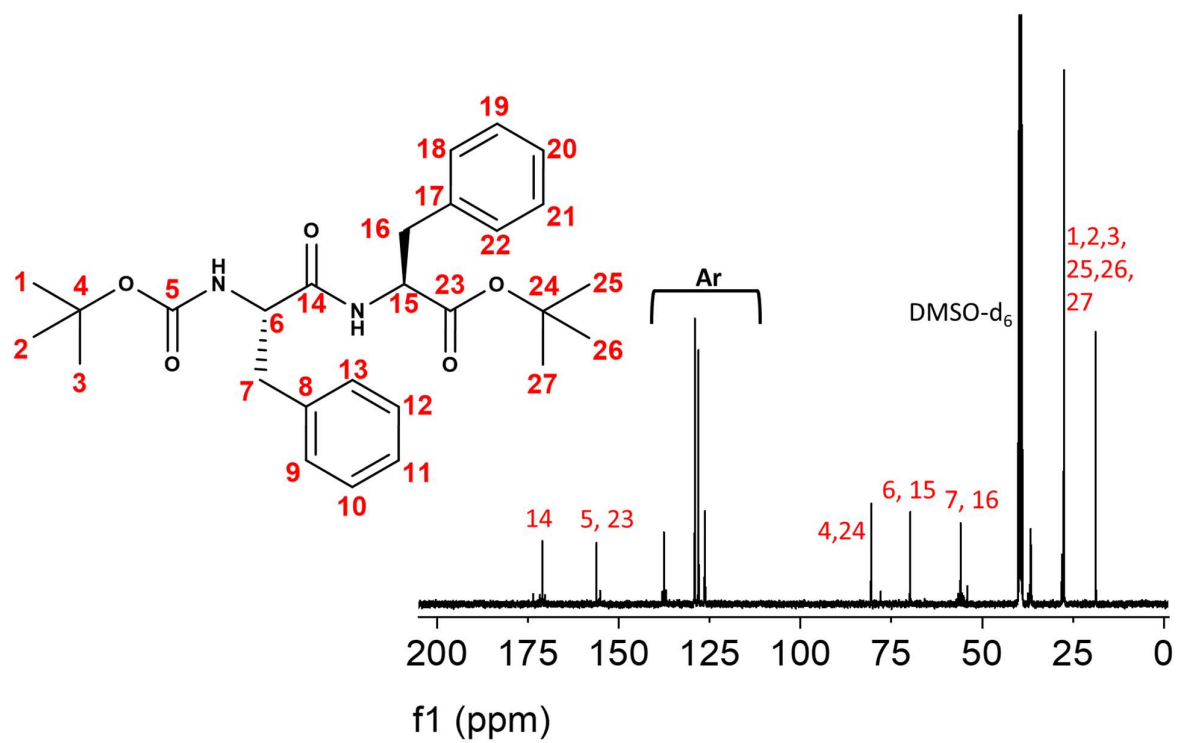


Figure A.2.45. Annotated ¹³C NMR spectrum (100 MHz, DMSO-d₆) of FF-Protected.

Appendix

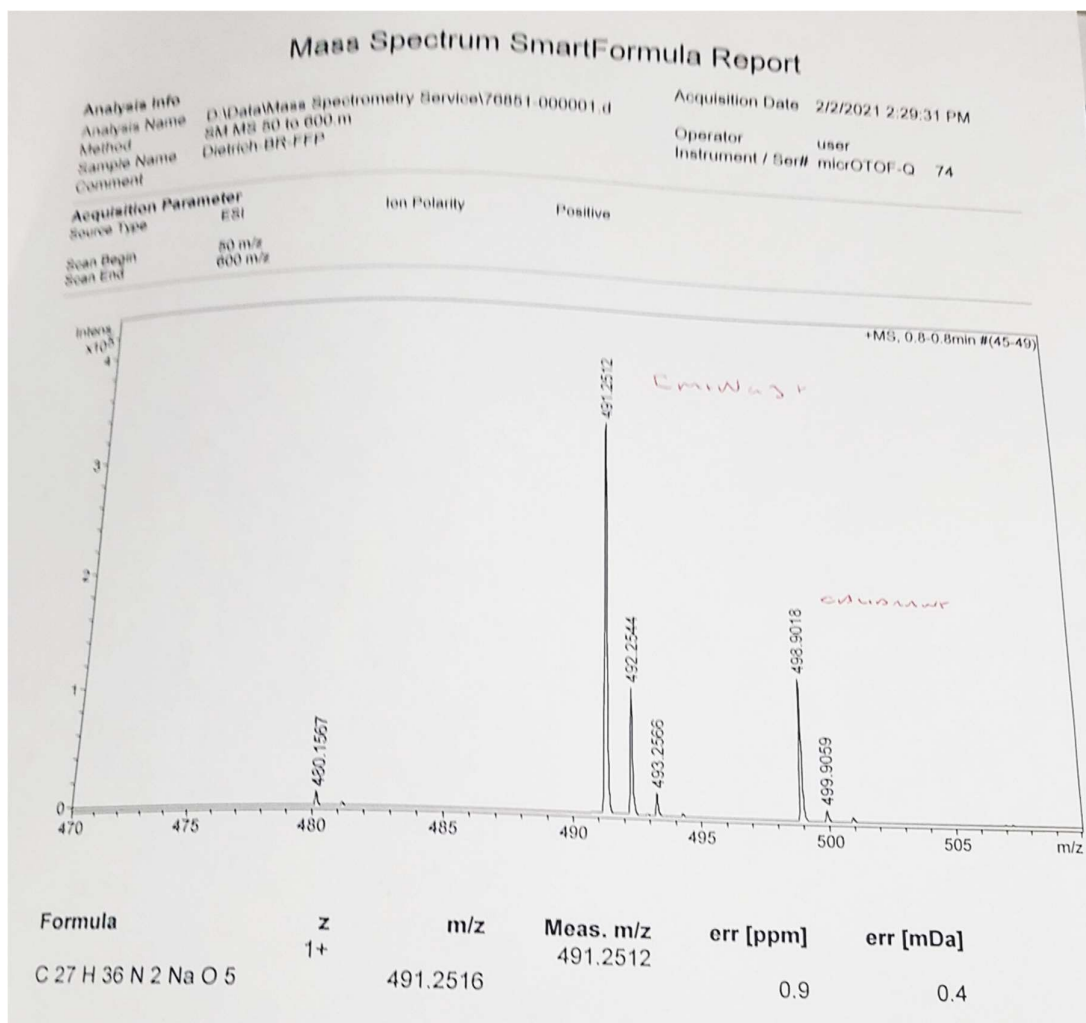


Figure A.2.46. HRSM report of FF-Protected in ethanol.

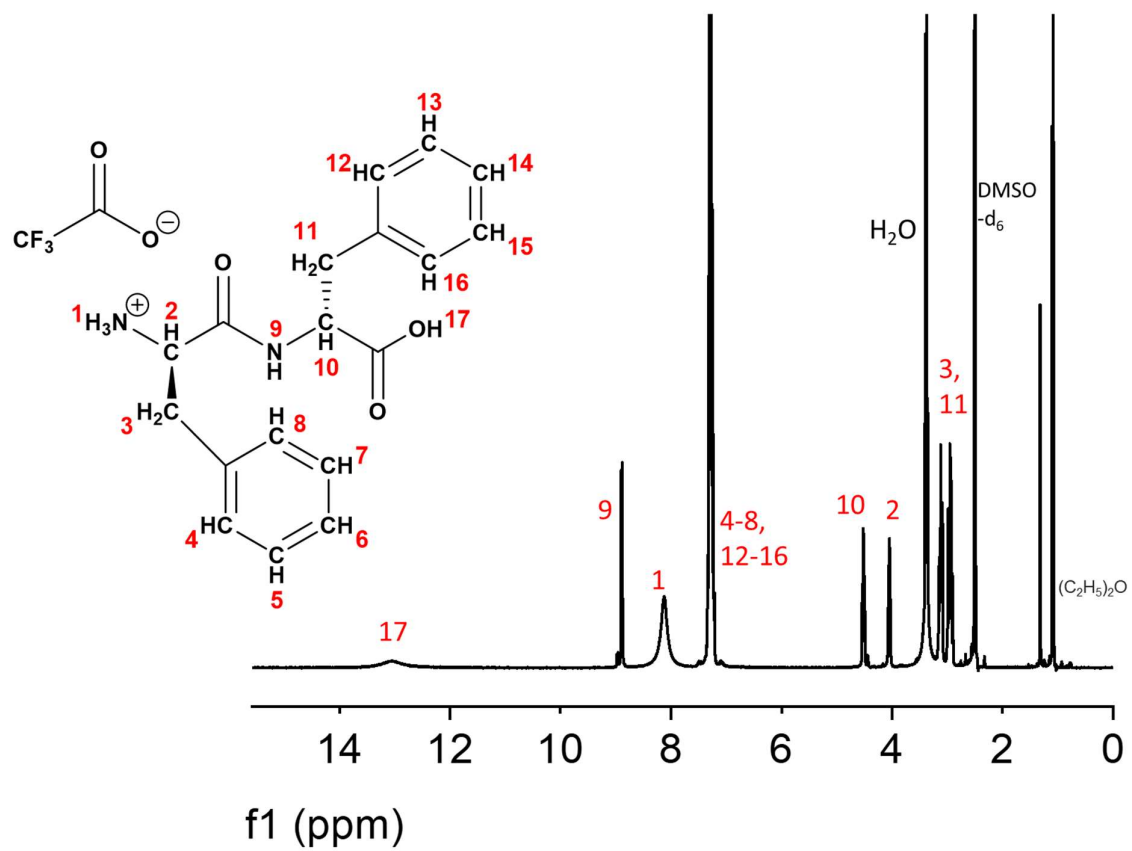


Figure A.2.47. Annotated ^1H NMR spectrum (400 MHz, DMSO-d₆) of FF-Deprotected.

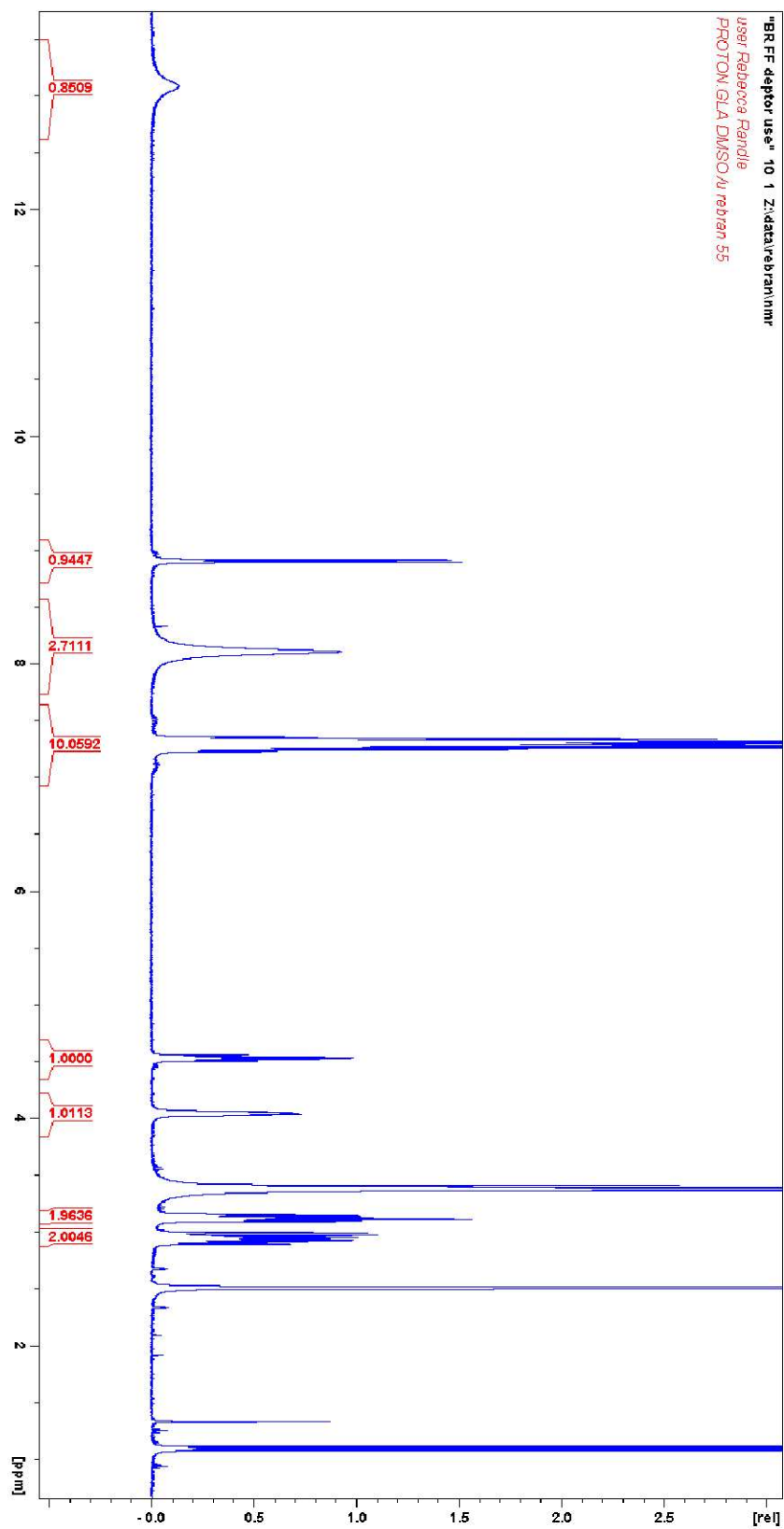


Figure A.2.48. ^1H NMR spectrum showing integration (400 MHz, DMSO-d_6) of FF-Deprotected.

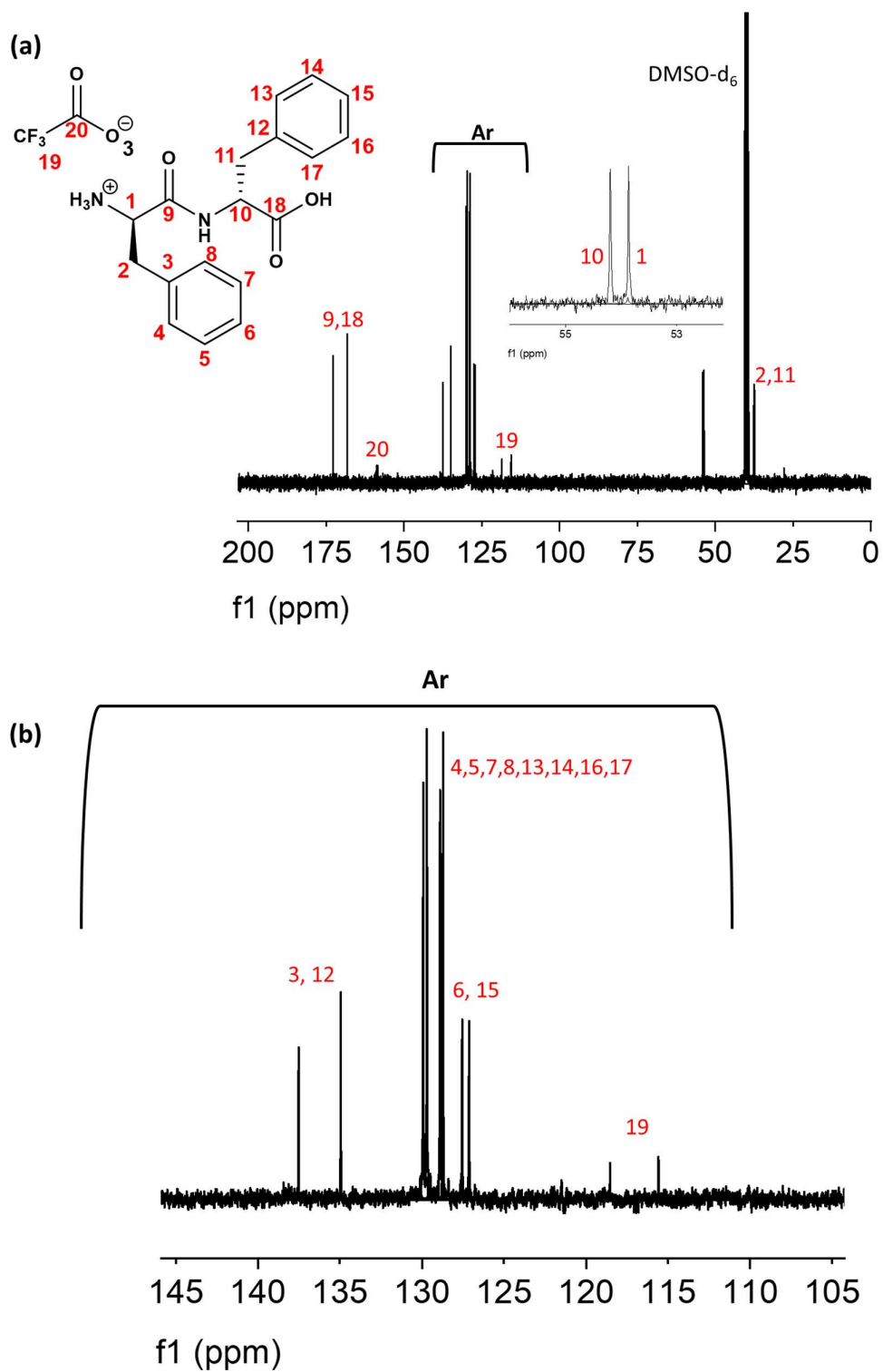


Figure A.2.49. Annotated ¹³C NMR spectrum (100 MHz, DMSO-d₆) of FF-Deprotected (a) full spectra with expanded 55-53 ppm (b) enhanced section marked Ar showing the aromatic carbon environments.

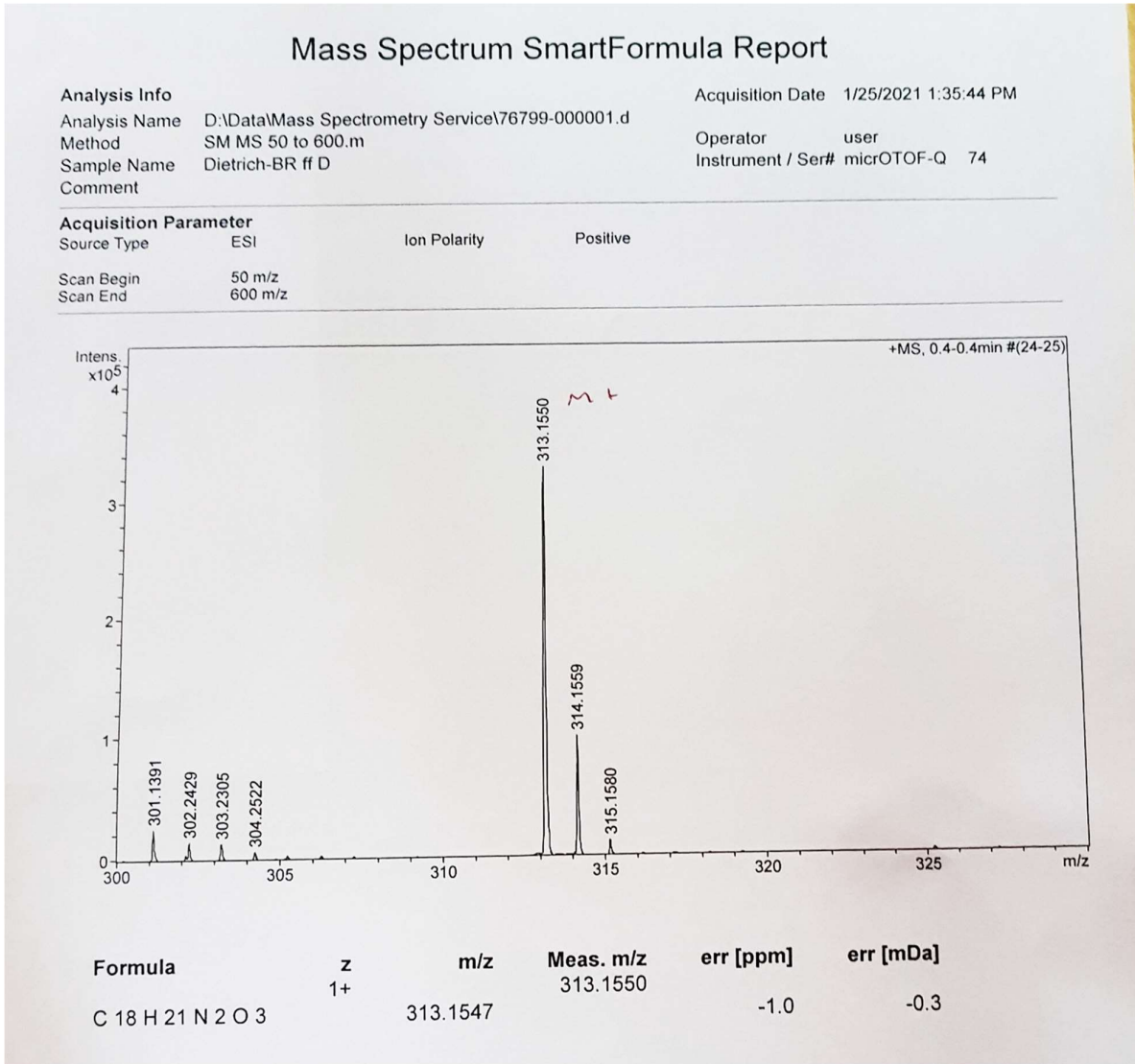


Figure A.2.50. HRSM report of FF-Deprotected in ethanol.

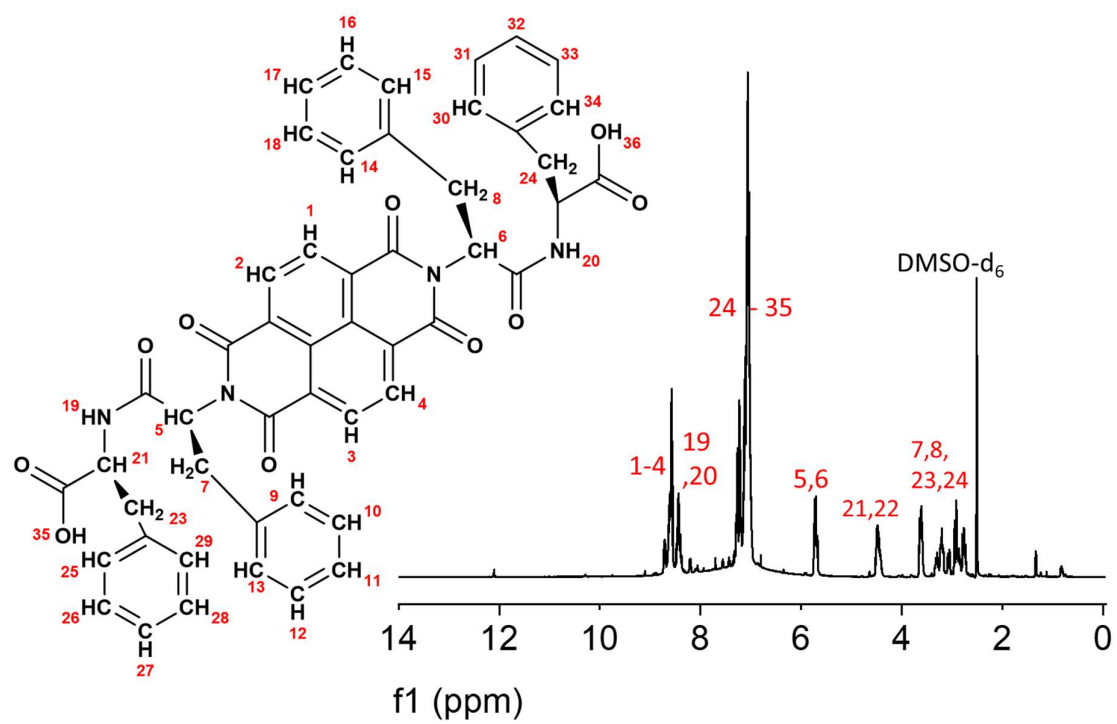


Figure A.2.51. Annotated ^1H NMR spectrum (400 MHz, DMSO- d_6 + TFA) of NDI-FF.

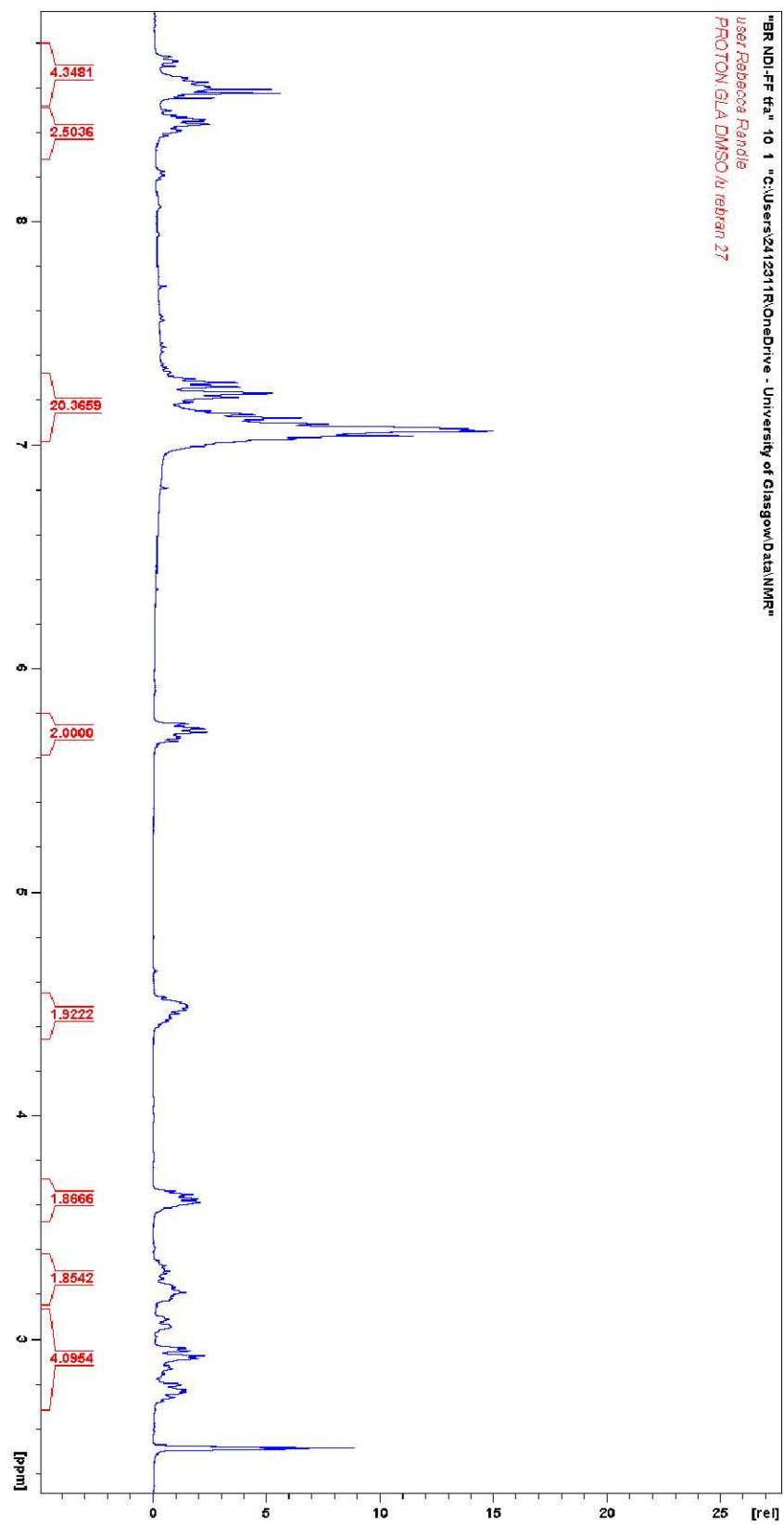


Figure A.2.52. ^1H NMR spectrum showing integration (400 MHz, DMSO-d_6) of NDI-FF.

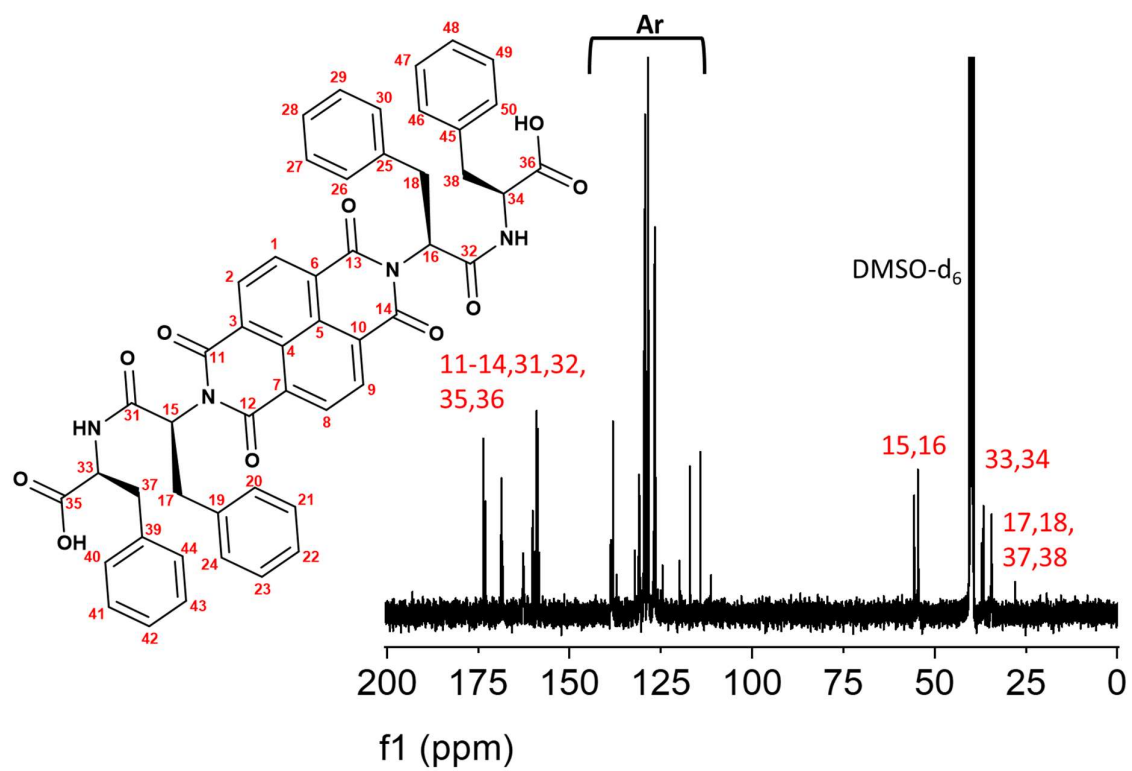


Figure A.2.53. Annotated ¹³C NMR spectrum (100 MHz, DMSO-d₆ + TFA) of NDI-FF.

Appendix

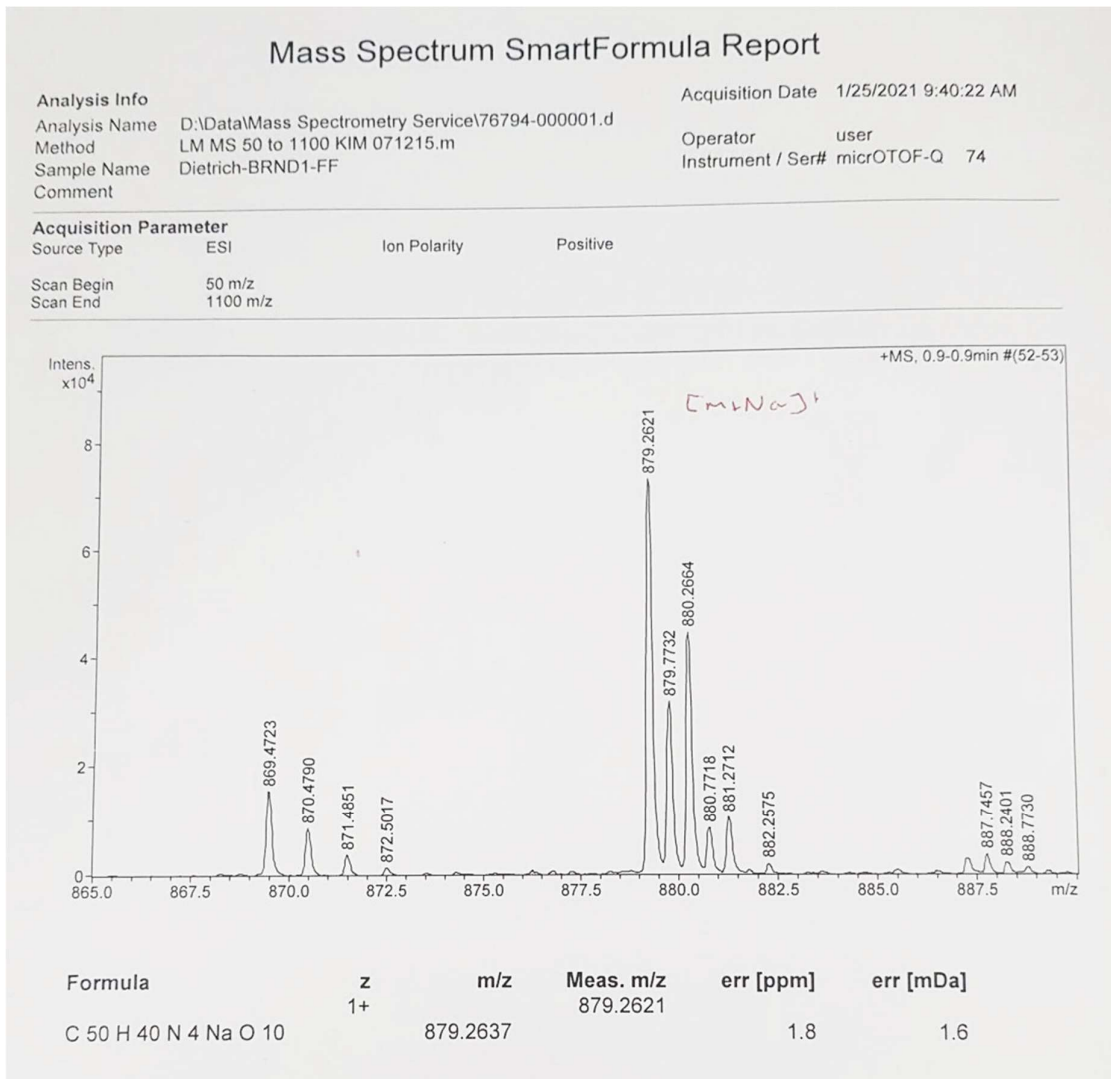


Figure A.2.54. HRMS report of NDI-FF in ethanol.

A.3 Chapter 3 appendices

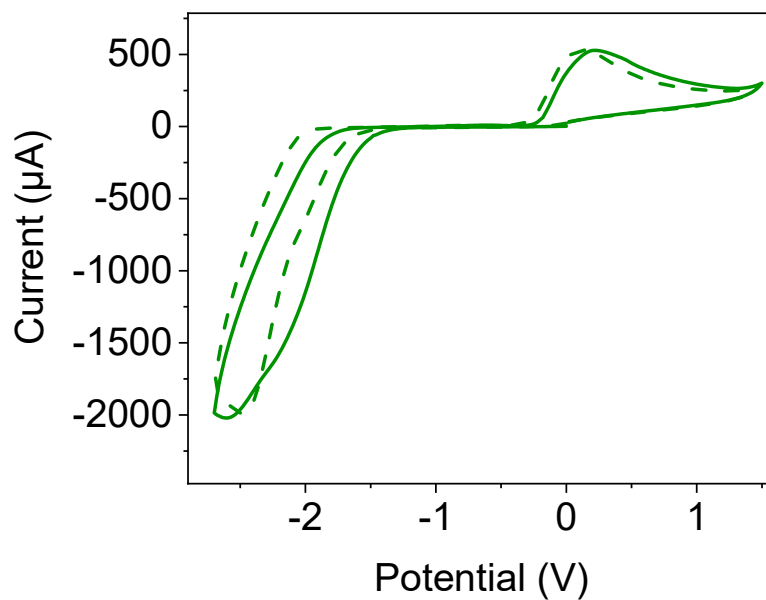


Figure A.3.1. Cyclic voltammograms collected from buffered (dashed line) and unbuffered (solid line) 10 mg/mL solutions of **NDI-I** adjusted to pH 9 and pH 9 respectively. Voltammograms measured using a 1x 1 FTO glass window cell. The scan rate of the cyclic voltammograms was 0.1 V/s.

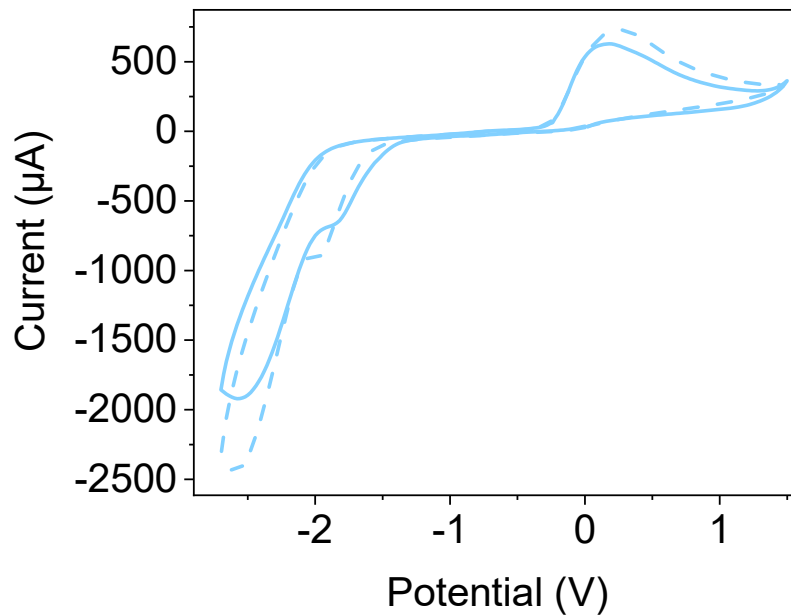


Figure A.3.2. Cyclic voltammograms collected from buffered (dashed line) and unbuffered (solid line) 10 mg/mL solutions of **NDI-V** adjusted to pH 9 and pH 9 respectively. Voltammograms measured using a 1x 1 FTO glass window cell. The scan rate of the cyclic voltammograms was 0.1 V/s.

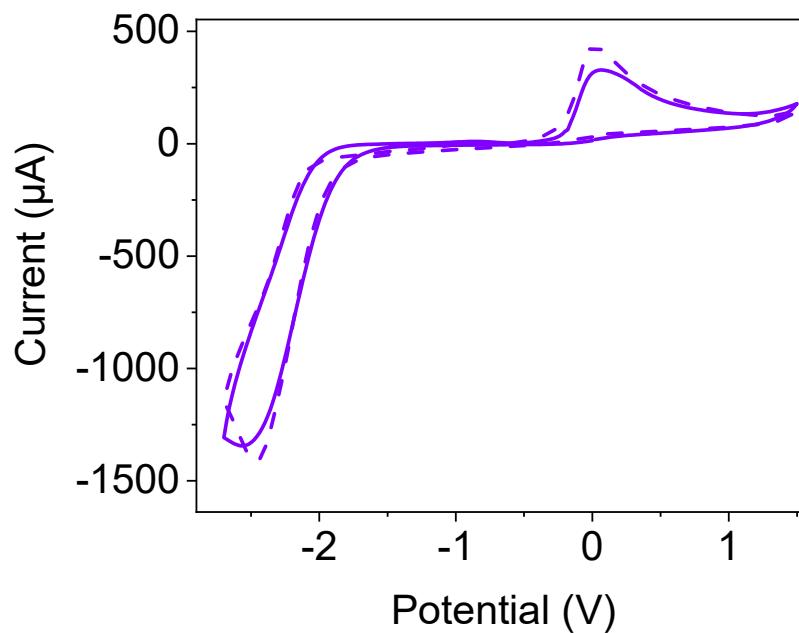


Figure A.3.3. Cyclic voltammograms collected from buffered (dashed line) and unbuffered (solid line) 10 mg/mL solutions of **NDI-F** adjusted to pH 6. Voltammograms measured using a 1x 1 FTO glass window cell. The scan rate of the cyclic voltammograms was 0.1 V/s.

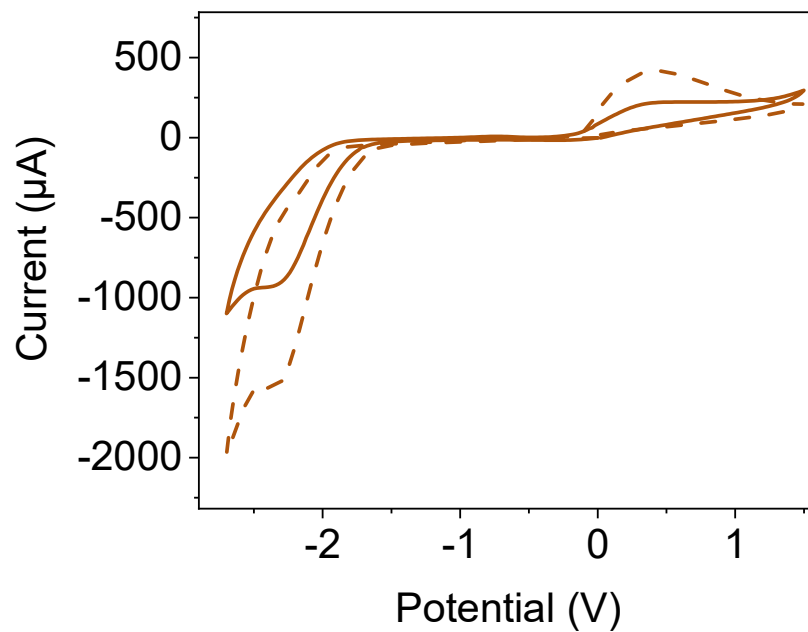


Figure A.3.4. Cyclic voltammograms collected from buffered (dashed line) and unbuffered (solid line) 10 mg/mL solutions of **NDI-GF** adjusted to pH 6. Voltammograms measured using a 1x 1 FTO glass window cell. The scan rate of the cyclic voltammograms was 0.1 V/s.

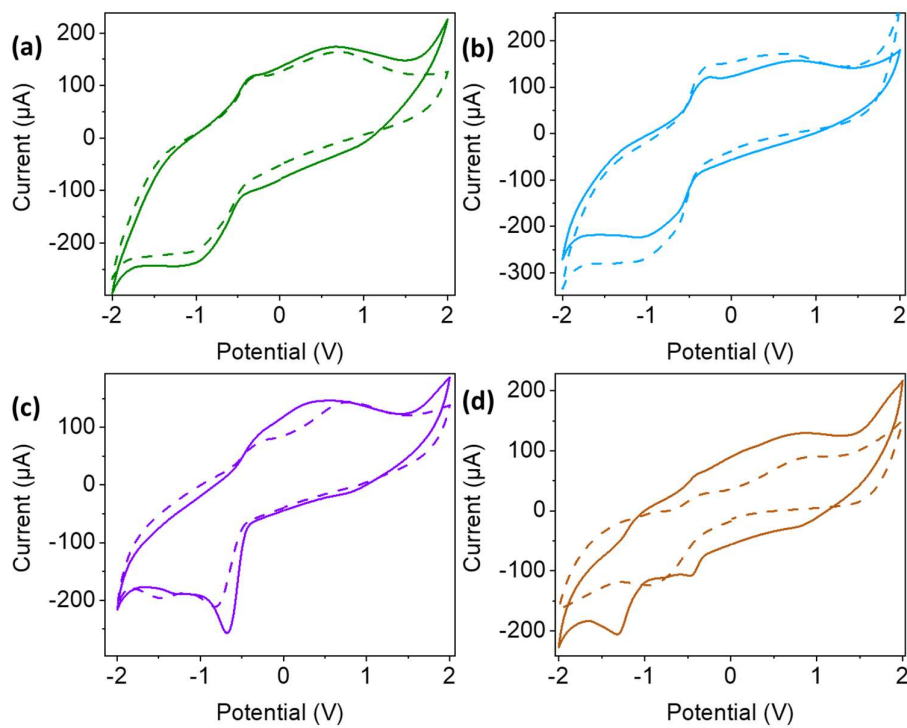


Figure A.3.5. Cyclic voltammogram collected from buffered (dashed line) and buffered (solid line) 10 mg/mL solution of (a) **NDI-I**, (b) **NDI-V** pH 9, (c) **NDI-F**, (d) **NDI-GF** pH 6. Voltammograms measured using a referenced classy carbon set up (vs Ag/AgCl). The scan rate of the cyclic voltammograms was 0.2 V/s.

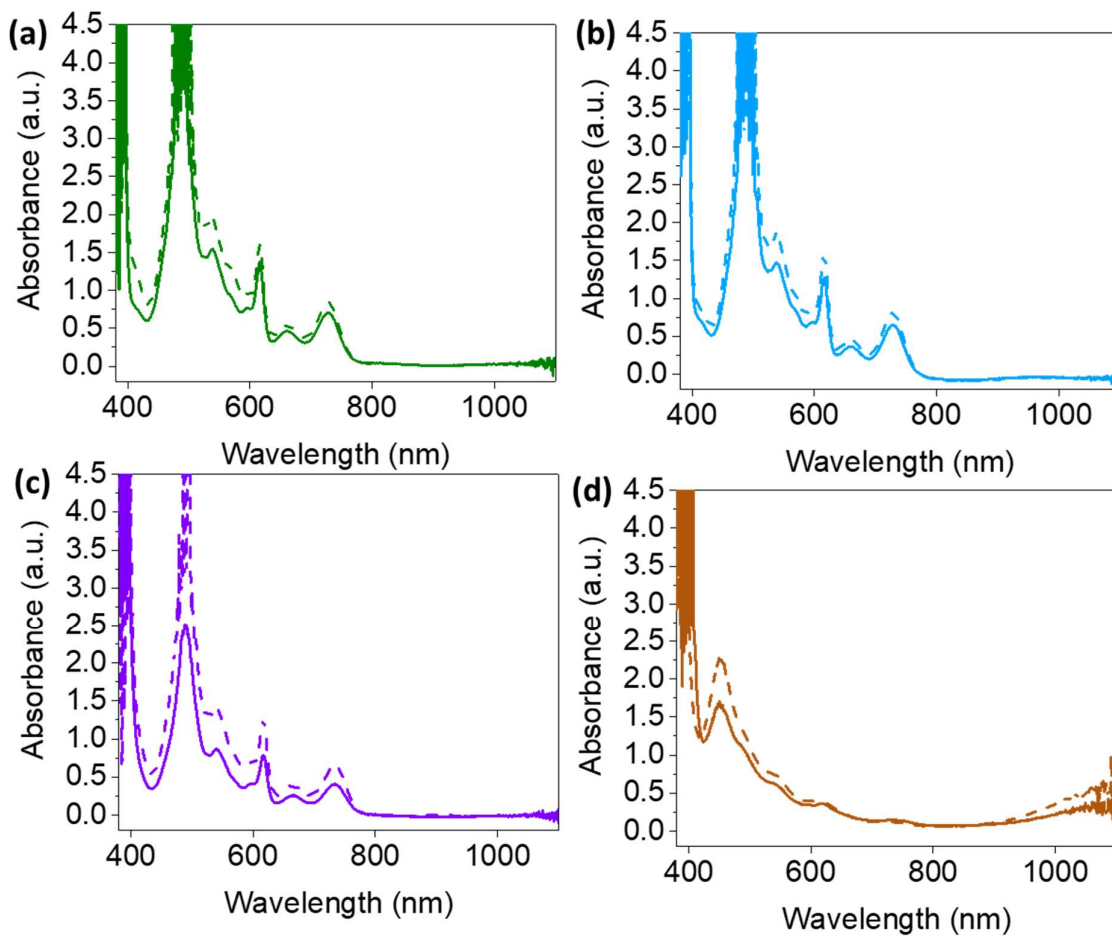


Figure A.3.6. Absorbance spectra collected from buffered (dashed line) and buffered (solid line) 10 mg/mL solution of (a) **NDI-I**, (b) **NDI-V** pH 9, (c) **NDI-F**, (d) **NDI-GF** pH 6 after a 10 second application of -2.5 V.

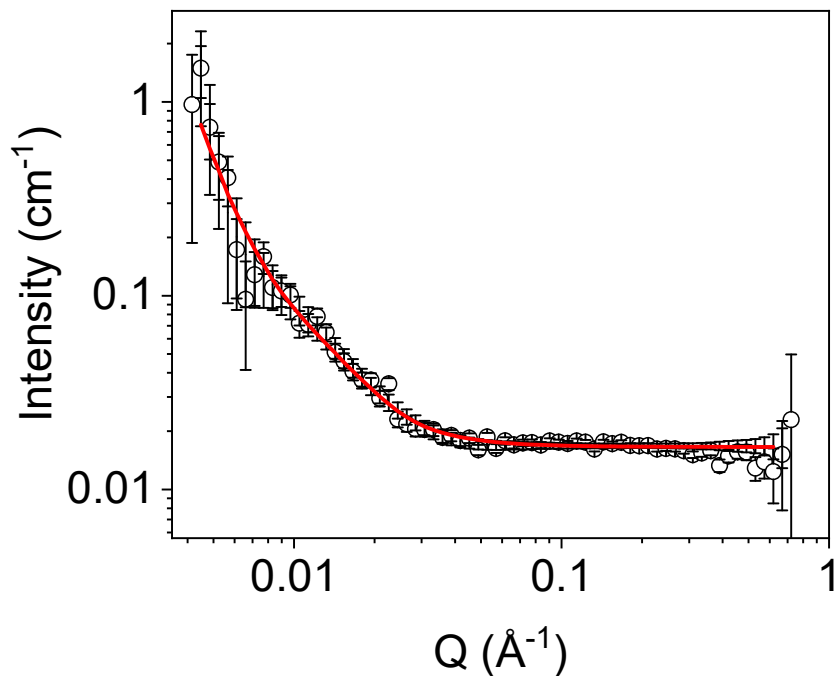


Figure A.3.7. Small angle neutron scattering data for a neutral solution of 10 mg/mL **NDI-I** at pH 12 (open circles) fitted to a flexible elliptical cylinder model combined with power law (red). Fit parameters can be found in Table A.3.1.

Table A.3.1. Parameters of SANS model fit seen in Figure A.3.7.

NDI-I pD 12	Flexible elliptical cylinder combined with power law	
	Value	Error
Scale a	1.57E-06	6.51E-08
Scale b	7.58E-22	1.67E-22
Background (cm ⁻¹)	0.016576	1.00E-04
Length (Å)	1.76E+03	3.87E+02
Kuhn length (Å)	84.985	6.5373
Radius (Å)	4.8951	0.15519
Axis ratio	25.898	0.819
Power	8.8107	3.92E-02
Range (Å ⁻¹)	0.00449-0.61892	
Chi ²	1.3882	

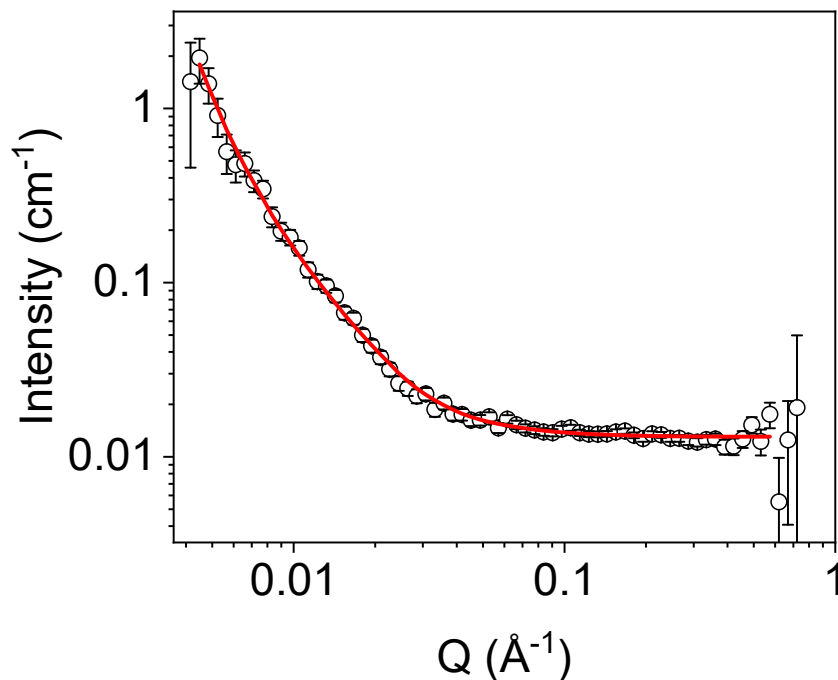


Figure A.3.8. Small angle neutron scattering data for a neutral solution of 10 mg/mL NDI-V at pD 12 (open circles) fitted to a flexible elliptical cylinder model combined with power law (red). Fit parameters can be found in Table A.3.2.

Table A.3.2. Parameters of SANS model fit seen in Figure A.3.8.

NDI-V pD 12	Flexible elliptical cylinder combined with power law	
	Value	Error
Scale a	7.05E-06	2.28E-07
Scale b	6.01E-10	5.76E-11
Background (cm ⁻¹)	0.013081	1.14E-04
Length (Å)	7.49E+09	4.92E+14
Kuhn length (Å)	120.89	6.074
Radius (Å)	5.4376	0.11327
Axis ratio	14.802	0.30733
Power	3.8965	1.94E-02
Range (Å ⁻¹)	0.00449-0.57308	
Chi ²	0.67995	

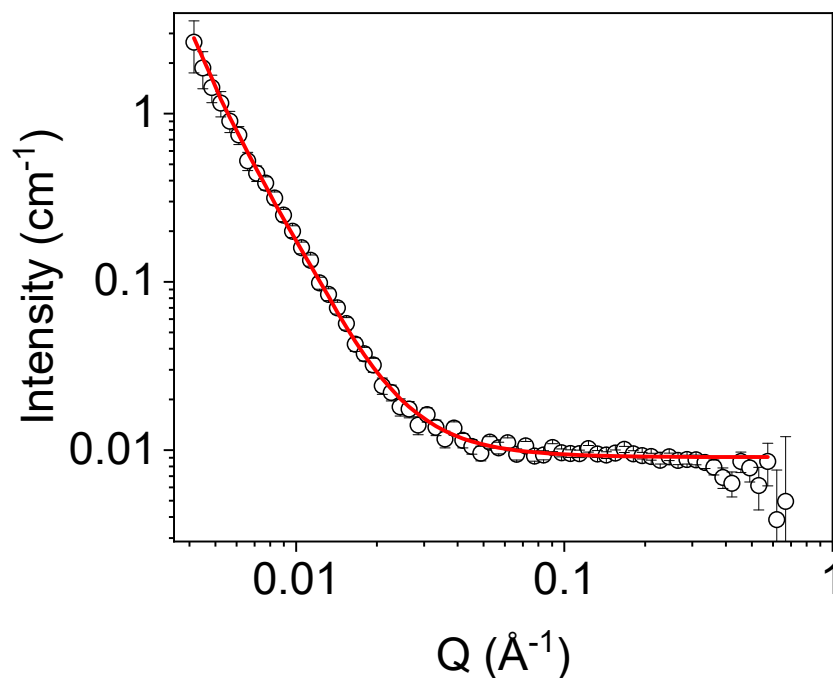


Figure A.3.9. Small angle neutron scattering data for a neutral solution of 10 mg/mL **NDI-F** at pD 12 (open circles) fitted to a flexible elliptical cylinder model combined with power law (red). Fit parameters can be found in Table A.3.3.

Table A.3.3. Parameters of SANS model fit seen in Figure A.3.9.

NDI-F pD 12	Flexible elliptical cylinder combined with power law	
	Value	Error
Scale a	1.14E-06	5.71E-08
Scale b	6.00E-09	2.24E-10
Background (cm ⁻¹)	0.009083	9.68E-05
Length (Å)	9.78E+02	1.97E+02
Kuhn length (Å)	146.31	18.9
Radius (Å)	5.00	0.255
Axis ratio	41.5	2.11
Power	3.5848	7.74E-03
Range (Å ⁻¹)	0.00416-0.57308	
Chi ²	0.83775	

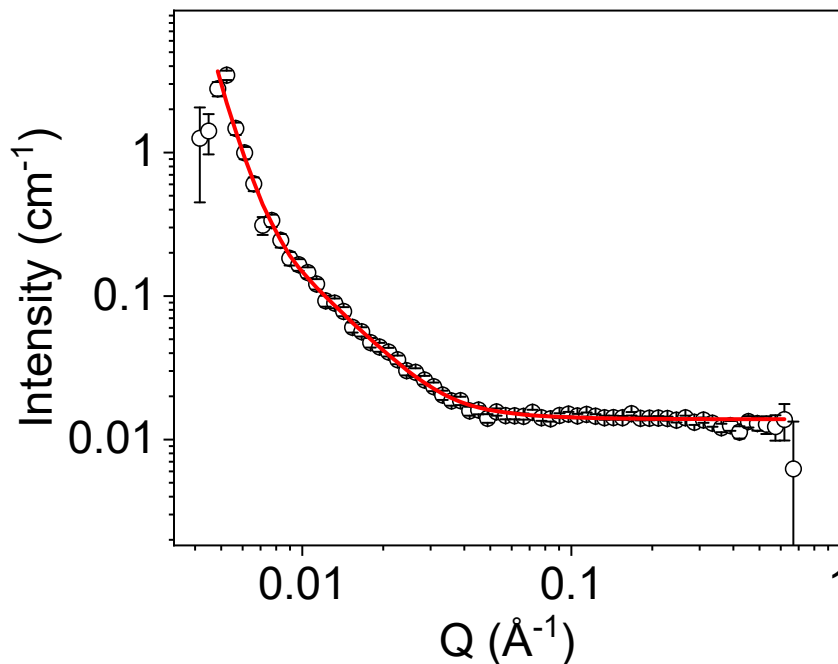


Figure A.3.10. Small angle neutron scattering data for a neutral solution of 10 mg/mL **NDI-GF** at pD 12 (open circles) fitted to a flexible elliptical cylinder model combined with power law (red). Fit parameters can be found in Table A.3.4.

Table A.3.4. Parameters of SANS model fit seen in Figure A.3.10.

NDI-GF pD 12	Flexible elliptical cylinder combined with power law	
	Value	Error
Scale a	2.40E-06	7.95E-08
Scale b	5.11E-11	2.31E-12
Background (cm ⁻¹)	0.014015	9.90E-05
Length (Å)	1.73E+03	2.26E+02
Kuhn length (Å)	46.787	2.58
Radius (Å)	4.9323	0.011069
Axis ratio	18.10	0.040535
Power	4.5189	8.88E-03
Range (Å ⁻¹)	0.00485-0.61892	
Chi ²	2.4217	

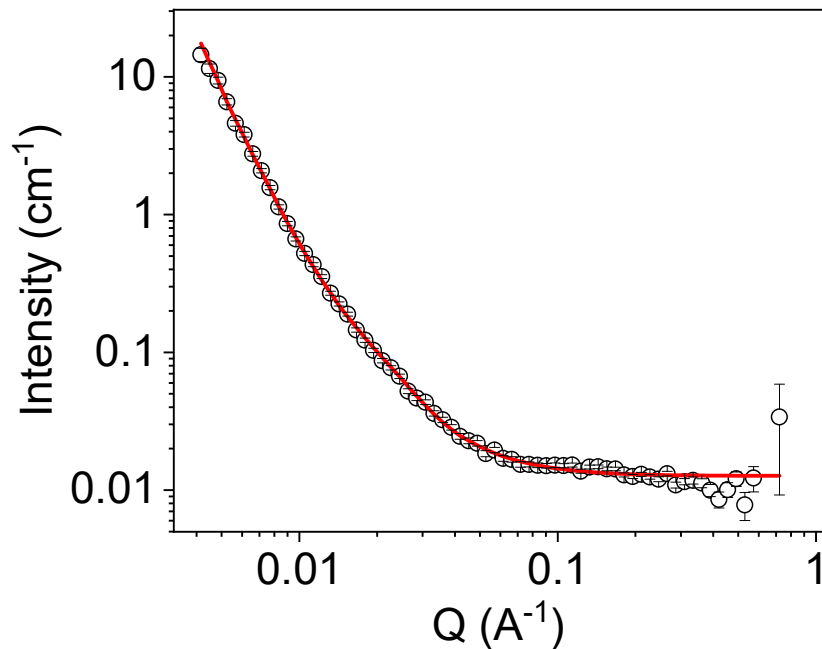


Figure A.3.11. Small angle neutron scattering data for a neutral solution of 10 mg/mL NDI-FF at pD 12 (open circles) fitted to a flexible elliptical cylinder model combined with power law (red). The fit parameters can be found in Table A.3.5.

Table A.3.5. Parameters of SANS model fit in Figure A.3.11.

NDI-FF pD 12	Flexible elliptical cylinder combined with power law	
	Value	Error
Scale a	1.26E-05	2.17E-07
Scale b	7.69E-09	8.42E-11
Background (cm ⁻¹)	0.012715	1.01E-04
Length (Å)	257.08	9.3823
Kuhn length (Å)	120.99	1.22
Radius (Å)	5.4954	8.83E-02
Axis ratio	19.818	3.15E-01
Power	3.8761	2.26E-03
Range (Å ⁻¹)	0.00416-0.72191	
Chi ²	2.1666	

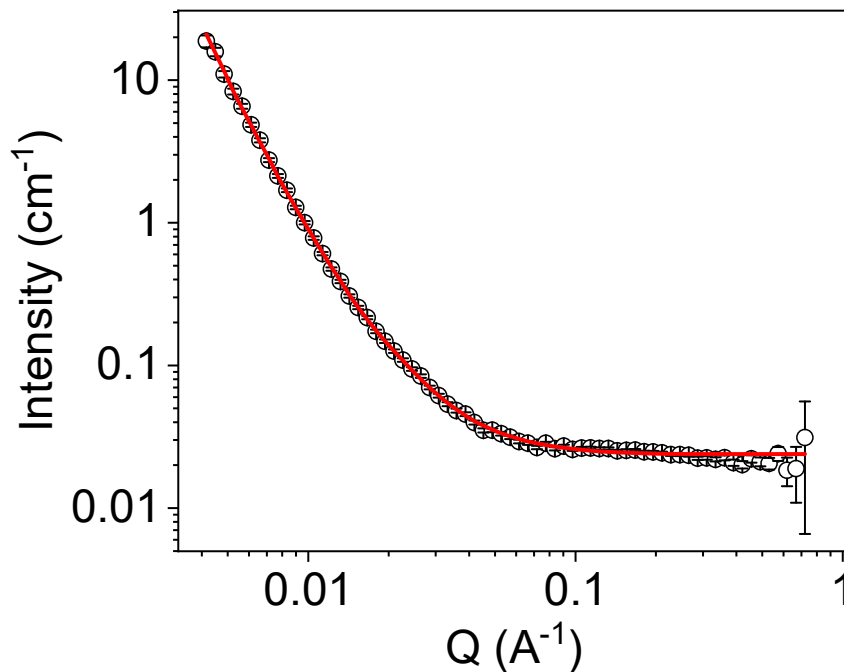


Figure A.3.12. Small angle neutron scattering data for a neutral buffered solution of 10 mg/mL NDI-FF at pH 7 (open circles) fitted to a flexible elliptical cylinder model combined with power law (red). The fit parameters can be found in Table A.3.5.

Table A.3.6. Parameters of SANS model fit in Figure A.3.12.

NDI-FF Neutral	Flexible elliptical cylinder combined with power law	
	Value	Error
Scale a	7.93E-06	1.25E-07
Scale b	2.77E-08	2.49E-10
Background (cm ⁻¹)	0.023895	1.07E-04
Length (Å)	205.18	5.9816
Kuhn length (Å)	133.99	9.65
Radius (Å)	10.036	1.78E-02
Ratio Axis	24.877	4.15E-01
Power	3.679	1.89E-03
Range (Å ⁻¹)	0.00416-0.72191	
Chi ²	1.8468	

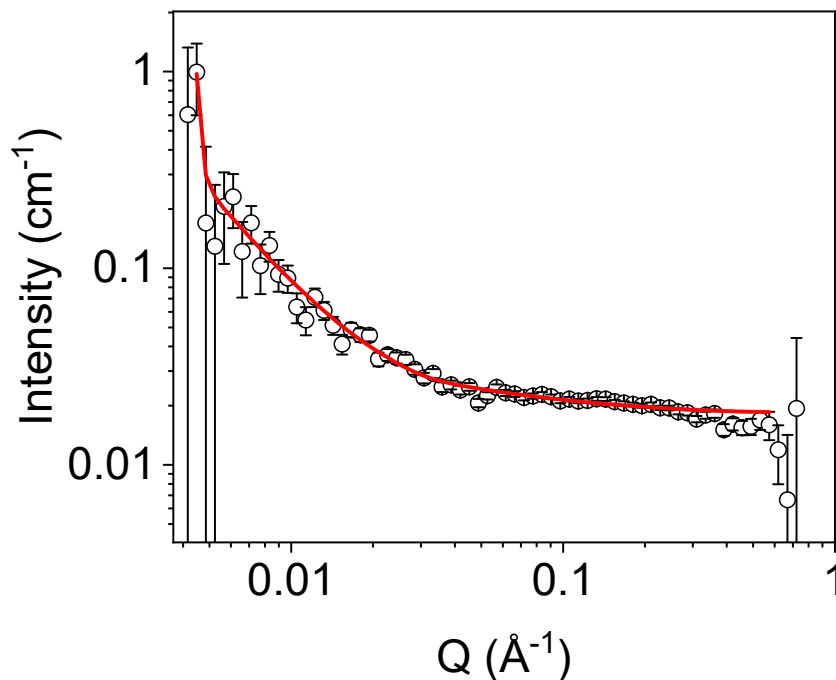


Figure A.3.13. Small angle neutron scattering data for a neutral buffered solution of 10 mg/mL NDI-I at pH 9 (open circles) fitted to a flexible cylinder model combined with power law (red). Fit parameters can be found in Table A.3.7.

Table A.3.7. Parameters of SANS model fit seen in Figure A.3.13.

NDI-I Neutral	Flexible cylinder combined with power law	
	Value	Error
Scale a	7.98E-04	2.16E-05
Scale b	3.36E-36	2.44E-36
Background (cm ⁻¹)	0.018544	1.04e-04
Length (Å)	3.58E+05	1.21E+05
Kuhn length (Å)	118.42	6.784
Radius (Å)	5.2269	0.072676
Power	14.374	0.12386
Range	0.00449-0.57308	
Chi ²	1.8877	

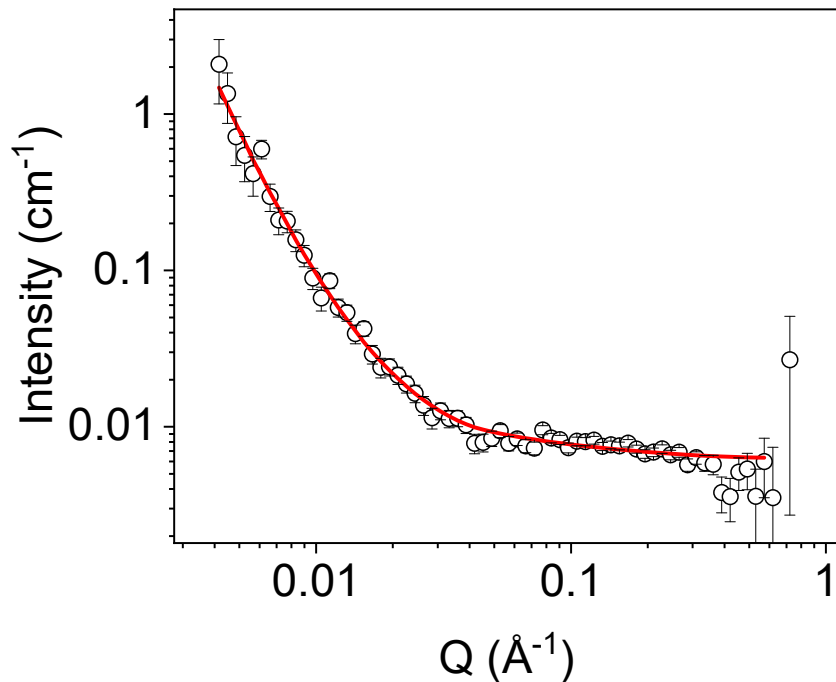


Figure A.3.14. Small angle neutron scattering data for a neutral solution of 10 mg/mL **NDI-I** at pH 6 (open circles) fitted to a flexible elliptical cylinder model combined with power law (red). Fit parameters can be found in Table A.3.8.

Table A.3.8. Parameters of SANS model fit seen in Figure A.3.14.

NDI-I pH 6	Flexible elliptical cylinder combined with power law	
	Value	Error
Scale a	4.24E-04	2.12E-05
Scale b	3.89E-09	2.59E-10
Background (cm ⁻¹)	0.0063224	9.74E-05
Length (Å)	1.95E+10	2.36E+10
Kuhn length (Å)	89.942	8.14
Radius (Å)	5.0167	1.28E-01
Axis ratio	3.5369	0.013796
Power	0.0063224	9.74E-05
Range	0.00416-0.57308	
Chi ²	1.1865	

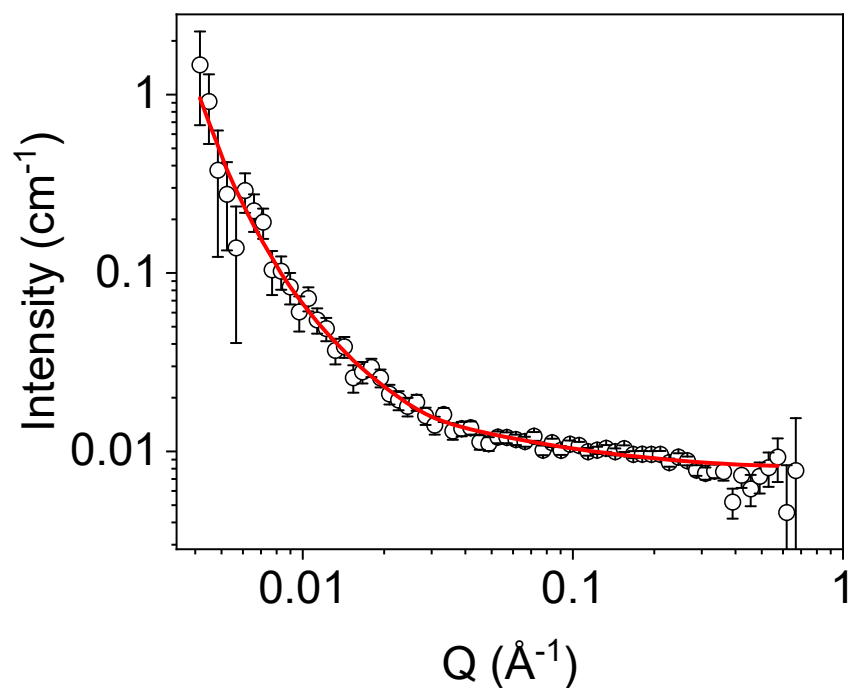


Figure A.3.15. Small angle neutron scattering data for a neutral buffered solution of 10 mg/mL **NDI-V** at pH 9 (open circles) fitted to a flexible cylinder model combined with power law (red). Fit parameters can be found in Table A.3.9.

Table A.3.9. Parameters of SANS model fit seen in Figure A.3.15.

NDI-V Neutral	Flexible cylinder combined with power law	
	Value	Error
Scale a	6.93E-04	2.50E-05
Scale b	9.21E-12	1.92E-12
Background (cm ⁻¹)	0.008282	9.96E-05
Length (Å)	2.95E+12	2.78E+12
Kuhn length (Å)	111.38	8.13
Radius (Å)	5.18	0.1254
Power	4.5031	4.05E-02
Range	0.00416-0.57308	
Chi ²	0.98001	

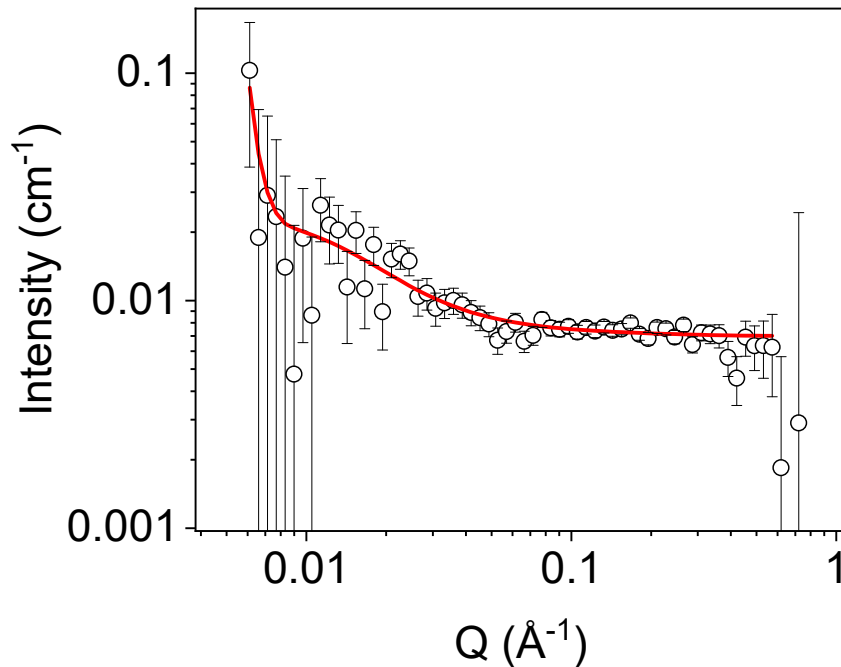


Figure A.3.16. Small angle neutron scattering data for a neutral solution of 10 mg/mL **NDI-V** at pH 6 (open circles) fitted to a flexible elliptical cylinder model combined with power law (red). Fit parameters can be found in Table A.3.10.

Table A.3.10. Parameters of SANS model fit seen in Figure A.3.16.

NDI-V pH 6	Flexible elliptical cylinder combined with power law	
	Value	Error
Scale a	1.54E-04	1.53E-05
Scale b	3.02E-31	2.73E-31
Background (cm ⁻¹)	0.006998	9.73E-05
Length (Å)	1.17E+03	4.74E+02
Kuhn length (Å)	41.85	7.89
Radius (Å)	5.00	2.53E-01
Axis ratio	12.899	1.68E-01
Power	0.006998	9.73E-05
Range	0.00611-0.57308	
Chi ²	0.77827	

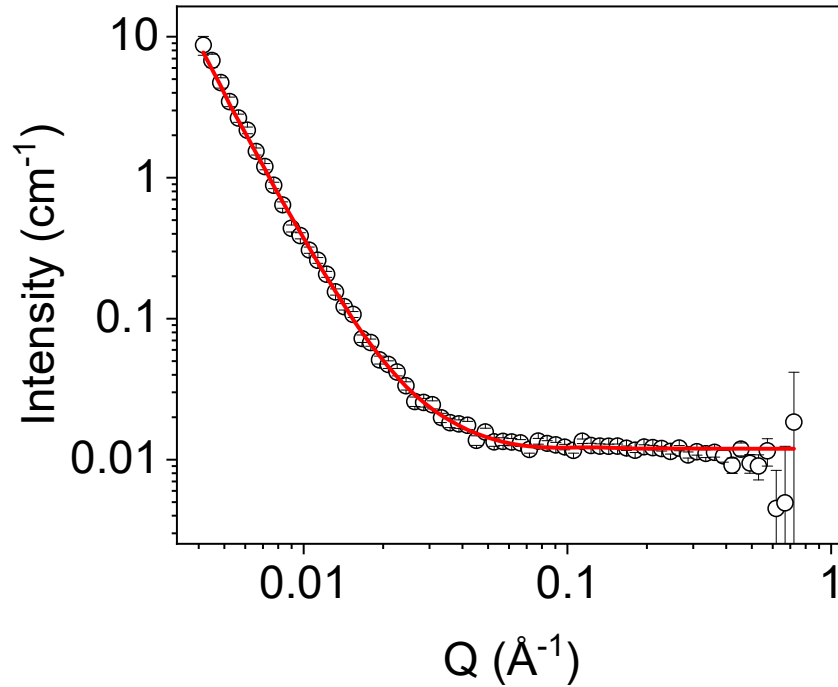


Figure A.3.17. Small angle neutron scattering data for a neutral solution of 10 mg/mL NDI-F at pH 9 (open circles) fitted to a hollow cylinder model combined with power law (red). Fit parameters can be found in Table A.3.11.

Table A.3.11. Parameters of SANS model fit seen in Figure A.3.17.

NDI-F pH 9	Hollow cylinder combined with power law	
	Value	Error
Scale a	4.22E-05	4.36E-06
Scale b	4.64E-08	6.34E-10
Background (cm ⁻¹)	0.011957	9.97E-05
Length (Å)	8.05E+02	2.08E+03
Radius (Å)	25.379	3.32
Thickness (Å)	7.8059	7.82E-02
Power	3.4114	2.91E-03
Range	0.00416-0.72191	
Chi ²	1.349	

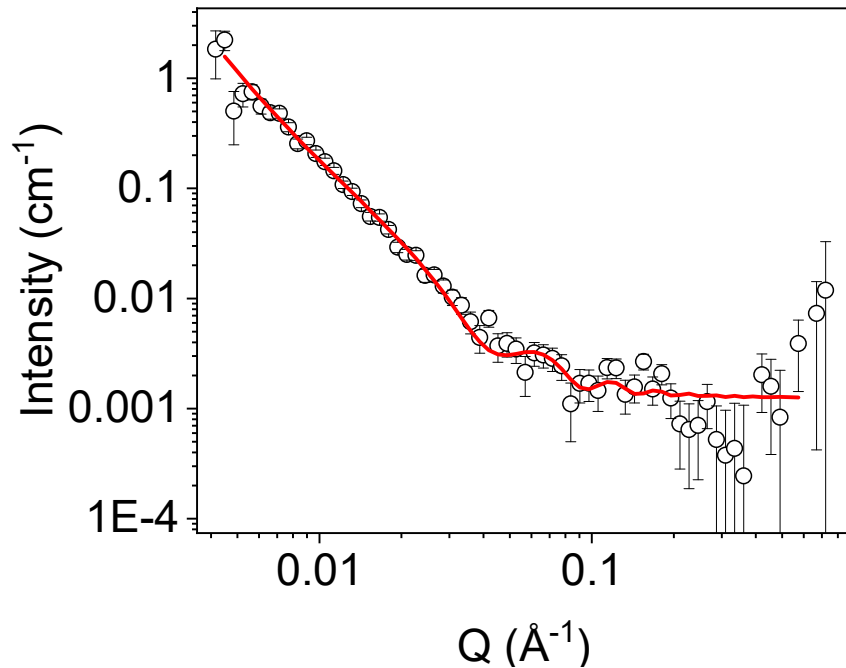


Figure A.3.18. Small angle neutron scattering data for a neutral buffered solution of 10 mg/mL **NDI-F** at pH 6 (open circles) fitted to a hollow cylinder model combined with power law (red). Fit parameters can be found in Table A.3.12.

Table A.3.12. Parameters of SANS model fit seen in Figure A.3.18.

NDI-F Neutral	Hollow cylinder combined with power law	
	Value	Error
Scale a	5.02E-05	2.63E-06
Scale b	1.11E-07	3.32E-09
Background (cm ⁻¹)	0.001293	9.94E-05
Length (Å)	3.93E+02	1.23E+02
Radius (Å)	52.325	2.1714
Thickness (Å)	11.761	0.62411
Power	3.0107	6.48E-03
Range	0.00449-00.57308	
Chi ²	1.4316	

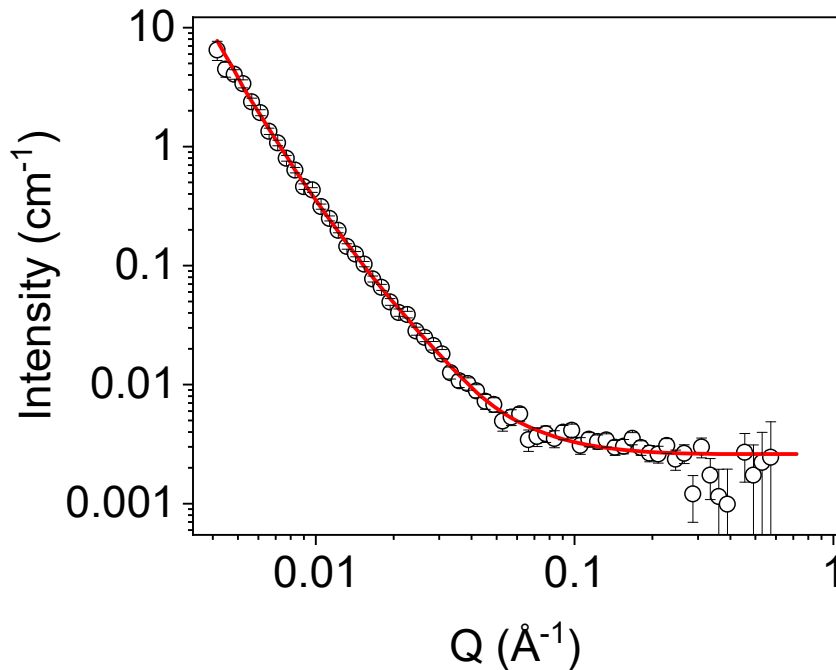


Figure A.3.19. Small angle neutron scattering data for a neutral solution of 10 mg/mL **NDI-GF** at pD 9 (open circles) fitted to a flexible elliptical cylinder model combined with power law (red). Fit parameters can be found in Table A.3.13.

Table A.3.13. Parameters of SANS model fit seen in Figure A.3.19.

NDI-GF pD 9	Flexible elliptical cylinder combined with power law	
	Value	Error
Scale a	8.43E-06	2.51E-07
Scale b	1.01E-08	1.73E-10
Background (cm ⁻¹)	0.002608	9.53E-05
Length (Å)	1566.50	475.31
Kuhn length (Å)	126.55	9.41
Radius (Å)	7.2637	1.46E-01
Axis ratio	10.354	2.06E-01
Power	3.6801	3.56E-03
Range	0.00416-0.72191	
Chi ²	0.95665	

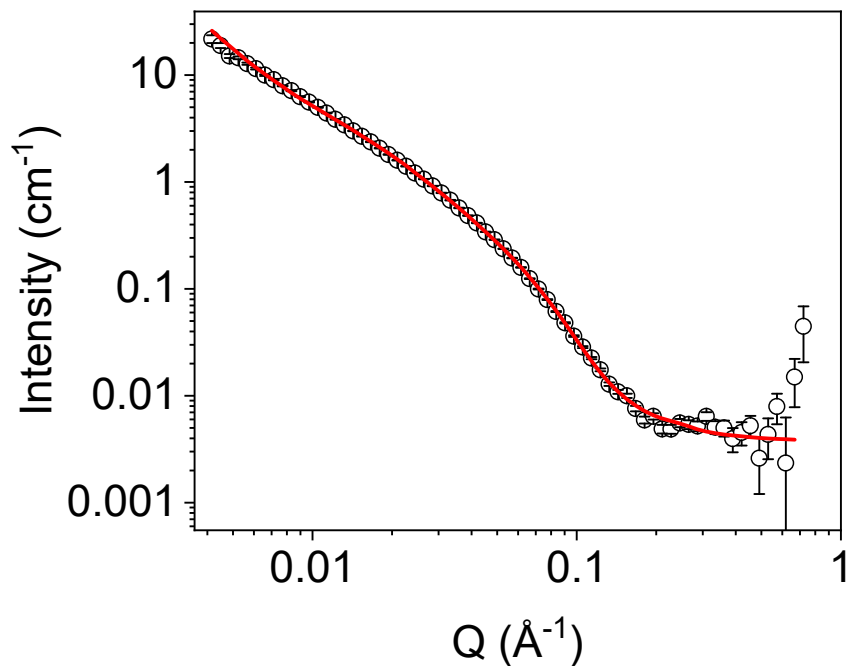


Figure A.3.20. Small angle neutron scattering data for a neutral buffered solution of 10 mg/mL **NDI-GF** at pD 6 (open circles) fitted to a flexible elliptical cylinder model combined with power law (red). Fit parameters can be found in Table A.3.14.

Table A.3.14. Parameters of SANS model fit seen in Figure A.3.20.

NDI-GF Neutral	Flexible elliptical cylinder combined with power law	
	Value	Error
Scale a	4.99E-05	1.76E-06
Scale b	4.99E-05	1.79E-07
Background (cm ⁻¹)	0.003755	1.09E-03
Length (Å)	762.08	5.98
Kuhn length (Å)	60.074	2.32E-02
Radius (Å)	19.512	2.07E-02
Ratio Axis	1.8167	1.82E-03
Power	2.36	8.73E-04
Range	0.00416-0.66844	
Chi ²	4.8026	

Appendix

Table A.3.15. Tabulated transmittance taken at the λ_{max} of the reduced state for buffered 10 mg/mL **NDI-GF**, **NDI-I**, **NDI-V**, **NDI-F** and **NDI-FF** after 10 seconds of application of -2.5 V unless stated otherwise. Data collected in a 1 x 1 cm FTO window set up.

		Transmittance at 450 nm (%T)
NDI-GF 10 mg/mL at pH 6	Neutral State	84.79
	Reduced State	7.22
Water		96.34
		Transmittance at 490 nm (%T)
NDI-I 10 mg/mL at pH 9	Neutral State	97.37
	Reduced State (10 seconds)	0.12
	Neutral State	95.35
	Reduced State (2 seconds)	3.23
NDI-V 10 mg/mL at pH 9	Neutral State	83.24
	Reduced State	0.10
	Neutral State	88.08
	Reduced State (2 seconds of -2.5 V applied)	4.17
NDI-F 10 mg/mL at pH 6	Neutral State	91.98
	Reduced State	2.78
Water		98.74

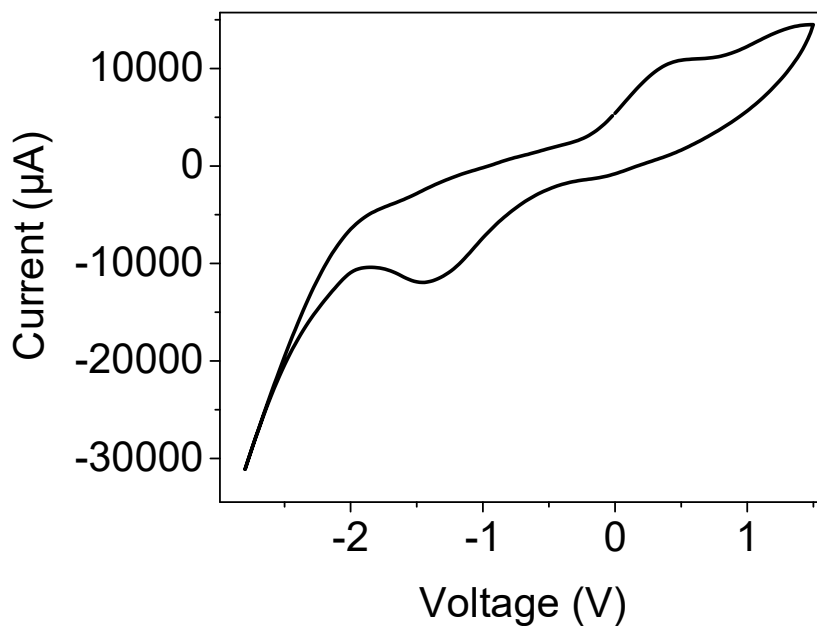


Figure A.3.21. Cyclic voltammogram showing Reduction and oxidation potentials taken from cyclic voltammograms of 10 mg/mL hydroquinone with 10 % 0.1 M NaCl. Measurements performed in 5 x 5 FTO window set up. The scan rate of the cyclic voltammograms was 0.5 V/s.

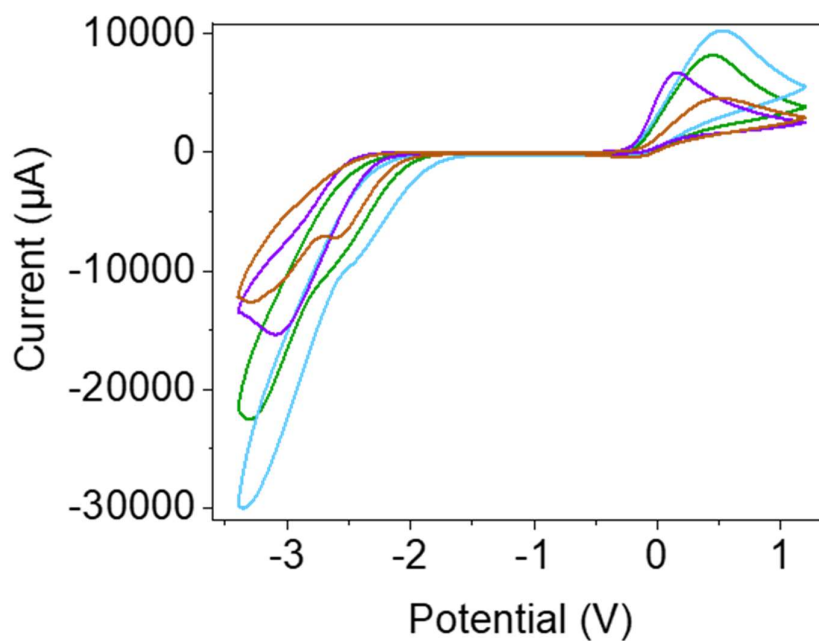


Figure A.3.22. Cyclic voltammograms collected from buffered 10 mg/mL solutions of **NDI-I** (green), **NDI-V** (blue), **NDI-F** (purple) and **NDI-GF** (brown) adjusted to their respective ideal pH (pH 9 for **NDI-I** and **NDI-V** and pH 6 for **NDI-F** and **NDI-GF**). Voltammograms measured using a 5 x 5 FTO glass window cell at 0.1 V/s scan rate.

A.3.1 Development of cyclability testing

Initial trials of cyclability were performed using **NDI-I** to conserve material. As NDI are photochromic,¹⁻¹⁰ cycling experiments were setup in a dark room without natural light. The only light upon the NDI solution was that cast by a small hand torch above an ultraviolet (UV) filter lens. This setup was found not to visually discolour the solution when left without any applied potential. These precautions were taken to eliminate any interference caused by photoinduced reduced species into the experiment. A UV filtering film was also applied to the outside of the FTO glass. The effect of a UV filter upon natural sunlight can be seen in Figure A.3.23. Cycling tests were performed using solutions at 10 mg/mL in 5 x 5 cm FTO window cells. This size of window allowed observation by camera.



Figure A.3.23. Images of FTO windows filled with **NDI-I** at 10 mg/mL exposed to natural daylight without (A) and with (B) UV filter protective film. A1 and B1 represent the solution at the start of the experiments and images following were taken every 30 minutes of exposure to natural light, starting with A1 and B2 until A7 and B7 (images after 3 hours 30 minutes).

As **NDI-I** was switched between states, a discolouration of the neutral state was observed, Figure A.3.24(a). Electrochemical oxidation also became less efficient as cycling progressed, Figure A.3.24(b). When this state was noticeable to the eye, the experiment was stopped. The effect of buffering the NDI solution to its ideal pH was found to increase the number of cycles achieved within the experiment, Figure A.3.24(b). In unbuffered solutions, pH decreases, resulting in less efficient electrochemical processes as aggregation changes (Chapter 2).

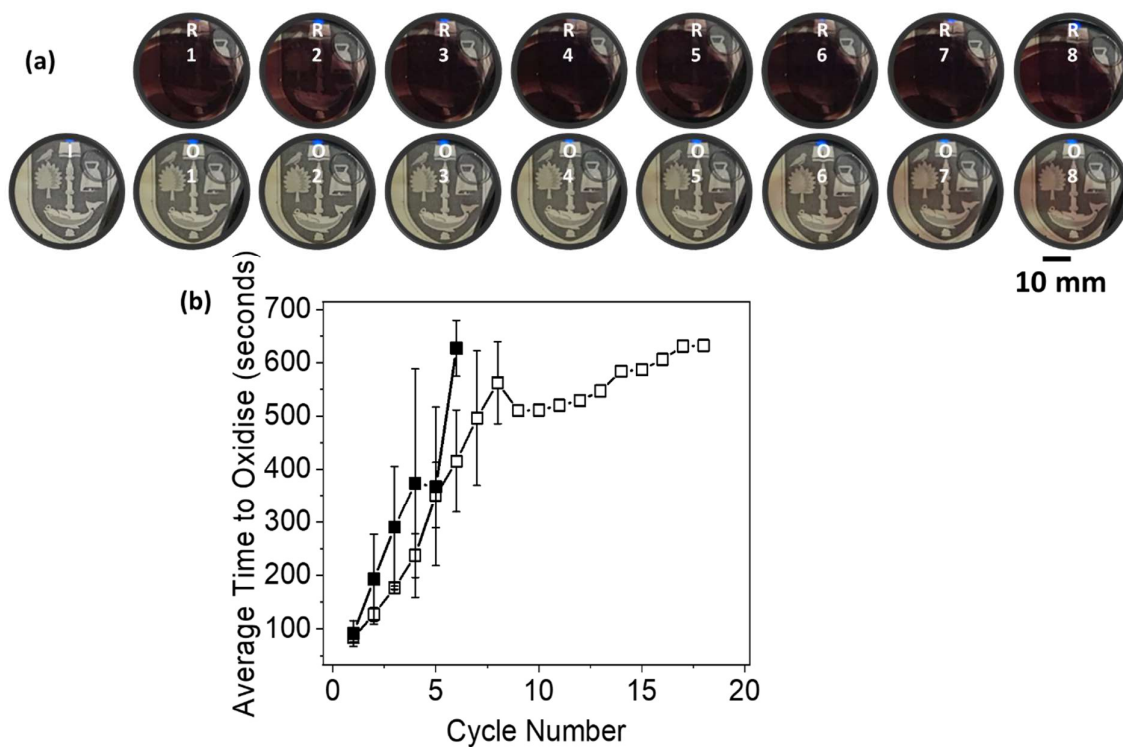


Figure A.3.24. (a) Images of FTO glass window filled with **NDI-I** at 10 mg/mL and buffered at pH 9 during one of the triplicated runs of this cycling experiment. Images captured before the experiment (I) and at the point of full reduction (R) and oxidation (O) for each cycle. (b) Plot showing how time to reach a state of full oxidation (i.e. without discolouration of the neutral state) fluctuates with cycling for buffered (open squares) and unbuffered (filled squares) solutions of 10 mg/mL **NDI-I**. Measurements are taken as an average of triplicate measurements and error bars calculated from standard deviation.

A cyclic voltammetry measurement was performed after each electrochemical reduction and oxidation procedure to probe the system further, Figure A.3.25-Figure A.3.26. Within the first 5 cycles the reduction peak shifts from -3.1 to -2.8 V for unbuffered solutions, Figure A.3.27(a). This trend is suppressed with the addition of a buffer, Figure A.3.27(a). The oxidation peak shifts more significantly by approximately 0.6 V over 50 cycles in unbuffered solutions whereas this change is only approximately 0.15 V in buffered solutions, Figure A.3.27(b). These observations suggest that significant shifting in peaks is due to a change in pH but that some shifting occurs as a result of cycling between neutral and reduced states.

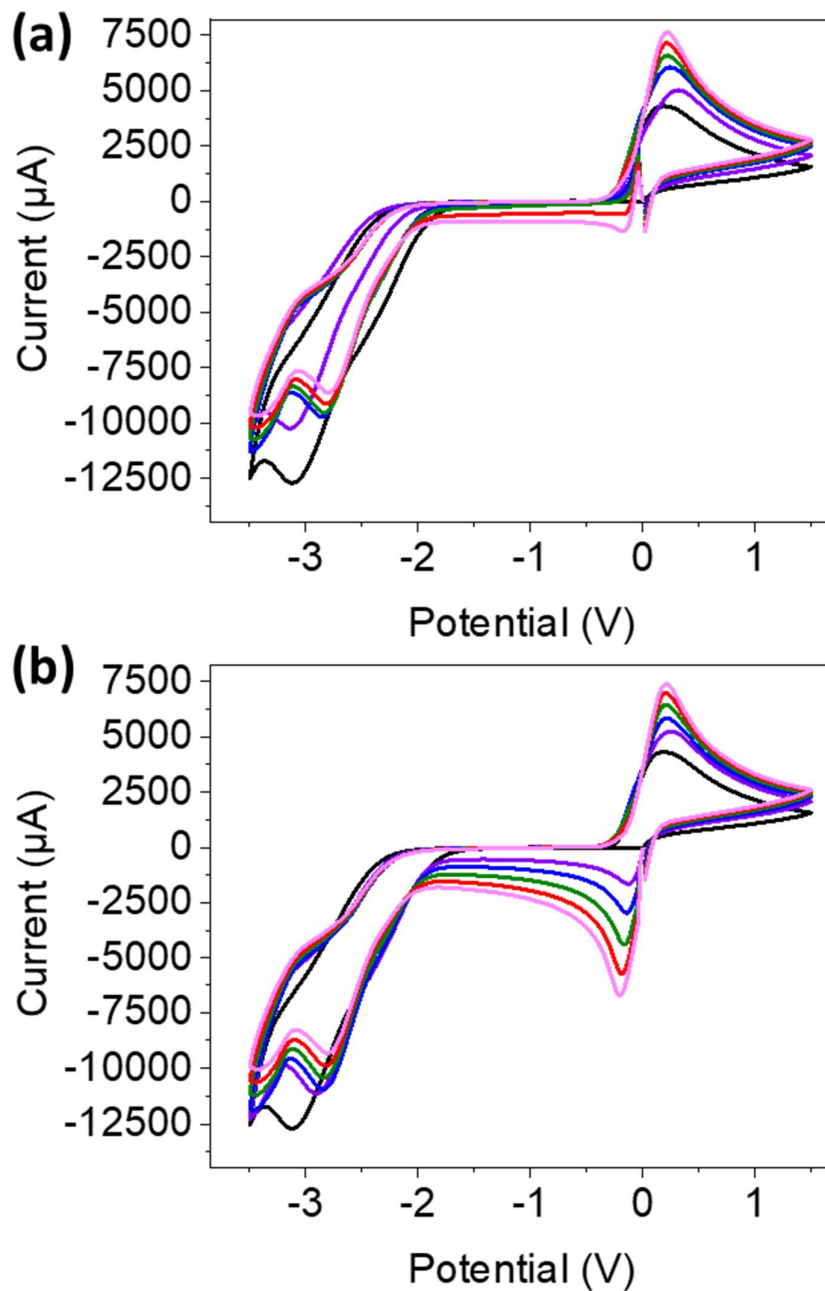


Figure A.3.25. Cyclic voltammograms performed before (black) and during a cycling experiment using unbuffered 10 mg/mL solutions of NDI-I at pH 9. Cyclic voltammograms were taken after the reduction process (a) and the oxidation process (b) had completed. Measurements taken during cycle 1 (purple), 2 (blue), 3 (green), 4 (red) and 5 (pink).

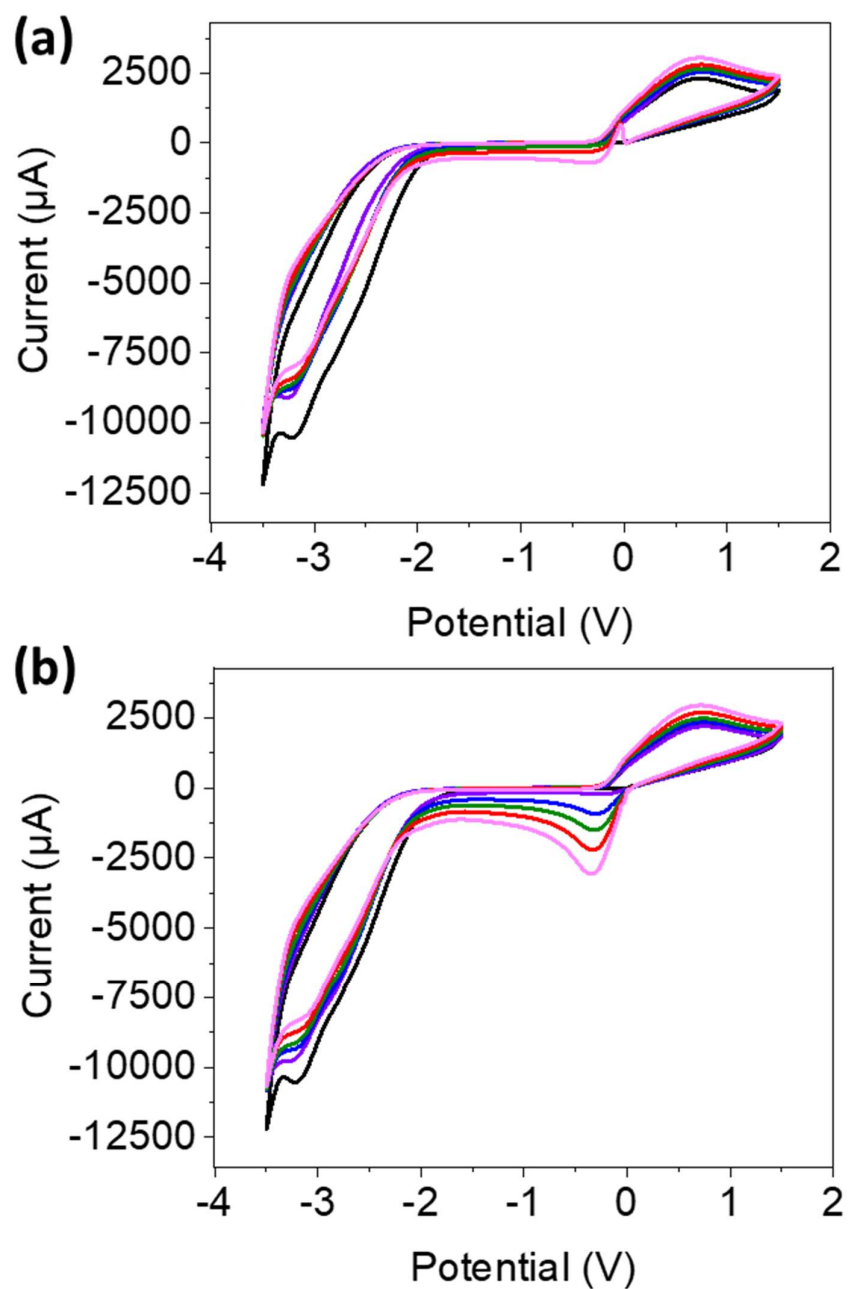


Figure A.3.26. Cyclic voltammograms performed before (**black**) and during a cycling experiment using buffered 10 mg/mL solutions of **NDI-I** at pH 9. Cyclic voltammograms were taken after the reduction process (a) and the oxidation process (b) had completed. Measurements taken during cycle 1 (**purple**), 2 (**blue**), 3 (**green**), 4 (**red**) and 5 (**pink**).

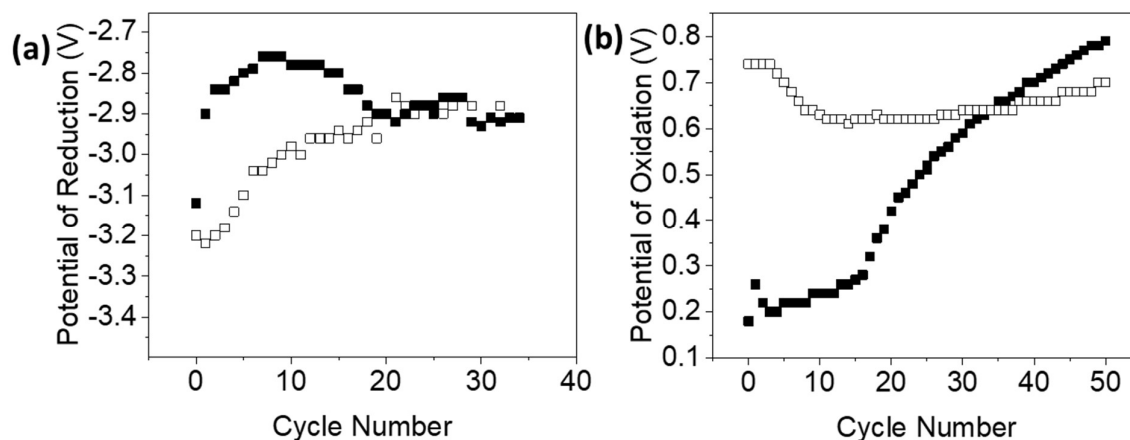


Figure A.3.27. Plot showing the shifting of the (a) reduction potential and (b) oxidation potential with cycling based on cyclic voltammetry measurements taken after each cycle. Measurements carried out using buffered (open squares) and non-buffered (filled squares) 10 mg/mL **NDI-I**.

As the reduction peak shifts to a lower potential, production of the radical anion will become more prevalent as the original reduction potential is applied. As the oxidation potential shifts to a higher potential, oxidation will become more energy intensive and less efficient. Both factors will result in an increase in oxidation time to reverse the larger concentration of radical anion produced. These observations explain the gradual increase in oxidation time with cycling and the discolouration observed in the oxidised state.

A second small reduction peak is observed to appear over time, Figure A.3.25-Figure A.3.26. The peak gradually appears around -0.2 V and grows with cycling and is only present in the cyclic voltammograms measured after the oxidation process. This observation which could suggest that a small amount of reduced material is still present and has diffused away from the working electrode surface and is partially oxidised by the counter electrode during CV scans, forming a negative peak around -0.2 V. Data suggests that the oxidative processes are not as efficient as the reductive processes. Therefore, an electrochemical script was created to maximise the efficiency of electrochemical oxidation.

A.3.2 The influence of electrochemical script

In order to reduce any negative effects caused by shifting in the oxidation potential, a new electrochemical procedure was devised. Instead of applying a fixed potential during the oxidation step of the on-off cycles, a sweeping potential would be applied. In this procedure, potential gradually increased in steps of 0.05 V every 5 seconds from 0.1 V to 0.95 V. This process cycles for 10 minutes. A visual representation of this method is shown in Figure A.3.28(a-b).

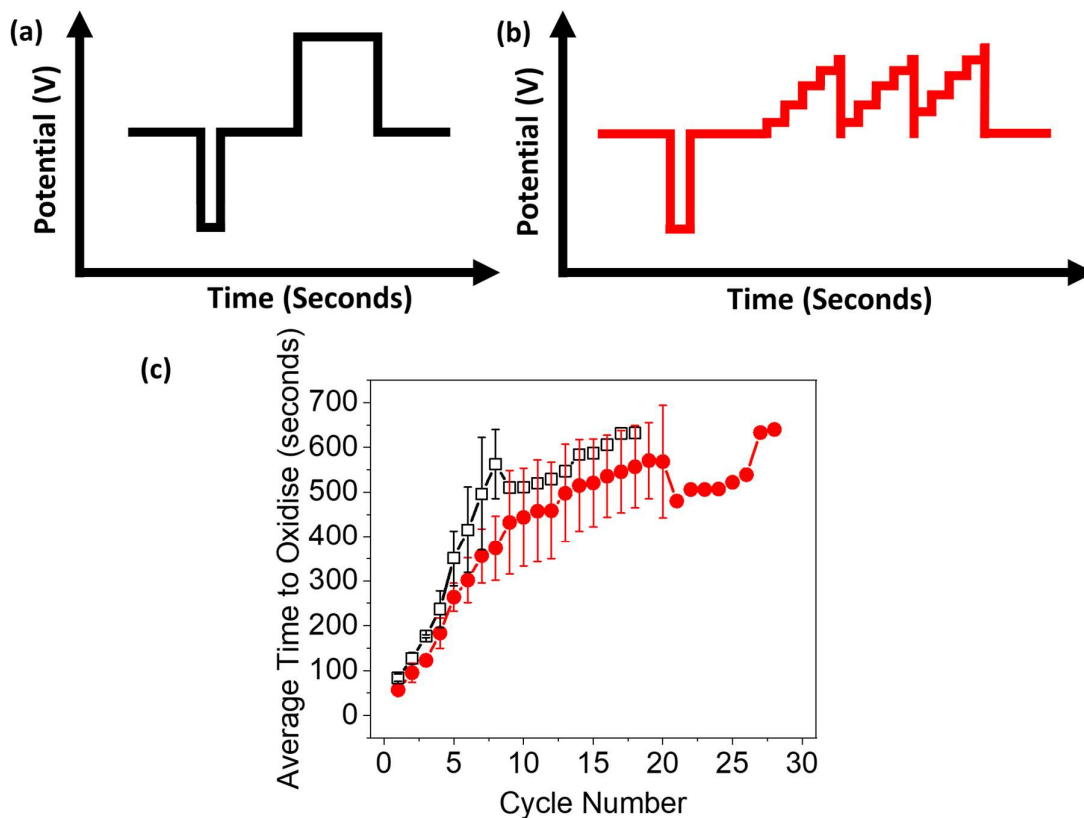


Figure A.3.28. Simplified schematic representation of the electrochemical procedure containing a fixed potential (a) and sweep potential (b) oxidation method. Potential axis is not to scale. (c) Plot showing how time to reach a state of full oxidation (i.e. without discolouration of the neutral state) fluctuates with cycling of 10 mg/mL buffered NDI-I with a fixed potential (open squares) and sweep potential (filled circles) methods. Measurements are taken as an average of triplicate measurements and error bars calculated from standard deviation.

A sweeping potential method reduces the average time of oxidation consistently compared to a fixed potential method, Figure A.3.28(c). Sweeping potential also increases the number of cycles that can be performed before the neutral state becomes discoloured to 28, Figure A.3.28(c).

Another method used was “flickering”. A flickering method is defined as applying a positive potential followed by a negative potential of the same magnitude (for example, applying 1 V, then -1 V). By applying a positive potential to the working electrode, the corresponding negative potential flows through the counter electrode, and vice versa. In this way, we hope to account for diffusion within the cell away from the working electrode surface which is represented as a cartoon in Figure A.3.29.

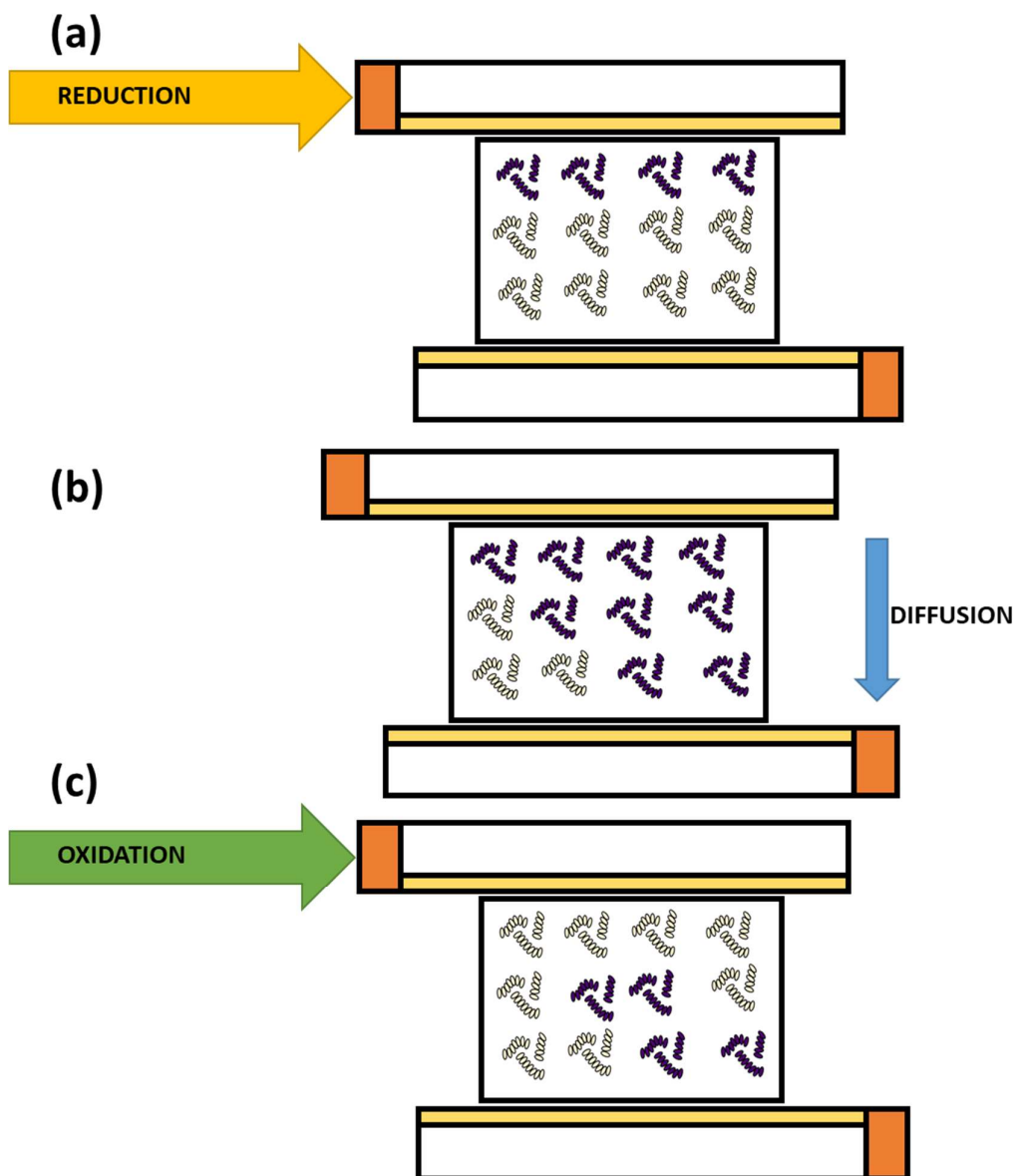


Figure A.3.29. Schematic showing how after reduction (a) diffusion away from the electrode surface (b) may compromise the efficiency of electrochemical oxidation when oxidising potential is applied (c).

Two different procedures were used which are described as short and long flicker methods. Both are based upon the sweep potential oxidation method because this method improved cyclability, Figure A.3.28(c). The “short flicker method” is shown schematically in Figure A.3.30(b) and the “long flicker” method is shown schematically in Figure A.3.30(c). The short flicker method involved flicking between positive and negative potentials before increasing in magnitude (i.e. 0.1 V followed by -0.1 V followed by 0.15 V etc.). The long flicker method involved flicking between positive and negative sweeps (i.e. sweeping from 0.1 V to 0.95 V followed by -0.1 V to -0.95 V).

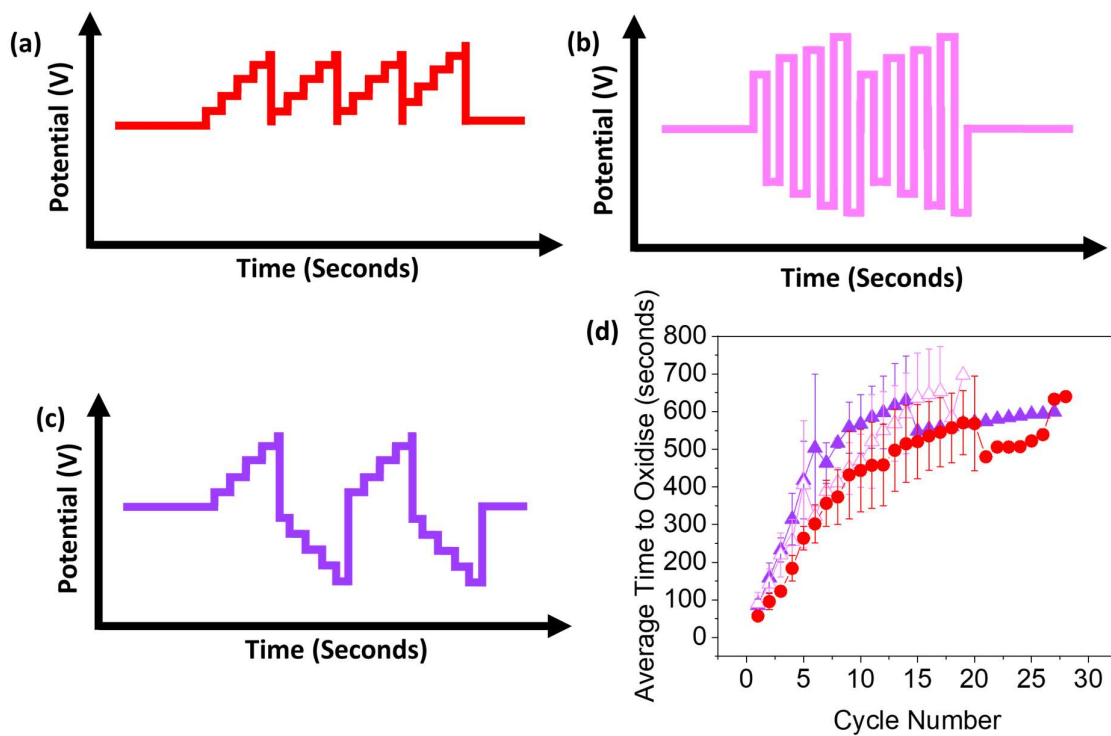


Figure A.3.30. Simplified schematic representation of the electrochemical oxidation procedure defined as (a) the sweep method, (b) a short flicker method and (c) a long flicker method. Potential axis is not to scale. (d) Plot showing how time to reach a state of full oxidation (i.e. without discolouration of the neutral state) fluctuates with cycling of 10 mg/mL buffered **NDI-I** with a sweep potential (red circles), short (pink open triangles) and long (purple filled triangles) flicker methods. Measurements are taken as an average of triplicate measurements and error bars calculated from standard deviation.

From Figure A.3.30(d), it is apparent that the difference in performance between flicking methods is minimal and the best scripting method is a sweeping potential. This method is used moving forward.

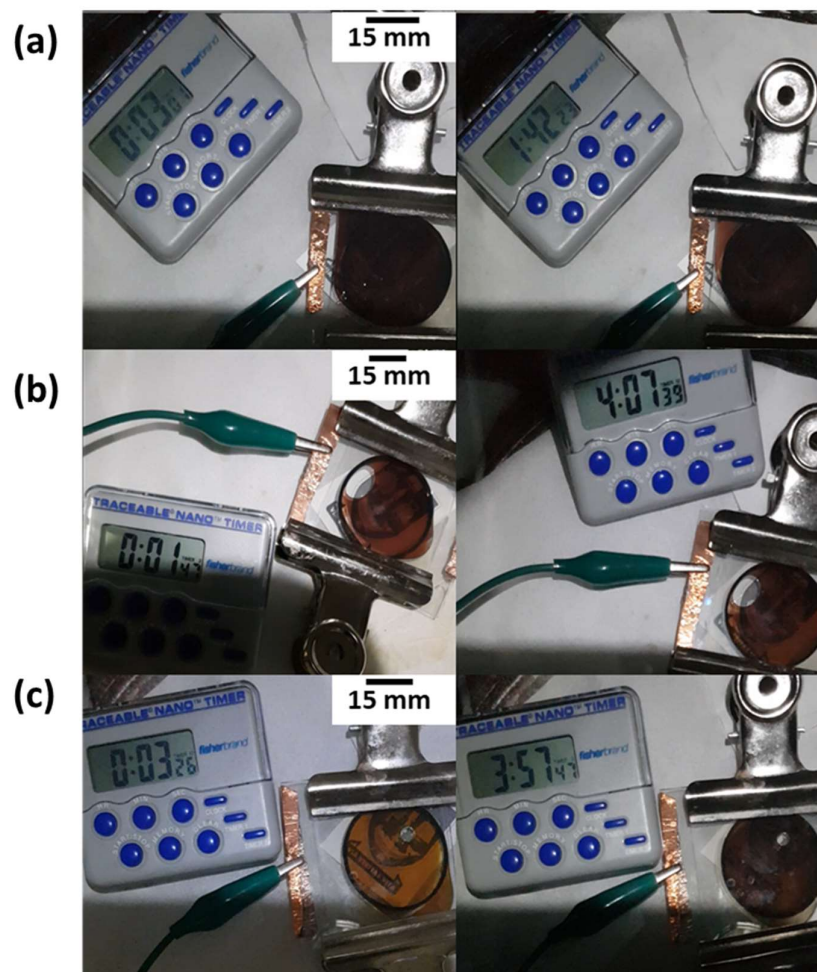


Figure A.3.31. Images of the reduced state at the start (left) and end (right) of cycling experiments. Buffered solutions of 10 mg/mL **NDI-V** (a), **NDI-F** (b) and **NDI-GF** (c) were used adjusted to their respective ideal pH (pH 9 for **NDI-V** and pH 6 for **NDI-F** and **NDI-GF**). The time at the start and end of the experiment is shown on a stopwatch.

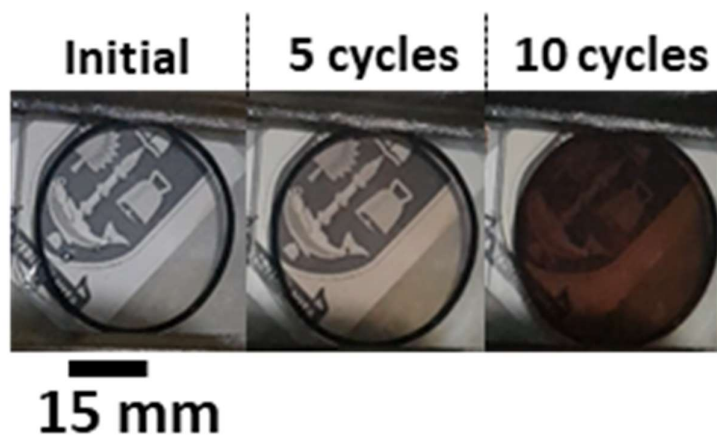


Figure A.3.32. Images of oxidised state after periods of cycling. Solution of buffered 10 mg/mL NDI-V at pH 9 used.

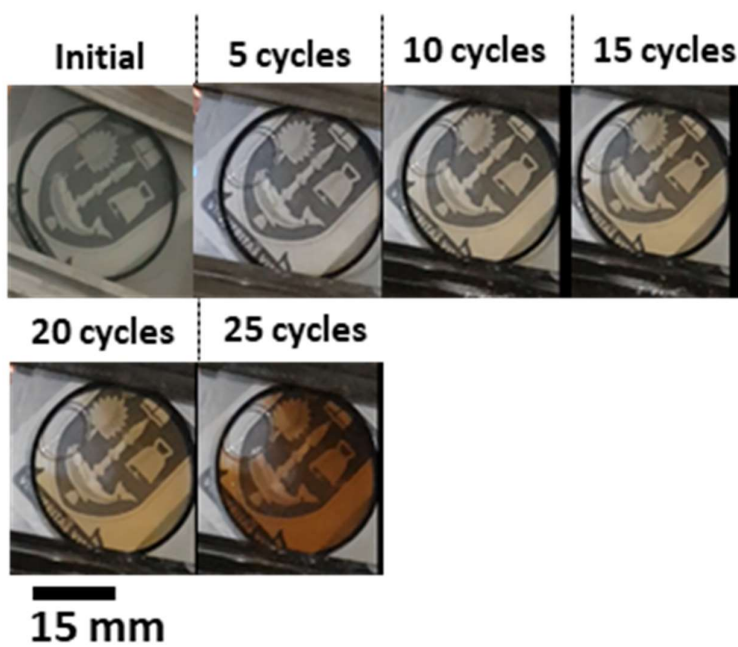


Figure A.3.33. Images of oxidised state after periods of cycling. Solution of buffered 10 mg/mL NDI-F at pH 6 used.

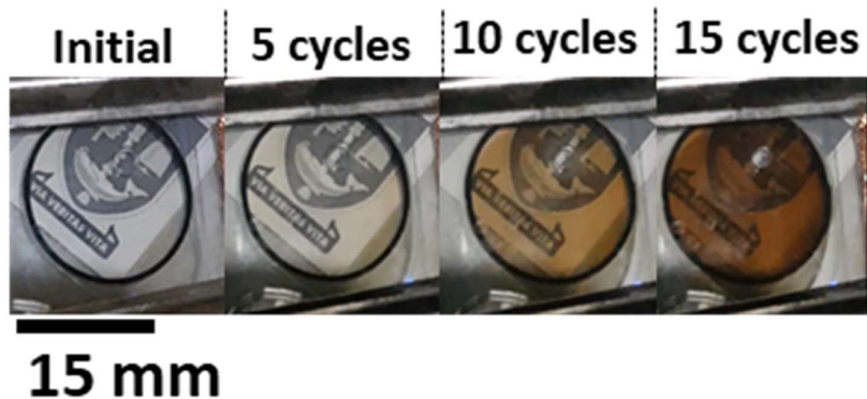


Figure A.3.34. Images of oxidised state after periods of cycling. Solution of buffered 10 mg/mL NDI-GF at pH 6 used.

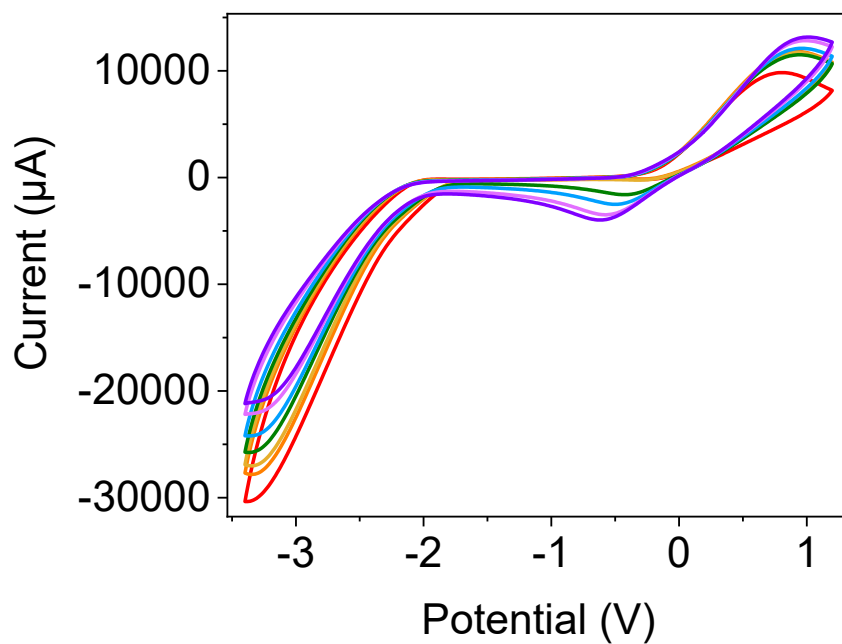


Figure A.3.35. Cyclic voltammogram collected from buffered 10 mg/mL solution of NDI-I adjusted to pH 9. Voltammograms measured using a 5 x 5 cm FTO window cell with a scan rate of 0.5 V/s. Measurements shown from scan number 1 (red), 5 (orange), 10 (yellow), 30 (green), 50 (blue), 80 (lilac) and 100 (purple).

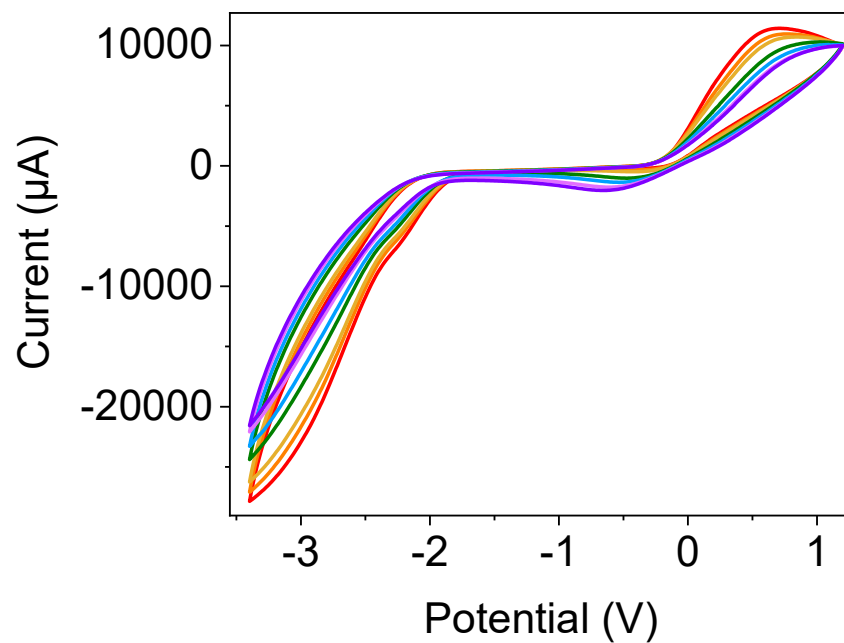


Figure A.3.36. Cyclic voltammogram collected from buffered 10 mg/mL solution of **NDI-V** adjusted to pH 9. Voltammograms measured using a 5 x 5 cm FTO window cell with a scan rate of 0.5 V/s. Measurements shown from scan number 1 (red), 5 (orange), 10 (yellow), 30 (green), 50 (blue), 80 (lilac) and 100 (purple).

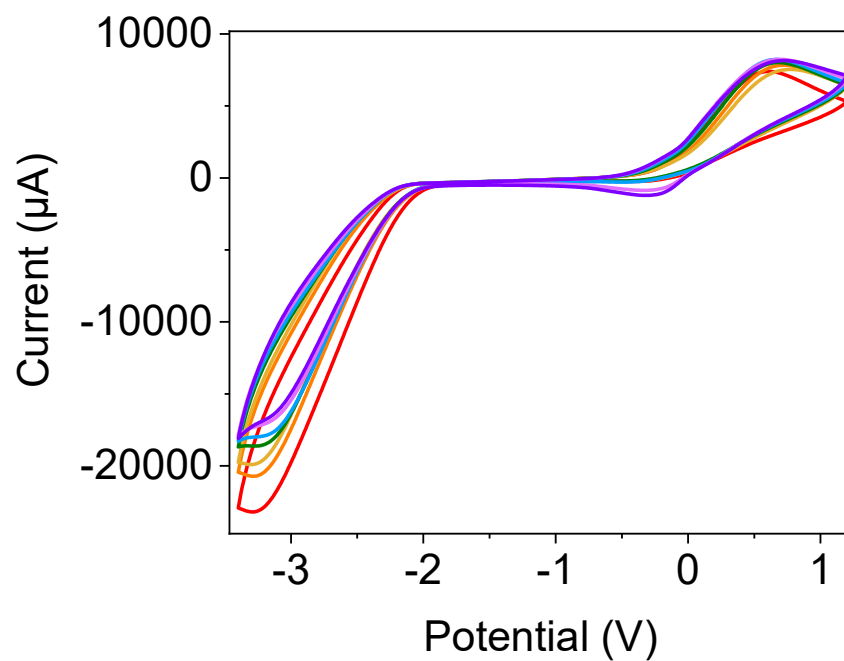


Figure A.3.37. Cyclic voltammogram collected from buffered 10 mg/mL solution of **NDI-F** adjusted to pH 6. Voltammograms measured using a 5 x 5 cm FTO window cell with a scan rate of 0.5 V/s. Measurements shown from scan number 1 (red), 5 (orange), 10 (yellow), 30 (green), 50 (blue), 80 (lilac) and 100 (purple).

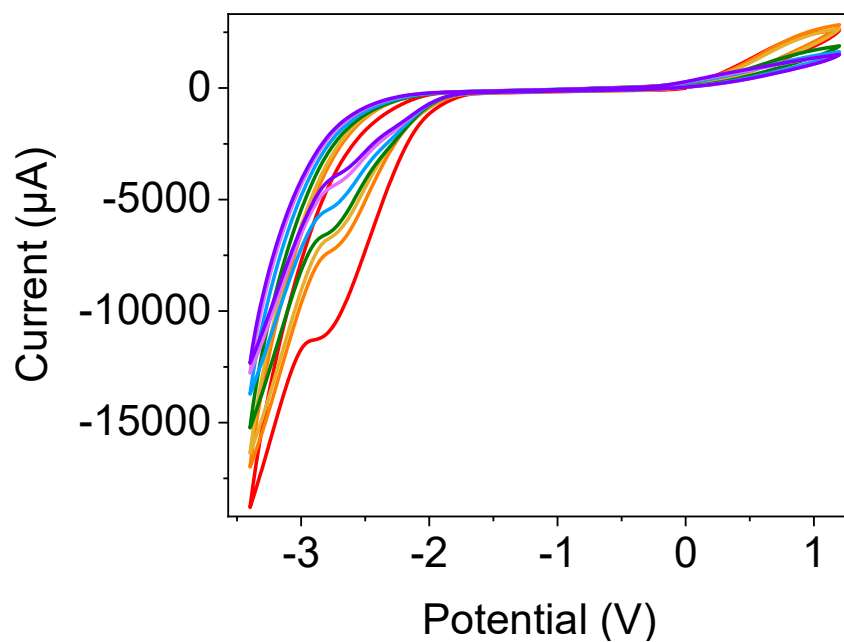


Figure A.3.38. Cyclic voltammogram collected from buffered 10 mg/mL solution of **NDI-GF** adjusted to pH 6. Voltammograms measured using a 5 x 5 cm FTO window cell with a scan rate of 0.5 V/s. Measurements shown from scan number 1 (red), 5 (orange), 10 (yellow), 30 (green), 50 (blue), 80 (lilac) and 100 (purple).

A.3.2 Explanation of NMR

In the case of **NDI-F**, the peaks corresponding to each environment of aggregate A (as seen in d-DMSO) (Chapter 2, 2.4.1.4) are as previously reported. In D₂O, a second set of peaks is observed which we hypothesize is a result of each R group either side of the NDI being slightly inequivalent which leads to two core environments (doublets) instead of one. A environments are highlighted in orange whereas the B environments are highlighted in blue in the same regions, Figure A.3.39-Figure A.3.40. While we call these aggregates for ease, we do not believe that there are two differently aggregated systems in solution, but that perhaps the R groups of the NDI are differently twisted or orientated from the core in some molecules, giving rise to inequality in environments.

The CH₂ environments of **NDI-F** are equivalent in aggregate B but not A, Figure A.3.40. At both high and low pD this second set of peaks are fairly small compared to the primary set of aggregate A, Figure A.3.39-Figure A.3.40. Integration for peaks attributed to aggregate A/B are as expected relative to one another, Figure A.3.41-Figure A.3.42.

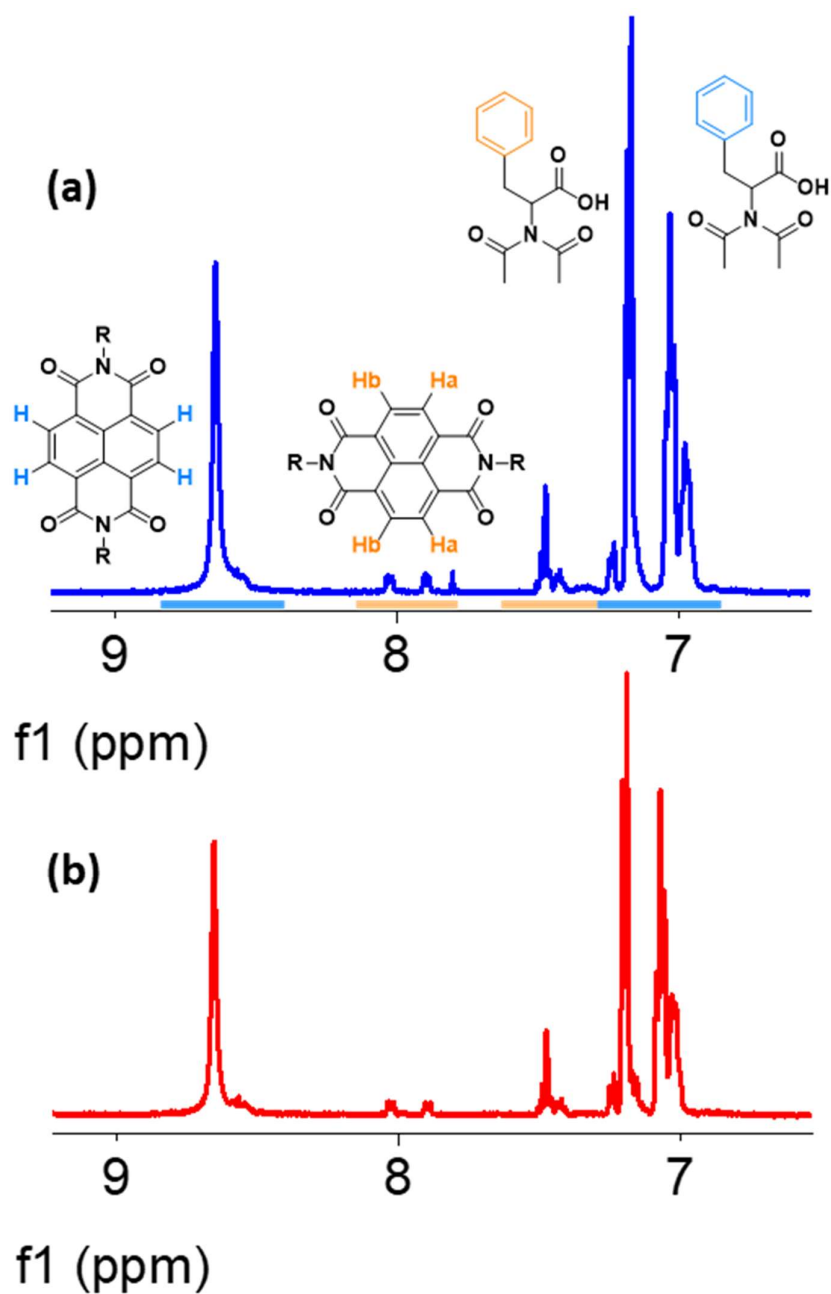


Figure A.3.39. Enlarged section of ¹H NMR spectra of 5 mg/mL NDI-F in D₂O at (a) pD 11 and (b) pD 6. Signals corresponding to different proton environments for aggregate A and B are highlighted alongside their assignment.

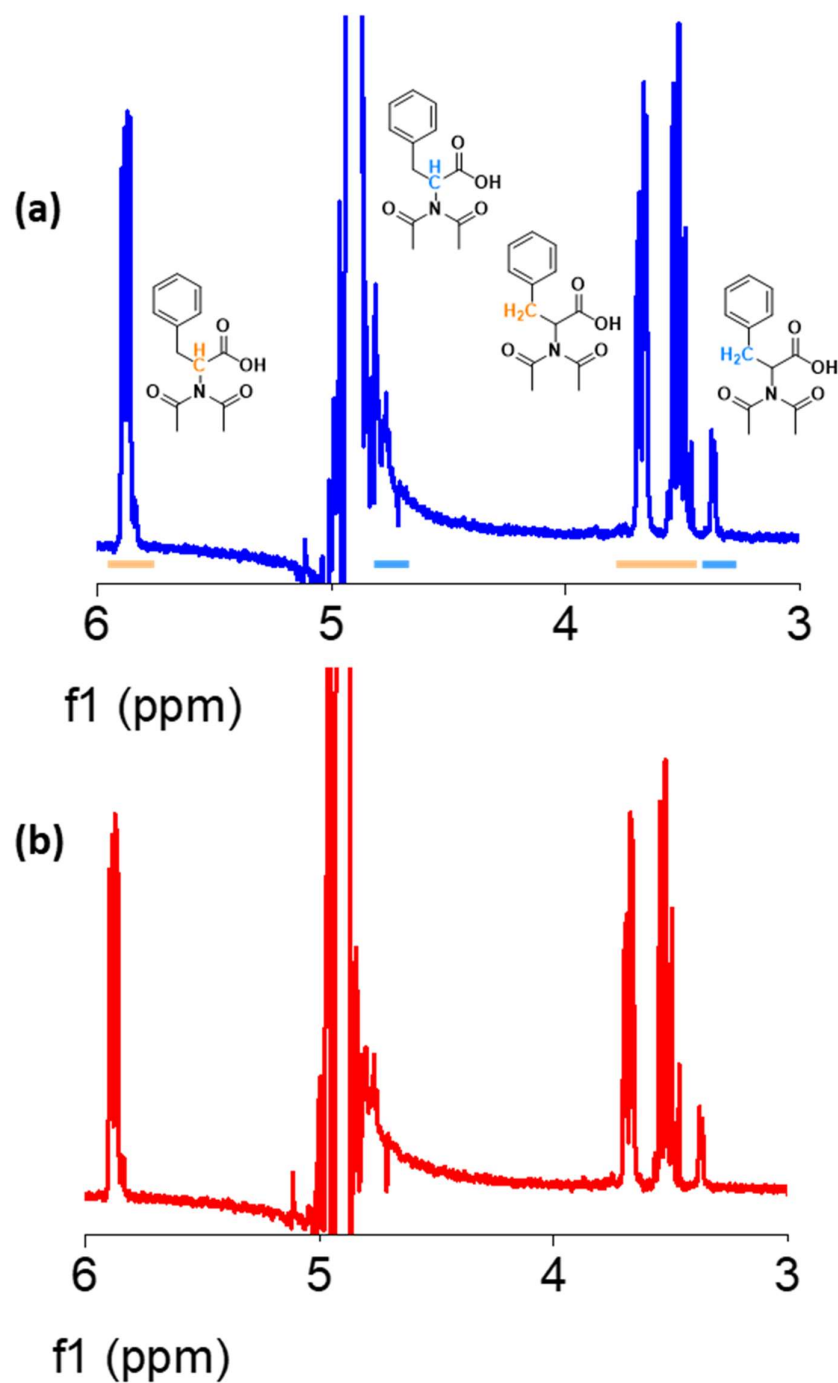


Figure A.3.40. Enlarged section of ^1H NMR spectra of 5 mg/mL NDI-F in D_2O at (a) pD 11 and (b) pD 6. Signals corresponding to different proton environments for aggregate A and B are highlighted alongside their assignment.

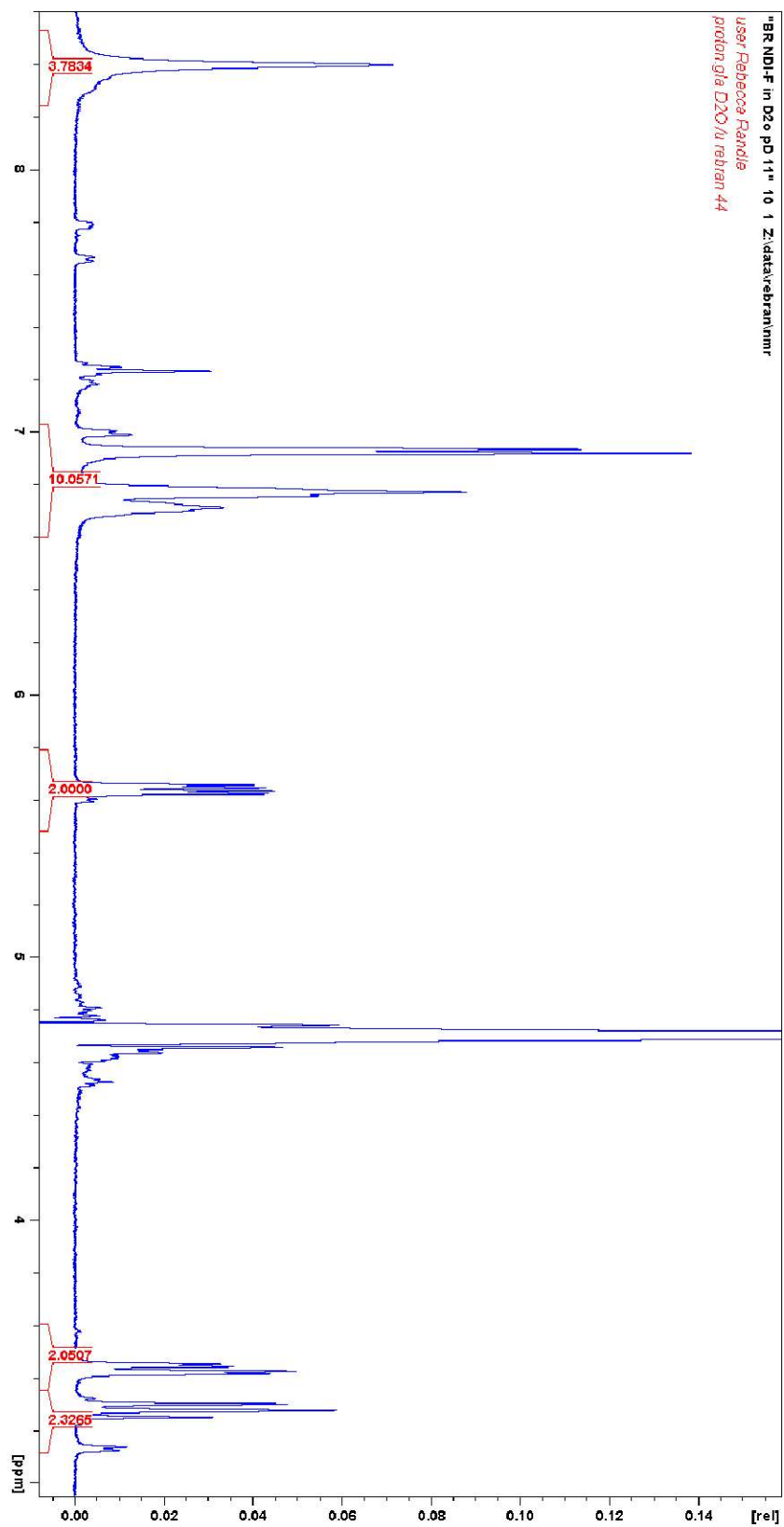


Figure A.3.41. ^1H NMR spectra of 5 mg/mL NDI-F in D_2O at pD 11 showing integration of aggregate A.

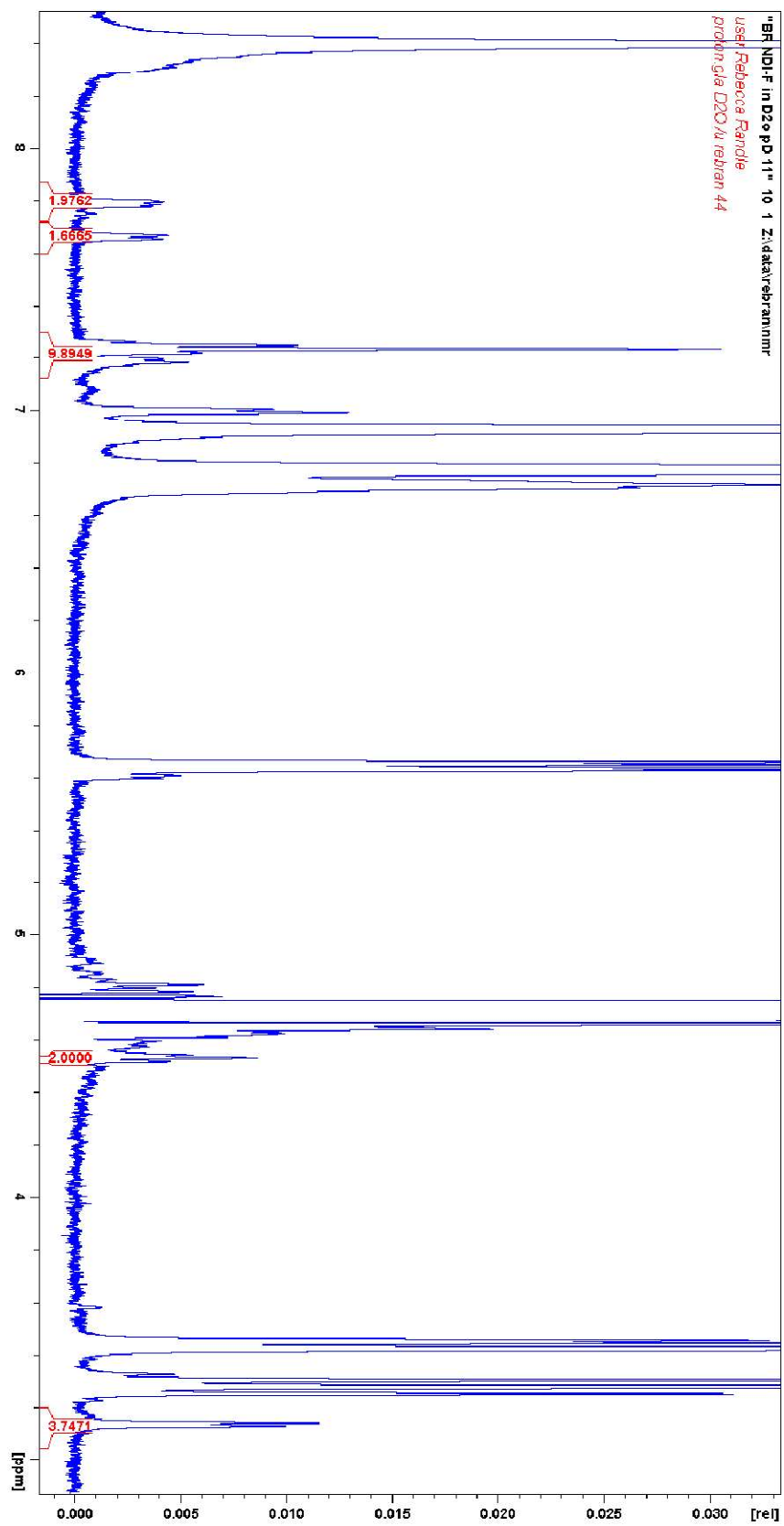


Figure A.3.42. ^1H NMR spectra of 5 mg/mL NDI-F in D_2O at pH 11 showing integration of aggregate B.

NDI-GF's ^1H NMR spectra in D_2O are more complex. As with **NDI-F**, two sets of environments are observed arising from an equivalent and inequivalent core aggregate. The set corresponding to aggregate B is far more intense at high pD than at low pD, Figure A.3.43-Figure A.3.46. This observation suggests that the ratio of the two sets of ^1H NMR peaks is dependent upon pH and therefore the reason for each R group being inequivalent may be a result of aggregation changing with pH (not 100 % of the molecules in either category). Some environments are hidden under a solvent peak but are shifted at higher temperatures, Figure A.3.45.

The ratio of aggregates is closer to 1:1 than with **NDI-F** which may be a result of the increased flexibility of **NDI-GF** in the glycine functionality, allowing more rotation of the bond. The aromatic environments are under integrated (particularly the singlet of equivalent core protons), Figure A.3.47 We believe this is due to some aggregation of molecules in D_2O affecting the core environments as the integration of these environments also changes with pD.

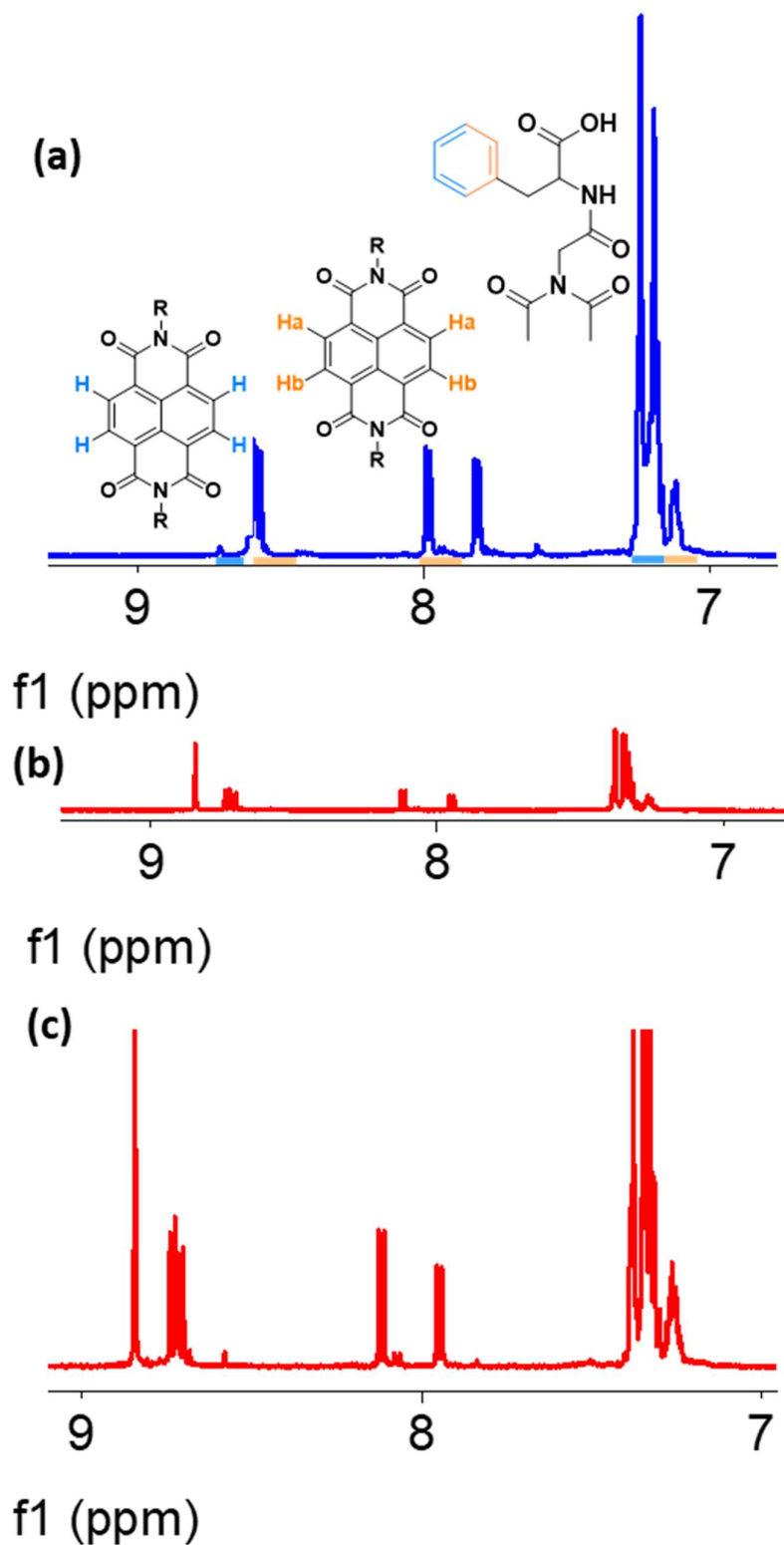


Figure A.3.43. Enlarged section of ^1H NMR spectra of 5 mg/mL NDI-GF in D_2O at (a) pH 11 and (b) pH 6. Due to low intensity of peaks at pH 6, a rescaled plot is shown (c). Signals corresponding to different proton environments for aggregate A and B are highlighted alongside their assignment.

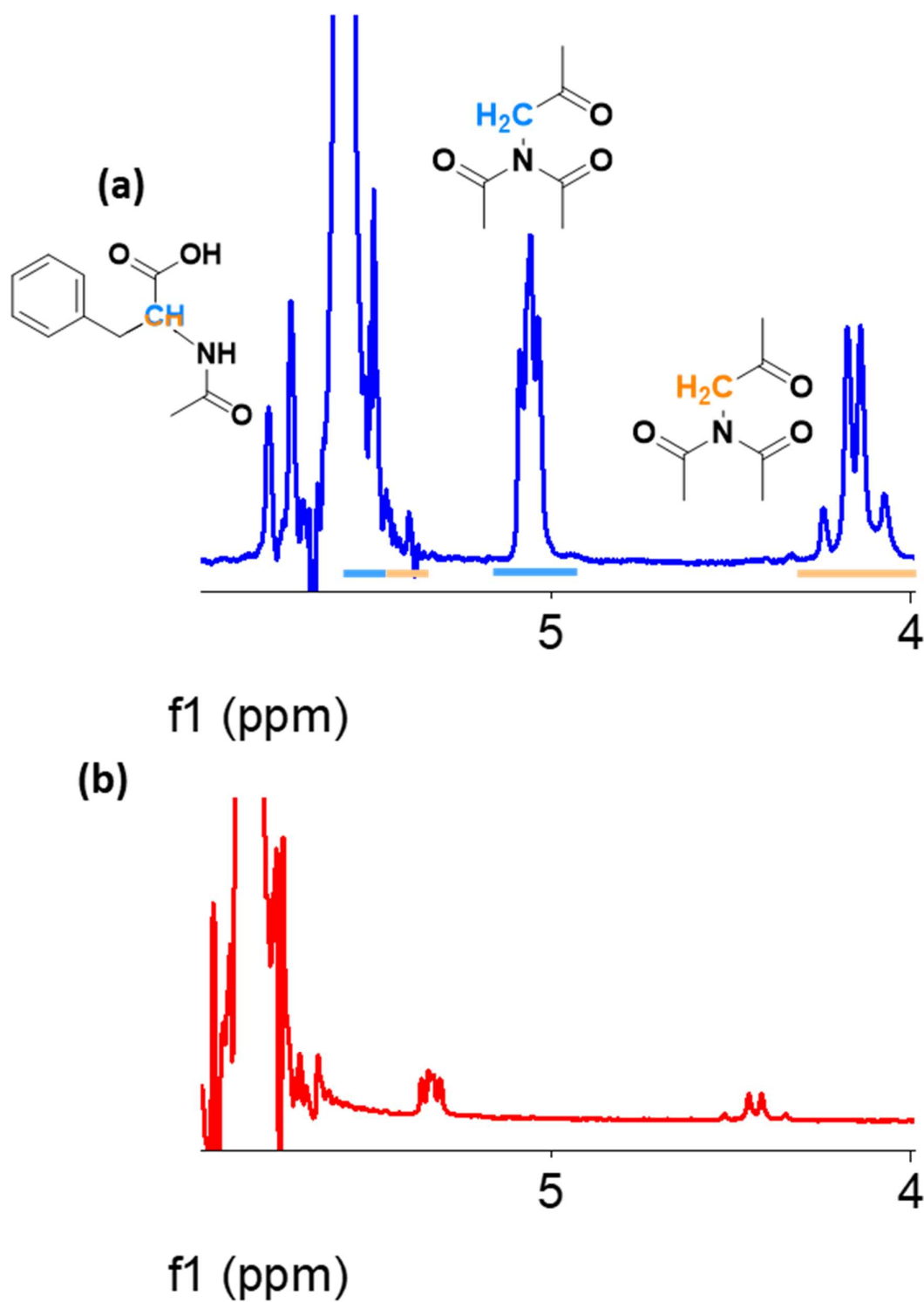


Figure A.3.44. Enlarged section of ¹H NMR spectra of 5 mg/mL NDI-GF in D₂O at (a) pD 11 and (b) pD 6. Signals corresponding to different proton environments for aggregate A and B are highlighted alongside their assignment.

Appendix

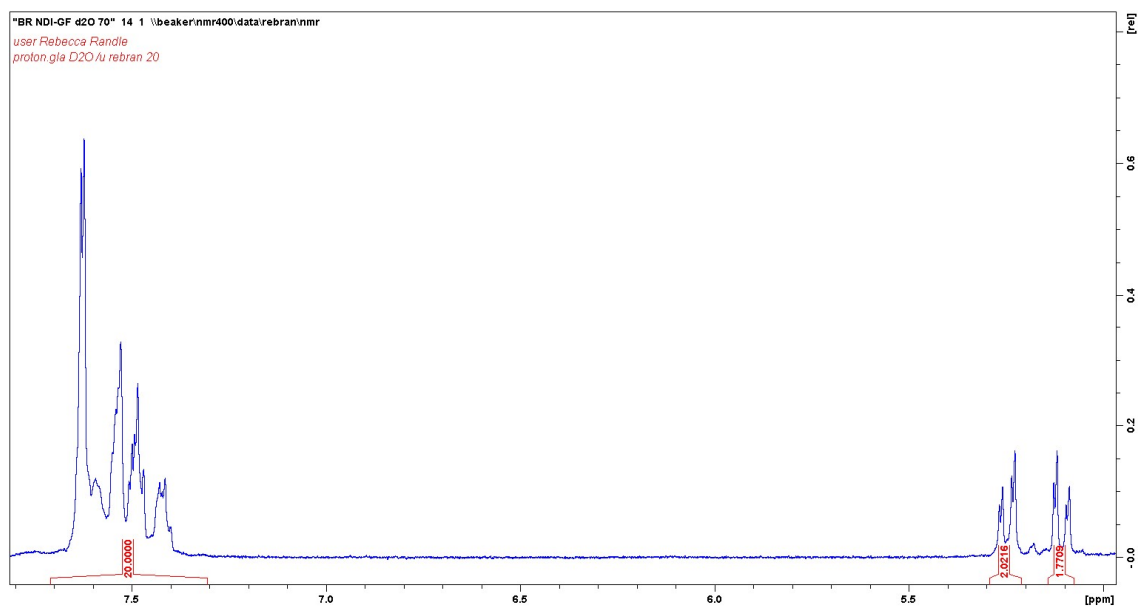


Figure A.3.45. Enlarged section of ^1H NMR spectra of 5 mg/mL **NDI-GF** in D_2O at 70 °C showing CH proton environments of each aggregate (and their relative integration) shifted from below the water peak.

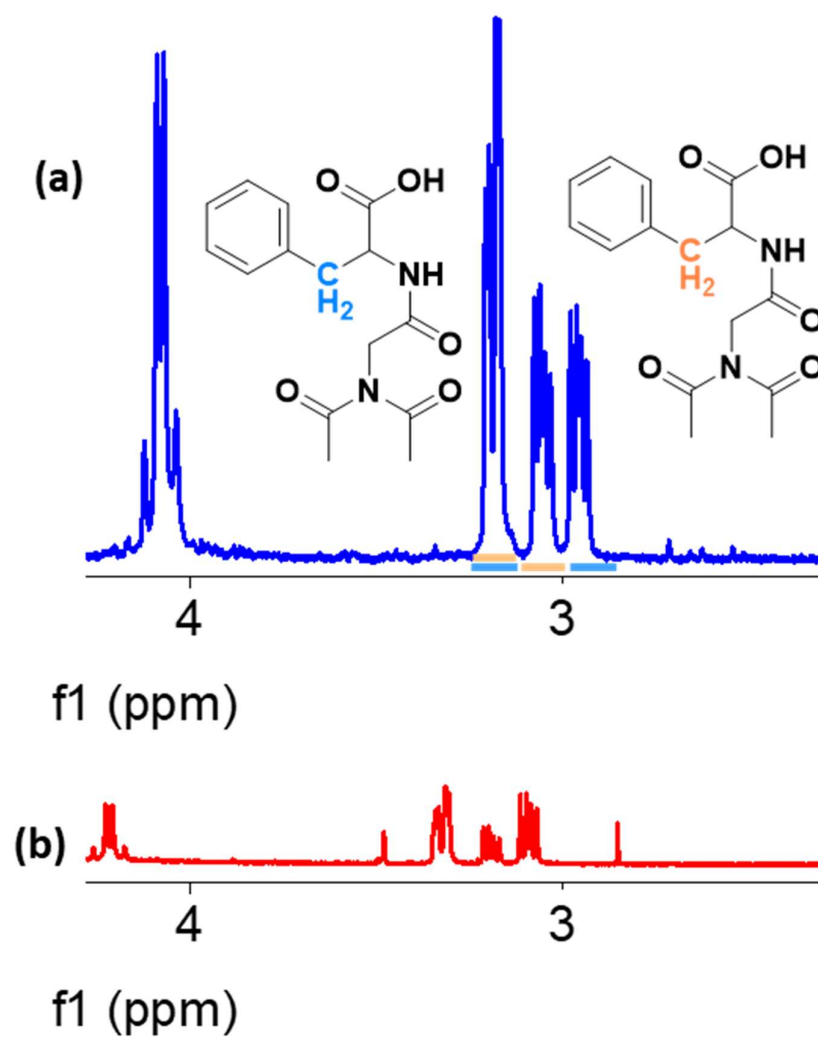


Figure A.3.46. Enlarged section of ^1H NMR spectra of 5 mg/mL NDI-GF in D_2O at (a) pD 11 and (b) pD 6. Signals corresponding to different proton environments for aggregate A and B are highlighted alongside their assignment.

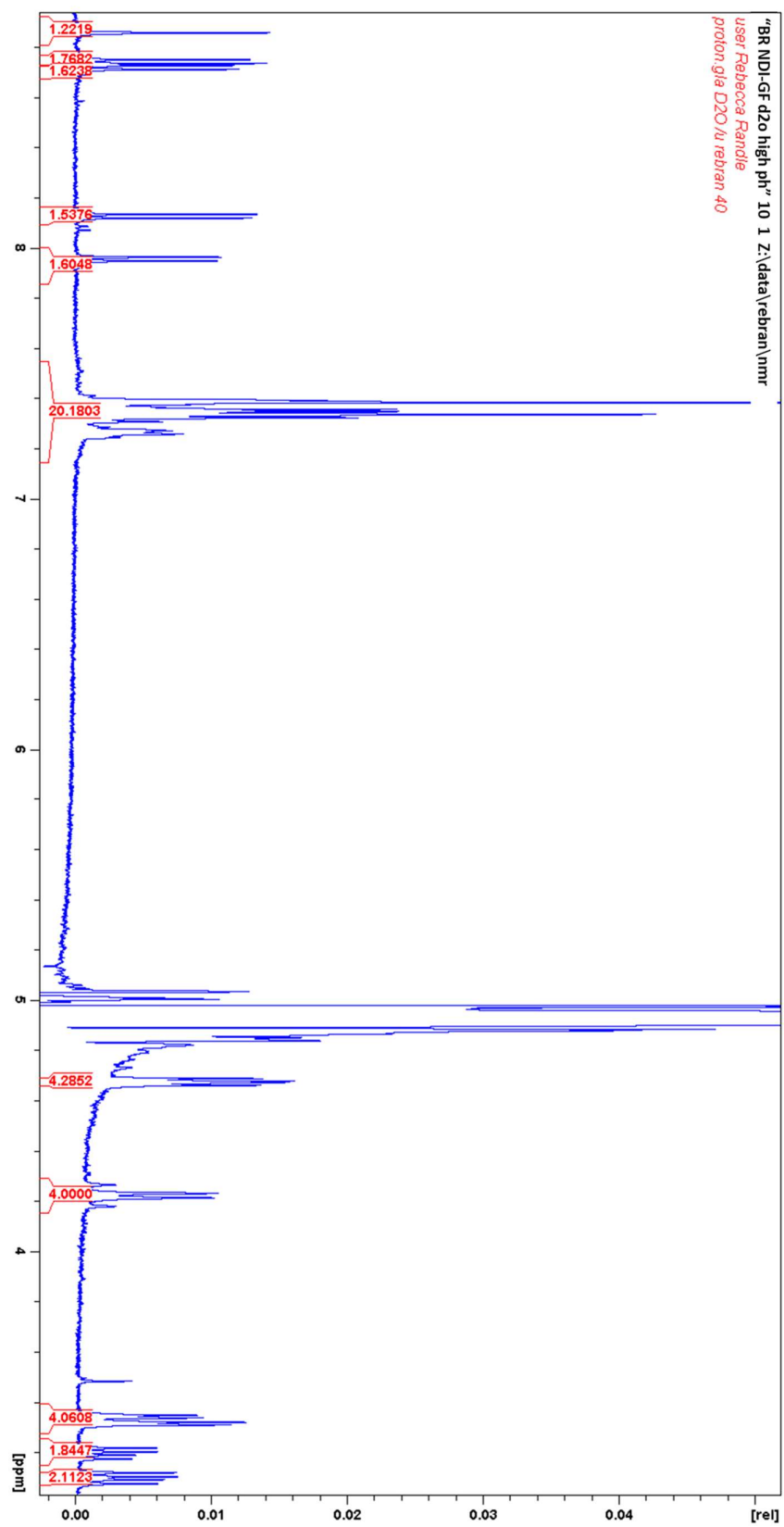


Figure A.3.47. ^1H NMR spectra of 5 mg/mL NDI-GF in D_2O at pH 11 showing integration.

Appendix

Increasing temperature to 50 and 70 °C did not result in any of the peaks converging, Figure A.3.48. Diffusion-ordered spectroscopy (DOSY) did not suggest different diffusion rate for each aggregate, Figure A.3.49-Figure A.3.56. Some impurities within D₂O (Figure A.3.57) cause small signals within the DOSY spectra that can be noted. For this reason, we do not think impurities are present in the NDI itself and that there are not two separate aggregates in solution with different diffusion coefficients.

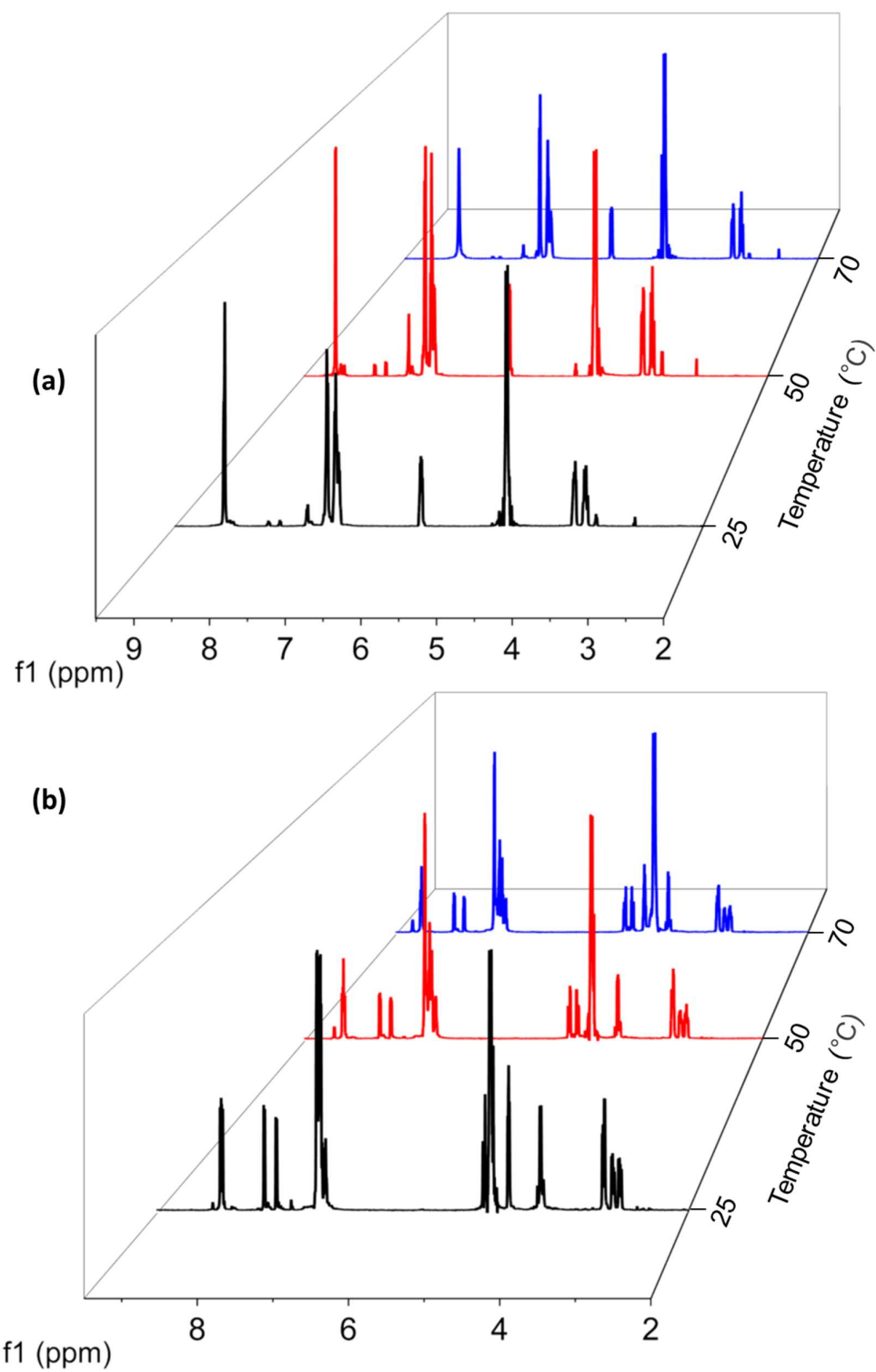


Figure A.3.48. ^1H NMR spectra of 5 mg/mL NDI-F (a) NDI-GF (b) in D_2O at (a) pD as temperature of the sample was increased.

Appendix

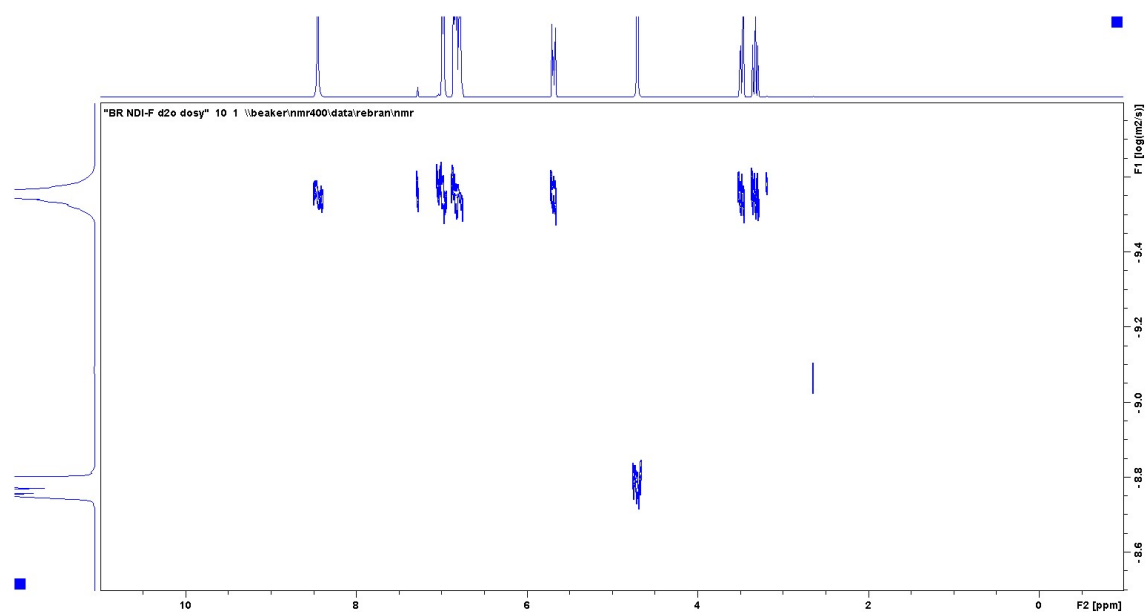


Figure A.3.49. DOSY spectra of 5 mg/mL NDI-F in D₂O at pD 11.

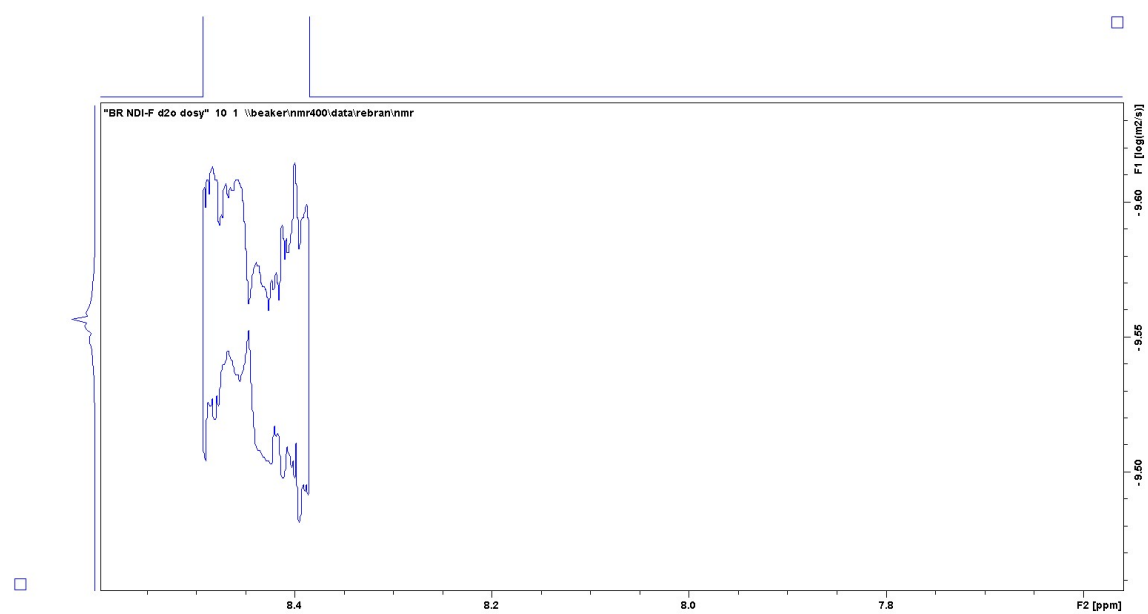


Figure A.3.50. Enlarged region of DOSY spectra of 5 mg/mL NDI-F in D₂O at pD 11.

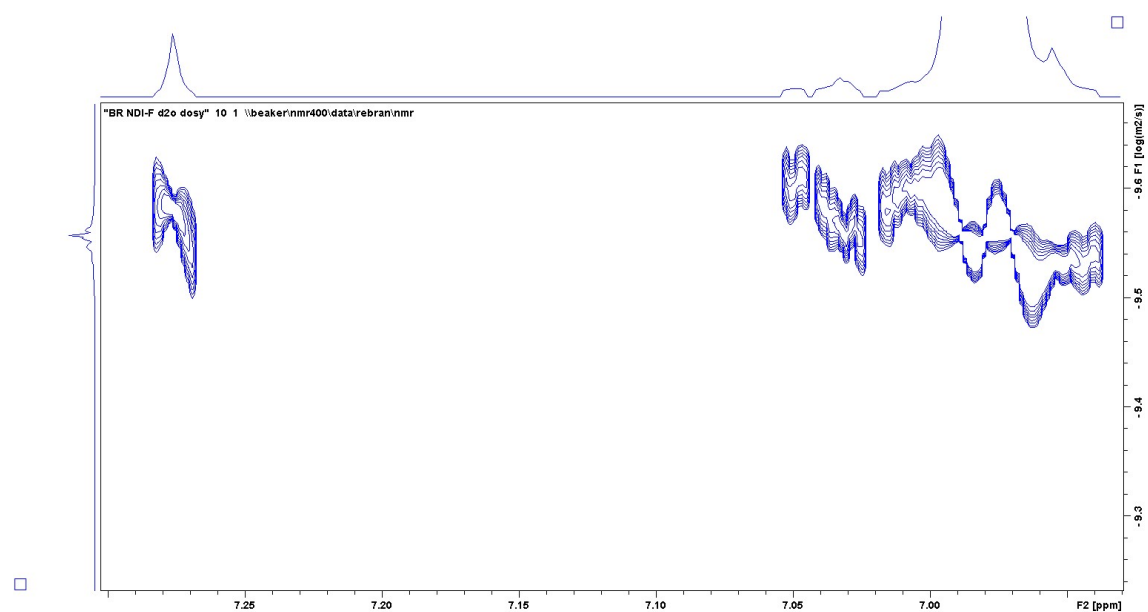


Figure A.3.51. Enlarged region of DOSY spectra of 5 mg/mL NDI-F in D₂O at pD 11.

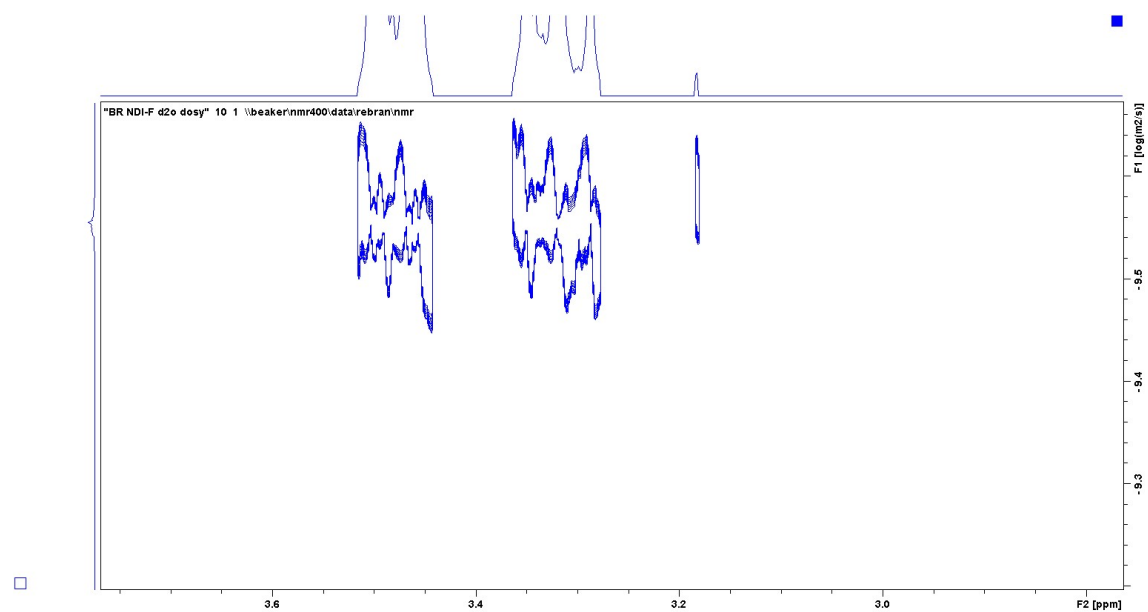


Figure A.3.52. Enlarged region of DOSY spectra of 5 mg/mL NDI-F in D₂O at pD 11.

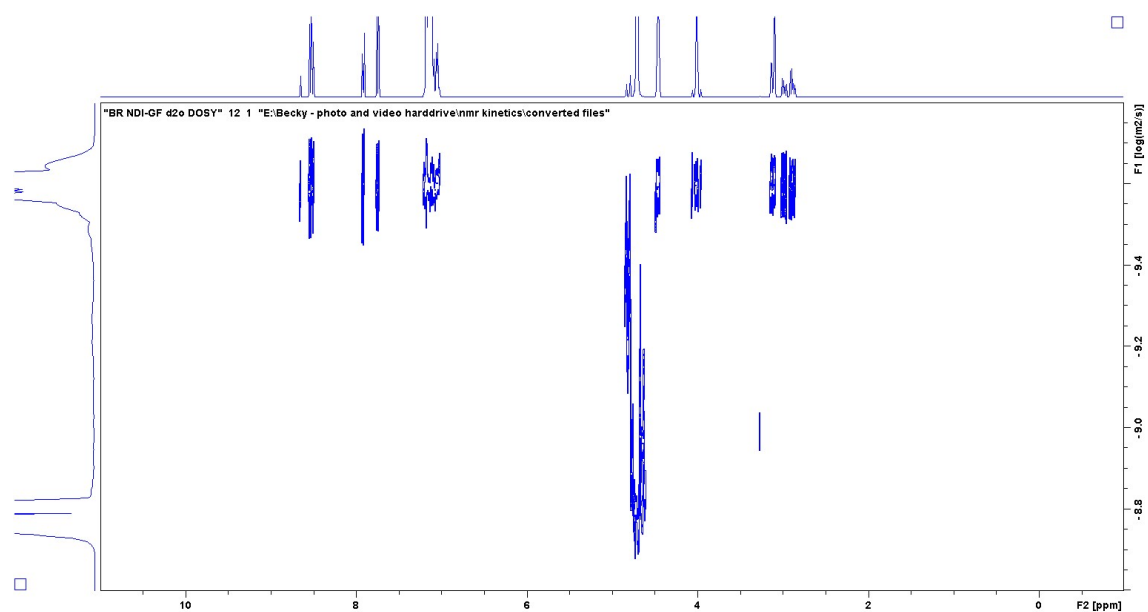


Figure A.3.53. DOSY spectra of 5 mg/mL NDI-GF in D₂O at pD 11.

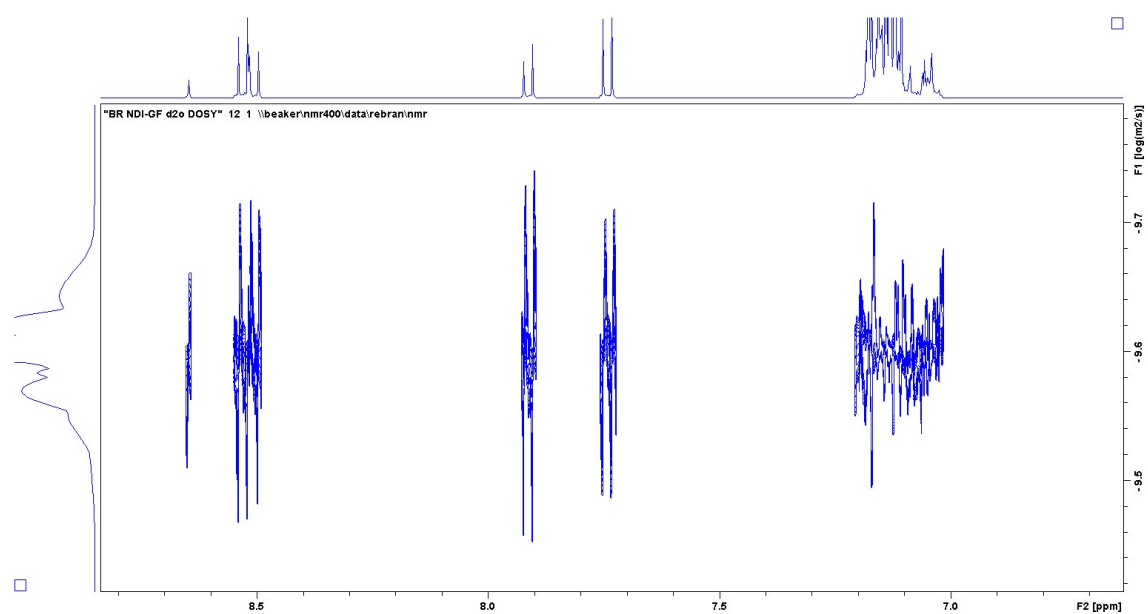


Figure A.3.54. Enlarged region of DOSY spectra of 5 mg/mL NDI-GF in D₂O at pD 11.

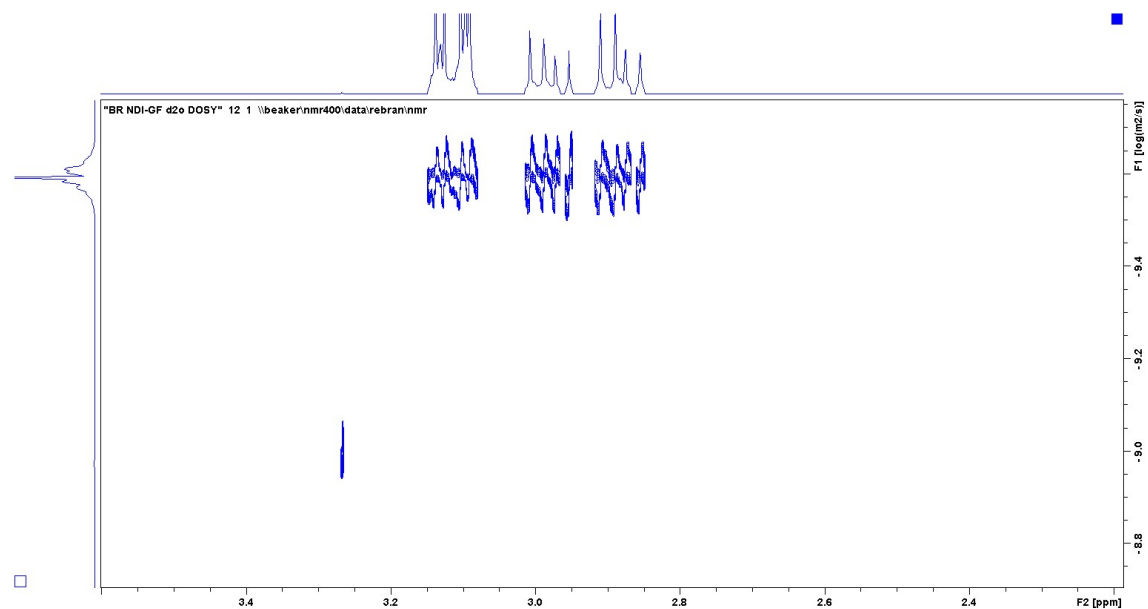


Figure A.3.55. Enlarged region of DOSY spectra of 5 mg/mL NDI-GF in D₂O at pD 11.

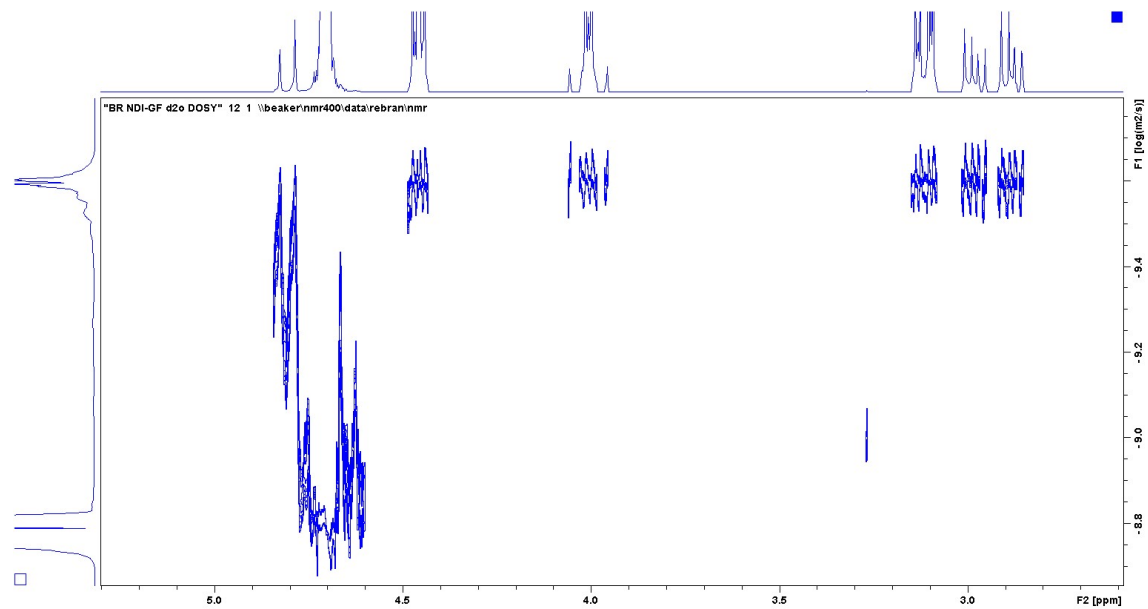


Figure A.3.56. Enlarged region of DOSY spectra of 5 mg/mL NDI-GF in D₂O at pD 11.

Appendix

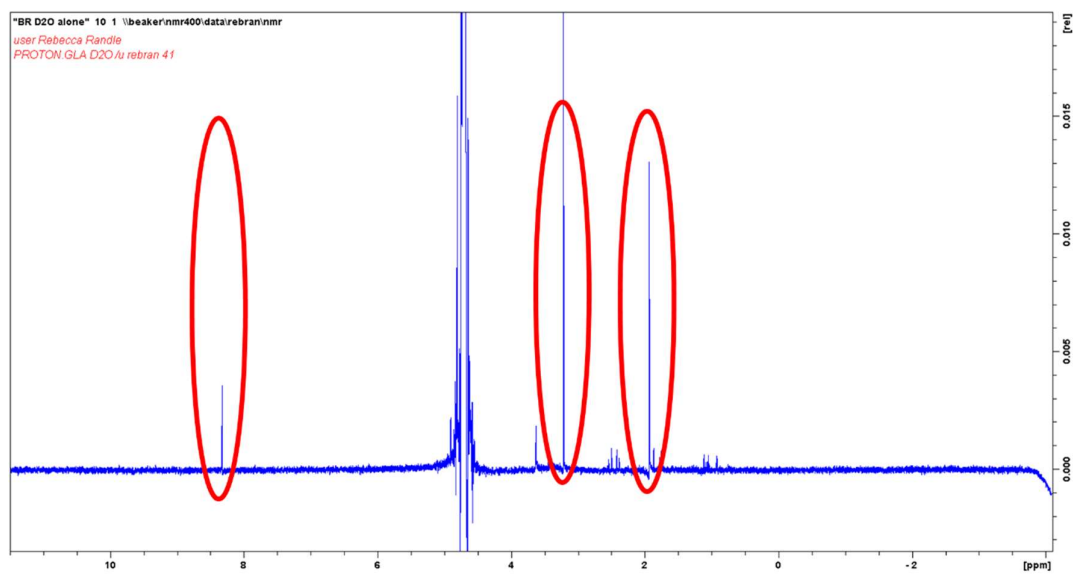


Figure A.3.57. ^1H NMR spectra of D_2O used in these experiments.

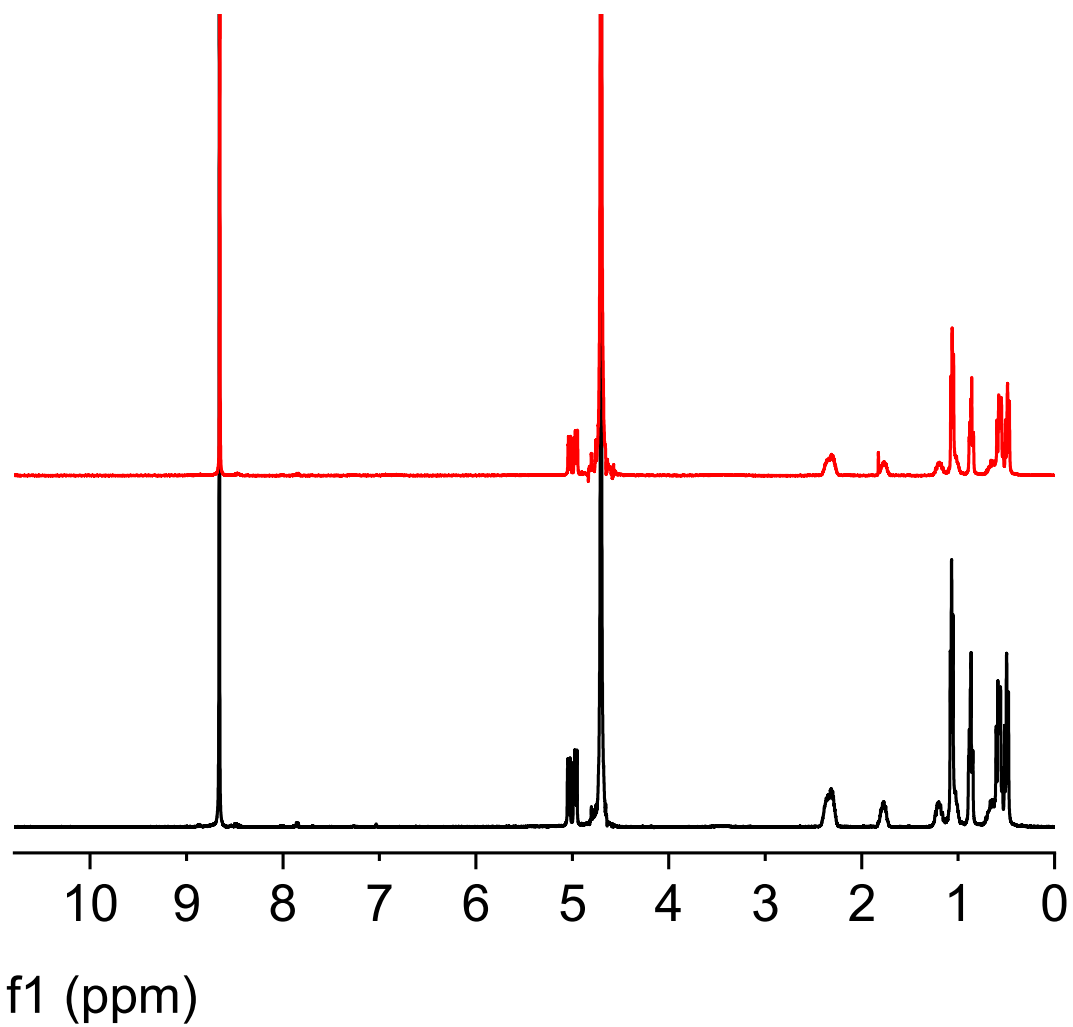


Figure A.3.58. ¹H NMR spectra of the neutral state of 10 mg/mL buffered **NDI-I** adjusted to pH 9 before (**black**) and after (**red**) excessive electrochemical cycling. Spectra taken after a period of 24 hours of relaxation following cycling.

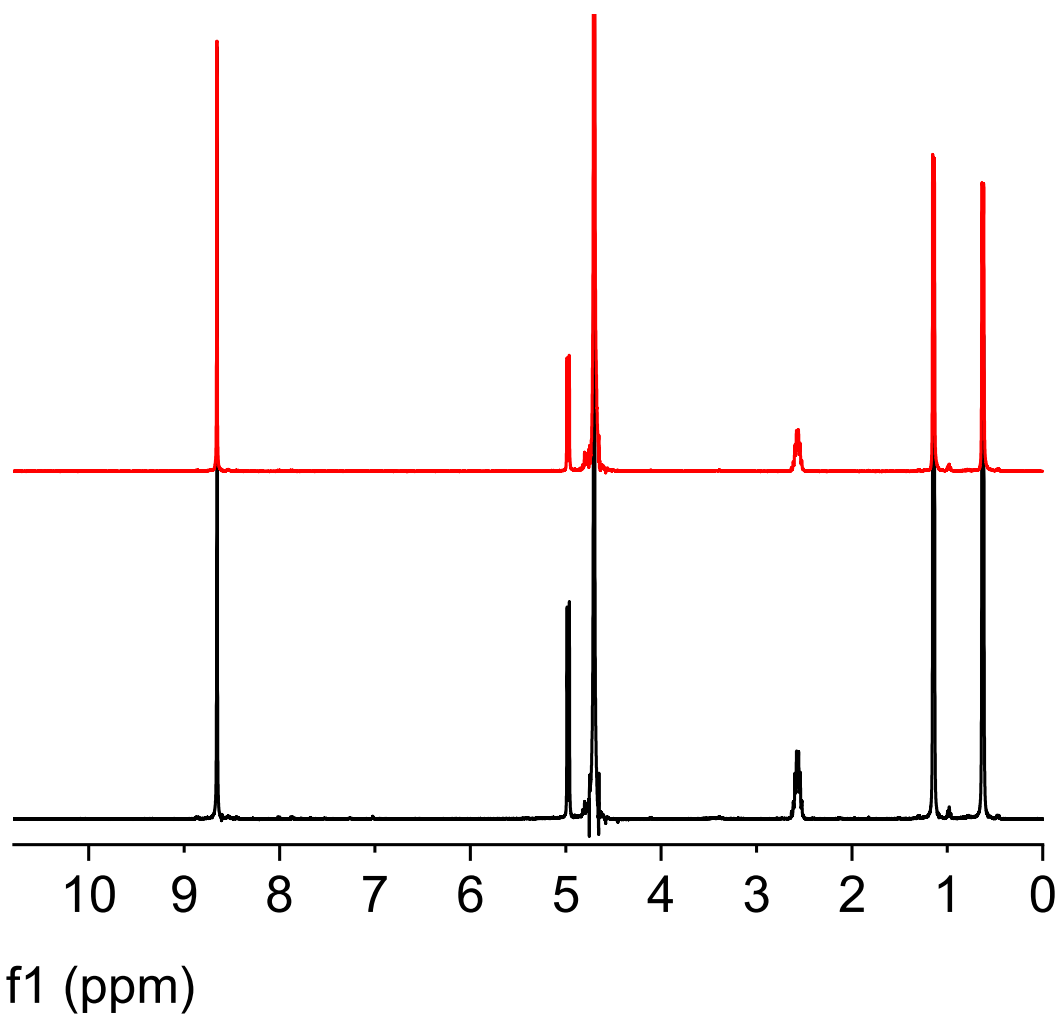


Figure A.3.59. ^1H NMR spectra of the neutral state of 10 mg/mL buffered **NDI-V** adjusted to pH 9 before (black) and after (red) excessive electrochemical cycling. Spectra taken after a period of 24 hours of relaxation following cycling.

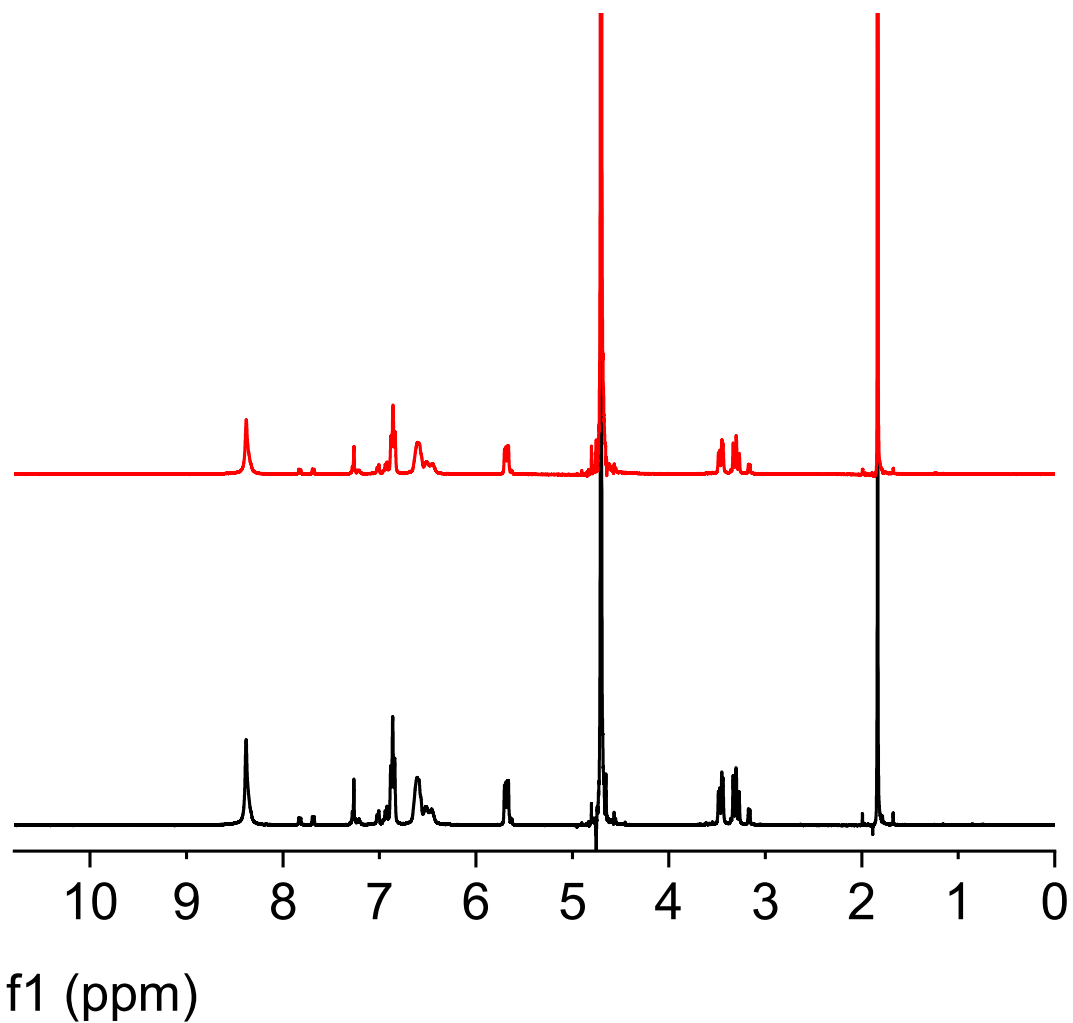


Figure A.3.60. ¹H NMR spectra of the neutral state of 10 mg/mL buffered **NDI-F** adjusted to pH 6 before (black) and after (red) excessive electrochemical cycling. Spectra taken after a period of 24 hours of relaxation following cycling.

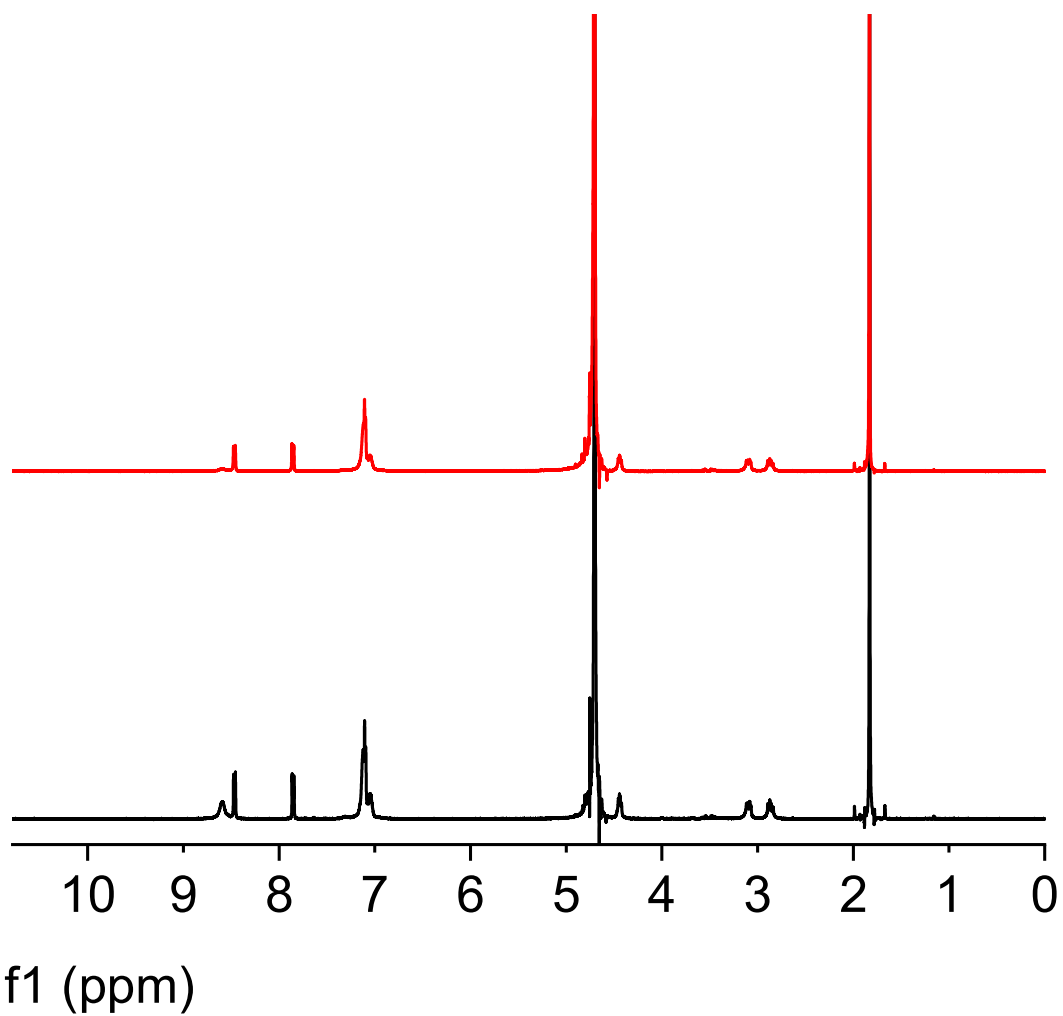


Figure A.3.61. ¹H NMR spectra of the neutral state of 10 mg/mL buffered **NDI-GF** adjusted to pH 6 before (black) and after (red) excessive electrochemical cycling. Spectra taken after a period of 24 hours of relaxation following cycling.

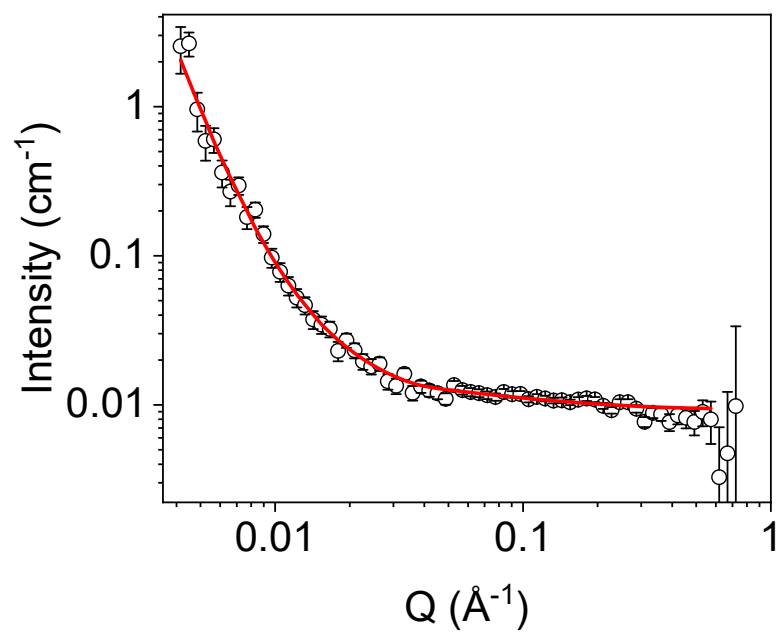


Figure A.3.62. Small angle neutron scattering data for a neutral buffered solution of 10 mg/mL **NDI-I** at pH 9 after one electrochemical cycle and relaxation for several days for several days (open circles) fitted to a flexible cylinder model combined with power law (red). Fit parameters can be found in Table A.3.16.

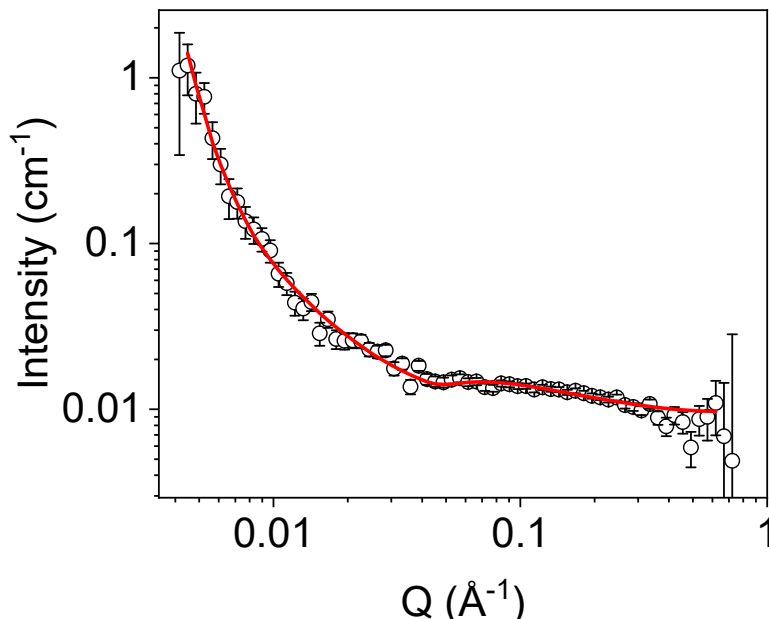


Figure A.3.63. Small angle neutron scattering data for a neutral buffered solution of 10 mg/mL NDI-I at pH 9 after 50 electrochemical cycles applying -2.7 V for 10 seconds and a sweeping oxidation potential between 0.1 and 0.95 V in order to switch between a neutral and reduced state followed by a relaxation period of several days (open circles) fitted to a flexible cylinder model combined with power law (red). Fit parameters can be found in Table A.3.16.

Table A.3.16. Parameters of SANS model fits seen in Figure A.3.62 and Figure A.3.63.

NDI-I electrochemically reduced and relaxed	Flexible cylinder combined with power law	
	Value	Error
Scale a	5.92E-04	2.54E-05
Scale b	1.44E-10	9.94E-12
Background (cm ⁻¹)	0.009279	9.99E-05
Length (Å)	2.39E+30	2.72E+30
Kuhn length (Å)	94.932	7.9
Radius (Å)	5.046	0.11151
Power	4.192	0.013739
Range	0.00416-0.57308	
Chi ²	1.1071	

NDI-I 50 electrochemical cycles and relaxed	Flexible cylinder combined with power law	
	Value	Error
Scale a	1.40E-03	3.51E-05
Scale b	5.23E-15	8.27E-16
Background (cm ⁻¹)	0.0096984	1.01E-04
Length (Å)	3.56E+95	2.56E+94
Kuhn length (Å)	72.727	2.5708
Radius (Å)	5.315	7.06E-02
Power	5.9971	2.96E-02
Range	0.00449-0.61892	
Chi ²	1.0179	

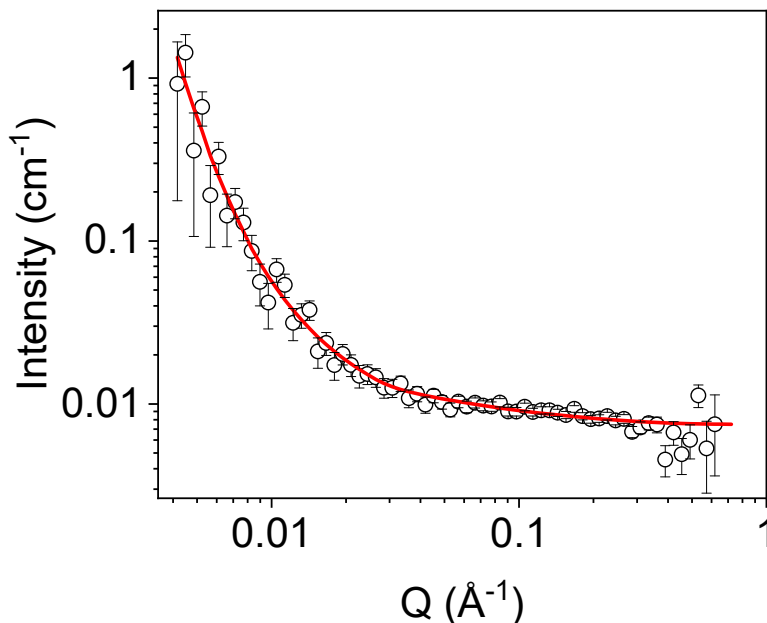


Figure A.3.64. Small angle neutron scattering data for a neutral buffered solution of 10 mg/mL **NDI-V** at pH 9 after one electrochemical cycle and relaxation for several days (open circles) fitted to a flexible cylinder model combined with power law (red). Fit parameters can be found in Table A.3.17.

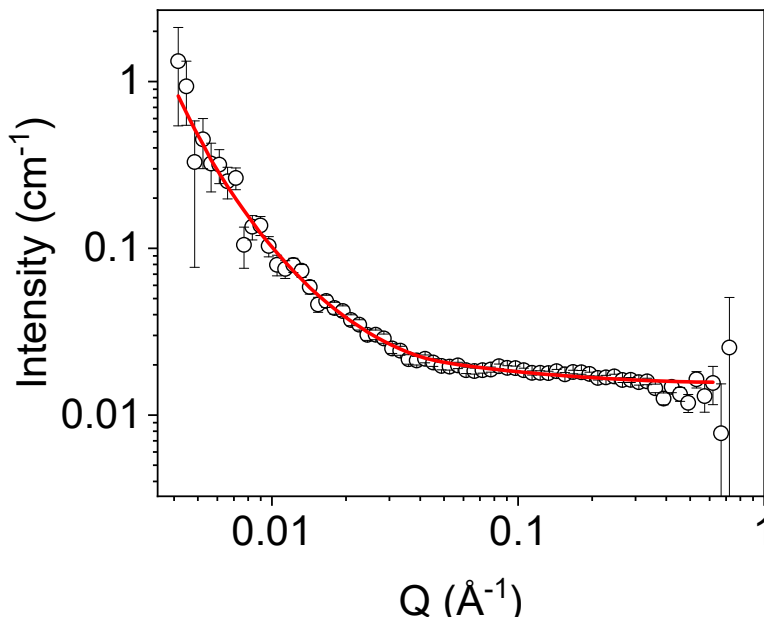


Figure A.3.65. Small angle neutron scattering data for a neutral buffered solution of 10 mg/mL **NDI-V** at pH 9 after 50 electrochemical cycles applying -2.7 V for 10 seconds and a sweeping oxidation potential between 0.1 and 0.95 V in order to switch between a neutral and reduced state followed by a relaxation period of several days (open circles) fitted to a flexible cylinder model combined with power law (red). Fit parameters can be found in Table A.3.17.

Table A.3.17. Parameters of SANS model fits seen in Figure A.3.64 and Figure A.3.65.

NDI-V electrochemically reduced and relaxed	Flexible cylinder combined with power law	
	Value	Error
Scale a	5.31E-04	2.53E-05
Scale b	2.91E-12	4.25E-13
Background (cm ⁻¹)	0.007503	9.91E-05
Length (Å)	5.40E+13	6.96E+14
Kuhn length (Å)	115.62	11.5
Radius (Å)	5.15	0.127
Power	4.7965	2.82E-02
Range	0.00416-0.72191	
Chi ²	1.0343	

NDI-V 50 electrochemical cycles and relaxed	Flexible cylinder combined with power law	
	Value	Error
Scale a	8.61E-04	2.44E-05
Scale b	1.43E-10	2.85E-11
Background (cm ⁻¹)	1.59E-02	1.55E-04
Length (Å)	2.26E+10	1.45E+11
Kuhn length (Å)	81.133	3.9229
Radius (Å)	4.9449	7.15E-02
Power	3.9739	3.99E-02
Range	0.00416-0.61892	
Chi ²	1.3035	

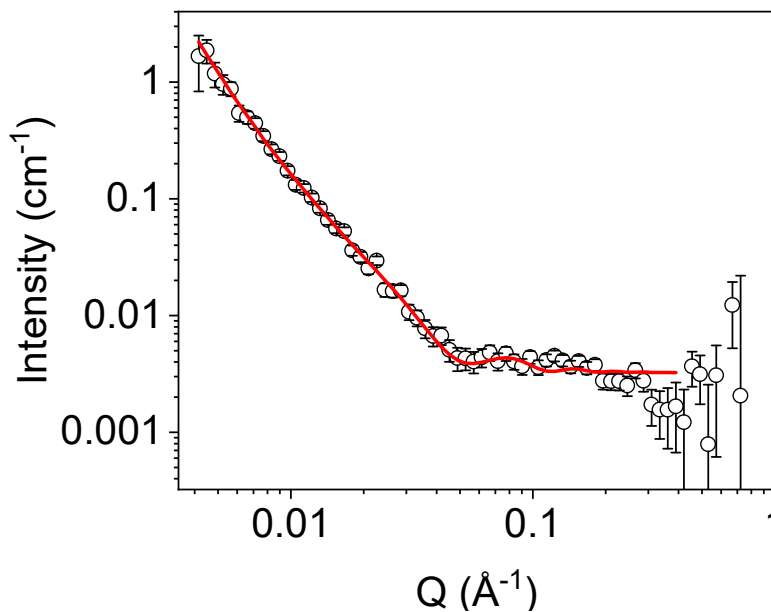


Figure A.3.66. Small angle neutron scattering data for a neutral buffered solution of 10 mg/mL **NDI-F** at pH 6 after application of -2.7 V for 5 minutes and relaxing for several days (open circles) fitted to a hollow cylinder model combined with power law (red). Fit parameters can be found in Table A.3.18.

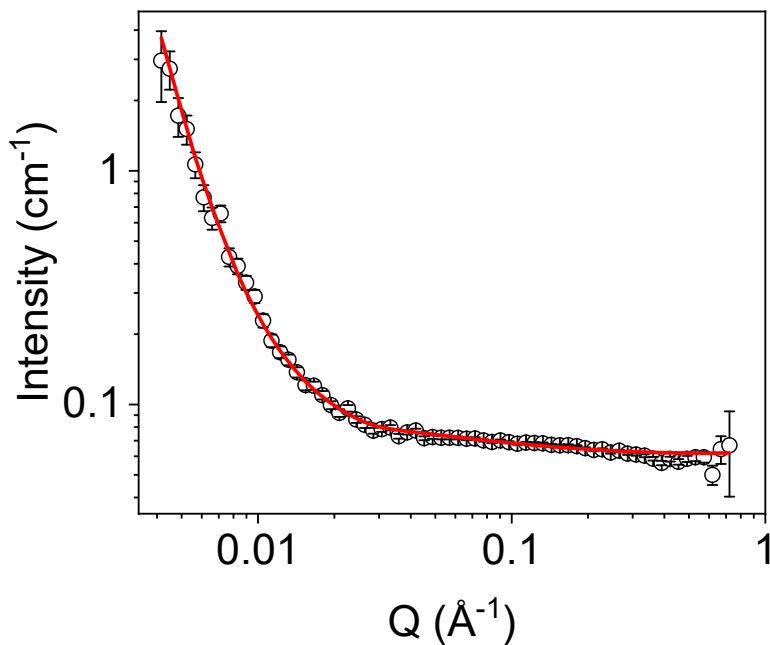


Figure A.3.67. Small angle neutron scattering data for a neutral buffered solution of 10 mg/mL **NDI-F** at pH 6 after 50 electrochemical cycles applying -2.7 V for 10 seconds and a sweeping oxidation potential between 0.1 and 0.95 V in order to switch between a neutral and reduced state followed by a relaxation period of several days (open circles) fitted to a flexible cylinder model combined with power law (red). Fit parameters can be found in Table A.3.18.

Table A.3.18. Parameters of SANS model fits seen in Figure A.3.66 and Figure A.3.67.

NDI-F electrochemically reduced and relaxed	Hollow cylinder combined with power law	
	Value	Error
Scale a	4.17E+01	2.21
Scale b	4.40E-08	1.14E-09
Background (cm ⁻¹)	0.003242	1.01E-04
Length (Å)	3.94E+02	1.15E+02
Radius (Å)	41.80	2.18
Thickness (Å)	10.536	0.5527
Power	3.1933	6.85E-03
Range	0.00416-0.39003	
Chi ²	1.146	

NDI-F 50 electrochemical cycles and relaxed	Flexible cylinder combined with power law	
	Value	Error
Scale a	1.85E-03	3.26E-05
Scale b	5.63E-10	3.00E-11
Background (cm ⁻¹)	0.061958	1.26E-04
Length (Å)	5.38E+38	2.94E+39
Kuhn length (Å)	111.96	4.2725
Radius (Å)	6.3855	5.94E-02
Power	4.0189	1.06E-02
Range	0.00416-0.72191	
Chi ²	2.6594	

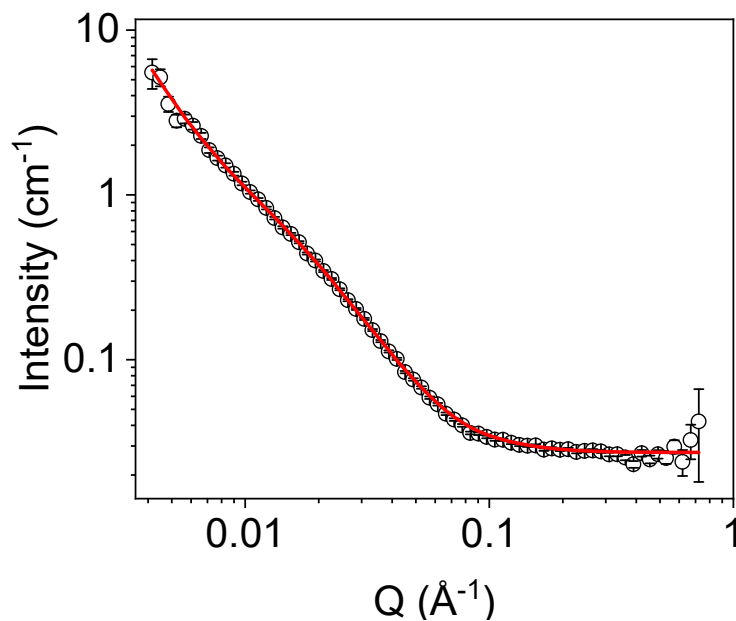


Figure A.3.68. Small angle neutron scattering data for a neutral buffered solution of 10 mg/mL **NDI-GF** at pD after one electrochemical cycle and relaxation for several days for several days (open circles) fitted to a flexible elliptical cylinder model combined with power law (red). Fit parameters can be found in Table A.3.19.

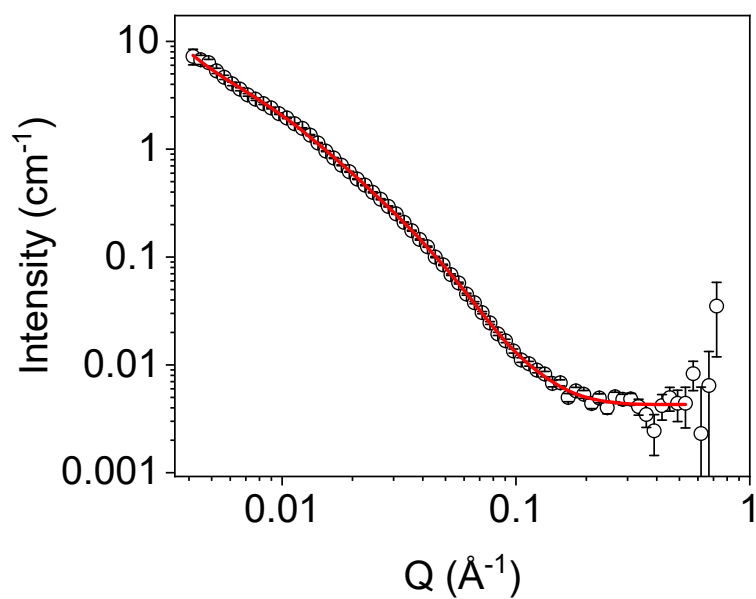


Figure A.3.69. Small angle neutron scattering data for a neutral buffered solution of 10 mg/mL **NDI-GF** at pH 6 after 50 electrochemical cycles applying -2.7 V for 10 seconds and a sweeping oxidation potential between 0.1 and 0.95 V in order to switch between a neutral and reduced state followed by a relaxation period of several days (open circles) fitted to a flexible elliptical cylinder model combined with power law (red). Fit parameters can be found in Table A.3.19.

Appendix

Table A.3.19. Parameters of SANS model fits seen in Figure A.3.68-Figure A.3.69.

NDI-GF electrochemically reduced and relaxed	Flexible elliptical cylinder combined with power law	
	Value	Error
Scale a	1.19E-04	7.87E-07
Scale b	3.32E-06	4.76E-08
Background (cm ⁻¹)	0.02576	0.001137
Length (Å)	1.32E+03	27.868
Kuhn length (Å)	45.638	0.3583
Radius (Å)	7.1657	1.96E-02
Ratio Axis	6.2301	1.69E-02
Power	2.5443	2.35E-02
Range	0.00416-0.72191	
Chi ²	1.5126	
NDI-GF 50 electrochemical cycles and relaxed	Flexible elliptical cylinder combined with power law	
	Value	Error
Scale a	1.18E ⁻⁰⁴	2.95E-07
Scale b	3.09E-07	9.02E-09
Background (cm ⁻¹)	0.004282	1.05E-04
Length (Å)	6.48E+03	1.46E+02
Kuhn length (Å)	15.262	5.56E-02
Radius (Å)	8.8361	1.32E-02
Ratio Axis	4.7215	6.99E-03
Power	2.9474	6.33E-03
Range	0.00416-0.53063	
Chi ²	1.6282	

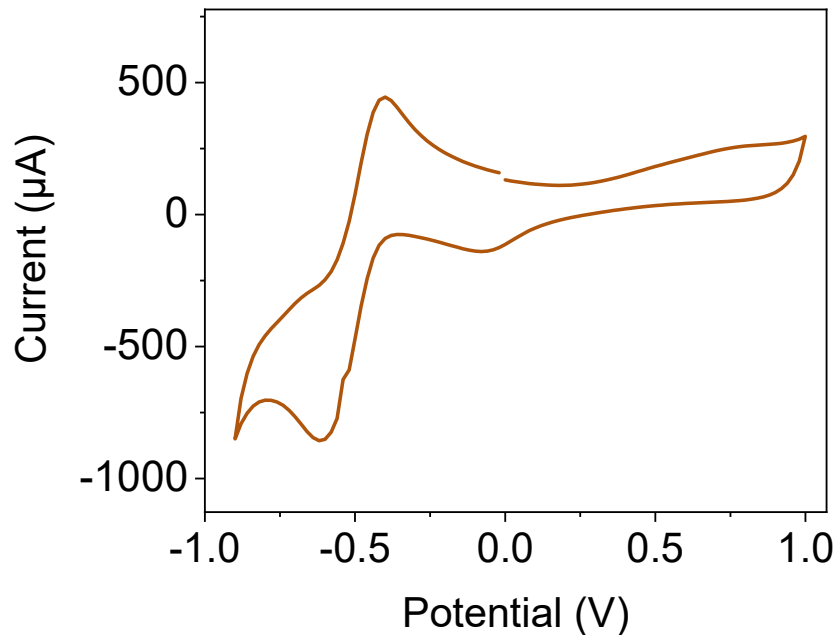
A.3.3 *In situ* measurement

Figure A.3.70. Cyclic voltammogram of buffered **NDI-GF** collected at pH 6 at 10 mg/mL within spectro-electrochemical cell setup (vs Pt). The scan rate of the cyclic voltammograms was 0.2 V/s.

The initial Kuhn length of a solution of **NDI-GF** is approximately 20 Å lower than that calculated from the fit to the measurement in a standard cuvette, calculated radius is approximately 8 Å larger and the axis ratio approximately 2 units smaller, Table A.3.14 and Table A.3.20. The Kuhn length of **NDI-I** and **NDI-V** are also estimated lower in the spectro-electrochemical cell by approximately 34 Å, Table A.3.7-Table A.3.9 and Table A.3.21-Table A.3.22. The radii of both **NDI-I** and **NDI-V** are consistent between the data collected in the spectro-electrochemical cell and in a cuvette, Table A.3.7-Table A.3.9 and Table A.3.21-Table A.3.22.

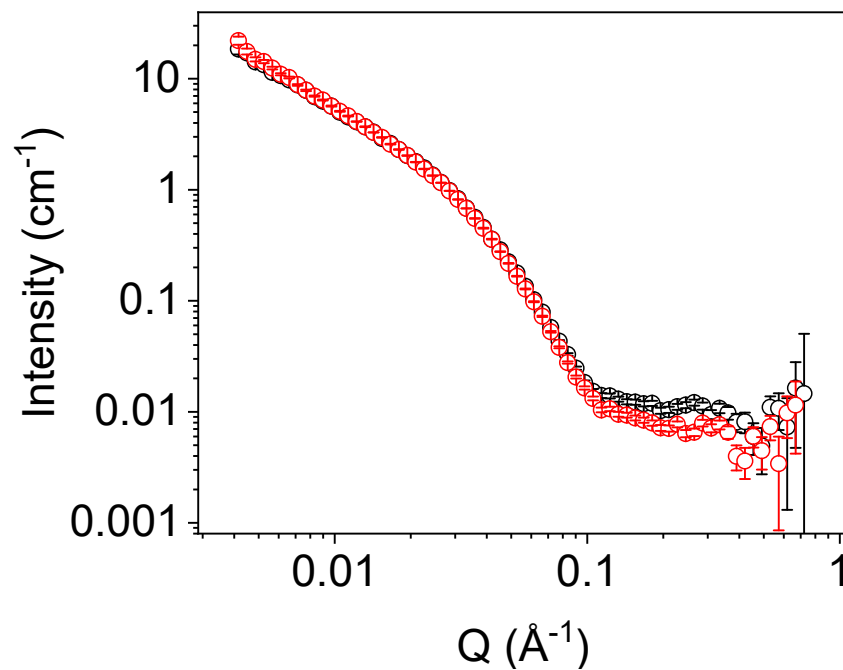


Figure A.3.71. Small angle neutron scattering data for a neutral buffered solution of 10 mg/mL **NDI-GF** at pH 6 in a spectro-electrochemical cell (**black**) and in a standard quartz cuvette (**red**) performed on the exact same solution in the same ISIS visit.

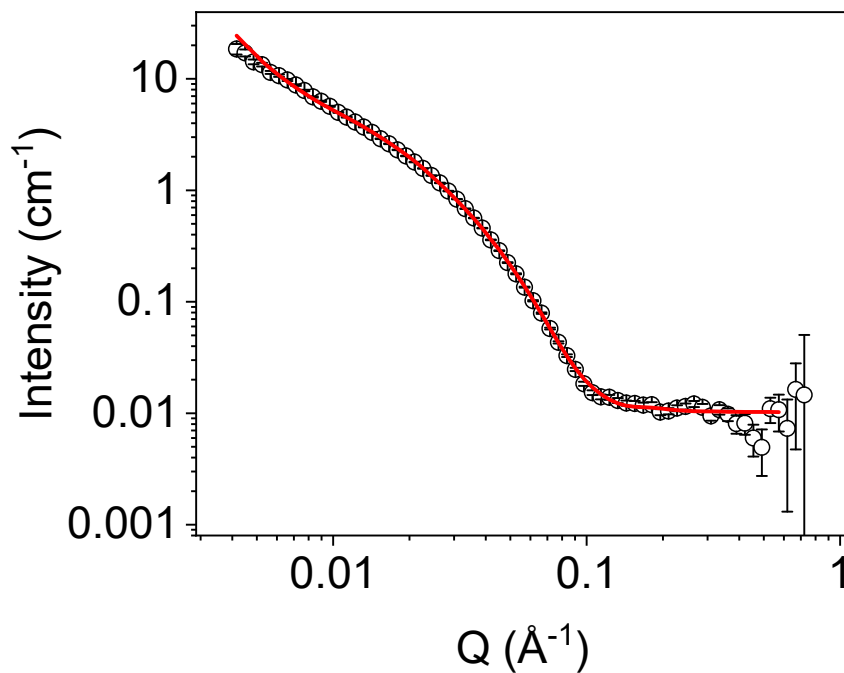


Figure A.3.72. Small angle neutron scattering data for a neutral buffered solution of 10 mg/mL NDI-GF at pD 6 (open circles) fitted to a flexible elliptical cylinder model combined with power law (red). Data taken in spectro-electrochemical cell. Fit parameters can be found in Table A.3.20.

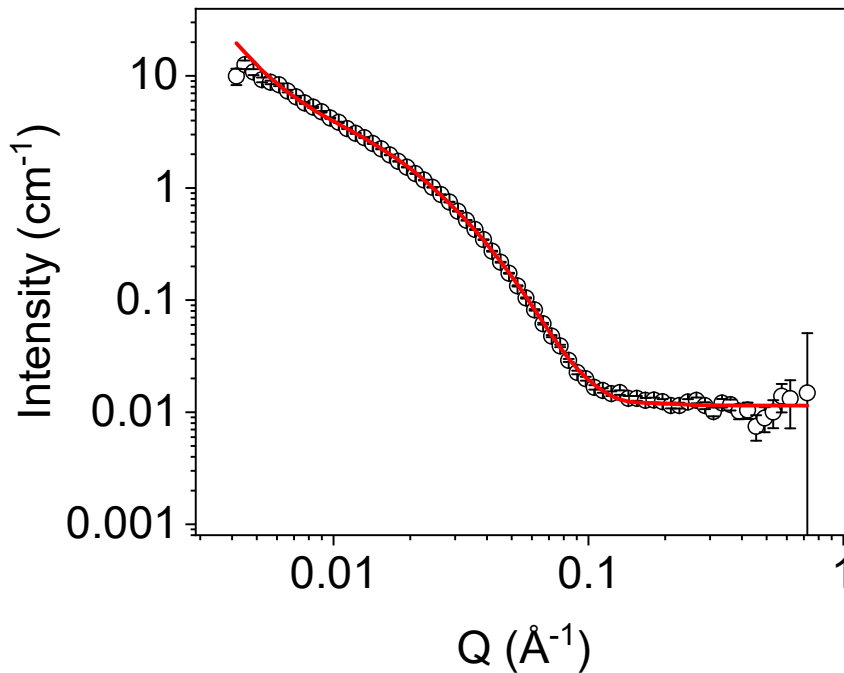


Figure A.3.73. Small angle neutron scattering data for a buffered reduced solution of 10 mg/mL NDI-GF at pD 6 (open circles) fitted to a flexible elliptical cylinder model combined with power law (red). Data taken in spectro-electrochemical cell. Fit parameters can be found in Table A.3.20.

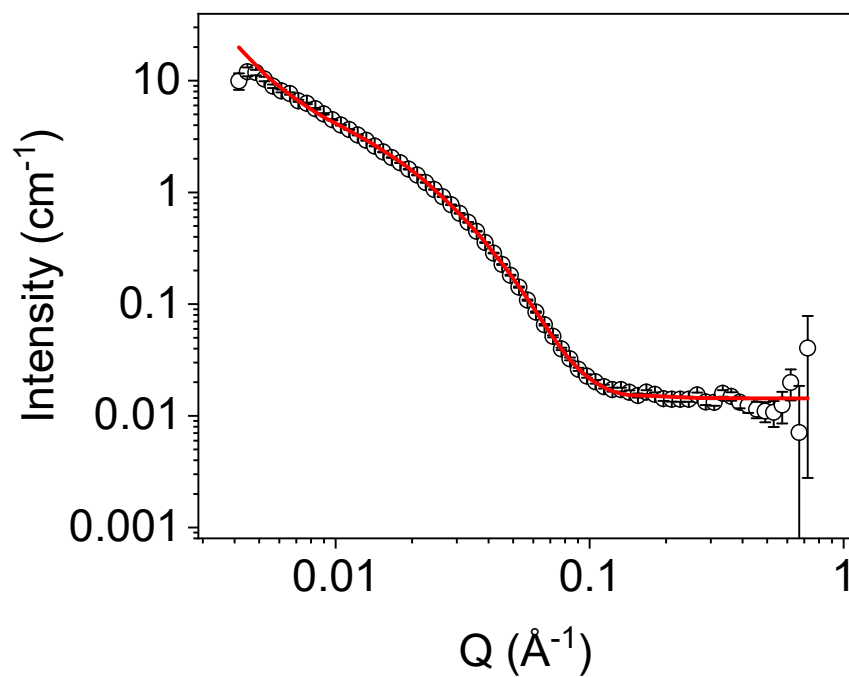


Figure A.3.74. Small angle neutron scattering data for a buffered electrochemically oxidised solution of 10 mg/mL **NDI-GF** at pH 6 (open circles) fitted to a flexible elliptical cylinder model combined with power law (red). Data taken in spectro-electrochemical cell. Data taken in spectro-electrochemical cell. Fit parameters can be found in Table A.3.20.

Table A.3.20. Parameters of SANS model fits seen in Figure A.3.72-Figure A.3.74.

NDI-GF neutral	Flexible elliptical cylinder combined with power law	
	Value	Error
Scale a	6.76E-04	1.03E-06
Scale b	3.10E-06	2.72E-08
Background (cm ⁻¹)	0.01023	1.53E-04
Length (Å)	1031.50	6.00
Kuhn length (Å)	40.947	0.11339
Radius (Å)	25.132	0.02613
Ratio Axis	1.9368	0.001881
Power	2.8273	1.93E-03
Range	0.00416-0.57308	
Chi ²	4.8588	
NDI-GF electrochemically reduced	Flexible elliptical cylinder combined with power law	
	Value	Error
Scale a	4.89E-04	8.83E-07
Scale b	1.42E-06	1.51E-08
Background (cm ⁻¹)	0.011439	1.52E-04
Length (Å)	985.70	6.67
Kuhn length (Å)	43.057	0.14539
Radius (Å)	23.333	0.028803
Ratio Axis	2.1808	0.002541
Power	2.9305	2.31E-03
Range	0.00416-0.72191	
Chi ²	4.0192	
NDI-GF electrochemically oxidised	Flexible elliptical cylinder combined with power law	
	Value	Error
Scale a	5.32E-04	9.46E-07
Scale b	1.73E-06	1.81E-08
Background (cm ⁻¹)	0.014325	1.54E-04
Length (Å)	958.25	6.43
Kuhn length (Å)	45.445	0.15312
Radius (Å)	24.908	0.030349
Ratio Axis	2.0408	0.002335
Power	2.8958	2.29E-03
Range	0.00416-0.72191	
Chi ²	4.1256	

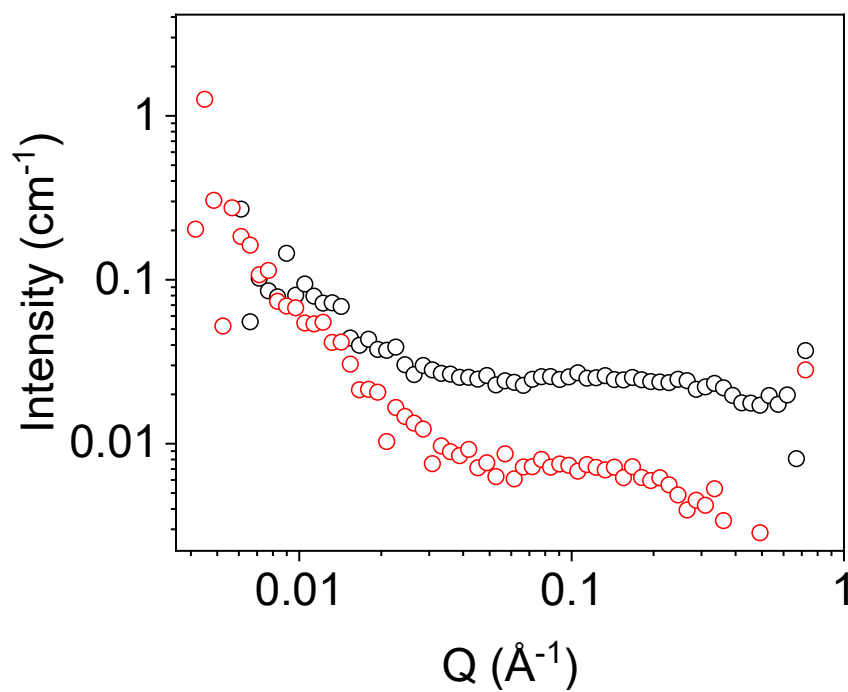


Figure A.3.75. Small angle neutron scattering data for a neutral buffered solution of 10 mg/mL **NDI-I** at pD 9 in a spectro-electrochemical cell (**black**) and in a standard quartz cuvette (**red**).

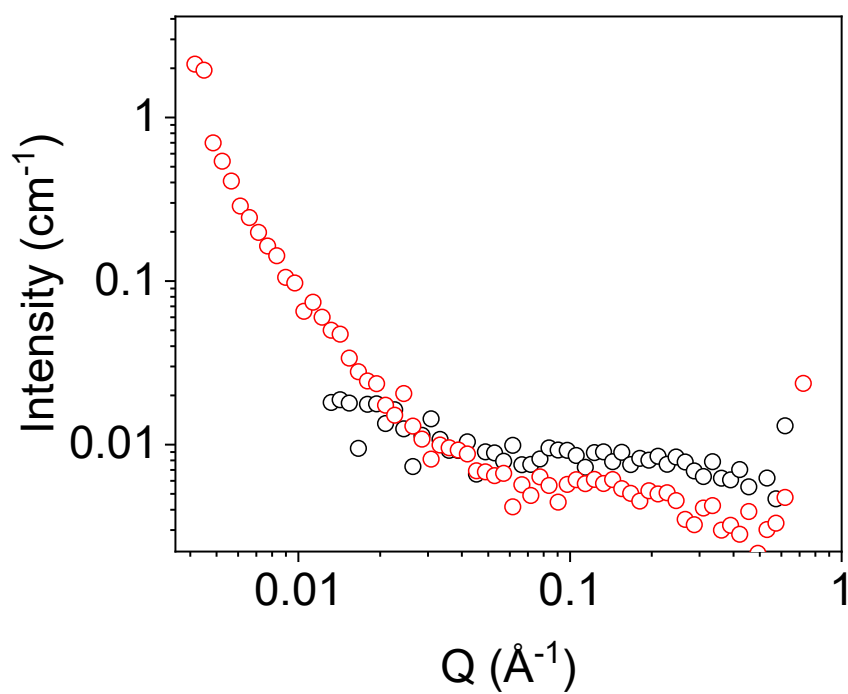


Figure A.3.76. Small angle neutron scattering data for a neutral buffered solution of 10 mg/mL **NDI-V** at pD 9 in a spectro-electrochemical cell (**black**) and in a standard quartz cuvette (**red**).

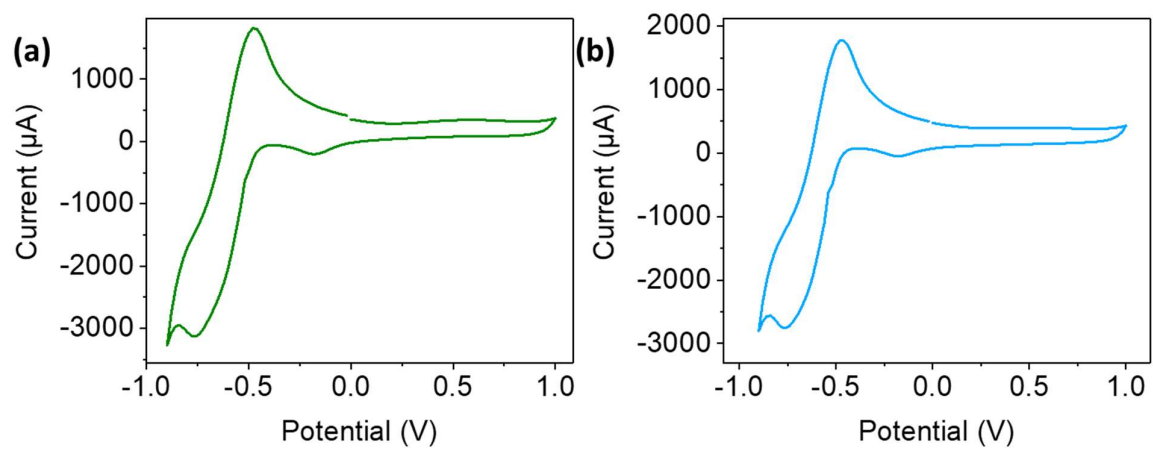


Figure A.3.77. Cyclic voltammograms of buffered 10 mg/mL **NDI-I** and **NDI-V** collected at pH 9 at 10 mg/mL within spectro-electrochemical cell setup (vs Pt). The scan rate of the cyclic voltammograms was 0.2 V/s.

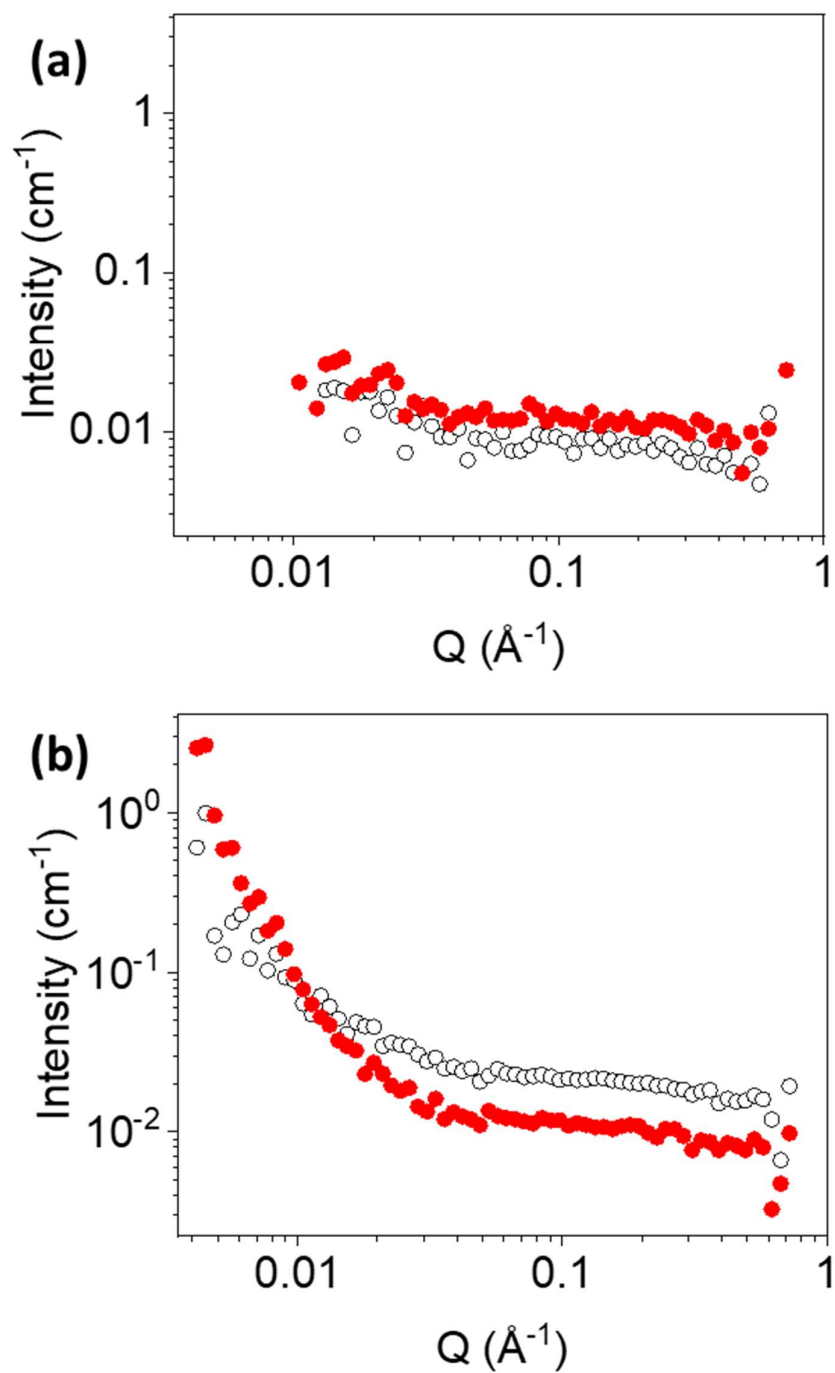


Figure A.3.78. Small angle neutron scattering data for a buffered solution of 10 mg/mL NDI-I at pH 9 in a neutral state before electrochemical reduction (black) and after one electrochemical reduction and oxidation (red). Measurements taken in (a) spectro-electrochemical cell and (b) in a standard quartz cuvette.

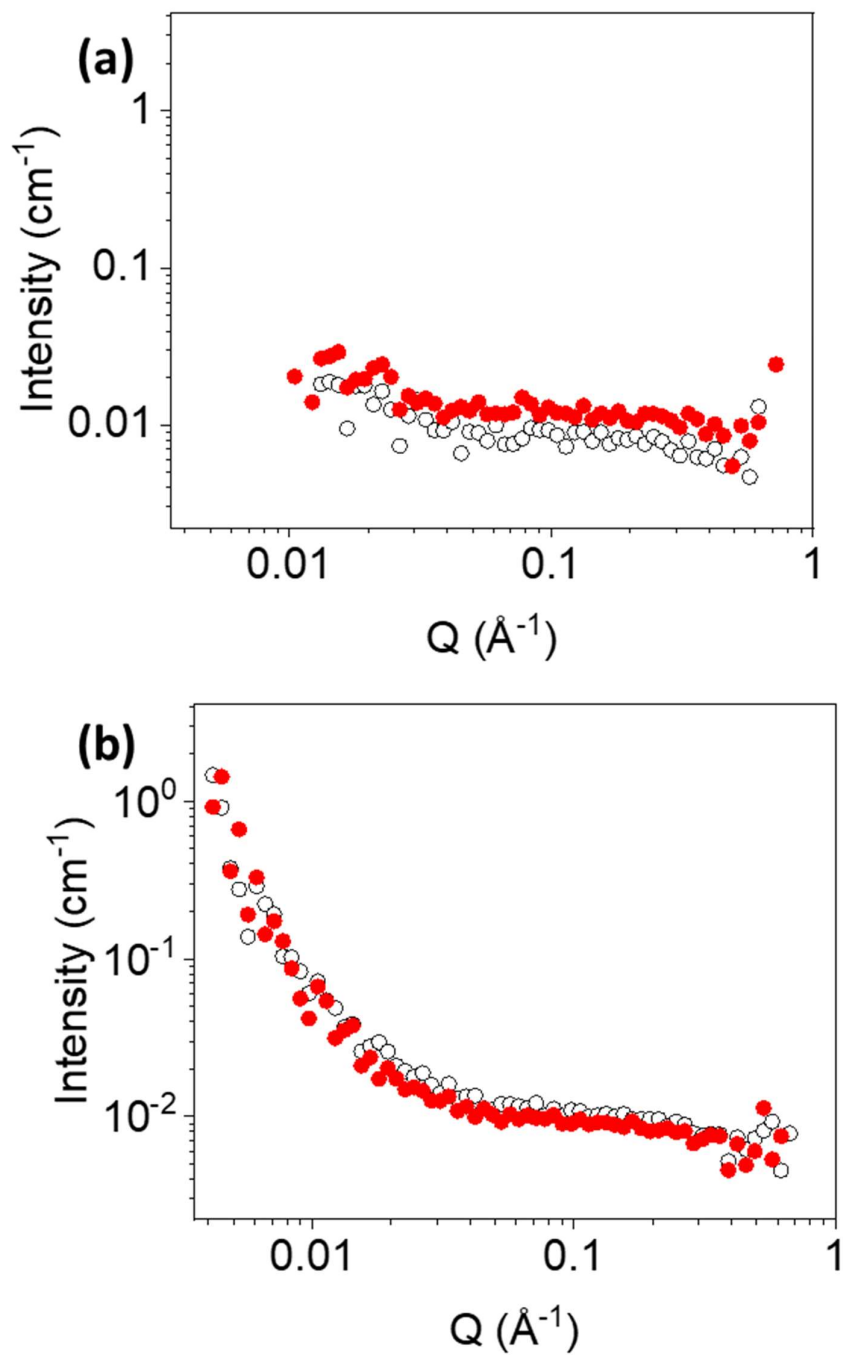


Figure A.3.79. Small angle neutron scattering data for a buffered solution of 10 mg/mL **NDI-V** at pD 9 in a neutral state before electrochemical reduction (**black**) and after one electrochemical reduction and oxidation (**red**). Measurements taken in (a) spectro-electrochemical cell and (b) in a standard quartz cuvette.

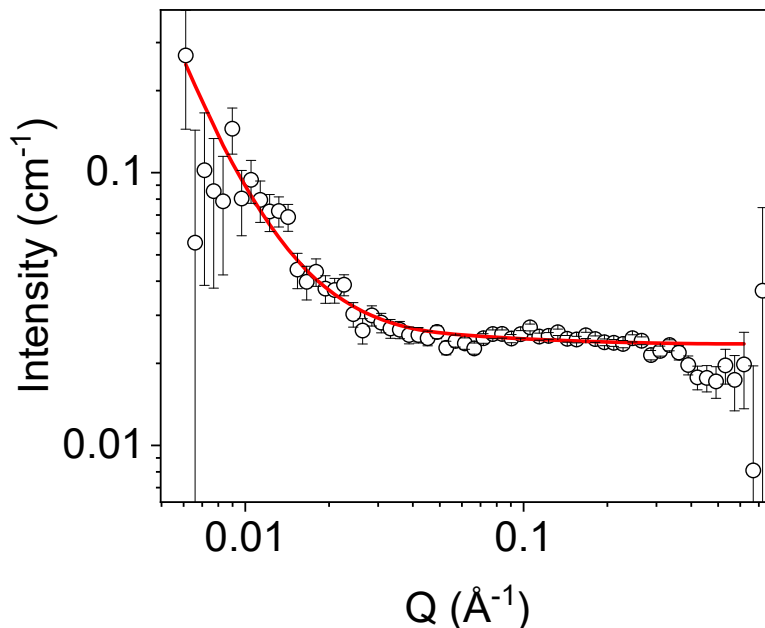


Figure A.3.80. Small angle neutron scattering data for a neutral buffered solution of 10 mg/mL NDI-I at pH 9 (open circles) fitted to a flexible elliptical cylinder model combined with power law (red). Data taken in spectro-electrochemical cell. Data taken in spectro-electrochemical cell. Fit parameters can be found in Table A.3.21.

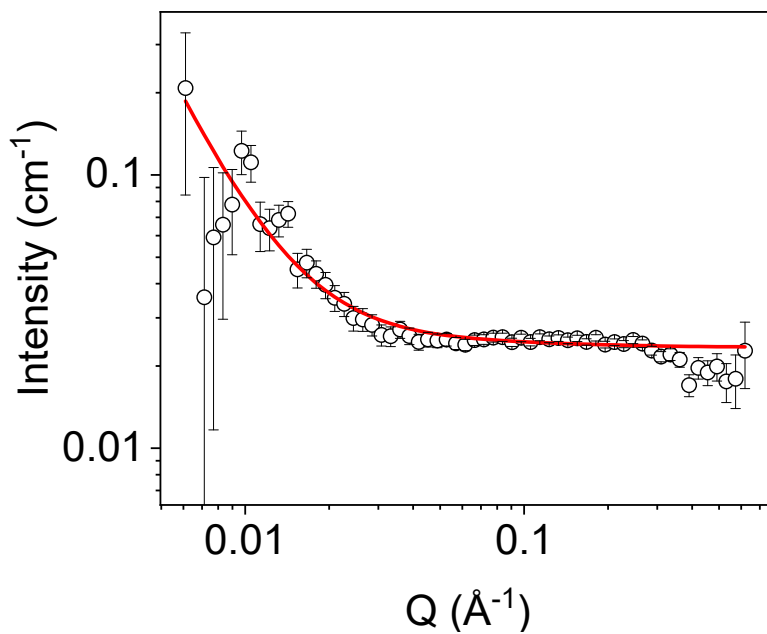


Figure A.3.81. Small angle neutron scattering data for a buffered reduced solution of 10 mg/mL NDI-I at pH 9 (open circles) fitted to a flexible elliptical cylinder model combined with power law (red). Data taken in spectro-electrochemical cell. Fit parameters can be found in Table A.3.21.

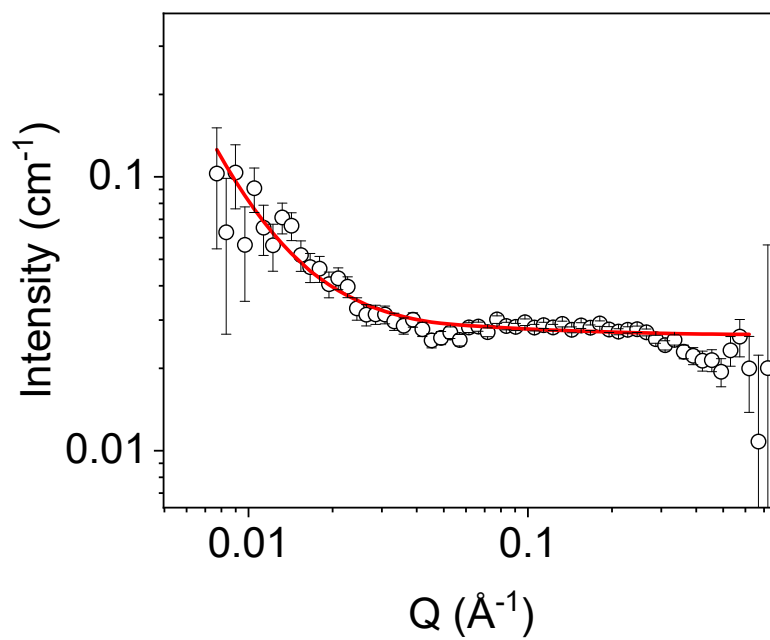


Figure A.3.82. Small angle neutron scattering data for a buffered electrochemically oxidised solution of 10 mg/mL NDI-I at pH 9 (open circles) fitted to a flexible elliptical cylinder model combined with power law (red). Data taken in spectro-electrochemical cell. Fit parameters can be found in Table A.3.21.

Table A.3.21. Parameters of SANS model fits shown in Figure A.3.80-Figure A.3.82.

NDI-I neutral	Flexible cylinder combined with power law	
	Value	Error
Scale a	2.22E-04	2.22E-05
Scale b	5.95E-08	8.36E-09
Background (cm ⁻¹)	0.023571	1.51e-04
Length (Å)	1.36E+12	3.26E+13
Kuhn length (Å)	84.598	1.45E+01
Radius (Å)	6.1236	3.13E-01
Power	2.8822	0.031443
Range	0.00611-0.61892	
Chi ²	2.0162	
NDI-I electrochemically reduced	Flexible cylinder combined with power law	
	Value	Error
Scale a	2.91E-04	2.68E-05
Scale b	8.26E-08	1.51E-08
Background (cm ⁻¹)	0.023493	0.001513
Length (Å)	2.57E+03	3.26E+03
Kuhn length (Å)	78.233	1.41E+01
Radius (Å)	4.9999	2.34E-01
Power	2.7499	0.041016
Range	0.00611-0.61892	
Chi ²	1.8964	
NDI-I electrochemically oxidised	Flexible cylinder combined with power law	
	Value	Error
Scale a	3.94E-04	3.17E-05
Scale b	1.30E-08	3.98E-09
Background (cm ⁻¹)	0.026594	1.52E-04
Length (Å)	1.48E+13	2.88E+14
Kuhn length (Å)	79.44	1.11E+01
Radius (Å)	5.0692	2.07E-01
Power	3.0679	0.067884
Range	0.0077-0.61892	
Chi ²	2.3304	

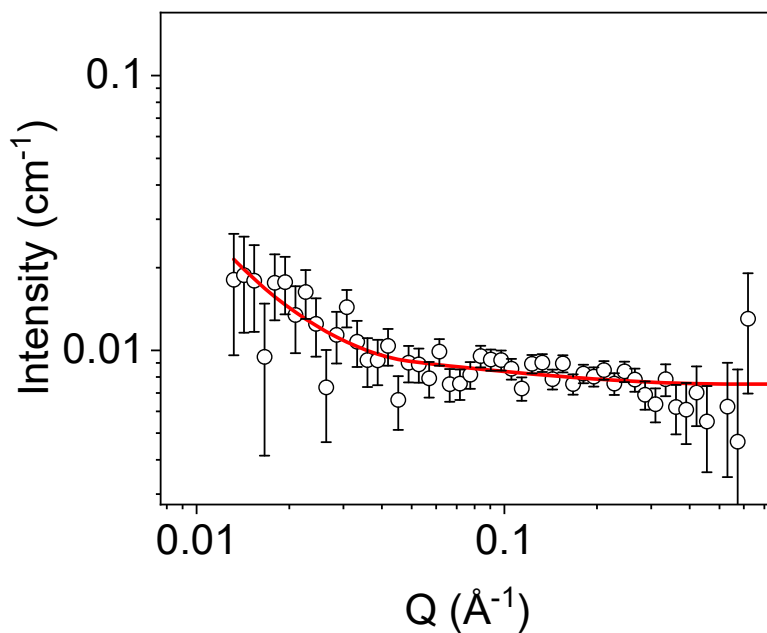


Figure A.3.83. Small angle neutron scattering data for a neutral buffered solution of 10 mg/mL **NDI-V** at pD 9 (open circles) fitted to a flexible elliptical cylinder model (red). Data taken in spectro-electrochemical cell. Fit parameters can be found in Table A.3.22.

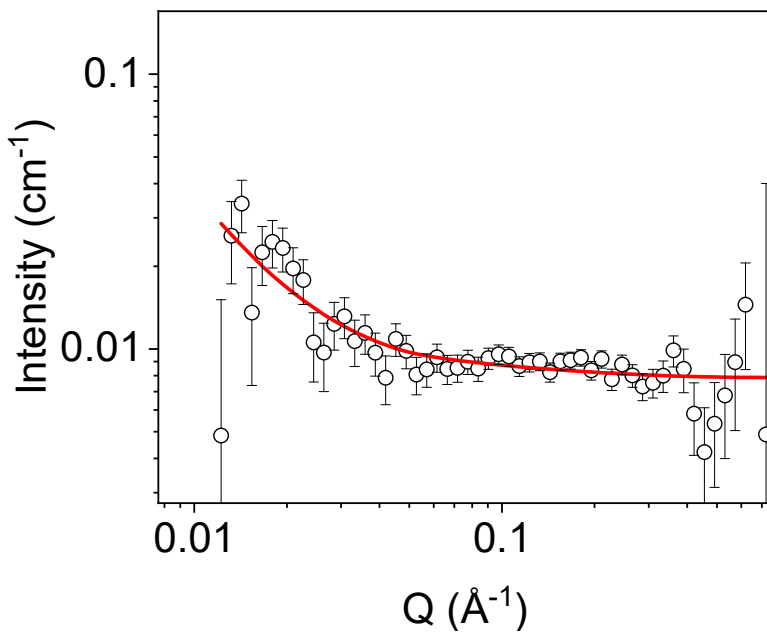


Figure A.3.84. Small angle neutron scattering data for a buffered reduced solution of 10 mg/mL **NDI-V** at pD 9 (open circles) fitted to a flexible elliptical cylinder model (red). Data taken in spectro-electrochemical cell. Fit parameters can be found in Table A.3.22.

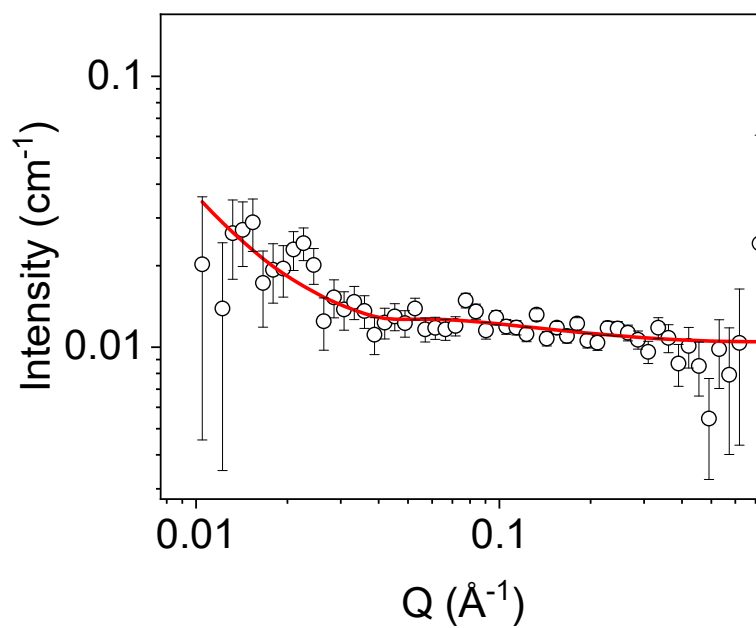


Figure A.3.85. Small angle neutron scattering data for a buffered electrochemically oxidised solution of 10 mg/mL NDI-V at pH 9 (open circles) fitted to a flexible elliptical cylinder model (red). Data taken in spectro-electrochemical cell. Fit parameters can be found in Table A.3.22.

Table A.3.22. Parameters of SANS model fits shown in Figure A.3.83-Figure A.3.85.

NDI-V neutral		Flexible cylinder combined
	Value	Error
Scale	2.02E-04	3.32E-05
Background (cm ⁻¹)	0.007539	1.88E-04
Length (Å)	1.49E+18	4.14E+19
Kuhn length (Å)	81.1380	18.6320
Radius (Å)	6.2426	0.4570
Range	0.0132-0.72191	
Chi ²	0.91148	
NDI-V electrochemically reduced		Flexible cylinder
	Value	Error
Scale	2.91E-04	6.15E-03
Background (cm ⁻¹)	0.007878	0.002162
Length (Å)	1.77E+06	3.20E+06
Kuhn length (Å)	70.012	12.23
Radius (Å)	5.0912	0.26567
Range	0.0132-0.61892	
Chi ²	0.91741	
NDI-V electrochemically oxidised		Flexible cylinder
	Value	Error
Scale	6.39E-04	5.50E-05
Background (cm ⁻¹)	0.010479	1.47E-04
Length (Å)	9.18E+74	2.22E+70
Kuhn length (Å)	80.473	11.5680
Radius (Å)	5.0978	0.2293
Range	0.01048-0.72191	
Chi ²	1.232	

A.3.E Chapter 3 experimental appendices

A.3.E.1 The influence of temperature

The temperature in the room in which the experiments were undertaken was recorded over several days, both in and out of working hours. Weekdays and weekends were recorded to ascertain how much difference in temperature was caused by people working in the lab. Temperature could be a factor in the speed of the redox reactions occurring in the FTO window. The ability to perform without detriment whilst temperature fluctuates is important for any commercial application and so temperature controlled experiments will help to assess how much temperature changes are responsible for the cyclability measurements collected.

During the working day there is a variation in temperature of around 2 °C (starting from 9 am), and almost 4 °C throughout the week,, Figure A.3.86. Without workers (at weekends) variation of temperature was a lot less. In a temperature-controlled environment set to 18 °C, cycling experiments were undertaken. By keeping the temperature constant, any fluctuation in temperature can be eliminated as a factor for trends that have been previously observed. It should be noted that temperature-controlled conditions made no difference to the intensity of colouration achieved by a 10 second reduction.

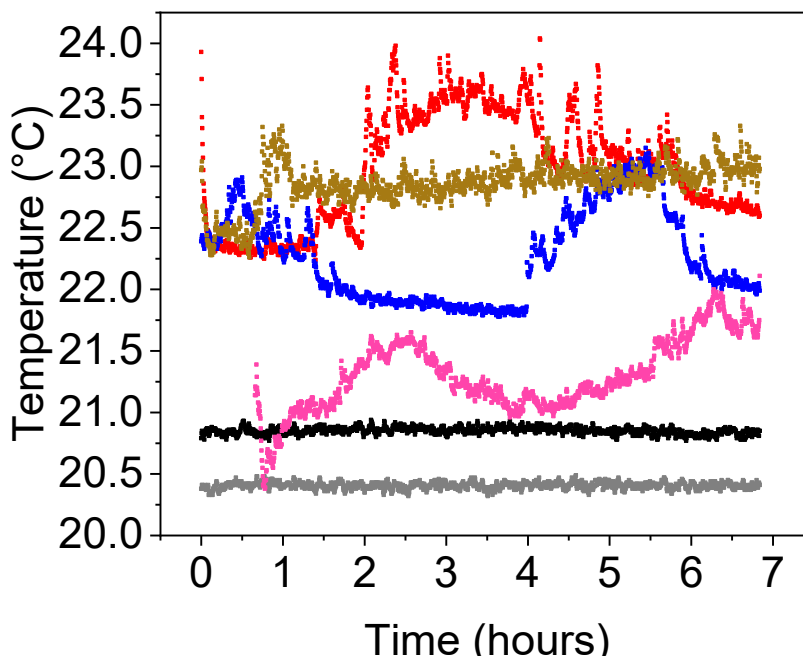


Figure A.3.86. Plot showing the fluctuation in of the room temperature of the lab over the course of weekdays (red, blue, beige, pink) and weekends (black, grey).

NDI-GF performs comparably in temperature controlled conditions whereas **NDI-V** and **NDI-F**, have an improved performance, Figure A.3.87(b)-(d). **NDI-I** demonstrates faster oxidation times in temperature-controlled conditions but the cyclability itself is not improved, Figure A.3.87(a). The trend of increasing oxidation time with cyclability is still observed for all NDIs, Figure A.3.87. Temperature fluctuation is therefore not causing this observed increase in oxidation time. These data suggest that some NDIs are more sensitive to temperature than others but that ultimately, variation in temperature has no significant impact upon cyclability. A temperature controlled room is not viable for any commercial product and so a requirement of 18 °C to improve cyclability is not a solution. This experiment highlights those NDIs unsuitable for such application (**NDI-V** and **NDI-GF**). **NDI-I** and **NDI-F** are still the best performing NDIs in terms of cyclability

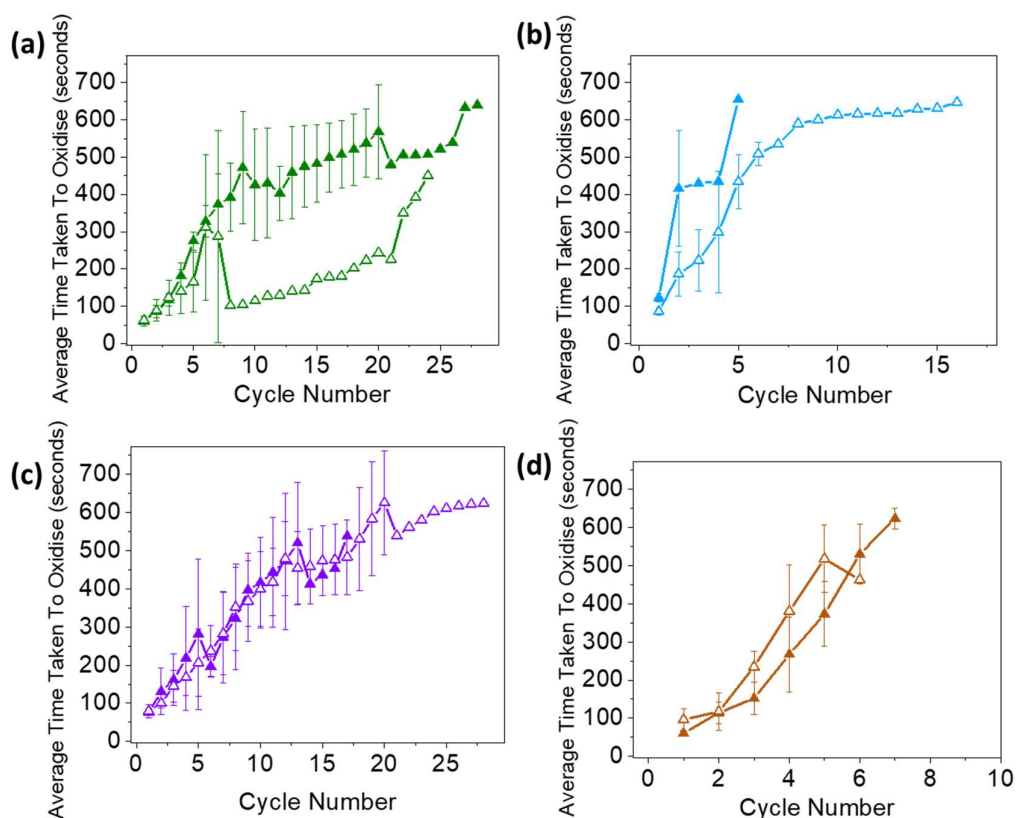


Figure A.3.87. Plot showing how time to reach a state of full oxidation (i.e., without discolouration of the neutral state) fluctuates with cycling from neutral to reduced state and back in standard (filled triangles) and temperature-controlled experiments (open triangles). Experiments undertaken using 10 mg/mL buffered solutions of (a) **NDI-I**, (b) **NDI-V**, (c) **NDI-F** and (d) **NDI-GF** at their respective 'idea' pH. Measurements are taken as an average of triplicate measurements and error bars calculated from standard deviation. Reduced state is achieved by applying -2.7 V for 10 seconds and oxidation achieved by applying a potential sweep between 0.1 and 0.95 V in 0.05 V increments every 5 seconds.

A.4 Chapter 4 appendices

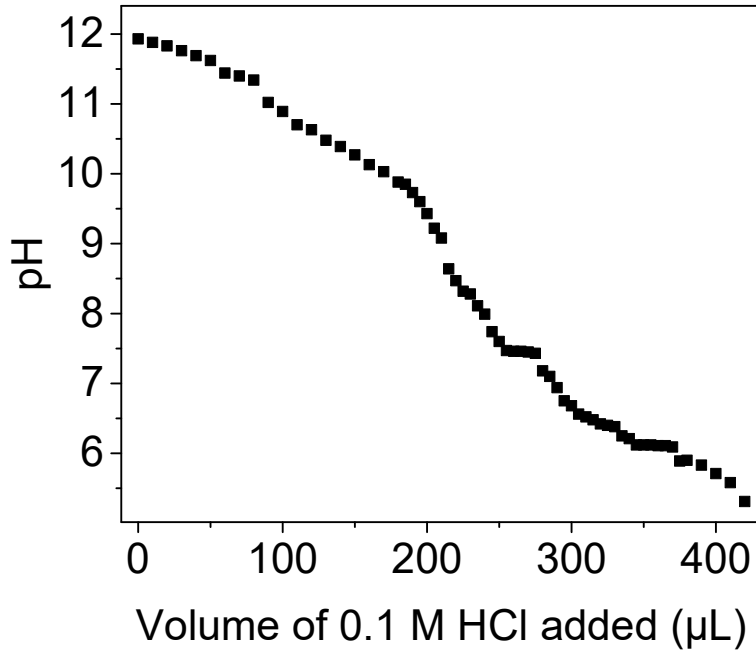


Figure A.4.1. pH titration data taken of 5 mg/mL 1-NapFF with background electrolyte.

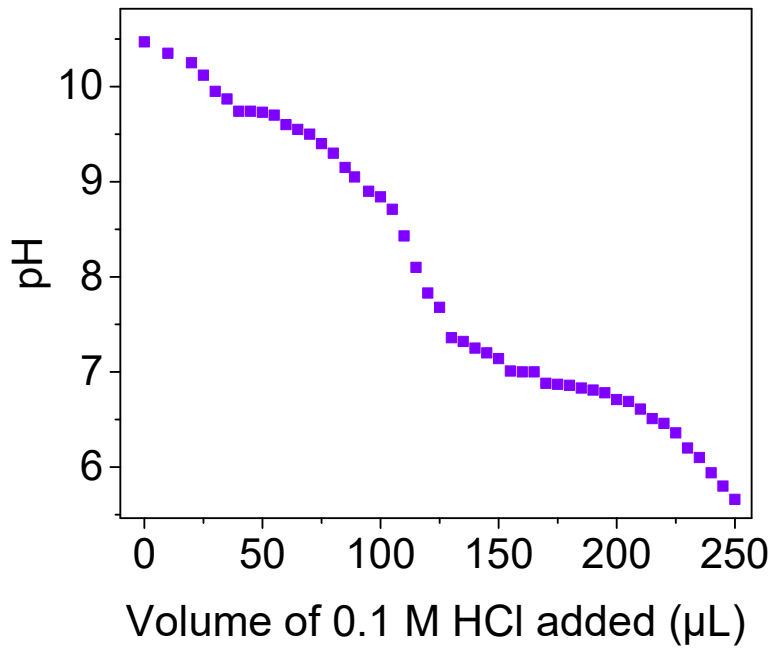


Figure A.4.2. pH titration data taken of 5 mg/mL NDI-F with background electrolyte.

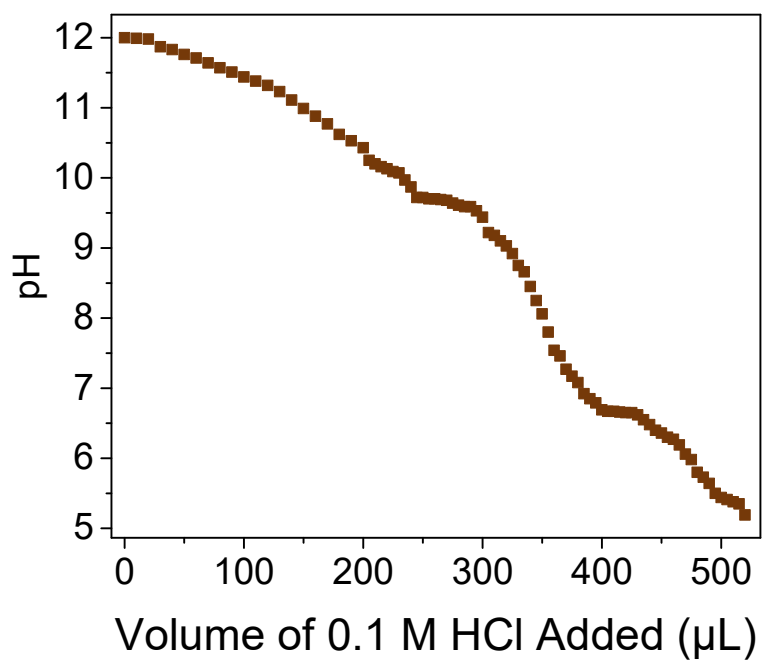


Figure A.4.3. pH titration data taken of 5 mg/mL NDI-GF with background electrolyte.

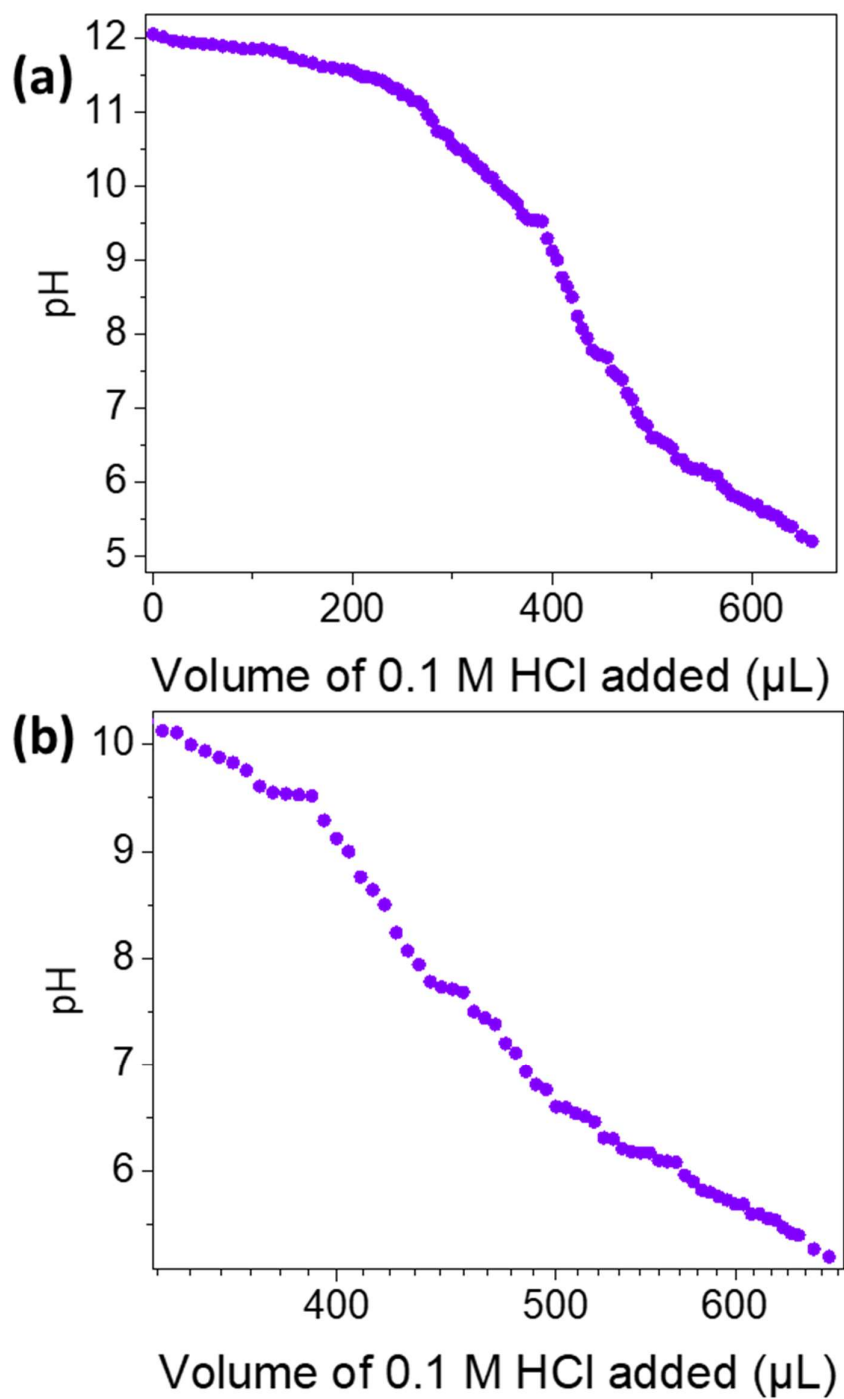


Figure A.4.4. pH titration data taken of 5:5 mg/mL NDI-F:1-NapFF with background electrolyte.

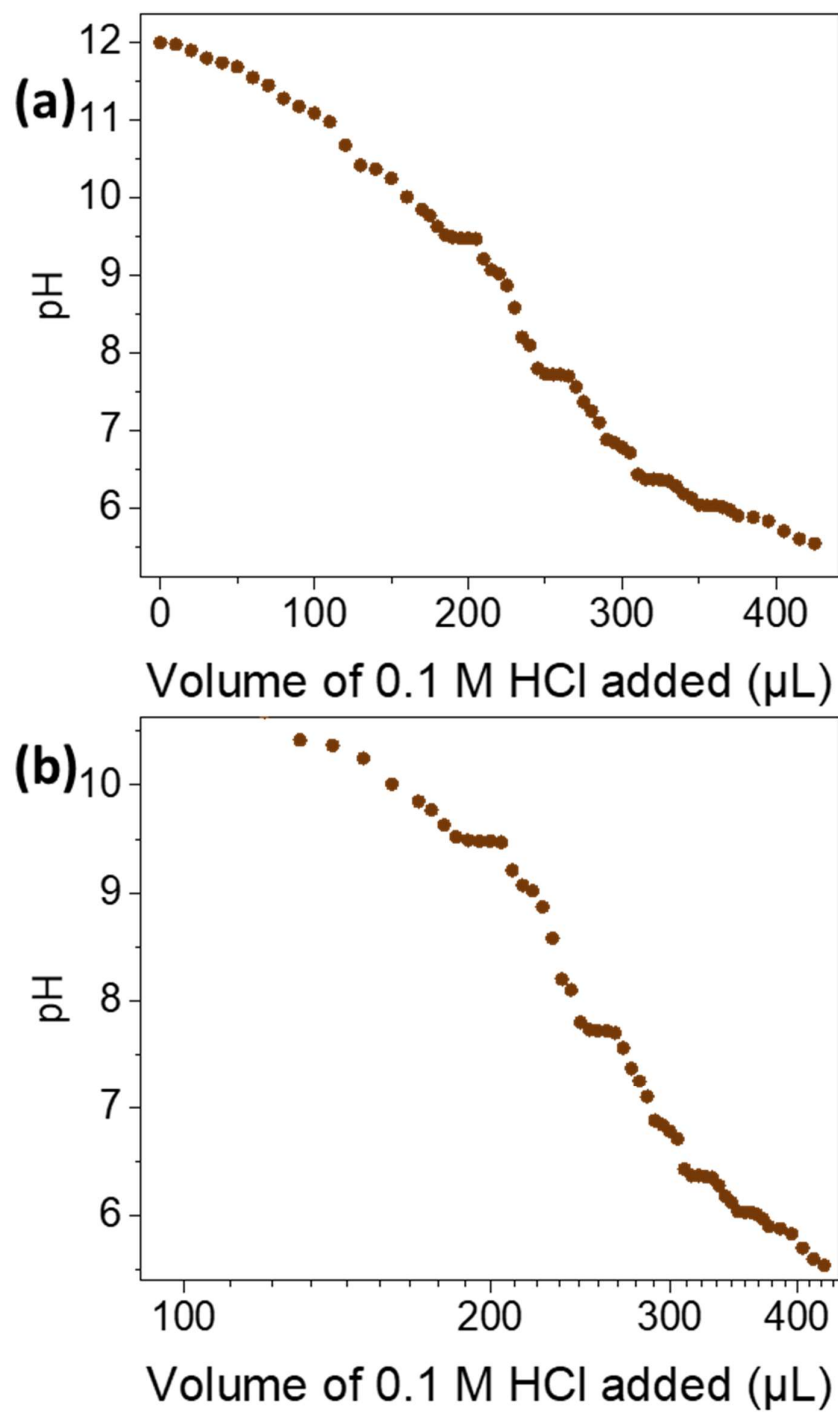


Figure A.4.5. pH titration data taken of 5:5 mg/mL NDI-GF:1-NapFF with background electrolyte.

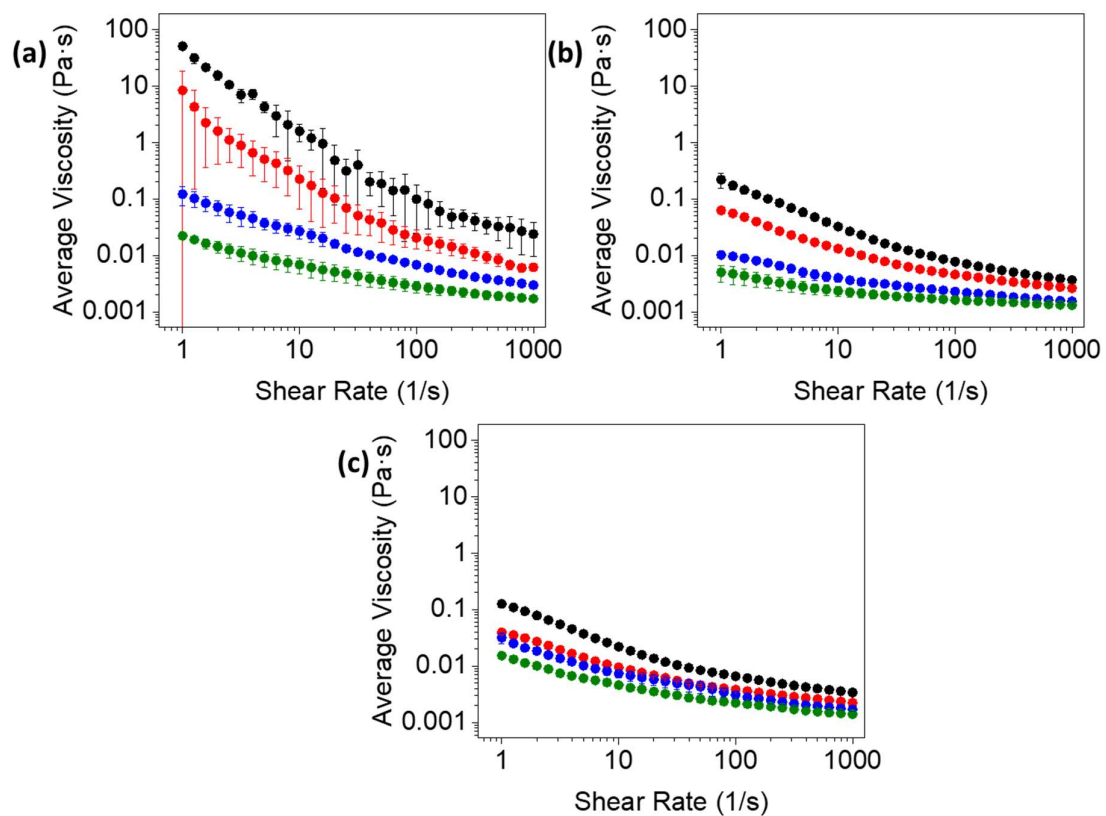


Figure A.4.6. Viscosity measurements of **1-NapFF** at 5 (black), 2.5 (red), 1.25 (blue) and 0.625 (green) mg/mL at pH 6 (a), 9 (b) and 12 (c). Measurements are taken as an average of triplicate measurements and error bars calculated from standard deviation. Background electrolyte present.

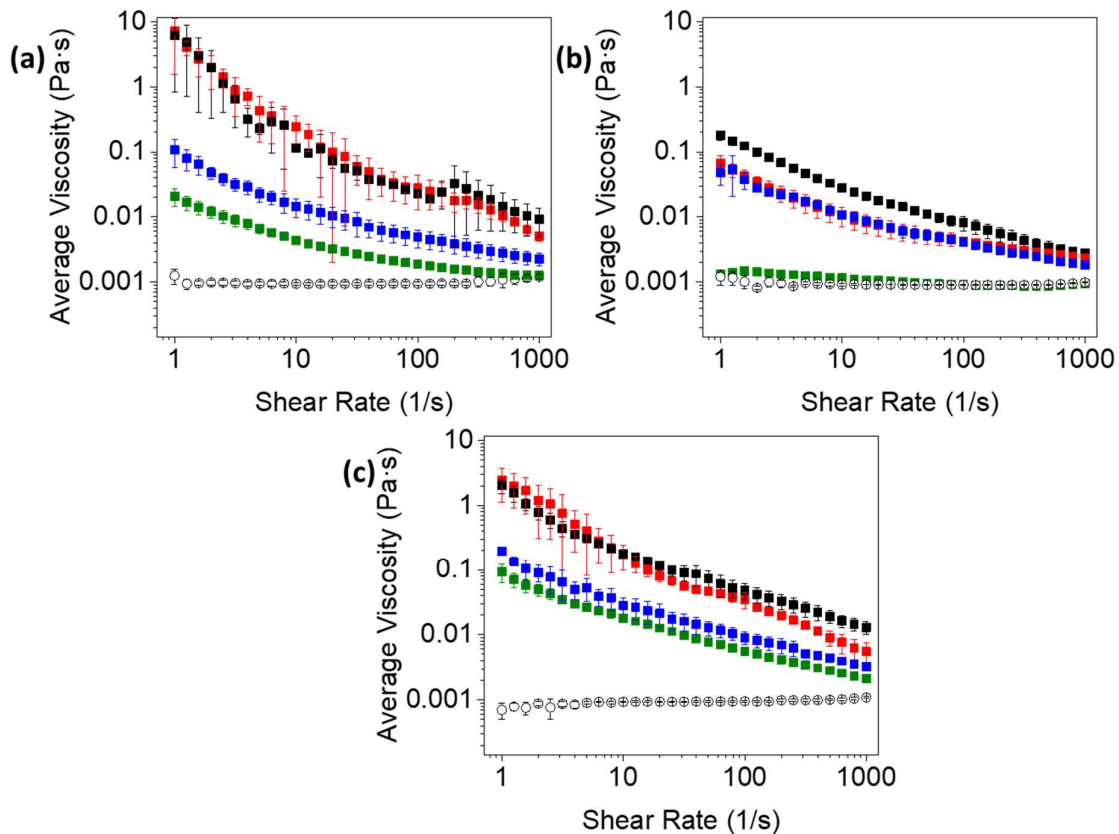


Figure A.4.7. Viscosity measurements of NDI-F:1-NapFF at 5:5 (black), 5:2.5 (red), 5:1.25 (blue), 5:0.625 (green) and 5:0 (open circles) mg/mL at pH 6 (a), 9 (b) and 12 (c). Measurements are taken as an average of triplicate measurements and error bars calculated from standard deviation. Background electrolyte present.

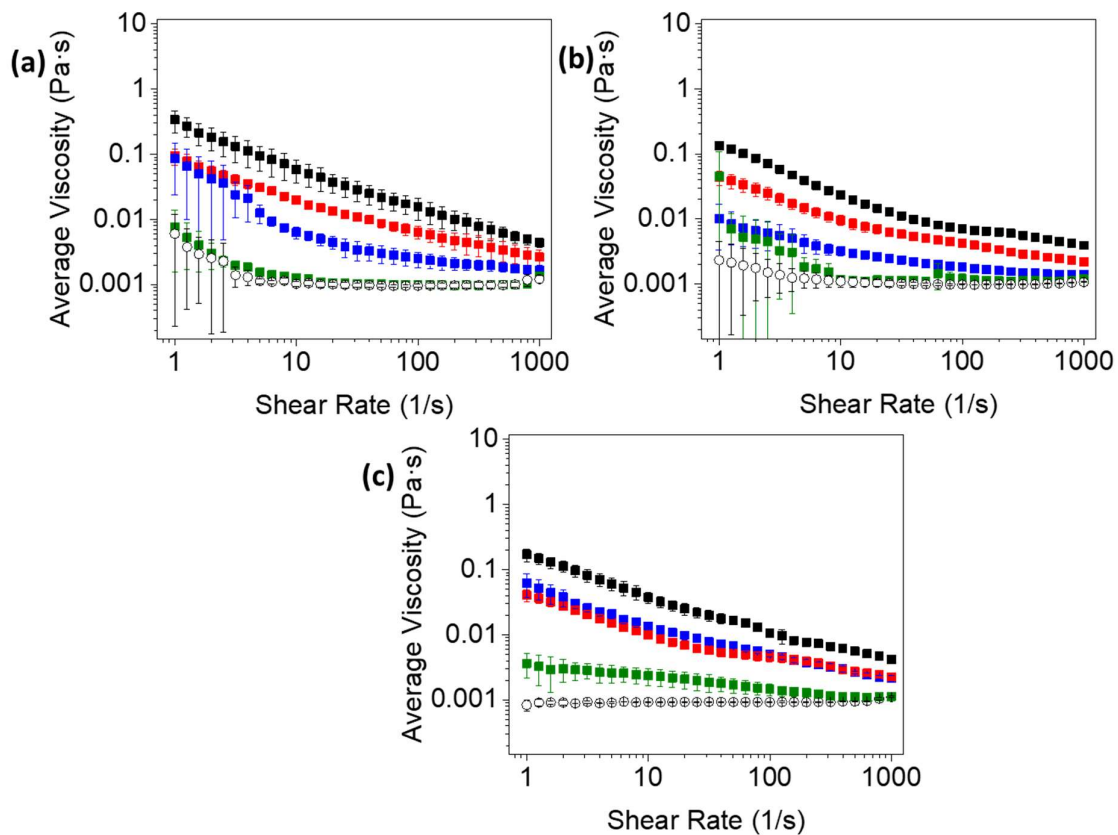


Figure A.4.8. Viscosity measurements of NDI-GF:1-NapFF at 5:5 (black), 5:2.5 (red), 5:1.25 (blue), 5:0.625 (green) and 5:0 (open circles) mg/mL at pH 6 (a), 9 (b) and 12 (c). Measurements are taken as an average of triplicate measurements and error bars calculated from standard deviation. Background electrolyte present.

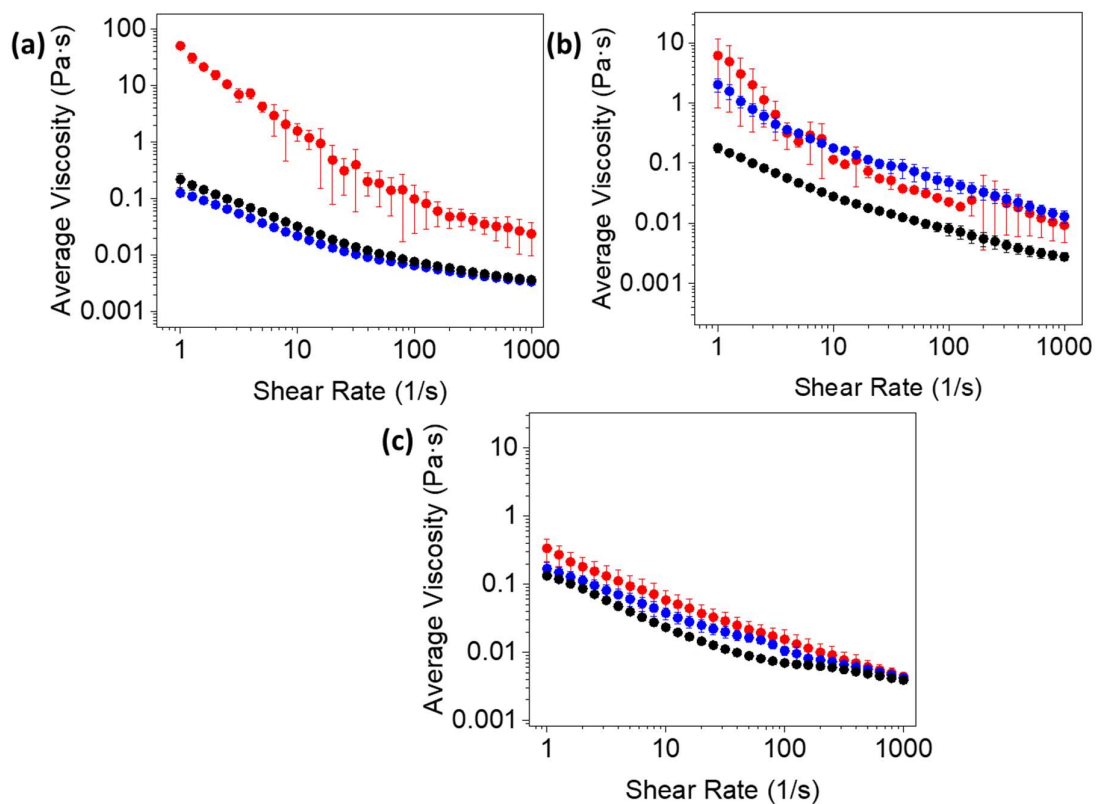


Figure A.4.9. Viscosity measurements of (a) 5 mg/mL **1-NapFF** and 5:5 mg/mL (b) **NDI-F:1-NapFF** and (c) **NDI-GF:1-NapFF** at pH 6 (red), 9 (black) and 12 (blue). Measurements are taken as an average of triplicate measurements and error bars calculated from standard deviation. Background electrolyte present.

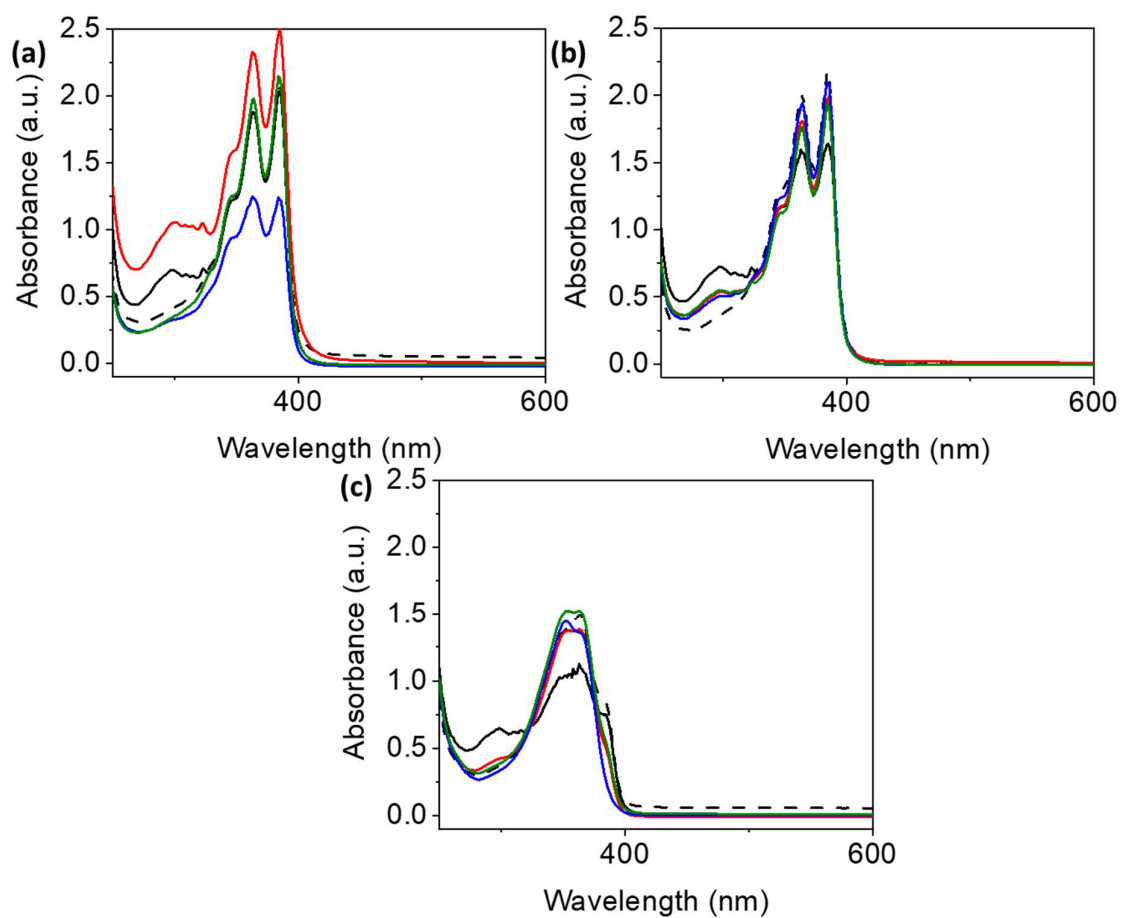


Figure A.4.10. Absorbance spectra of neutral NDI-F:1-NapFF at 5:5 (black), 5:2.5 (red), 5:1.25 (blue), 5:0.625 (green) and 5:0 (dashed line) mg/mL at pH 6 (a), 9 (b) and 12 (c). Background electrolyte present.

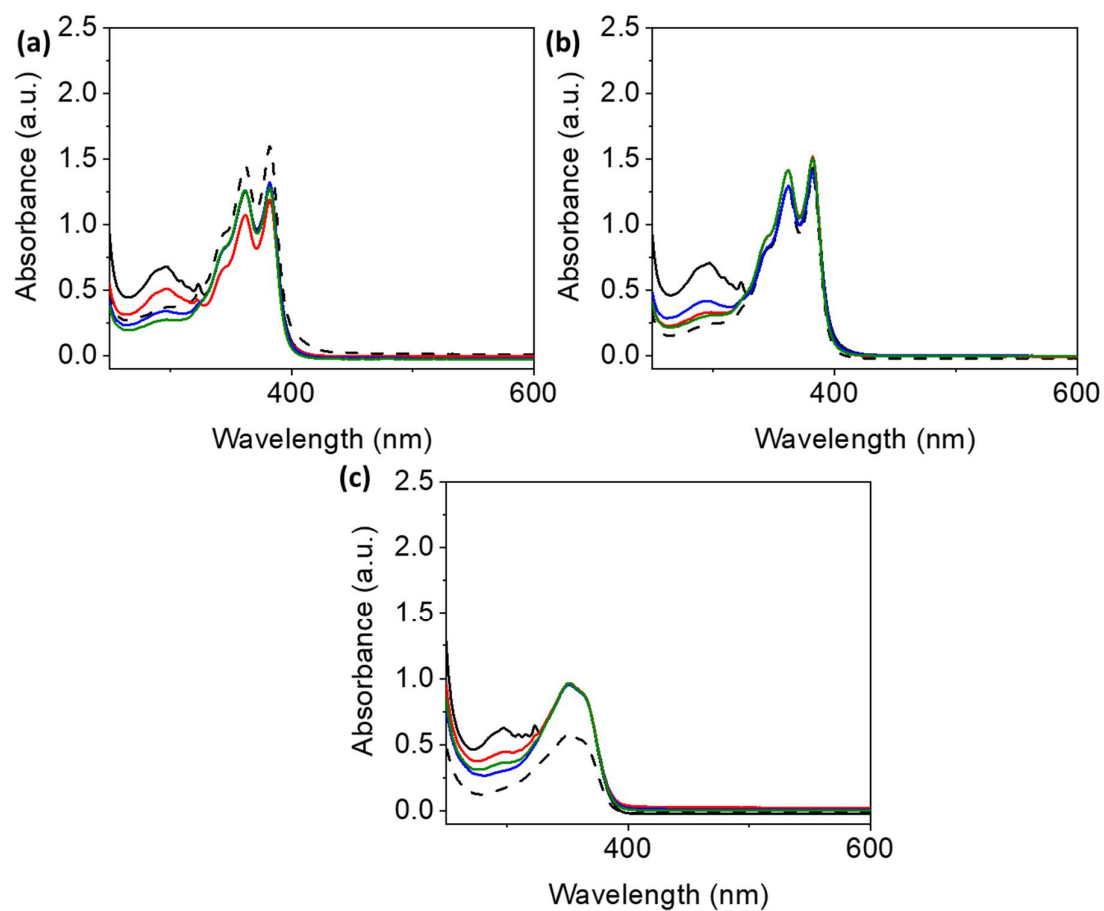


Figure A.4.11. Absorbance spectra of neutral **NDI-GF:1-NapFF** at 5:5 (black), 5:2.5 (red), 5:1.25 (blue), 5:0.625 (green) and 5:0 (dashed line) mg/mL at pH 6 (a), 9 (b) and 12 (c). Background electrolyte present.

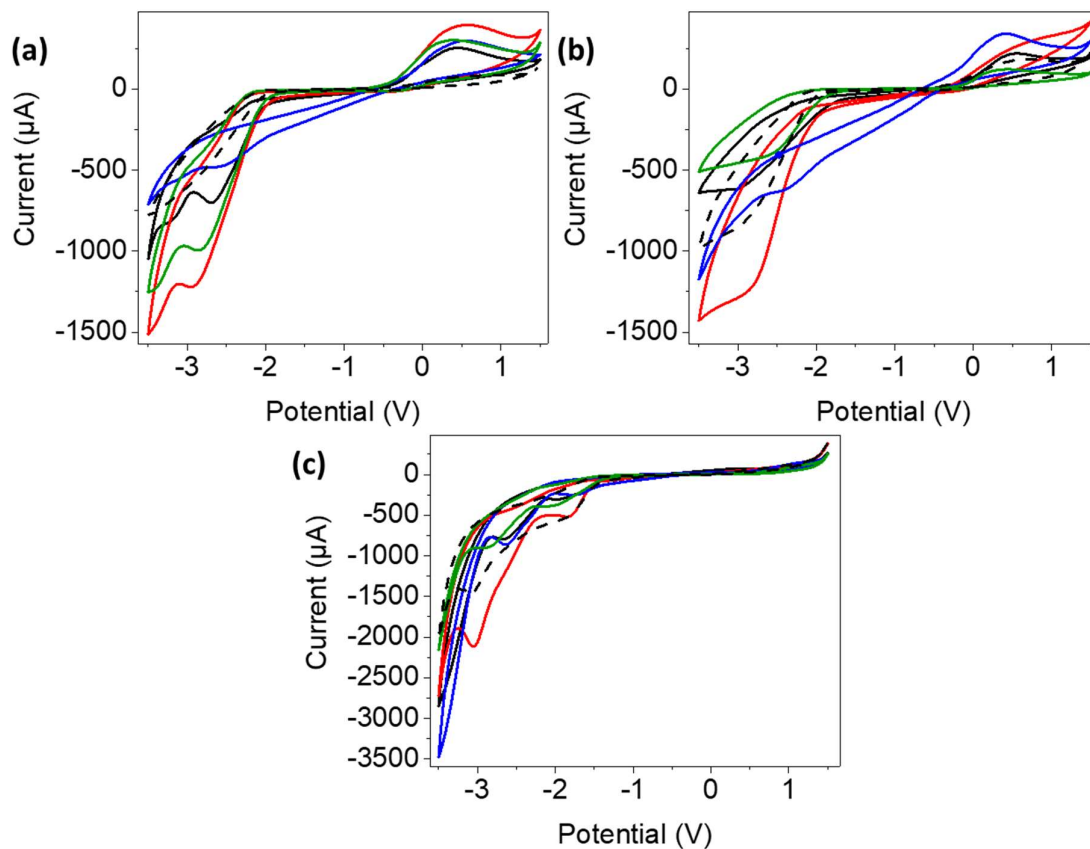


Figure A.4.12. Cyclic voltammograms of NDI-F:1-NapFF at 5:5 (black), 5:2.5 (red), 5:1.25 (blue), 5:0.625 (green) and 5:0 (dashed line) mg/mL at pH 6 (a), 9 (b) and 12 (c). Scan rate used was 0.2 V/s. Performed in 1 x 1 FTO window cells.

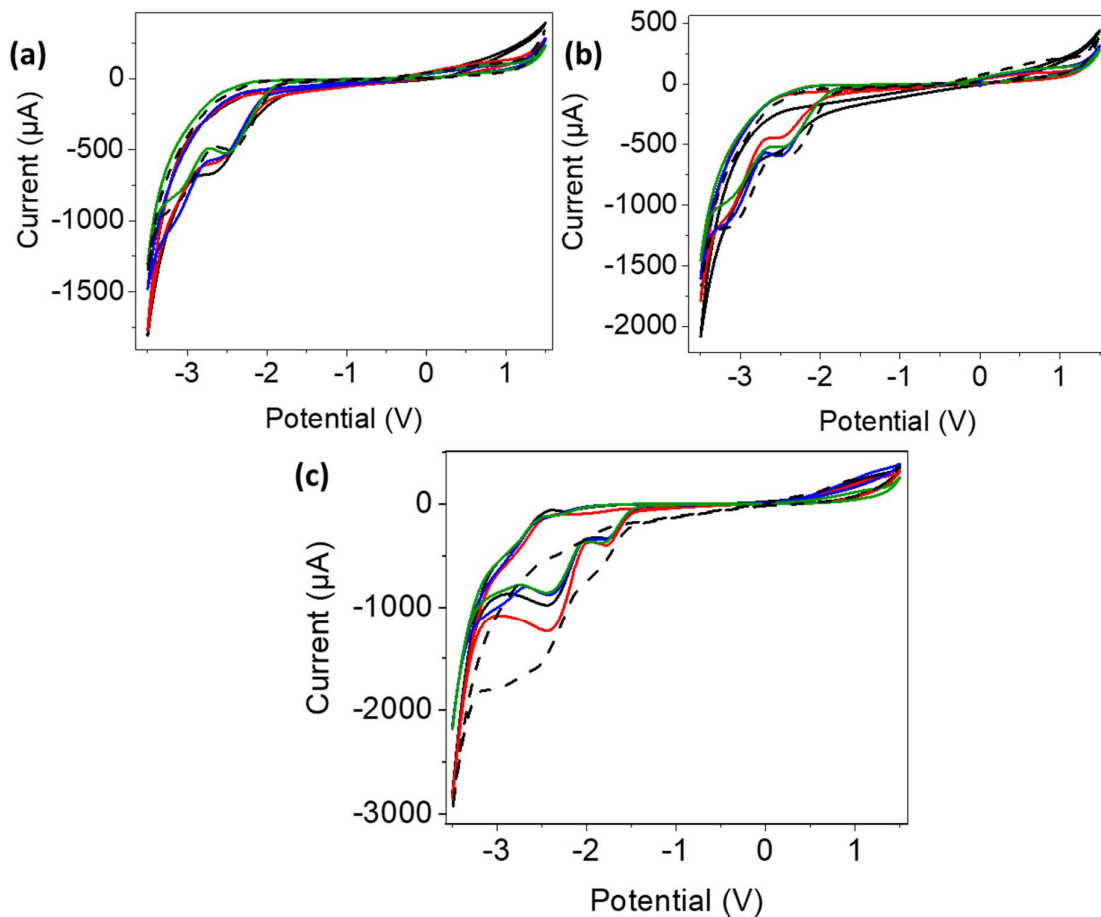


Figure A.4.13. Cyclic voltammograms of NDI-GF:1-NapFF at 5:5 (black), 5:2.5 (red), 5:1.25 (blue), 5:0.625 (green) and 5:0 (dashed line) mg/mL at pH 6 (a), 9 (b) and 12 (c). Scan rate used was 0.2 V/s. Performed in 1 x 1 FTO window cells.

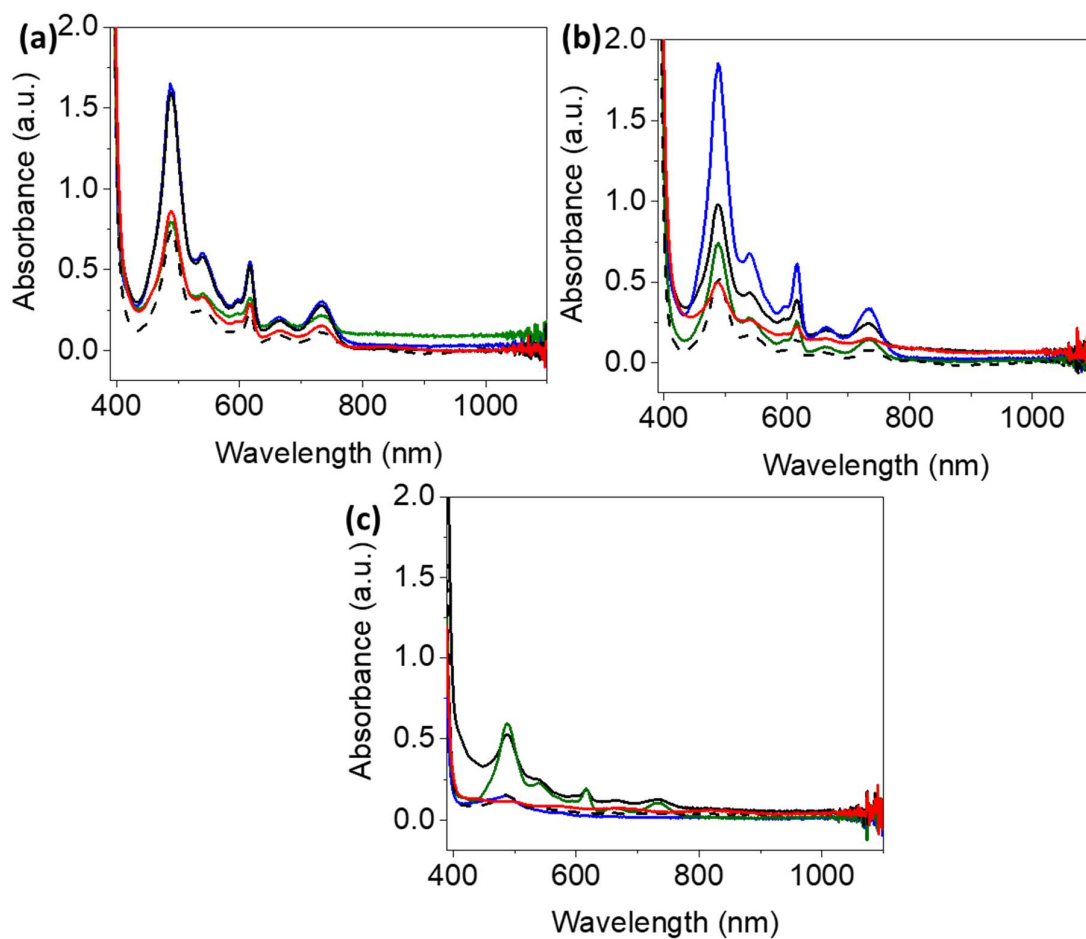


Figure A.4.14. Absorbance spectra of reduced solutions of **NDI-F:1-NapFF** at 5:5 (black), 5:2.5 (red), 5:1.25 (blue), 5:0.625 (green) and 5:0 (dashed line) mg/mL at pH 6 (a), 9 (b) and 12 (c). Spectra taken after 10 second application of -2.5 V. Solutions contain background electrolyte.

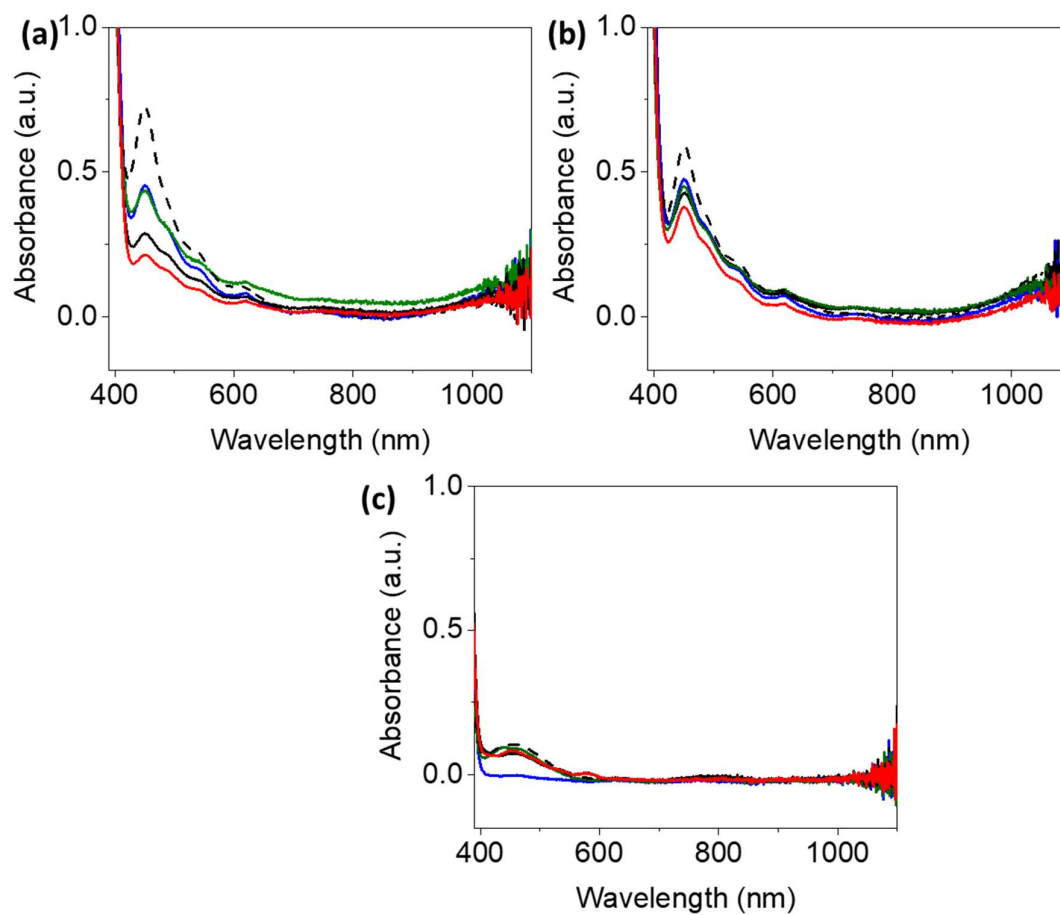


Figure A.4.15. Absorbance spectra of reduced solutions of **NDI-GF:1-NapFF** at 5:5 (black), 5:2.5 (red), 5:1.25 (blue), 5:0.625 (green) and 5:0 (dashed line) mg/mL at pH 6 (a), 9 (b) and 12 (c). Spectra taken after 10 second application of -2.5 V. Solutions contain background electrolyte.

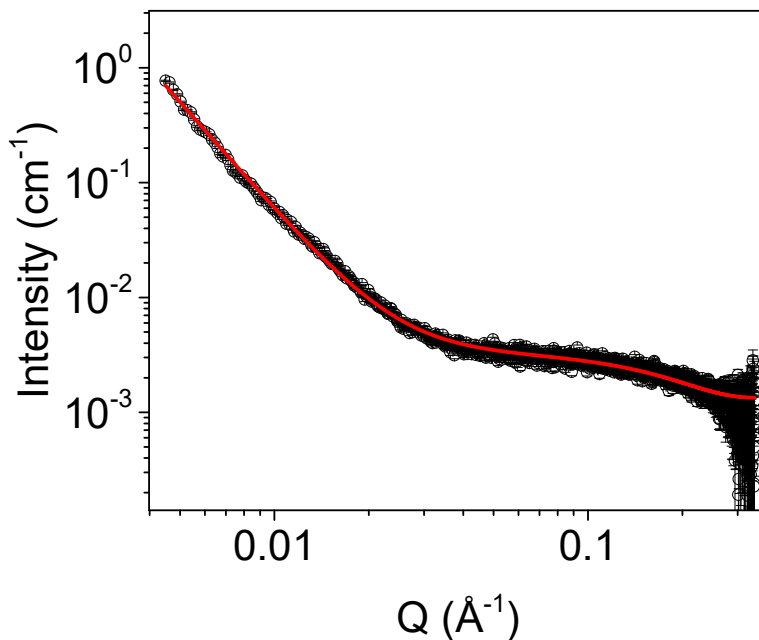


Figure A.4.16. Small angle X-ray scattering data for a solution of 5 mg/mL **NDI-F** at pH 6 (open circles) fitted to a hollow cylinder model combined with power law (red). Fit parameters can be found in Table A.4.1.

Table A.4.1. Parameters of SAXS model fit seen in Figure A.4.16.

NDI-F 5 mg/mL pH 6	Hollow cylinder combined with power law	
	Value	Error
Scale A	2.26E-04	7.92E-07
Scale B	3.14E-08	6.89E-11
Background	0.001334	3.34E-06
Length (Å)	20.505	0.094302
Radius (Å)	4.7409	0.033889
Thickness (Å)	5.0782	0.0155
Power	3.1291	4.60E-04
Range (Å ⁻¹)	0.0045-0.3397383	
Chi ²	2.5528	

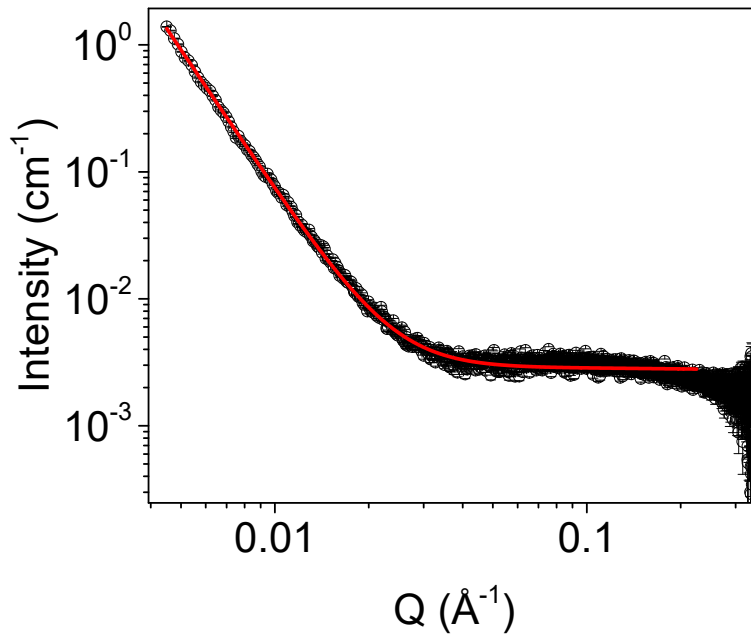


Figure A.4.17. Small angle X-ray scattering data for a solution of 5 mg/mL **NDI-F** at pH 9 (open circles) fitted to a hollow cylinder model combined with power law (red). Fit parameters can be found in Table A.4.2.

Table A.4.2. Parameters of SAXS model fit seen in Figure A.4.17.

NDI-F 5 mg/mL pH 9	Hollow cylinder combined with power law	
	Value	Error
Scale A	1.56E-05	1.14E-06
Scale B	3.41E-09	5.33E-12
Background	0.002783	9.40E-12
Length (Å)	14.1	1.40
Radius (Å)	6.259	1.08
Thickness (Å)	4	0.320
Power	3.6624	3.15E-04
Range (Å ⁻¹)	0.0045-0.22524434	
Chi ²	4.355	

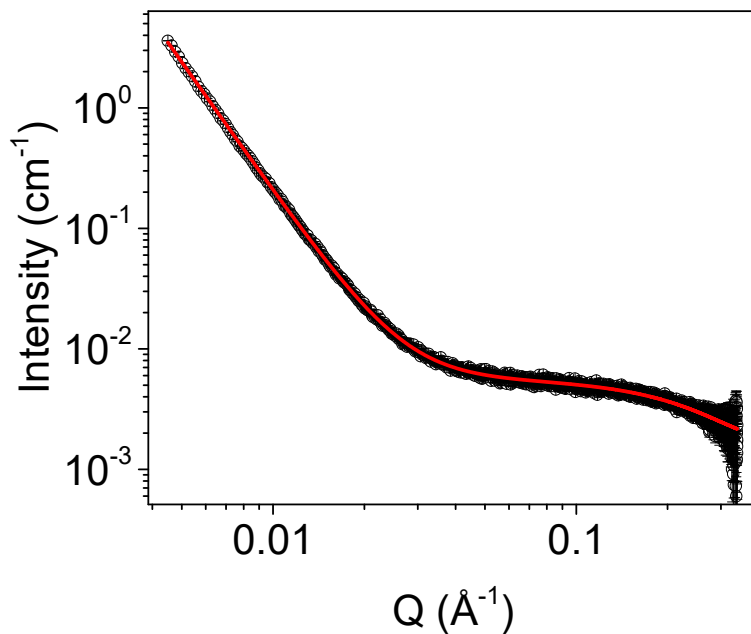


Figure A.4.18. Small angle X-ray scattering data for a solution of 5 mg/mL **NDI-F** at pH 12 (open circles) fitted to a sphere model combined with power law (red). Fit parameters can be found in Table A.4.3.

Table A.4.3. Parameters of SAXS model fit seen in Figure A.4.18.

NDI-F 5 mg/mL pH 12	Sphere combined with power law	
	Value	Error
Scale A	6.68E-04	9.67E-07
Scale B	1.58E-08	1.01E-11
Background	0.0017806	3.43E-06
Radius (Å)	9.1026	5.50E-03
Power	3.5557	1.29E-03
Range (Å ⁻¹)	0.0045-0.3397383	
Chi ²	1.8197	

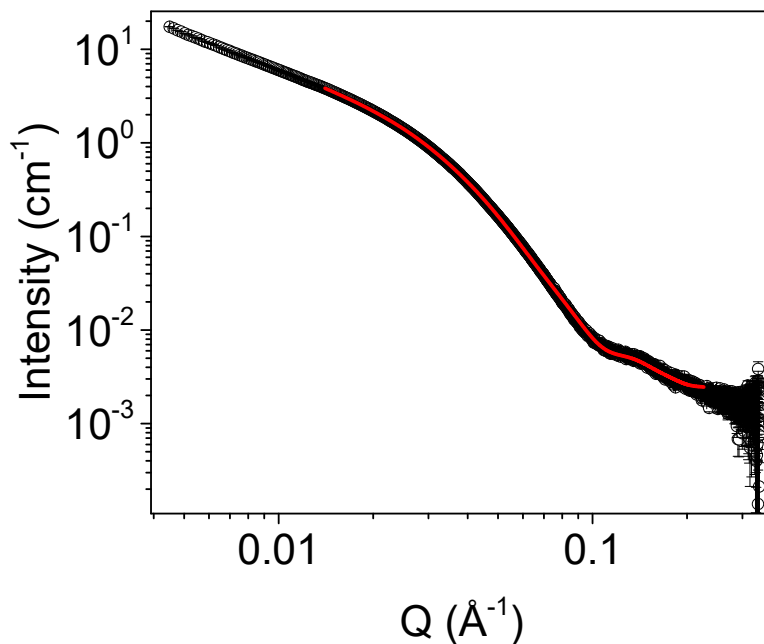


Figure A.4.19. Small angle X-ray scattering data for a solution of 5 mg/mL **NDI-GF** at pH 6 (open circles) fitted to a flexible elliptical cylinder model combined with power law (red). Fit parameters can be found in Table A.4.4.

Table A.4.4. Parameters of SAXS model fit seen in Figure A.4.19.

NDI-GF 5 mg/mL pH 6	Flexible elliptical cylinder combined with power law	
	Value	Error
Scale A	3.61E-04	2.81E-08
Scale B	3.99E-06	1.27E-09
Background	0.001984	4.24E-06
Length (Å)	423.94	0.11
Kuhn length (Å)	70.994	0.0148
Radius (Å)	32.551	2.15E-03
Axis Ratio	2.042	1.24E-04
Power	2.97	8.36E-05
Range (Å ⁻¹)	0.014-0.226	
Chi ²	6.537	

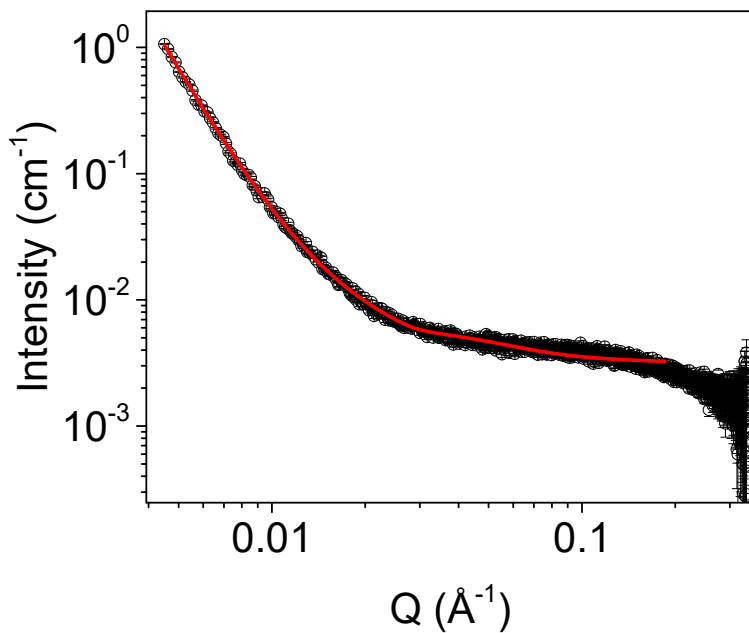


Figure A.4.20. Small angle X-ray scattering data for a solution of 5 mg/mL **NDI-GF** at pH 9 (open circles) fitted to a flexible elliptical cylinder model combined with power law (red). Fit parameters can be found in Table A.4.5.

Table A.4.5. Parameters of SAXS model fit seen in Figure A.4.20.

NDI-GF 5 mg/mL pH 9	Flexible elliptical cylinder combined with power law	
	Value	Error
Scale A	5.15E-06	2.31E-08
Scale B	1.02E-10	2.72E-13
Background	0.003172	4.68E-06
Length (Å)	1.34E+58	1.52E+50
Kuhn length (Å)	114.96	0.812
Radius (Å)	6.0285	0.0169
Axis Ratio	6.642	0.0185
Power	4.25	5.20E-03
Range (Å ⁻¹)	0.0045-0.18533502	
Chi ²	3.6122	

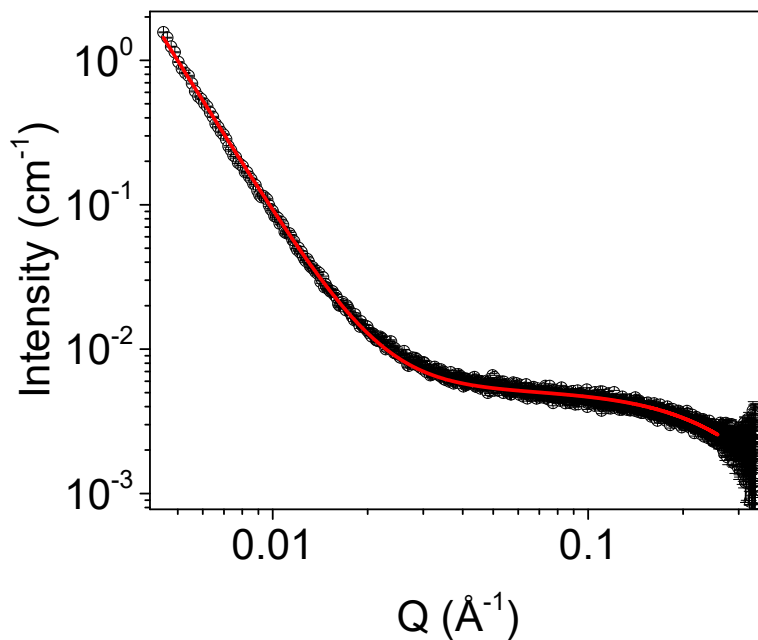


Figure A.4.21. Small angle X-ray scattering data for a solution of 5 mg/mL **NDI-GF** at pH 12 (open circles) fitted to a sphere model combined with power law (red). Fit parameters can be found in Table A.4.6.

Table A.4.6. Parameters of SAXS model fit seen in Figure A.4.21.

NDI-GF 5 mg/mL pH 12	Sphere combined with power law	
	Value	Error
Scale A	8.15E-04	1.06E-06
Scale B	8.57E-09	1.18E-11
Background	0.0011828	3.41E-06
Radius (Å)	8.6548	0.0046768
Power	3.5035	1.28E-04
Range (Å ⁻¹)	0.0045-0.2754335	
Chi ²	2.8193	

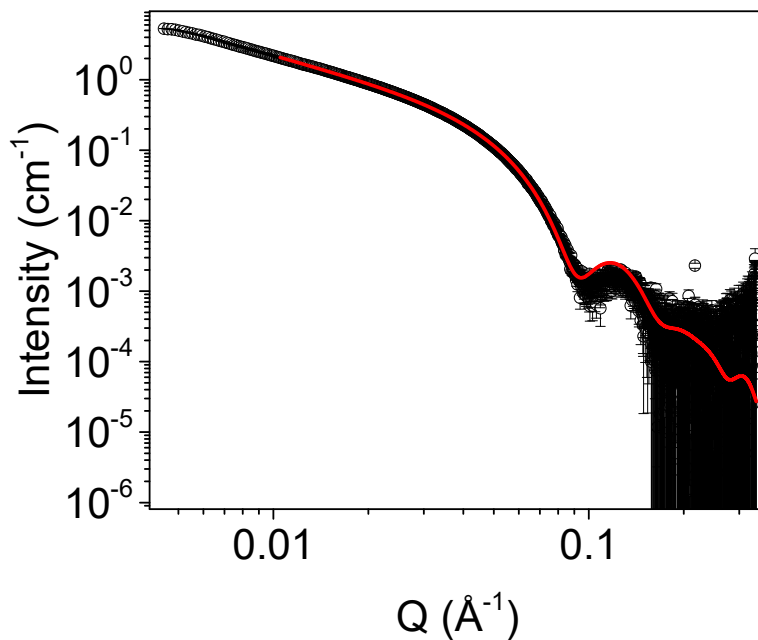


Figure A.4.22. Small angle X-ray scattering data for a solution of 5 mg/mL **1-NapFF** at pH 6 (open circles) fitted to a flexible elliptical cylinder model combined with power law (red). Fit parameters can be found in Table A.4.7.

Table A.4.7. Parameters of SAXS model fit seen in Figure A.4.22.

1-NapFF 5 mg/mL pH 6	Flexible elliptical cylinder combined with power law	
	Value	Error
Scale A	4.32E-04	6.19E-08
Scale B	2.48E-07	3.25E-10
Background	6.46E-27	5.08E-06
Length (Å)	310.63	0.03084
Kuhn length (Å)	310.32	0.97306
Radius (Å)	36.889	0.003665
Axis Ratio	1.2996	1.21E-04
Power	3.2179	3.12E-04
Range (Å ⁻¹)	0.010519111-0.3397383	
Chi ²	5.8737	

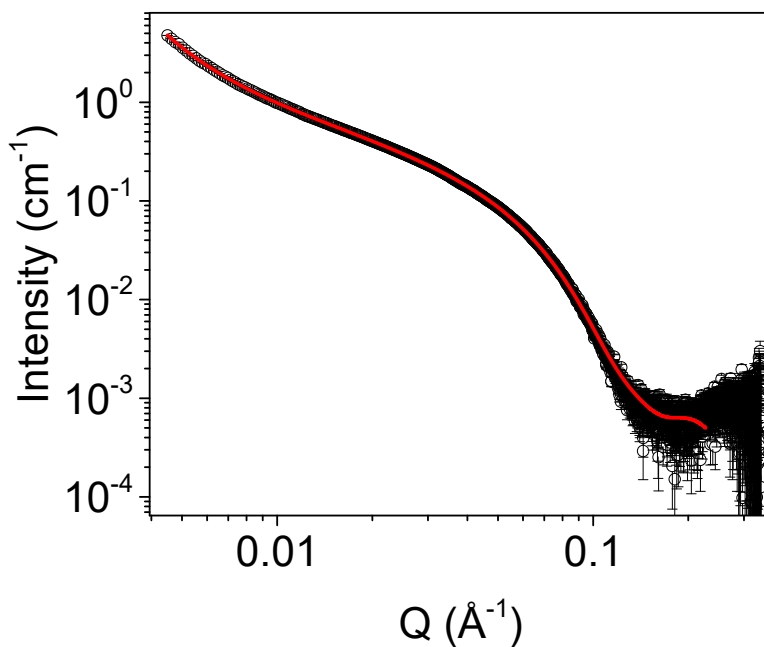


Figure A.4.23. Small angle X-ray scattering data for a solution of 5 mg/mL **1-NapFF** at pH 9 (open circles) fitted to a flexible elliptical cylinder model combined with power law (red). Fit parameters can be found in Table A.4.8.

Table A.4.8. Parameters of SAXS model fit seen in Figure A.4.23.

1-NapFF 5 mg/mL pH 9	Flexible elliptical cylinder combined with power law	
	Value	Error
Scale A	2.65E-04	3.25E-08
Scale B	5.03E-13	1.32E-15
Background	3.00E-04	3.95E-06
Length (Å)	9.854E+03	51.418
Kuhn length (Å)	420.78	0.41916
Radius (Å)	23.749	0.001891
Axis Ratio	1.7407	1.32E-04
Power	5.3284	0.004998
Range (Å ⁻¹)	0.0045-0.22715172	
Chi ²	4.9489	

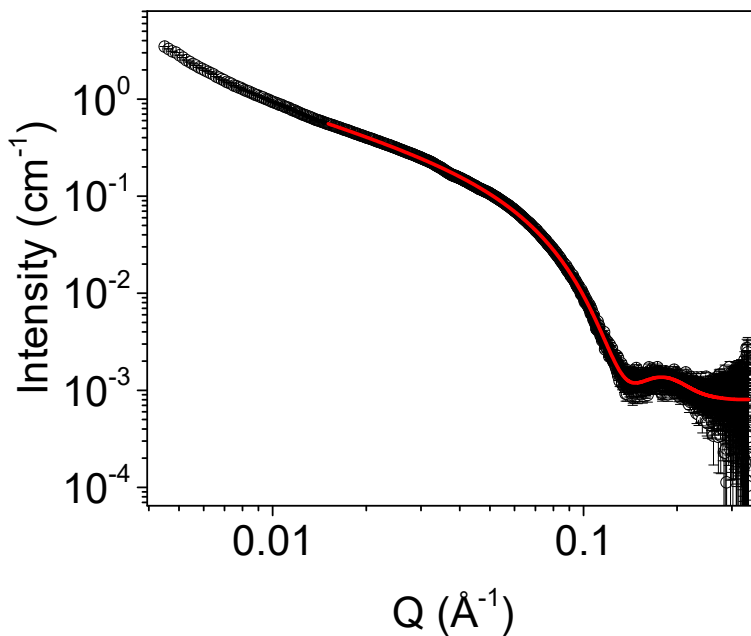


Figure A.4.24. Small angle X-ray scattering data for a solution of 5 mg/mL **1-NapFF** at pH 12 (open circles) fitted to a flexible elliptical cylinder model combined with power law (red). Fit parameters can be found in Table A.4.9. Shear alignment causing elliptical scattering plot and kink in data is evidenced in Figure A.4.25.

Table A.4.9. Parameters of SAXS model fit seen in Figure A.4.24.

1-NapFF 5 mg/mL pH 12	Flexible elliptical cylinder combined with power law	
	Value	Error
Scale A	4.26E-04	5.53E-08
Scale B	4.59E-08	7.69E-10
Background	7.55E-04	3.51E-06
Length (Å)	382.26	0.70815
Kuhn length (Å)	491.36	8.37
Radius (Å)	23.388	1.97E-03
Axis Ratio	1.3765	1.08E-04
Power	3.0871	0.034804
Range (Å ⁻¹)	0.015-0.3397383	
Chi ²	10.111	

Appendix

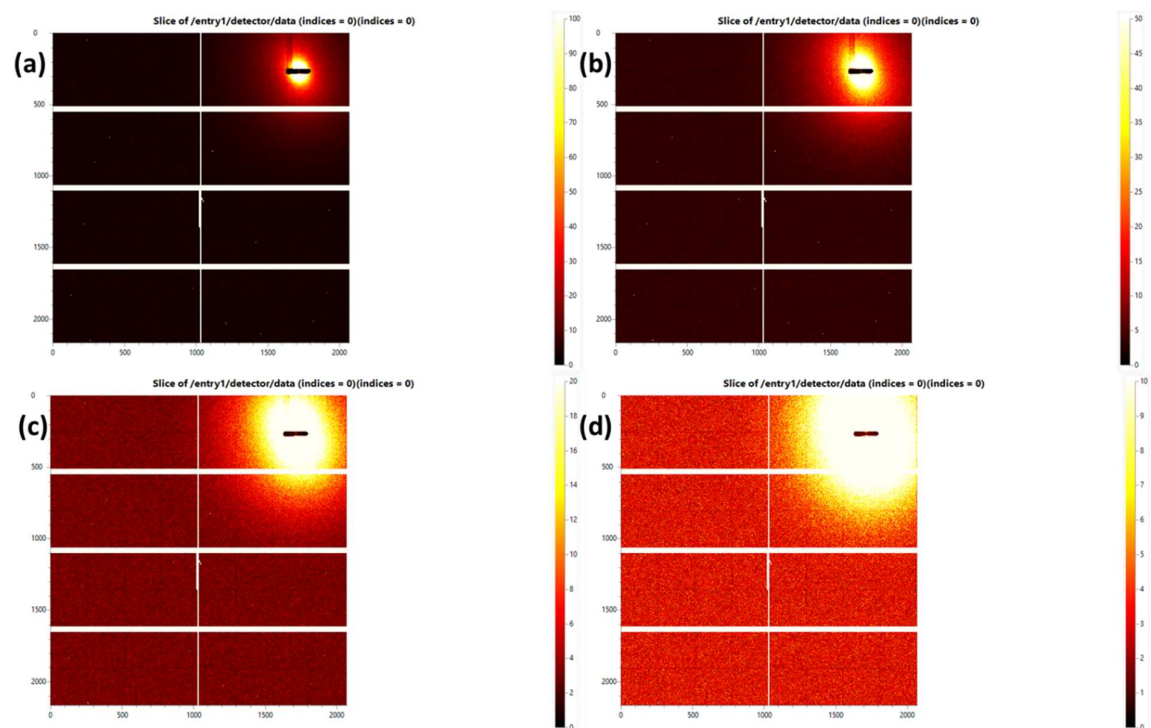


Figure A.4.25. Raw detector data of 2D scattering plots of measurement taken from for a solution of 5 mg/mL 1-NapFF at pH 12. Histogram plots are shown at a range of 0 to (a) 100, (b) 50, (c) 20 and (d) 10.

Appendix

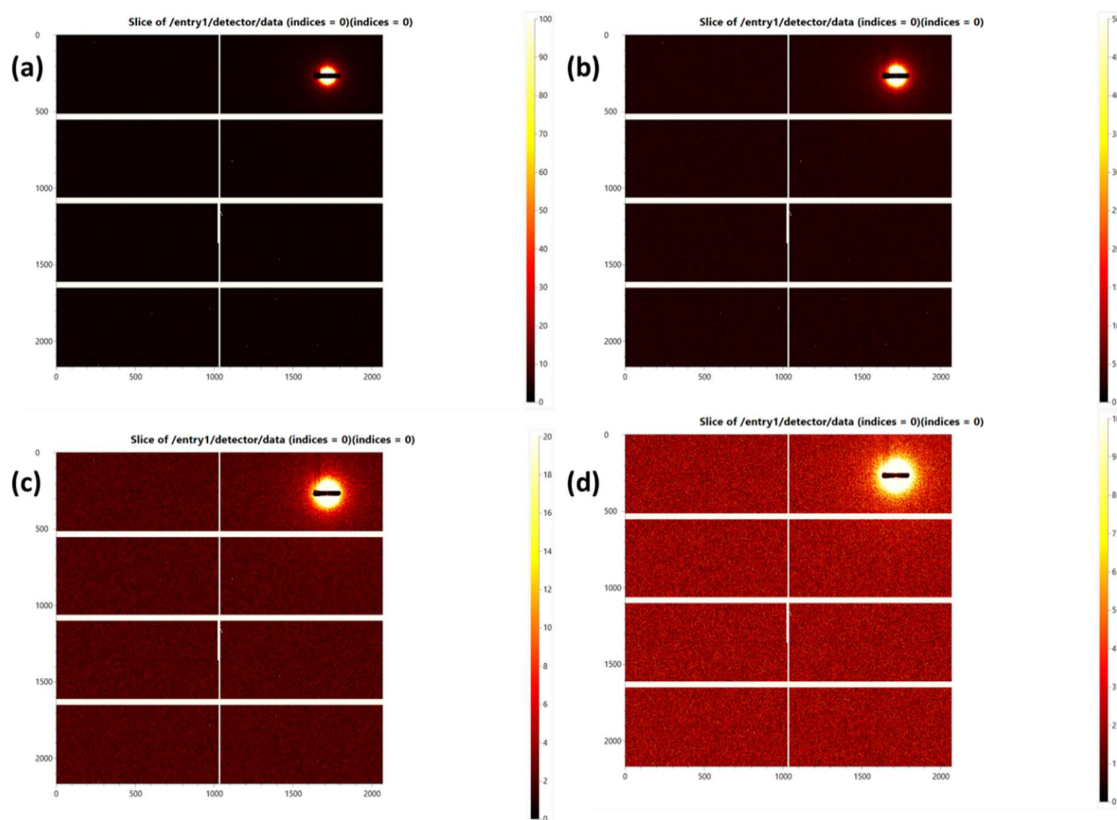


Figure A.4.26. Raw detector data of 2D scattering plots of measurement taken from for a solution of H_2O containing 50% 0.1 M NaCl. Histogram plots are shown at a range of 0 to (a) 100, (b) 50, (c) 20 and (d) 10. This data has no kinks and are shown as a control for no shear aligned sample.

Appendix

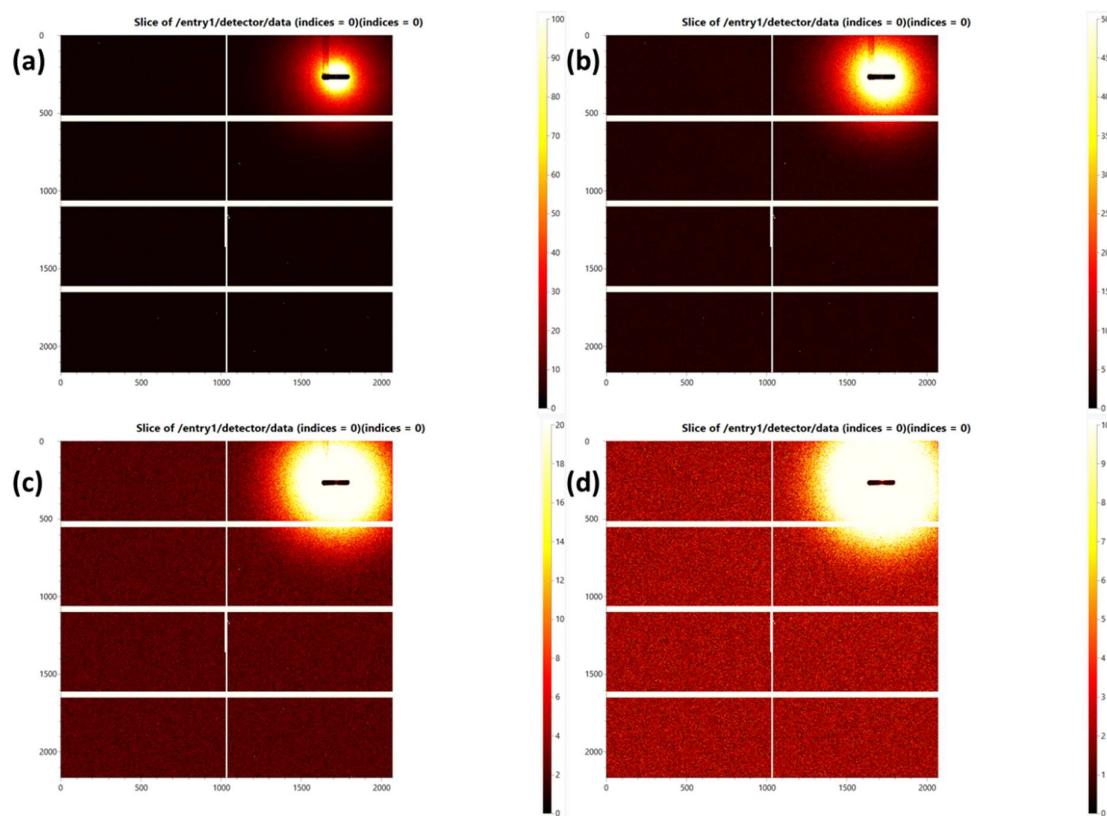


Figure A.4.27. Raw detector data of 2D scattering plots of measurement taken from for a solution of **NDI-F:1-NapFF** 5:5 mg/mL adjusted to pH 6. Histogram plots are shown at a range of 0 to (a) 100, (b) 50, (c) 20 and (d) 10. This data has no kinks and are shown as a control for no shear aligned sample.

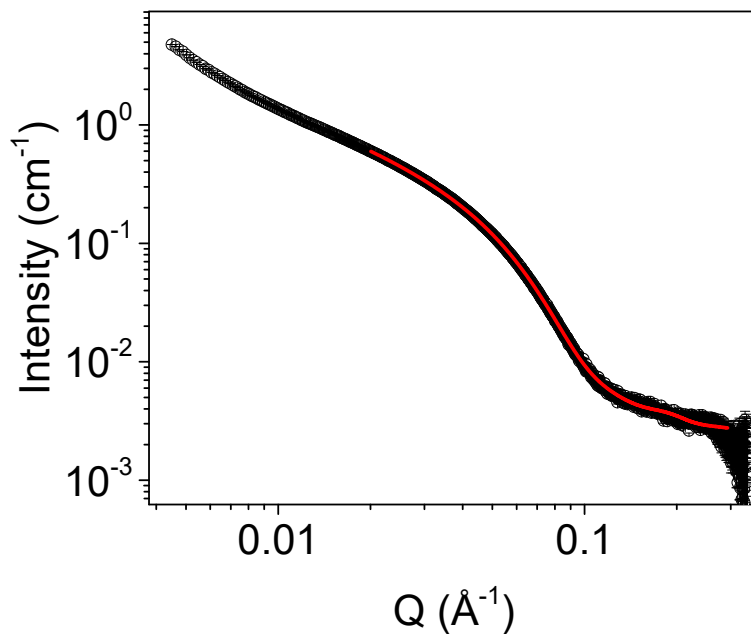


Figure A.4.28. Small angle X-ray scattering data for a solution of **NDI-GF:1-NapFF 5:5 mg/mL** at pH 6 (open circles) fitted to a flexible elliptical cylinder model combined with power law (red). Fit parameters can be found in Table A.4.10.

Table A.4.10. Parameters of SAXS model fit seen in Figure A.4.28.

NDI-GF:1-NapFF 5:5 mg/mL pH 6	Flexible elliptical cylinder combined with power law	
	Value	Error
Scale A	3.33E-04	4.48E-08
Scale B	4.17E-05	5.05E-08
Background	2.30E-03	3.66E-06
Length (Å)	1.82E+10	4.65E+10
Kuhn length (Å)	349.11	1.1876
Radius (Å)	26.331	2.79E-03
Axis Ratio	1.725	1.67E-04
Power	1.8485	3.88E-04
Range (Å ⁻¹)	0.02-0.292763	
Chi ²	2.1979	

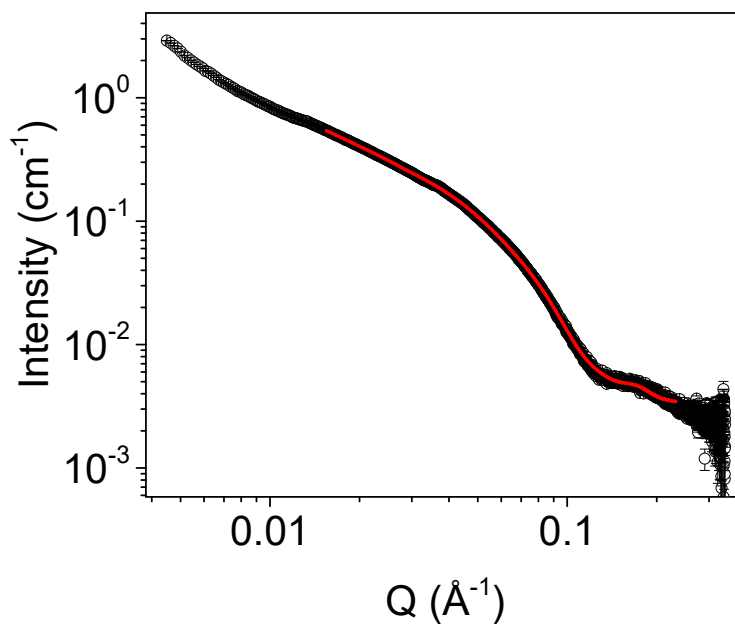


Figure A.4.29. Small angle X-ray scattering data for a solution of **NDI-GF:1-NapFF** 5:5 mg/mL at pH 9 (open circles) fitted to a flexible elliptical cylinder model combined with cylinder (red). Fit parameters can be found in Table A.4.11.

Table A.4.11. Parameters of SAXS model fit seen in Figure A.4.29.

NDI-GF:1-NapFF 5:5 mg/mL pH 9	Flexible elliptical cylinder combined with cylinder	
	Value	Error
Scale A	8.82E-05	3.13E-08
Scale B	3.96E-04	7.93E-08
Background	3.35E-03	4.17E-06
Length (Å)	2.28E+38	1.93E+30
Kuhn length (Å)	113.68	0.0732
Radius (Å)	14.579	3.79E-03
Axis Ratio	3.5921	8.93E-04
Length B (Å)	131.11	0.076227
Radius B (Å)	30.378	4.03E-03
Range (Å ⁻¹)	0.01549142-0.23165601	
Chi ²	3.5847	

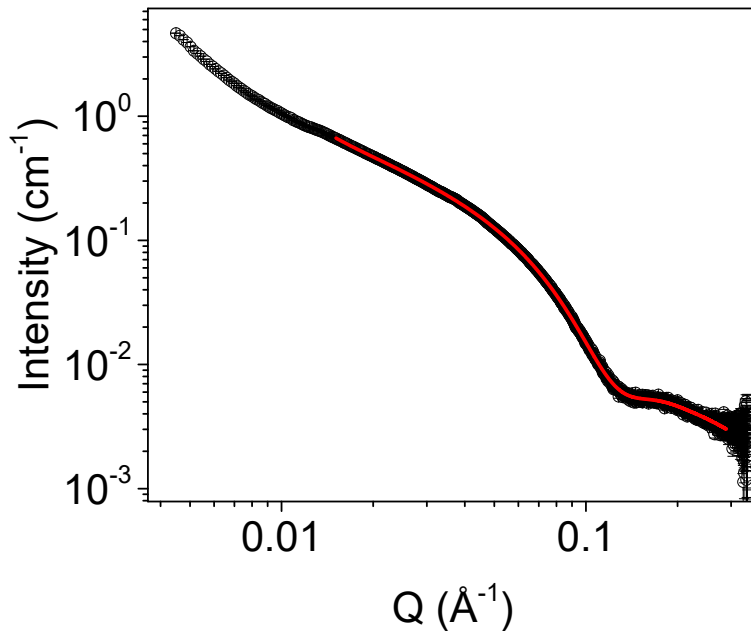


Figure A.4.30. Small angle X-ray scattering data for a solution of **NDI-GF:1-NapFF 5:5 mg/mL** at pH 12 (open circles) fitted to a flexible elliptical cylinder model combined with sphere (red). Fit parameters can be found in Table A.4.12.

Table A.4.12. Parameters of SAXS model fit seen in Figure A.4.30.

NDI-GF:1-NapFF 5:5 mg/mL pH 12	Flexible elliptical cylinder combined with sphere	
	Value	Error
Scale A	4.88E-04	5.86E-08
Scale B	1.72E-03	1.92E-06
Background	1.01E-03	3.74E-06
Length (Å)	3.74E+05	6.35E+03
Kuhn length (Å)	244.22	0.53744
Radius (Å)	22.896	1.82E-03
Axis Ratio	1.4604	1.08E-04
Radius B (Å)	6.9674	3.19E-03
Range (Å ⁻¹)	0.015-0.28923	
Chi ²	3.8119	

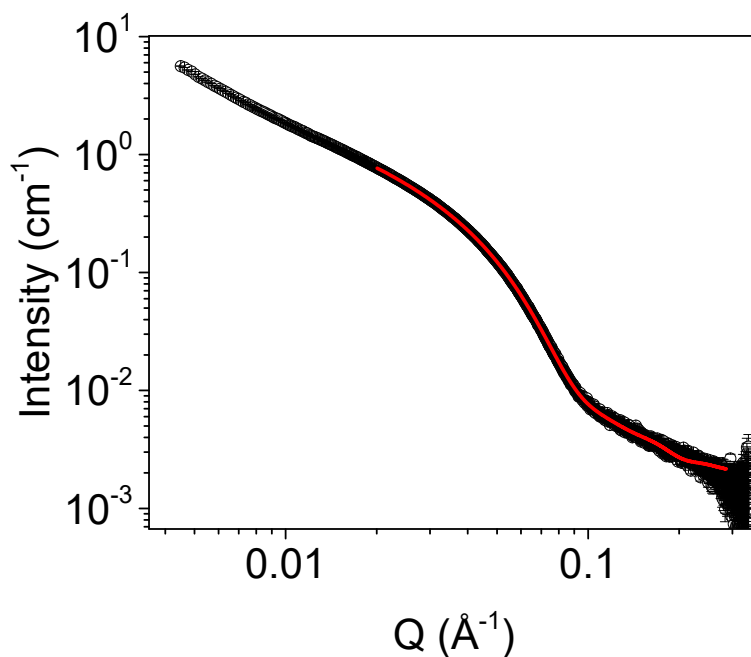


Figure A.4.31. Small angle X-ray scattering data for a solution of **NDI-GF:1-NapFF** 5:2.5 mg/mL at pH 6 (open circles) fitted to a flexible elliptical cylinder model combined with power law (red). Fit parameters can be found in Table A.4.13.

Table A.4.13. Parameters of SAXS model fit seen in Figure A.4.31.

NDI-GF:1-NapFF 5:2.5 mg/mL pH 6	Flexible elliptical cylinder combined with power law	
	Value	Error
Scale A	8.78E-03	1.15E-06
Scale B	2.41E-05	1.81E-08
Background	1.73E-03	3.67E-06
Length (Å)	207.72	0.17722
Kuhn length (Å)	202.7	0.44586
Radius (Å)	31.16	0.003393
Axis Ratio	1.6146	1.60E-04
Power	2.1885	2.31E-04
Range (Å ⁻¹)	0.02-0.0285959	
Chi ²	2.6725	

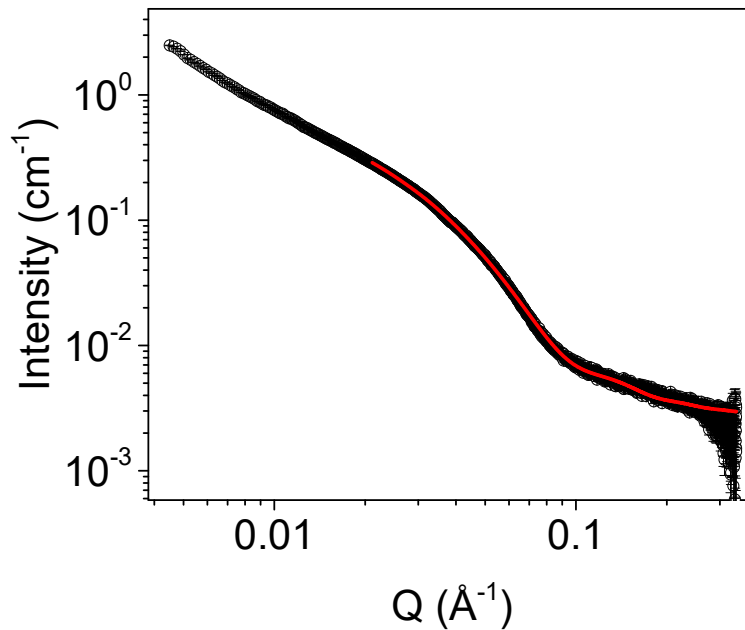


Figure A.4.32. Small angle X-ray scattering data for a solution of **NDI-GF:1-NapFF 5:2.5 mg/mL** at pH 9 (open circles) fitted to a flexible cylinder model combined with power law (red). Fit parameters can be found in Table A.4.14.

Table A.4.14. Parameters of SAXS model fit seen in Figure A.4.32.

NDI-GF:1-NapFF 5:2.5 mg/mL pH 9	Flexible cylinder combined with power law	
	Value	Error
Scale A	2.40E-03	6.17E-07
Scale B	3.92E-05	1.38E-08
Background	2.63E-03	3.53E-06
Length (Å)	409.53	1.20E-03
Kuhn length (Å)	40.953	0.027106
Radius (Å)	36.884	6.48E-03
Power	2.0339	8.52E-05
Range (Å ⁻¹)	0.021-0.3397383	
Chi ²	4.9983	

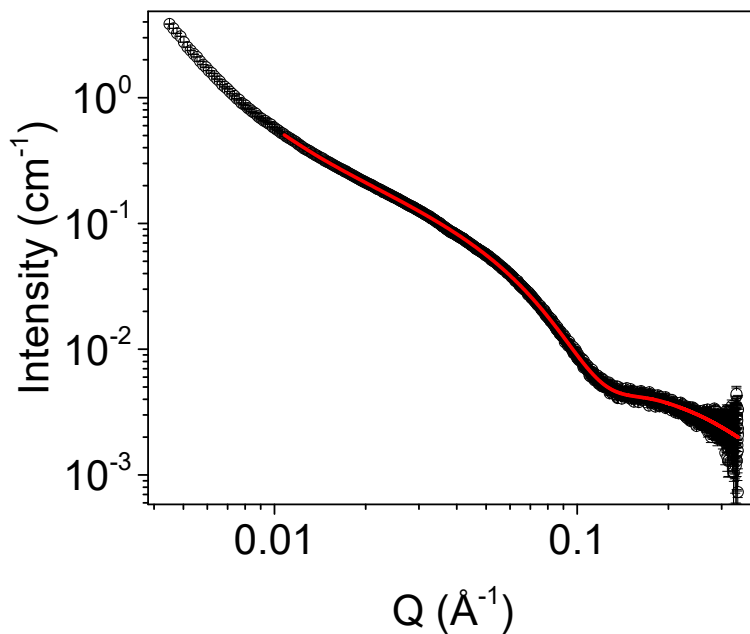


Figure A.4.33. Small angle X-ray scattering data for a solution of **NDI-GF:1-NapFF 5:2.5 mg/mL** at pH 12 (open circles) fitted to a flexible elliptical cylinder model combined with sphere (red). Fit parameters can be found in Table A.4.15.

Table A.4.15. Parameters of SAXS model fit seen in Figure A.4.33.

NDI-GF:1-NapFF 5:2.5 mg/mL pH 12	Flexible elliptical cylinder combined with sphere	
	Value	Error
Scale A	5.33E-03	1.03E-06
Scale B	0.040735	4.85E-05
Background	7.14E-04	3.53E-06
Length (Å)	1.16E+04	93.269
Kuhn length (Å)	250.75	0.31285
Radius (Å)	22.426	2.73E-03
Axis Ratio	1.4675	1.67E-04
Radius B (Å)	6.8386	3.28E-03
Range (Å ⁻¹)	0.0107808-0.339738	
Chi ²	2.861	

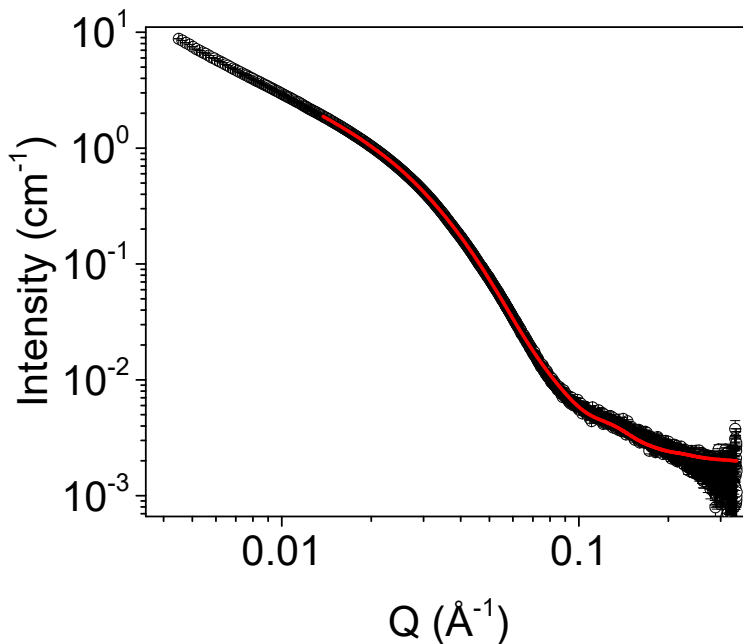


Figure A.4.34. Small angle X-ray scattering data for a solution of **NDI-GF:1-NapFF** 5:1.25 mg/mL at pH 6 (open circles) fitted to a flexible elliptical cylinder model combined with power law (red). Fit parameters can be found in Table A.4.16.

Table A.4.16. Parameters of SAXS model fit seen in Figure A.4.34.

NDI-GF:1-NapFF 5:1.25 mg/mL pH 6 Flexible elliptical cylinder combined with power law		
	Value	Error
Scale A	3.51E-03	4.14E-07
Scale B	6.19E-06	2.01E-09
Background	1.89E-03	3.52E-06
Length (Å)	501.31	0.1568
Kuhn length (Å)	59.577	0.017406
Radius (Å)	35.571	3.31E-03
Axis Ratio	1.8734	1.60E-04
Power	2.6917	8.11E-05
Range (Å ⁻¹)	0.013790367-0.3397383	
Chi ²	5.3705	

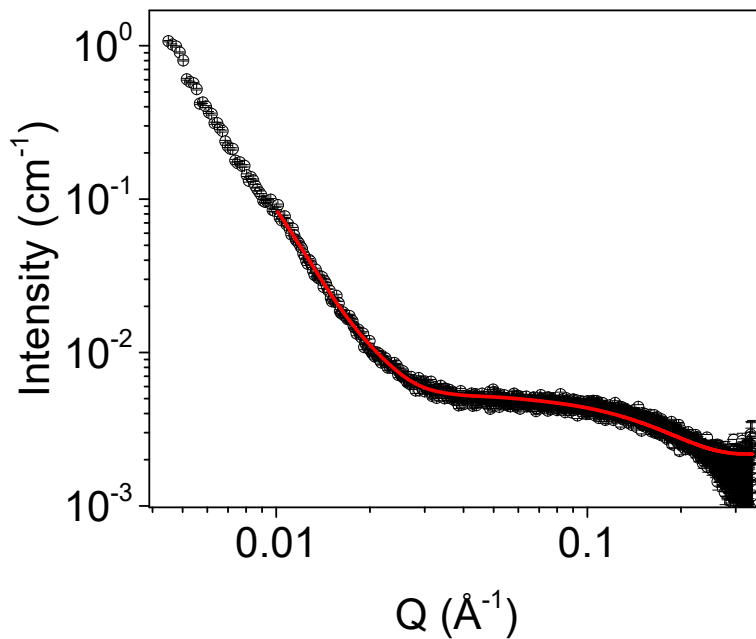


Figure A.4.35. Small angle X-ray scattering data for a solution of **NDI-GF:1-NapFF** 5:1.25 mg/mL at pH 9 (open circles) fitted to a flexible elliptical cylinder model combined with cylinder (red). Fit parameters can be found in Table A.4.17.

Table A.4.17. Parameters of SAXS model fit seen in Figure A.4.35.

NDI-GF:1-NapFF 5:1.25 mg/mL pH 9 Flexible elliptical cylinder combined with cylinder		
	Value	Error
Scale A	1.05E-05	3.50E-08
Scale B	4.15E-03	9.51E-06
Background	2.17E-03	3.36E-06
Length (Å)	4.21E+10	2.73E+12
Kuhn length (Å)	50.165	0.23662
Radius (Å)	84.213	0.6221
Axis Ratio	2.955	0.014281
Length B (Å)	21.391	0.063256
Radius B (Å)	12.252	0.018069
Range (Å ⁻¹)	0.01-0.3397383	
Chi ²	3.2094	

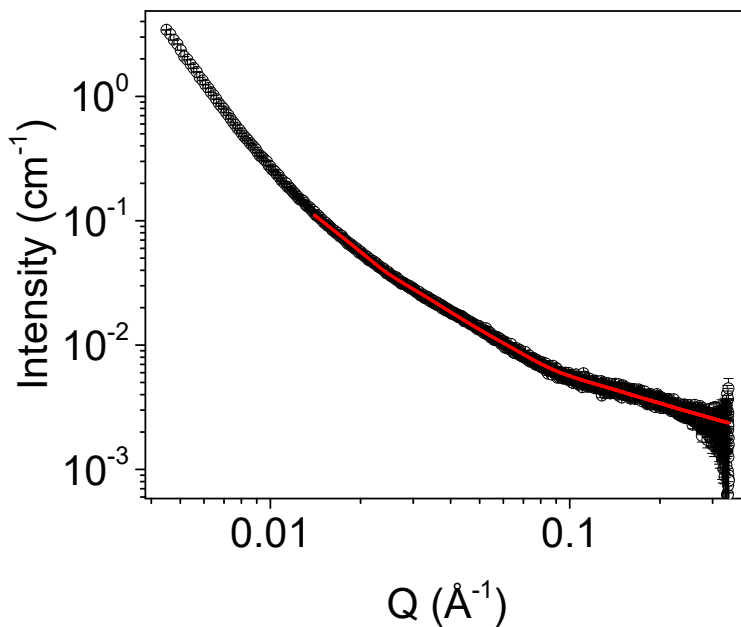


Figure A.4.36. Small angle X-ray scattering data for a solution of **NDI-GF:1-NapFF** 5:1.25 mg/mL at pH 12 (open circles) fitted to a flexible elliptical cylinder model combined with cylinder (red). Fit parameters can be found in Table A.4.18.

Table A.4.18. Parameters of SAXS model fit seen in Figure A.4.36.

NDI-GF:1-NapFF 5:1.25 mg/mL pH 12	Flexible elliptical cylinder combined with cylinder	
	Value	Error
Scale A	2.80E-04	2.47E-07
Scale B	2.27E-02	2.49E-05
Background	1.78E-03	3.45E-06
Length (Å)	1.39E+32	2.70E+30
Kuhn length (Å)	136.97	0.2122
Radius (Å)	29.262	0.022982
Axis Ratio	2.8972	2.07E-03
Length B (Å)	84.463	0.26049
Radius B (Å)	4.9961	2.92E-03
Range (Å ⁻¹)	0.014-0.339738	
Chi ²	2.1395	

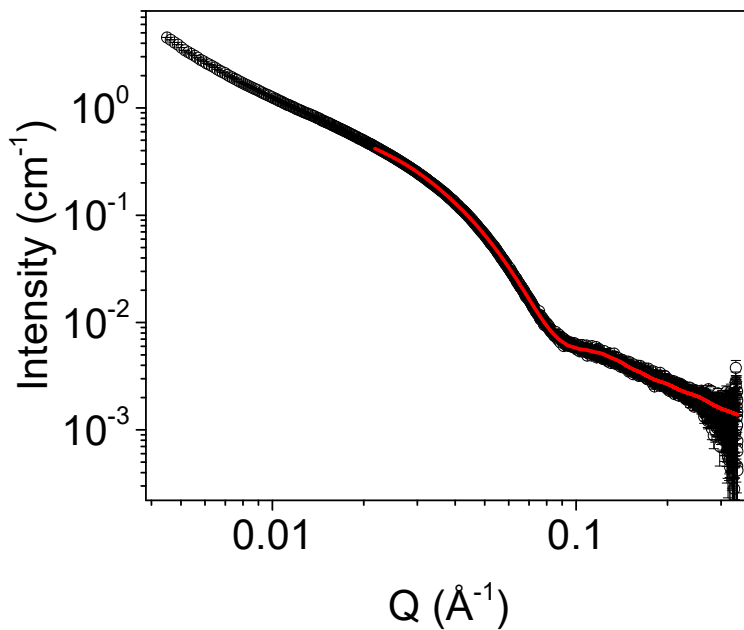


Figure A.4.37. Small angle X-ray scattering data for a solution of **NDI-GF:1-NapFF** 5:0.625 mg/mL at pH 6 (open circles) fitted to a flexible elliptical cylinder model combined with cylinder (red). Fit parameters can be found in Table A.4.19.

Table A.4.19. Parameters of SAXS model fit seen in Figure A.4.37.

NDI-GF:1-NapFF 5:0.625 mg/mL pH 6	Flexible elliptical cylinder combined with cylinder	
	Value	Error
Scale A	1.10E-03	2.14E-07
Scale B	6.72E-03	7.08E-06
Background	7.08E-04	3.88E-06
Length (Å)	307.36	0.381936
Kuhn length (Å)	76.839	5.95E-05
Radius (Å)	34.958	6.25E-03
Axis Ratio	1.3708	2.08E-04
Length B (Å)	2.74E+03	13.979
Radius B (Å)	4.8971	2.78E-03
Range (Å ⁻¹)	0.0217722231-0.3397383	
Chi ²	4.2863	

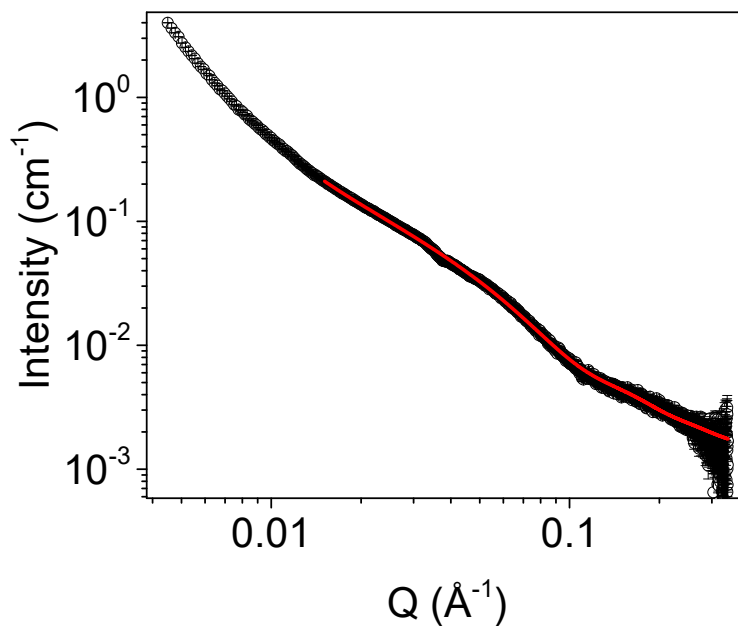


Figure A.4.38. Small angle X-ray scattering data for a solution of **NDI-GF:1-NapFF** 5:0.625 mg/mL at pH 9 (open circles) fitted to a flexible cylinder model combined with power law (red). Fit parameters can be found in Table A.4.20. Shear alignment causing elliptical scattering plot and kink in data is evidenced in Figure A.4.39.

Table A.4.20. Parameters of SAXS model fit seen in Figure A.4.37.

NDI-GF:1-NapFF 5:0.625 mg/mL pH 9		
Flexible cylinder combined with power law		
	Value	Error
Scale A	4.02E-04	2.85E-07
Scale B	1.68E-04	7.13E-08
Background	8.24E-04	3.51E-06
Length (Å)	2.39E+06	2.81E+10
Kuhn length (Å)	207.73	1.0138
Radius (Å)	31.442	0.014939
Power	1.5855	1.28E-04
Range (Å ⁻¹)	0.015-0.3397383	
Chi ²	6.401	

Appendix

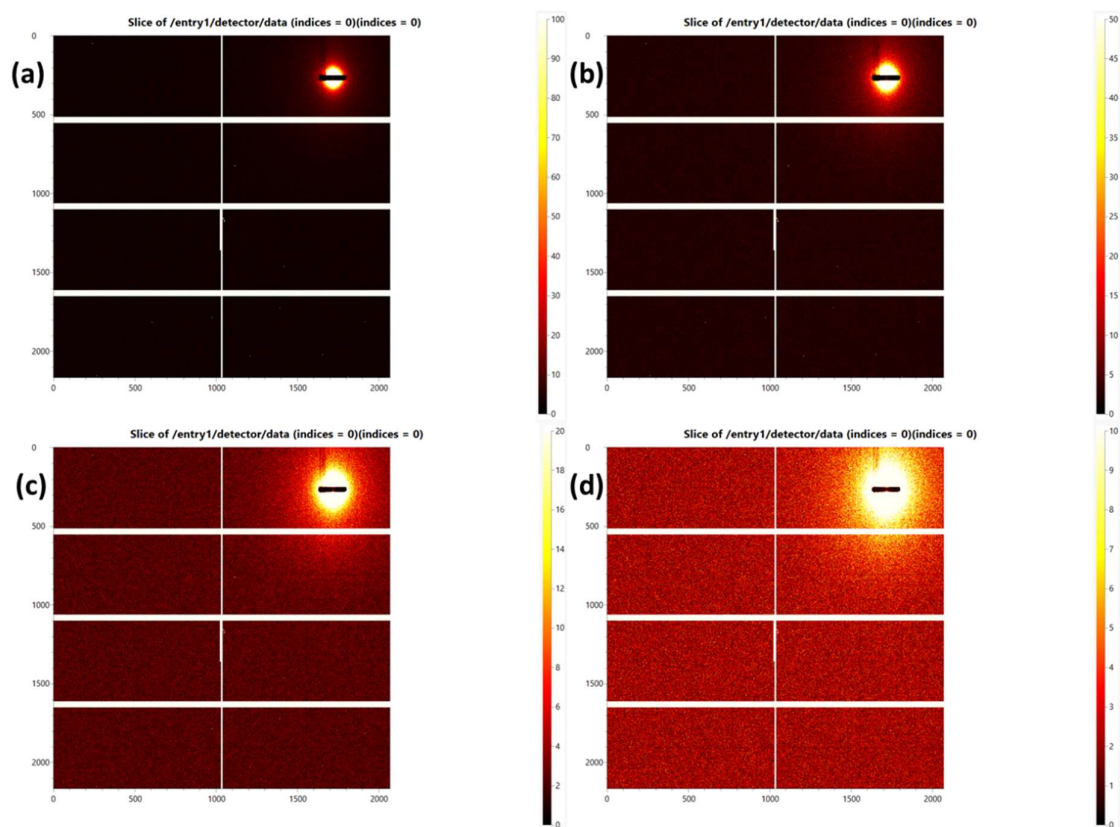


Figure A.4.39. Raw detector data of 2D scattering plots of measurement taken from for a solution of **NDI-GF:1-NapFF** 5:0.625 mg/mL adjusted to pH 9. Histogram plots are shown at a range of 0 to (a) 100, (b) 50, (c) 20 and (d) 10.

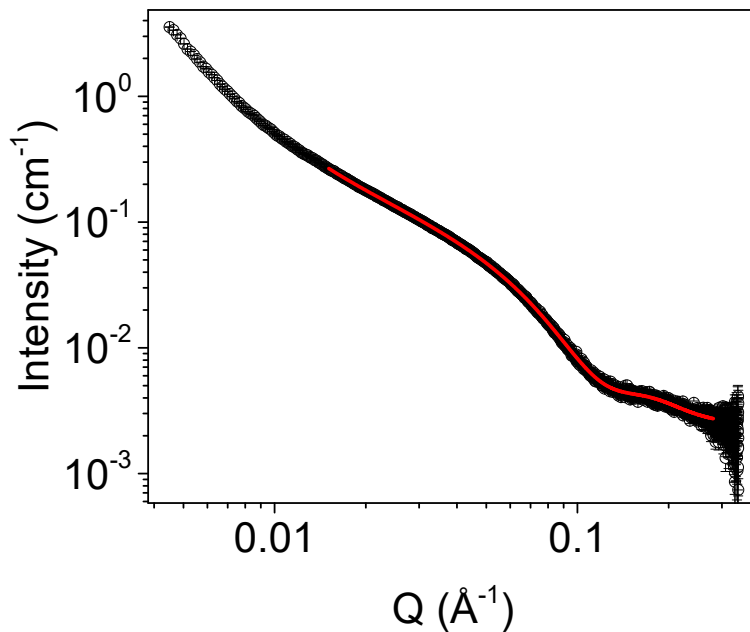


Figure A.4.40. Small angle X-ray scattering data for a solution of **NDI-GF:1-NapFF** 5:0.625 mg/mL at pH 12 (open circles) fitted to a flexible cylinder model combined with sphere (red). Fit parameters can be found in Table A.4.21.

Table A.4.21. Parameters of SAXS model fit seen in Figure A.4.40.

NDI-GF:1-NapFF 5:0.625 mg/mL pH 12	Flexible elliptical cylinder combined with sphere	
	Value	Error
Scale A	1.11E-03	2.61E-07
Scale B	1.41E-03	3.27E-06
Background	2.55E-03	3.62E-06
Length (Å)	9.84E+03	88.729
Kuhn length (Å)	211.42	0.36517
Radius (Å)	23.906	3.63E-03
Axis Ratio	1.3493	1.89E-04
Radius B (Å)	12.236	0.012813
Range (Å ⁻¹)	0.0150989-0.280856	
Chi ²	1.5755	

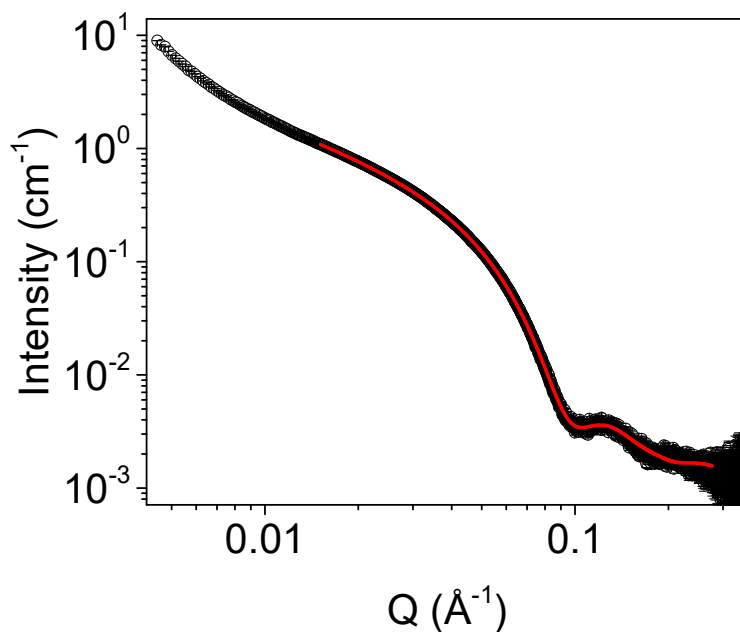


Figure A.4.41. Small angle X-ray scattering data for a solution of **NDI-F:1-NapFF** 5:5 mg/mL at pH 6 (open circles) fitted to a flexible elliptical cylinder model combined with hollow cylinder (red). Fit parameters can be found in Table A.4.22.

Table A.4.22. Parameters of SAXS model fit seen in Figure A.4.41.

NDI-F:1-NapFF 5:5 mg/mL pH 6	Flexible elliptical cylinder combined with hollow cylinder	
	Value	Error
Scale A	4.37E-04	4.44E-08
Scale B	6.06E-05	7.30E-07
Background	1.51E-03	3.61E-06
Length (Å)	385.26	0.57189
Kuhn length (Å)	317.28	0.48714
Radius (Å)	32.967	2.44E-03
Axis Ratio	1.4234	9.77E-05
Length B (Å)	26.528	0.48276
Radius B (Å)	6.6582	0.14774
Thickness B (Å)	5.0637	0.058302
Range (Å ⁻¹)	0.15-0.27666849	
Chi ²	2.339	

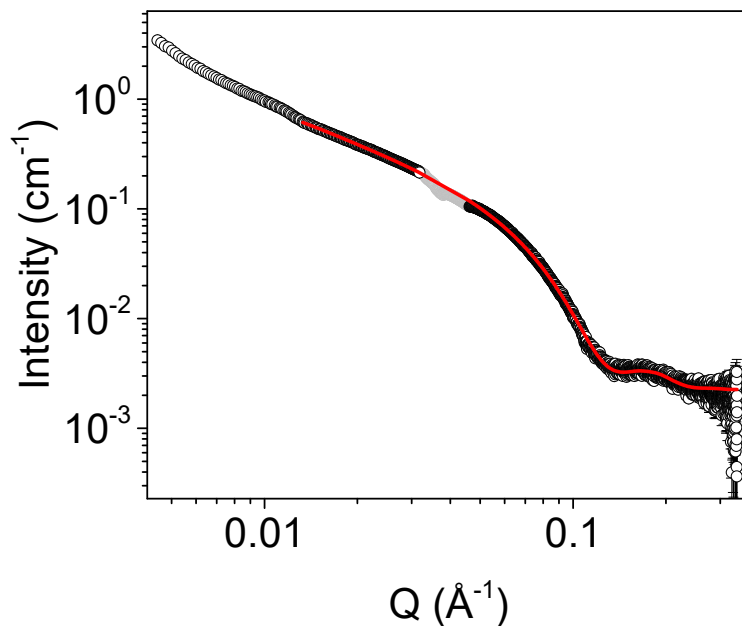


Figure A.4.42. Small angle X-ray scattering data for a solution of **NDI-F:1-NapFF** 5:5 mg/mL at pH 9 (open circles) fitted to a flexible elliptical cylinder model combined with hollow cylinder (red). Part of the data has been cut out (grey) due to a large kink. Fit parameters can be found in Table A.4.23. Shear alignment causing elliptical scattering plot and kink in data is evidenced in Figure A.4.43.

Table A.4.23. Parameters of SAXS model fit seen in Figure A.4.42.

NDI-F:1-NapFF 5:5 mg/mL pH 9	Flexible elliptical cylinder combined with hollow cylinder	
	Value	Error
Scale A	2.02E-04	8.14E-08
Scale B	3.58E-04	8.63E-08
Background	2.24E-03	3.56E-06
Length (Å)	392.9	1.1269
Kuhn length (Å)	242.53	0.46784
Radius (Å)	19.3	4.69E-03
Axis Ratio	1.3823	3.31E-04
Length B (Å)	4.43E+03	13.779
Radius B (Å)	5.9122	4.93E-03
Thickness B (Å)	23.423	4.16E-03
Range (Å ⁻¹)	0.0133-0.34	
Chi ²	9.4607	

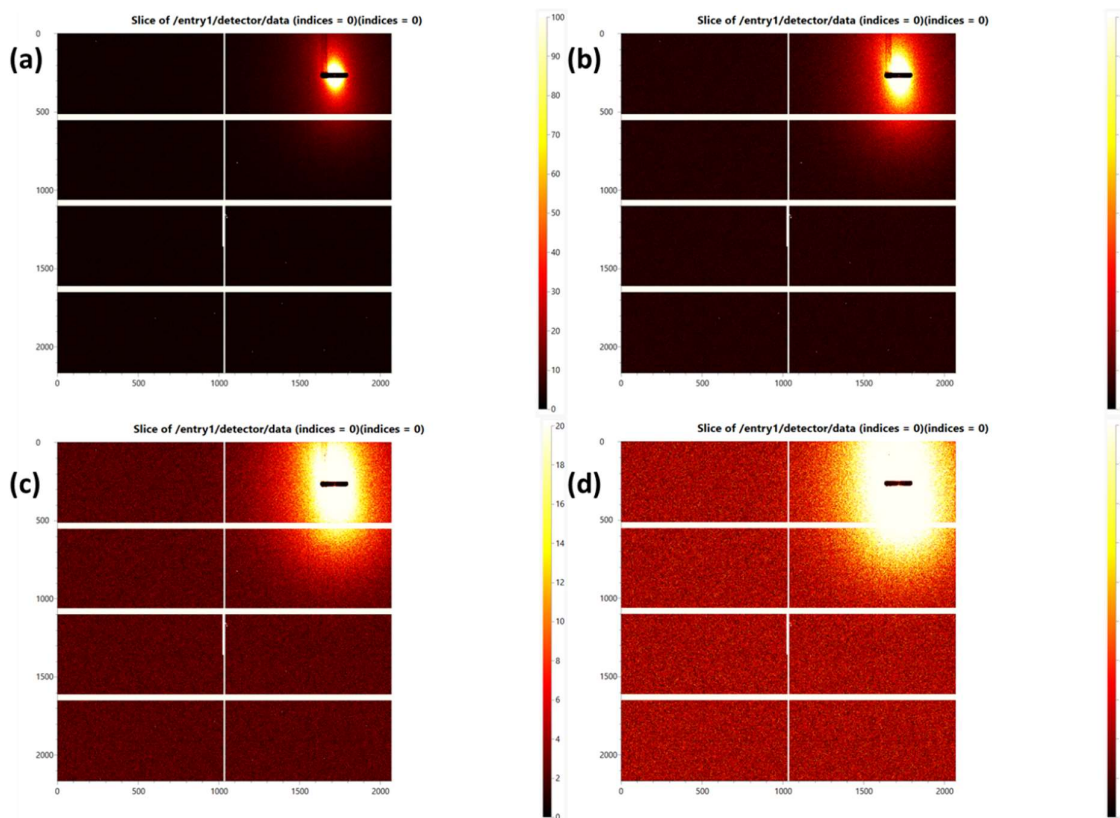


Figure A.4.43. Raw detector data of 2D scattering plots of measurement taken from for a solution of **NDI-F:1-NapFF** 5:5 mg/mL adjusted to pH 9. Histogram plots are shown at a range of 0 to (a) 100, (b) 50, (c) 20 and (d) 10.

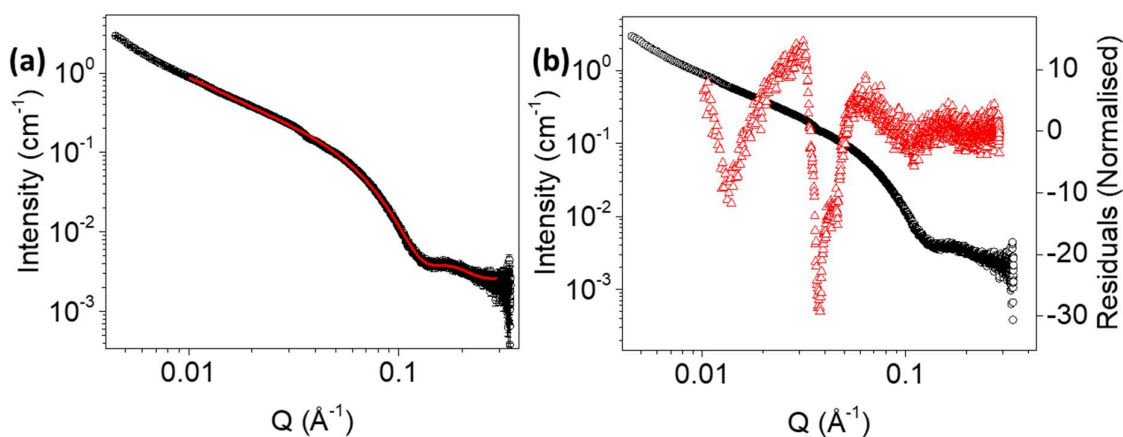


Figure A.4.44. Small angle X-ray scattering data for a solution of **NDI-F:1-NapFF** 5:5 mg/mL at pH 12 (open circles) fitted to a flexible cylinder model combined with hollow cylinder (red). A small kink results in a higher χ^2 value shown by (b) the residuals of the fit (open triangles). Fit parameters can be found in Table A.4.24. Shear alignment causing elliptical scattering plot and kink in data is evidenced in Figure A.4.45.

Table A.4.24. Parameters of SAXS model fit seen in Figure A.4.44.

NDI-F:1-NapFF 5:5 mg/mL pH 12 Flexible cylinder combined with hollow cylinder		
	Value	Error
Scale A	4.92E-04	8.22E-08
Scale B	1.59E-04	8.60E-08
Background	2.54E-03	3.68E-06
Length (Å)	616.35	1.4287
Kuhn length (Å)	302.58	0.28857
Radius (Å)	24.78	2.56E-03
Length B (Å)	4.96E+03	40.034
Radius B (Å)	14.286	0.013431
Thickness B (Å)	16.423	7.84E-03
Range (Å ⁻¹)	0.01-0.28923011	
Chi ²	19.635	

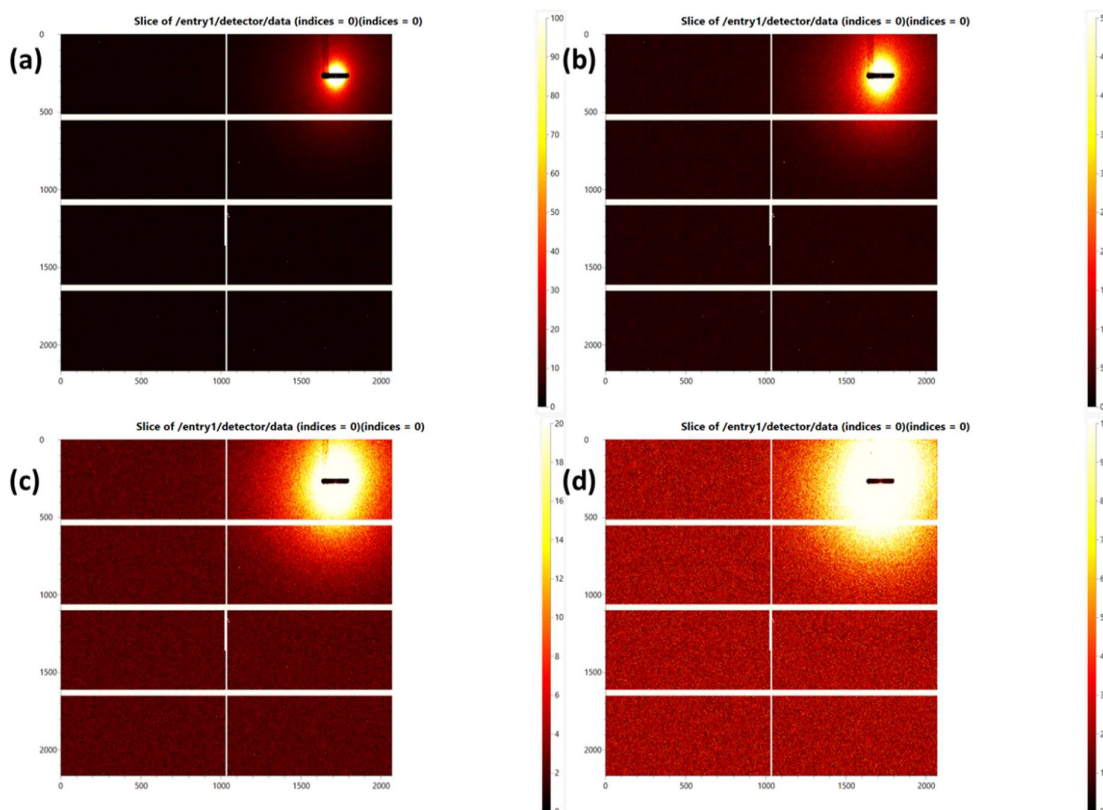


Figure A.4.45. Raw detector data of 2D scattering plots of measurement taken from for a solution of NDI-F:1-NapFF 5:5 mg/mL adjusted to pH 12. Histogram plots are shown at a range of 0 to (a) 100, (b) 50, (c) 20 and (d) 10.

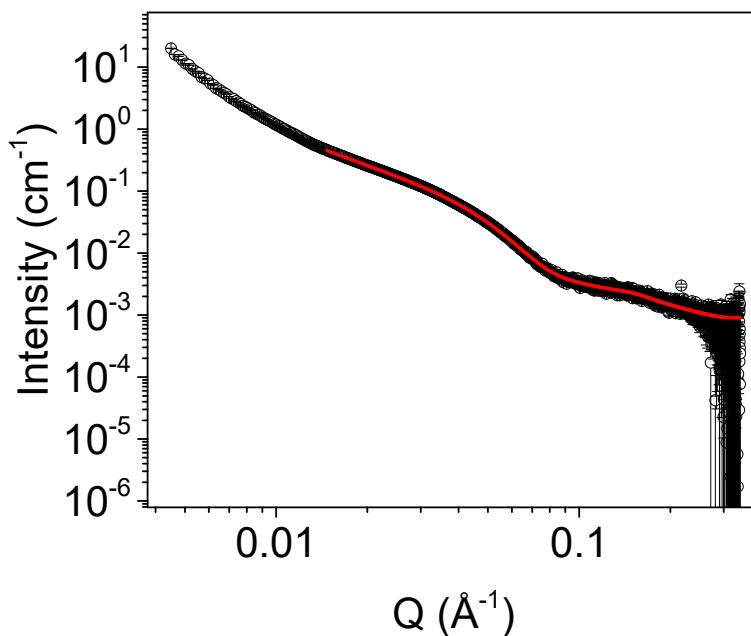


Figure A.4.46. Small angle X-ray scattering data for a solution of **NDI-F:1-NapFF 5:2.5 mg/mL** at pH 6 (open circles) fitted to a flexible elliptical cylinder model combined with cylinder (red). Fit parameters can be found in Table A.4.25.

Table A.4.25. Parameters of SAXS model fit seen in Figure A.4.46.

NDI-F:1-NapFF 5:2.5 mg/mL pH 6	Flexible elliptical cylinder combined with cylinder	
	Value	Error
Scale A	2.24E-03	5.01E-07
Scale B	7.66E-03	1.59E-05
Background	7.36E-04	3.96E-06
Length (Å)	6.67E+03	40.783
Kuhn length (Å)	162.02	0.11674
Radius (Å)	34.097	5.81E-03
Axis Ratio	1.6426	2.53E-04
Length B (Å)	179.98	3.0406
Radius B (Å)	6.5195	7.41E-03
Range (Å ⁻¹)	0.014706318-0.23178686	
Chi ²	2.1574	

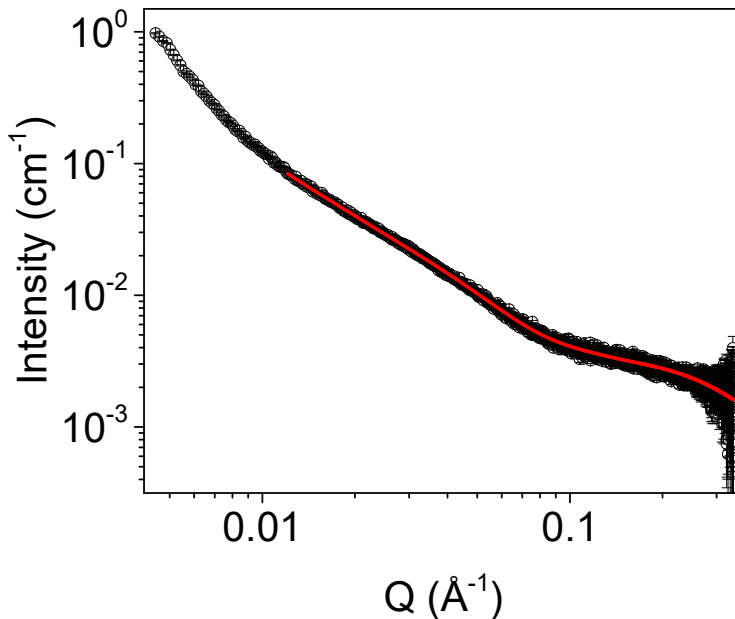


Figure A.4.47. Small angle X-ray scattering data for a solution of **NDI-F:1-NapFF** 5:2.5 mg/mL at pH 9 (open circles) fitted to a flexible elliptical cylinder model combined with sphere (red). Fit parameters can be found in Table A.4.26.

Table A.4.26. Parameters of SAXS model fit seen in Figure A.4.47.

NDI-F:1-NapFF 5:2.5 mg/mL pH 9	Flexible elliptical cylinder combined with sphere	
	Value	Error
Scale A	4.42E-04	3.71E-07
Scale B	0.028788	4.37E-05
Background	7.19E-04	3.40E-06
Length (Å)	2.52E+03	33.126
Kuhn length (Å)	193.59	0.57129
Radius (Å)	19.219	0.010499
Axis Ratio	2.3892	1.25E-03
Radius B (Å)	6.9612	4.21E-03
Range (Å ⁻¹)	0.012-0.3397383	
Chi ²	1.6707	

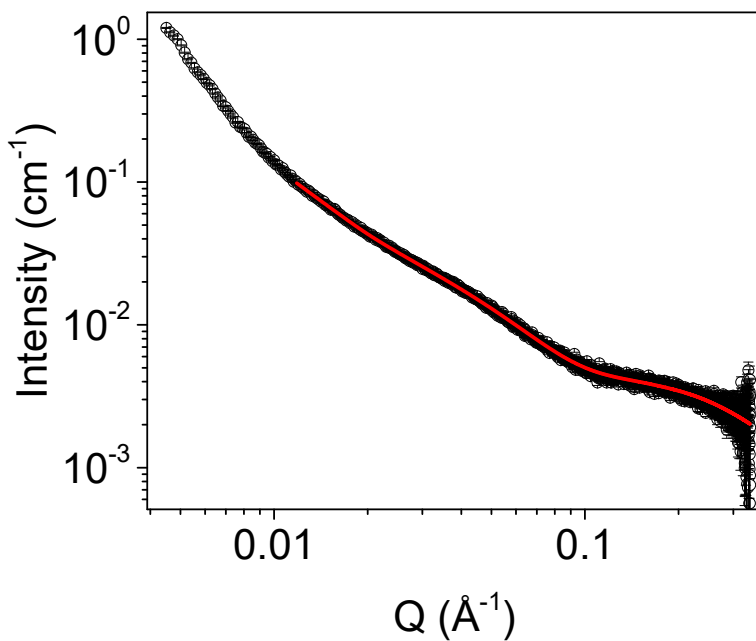


Figure A.4.48. Small angle X-ray scattering data for a solution of **NDI-F:1-NapFF** 5:2.5 mg/mL at pH 12 (open circles) fitted to a flexible elliptical cylinder model combined with sphere (red). Fit parameters can be found in Table A.4.27.

Table A.4.27. Parameters of SAXS model fit seen in Figure A.4.48.

NDI-F:1-NapFF 5:2.5 mg/mL pH 12	Flexible elliptical cylinder combined with sphere	
	Value	Error
Scale A	7.36E-04	5.68E-07
Scale B	0.031674	4.12E-05
Background	1.03E-03	3.44E-06
Length (Å)	1.46E+04	459.65
Kuhn length (Å)	171.02	0.4051
Radius (Å)	21.403	0.010119
Axis Ratio	1.7393	7.79E-04
Radius B (Å)	7.1664	3.74E-03
Range (Å ⁻¹)	0.011827613-0.3397383	
Chi ²	1.5793	

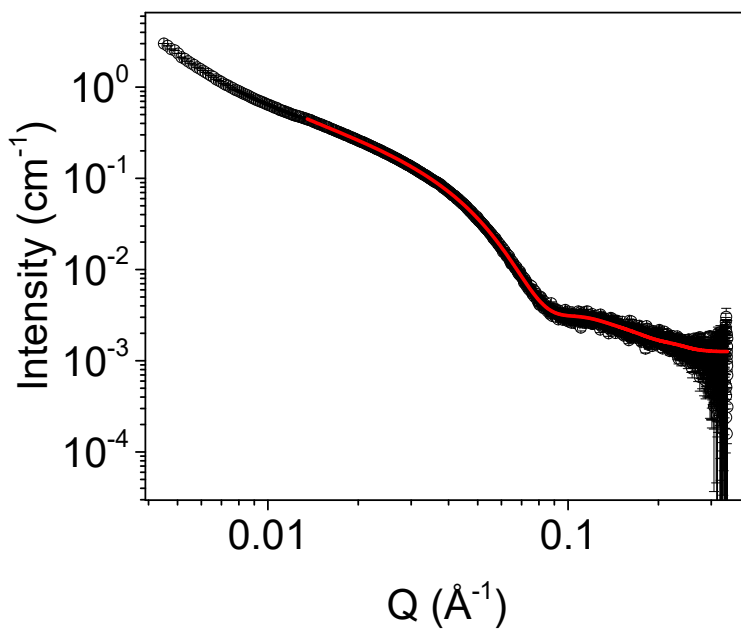


Figure A.4.49. Small angle X-ray scattering data for a solution of **NDI-F:1-NapFF** 5:1.25 mg/mL at pH 6 (open circles) fitted to a flexible elliptical cylinder model combined with hollow cylinder (red). Fit parameters can be found in Table A.4.28.

Table A.4.28. Parameters of SAXS model fit seen in Figure A.4.49.

NDI-F:1-NapFF 5:1.25 mg/mL pH 6	Flexible elliptical cylinder combined with hollow cylinder	
	Value	Error
Scale A	3.04E-03	6.07E-07
Scale B	4.61E-03	1.97E-05
Background	1.25E-03	3.45E-06
Length (Å)	1.36E+04	156.31
Kuhn length (Å)	330.09	1.275
Radius (Å)	34.879	5.17E-03
Axis Ratio	1.4808	1.99E-04
Length B (Å)	21.781	0.12918
Radius B (Å)	5.0231	0.043872
Thickness (Å)	5.0486	0.019501
Range (Å ⁻¹)	0.013528666-0.3397383	
Chi ²	1.9196	

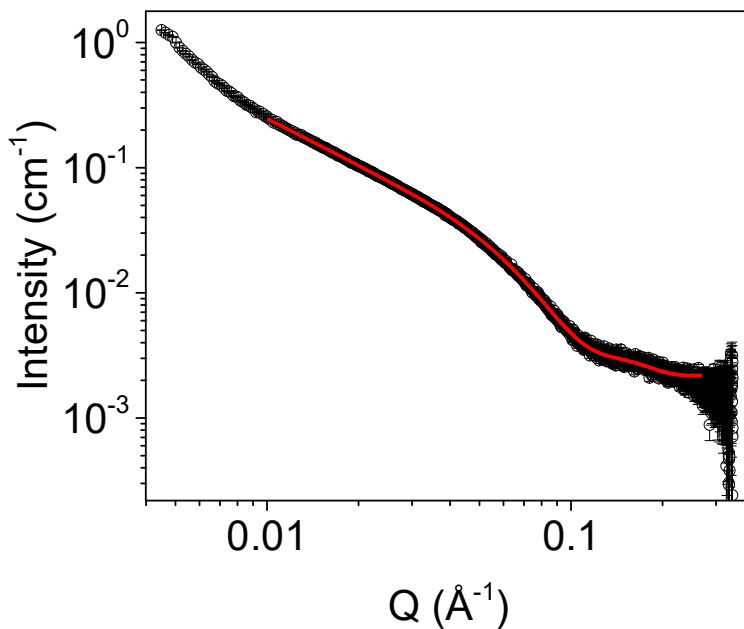


Figure A.4.50. Small angle X-ray scattering data for a solution of **NDI-F:1-NapFF 5:1.25 mg/mL** at pH 9 (open circles) fitted to a flexible cylinder model combined with hollow cylinder (red). Fit parameters can be found in Table A.4.29.

Table A.4.29. Parameters of SAXS model fit seen in Figure A.4.50.

NDI-F:1-NapFF 5:1.25 mg/mL pH 9	Flexible cylinder combined with hollow cylinder	
	Value	Error
Scale A	1.25E-03	1.45E-06
Scale B	1.44E-03	6.27E-07
Background	2.16E-03	3.58E-06
Length (Å)	263	454.48
Kuhn length (Å)	286.86	0.73692
Radius (Å)	15.674	4.28E-03
Length B (Å)	298.02	2.6231
Radius B (Å)	12.942	0.031054
Thickness (Å)	17.047	0.017152
Range (Å ⁻¹)	0.01-0.26659302	
Chi ²	1.9601	

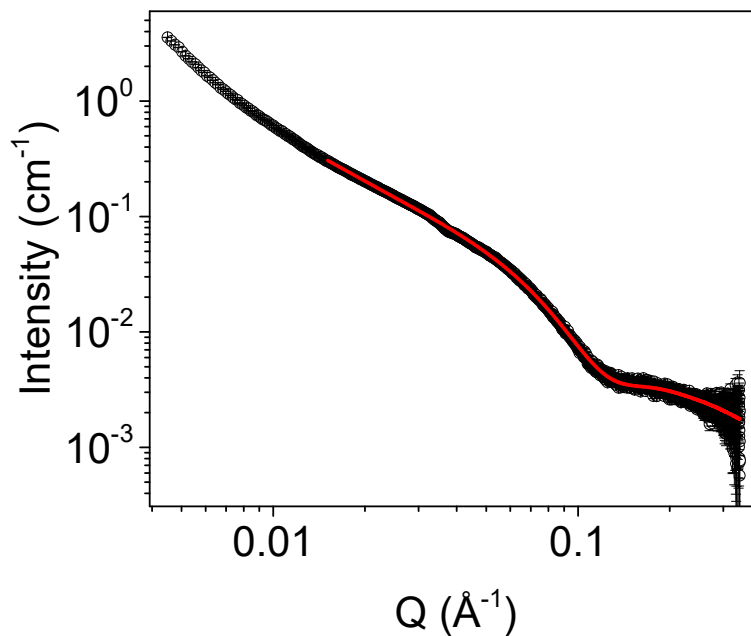


Figure A.4.51. Small angle X-ray scattering data for a solution of **NDI-F:1-NapFF** 5:1.25 mg/mL at pH 12 (open circles) fitted to a flexible elliptical cylinder model combined with sphere (red). Fit parameters can be found in Table A.4.30. Shear alignment causing elliptical scattering plot and kink in data is evidenced in Figure A.4.52.

Table A.4.30. Parameters of SAXS model fit seen in Figure A.4.51.

NDI-F:1-NapFF 5:1.25 mg/mL pH 12		
Flexible elliptical cylinder combined with sphere		
	Value	Error
Scale A	4.04E-04	3.52E-06
Scale B	4.58E-03	1.00E-06
Background	4.60E-02	6.24E-05
Length (Å)	214	7.4733
Kuhn length (Å)	208.48	0.2878
Radius (Å)	22.384	3.13E-03
Axis Ratio	1.441	1.87E-04
Radius B (Å)	6.1026	3.24E-03
Range (Å ⁻¹)	0.015-0.3397383	
Chi ²	7.0611	

Appendix

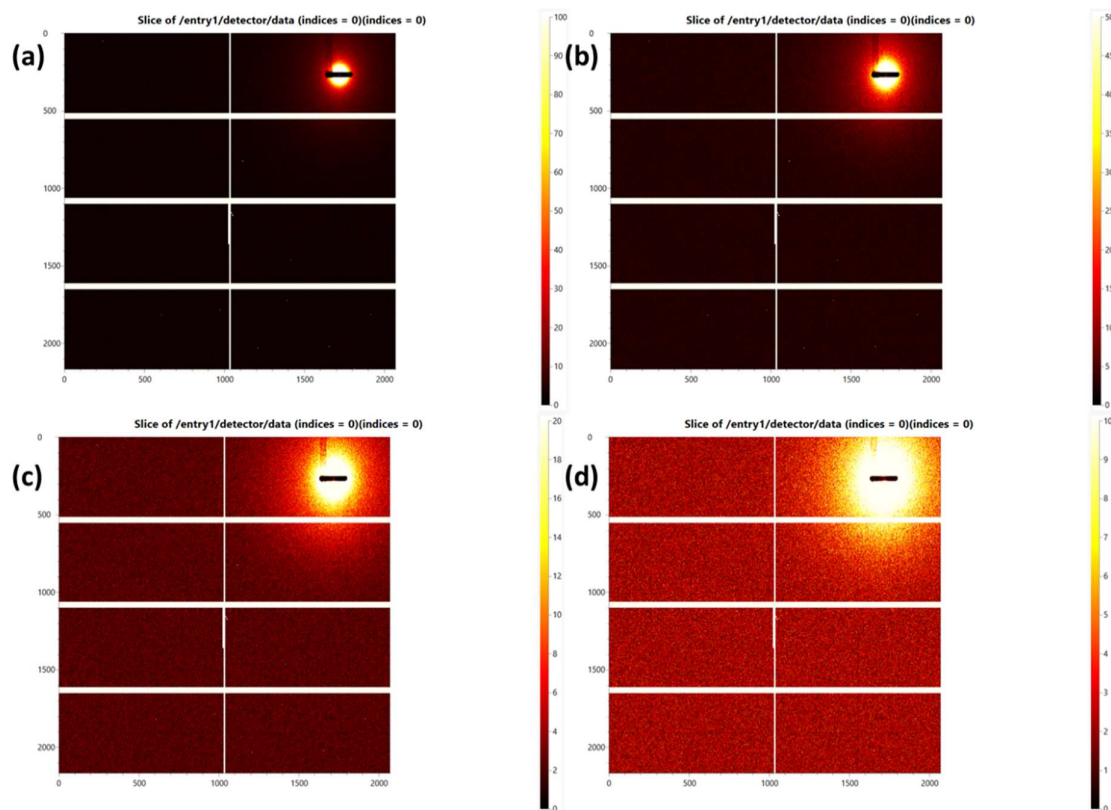


Figure A.4.52. Raw detector data of 2D scattering plots of measurement taken from for a solution of NDI-F:1-NapFF 5:1.25 mg/mL adjusted to pH 12. Histogram plots are shown at a range of 0 to (a) 100, (b) 50, (c) 20 and (d) 10.

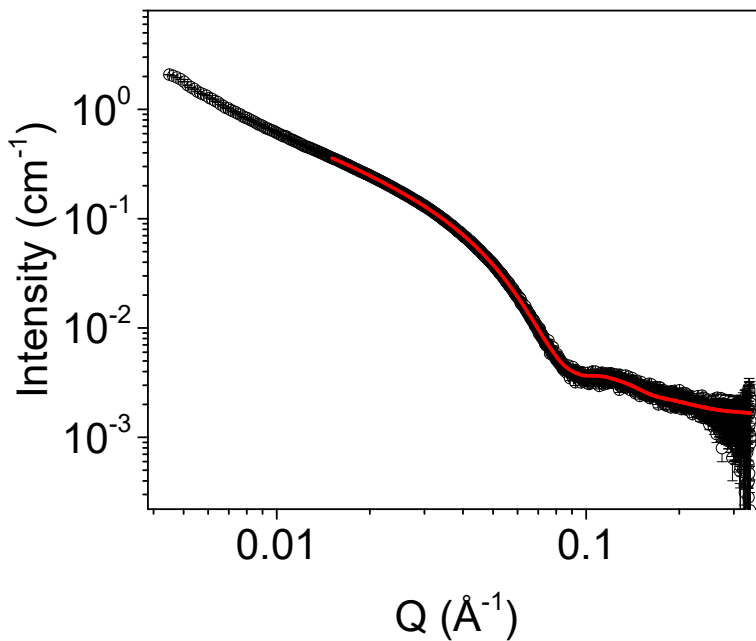


Figure A.4.53. Small angle X-ray scattering data for a solution of **NDI-F:1-NapFF** 5:0.625 mg/mL at pH 6 (open circles) fitted to a flexible elliptical cylinder model combined with cylinder (red). Fit parameters can be found in Table A.4.31.

Table A.4.31. Parameters of SAXS model fit seen in Figure A.4.53.

NDI-F:1-NapFF 5:0.625 mg/mL pH 6	Flexible elliptical cylinder combined with cylinder	
	Value	Error
Scale A	7.87E-04	1.73E-07
Scale B	7.99E-04	1.99E-06
Background	1.64E-03	3.45E-06
Length (Å)	341.48	0.50947
Kuhn length (Å)	240.99	0.28554
Radius (Å)	35.814	5.86E-03
Axis Ratio	1.3442	1.96E-04
Length B (Å)	4.95E+03	48.856
Radius B (Å)	9.2622	0.13251
Range (Å ⁻¹)	0.015-0.3397383	
Chi ²	2.1487	

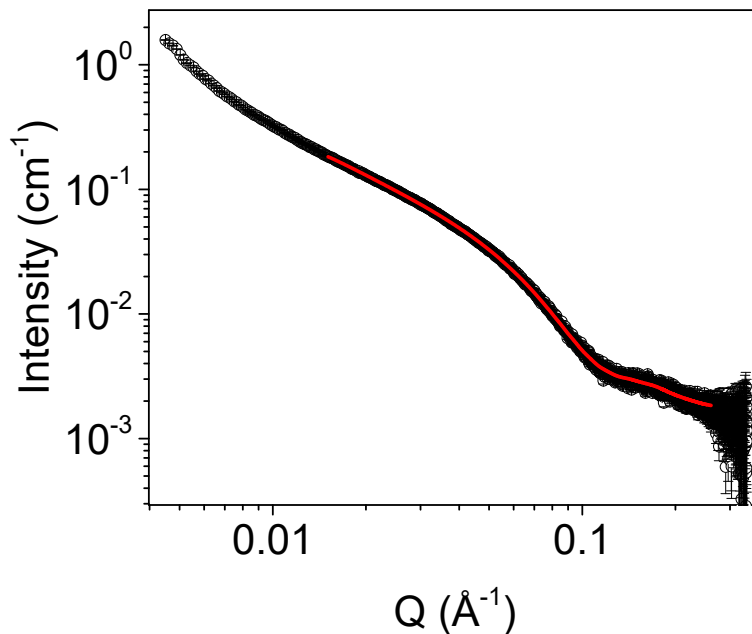


Figure A.4.54. Small angle X-ray scattering data for a solution of **NDI-F:1-NapFF** 5:0.625 mg/mL at pH 9 (open circles) fitted to a flexible elliptical cylinder model combined with cylinder (red). Fit parameters can be found in Table A.4.31.

Table A.4.32. Parameters of SAXS model fit seen in Figure A.4.53.

NDI-F:1-NapFF 5:0.625 mg/mL pH 9	Flexible elliptical cylinder combined with cylinder	
	Value	Error
Scale A	6.62E-04	2.18E-07
Scale B	9.30E-04	1.62E-06
Background	1.69E-03	3.62E-06
Length (Å)	355.18	0.85363
Kuhn length (Å)	228.08	0.36735
Radius (Å)	26.512	5.75E-03
Axis Ratio	1.3059	2.59E-04
Length B (Å)	3.16E+03	35.313
Radius B (Å)	10.073	9.91E-03
Range (Å ⁻¹)	0.015-0.26044306	
Chi ²	1.825	

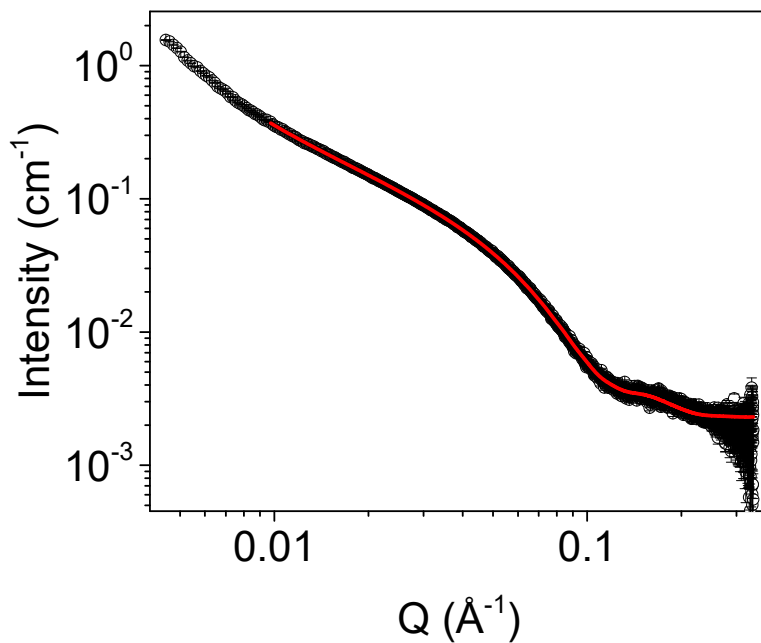


Figure A.4.55. Small angle X-ray scattering data for a solution of **NDI-F:1-NapFF** 5:0.625 mg/mL at pH 12 (open circles) fitted to a flexible elliptical cylinder model combined with hollow cylinder (red). Fit parameters can be found in Table A.4.33.

Table A.4.33. Parameters of SAXS model fit seen in Figure A.4.55.

NDI-F:1-NapFF 5:0.625 mg/mL pH 12	Flexible elliptical cylinder combined with cylinder	
	Value	Error
Scale A	8.54E-04	2.38E-07
Scale B	7.32E-04	1.10E-06
Background	2.29E-03	3.45E-06
Length (Å)	1.19E+04	163.56
Kuhn length (Å)	344.68	1.2153
Radius (Å)	28.224	5.00E-03
Axis Ratio	1.1715	1.90E-04
Length B (Å)	4.55E+03	36.469
Radius B (Å)	12.723	0.011025
Range (Å ⁻¹)	0.0097340094-0.3397383	
Chi ²	2.1225	

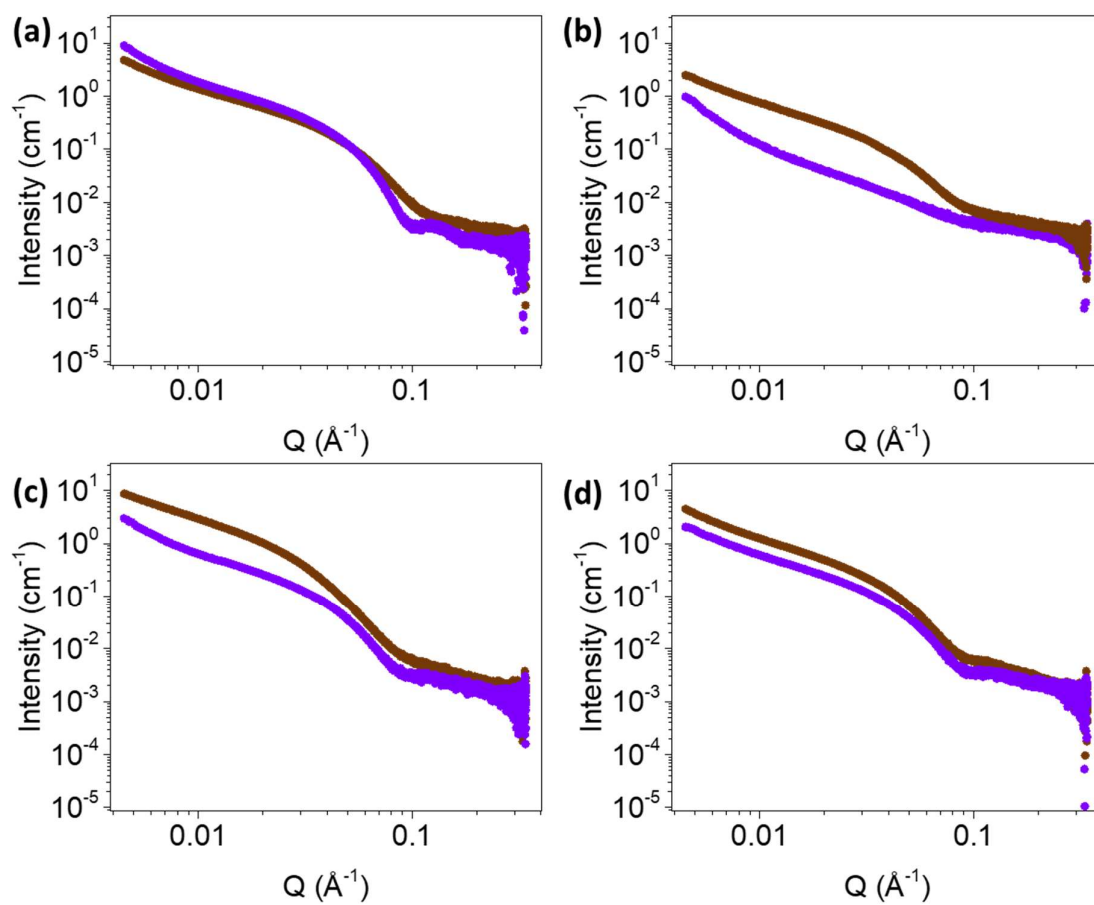


Figure A.4.56. SAXS data of NDI-F:1-NapFF (purple) and NDI-GF:1-NapFF (brown) at (a) 5:5, (b) 5:2.5, (c) 5:1.25 and (d) 5:0.625 mg/mL ratios. Solutions at pH 6.

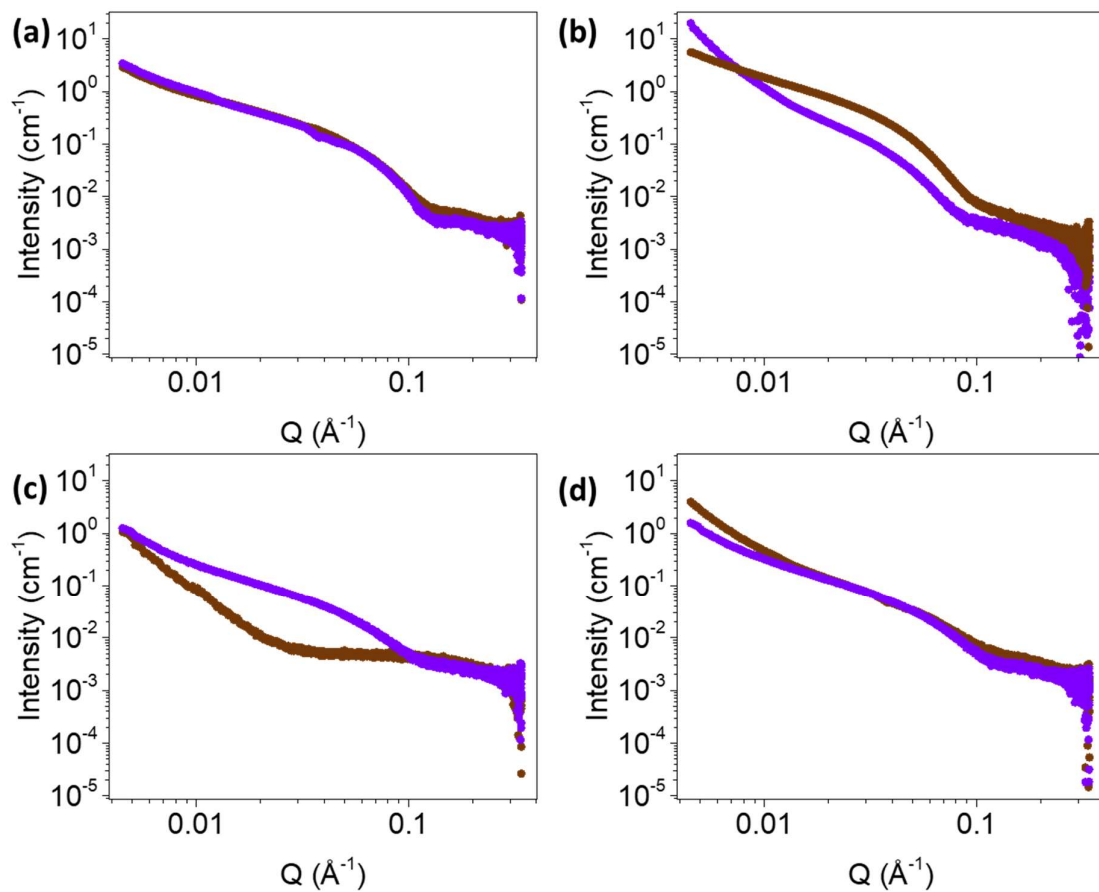


Figure A.4.57. SAXS data of NDI-F:1-NapFF (purple) and NDI-GF:1-NapFF (brown) at (a) 5:5, (b) 5:2.5, (c) 5:1.25 and (d) 5:0.625 mg/mL ratios. Solutions at pH 9.

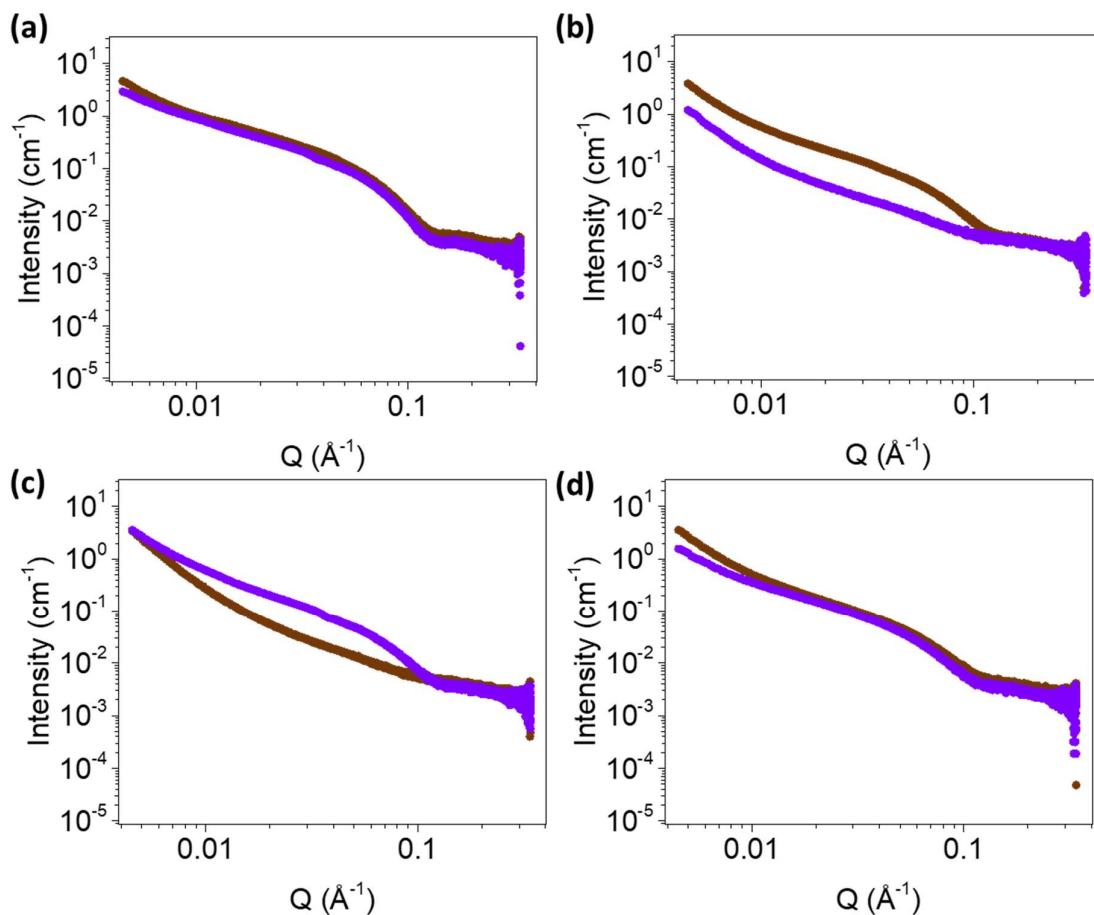


Figure A.4.58. SAXS data of **NDI-F:1-NapFF** (purple) and **NDI-GF:1-NapFF** (brown) at (a) 5:5, (b) 5:2.5, (c) 5:1.25 and (d) 5:0.625 mg/mL ratios. Solutions at pH 12.

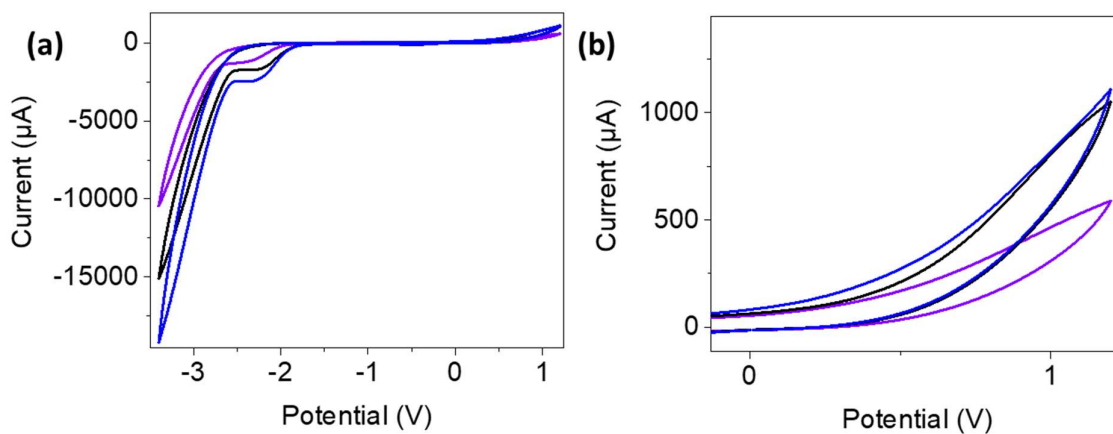


Figure A.4.59. Cyclic voltammograms of **NDI-F** (purple) and **NDI-F:1-NapFF** (black) at a 5 and 5:5 mg/mL concentration respectively at pH 6. **NDI-F:1-NapFF** at 5:1.25 mg/mL at pH 9 is also shown (blue). Voltammograms performed in 5 x 5 FTO window cell at 0.2 V/s scan rate. (a) full voltammogram and (b) expanded between 0-1 V is shown for clarity.

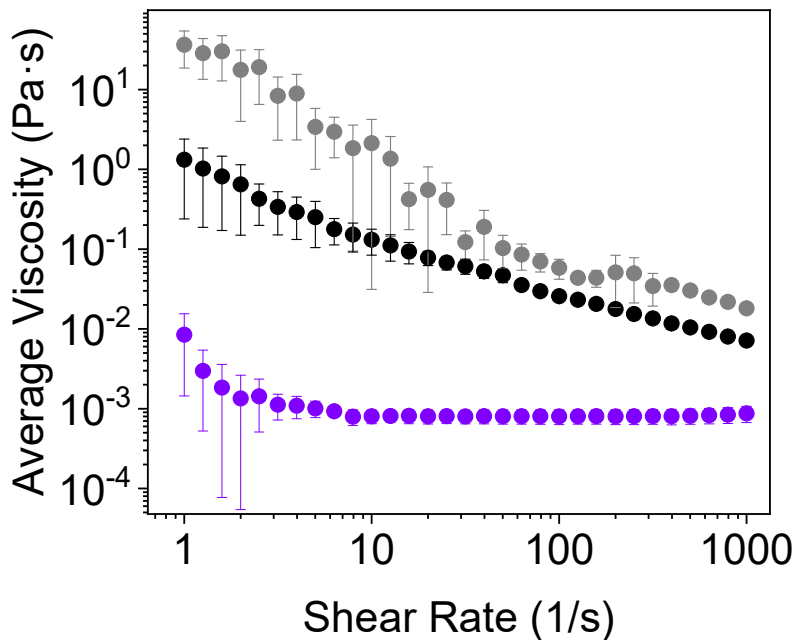


Figure A.4.60. Viscosity measurements of **NDI-F:1-NapFF** at 5:5 mg/mL (**black**), **NDI-F** at 5 mg/mL (**purple**) and **1-NapFF** at 5 mg/mL (**grey**). All solutions buffered at pH 6. Measurements are taken as an average of triplicate measurements and error bars calculated from standard deviation.

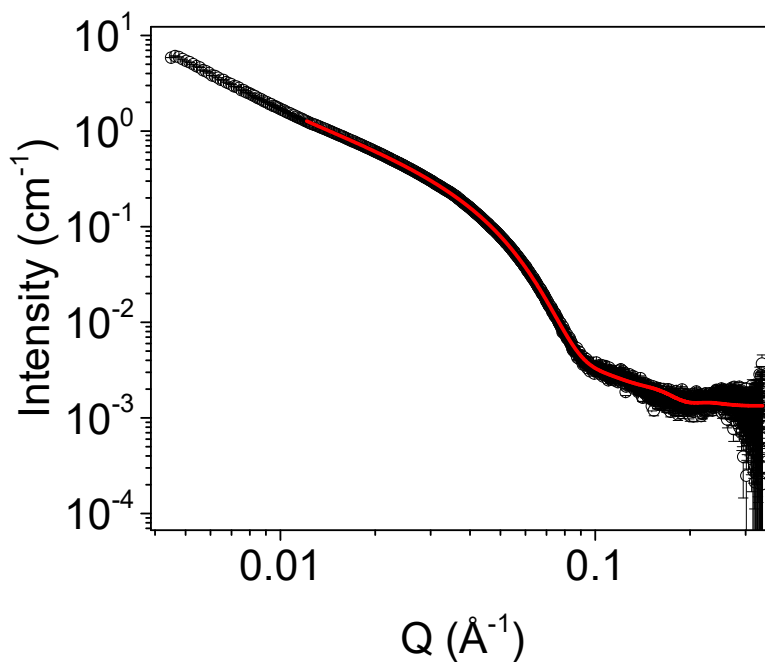


Figure A.4.61. Small angle X-ray scattering data for a solution of 5 mg/mL buffered **1-NapFF** at pH 6 (open circles) fitted to a flexible elliptical cylinder model combined with power law (**red**). Fit parameters can be found in Table A.4.34.

Table A.4.34. Parameters of SAXS model fit seen in Figure A.4.61.

1-NapFF buffered 5 mg/mL pH 6		Flexible elliptical cylinder combined with power law
	Value	Error
Scale A	2.40E-04	3.08E-08
Scale B	3.39E-07	2.43E-10
Background	1.31E-03	3.52E-06
Length (Å)	250.95	0.23673
Kuhn length (Å)	308.02	1.0143
Radius (Å)	32.945	3.18E-03
Axis Ratio	1.5991	1.43E-04
Power	3.1981	1.75E-04
Range (Å ⁻¹)	0.012119029-0.33973727	
Chi ²	3.1229	

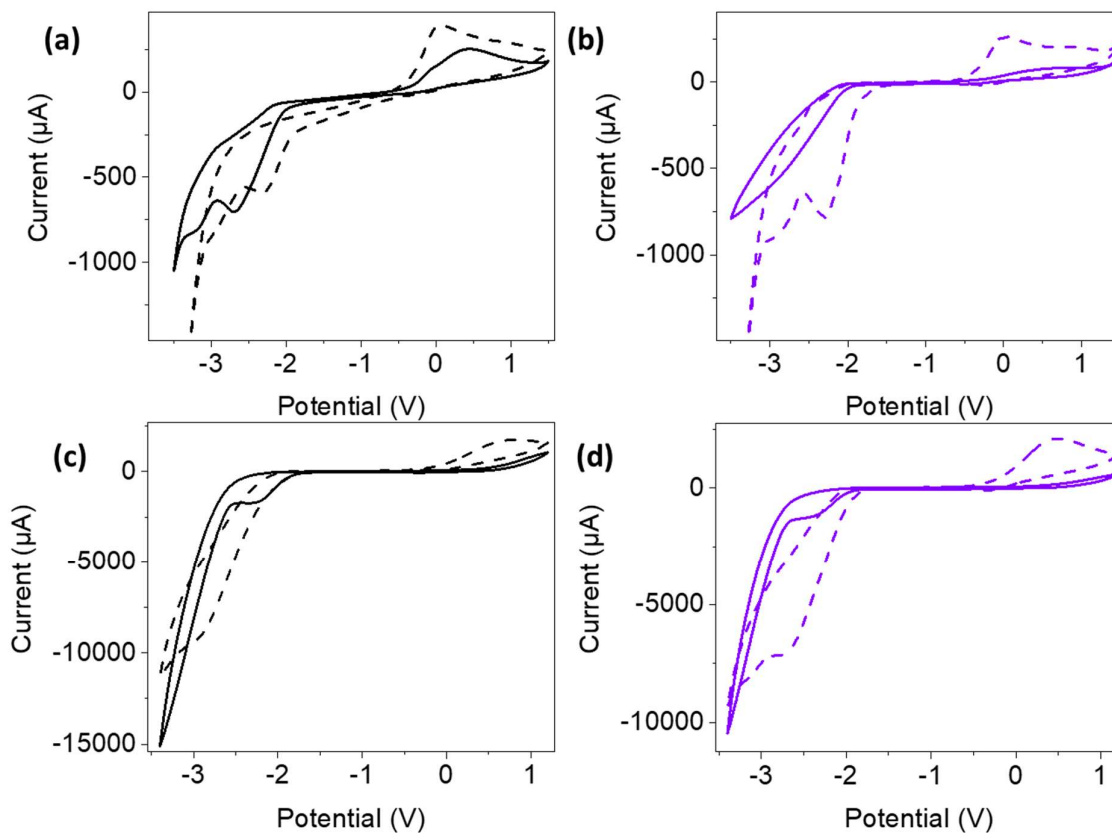


Figure A.4.62. Cyclic voltammograms taken at 0.2 V/s of (a/d) NDI-F 5 mg/mL and (a/c) NDI-F:1-NapFF 5:5 mg/mL buffered (dashed line) and unbuffered (solid line) at pH 6 in (a-b) 1 x 1 and (c-d) 5 x 5 FTO window cells.

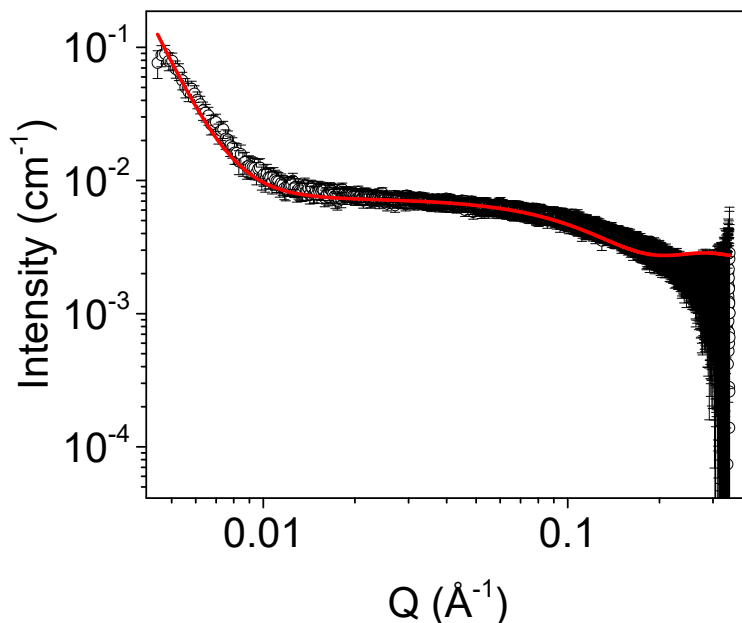


Figure A.4.63. Small angle X-ray scattering data for a solution of 5 mg/mL NDI-F buffered at pH 6 (open circles) fitted to a hollow cylinder model combined with power law (red). Fit parameters can be found in Table A.4.35.

Table A.4.35. Parameters of SAXS model fit seen in Figure A.4.63.

NDI-F 5 mg/mL pH 6	Hollow cylinder combined with power law	
	Value	Error
Scale A	2.68E-04	9.50E-06
Scale B	3.93E-13	3.66E-13
Background	0.002592	1.17E-05
Length (Å)	21.919	0.16779
Radius (Å)	9.1247	0.1064
Thickness (Å)	5.2739	0.035929
Power	4.8905	0.18175
Range (Å ⁻¹)	0.0045-0.34	
Chi ²	1.0233	

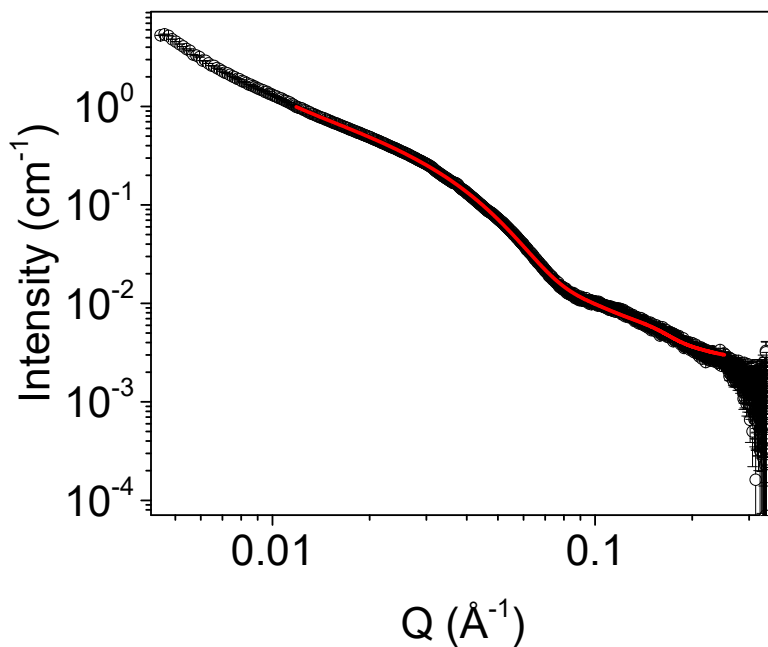


Figure A.4.64. Small angle X-ray scattering data for a solution of **NDI-F:1-NapFF** 5:5 mg/mL buffered at pH 6 (open circles) fitted to a flexible elliptical cylinder model combined with hollow cylinder (red). Fit parameters can be found in Table A.4.36.

Table A.4.36. Parameters of SAXS model fit seen in Figure A.4.64.

NDI-F:1-NapFF 5:5 mg/mL pH 6	Flexible elliptical cylinder combined with hollow cylinder	
	Value	Error
Scale A	1.98E-04	2.59E-08
Scale B	4.75E-04	4.91E-07
Background	0.002751	3.90E-06
Length (Å)	9.61E+03	1.106E+03
Kuhn length (Å)	304.54	0.57256
Radius (Å)	32.898	0.003192
Axis Ratio	1.718	1.54E-04
Length B (Å)	40.321	0.079107
Radius B (Å)	4.8418	0.010837
Thickness B (Å)	6.3351	0.00562
Range (Å ⁻¹)	0.0118563-0.251462	
Chi ²	12.461	

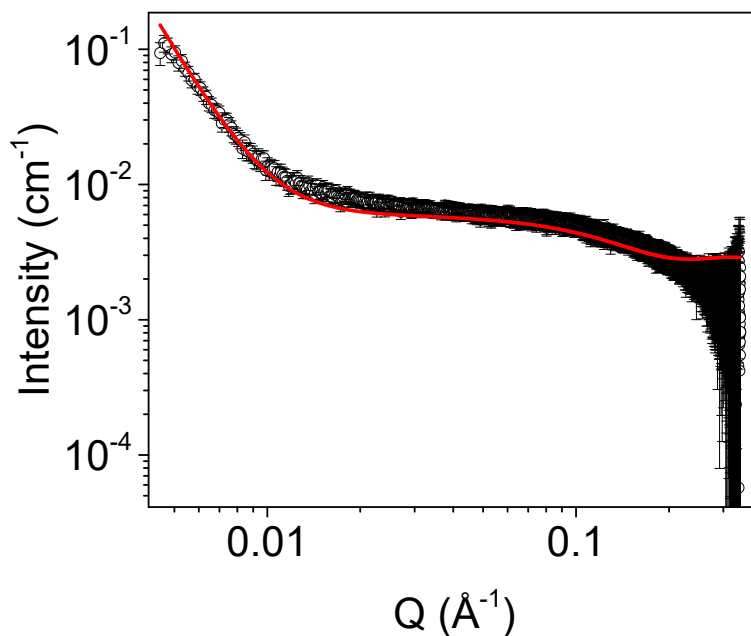


Figure A.4.65. Small angle X-ray scattering data for a solution of **NDI-F** 5 mg/mL buffered at pH 6 and electrochemically cycled once (open circles) fitted to a flexible elliptical cylinder model combined with power law (red). Solutions were relaxed for several days prior to measurement. Fit parameters can be found in Table A.4.37.

Table A.4.37. Parameters of SAXS model fit seen in Figure A.4.65.

NDI-F 5 mg/mL at pH 6 and electrochemically cycled once	Flexible elliptical cylinder combined with power law	
	Value	Error
Scale A	2.21E-04	2.09E-06
Scale B	9.70E-11	1.77E-12
Background	2.73E-03	1.17E-05
Length (Å)	21.39	0.16561
Radius (Å)	9.4351	0.11338
Thickness (Å)	5.0627	0.032683
Power	3.9098	4.66E-03
Range (Å ⁻¹)	0.0045-0.34	
Chi ²	1.1616	

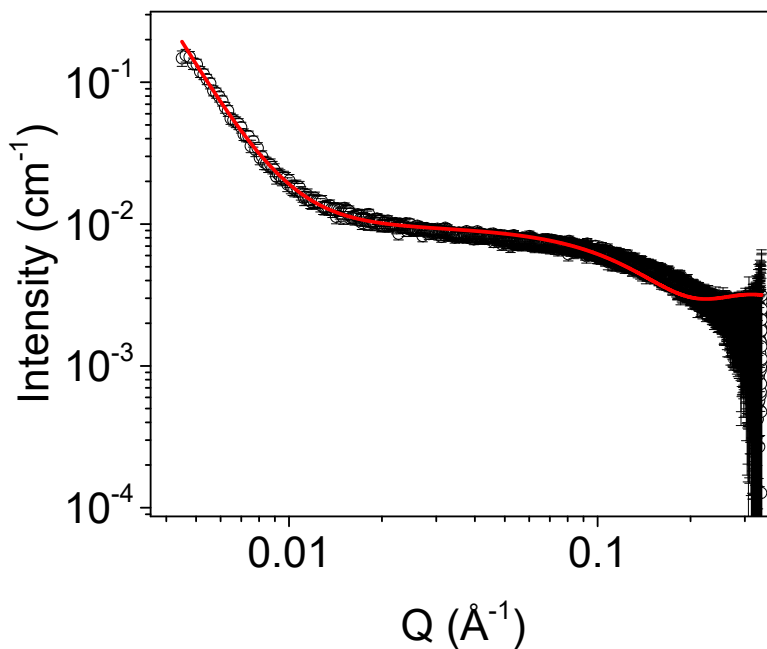


Figure A.4.66. Small angle X-ray scattering data for a solution of **NDI-F** 5 mg/mL buffered at pH 6 and electrochemically cycled 50 times (open circles) fitted to a flexible elliptical cylinder model combined with power law (red). Solutions were relaxed for several days prior to measurement. Fit parameters can be found in Table A.4.38.

Table A.4.38. Parameters of SAXS model fit seen in Figure A.4.66.

NDI-F 5 mg/mL at pH 6 and electrochemically 50 cycles	Flexible elliptical cylinder combined with power law	
	Value	Error
Scale A	3.83E-04	1.84E-06
Scale B	3.88E-10	1.05E-10
Background	2.88E-03	1.19E-05
Length (Å)	24.878	0.14172
Radius (Å)	9.4517	0.071064
Thickness (Å)	5.2611	0.024297
Power	3.6971	0.054138
Range (Å ⁻¹)	0.0045-0.34	
Chi ²	1.0877	

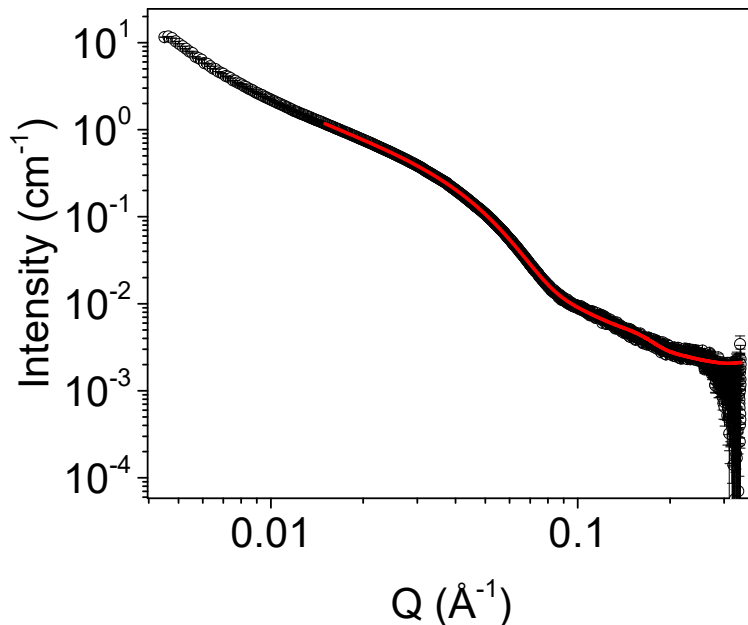


Figure A.4.67. Small angle X-ray scattering data for a solution of **NDI-F:1-NapFF** 5:5 mg/mL buffered at pH 6 and electrochemically cycled once (open circles) fitted to a flexible elliptical cylinder model combined with hollow cylinder (red). Solutions were relaxed for several days prior to measurement. Fit parameters can be found in Table A.4.39.

Table A.4.39. Parameters of SAXS model fit seen in Figure A.4.67.

NDI-F:1-NapFF 5:5 mg/mL at pH 6 and electrochemically cycled once		
Flexible elliptical cylinder combined with hollow cylinder		
	Value	Error
Scale A	3.15E-04	3.07E-08
Scale B	3.77E-04	4.80E-07
Background	2.07E-03	3.56E-06
Length (Å)	3.75E+03	7.4858
Kuhn length (Å)	298.49	0.21687
Radius (Å)	32.004	2.22E-03
Axis Ratio	1.6815	1.09E-04
Length (Å) B	45.684	0.12587
Radius (Å) B	4.8693	0.013661
Thickness (Å) B	6.5279	7.22E-03
Range (Å ⁻¹)	0.010936766-0.33973727	
Chi ²	5.034	

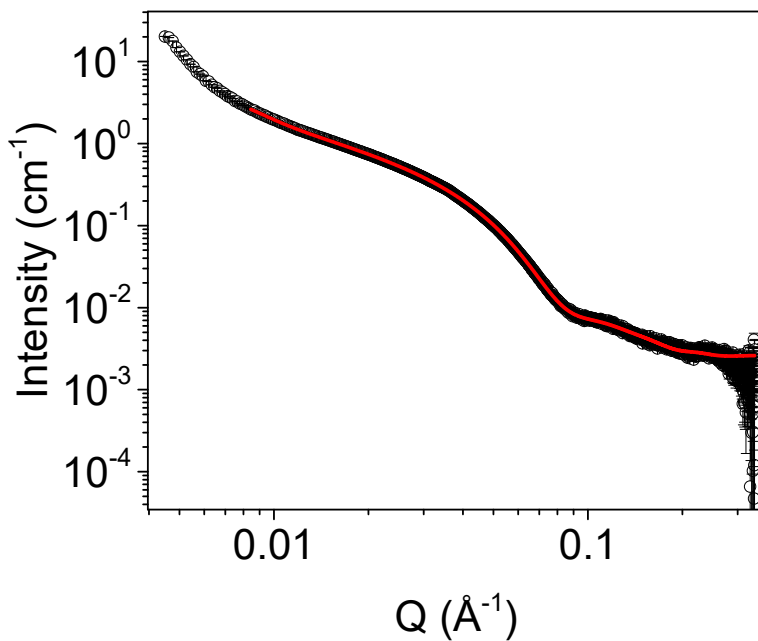


Figure A.4.68. Small angle X-ray scattering data for a solution of **NDI-F:1-NapFF** 5:5 mg/mL buffered at pH 6 and electrochemically cycles 50 times (open circles) fitted to a flexible elliptical cylinder model combined with hollow cylinder (red). Solutions were relaxed for several days prior to measurement. Fit parameters can be found in Table A.4.40.

Table A.4.40. Parameters of SAXS model fit seen in Figure A.4.68.

NDI-F:1-NapFF 5:5 mg/mL at pH 6 and electrochemically 50 cycles		Flexible elliptical cylinder combined with hollow cylinder	
	Value	Error	
Scale A	3.43E-04	3.26E-08	
Scale B	2.01E-04	4.00E-07	
Background	2.52E-03	3.58E-06	
Length (Å)	1.35E+05	1098.7	
Kuhn length (Å)	307.39	0.15327	
Radius (Å)	34.873	2.29E-03	
Axis Ratio	1.5243	9.44E-05	
Length (Å)	48.906	0.21743	
Radius (Å)	4.7426	0.022453	
Thickness (Å)	7.4649	0.012701	
Range (Å ⁻¹)	0.0084408771-0.33973727		
Chi ²	4.9949		

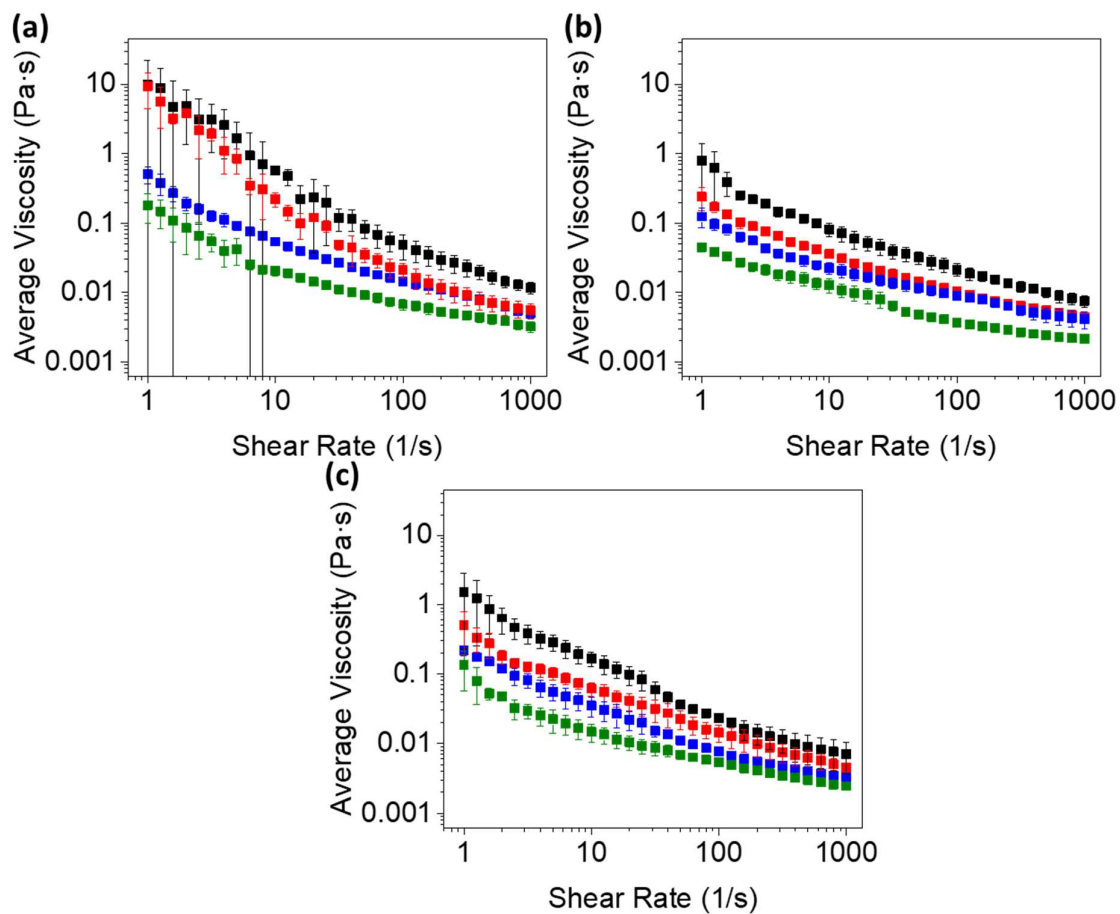


Figure A.4.69. Viscosity measurements 1-NapFF after heat cooling at 40 °C at (a) pH 6, (b) 9 and (c) 12. Solutions at 5 (black), 2.5 (red), 1.25 (blue), 0.625 (green) and 5:0 (open circles) mg/mL. Measurements are taken as an average of triplicate measurements and error bars calculated from standard deviation.

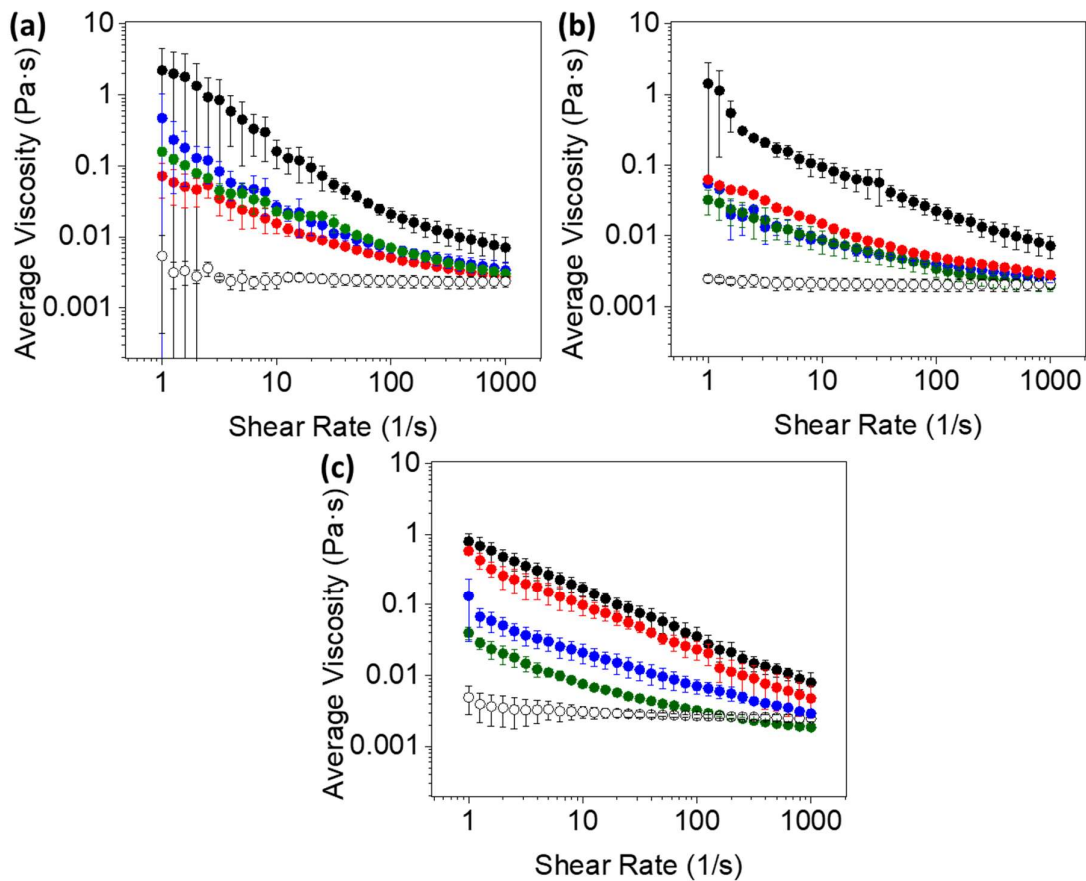


Figure A.4.70. Viscosity measurements NDI-F:1-NapFF after heat cooling at 40 °C at (a) pH 6, (b) 9 and (c) 12. Solutions at 5:5 (black), 5:2.5 (red), 5:1.25 (blue), 5:0.625 (green) and 5:0 (open circles) mg/mL. Measurements are taken as an average of triplicate measurements and error bars calculated from standard deviation.

Appendix

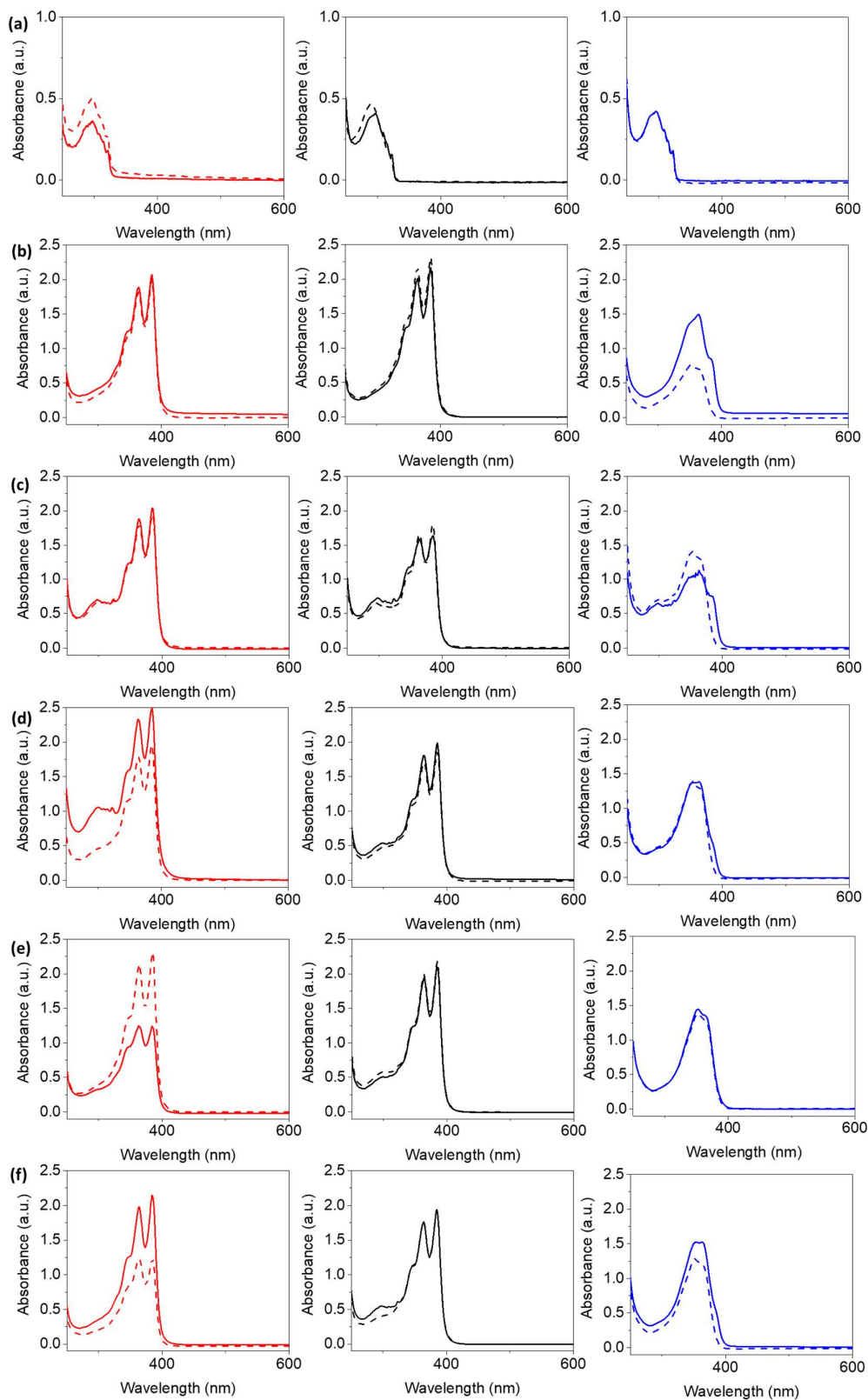


Figure A.4.71. Absorbance spectra of neutral **NDI-F:1-NapFF** before (solid line) and after (dashed line) heat-cooling at 40 °C at (a) 0:5, (b) 5:0, (c) 5:5, (d) 5:2.5, (e) 5:1.25 and (f) 5:0.625 mg/mL at pH 6 (red), 9 (black) and 12 (blue).

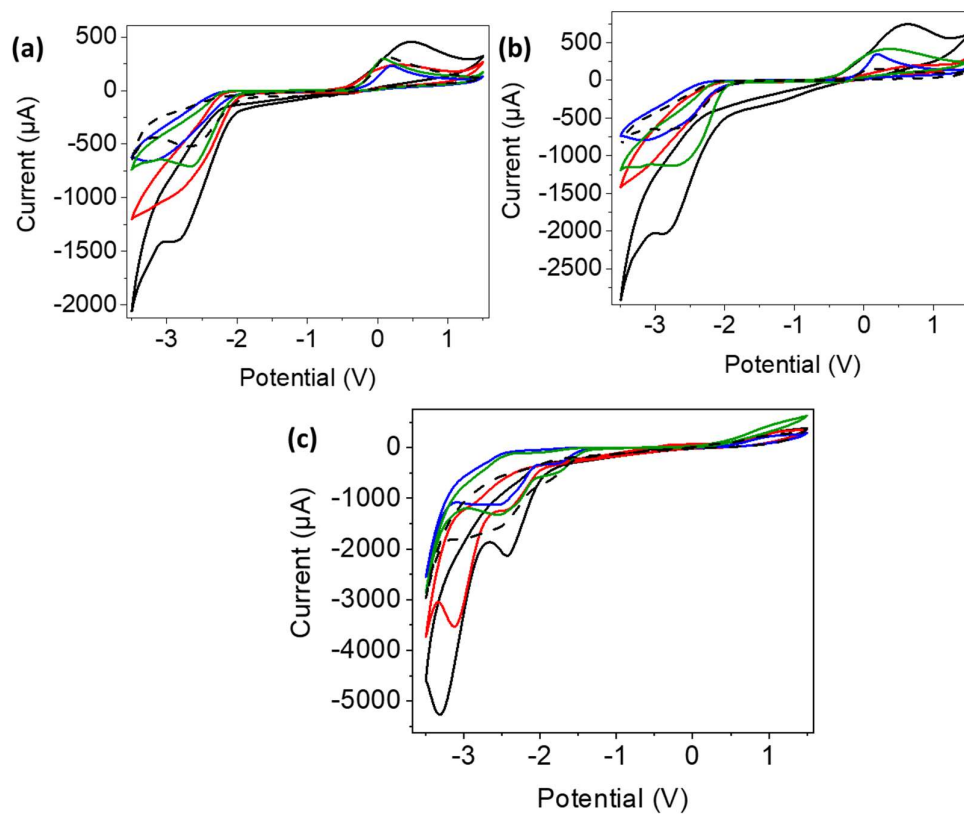


Figure A.4.72. Cyclic voltammograms of NDI-F:1-NapFF at 5:5 (black), 5:2.5 (red), 5:1.25 (blue), 5:0.625 (green) and 5:0 (dashed line) mg/mL at pH 6 (a), 9 (b) and 12 (c) after heat-cooling at 40 °C. Scan rate used was 0.2 V/s. Performed in 1 x 1 FTO window cells.

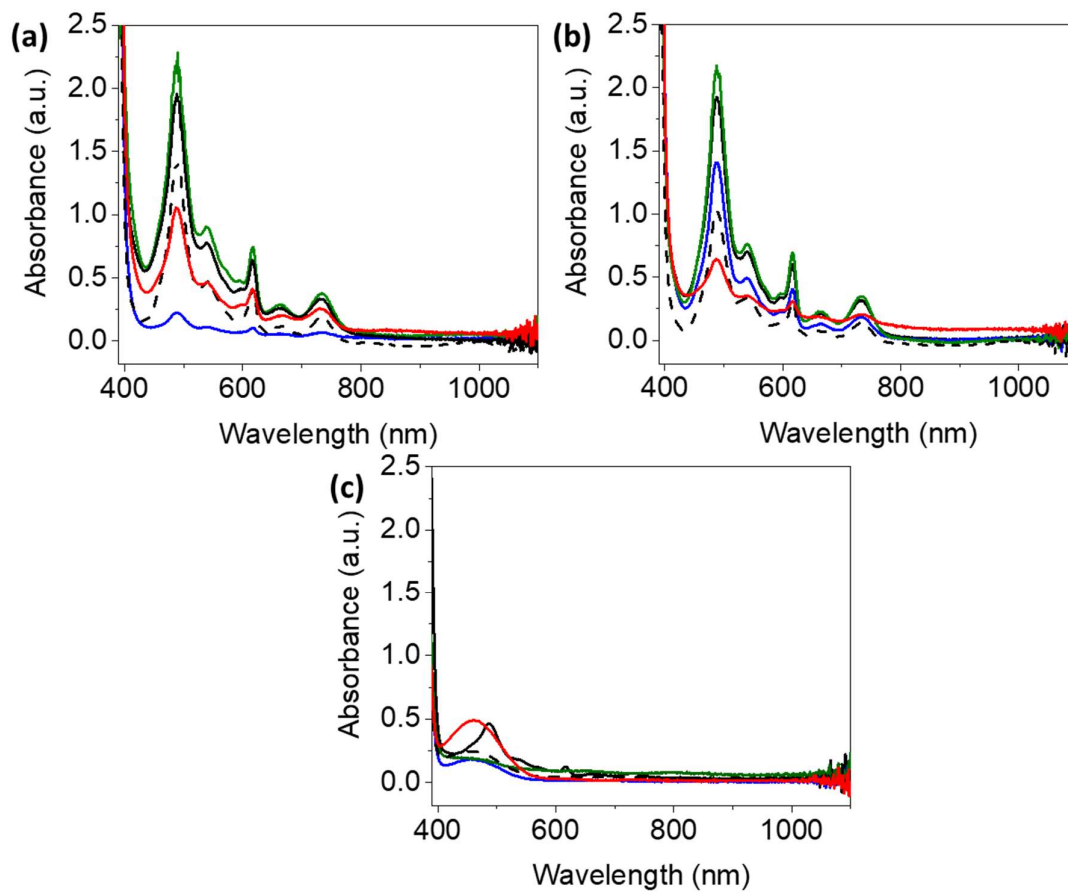


Figure A.4.73. Absorbance spectra of reduced solutions (heat-cooled at 40 °C) of **NDI-F:1-NapFF** at 5:5 (black), 5:2.5 (red), 5:1.25 (blue), 5:0.625 (green) and 5:0 (dashed line) mg/mL at pH 6 (a), 9 (b) and 12 (c). Spectra taken after 10 second application of -2.5 V.

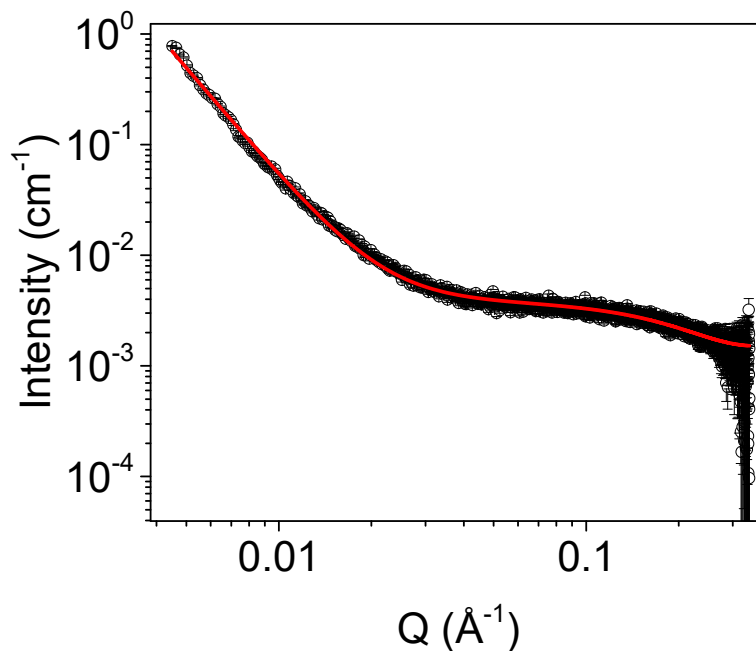


Figure A.4.74. Small angle X-ray scattering data for a solution of **NDI-F** 5 mg/mL at pH 6 after heat-cooling (heated to 40 °C and allowed to cool) (open circles) fitted to a hollow cylinder model combined with power law (red). Fit parameters can be found in Table A.4.41.

Table A.4.41. Parameters of SAXS model fit seen in Figure A.4.74.

NDI-F 5 mg/mL pH 6 heat-cooled	Hollow cylinder combined with power law	
	Value	Error
Scale A	3.38E-04	9.50E-07
Scale B	1.50E-08	3.61E-11
Background	1.50E-03	3.70E-06
Length (Å)	16.812	0.058688
Radius (Å)	4.6741	0.027332
Thickness (Å)	5.0526	0.012555
Power	3.2663	4.99E-04
Range (Å ⁻¹)	0.0045-0.18978393	
Chi ²	2.3593	

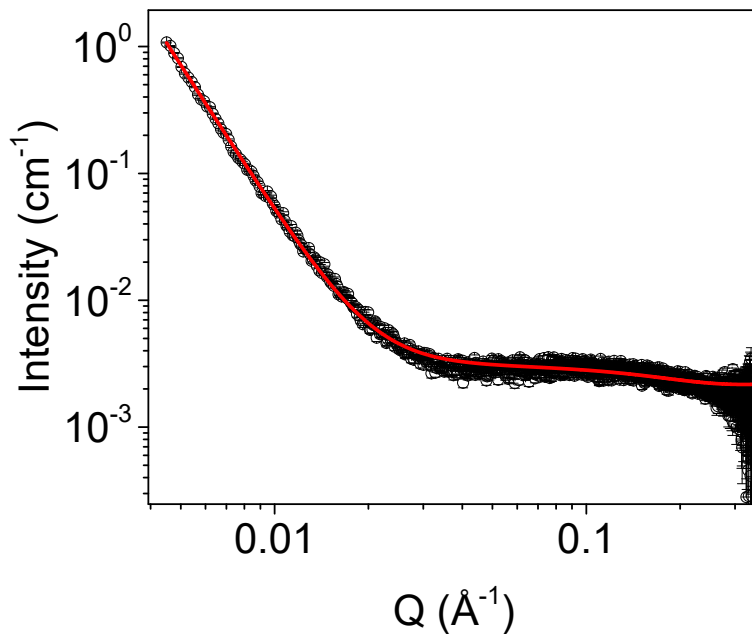


Figure A.4.75. Small angle X-ray scattering data for a solution of **NDI-F** 5 mg/mL at pH 9 after heat-cooling (heated to 40 °C and allowed to cool) (open circles) fitted to a hollow cylinder model combined with power law (red). Fit parameters can be found in Table A.4.42.

Table A.4.42. Parameters of SAXS model fit seen in Figure A.4.75.

NDI-F 5 mg/mL pH 9 heat-cooled	Hollow cylinder combined with power law	
	Value	Error
Scale A	1.00E-04	3.70E-06
Scale B	1.09E-09	2.46E-12
Background	2.05E-03	3.34E-06
Length (Å)	20.524	0.17472
Radius (Å)	5.545	0.10166
Thickness (Å)	4.9382	0.1621
Power	3.8139	4.13E-04
Range (Å ⁻¹)	0.0045-0.3397383	
Chi ²	2.5829	

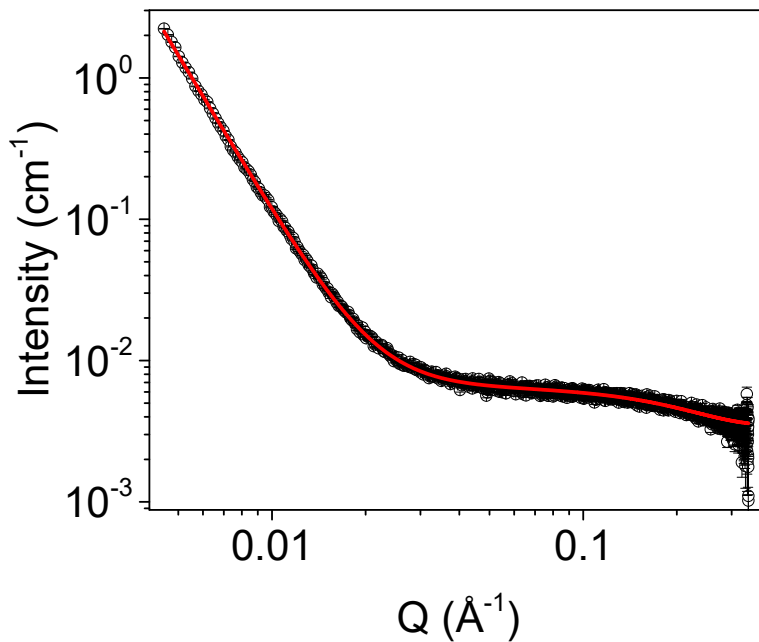


Figure A.4.76. Small angle X-ray scattering data for a solution of **NDI-F** 5 mg/mL at pH 12 after heat-cooling (heated to 40 °C and allowed to cool) (open circles) fitted to a hollow cylinder model combined with power law (red). Fit parameters can be found in Table A.4.43.

Table A.4.43. Parameters of SAXS model fit seen in Figure A.4.76.

NDI-F 5 mg/mL pH 12 heat-cooled	Sphere with power law	
	Value	Error
Scale A	3.22E-04	6.70E-07
Scale B	4.81E-09	4.98E-12
Background	0.0035152	3.45E-06
Radius (Å)	10.735	9.46E-03
Power	3.6843	2.62E-03
Range (Å ⁻¹)	0.0045-0.3397383	
Chi ²	2.0426	

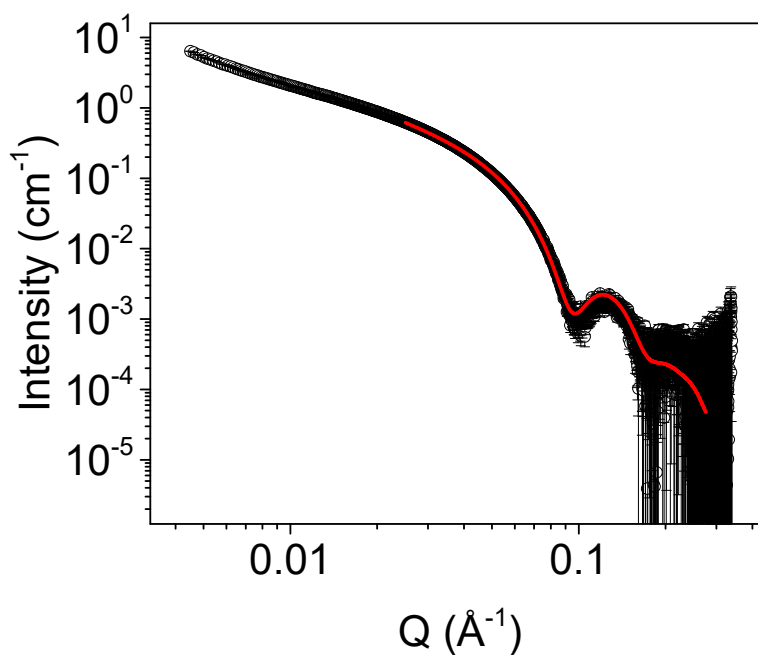


Figure A.4.77. Small angle X-ray scattering data for a solution of **1-NapFF** 5 mg/mL at pH 6 after heat-cooling (heated to 40 °C and allowed to cool) (open circles) fitted to a hollow cylinder model combined with power law (red). Fit parameters can be found in Table A.4.44.

Table A.4.44. Parameters of SAXS model fit seen in Figure A.4.77.

1-NapFF 5 mg/mL pH 6 heat-cooled	Flexible elliptical cylinder combined with power law	
	Value	Error
Scale A	4.45E-04	1.01E-07
Scale B	1.21E-08	3.79E-11
Background	2.10E-08	3.59E-06
Length (Å)	263.94	0.81312
Kuhn Length (Å)	307.63	1.37E+02
Radius (Å)	35.745	3.24E-03
Axis Ratio	1.3025	1.09E-04
Power	4.1329	4.30E-04
Range (Å ⁻¹)	0.025-0.27614509	
Chi ²	11.491	

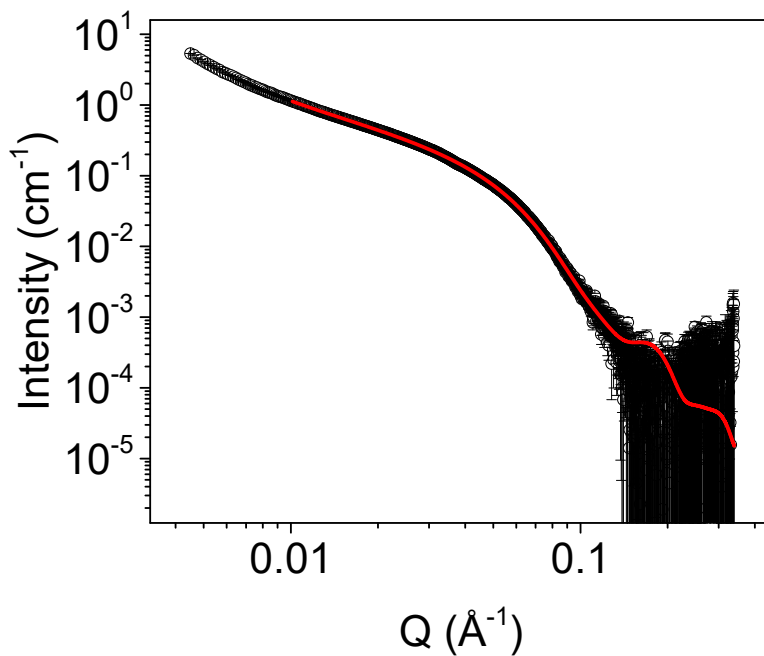


Figure A.4.78. Small angle X-ray scattering data for a solution of **1-NapFF** 5 mg/mL at pH 9 after heat-cooling (heated to 40 °C and allowed to cool) (open circles) fitted to a hollow cylinder model combined with power law (red). Fit parameters can be found in Table A.4.45.

Table A.4.45. Parameters of SAXS model fit seen in Figure A.4.78. χ^2 is higher for this fit likely due to noisy data at high Q (Figure A.4.78) leading to a poor fit of the model over approximately 0.1 \AA^{-1} .

1-NapFF 5 mg/mL pH 9 heat-cooled	Flexible elliptical cylinder combined with power law	
	Value	Error
Scale A	2.15E-04	2.77E-08
Scale B	9.23E-13	2.36E-14
Background	9.68E-08	3.44E-06
Length (Å)	5398	25.703
Kuhn Length (Å)	427.05	0.5653
Radius (Å)	27.794	2.49E-03
Axis Ratio	1.7526	1.47E-04
Power	5.243	5.75E-03
Range (Å ⁻¹)	0.01-0.3397383	
Chi ²	6.3448	

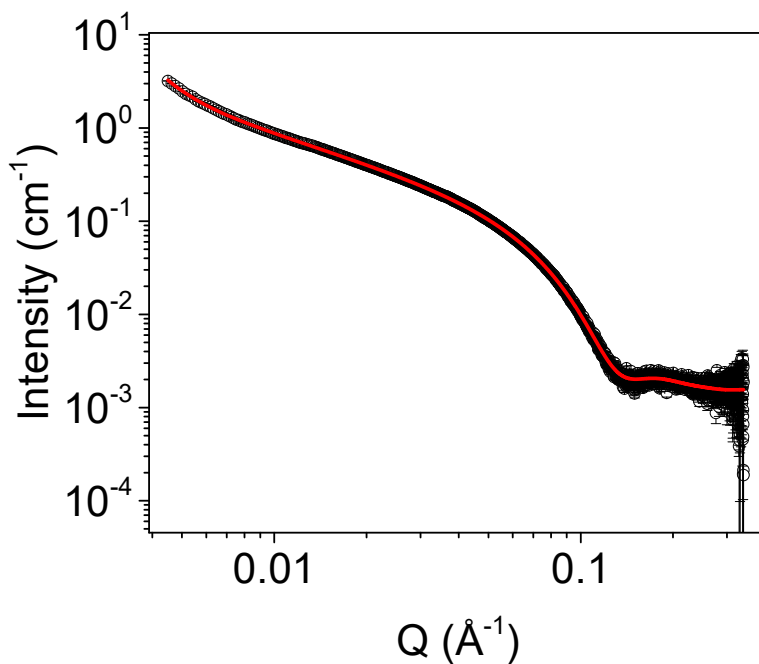


Figure A.4.79. Small angle X-ray scattering data for a solution of **1-NapFF** 5 mg/mL at pH 12 after heat-cooling (heated to 40 °C and allowed to cool) (open circles) fitted to a hollow cylinder model combined with power law (red). Fit parameters can be found in Table A.4.46.

Table A.4.46. Parameters of SAXS model fit seen in Figure A.4.79.

1-NapFF 5 mg/mL pH 12 heat-cooled	Flexible elliptical cylinder combined with power law	
	Value	Error
Scale A	3.96E-04	4.71E-08
Scale B	5.76E-18	4.41E-20
Background	1.51E-03	3.53E-06
Length (Å)	547.81	0.89307
Kuhn Length (Å)	2.47E+04	248.35
Radius (Å)	22.922	1.71E-03
Axis Ratio	1.453	1.03E-04
Power	7.2691	1.44E-03
Range (Å ⁻¹)	0.0045-0.3397383	
Chi ²	2.5879	

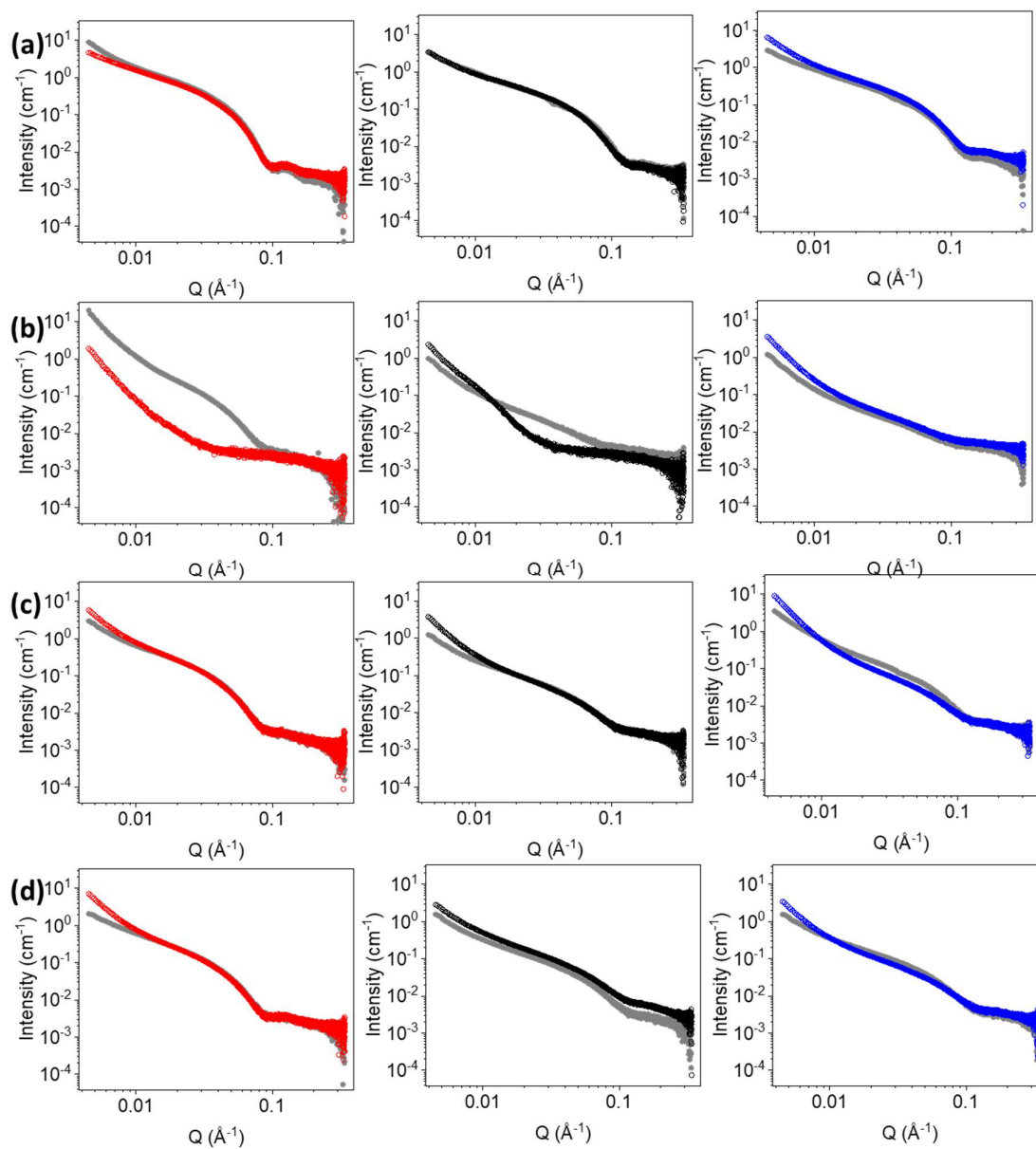


Figure A.4.80. SAXS data of NDI-F:1-NapFF before (grey) and after (open circles) a heat-cool transition (heated to 40 °C and allowed to cool) at pH 6 (red), 9 (black) and 12 (blue) at (a) 5:5, (b) 5:2.5, (c) 5:1.25 and (d) 5:0.625 mg/mL.

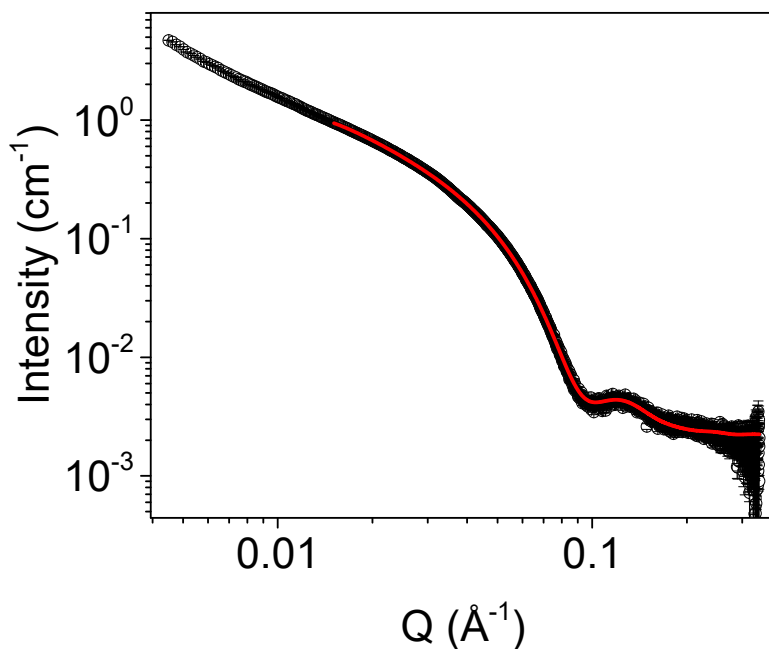


Figure A.4.81. Small angle X-ray scattering data for a solution of **NDI-F:1-NapFF** 5:5 mg/mL at pH 6 after heat-cooling (heated to 40 °C and allowed to cool) (open circles) fitted to a flexible elliptical model combined with hollow cylinder (red). Fit parameters can be found in Table A.4.47.

Table A.4.47. Parameters of SAXS model fit seen in Figure A.4.81.

NDI-F:1-NapFF 5:5 mg/mL pH 6 heat-cooled	Flexible elliptical cylinder combined with hollow cylinder	
	Value	Error
Scale A	6.80E-05	3.82E-07
Scale B	3.74E-04	4.24E-08
Background	2.21E-03	3.55E-06
Length (Å)	287.5	0.16084
Kuhn Length (Å)	215.71	0.12837
Radius (Å)	34.066	2.81E-03
Axis Ratio	1.38	1.05E-04
Length B (Å)	179.88	8.3362
Radius B (Å)	4.5461	0.0579
Thickness B (Å)	6.6336	0.031307
Range (Å ⁻¹)	0.15-0.27666849	
Chi ²	4.8944	

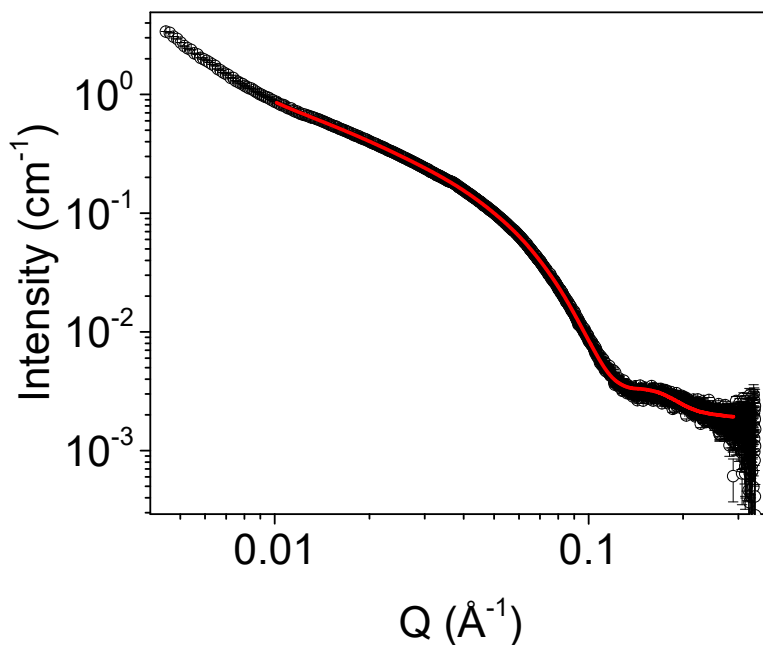


Figure A.4.82. Small angle X-ray scattering data for a solution of **NDI-F:1-NapFF** 5:5 mg/mL at pH 9 after heat-cooling (heated to 40 °C and allowed to cool) (open circles) fitted to a flexible elliptical model combined with hollow cylinder (red). Fit parameters can be found in Table A.4.48.

Table A.4.48. Parameters of SAXS model fit seen in Figure A.4.82.

NDI-F:1-NapFF 5:5 mg/mL pH 9 heat-cooled	Flexible elliptical cylinder combined with hollow cylinder	
	Value	Error
Scale A	2.44E-04	4.28E-08
Scale B	1.81E-04	7.86E-08
Background	1.87E-03	3.62E-06
Length (Å)	1.10E+05	2.24E+03
Kuhn Length (Å)	343.64	1.07
Radius (Å)	21.126	2.42E-03
Axis Ratio	1.7501	1.90E-03
Length B (Å)	284.86	0.8212
Radius B (Å)	9.9386	0.019015
Thickness B (Å)	20.902	0.013645
Range (Å ⁻¹)	0.01-0.28936096	
Chi ²	3.5318	

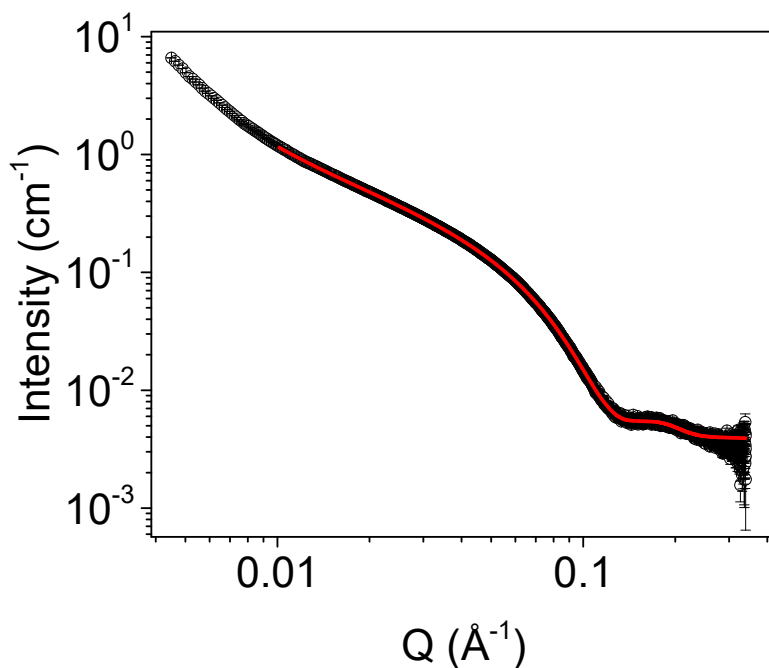


Figure A.4.83. Small angle X-ray scattering data for a solution of **NDI-F:1-NapFF** 5:5 mg/mL at pH 12 after heat-cooling (heated to 40 °C and allowed to cool) (open circles) fitted to a flexible elliptical model combined with cylinder (red). Fit parameters can be found in Table A.4.49.

Table A.4.49. Parameters of SAXS model fit seen in Figure A.4.83.

NDI-F:1-NapFF 5:5 mg/mL pH 12 heat-cooled	Flexible elliptical cylinder combined with cylinder	
	Value	Error
Scale A	5.17E-04	6.04E-08
Scale B	1.55E-04	2.85E-07
Background	3.87E-03	3.66E-06
Length (Å)	1536.2	1.10E-03
Kuhn Length (Å)	384.05	0.55395
Radius (Å)	24.837	1.83E-03
Axis Ratio	1.2823	8.87E-05
Length B (Å)	3721.8	34.204
Radius B (Å)	11.559	0.012833
Range (Å ⁻¹)	0.01-0.339738	
Chi ²	2.803	

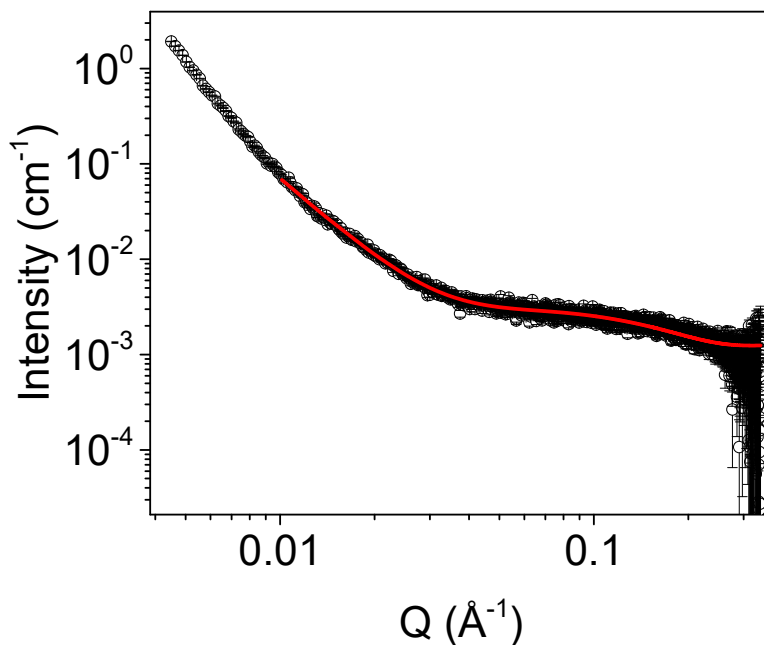


Figure A.4.84. Small angle X-ray scattering data for a solution of **NDI-F:1-NapFF** 5:2.5 mg/mL at pH 6 after heat-cooling (heated to 40 °C and allowed to cool) (open circles) fitted to a flexible elliptical model combined with cylinder (red). Fit parameters can be found in Table A.4.50.

Table A.4.50. Parameters of SAXS model fit seen in Figure A.4.84.

NDI-F:1-NapFF 5:2.5 mg/mL pH 6 heat-cooled	Flexible elliptical cylinder combined with cylinder	
	Value	Error
Scale A	4.70E-06	1.54E-08
Scale B	2.30E-03	8.73E-06
Background	1.24E-03	3.33E-06
Length (Å)	1.36E+04	6.72E+03
Kuhn Length (Å)	62.822	0.29529
Radius (Å)	50.428	0.25753
Axis Ratio	10.748	0.036931
Length B (Å)	22.469	0.11169
Radius B (Å)	12.696	0.031313
Range (Å ⁻¹)	0.01-0.3397383	
Chi ²	2.2681	

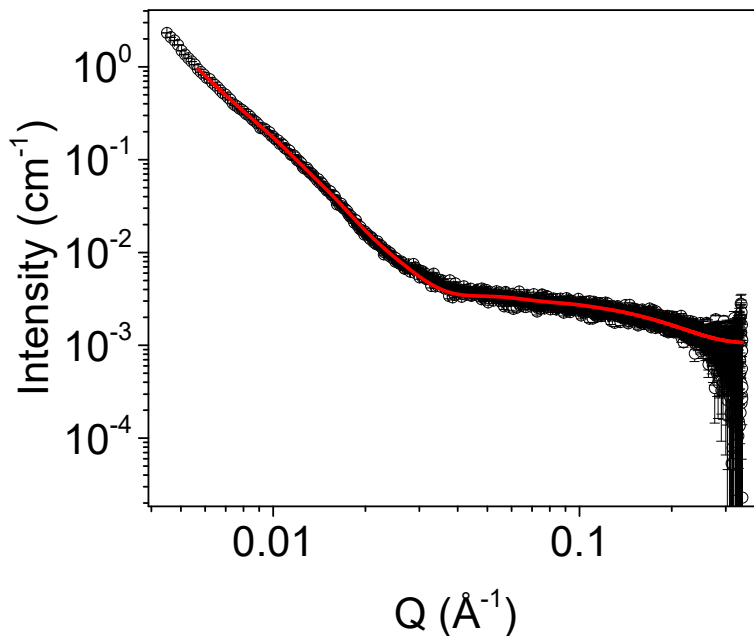


Figure A.4.85. Small angle X-ray scattering data for a solution of **NDI-F:1-NapFF** 5:2.5 mg/mL at pH 9 after heat-cooling (heated to 40 °C and allowed to cool) (open circles) fitted to a flexible elliptical model combined with sphere (red). Fit parameters can be found in Table A.4.51.

Table A.4.51. Parameters of SAXS model fit seen in Figure A.4.85.

NDI-F:1-NapFF 5:2.5 mg/mL pH 9 heat-cooled	Flexible elliptical cylinder combined with sphere	
	Value	Error
Scale A	3.80E-03	1.15E-05
Scale B	3.82E-05	3.75E-08
Background	1.08E-03	3.42E-06
Length (Å)	8.93E+40	1.17E+40
Kuhn Length (Å)	157.15	0.22194
Radius (Å)	83.318	0.12642
Axis Ratio	6.7222	7.34E-03
Radius B (Å)	12.305	0.015917
Range (Å ⁻¹)	0.0056776521-0.3397383	
Chi ²	2.3503	

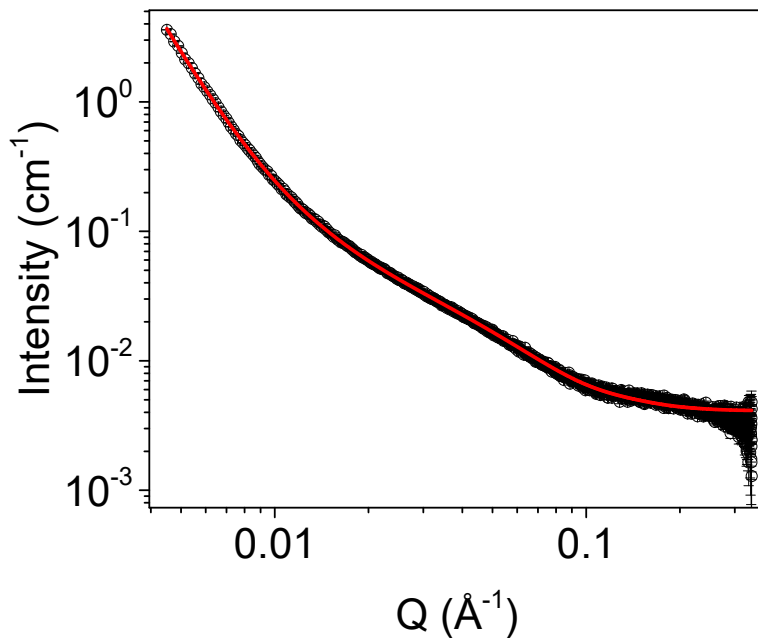


Figure A.4.86. Small angle X-ray scattering data for a solution of **NDI-F:1-NapFF** 5:2.5 mg/mL at pH 12 after heat-cooling (heated to 40 °C and allowed to cool) (open circles) fitted to a flexible elliptical model combined with power law (red). Fit parameters can be found in Table A.4.52.

Table A.4.52. Parameters of SAXS model fit seen in Figure A.4.86.

NDI-F:1-NapFF 5:2.5 mg/mL pH 12 heat-cooled		
Flexible elliptical cylinder combined with power law		
	Value	Error
Scale A	9.40E-04	5.39E-07
Scale B	2.68E-10	2.51E-13
Background	4.12E-03	3.59E-06
Length (Å)	2374.9	9.53E-03
Kuhn Length (Å)	237.49	0.56692
Radius (Å)	8.9616	3.11E-03
Axis Ratio	4.1282	1.41E-03
Power	4.2976	1.83E-04
Range (Å ⁻¹)	0.0045-0.3397383	
Chi ²	3.4598	

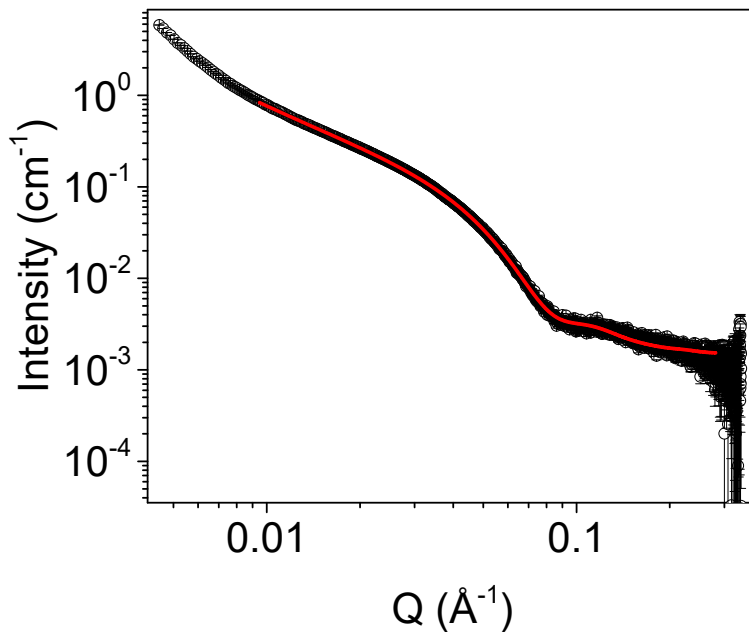


Figure A.4.87. Small angle X-ray scattering data for a solution of **NDI-F:1-NapFF** 5:1.25 mg/mL at pH 6 after heat-cooling (heated to 40 °C and allowed to cool) (open circles) fitted to a flexible elliptical model combined with power law (red). Fit parameters can be found in Table A.4.53.

Table A.4.53. Parameters of SAXS model fit seen in Figure A.4.87.

NDI-F:1-NapFF 5:1.25 mg/mL pH 6 heat-cooled		
Flexible elliptical cylinder combined with power law		
	Value	Error
Scale A	2.66E-03	5.70E-07
Scale B	1.17E-05	1.38E-08
Background	1.36E-03	3.53E-06
Length (Å)	3935.3	8.76E-03
Kuhn Length (Å)	393.71	0.65811
Radius (Å)	37.002	5.59E-03
Axis Ratio	1.4004	1.94E-04
Power	2.0602	3.12E-04
Range (Å ⁻¹)	0.0094723089-0.28111739	
Chi ²	3.5462	

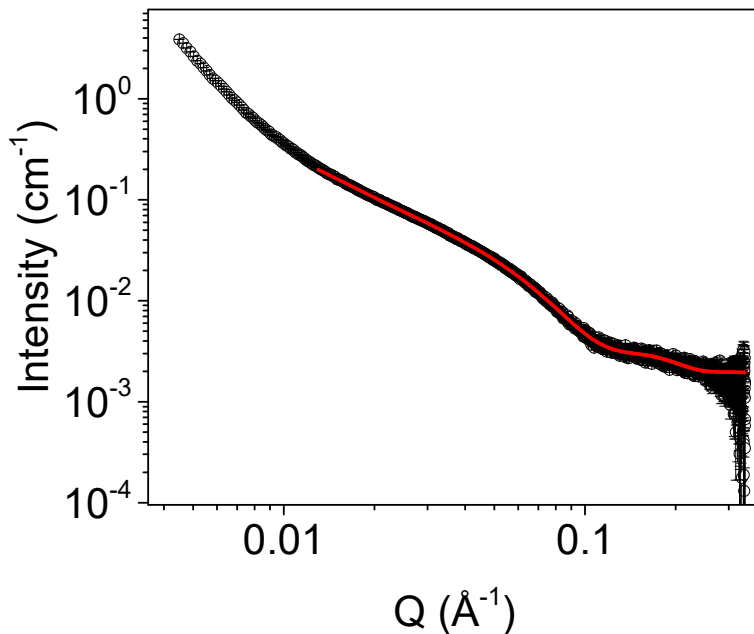


Figure A.4.88. Small angle X-ray scattering data for a solution of **NDI-F:1-NapFF** 5:1.25 mg/mL at pH 9 after heat-cooling (heated to 40 °C and allowed to cool) (open circles) fitted to a flexible elliptical model combined with hollow cylinder (red). Fit parameters can be found in Table A.4.54.

Table A.4.54. Parameters of SAXS model fit seen in Figure A.4.88.

NDI-F:1-NapFF 5:1.25 mg/mL pH 9 heat-cooled	Flexible elliptical cylinder combined with hollow cylinder	
	Value	Error
Scale A	9.79E-04	5.28E-07
Scale B	1.84E-03	1.57E-06
Background	1.94E-03	3.41E-06
Length (Å)	6.33E+03	112.65
Kuhn Length (Å)	130.22	0.17973
Radius (Å)	10.451	3.48E-03
Axis Ratio	3.636	0.001189
Length B (Å)	372.94	4.3216
Radius B (Å)	11.759	0.021534
Thickness B (Å)	16.355	0.012011
Range (Å ⁻¹)	0.013005265-0.3397383	
Chi ²	2.0067	

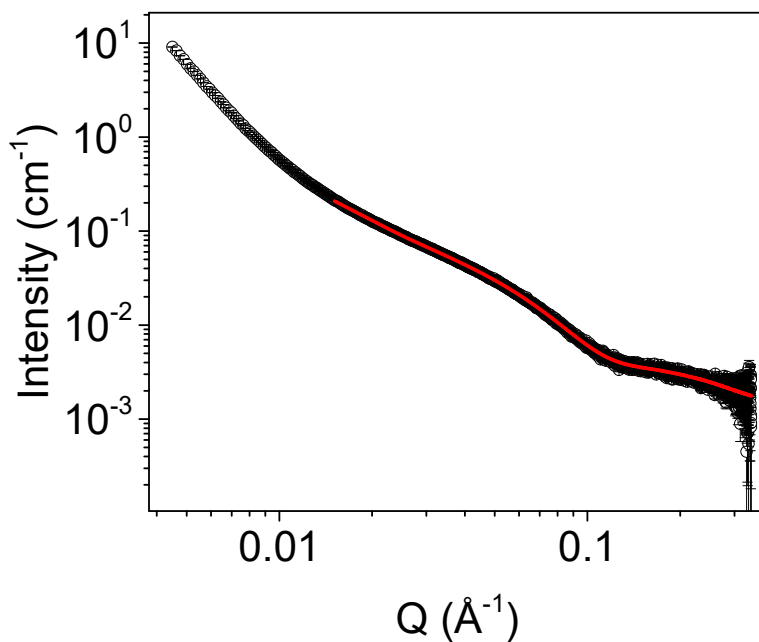


Figure A.4.89. Small angle X-ray scattering data for a solution of **NDI-F:1-NapFF** 5:1.25 mg/mL at pH 12 after heat-cooling (heated to 40 °C and allowed to cool) (open circles) fitted to a flexible elliptical model combined with sphere (red). Fit parameters can be found in Table A.4.55.

Table A.4.55. Parameters of SAXS model fit seen in Figure A.4.89.

NDI-F:1-NapFF 5:1.25 mg/mL pH 12 heat-cooled	Flexible elliptical cylinder combined with sphere	
	Value	Error
Scale A	2.45E-03	7.68E-07
Scale B	1.40E-02	2.69E-05
Background	1.37E-03	3.45E-06
Length (Å)	1.18E+04	147.02
Kuhn Length (Å)	138.49	0.12185
Radius (Å)	21.721	4.33E-03
Axis Ratio	1.5779	2.95E-04
Radius B (Å)	8.5485	6.95E-03
Range (Å ⁻¹)	0.015-0.3397383	
Chi ²	1.7716	

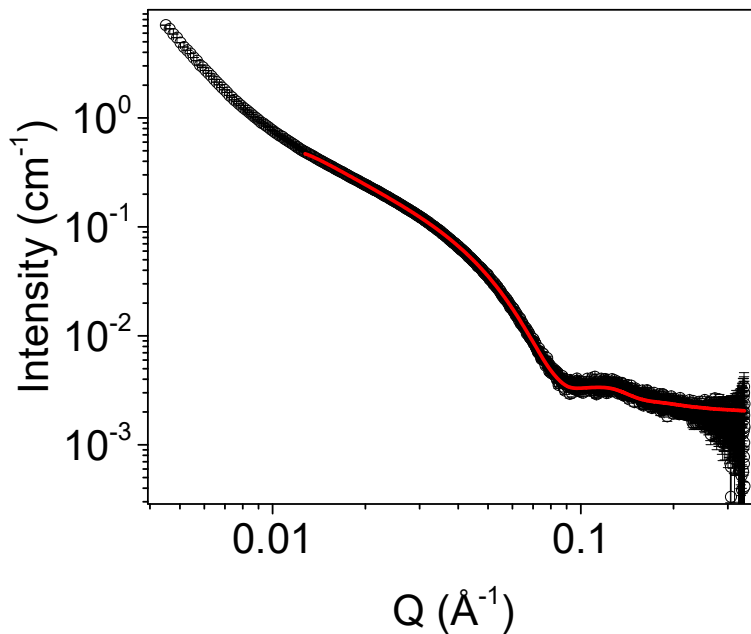


Figure A.4.90. Small angle X-ray scattering data for a solution of **NDI-F:1-NapFF** 5:0.625 mg/mL at pH 6 after heat-cooling (heated to 40 °C and allowed to cool) (open circles) fitted to a flexible elliptical model combined with cylinder (red). Fit parameters can be found in Table A.4.56.

Table A.4.56. Parameters of SAXS model fit seen in Figure A.4.90.

NDI-F:1-NapFF 5:0.625 mg/mL pH 6 heat-cooled	Flexible elliptical cylinder combined with cylinder	
	Value	Error
Scale A	7.74E-04	1.84E-07
Scale B	5.86E-04	3.15E-06
Background	2.01E-03	4.68E-06
Length (Å)	502.61	1.1139
Kuhn Length (Å)	236.34	0.20972
Radius (Å)	8.0352	0.023693
Axis Ratio	1.301	1.95E-04
Length B (Å)	5408.3	110.065
Radius B (Å)	36.259	6.08E-03
Range (Å ⁻¹)	0.015-0.3397383	
Chi ²	2.2282	

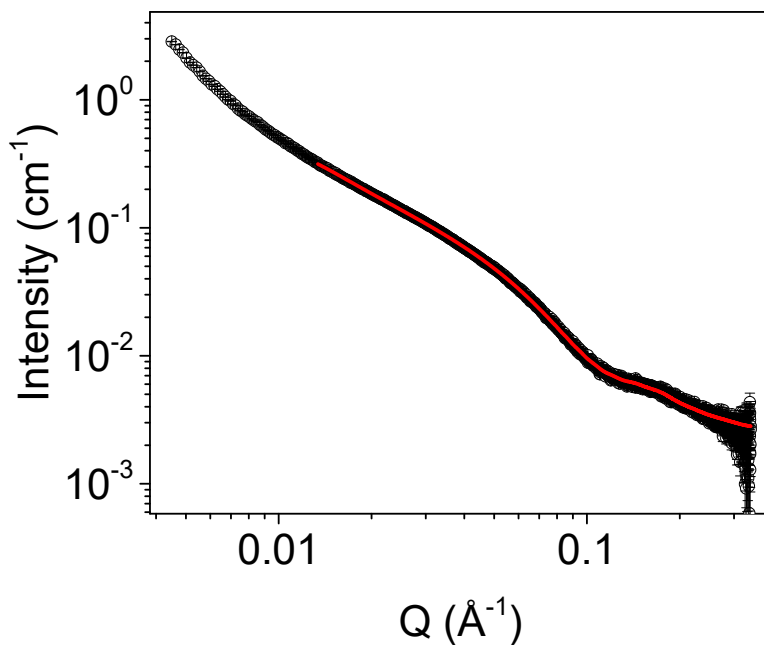


Figure A.4.91. Small angle X-ray scattering data for a solution of **NDI-F:1-NapFF** 5:0.625 mg/mL at pH 9 after heat-cooling (heated to 40 °C and allowed to cool) (open circles) fitted to a flexible elliptical model combined with cylinder (red). Fit parameters can be found in Table A.4.57.

Table A.4.57. Parameters of SAXS model fit seen in Figure A.4.91.

NDI-F:1-NapFF 5:0.625 mg/mL pH 9 heat-cooled	Flexible elliptical cylinder combined with cylinder	
	Value	Error
Scale A	1.02E-03	2.84E-07
Scale B	3.04E-03	2.26E-06
Background	2.69E-03	3.53E-06
Length (Å)	530.53	2.0296
Kuhn Length (Å)	242.51	0.28957
Radius (Å)	30.098	5.40E-03
Axis Ratio	1.041	1.68E-04
Length B (Å)	3135.9	13.455
Radius B (Å)	8.6648	3.64E-03
Range (Å ⁻¹)	0.013397816-0.3397383	
Chi ²	2.2613	

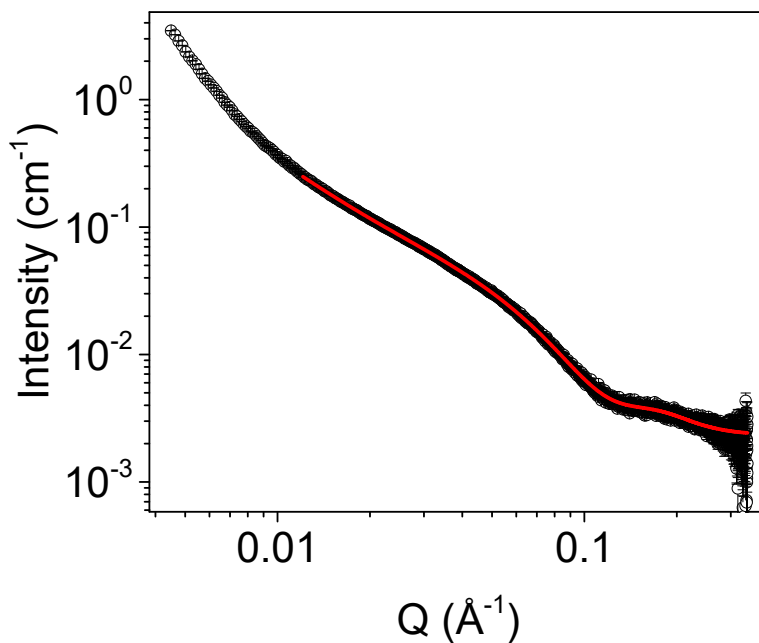


Figure A.4.92. Small angle X-ray scattering data for a solution of **NDI-F:1-NapFF** 5:0.625 mg/mL at pH 12 after heat-cooling (heated to 40 °C and allowed to cool) (open circles) fitted to a flexible elliptical model combined with sphere (red). Fit parameters can be found in Table A.4.58.

Table A.4.58. Parameters of SAXS model fit seen in Figure A.4.92.

NDI-F:1-NapFF 5:0.625 mg/mL pH 12 heat-cooled	Flexible elliptical cylinder combined with sphere	
	Value	Error
Scale A	7.12E-04	2.24E-07
Scale B	1.22E-03	3.24E-06
Background	2.41E-03	3.48E-06
Length (Å)	4248.9	30.728
Kuhn Length (Å)	193.67	0.27866
Radius (Å)	24.494	4.78E-03
Axis Ratio	1.2811	2.33E-04
Radius B (Å)	12.073	0.014214
Range (Å ⁻¹)	0.012-0.3397383	
Chi ²	1.7946	

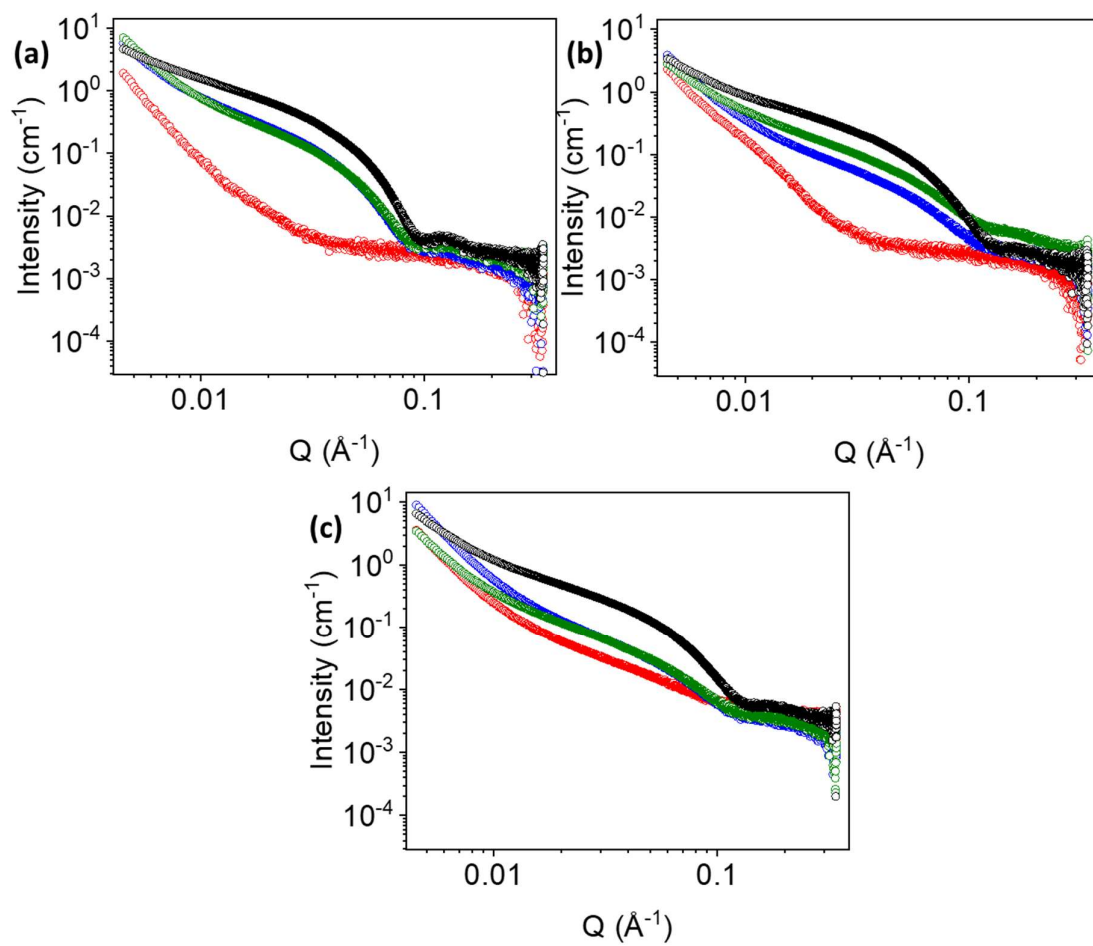


Figure A.4.93. SAXS data of NDI-F:1-NapFF after heat-cooling (heated to 40 °C and allowed to cool) at 5:5 (black), 5:2.5 (red), 5:1.25 (blue) and 5:0.625 (green) mg/mL at pH 6 (a), 9 (b) and 12 (c).

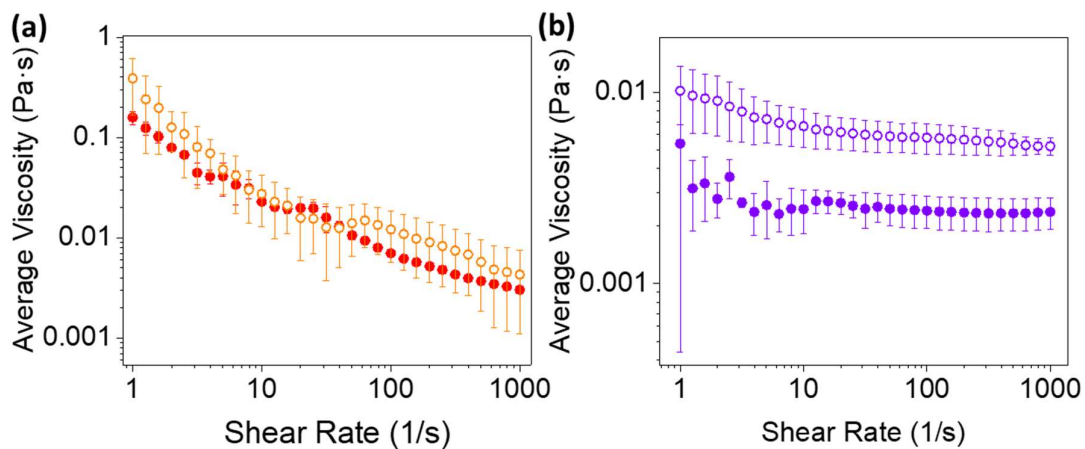


Figure A.4.94. Viscosity measurements (a) **NDI-F:1-NapFF** 5:0.625 mg/mL and (b) **NDI-F** 5 mg/mL after heat cooling at 40 °C. Solutions at pH 6 buffered (open circles) and unbuffered (filled circles). Measurements are taken as an average of triplicate measurements and error bars calculated from standard deviation.

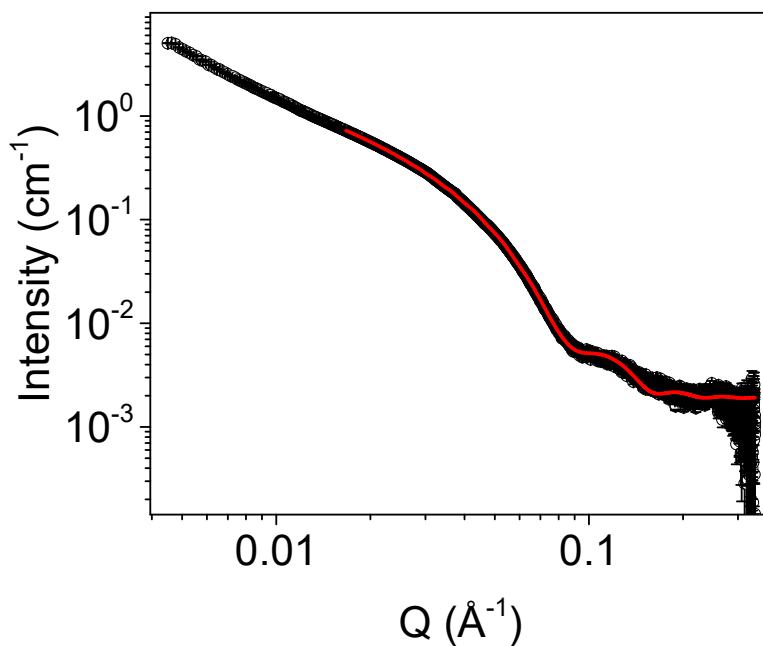


Figure A.4.95. Small angle X-ray scattering data for a solution of **NDI-F:1-NapFF** 5:0.625 mg/mL at buffered at pH 6 after heat-cooling (heated to 40 °C and allowed to cool) (open circles) fitted to a flexible elliptical model combined with cylinder (red). Fit parameters can be found in Table A.4.59.

Table A.4.59. Parameters of SAXS model fit seen in Figure A.4.95.

NDI-F:1-NapFF 5:0.625 mg/mL pH 6 heat-cooled buffered		Flexible elliptical cylinder combined with cylinder	
	Value	Error	
Scale A	1.77E-03	3.06E-07	
Scale B	1.93E-04	9.54E-08	
Background	1.88E-03	3.51E-06	
Length (Å)	303.56	0.80161	
Kuhn Length (Å)	201.23	0.40333	
Radius (Å)	16.406	8.33E-03	
Axis Ratio	5.1161	2.35E-03	
Length B (Å)	1.04E+04	7.0388	
Radius B (Å)	43.138	5.61E-03	
Range (Å ⁻¹)	0.016716719-0.33973727		
Chi ²	6.6238		

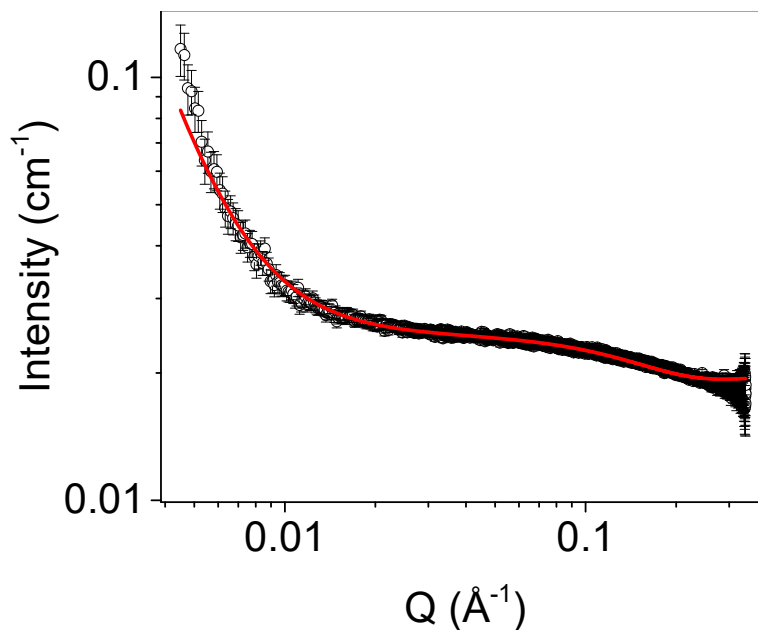
**Figure A.4.96.** Small angle X-ray scattering data for a solution of **NDI-F** 5 mg/mL at buffered at pH 6 after heat-cooling (heated to 40 °C and allowed to cool) (open circles) fitted to a hollow cylinder model combined with power law (red). Fit parameters can be found in Table A.4.60.

Table A.4.60. Parameters of SAXS model fit seen in Figure A.4.96.

NDI-F 5 mg/mL pH 6 heat-cooled buffered		Hollow cylinder combined with power law	
	Value	Error	
Scale A	3.08E-04	1.6859-06	
Scale B	1.80E-09	4.37E-11	
Background	1.97E-02	9.35E-06	
Length (Å)	19.72	0.10064	
Radius (Å)	6.7749	0.061828	
Thickness (Å)	7.2061	0.11269	
Range (Å ⁻¹)	0.0045-0.34		
Chi ²	1.1831		

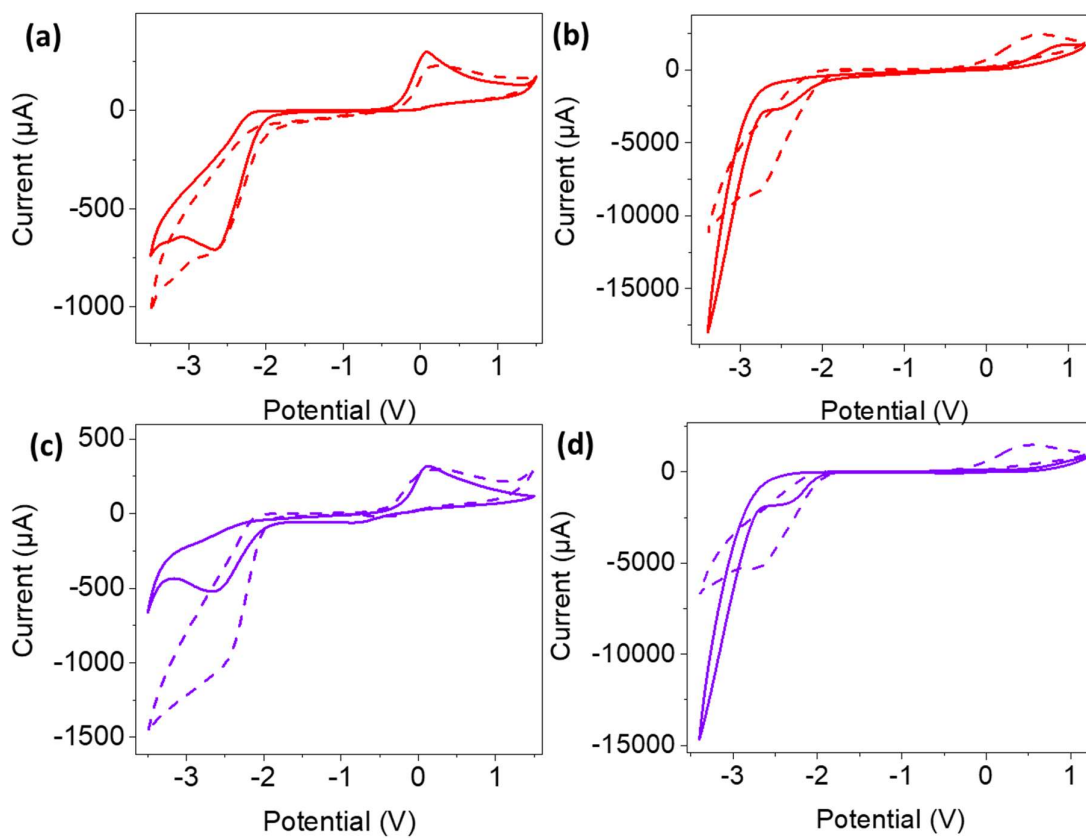


Figure A.4.97. Cyclic voltammograms taken at 0.2 V/s of heat-cooled (heated to 40 °C and allowed to cool) (a-b) **NDI-F:1-NapFF 5:0.625 mg/mL** and (b-c) **NDI-F 5 mg/mL buffered** (dashed line) and unbuffered (solid line) at pH 6 in (a/c) 1 x 1 and (b/d) 5 x 5 FTO window cells.

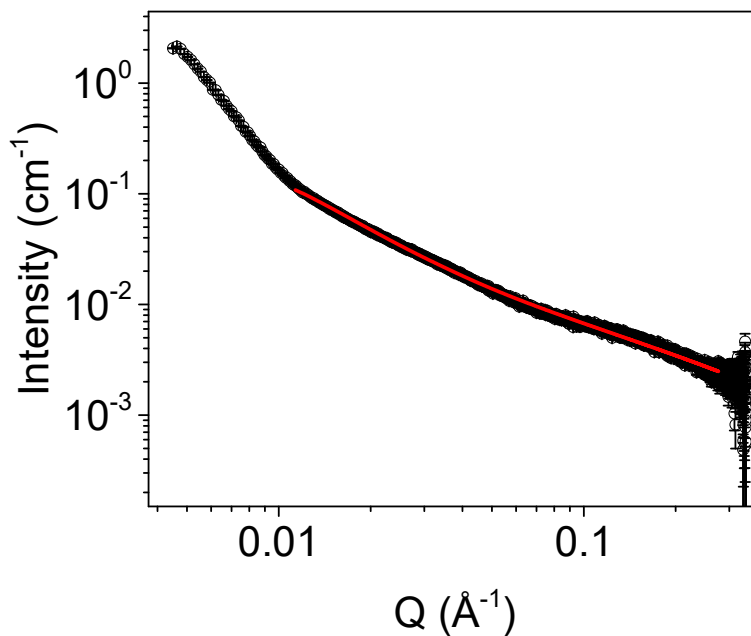


Figure A.4.98. Small angle X-ray scattering data for a solution of **NDI-F:1-NapFF** 5:0.625 mg/mL buffered at pH 6, heat-cooled (heated to 40 °C and allowed to cool) and electrochemically cycles once (open circles) fitted to a flexible cylinder model (red). Solutions were relaxed for several days prior to measurement. Fit parameters can be found in Table A.4.61.

Table A.4.61. Parameters of SAXS model fit seen in Figure A.4.98.

NDI-F:1-NapFF 5:0.625 mg/mL at pH 6 heat-cooled and electrochemically cycled once	Flexible cylinder	
	Value	Error
Scale	7.68E-03	3.69E+96
Background	1.21E-03	3.58E-06
Length (Å)	1.32E+03	10.173
Kuhn length (Å)	98.875	0.13349
Radius (Å)	5	8.93E-04
Range (Å ⁻¹)	0.011330854-0.27615779	
Chi ²	4.235	

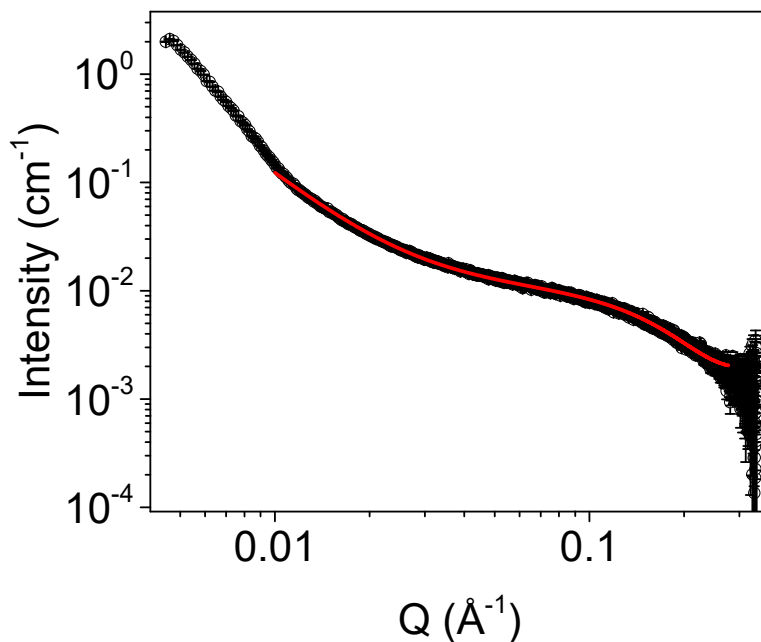


Figure A.4.99. Small angle X-ray scattering data for a solution of **NDI-F:1-NapFF** 5:0.625 mg/mL buffered at pH 6, heat-cooled (heated to 40 °C and allowed to cool) and electrochemically cycles 50 times (open circles) fitted to a flexible cylinder model combined (red). Solutions were relaxed for several days prior to measurement. Fit parameters can be found in Table A.4.62.

Table A.4.62. Parameters of SAXS model fit seen in Figure A.4.99.

NDI-F:1-NapFF 5:0.625 mg/mL at pH 6, heat-cooled and electrochemically cycles 50 times	Flexible cylinder	
	Value	Error
Scale	5.67E-03	3.18E-06
Background	9.76E-04	3.48E-06
Length (Å)	6.79E+44	1.26E+40
Kuhn length (Å)	112.73	0.14531
Radius (Å)	6.8581	2.09E-03
Range (Å ⁻¹)	0.017110807-0.31044342	
Chi ²	6.55	

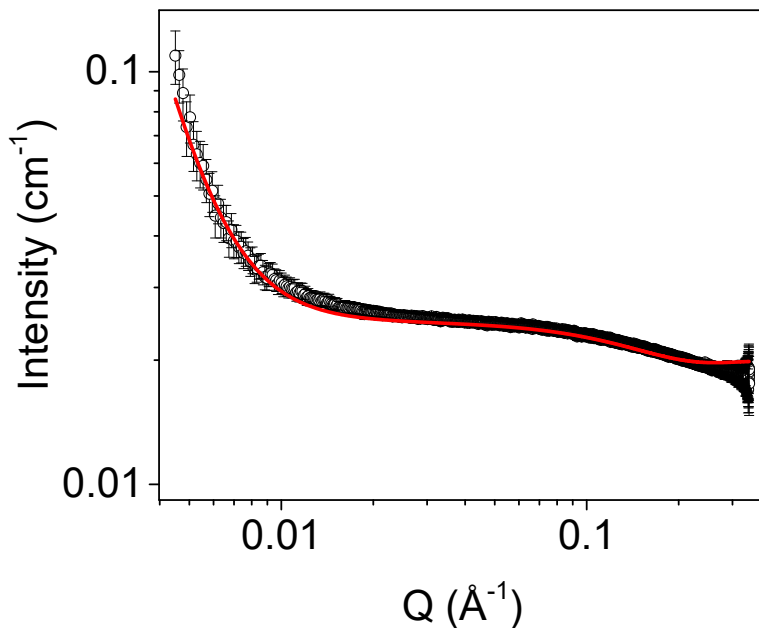


Figure A.4.100. Small angle X-ray scattering data for a solution of **NDI-F** 5 mg/mL buffered at pH 6, heat-cooled (heated to 40 °C and allowed to cool) and electrochemically cycles once (open circles) fitted to a hollow cylinder model combined with power law (red). Solutions were relaxed for several days prior to measurement. Fit parameters can be found in Table A.4.63.

Table A.4.63. Parameters of SAXS model fit seen in Figure A.4.100.

NDI-F 5 mg/mL at pH 6 heat-cooled and electrochemically cycled once	Hollow cylinder combined with power law	
	Value	Error
Scale A	4.66E-04	2.50E-06
Scale B	1.55E-09	5.63E-11
Background	1.96E-02	1.24E-05
Length (Å)	18.588	0.085496
Radius (Å)	4.9871	0.019028
Thickness (Å)	8.1499	0.05741
Power	3.2369	6.88E-03
Range (Å ⁻¹)	0.0045-0.34	
Chi ²	1.002	

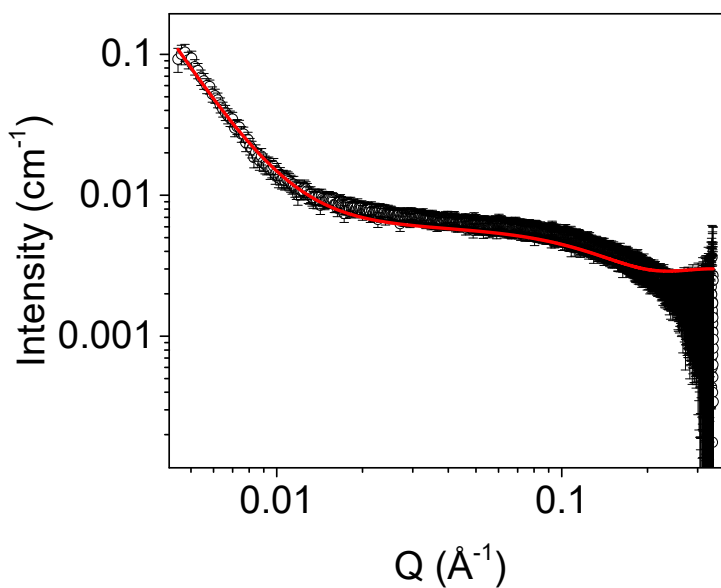


Figure A.4.101. Small angle X-ray scattering data for a solution of **NDI-F** 5 mg/mL buffered at pH 6, heat-cooled (heated to 40 °C and allowed to cool) and electrochemically cycles 50 times (open circles) fitted to a flexible elliptical cylinder model combined with cylinder (red). Solutions were relaxed for several days prior to measurement. Fit parameters can be found in Table A.4.64.

Table A.4.64. Parameters of SAXS model fit seen in Figure A.4.101.

NDI-F 5 mg/mL at pH 6 heat-cooled and electrochemically cycled 50 times	Hollow cylinder combined with power law	
	Value	Error
Scale A	2.03E-04	2.00E-06
Scale B	6.65E-09	1.80E-09
Background	2.87E-03	1.17E-05
Length (Å)	25.417	0.28348
Radius (Å)	8.8805	0.13457
Thickness (Å)	5.217	0.032194
Power	3.0631	0.056069
Range (Å ⁻¹)	0.0045-0.34	
Chi ²	1.2882	

A.4.E Chapter 4 experimental appendices

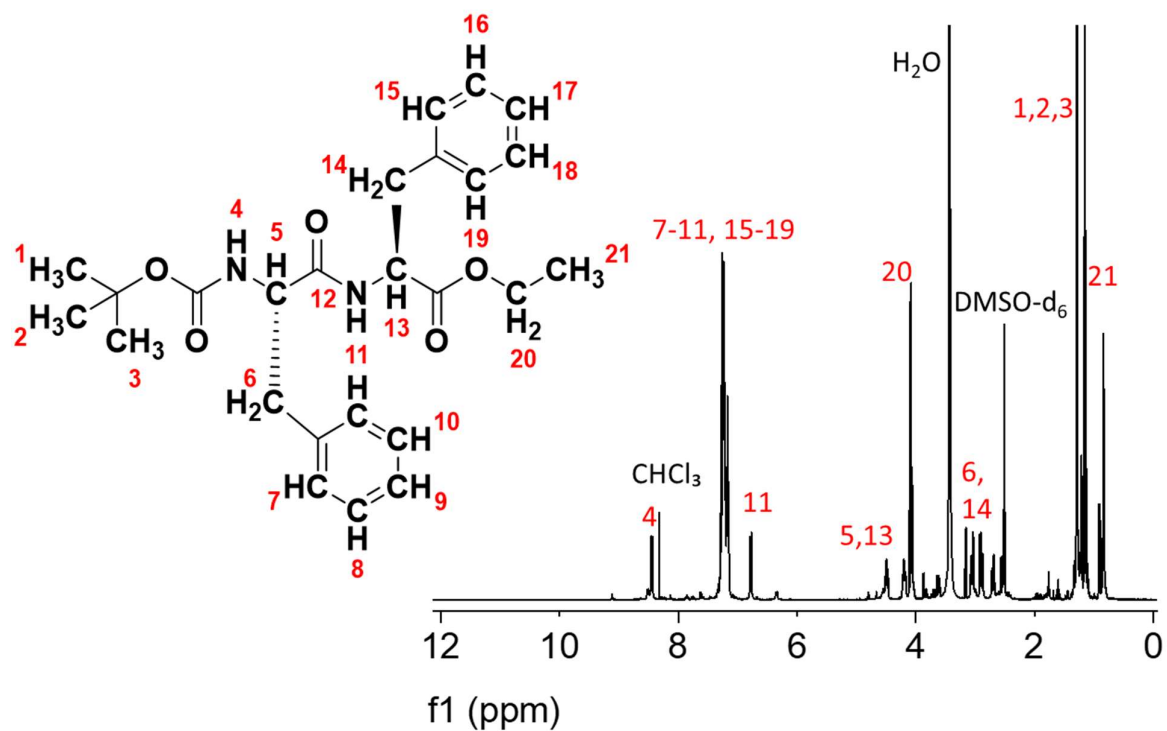


Figure A.4.102. Annotated ¹H NMR spectrum (400 MHz, DMSO-d₆) of FF-OEt – Protected.

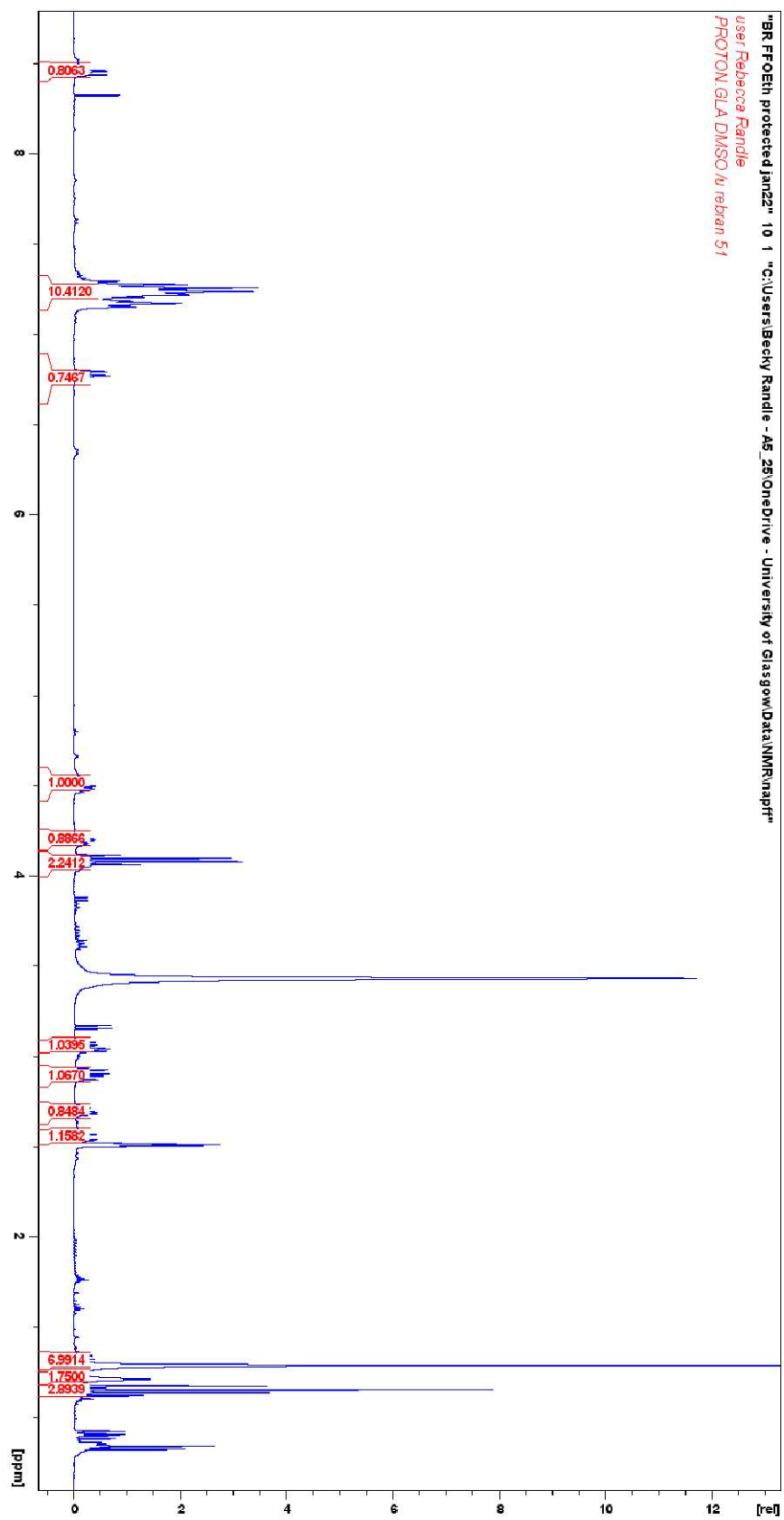


Figure A.4.103. ¹H NMR spectrum showing integrals (400 MHz, DMSO-d₆) of FF-OEt – Protected.

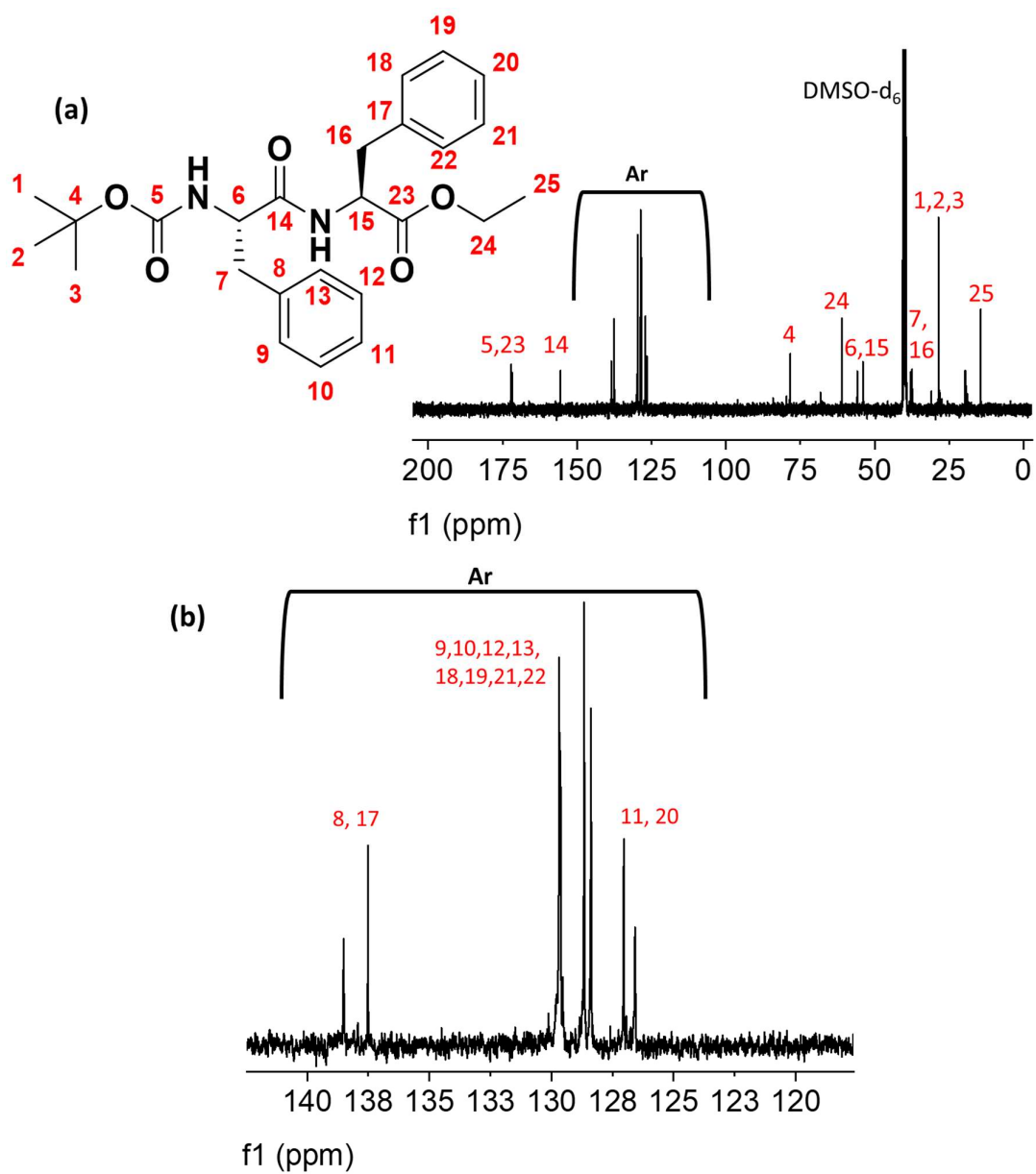


Figure A.4.104. Annotated ^{13}C NMR spectrum (100 MHz, DMSO-d_6) of FF-OEt - Protected. (a) full spectra (b) enhanced section marked Ar showing the aromatic carbon environments.

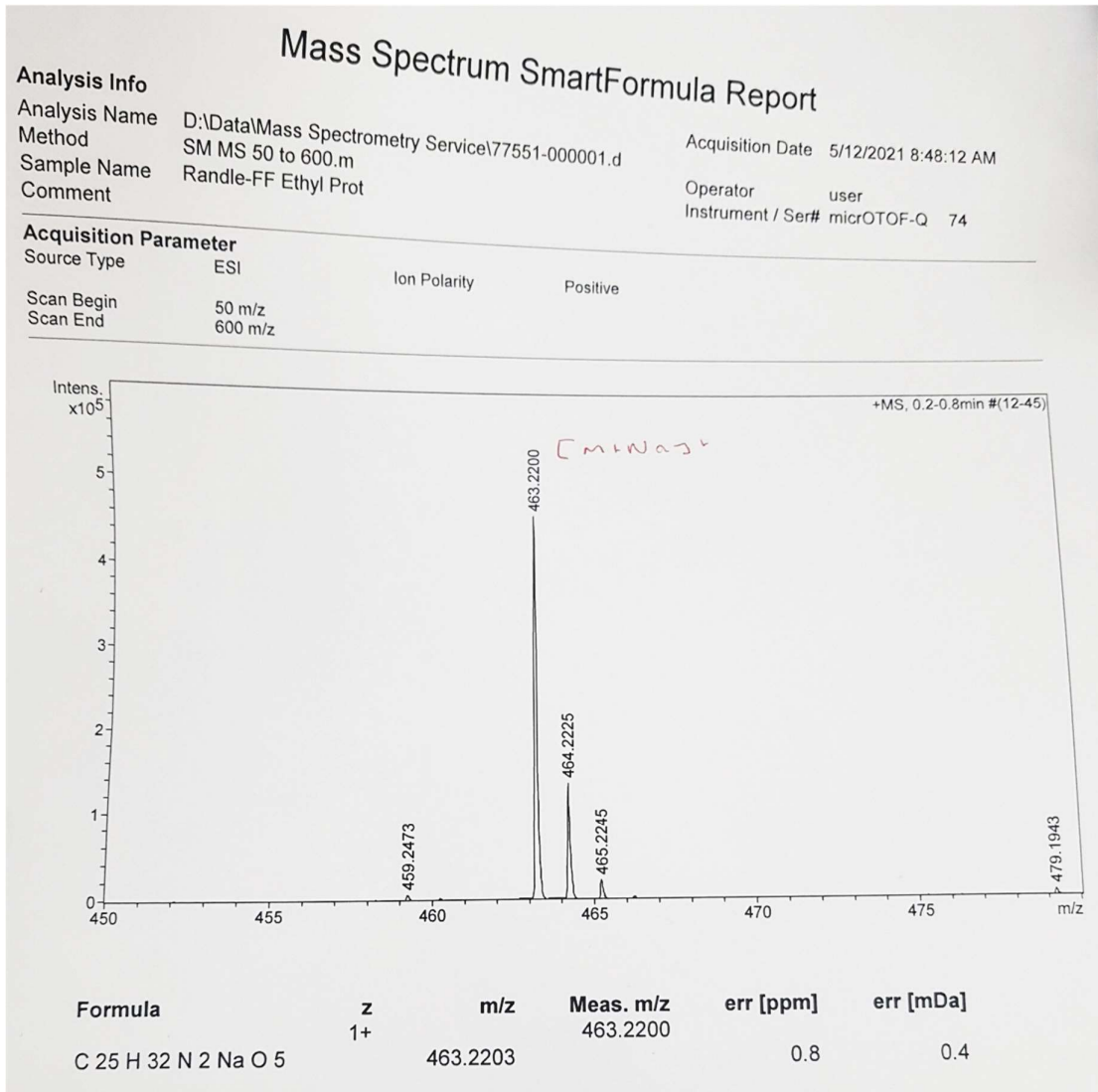


Figure A.4.105. HRMS report of FF-OEt – Protected in ethanol.

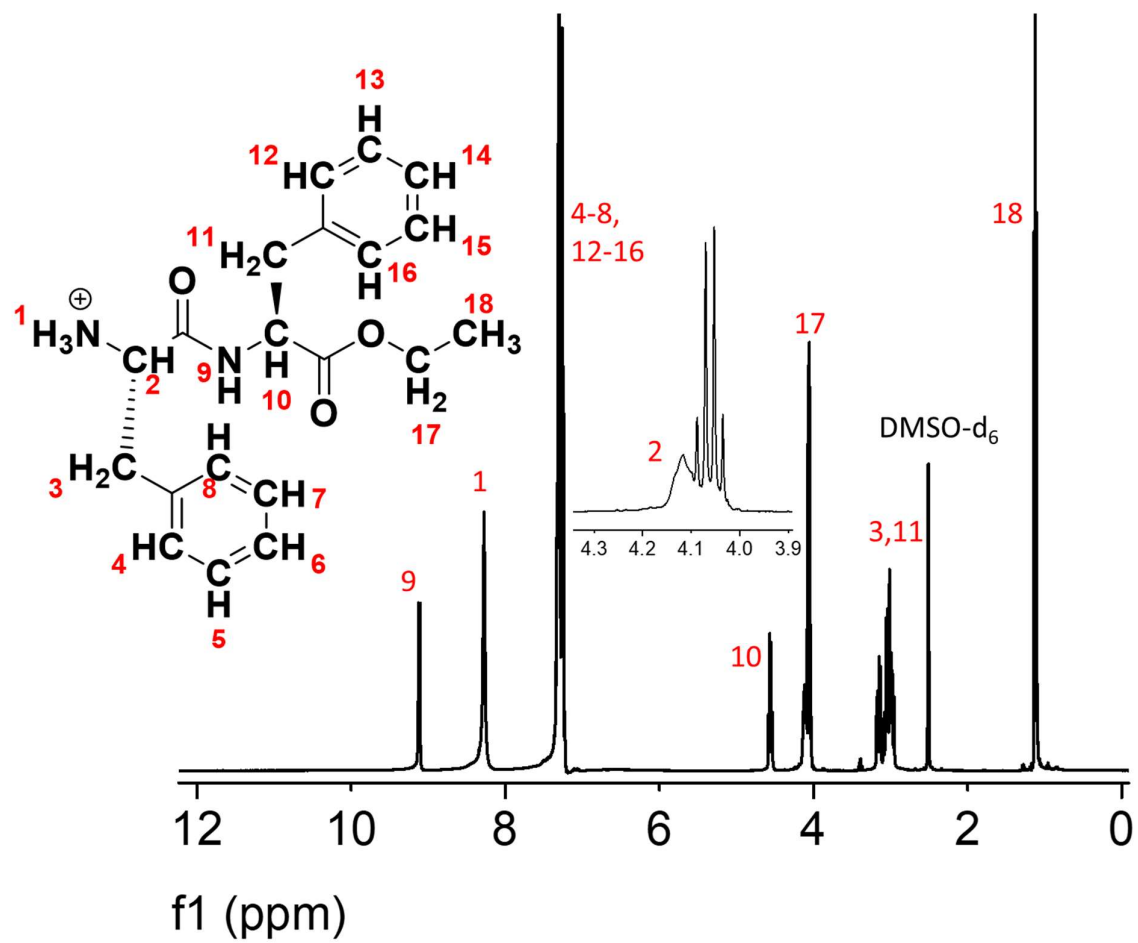


Figure A.4.106. Annotated ¹H NMR spectrum (400 MHz, DMSO-d₆) of FF-OEt – Deprotected with expanded 4.3-3.9 ppm.

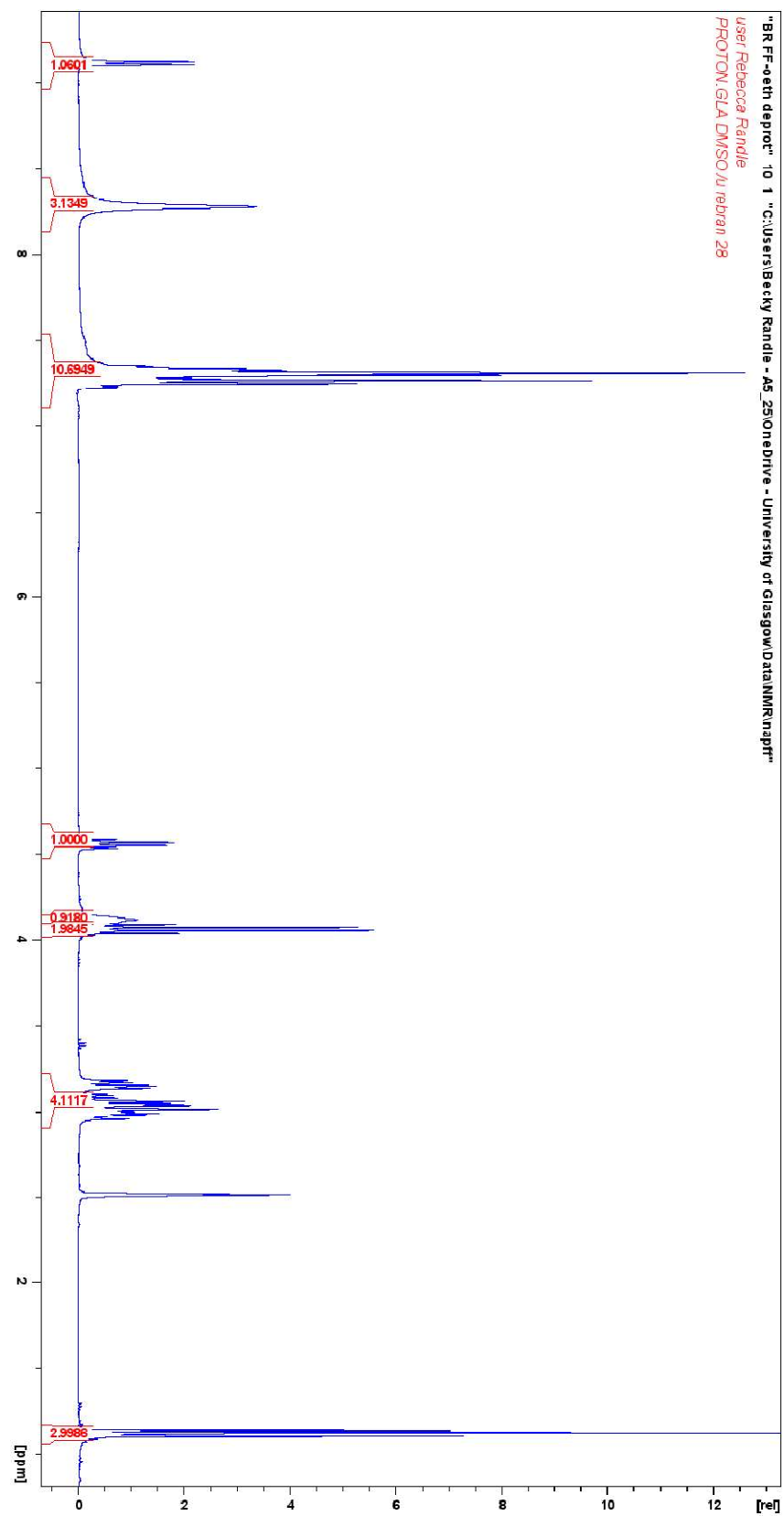


Figure A.4.107. ¹H NMR spectrum showing integrals (400 MHz, DMSO-d₆) of FF-OEt – Deprotected.

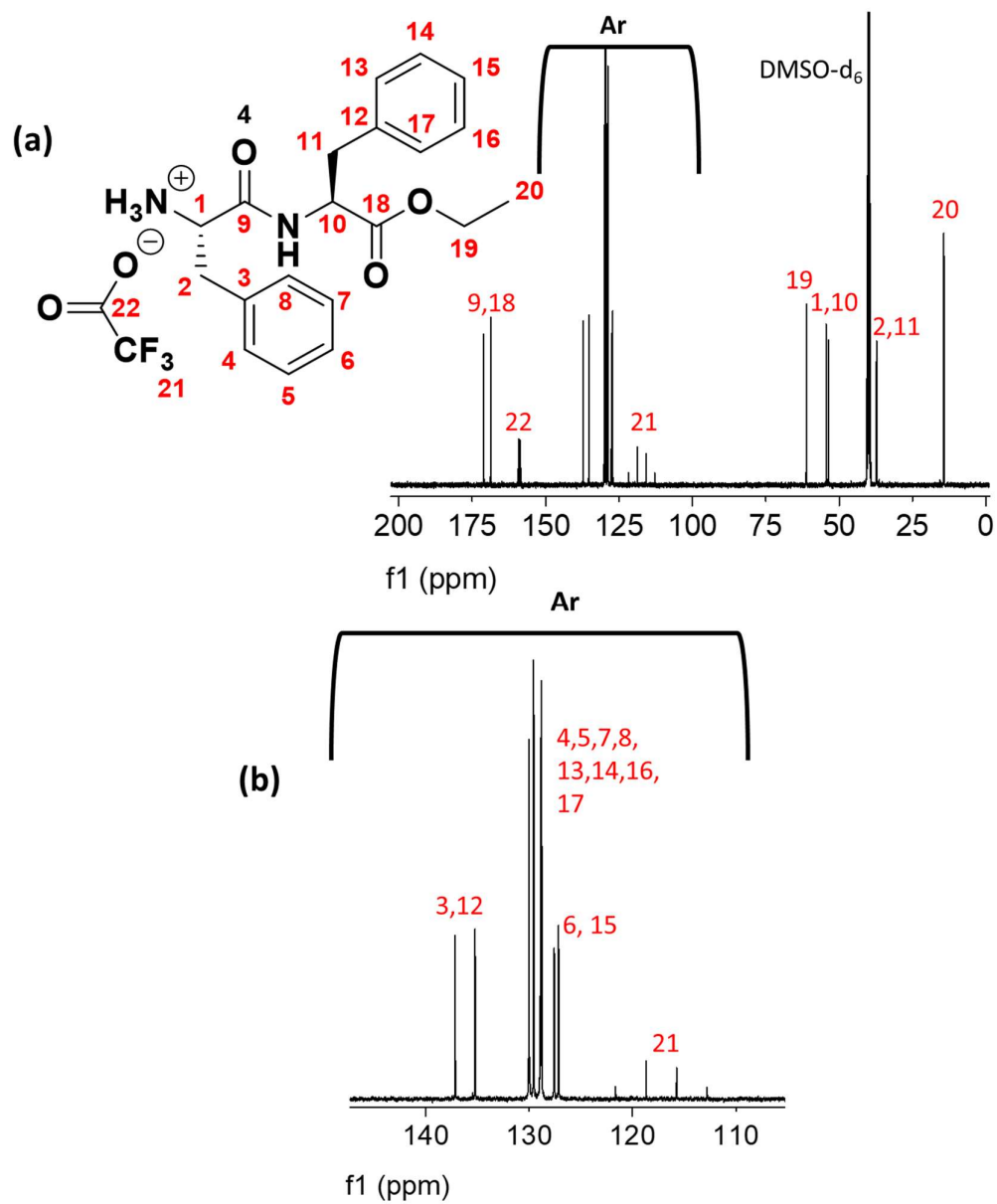


Figure A.4.108. Annotated ^{13}C NMR spectrum (100 MHz, DMSO-d_6) of FF-OEt - Deprotected. (a) full spectra (b) enhanced section marked Ar showing the aromatic carbon environments.

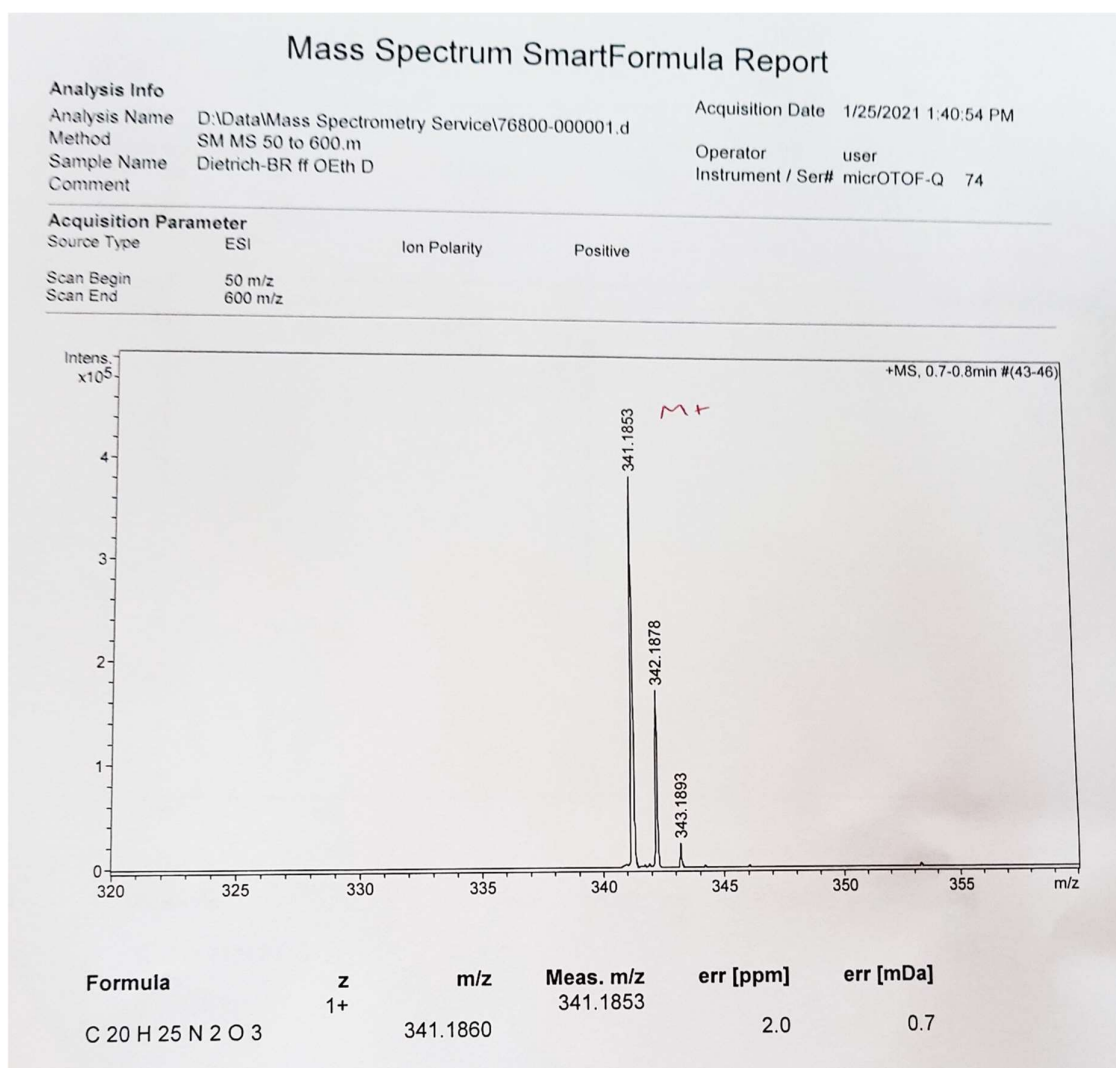


Figure A.4.109. HRMS report of FF-OEt – Deprotected in ethanol.

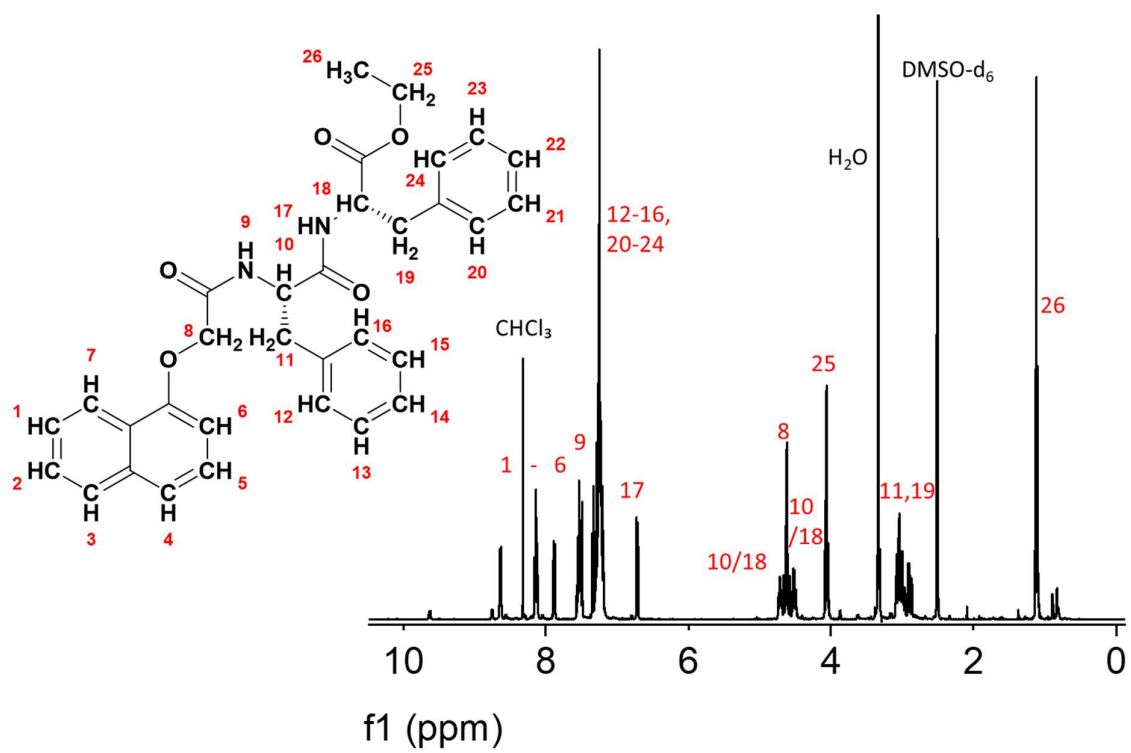


Figure A.4.110. Annotated ^1H NMR spectrum (400 MHz, DMSO-d_6) of 1-NapFF - Protected.

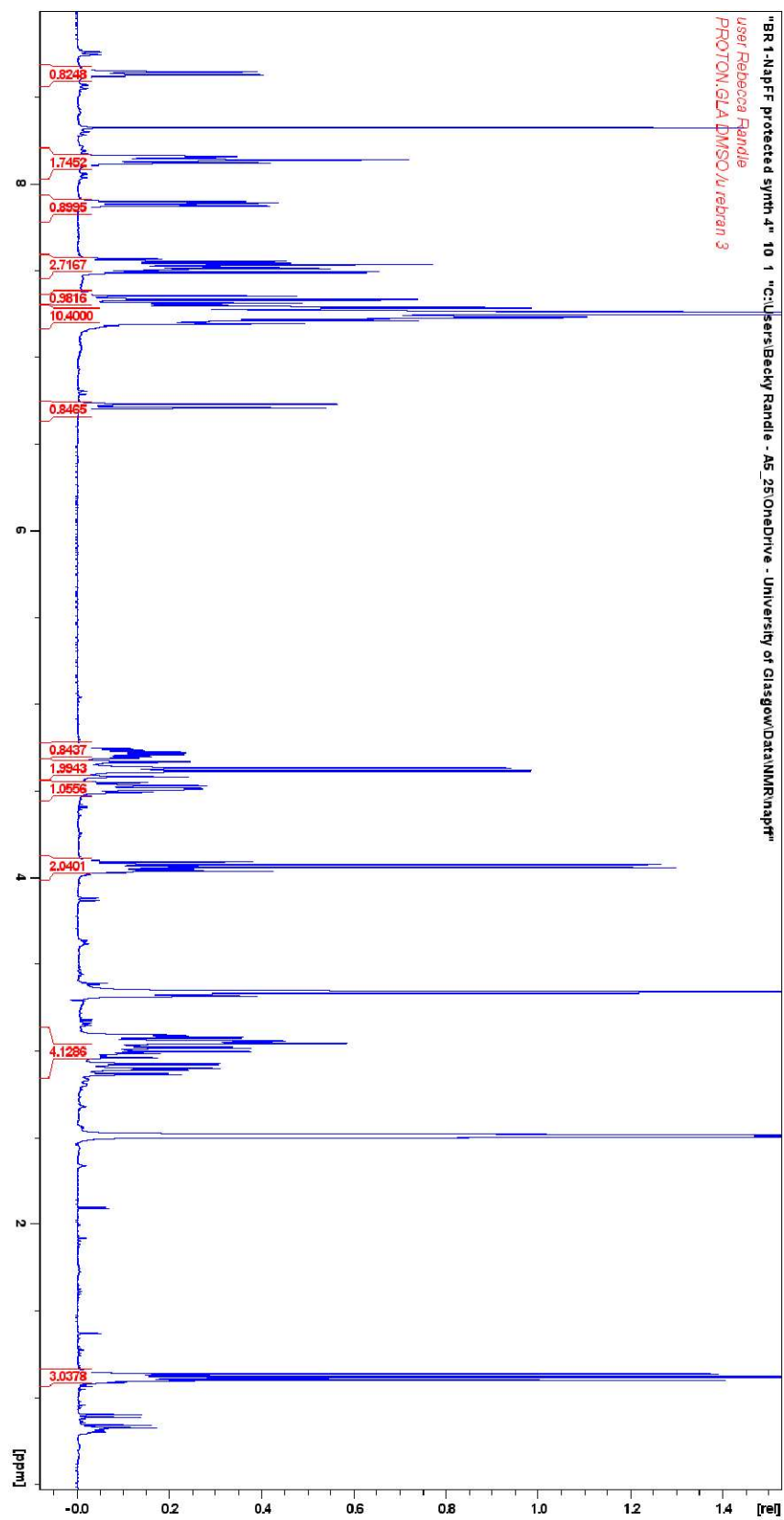
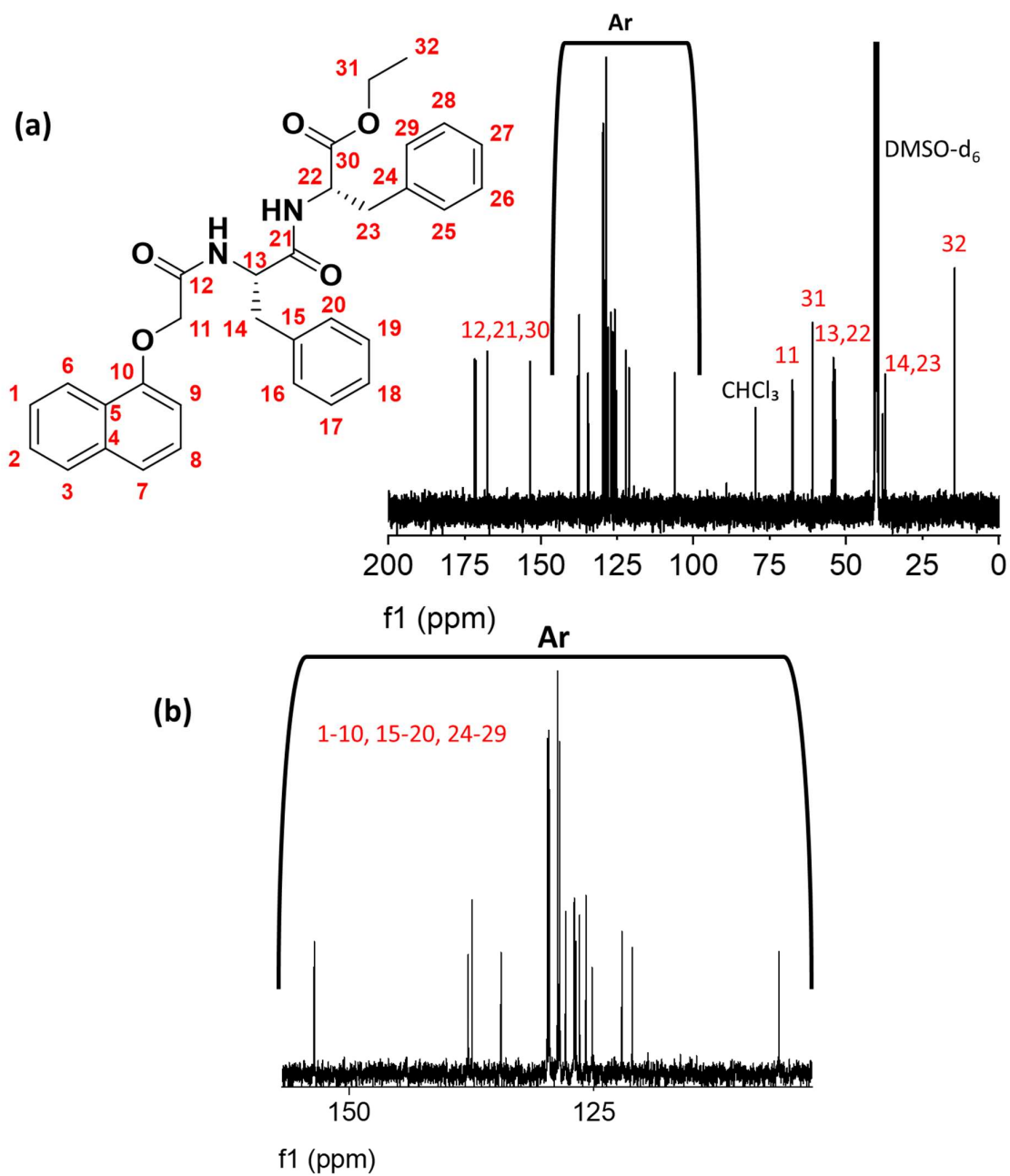


Figure A.4.111. ^1H NMR spectrum showing integrals (400 MHz, $\text{DMSO}-d_6$) of **1-NapFF** - Protected.



Appendix

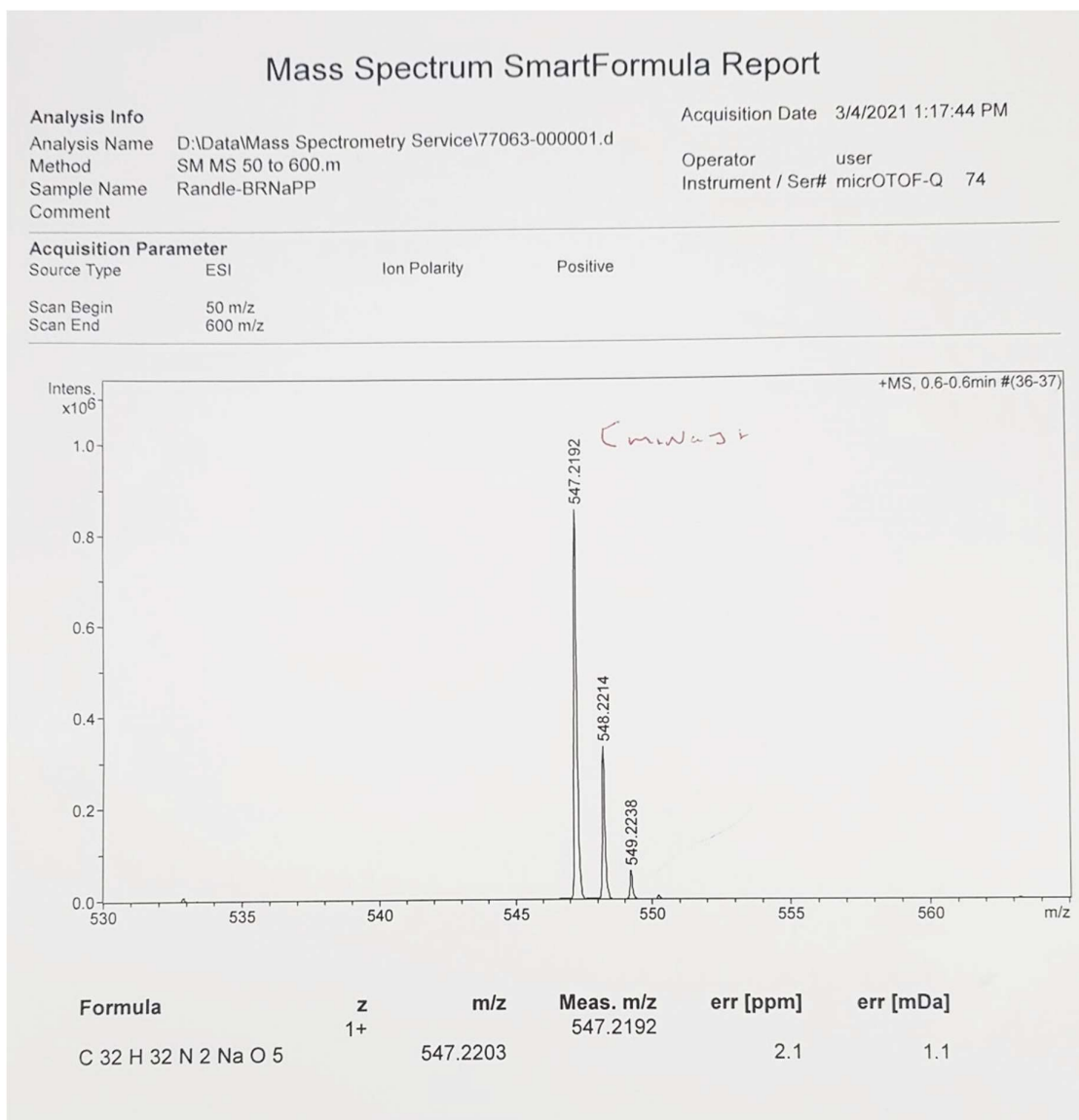


Figure A.4.113. HRMS report of 1-NapFF – Protected in ethanol.

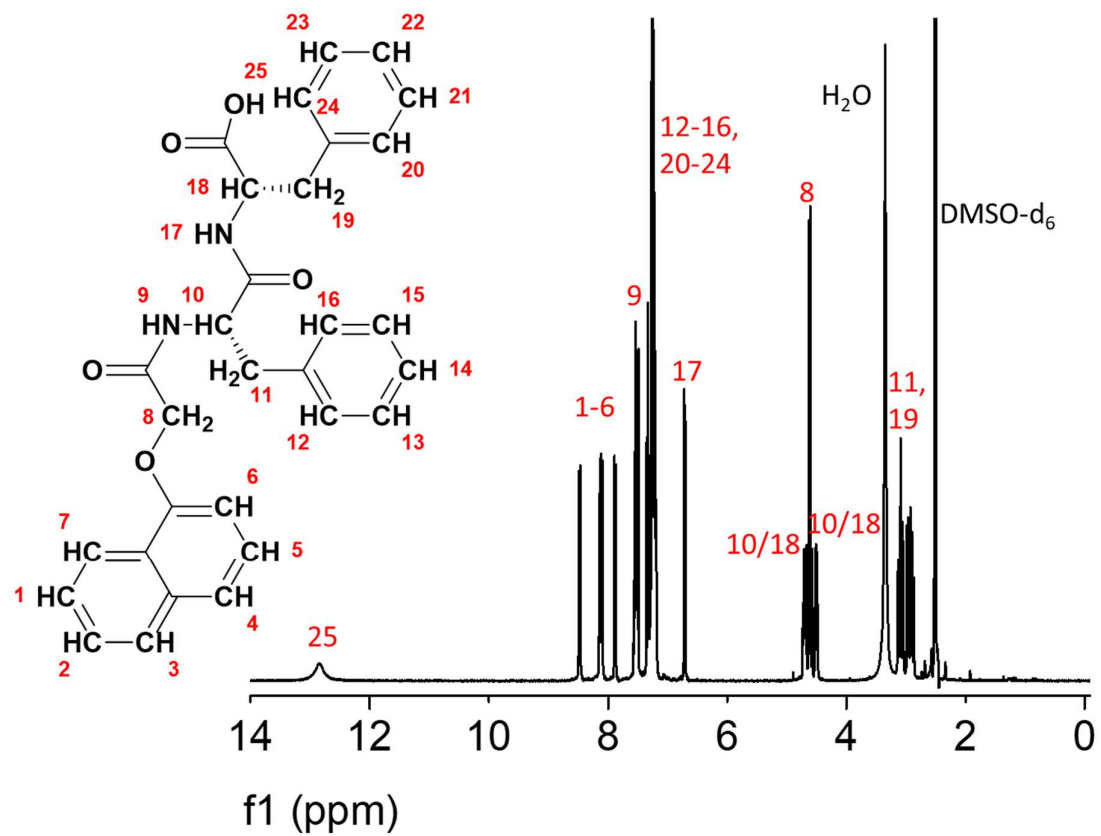


Figure A.4.114. Annotated ¹H NMR spectrum (400 MHz, DMSO-d₆) of 1-NapFF.

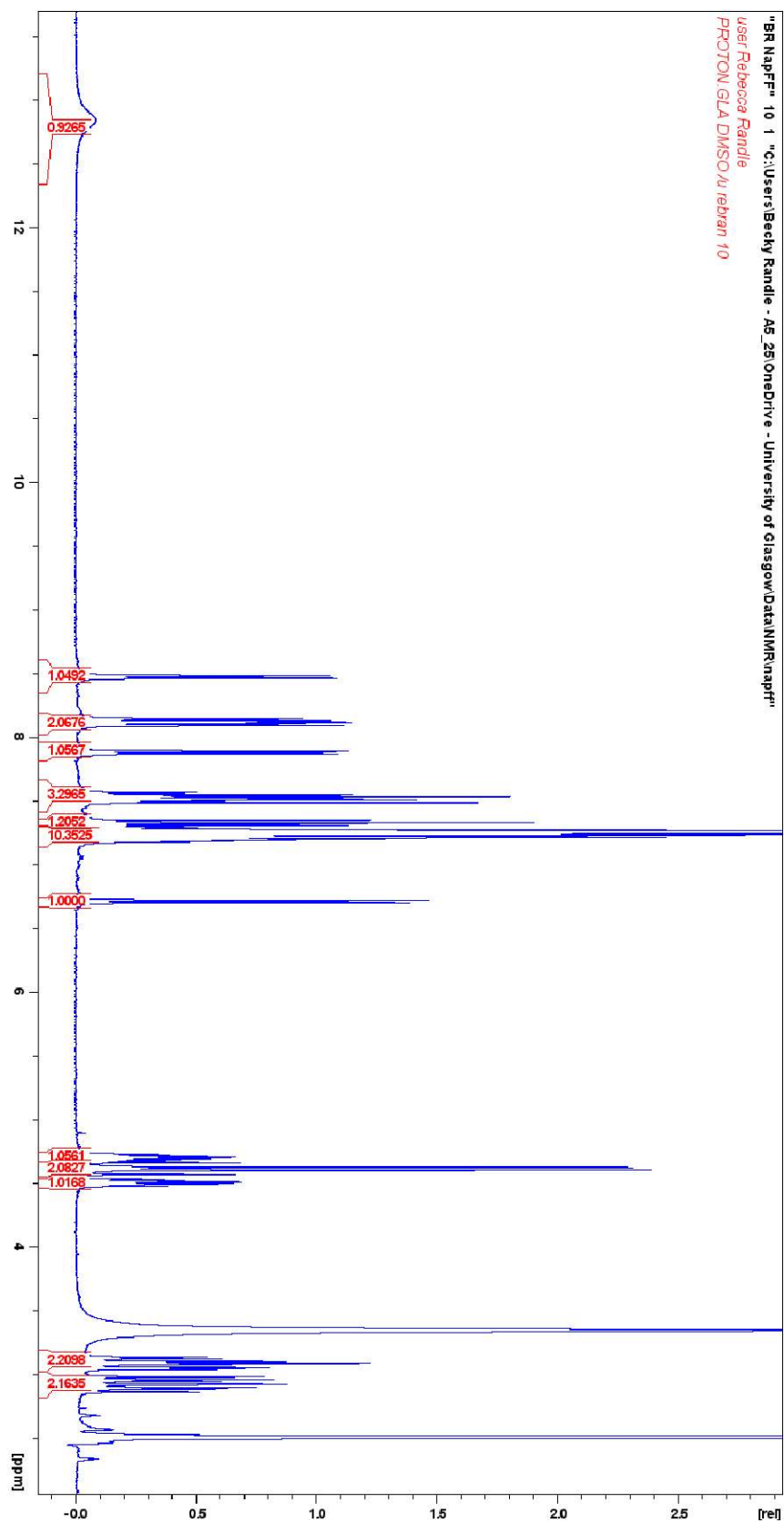


Figure A.4.115. ^1H NMR spectrum showing integrals (400 MHz, DMSO-d_6) of 1-NapFF.

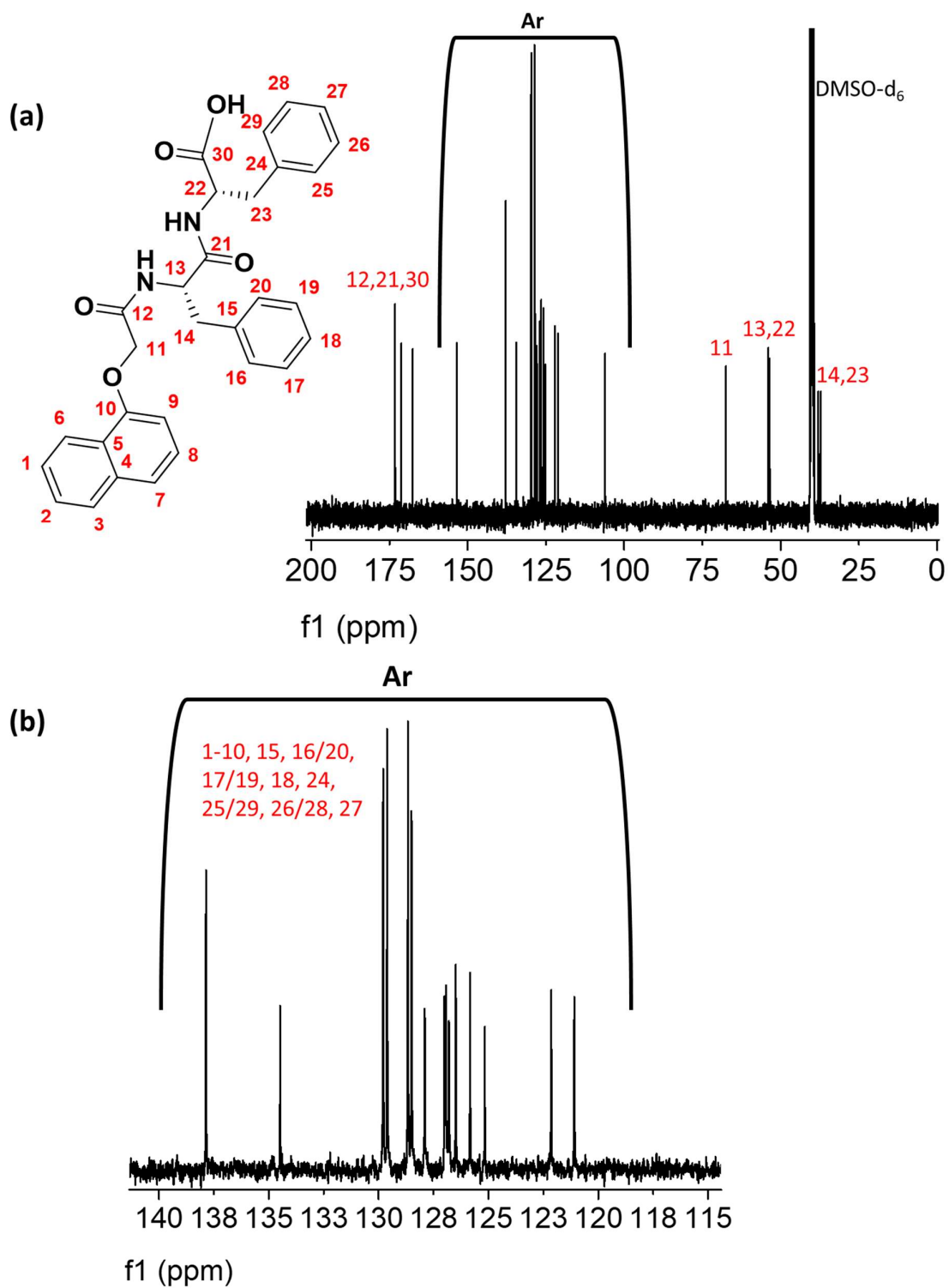


Figure A.4.116. Annotated ^{13}C NMR spectrum (100 MHz, DMSO-d₆) of **1-NapFF** (a) full spectra (b) enhanced section marked Ar showing the aromatic carbon environments.

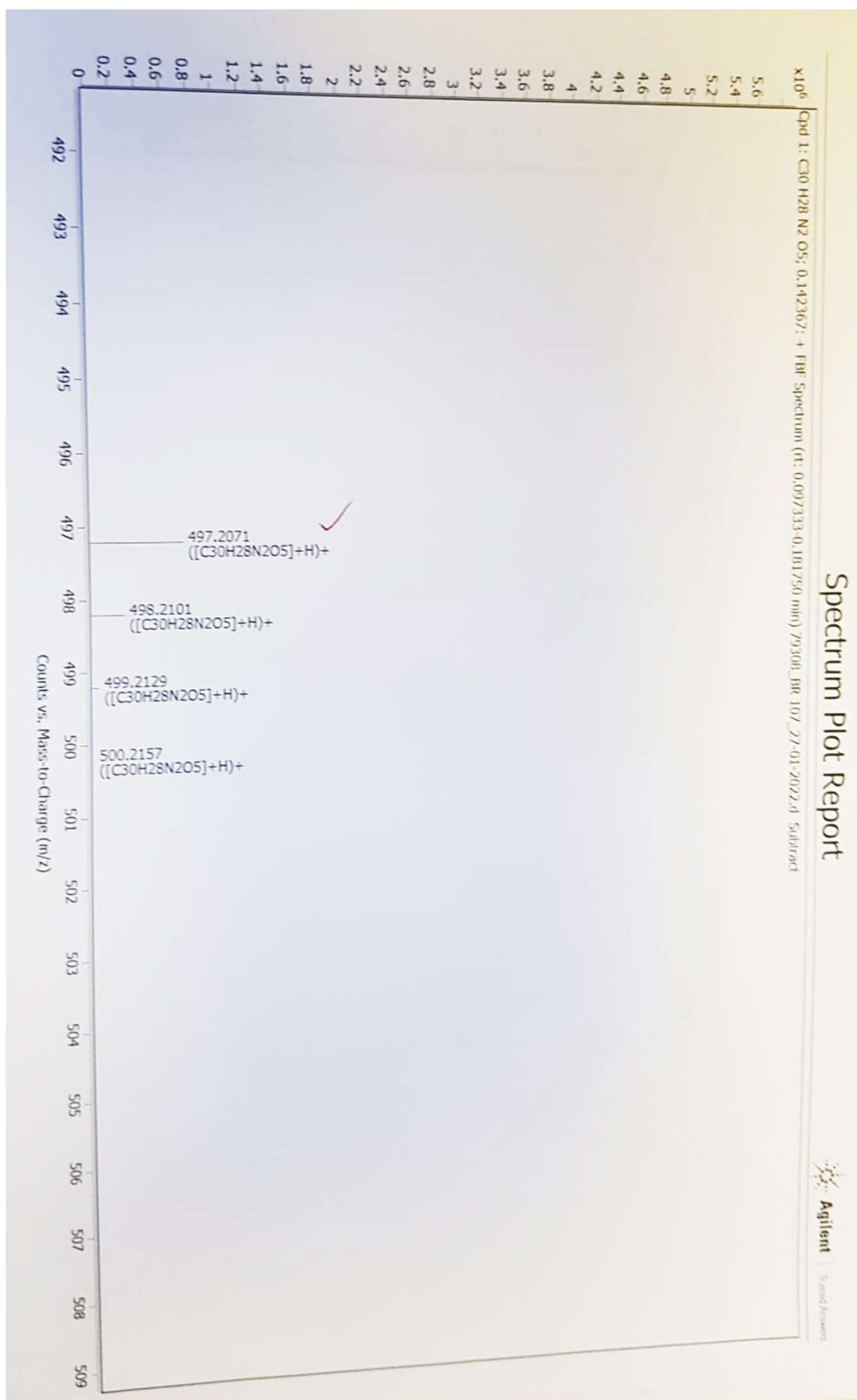


Figure A.4.117. HRSM report of 1-NapFF in ethanol.

References

- 1 L. Gonzalez, C. Liu, B. Dietrich, H. Su, S. Sproules, H. Cui, D. Honecker, D. J. Adams and E. R. Draper, *Commun. Chem.*, 2018, **1** (77), 1-8.
- 2 Y. Fukutomi, M. Nakano, J.-Y. Hu, I. Osaka and K. Takimiya, *J. Am. Chem. Soc.*, 2013, **15**, 3.
- 3 M. Wang, Yuan, Jiang, Yuqian, Zhu, Xuefeng, Liu, *J. Phys. Chem. Lett.*, 2019, **10**, 5861–5867.
- 4 S. V. Bhosale, C. H. Jani and S. J. Langford, *Chem. Soc. Rev.*, 2008, **37**, 331–342.
- 5 S. V. Bhosale, M. al Kobaisi, R. W. Jadhav, P. P. Morajkar, L. A. Jones and S. George, *Chem. Soc. Rev.*, 2021, **50**, 9845-9998
- 6 M. al Kobaisi, S. v. Bhosale, K. Latham, A. M. Raynor and S. v. Bhosale, *Chem. Rev.*, 2016, **116**, 11685–11796.
- 7 G. Andric, A. F. Boas, B. M. Bond, D. D. Fallon, A. P. Ghiggino, C. Hogan, A. A. Hutchison, C. A-P Lee, A. J. Langford, D. R. Pilbrow, B. J. Troup and C. P. Woodward, *Aust. J. Chem.*, 2004, **57**, 1011–1019.
- 8 T. Liu, Y. Chen, Z.-L. Sun, J. Liu and J.-J. Liu, *J. Solid State Chem.*, 2019, **277**, 216–220.
- 9 J. E. Rogers, S. J. Weiss and L. A. Kelly, *J. Am. Chem. Soc.*, 2000, **122**, 427–436.
- 10 Y. Matsunaga, K. Goto, K. Kubono, K. Sako and T. Shinmyozu, *Chem. Eur. J.*, 2014, **20**, 7309–f7316.